

General Disclaimer

One or more of the Following Statements may affect this Document

- This document has been reproduced from the best copy furnished by the organizational source. It is being released in the interest of making available as much information as possible.
- This document may contain data, which exceeds the sheet parameters. It was furnished in this condition by the organizational source and is the best copy available.
- This document may contain tone-on-tone or color graphs, charts and/or pictures, which have been reproduced in black and white.
- This document is paginated as submitted by the original source.
- Portions of this document are not fully legible due to the historical nature of some of the material. However, it is the best reproduction available from the original submission.

January 1975
6906

FINAL REPORT
AIRBORNE VISIBLE LASER OPTICAL COMMUNICATIONS
(AVLOC)
PROGRAM

Submitted to

NASA

George C. Marshall Space Flight Center
Huntsville, Alabama

Prepared by
John H. Ward

(NASA-CR-120720) AIRBORNE VISIBLE LASER
OPTICAL COMMUNICATIONS PROGRAM (AVLOC)
Final Report (ITT Gilfillan, Inc.) 503 p HC
\$12.75 CSCL 20E

N76-18429

G3/36 13856 Unclassified

ITT GILFILLAN
7821 Orion Avenue, P.O. Box 7713
Van Nuys, California 91409

FOREWORD

This document is the final report on Contract NAS8-20629 entitled "A Narrow Beam, Broad Bandwidth Optical Communications System." (Later known as the Airborne Visible Laser Optical Communications, AVLOC, Program subsequent to contract Modification No. 9.) The program is sponsored by the George C. Marshall Space Flight Center of the National Aeronautics and Space Administration, Huntsville, Alabama. The technical representative for the Government contracting officer is Dr. Joseph L. Randall and the cognizant Government program manager is Mr. Wayne Wagnon.

This work was performed by the Aerospace/Optical Division of International Telephone and Telegraph Corporation, San Fernando, California. (The Aerospace/Optical Division has more recently merged with the ITT Gilfillan Division.) The principal contributors to the program were Mr. John H. Ward, program manager and technical director, and Messrs. V. Hammock, E. R. Marcusen, J. R. Priebe, J. J. Redmann, R. R. Waer, and R. W. Yancey.

TABLE OF CONTENTS

1.	INTRODUCTION	1-1
1.1	System Discussion	1-7
1.2	Historical Background	1-10
2.	SYSTEM MATHEMATICAL MODEL	2-1
2.1	Performance of an Ideal System	2-1
2.2	Calculation of Model System's Performance Under Noise Conditions	2-12
2.3	Data, Communications Channel	2-25
2.4	Radiometric Analysis	2-32
2.5	Adaptive Signal Processing Threshold Analysis	2-49
2.6	Analysis of the Ground Based Acquisition System	2-64
2.7	System Performance Prediction	2-71
2.8	GBAA System Design	2-101
2.9	Additional Laser Candidate Consideration	2-108
3.	AIRBORNE OPTICAL COMMUNICATIONS PACKAGE (AOCP)	3-1
3.1	General	3-1
3.2	Common Optics Subsystem	3-16
3.3	Receiver Subsystem	3-25
3.4	Transmitter Subsystem	3-89
3.5	TV Acquisition Aid	3-124
3.6	Down Link Communications Equipment	3-132
3.7	AOCP Calibration and Test	3-140
4.	REMOTE EQUIPMENT RACK (RER)	4-1
5.	CUBE CORNER ASSEMBLY	5-1
6.	GROUND CHECKOUT EQUIPMENT (GCE)	6-1
7.	GROUND BASED ACQUISITION AID (GBAA)	7-1
7.1	Overall System Description	7-1
7.2	Transmitter Subsystem	7-16
7.3	Receiver Subsystem	7-34

TABLE OF CONTENTS (Continued)

7.4	Control and Display	7-49
7.5	GBAA Laser Radar Target Tracker	7-57
7.6	Mechanical Configuration	7-61
7.7	System Alignment and Calibration Test	7-67
8. SYSTEM INTEGRATION AND TEST		
8.1	Introduction	8-1
8.2	Interface	8-1
8.3	MSFC Field Tests	8-4
9. FLIGHT OPERATIONS		
APPENDIX A		
APPENDIX B		
APPENDIX C		
APPENDIX D		
APPENDIX E		
APPENDIX F		

1.0 INTRODUCTION

This document constitutes the final report on Contract NAS8-20629.

The purpose of this report is to describe the design, development and operation of airborne and ground-based laser communications and laser radar hardware in support of the Airborne Visible Laser Optical Communications (AVLOC) program at NASA Marshall Space Flight Center. This has been a highly successful pioneering program contributing much knowledge toward the realization of operational laser communications systems. ITTG is very pleased to have been associated with this development and values highly the experience gained.

The major emphasis on this contract was to develop a highly flexible test bed for the evaluation of laser communications systems techniques and components in an operational environment. The historical trend in communications has been to higher and higher frequencies. Hence, it is not surprising that engineers have sought to apply the laser in communications systems since it was first introduced around 1960. Their interest in this application of the laser stems, largely, from the promise of greater information capacities and communication distances than had been realized heretofore.

The properties of laser radiation which make these improvements possible are its short wavelength and its relatively high degree of coherence, as compared with other sources of optical radiation. However, the real advantage in communications at optical frequencies lies in the ability to form

narrow beamwidths with small "antennas." For the first time, a source of optical radiation is available which approaches a carrier in spectral purity suggesting the use of many of the coherent detection techniques that have been developed to a high degree of sophistication in the rf spectral region.

Unfortunately, the performance of a coherent detection system at optical frequencies, particularly at the visible wavelengths, is severely limited by a turbulent transmission medium such as the atmosphere through which any ground-based system must operate. Under these conditions, the simpler photon-counting receiver can still be used to exploit many of the laser properties in communications.

When comparisons between approaches are made, consideration must be given to the performance of the overall communications system. A comparison of laser efficiency alone, for example, is inadequate for judging the performance of optical communications systems. A photon-counting system is considerably simpler and less critical of mechanical alignment than a heterodyne or homodyne system and is potentially more reliable. Further, the use of visible or near-visible wavelengths, which exhibit impractically small coherence apertures in a turbulent medium are very desirable from the detector standpoint. High detectivity, large gain-bandwidth product detectors are available in this spectral region. Many of these detectors can be "electronically gimballed" to provide a large search/acquisition field-of-view and a small, low-noise field-of-view for tracking and

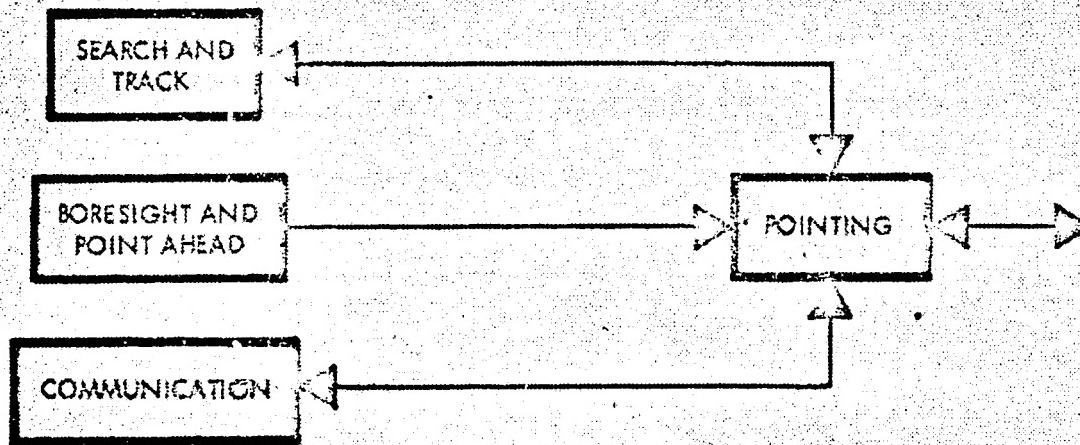
communicating. The high degree of background spatial filtering offered by these devices when combined with currently available narrow bandpass optical filters, virtually eliminates the optical background problem. These acquisition and tracking techniques make the handling of extremely narrow (fractional arc second) transmitted beamwidths practical.

The basic justification for communications at optical frequencies lies either in the need for extremely wide information bandwidth or in the need for the very high "antenna" gains available. The latter provides a number of useful advantages including extreme link privacy and efficient utilization of transmitted power for very long range (inter planetary) communications. Also, laser communications system performance is most readily and inexpensively obtained through narrower beam handling. The basic laser communications system elements are illustrated by the block diagram of Figure 1-1. It becomes apparent, as a result of experience in the design and development of systems of this type, that the major systems emphasis should be placed on narrow beam handling. Communications per se becomes almost secondary for data rates up to several hundred megabits per second.

The specific program objectives are: 1) Evaluation of optical acquisition, tracking and pointing techniques, as well as optical communications systems performance in an aerospace environment, and 2) determine turbulence effects on laser beams propagating vertically through the atmosphere. To accomplish these objectives, the experiment is to establish a two-way laser communications link between a high altitude aircraft (50,000 to 70,000 foot altitude) and a ground station. The experimental system has the capability of automatic acquisition at each terminal and auto

7778-30

BASIC ELEMENTS



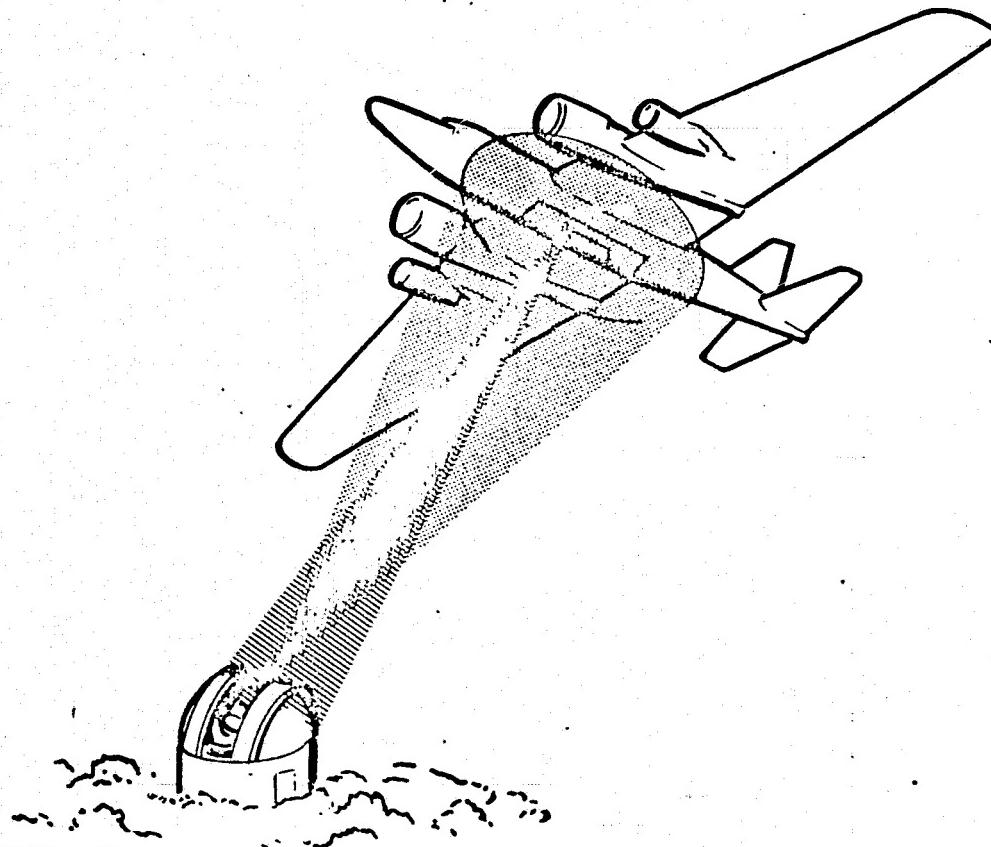
TECHNOLOGIES INVOLVED

- NARROW BEAM HANDLING
- COMMUNICATIONS

Figure 1-1. Laser Information Transfer Systems

track and continuous closed loop point to maintain communications as the aircraft "orbits" the ground station. Figure 1-2 shows an artist concept of this configuration.

A comprehensive experiment measurements plan pursuant to these technical objectives was prepared by the technical staff of NASA/MSFC. The objectives fall into three categories: 1) To evaluate system techniques for wide angle acquisition, precision tracking and pointing in a real and dynamic environment, and to evaluate quantitatively the performance of the direct detection communications link; 2) Prove certain system components as related to their suitability to the environment - particularly with respect to narrow beam handling, and 3) Advance the understanding of the effects of atmospheric propagation on the performance of an optical communications link.



7778 - 22

Figure 1-2. Airborne Visible Laser Optical Communications (AVLOC) Experiment

OBJECTIVES

- EVALUATE INTEGRATED OPTICAL COMMUNICATION SYSTEM TECHNIQUE
 - ✓ ACQUISITION
 - ✓ TRACKING
 - ✓ POINTING
 - ✓ COMMUNICATIONS
- PROVE COMPONENTS
- ADVANCE KNOWLEDGE IN ATMOSPHERIC OPTICS
 - ✓ UP-LINK ATMOSPHERIC PROPAGATION MEASUREMENT
 - ✓ SIMULTANEOUS DOWN-LINK SCINTILLATION CORRELATIONS
 - ✓ UP-LINK APERTURE AVERAGING EFFECTS

1.1 System Discussion

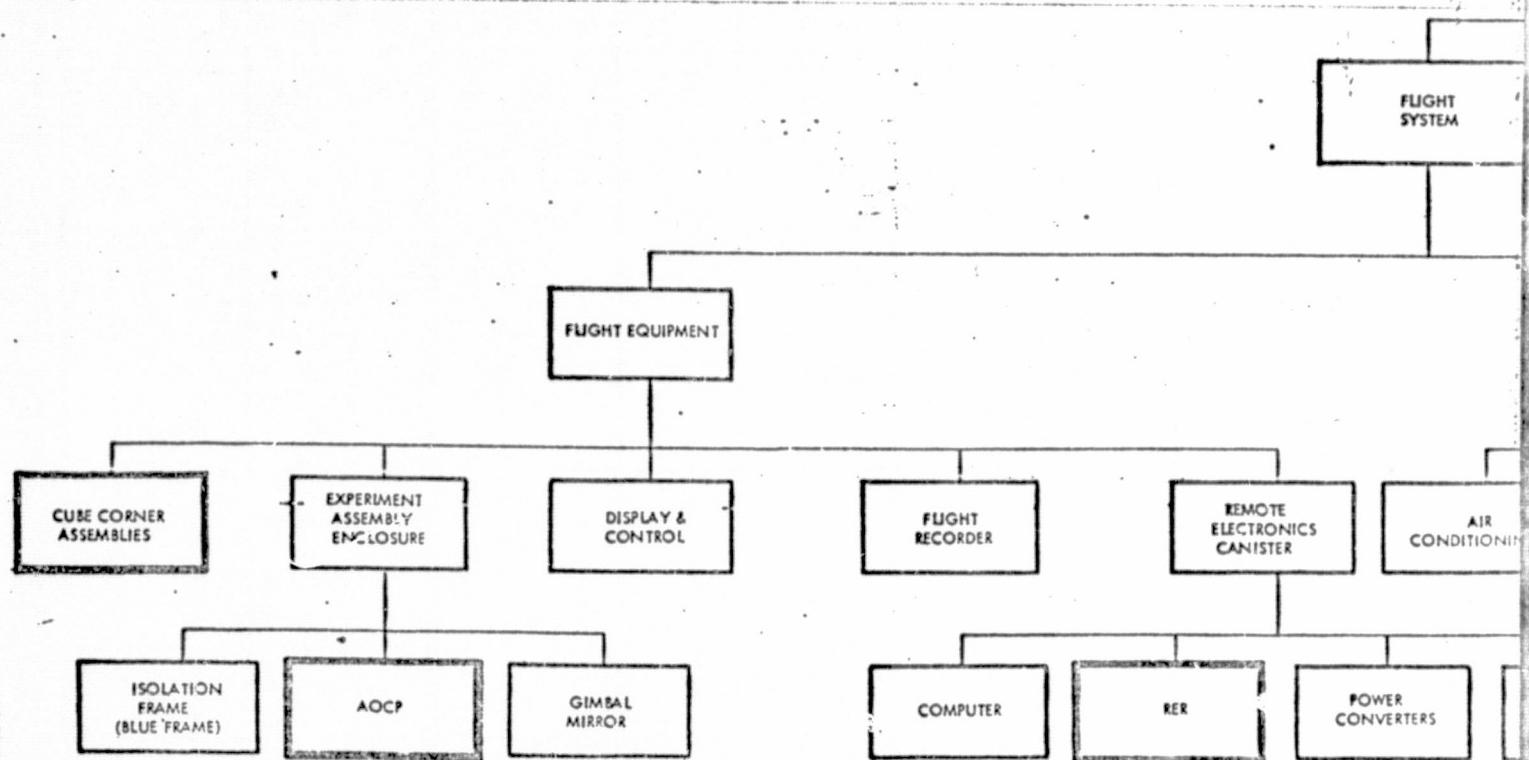
In order to place the ITTG effort in this program into proper perspective, an overall AVLOC program system hardware tree is presented in the block diagram shown in Figure 1-3. This program tree emphasizes the ITTG items and attempts to show their relation to the other program elements.

These items indicated by heavy outlines will be described in detail in the following report sections. Major contributions were made in the interface area as well and will be described where appropriate in the hardware sections. Further, ITTG has previously submitted safety plans, interface control documents, cabling, operation and maintenance manuals, and operating plan inputs which will not be repeated in this report. It should also be noted that some system design modifications and improvements have been made by NASA/MSFC technical personnel subsequent to the first flight test series and will not be reported herein.

The following sections will present the design and analysis for the major deliverable hardware items. The approach taken in organizing this report is to discuss each deliverable item firstly at a top level interim of the design parameters and overall specifications and then to break the system down into a logical set of subsystems either functional blocks or critical components. The system hardware tree provided with each item serves to interrelate the various system elements.

ITTG has designed equipment for both the flight system and the ground system. The flight system items include the cube corner assemblies, the AOCP, the Remote Equipment Rack (RER), and the Ground Checkout Equipment (GCE). ITT ground system hardware consists of the Ground Based Acquisition Aid (GBAA). One of the more difficult yet successful aspects of the program was that of interface between two prime contractors having overlapping responsibilities and complex interrelationships. The success of this dual contractor approach was due to the excellent personal relationships and singleness of purpose on the part of all program personnel and to the outstanding leadership and guidance offered by the NASA/MSFC technical and management personnel. Cooperation among contractor technical personnel, side-by-side working relationships, and free exchange of design data were essential to the success of this difficult program arrangement. ITTG wishes to compliment the CCSD personnel for their contribution as system integration contractor for supporting this cooperative attitude.

AVLOC P



FOLDOUT FRAME

6705-54

PROGRAM HARDWARE TREE

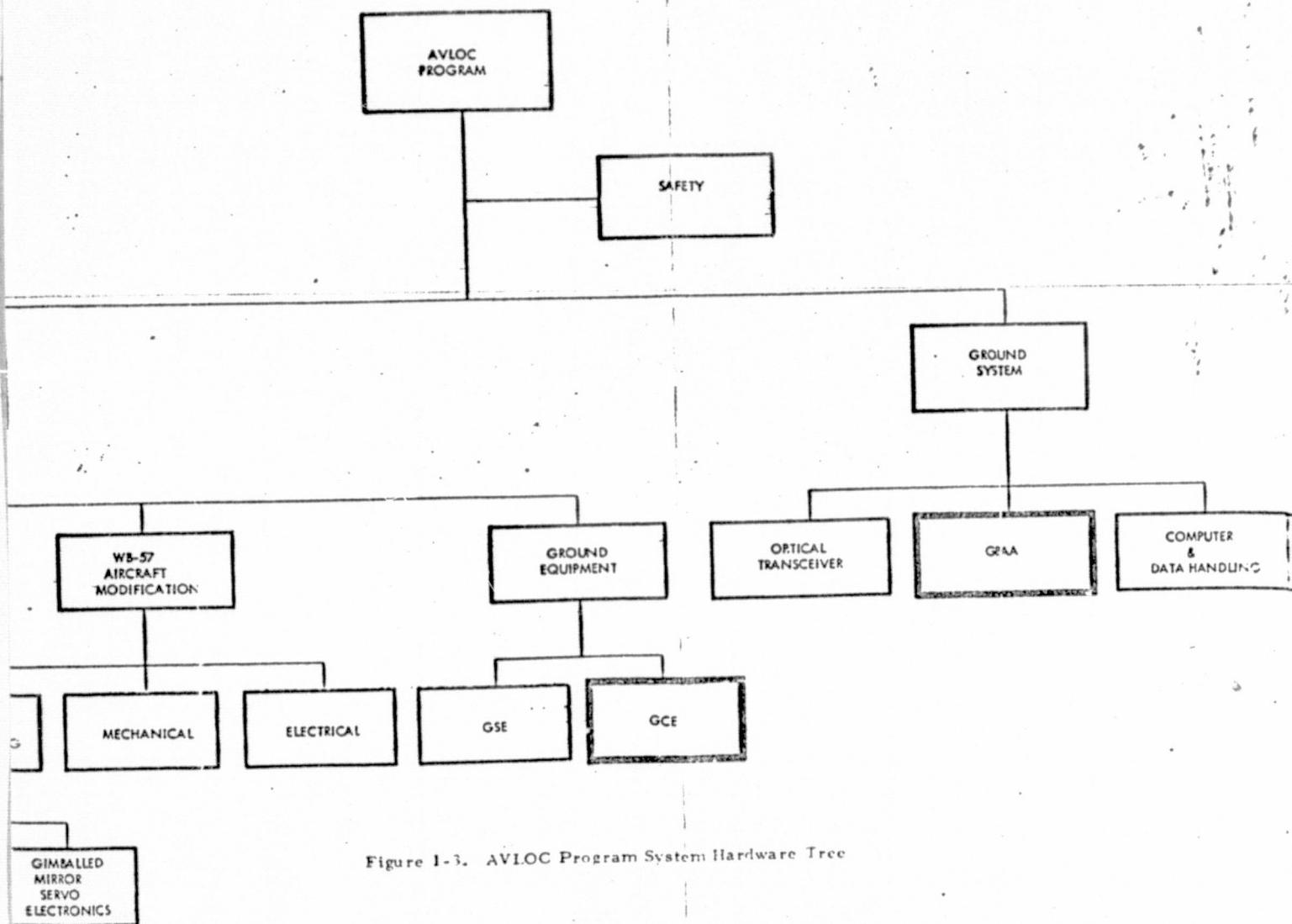


Figure 1-3. AVLOC Program System Hardware Tree

1-9

FOLDOUT FRAME 2

REPRODUCIBILITY OF THE
ORIGINAL PAGE IS POOR

Field tests from the ITTG rooftop dome at San Fernando, California, to a mountain site 5 miles away were conducted, using an 8-inch aperture collecting telescope at the receiver terminal.

The second Interim Report (Reference 2), prepared by John R. Priebe, and dated 15 September 1969, covers the next 23 months. It describes improvements in the equipment, including the additions of pulse shaping and thresholding circuits in the communication system, and the provision for simultaneously monitoring and recording Bit Error Rate (BER), Photomultiplier Current, and mean square value of the signal fluctuations. The report also develops a mathematical model for estimating performance of the communication system under ideal and noisy conditions. The report contains a summary of experimental data gathered under a variety of atmospheric conditions, using the nominal 5 mile range from a converted trailer to the mobile unit atop a nearby mountain. The addition of a 22-inch diameter telescope for the receiver (in place of the 8-inch unit used previously) permitted measurement of aperture averaging effects.

Because of the in-depth coverage of activities and results provided in the comprehensive Interim Reports, no additional information is presented in this document on the period from July, 1966 through September, 1969.

On 27 October 1969, ITT submitted to NASA/MSFC a proposal (Reference 3) entitled, "Aircraft Optical Communications Package and Optical Acquisition Equipment," in response to NASA RFQ 1-0-40-02596.

ITT was selected by NASA to design and build the equipment for the Aircraft Visible Laser Optical Communications (AVLOC) program as a result of this proposal; and the work was performed under an extension of Contract NAS8-20629.

The equipment consisted of:

- 1) A Ground-Based Acquisition Aid (GBAA), which is a pulsed laser tracking radar used to acquire and track the cooperative target aircraft carrying the aircraft optical communication terminal.
- 2) Precision optical retroreflectors, for attachment to the aircraft.
- 3) An Aircraft Optical Communications Package (AOCP), with auxiliary equipment located in Remote Equipment Racks (RER). This equipment included a TV Tracker (provided by ITT on loan to NASA), a laser transceiver, atmospheric scintillation measurement devices, and various commandable functions for varying experiment parameters.
- 4) Ground Checkout Equipment (GCE), for exercising, testing, aligning, and boresighting the AOCP, simulating the up-link optical communication system, and exercising the gimbal mirror and computer

provided by the Integrating Contractor, Chrysler Corporation Space Division (CCSD).

This equipment is discussed in more detail in subsequent sections. Operation and Maintenance Manuals (References 4 and 5) and engineering drawings have been provided previously.

A list of important dates in the AVLOC program follows:

6-7 May 1970	Preliminary Requirements Review
5-6 August 1970	Preliminary Design Review
15 October 1970	Critical Design Review
June 1971	AOCP and GCE shipped to NASA/Michoud Facility
September 1971	GBAA shipped to MSFC
October 1971	Retroreflectors shipped, 32 to CCSD, 3 to MSFC
12 October 1971	AOCP and GCE shipped from Michoud to MSFC for further test and evaluation, and subsequent integration with CCSD equipment.
May 1972	AOCP and GCE shipped to Kirtland AFB, New Mexico, for integration by General Dynamics into RB-57 Aircraft, along with CCSD equipment.

16 August 1972

GBAA successfully acquired RB-57

Aircraft, and tracked it for about
two hours.

August 1972

Integration and testing of equipment
in aircraft completed, and the air-
craft transferred from the Air Force
to NASA. All equipment sent to
Ellington AFB, Texas (near Houston).

SECTION 2.

2. SYSTEM MATHEMATICAL MODEL

In the following paragraphs a mathematical model is developed for use in predicting potential performance of the Optical Communications System. First discussed is the ideal system, one limited by only the most fundamental types of noise. This ideal model is then modified to include the most common sources of noise, encountered in photon-counting communications systems operating in the field. A list of symbols and abbreviations used in this discussion is presented in Table 2-1.

2.1 Performance of an Ideal System

An ideal optical communications system has its performance limited by design parameters (such as laser power, modulation index, collection aperture diameter, etc.) and the fundamental fluctuations in the detected signal due to photocurrent shot noise. This section is concerned with introducing both these system concepts and the analytical techniques that will be expanded later to form a general model.

2.1.1 Sensor Photocurrent and Its Variance. - It is important to clarify first the term "modulation index," Figure 2-1 depicts a partially modulated binary pulse train. The peak amplitude of this train is A_p , and the minimum amplitude is A_m . The average amplitude is $\bar{A} = (A_p + A_m)/2$, assuming a long random and equally likely series of binary pulses. The modulation index M is defined as

$$M = \frac{A_p}{\bar{A}} - 1 = \frac{A_p - A_m}{A_p + A_m} \quad (2.1)$$

TABLE 2-1. LIST OF SYMBOLS AND ABBREVIATIONS

BER	Bit error rate
PSR	Pseudo-random
D/A	Digital-to-analog conversion
M	Modulation index
\bar{A}, A_m, A_p, A_s	Signal amplitudes
Var	Statistical variance
i_p, i_p, i_m	Photocurrents in electrons per second
Δt	Time interval in seconds, the inverse of the system bit transmission rate
N_t	Set number of photoelectrons per bit interval use as threshold decision value
\bar{N}, N_p, N_m, N_s	Number of photoelectrons per bit interval (defined from \bar{N})
k	Factor describing increase in current variance with a noisy amplification process
$\tilde{N}, \tilde{N}_p, \tilde{N}_m$	Random variables describing numbers of photoelectrons in an ideal system
P, Q	Tabulated probability error functions
a	Random variable describing noise multiplicative with signal

N, N_p, N_m

Random variables describing numbers of photoelectrons
in a noisy communication system

ρ

Coefficient of variation

m, σ^2

Mean and variance of a normal distribution

$g(x)$

Probability density function

Ψ

Line-of-sight zenith look angle

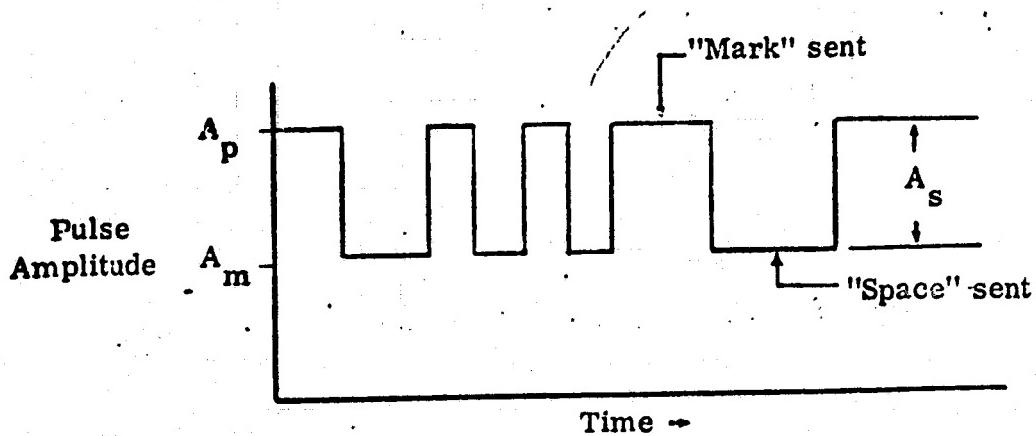


Figure 2-1. Partially Modulated Binary Pulse Train

In terms of the average amplitude \bar{A} , the peak amplitude can be written as $A_p = \bar{A}(M+1)$. In a like manner the minimum amplitude A_m can be written as $A_m = \bar{A}(1 - M)$. The signal amplitude A_s is defined as the difference between the maximum and minimum amplitudes. Consequently, it follows that $A_s = A_p - A_m = 2M\bar{A}$.

The amplitudes of Figure 2-1 may represent any of a number of types of information carriers. For instance, the peak amplitude A_p may represent peak numbers of photons, photoelectrons, photocurrent values, or other like quantities. In an ideal system, the average photoelectron current is directly proportional to the average radiation incident on the photosensor. Consequently, in using the system of subscripts introduced above with an average photoelectron current (electrons per second), of i , the resultant expression that represents a mark having been sent is the term $(1 + M) i$, and likewise, the photocurrent representing a space is $(1 - M) i$.

The shot noise fluctuations in a photocurrent are well described by a Poisson statistical distribution. Hence, the statistical variance of the number of photoelectrons counted during a time interval Δt is proportional to the product of the photocurrent, i_{pc} , and the sample period, Δt . In

equation form,

$$i_p = (1 + M)\bar{i}; \quad i_m = (1 - M)\bar{i}; \text{ and} \quad (2.2)$$

$$\text{var}\{i_{pc}\} = k i_{pc} \Delta t.$$

The constant of proportionality, $k \geq 1$, is used to describe the noise effects of amplification, such as dynode noise in a multiplier phototube.

2.1.2 The Bit Error Rate (BER) and Its Effects. - The product of the sample period, Δt , and the photoelectron current, i_{pc} , is the number, N , of electrons counted during a sample interval. The decision as to whether a space or mark was sent is made by comparing the number of photoelectrons counted with some threshold value N_t . If the number of electrons counted is greater than N_t , it is decided that a mark was sent. If the number counted is less than N_t , it is decided that a space was sent. Because of the variance in the values of i_{pc} , there is some statistical probability that, although a mark was sent, the product $i_{pc} \Delta t$ in the receiver will be less than N_t . Hence, the receiver logic circuitry will make an incorrect decision in such cases. The probability of making an incorrect decision during a sample interval is called the bit error rate (BER).

Although other factors such as signal-to-noise ratio could be used, bit error rate is more indicative of the quality of a digitally coded communications channel. For channels using non-digital modulation schemes, it is clear that the lower the system's potential bit error rate, the better the information transmission (as measured by fidelity, signal-to-noise ratio, or any other method), even though there is no linear relationship between these characteristics. The use of a system's potential bit error rate as a basis to judge its performance provides the advantage of easily considering the adverse effects of many and varied noise factors as a whole. For example, some criteria of performance require that all noise sources, to be combined, must have similar frequency spectra. These analytical techniques would have difficulty in estimating the simultaneous effects of signal current shot-noise and atmospheric turbulence.

It is of value to compare the subjective quality of a closed circuit video picture as a function of bit error rate in the communications channel. Figure 2-2 shows the resultant degradation in received picture quality as

7778-36

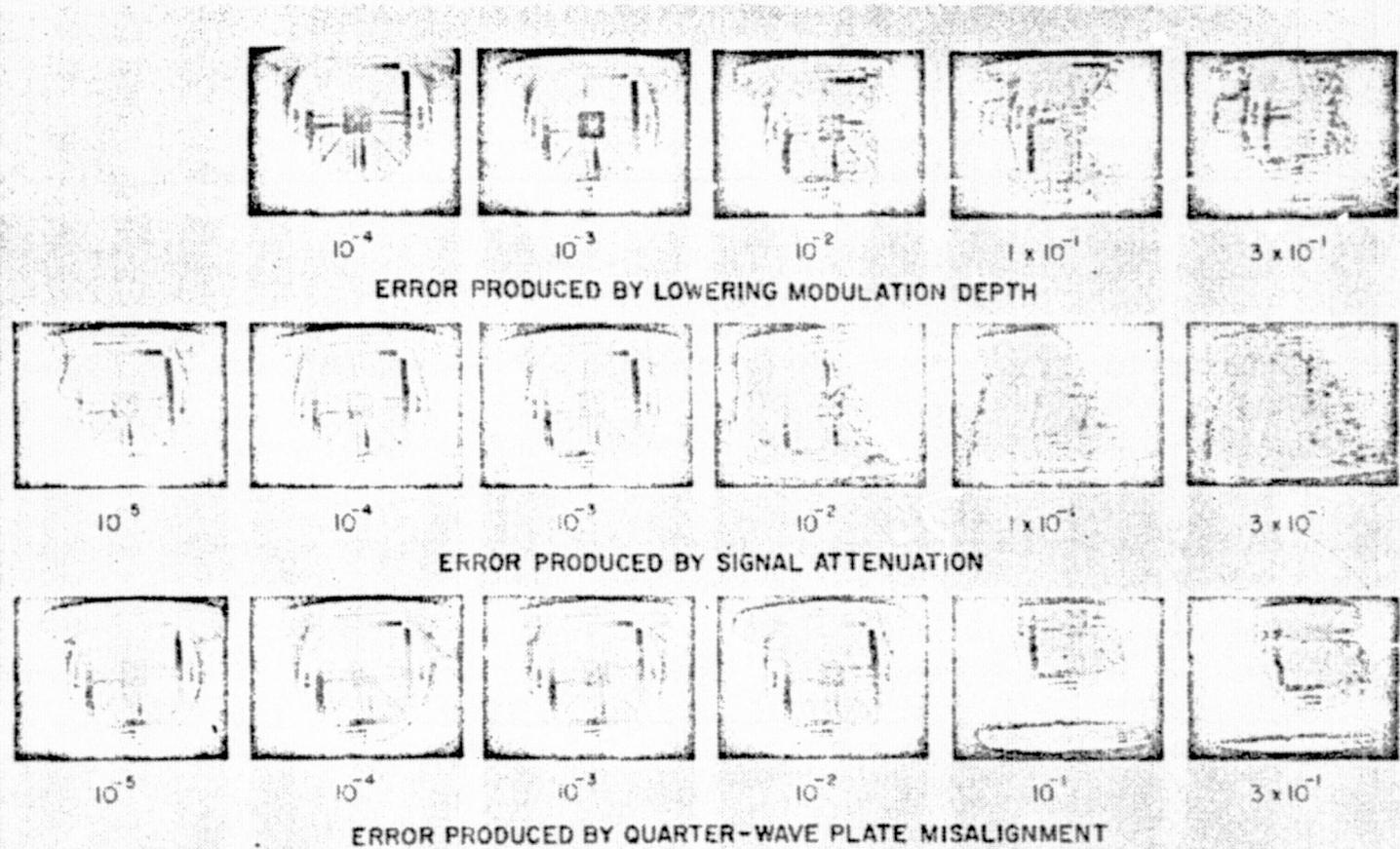


Figure 2-2. Video Picture Quality with Measured Bit Error Rate for Polarization Modulation

the BER is increased from 10^{-5} to 0.30, by attenuating the radiation of the transmitted laser beam. These photos were taken during a laboratory test of the Optical Communications System identical to the AOCP and ground station hardware.

2.1.3 Computation of the Ideal Single-Channel BER. - In a single-channel photon-counting type of digital system, a mark or space decision is based upon whether or not the number of photoelectrons counted in one photo-sensor during a bit interval is larger than some threshold value, N_t . An error occurs when either: (1) a signal is sent but not detected or, (2) when the threshold value is exceeded during an interval when no signal is sent. In equation form, the probability of an error during a bit interval (the bit error rate) is

$$\text{BER} = P \{ \text{signal sent} \} \cdot P \{ \text{noise and signal} \leq N_t \} \quad (2.3a)$$

$$+ P \{ \text{signal not sent} \} \cdot P \{ \text{noise} > N_t \}.$$

Since in the random MRZ coding considered here, the probability of a signal being sent during a sample bit interval is 1/2, Equation 3.3a becomes

$$\text{BER} = 1/2 P \{ \text{noise and signal} \leq N_t \} \quad (2.3b)$$

$$+ 1/2 P \{ \text{noise} > N_t \}.$$

The derivation of the system bit error rate discussed here is concerned with only the variations in the signal amplitude itself. These fluctuations in the modulated and unmodulated portions of the collected laser beam are caused by the inherent photocurrent shot noise. Using the above terminology, we correctly consider a mark to have been sent if the number of photo-electrons \tilde{N}_p counted during a sample period is larger than the threshold value N_t . We correctly decide that a space has been sent if we detect a smaller value \tilde{N}_m . Both \tilde{N}_p and \tilde{N}_m are random variables because of the effects of photocurrent shot noise. Intuitively, the threshold value N_t should be set at some number between the average values of \tilde{N}_p and \tilde{N}_m . One of the purposes of the following analysis is to determine the value of N_t which minimizes the system's bit error rate.

Equation 2.3 can be rewritten to include the variables \tilde{N}_p and \tilde{N}_m as

$$BER = \frac{1}{2} P\{\tilde{N}_p \leq N_t\} + \frac{1}{2} P\{\tilde{N}_m > N_t\}. \quad (2.4)$$

In terms of probability distributions, the components of the last equation are

$$P\{\tilde{N}_p \leq N_t\} = \int_{-\infty}^{N_t} dz P\{\tilde{N}_p = z\}, \quad (2.5a)$$

$$P\{\tilde{N}_m > N_t\} = \int_{N_t}^{\infty} dz P\{\tilde{N}_m = z\}. \quad (2.5b)$$

For large numbers of photoelectrons N the shot noise (Poisson) distributions are approximately normal.

Hence, keeping in mind that $\bar{N}(1+M)\Delta t = i_p$ and $\bar{N}(1-M)\Delta t = i_m$, we find that the combination of equations 2.2 and 2.5 results in

$$P\{\tilde{N}_p \leq N_t\} = \int_{-\infty}^{N_t} dz \frac{e^{-\frac{1}{2}\left(\frac{z - \bar{N}(1+M)}{\sqrt{\bar{N}k(1-M)}}\right)^2}}{\sqrt{2\pi} \sqrt{\bar{N}k(1+M)}}, \quad (2.6a)$$

$$P\{\tilde{N}_m > N_t\} = \int_{N_t}^{\infty} dz \frac{e^{-\frac{1}{2}\left(\frac{z - \bar{N}(1-M)}{\sqrt{\bar{N}k(1-M)}}\right)^2}}{\sqrt{2\pi} \sqrt{\bar{N}k(1-M)}}. \quad (2.6b)$$

We can use here the tabulated functions P and Q where:

$$P(r) = \frac{1}{\sqrt{2\pi}} \int_{-\infty}^r e^{-\frac{t^2}{2}} dt, \quad Q(r) = \frac{1}{\sqrt{2\pi}} \int_r^{\infty} e^{-\frac{t^2}{2}} dt; \quad (2.7)$$

so that Equation 3.4 for the bit error rate simplifies to

$$\text{BER} = \frac{1}{2} P\left(\frac{N_t - \bar{N}(1+M)}{\sqrt{k\bar{N}(1+M)}}\right) + \frac{1}{2} Q\left(\frac{N_t - \bar{N}(1-M)}{\sqrt{k\bar{N}(1-M)}}\right). \quad (2.8)$$

In this case, the bit error rate is minimized for a threshold value of

$$N_t = \bar{N} \sqrt{1 - M^2} \left[1 + \frac{k}{2M\bar{N}} \ln\left(\frac{1+M}{1-M}\right) \right]^{\frac{1}{2}} \approx \bar{N} \sqrt{(1 - M^2)}, \quad (2.9)$$

an approximation easily justified for large values of \bar{N} . With this optimum value of N_t , the bit error rate from Equation 2.8 is found to be

$$\text{BER} \Big| \begin{array}{l} \text{Single} \\ \text{Channel,} \\ \text{Optimum} \end{array} = Q\left[\sqrt{\frac{\bar{N}}{k}} \left(\sqrt{1+M} - \sqrt{1-M} \right)\right], \quad (2.10)$$

or approximately

$$Q\left[\sqrt{\frac{\bar{N}}{k}} \left(M + \frac{M^3}{8} + \frac{7M^5}{128} + \dots \right)\right].$$

Equation 2.10 is plotted in Figure 2-3 for two values of modulation index M.

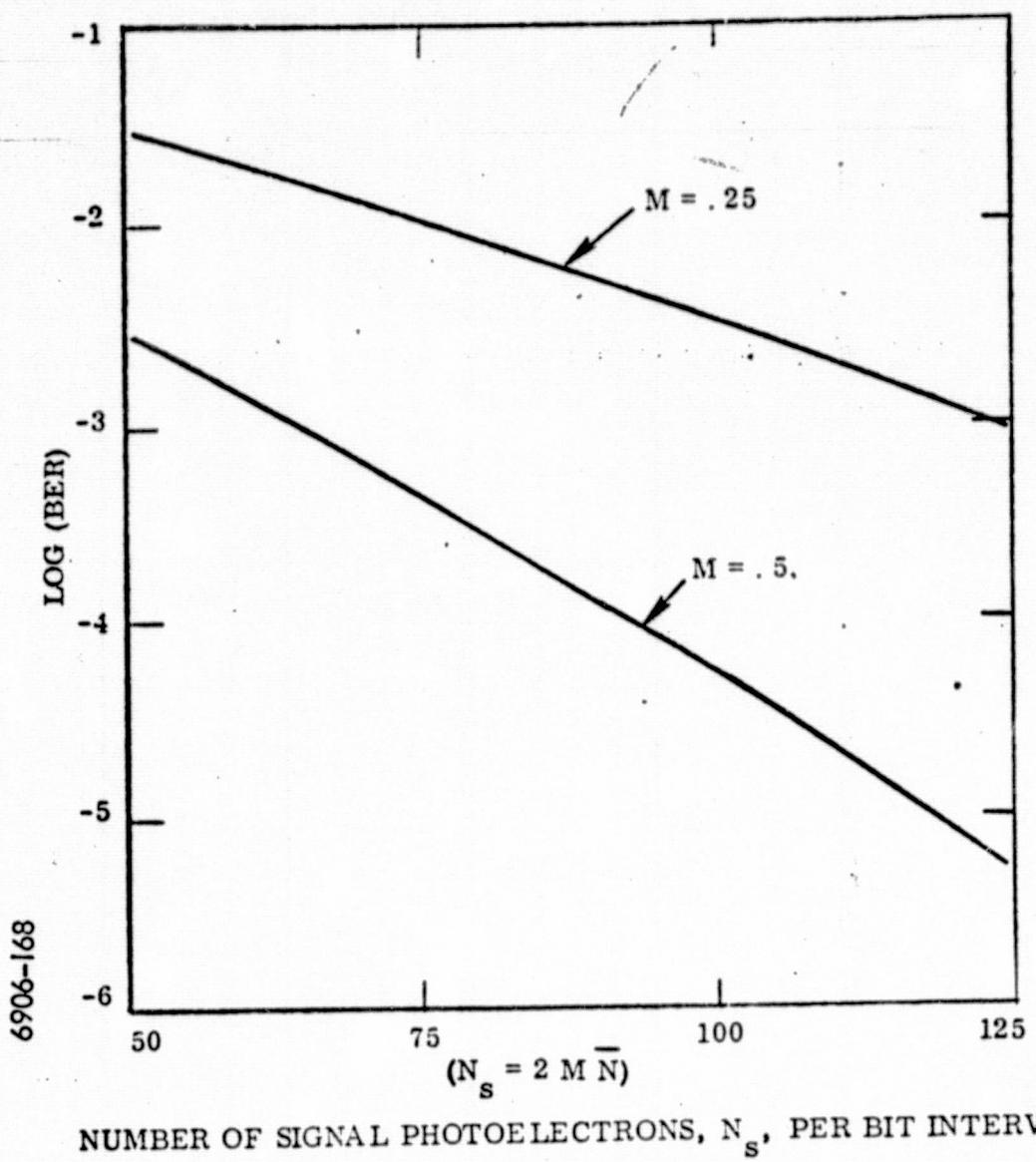


Figure 2-3. Single Channel Bit Error Rate (the Factor k is 1.6)

2.1.4 Computation of the Ideal Binary Channel BER. - Analysis of an ideally balanced binary system is somewhat simpler than that of the single channel, since there is no threshold value N_t to be considered. In this situation, the decision as to whether a mark or space was sent is based on which of two channels has the greater number of photoelectrons. Using subscripts 1 and 2 for the two channels, we can write the expression for the bit error rate, analogous to Equation 2.4 as

$$\text{BER} = \frac{1}{2} P\{\tilde{N}_{p_1} < \tilde{N}_{m_2}\} + \frac{1}{2} P\{\tilde{N}_{p_2} < \tilde{N}_{m_1}\}. \quad (2.11)$$

For a balanced symmetrical system, the two probabilities are equivalent, and we can write

$$\text{BER} = P\{\tilde{N}_{p_1} < \tilde{N}_{m_2}\} = P\{\tilde{N}_{p_1} - \tilde{N}_{m_2} < 0\}. \quad (2.12)$$

Written in terms of conditional probability distributions, the last equation is

$$\text{BER} = \int_{-\infty}^0 dz \int_{-\infty}^{\infty} dy P\{\tilde{N}_p = z + y\} \cdot P\{\tilde{N}_m = y\}. \quad (2.13)$$

Approximating the probabilities with normal distributions, as was done with Equation 2.6, the last expression can be arranged in explicit form as

$$\text{BER} = \int_{-\infty}^0 dz \int_{-\infty}^{\infty} dy \frac{e^{-\frac{1}{2} \left(\frac{z+y-\bar{N}(1+M)}{\sqrt{k\bar{N}(1+M)}} \right)^2}}{\sqrt{2\pi} \sqrt{k\bar{N}(1+M)}} \cdot \frac{e^{-\frac{1}{2} \left(\frac{y-\bar{N}(1-M)}{\sqrt{k\bar{N}(1-M)}} \right)^2}}{\sqrt{2\pi} \sqrt{k\bar{N}(1-M)}}. \quad (2.14)$$

This equation, where \bar{N} is the product $i \Delta t$ averaged on one photosensor, can be integrated directly to obtain the simpler form

$$\text{BER} \mid_{\substack{\text{Binary} \\ \text{Channel}, \\ \text{Optimum}}} = Q \left(M \sqrt{\frac{2 \bar{N}}{k}} \right) \quad (2.15)$$

The last equation is plotted in Figure 2-4 for modulation indices ranging from 0.3 to 0.8.

2.1.5 Comparison of Ideal Single Channel and Binary Channel Systems.

The practical differences between a single channel system and a binary channel system are mainly in the added complexity involved in the binary system's receiver. It is interesting to consider how great an advantage is gained from this additional receiver complexity. Given that the two systems would have the same types of photosensors, modulators, etc., we can calculate the increase in remote terminal laser power required by a single channel system to equal the performance (BER) of a binary channel system. By comparing Equations 2.10 and 2.15 we see that the single channel system's laser power must be increased by the factor

$$\text{Required Laser Power Increase} = 1 + \sqrt{1 - M^2} \quad (2.16)$$

For example, if the modulator used were capable of a modulation index of 0.5, the required single channel laser power increase would be about 87 percent.

Equation 2.16 implies that both types of systems have about the same performance when used at high modulation indices and very low noise levels.

2.2 Calculation of Model System's Performance Under Noise Conditions

In the optical communications system under study there are seven principal sources of noise. For convenience in analysis, all seven may be considered together at the photodetector, even though some noise factors may not actually exist at that point in the signal processing train. Those noise factors not present at the photodetector (such as noise in later amplifiers) can be replaced in analysis with an equivalent noise generator

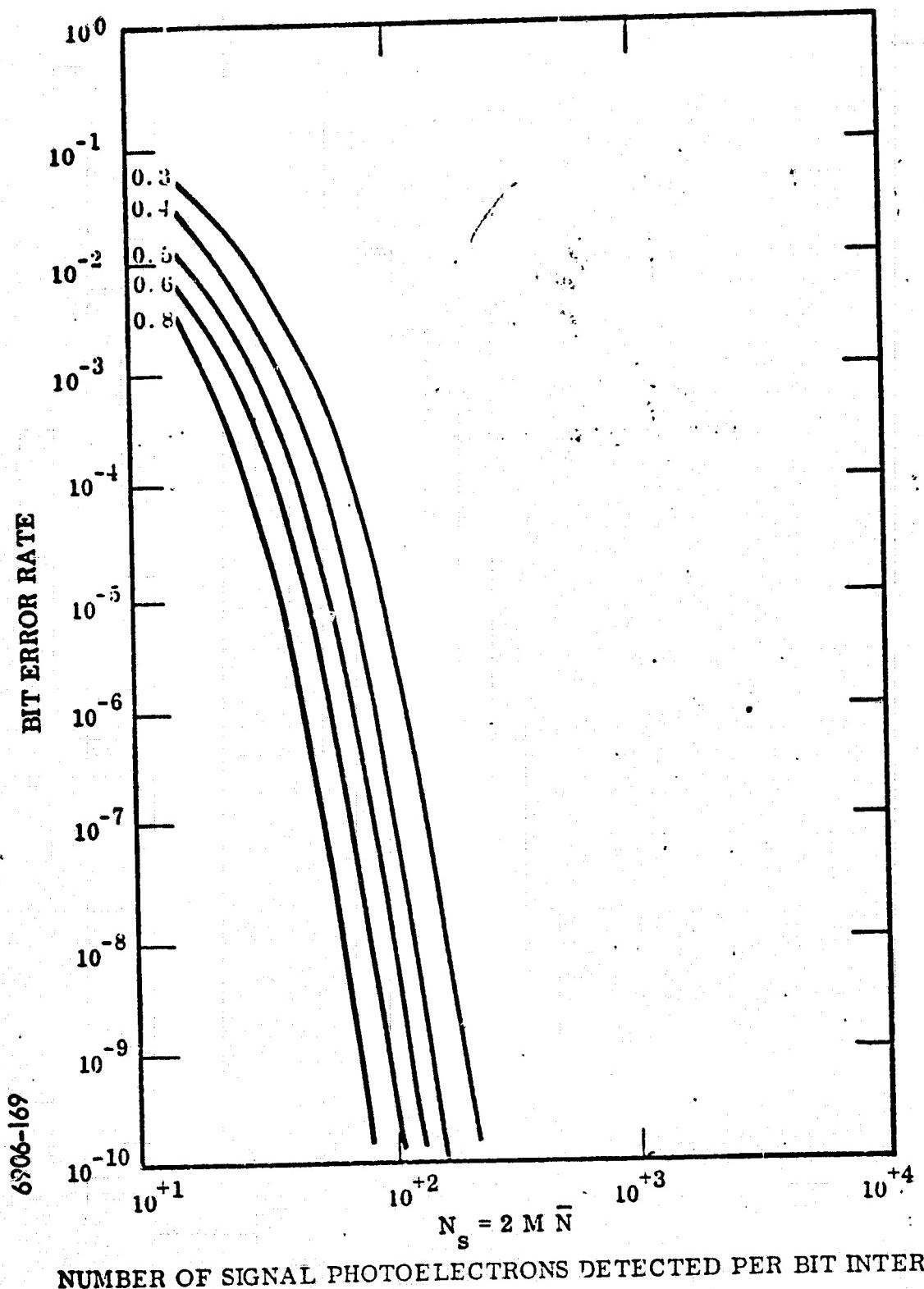


Figure 2-4. Binary-Channel BER in the Presence of Log-Normal Atmospheric Turbulence for $k = 1.6$ and $M = 0.4$

at the photodetector. The eight principal noise factors occurring in the system under study are as follows:

- a. Laser Generation Noise - a time varying factor multiplying the average radiative power from the laser. These fluctuations in laser power may be caused by power supply ripple, microphonics, etc.
- b. Atmospheric Scintillation Effects - these act in much the same manner as the Laser Generation noise above, but of course with different frequency and probability distributions.
- c. Signal and Background Shot Noise - variations in the photo-electron current that are proportional to the square root of the current.
- d. Background Modulation - a factor usually encountered in scanning systems, in which the background noise may be much greater than that predicted by shot noise calculations.
- e. Dark Current - in the system's photodetector, normally of concern only when operating with infrared sensitive sensors at low signal levels.
- f. Dynode Noise - significantly increases the fluctuations in photo-electron current during the first stages of amplification. If an electron multiplier type phototube were not used as the photo-sensor, the preamplifier would then be an important source of noise of this type.
- g. Johnson or Thermal Noise - usually of concern only if the sensor's load resistor precedes most of the signal amplification.

2.2.1 Sensor Photocurrent and Its Variance. - In a two level digital signal the seven noise factors discussed above can be combined into multiplicative and additive contributions to the sensor photocurrent, i_{pc} . For the condition of a "mark" being sent, the signal photocurrent i_p and its variance are described, as was done with Equation 2.2, by

$$i_p = a(1 + M) \bar{i} + \sum i_n; \hat{N}_p = i_p \Delta t \quad (2.17a)$$

$$\text{var}(i_{pc}) = k i_p \Delta t = k \hat{N}_p$$

For the conditions of a "space" being sent, the last equations take the form

$$i_m = a(1 - M) \bar{i} + \sum i_n; \text{ var}(i_{pc}) = i_m \Delta t = k \hat{N}_m. \quad (2.17b)$$

In the last equations, i_{pc} is the instantaneous photocurrent (in electrons per second) and the term a is the product of factors describing system radiometry, time varying atmospheric scintillation, and laser generation noise effects. The last term $\sum i_n$, represents the sum of the dc noise currents, such as background and detector dark current. In the equations for the photocurrent variance, $\text{var}(i_{pc})$, the coefficient k describes multiplicative amplifier or dynode noise, and as before, Δt represents the time interval over which the photocurrent is sampled.

2.2.2 General Form for the BER of a Noisy System. - But for an added complexity in the component Equations 2.5, the derivation of the system VER using Equations 2.17 follows that of Equation 2.2. In regards to the previous ideal system, it was assumed that the average signal irradiance on the photosensor was constant. Variations in the photoelectron current were due to shot noise alone. However, in the situation where the system suffers from phenomena such as atmospheric scintillation and its resultant time varying effects, the major variations in the sensor photocurrent can be due to similar variations in the signal irradiance on the photodector. Hence the term $P\{\tilde{N}_p = z\}$ in Equation 2.5a must be replaced with a more complex statistical expression. The term $P\{\tilde{N}_p = z\}$ is the probability that "z" photoelectrons will be counted during a sample interval if a "mark" is sent, and the long-term average number of photoelectrons counted is \bar{N} . However, in the presence of scintillation or fluctuating laser power, \bar{N} is not constant and must be replaced by a random variable \tilde{N} . The shot noise in the photocurrent still exists, but a parameter of its distribution, i.e., the population mean, is also a variable. For this reason we have a conditional distribution $P\{\tilde{N}_p = z; x\}$. This expression represents the probability that the number of photoelectrons counted for a "mark" sent be z , given that the mean number \tilde{N} is x . It can be seen that the original expression for $P\{\tilde{N}_p = z\}$ is replaced by

$$P\{\tilde{N}_p = z\} = \int_{-\infty}^{\infty} dx P\{\tilde{N}_p = z; x\} \cdot P\{\tilde{N} = x\}. \quad (2.18)$$

As a consequence, the form of Equations 2.5 for a single channel BER is changed to

$$P\{\tilde{N}_p \leq N_t\} = \int_{-\infty}^{\infty} dx \int_{-\infty}^{N_t} dz P\{\tilde{N}_p = z; x\} \cdot P\{\tilde{N} = x\}, \quad (2.19a)$$

$$P\{\tilde{N}_m > N_t\} = \int_{-\infty}^{\infty} dx \int_{N_t}^{\infty} dz P\{\tilde{N}_m = z; x\} \cdot P\{\tilde{N} = x\}. \quad (2.19b)$$

These, combined with Equation 2.4, describe the BER for a single channel system with additive and multiplicative noise.

To describe the BER for the binary channel system in a noisy environment, an expression similar to Equation 2.13 can be derived. Hence, written in terms of conditional probability distributions,

$$\text{BER}_{\text{Binary Channel}} = \int_{-\infty}^0 dz \int_{-\infty}^{\infty} dy \int_{-\infty}^{\infty} dx P\{\tilde{N}_p = z + y; \tilde{N} = x\} \cdot P\{\tilde{N}_m = y; \tilde{N} = x\} \cdot P\{\tilde{N} = x\}. \quad (2.20)$$

Equations 2.19 and 2.20 describe system BER with statistical expressions. In order to obtain numerical values, these terms must be replaced with algebraic expressions. The most important additional source of noise to be considered here is that due to atmospheric scintillation. It is well known that these turbulence induced statistical variations in beam transmittance do not follow the normal probability distribution. For this reason, the next section digresses somewhat to discuss the log-normal distribution, which is more appropriate for use in modeling atmospheric effects.

2.2.3 Log-Normal Probability Distribution. - The log-normal probability distribution is applied in situations where a series of independent random impulses c_j have effects on a phenomenon which are dependent on the instantaneous state x_j of the phenomenon. Furthermore, the magnitude of the change in state of the phenomenon, $x_{j+1} - x_j$, is proportional to the magnitude of the impulse c_j and some function $f(x_j)$ of the instantaneous state.

Here the state x_j of the phenomenon was produced by c_{j-1} . The equation for the effect of c_j is

$$x_{j+1} - x_j = c_j f(x_j) = \Delta x_j \quad (2.21)$$

In the present application, we consider the change (Δx_j) to be a variation in the radiant power transmitted by a turbulent atmosphere, and this variation to be equal to the product of the radiant power itself, i.e., $f(x_j) = x_j$, and the magnitude of a number of turbulent impulses c_j . As a consequence we can rearrange the last equation to obtain the form

$$c_j = \frac{\Delta x_j}{f(x_j)} = \frac{\Delta x_j}{x_j} \quad (2.22)$$

The sum $C = \sum c_j$ of a large number of impulses, which we assumed above to be independent, tends to have a normal distribution as implied by the central limit theorem. If each of the impulses c_j has only a very slight effect Δx_j , then the resulting state x_n caused by a very large number of impulses c , is

$$C = \sum_{j=0}^n c_j = \sum_{j=0}^n \frac{\Delta x_j}{x_j} \approx \int_{x_0}^{x_n} \frac{dx}{x} = \ln \frac{x_n}{x_0} \quad (2.23)$$

which, in the limit, has a logarithmic relationship to the impulses. Hence, we have a reasonable justification for writing the relationship

$$\ln x = u, \quad (3.24)$$

where x is a linear function of the instantaneous radiant flux transmitted through the atmosphere, and u is a normally distributed variable dependent on the characteristics of the atmospheric turbulence.

To relate the characteristic parameters of x to those of u , we assume the variate u to have a mean m and a variance σ^2 . The distribution function of u is

$$P\{u \leq U\} = \int_{-\infty}^U du \frac{e^{-\frac{(u-m)^2}{2\sigma^2}}}{\sqrt{2\pi \sigma^2}} . \quad (2.25)$$

The distribution function of x , $\phi(x)$, can be determined from Equation 2.25, since from Equation 2.24, x is a function of the random variable u . With the appropriate change of variables we find that

$$P\{x \leq X\} = \Phi(X) = \int_0^X \frac{dx}{x} \frac{e^{-\frac{(\ln x - m)^2}{2\sigma^2}}}{\sqrt{2\pi \sigma^2}} ; X \geq 0 . \quad (2.26)$$

The mean or expected value $E(x)$ of the variable x is given by the Stieltjes integral

$$E(x) = \int_0^\infty x d\Phi(x) = \exp \left[m + \frac{\sigma^2}{2} \right] . \quad (2.27)$$

In a similar manner the expected value of x^2 can be found to be

$$E(x^2) = \exp \left[2m + 2\sigma^2 \right] . \quad (2.28)$$

The variance of x is found from the well-known relationship

$$\text{Var } \{x\} = E(x^2) - E^2(x) = e^{2m+\sigma^2} [e^{\sigma^2} - 1] , \quad (2.29)$$

which leads directly to

$$\sigma^2 = \ln \left[1 + \frac{\text{Var } \{x\}}{E^2(x)} \right] = \ln \left[1 + \rho^2 \right], \quad (2.30)$$

where

$$\text{Var } \{x\} = \rho^2 E^2(x).$$

It is convenient to work with the normalized variable $x/E(x)$, which also has a log-normal distribution. In terms of the original parameters m and σ , we find that

$$E \left[\ln \frac{x}{E(x)} \right] = m - \left(m + \frac{\sigma^2}{2} \right) = -\frac{\sigma^2}{2}, \quad (2.31)$$

and

$$\text{Var} \left\{ \ln \frac{x}{E(x)} \right\} = \text{Var} \left\{ \ln(x) \right\} = \sigma^2. \quad (2.32)$$

The ratio $x/E(x)$ may be considered here to describe the instantaneous transmittance of the atmosphere between the remote and base terminals. Averaged over a sample interval, the photocurrent, i , and the number of photoelectrons counted, \tilde{N} , are related to the variable x above as

$$\frac{\tilde{N}}{\bar{N}} = \frac{\tilde{i}}{\bar{i}} = \frac{x}{E(x)}. \quad (2.33)$$

The distribution function for \tilde{N} is

$$\Phi(x) = P \{ \tilde{N} \leq x \} = \int_0^x \frac{dx}{x \sqrt{2\pi\sigma^2}} \exp - \left[\frac{\ln x - m}{\sqrt{2\sigma^2}} \right]^2. \quad (2.34)$$

- Using Equation 2.27 and the expression $E(\tilde{N}) = \bar{N}$, we find that the probability function for \tilde{N} is

$$\frac{d\Phi}{dx} = g(x) = \frac{1}{x\sqrt{\pi}} \exp -\frac{1}{2} \left[\frac{\sigma}{2} + \frac{1}{\sigma} \ln \frac{x}{\bar{N}} \right]^2 ,$$

(2.35)

$$g(x) = 0, x < 0 ;$$

where:

$$\sigma^2 = \ln \left[1 + \frac{\text{Var}\{\tilde{N}\}}{\bar{N}^2} \right]$$

(2.36)

2.2.4 Atmospheric Scintillation Effects - Typical Values. - The principal signal fluctuations encountered in a space-to-space optical communications link are those due to the impressed modulation and fundamental photocurrent shot noise. However, in a satellite-to-ground terminal situation, atmospheric scintillation along the space-to-earth link is expected to influence the system's bit error rate to a great extent, dominating the simpler effects of photocurrent shot noise.

Typical values for the log-amplitude variance, $C_\ell(0)$, for an optical path along the zenith angle ψ are estimated to be fairly well represented by the equation $C_\ell(0) = 0.73(\sec \psi)^{11/6}$. The coefficient 0.73 of course varies from day to day for different locations, and for most astronomical observations, is probably too large. The variance, $\text{Var}\{P_c\}$, of the detected beam's radiant power P is related to $C_\ell(0)$ by the equation

$$\text{Var}\{P_c\} = P^2 \theta \left[\exp \{4 C_\ell(0)\} - 1 \right] = P^2 \rho^2 ,$$

(2.37)

where θ is a complex function of the collector diameter, optical wavelength, and log-amplitude variance. Values of Equation 2.37 for collector diameters of 50, 100, and 150 cm are shown in Figure 2-5. It is clear that the relative fluctuations represented by the normalized variance ρ^2 in the collected radiant power will affect both the modulated and the unmodulated portions of the beam from the satellite terminal.

Figure 2-6 illustrates the effect of atmospheric scintillation on the transmitted signal. Figure 2-6A depicts the digitally coded laser beam, with a modulation index of 0.5 and average amplitude \bar{A} . The relative fluctuations in the effective transmittance of the atmospheric path are shown in Figure 2-6 B. For purposes of illustration, these fluctuations are pictured as varying at megahertz rates. In an actual system, these atmospheric scintillations would be concentrated below 100 hertz and would vary extremely slowly compared to the data rate. Figure 2-6 C illustrates the resultant signal amplitude as collected by the ground terminal. The modulation index itself is unchanged from that of the transmitted beam in Figure 2-6.

2.2.5 Noisy Single and Binary Channel BER. - We may use the variable $x = ai\Delta t$ in Equation 2.17 to obtain the definitions:

$$\begin{aligned}\hat{N}_p &= (1 + M)x + \sum i_n \Delta t, \\ \hat{N}_m &= (1 - M)x + \sum i_n \Delta t.\end{aligned}\quad (2.38)$$

With these substitutions, Equation 2.35 can be used to rewrite Equations 2.19 in the more general form:

$$P\{\hat{N}_p \leq N_t\} = \int_{-\infty}^{N_t} dz \int_0^{+\infty} dx g(x) \frac{e^{-\frac{1}{2} \left(\frac{z - \hat{N}_p}{\sqrt{k \hat{N}_p}} \right)^2}}{\sqrt{2\pi} \sqrt{k \hat{N}_p}} \quad (2.39a)$$

$$P\{\hat{N}_m > N_t\} = \int_{N_t}^{\infty} dz \int_0^{+\infty} dx g(x) \frac{e^{-\frac{1}{2} \left(\frac{z - \hat{N}_m}{\sqrt{k \hat{N}_m}} \right)^2}}{\sqrt{2\pi} \sqrt{k \hat{N}_m}} \quad (2.39b)$$

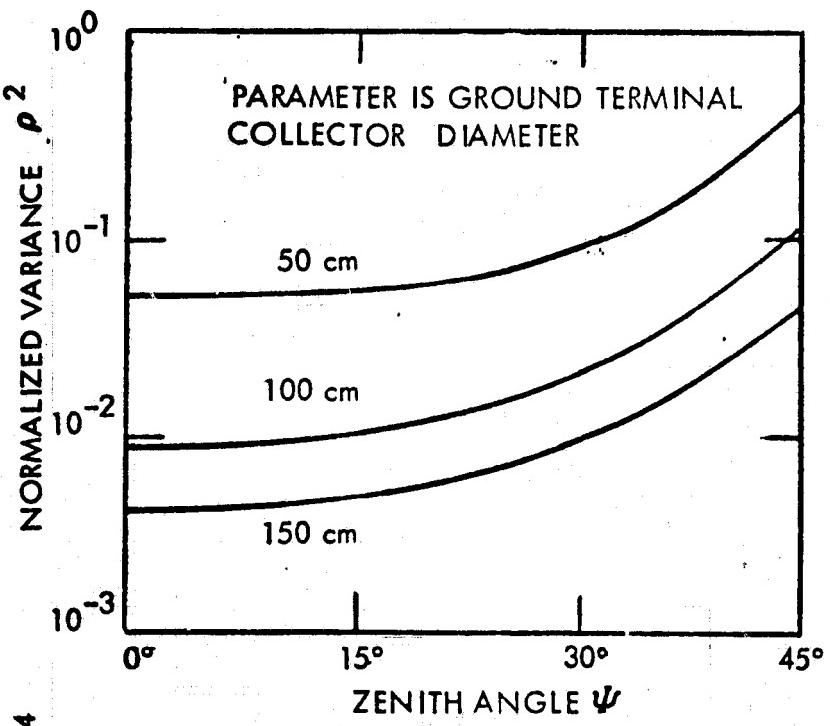
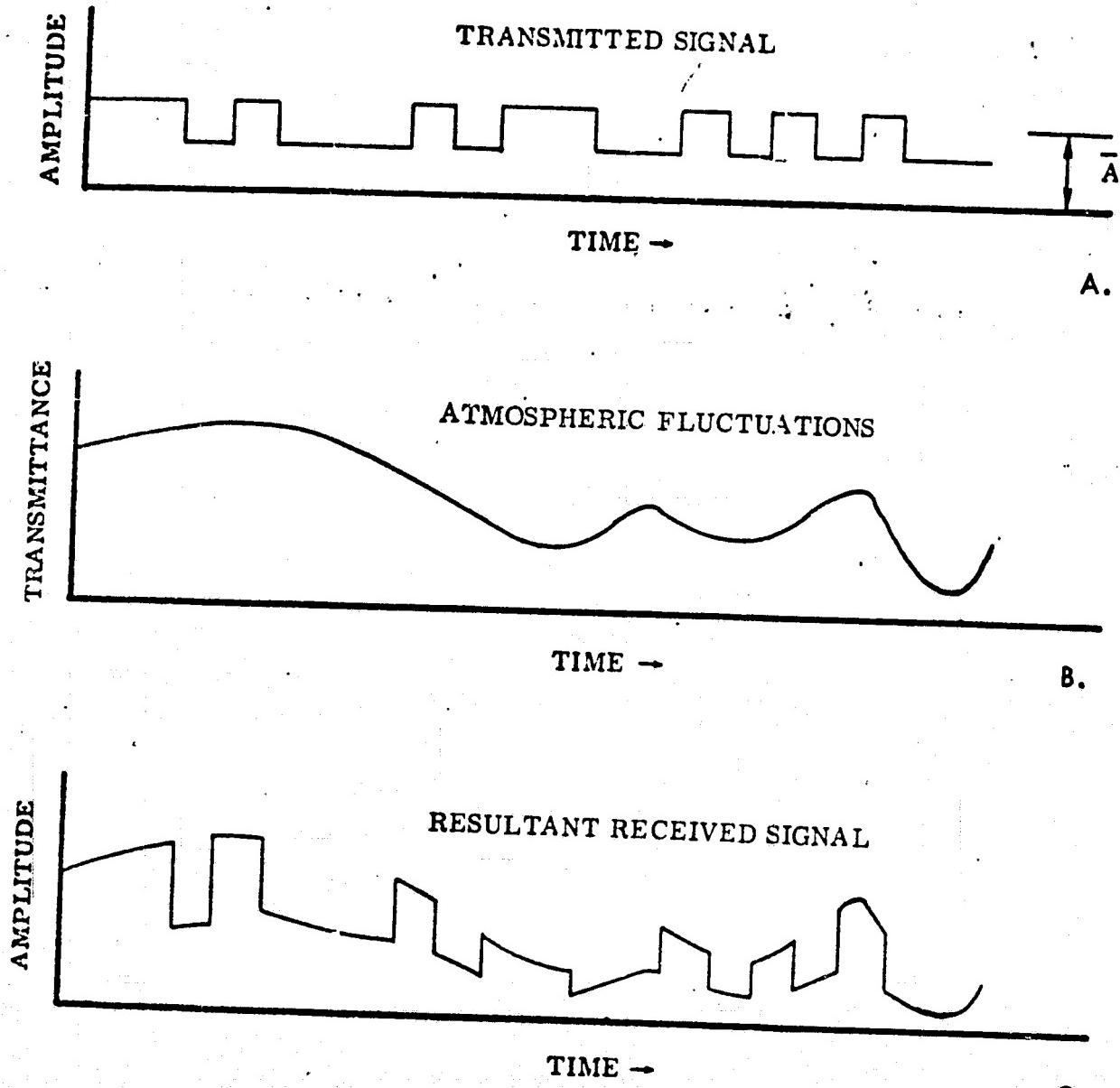


Figure 2-5. Variation in Scintillation Normalized Variance ρ^2 with Zenith Angle ψ



6906-170

Figure 2-6. Effects of Atmospheric Scintillation on a Digitally Coded Beam of Average Amplitude A

Using the expressions of Equation 2.7, we find that the noisy single channel BER is

$$\text{BER}_{\text{Single Channel}} = \frac{1}{2} \int_0^{\infty} dx g(x) \left[P \left(\frac{N_t - \hat{N}_p}{\sqrt{k \hat{N}_p}} \right) + Q \left(\frac{N_t - \hat{N}_m}{\sqrt{k \hat{N}_m}} \right) \right]. \quad (2.40)$$

The optimum value for the threshold setting N_t can be found by differentiation to be

$$N_t^2 = \hat{N}_m \hat{N}_p \left[1 + \frac{k \ln(\hat{N}_p / \hat{N}_m)}{\hat{N}_p - \hat{N}_m} \right],$$

or approximately

$$N_t \approx \sqrt{\hat{N}_m \hat{N}_p}. \quad (2.41)$$

Hence, by substituting this value for the threshold into Equation 2.40 we obtain the simpler form

$$\text{BER}_{\text{Optimum, Single Channel}} = \int_0^{\infty} dx g(x) Q \left[\frac{\sqrt{\hat{N}_p} - \sqrt{\hat{N}_m}}{\sqrt{k}} \right]. \quad (2.42)$$

In a similar manner, the expression for the balanced binary channel BER can be written from Equation 2.20 in explicit form as

$$\text{BER} \quad \begin{aligned} \text{Balanced Binary Channel} &= \int_{-\infty}^0 dz \int_0^\infty dy \int_0^\infty dx g(x) \frac{e^{-\frac{1}{2} \left(\frac{z+y-\hat{N}_p}{\sqrt{k\hat{N}_p}} \right)^2}}{\sqrt{2\pi} \sqrt{k\hat{N}_p}} \cdot \frac{e^{-\frac{1}{2} \left(\frac{y-\hat{N}_m}{\sqrt{k\hat{N}_m}} \right)^2}}{\sqrt{2\pi} \sqrt{k\hat{N}_m}} \end{aligned} \quad (2.43)$$

This expression may also be integrated to obtain the simpler form

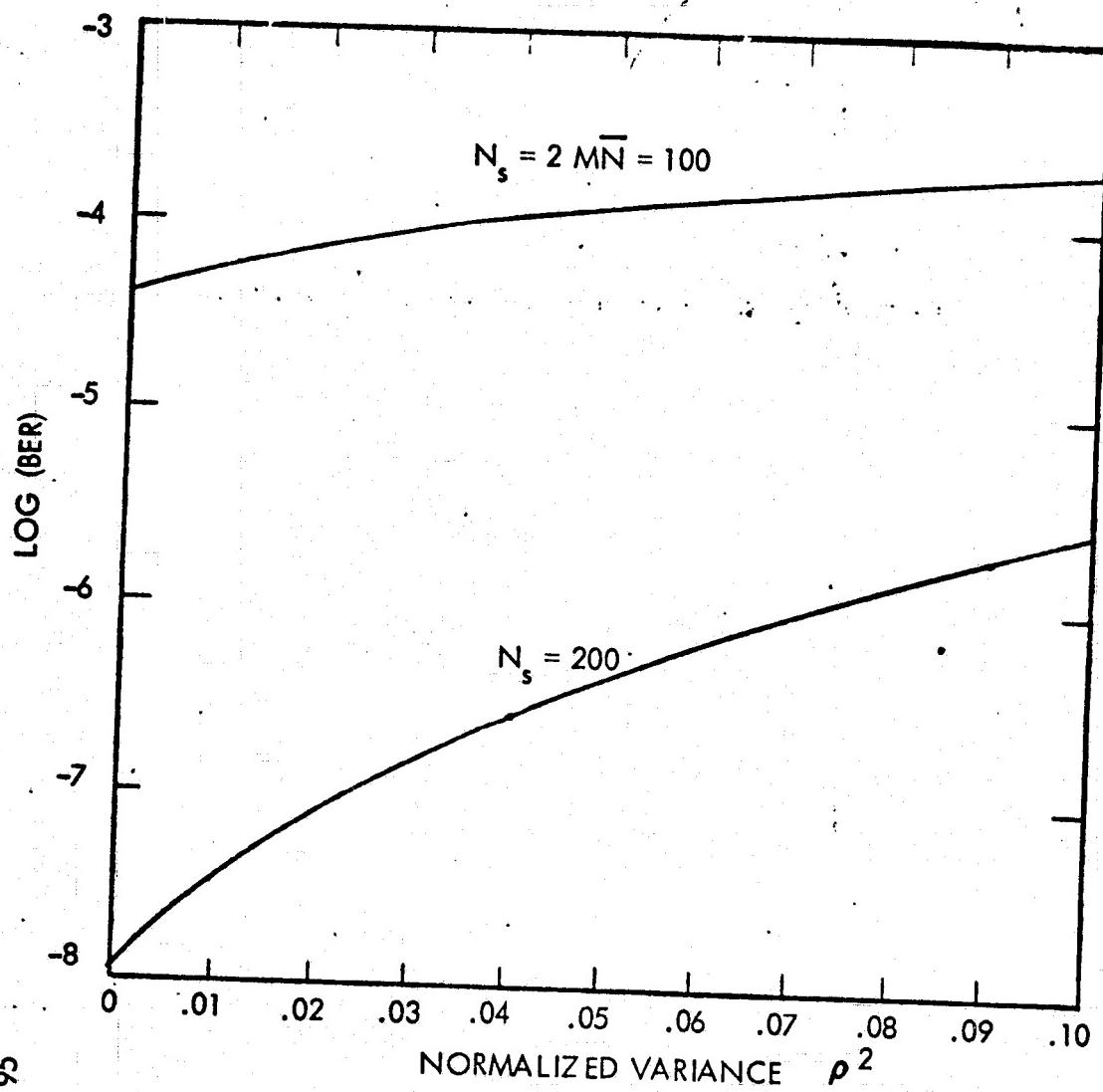
$$\text{BER} \quad \begin{aligned} \text{Balanced Binary Channel} &= \int_0^\infty dx g(x) Q \left[\frac{\frac{\hat{N}_p - \hat{N}_m}{\sqrt{k(\hat{N}_p + \hat{N}_m)}}}{\sqrt{k(\hat{N}_p + \hat{N}_m)}} \right] \end{aligned} \quad (2.44)$$

Equations 2.42 and 2.44 describe the performance of single and binary channel systems in the presence of additive noise. Measurements on the present optical communications system indicate that, in the laboratory and field tests performed, background noise and photosensor dark current are negligible i.e., $\Sigma_i \approx 0$. Representative values of system BER for these test conditions are plotted in Figures 2-7 and 2-8 for a dynode noise factor of 1.6.

2.3 Data, Communications Channel

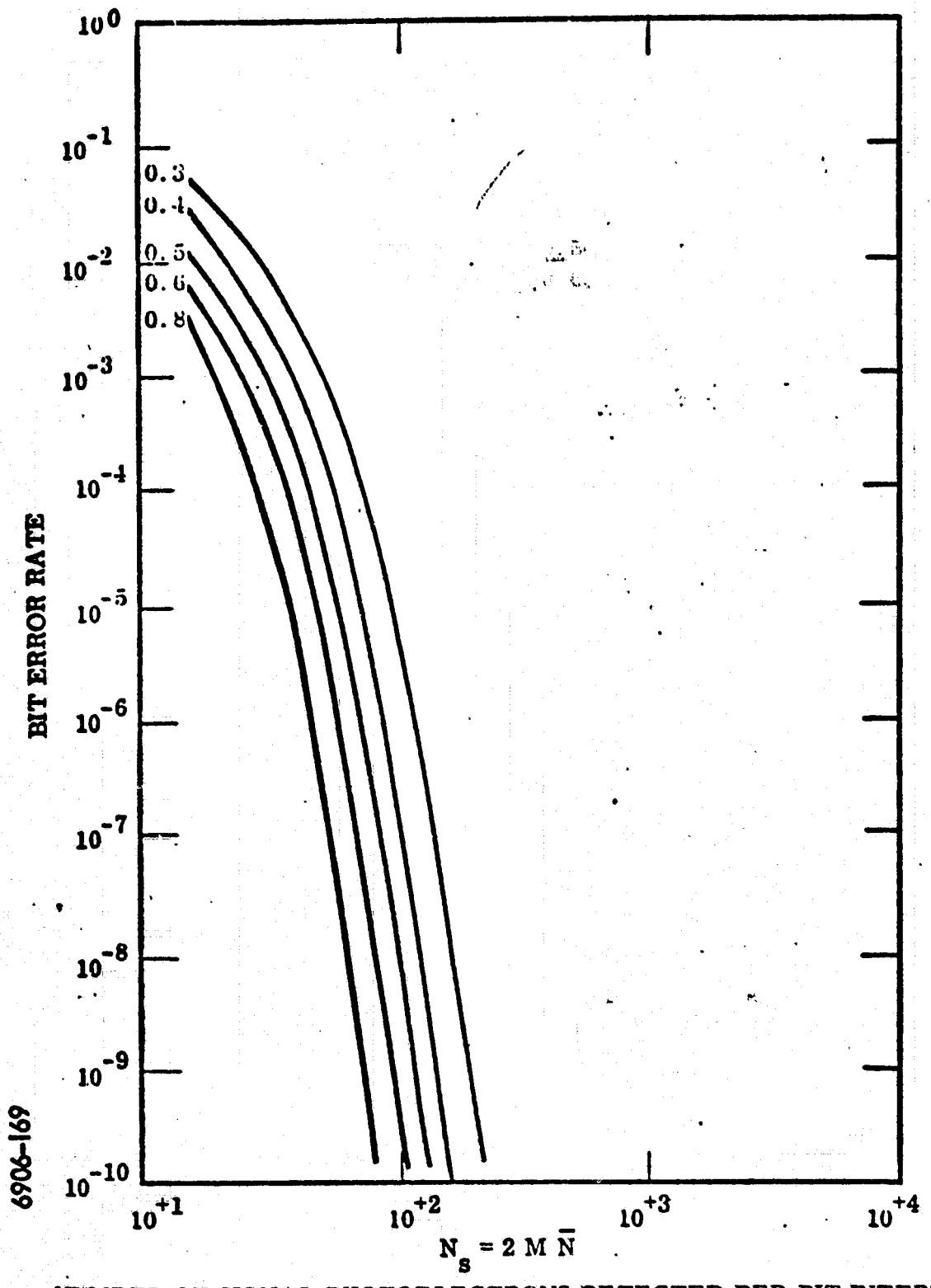
Although many complex parameters affect the performance of an optical communications system, four factors are of major concern in the system's evaluation. These are: laser power, signal beam modulation index, atmospheric scintillation, and the resulting bit error rate. Figure 2-9 is a portion of a recording tape generated with the engineering model during a field experiment. The raw data shown here are the bases for calculations that lead to evaluating system performance.

The two curves in the upper portion of Figure 2-9 are measurements of anode current of the system's photomultiplier tube sensor. The straight line at the top of the figure is the system's zero or dark level. This



6906 - 95

Figure 2-7. Single Channel Bit Error Rate in the Presence
of Log-Normal Turbulence for $k = 1.6$ and $M = 5.05$



NUMBER OF SIGNAL PHOTOELECTRONS DETECTED PER BIT INTERVAL N_s

Figure 2-8. Binary Channel Bit Error Rate with Modulation Index as the Parameter (Noise Factor k is 1.6)

2-28

7778-37

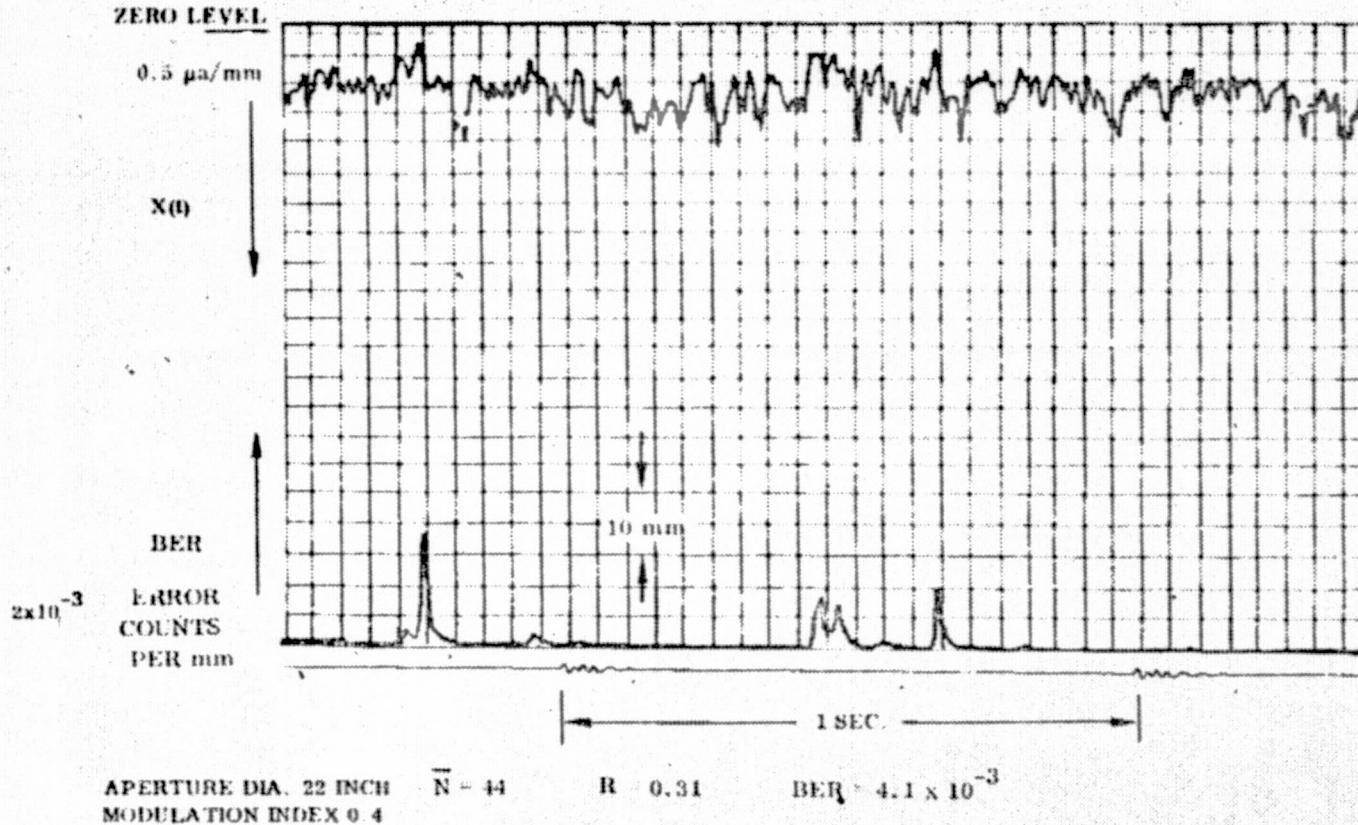


Figure 2-9. Integrated Error Output Data Sample

current measurement is made with all radiation blocked from the photo-sensor, and is an indication of the tube's dark current. The second curve from the top is a record of the tube's output current and shows the noisy effects of atmospheric scintillation. This curve was generated on the 5-mile test range at ITTG, San Fernando, California. The normalized variance determined from this data was $r=0.31$, the term r being an experimental estimate of the parameter ρ of equation 2.30. The laser beam was heavily attenuated with neutral density filters during this test run, limiting to 44 the average number of signal events per sample period.

The lowest curve of Figure 2-9 is a series of one second timing marks, used for setting the horizontal scale. The curve above these timing marks indicates the instantaneous system bit error rate, the output of the bit error detector. Under close inspection, it is seen that error bursts occur as a nonlinear, almost threshold function of the detected signal current. With a digital counter reading the output of the bit error detector, the bit error rate for the sample of Figure 2-9 was found to be 4.1×10^{-3} .

A 22 inch telescope was successful in allowing experimental control over the scintillation effects of atmospheric turbulence. The two photographs of Figure 2-10 show the irradiance distribution of the down-link laser beam across the full 22 inch aperture. These two photos were taken approximately 500 msec apart with the same exposure - 1/1000 second. The differences in scintillation and the resultant variations in detected radiant power are apparent.

It was pointed out that the system's bit error rate is a complex function of atmospheric scintillation amplitude r , the ratio of the measured standard deviation to the mean (of any linear function) of the detected signal radiation. The factor r is useful in predicting system performance and, as Figure 2-5 shows, is somewhat under the system designer's control in that scintillation amplitude is greatly affected by receiving aperture diameter. The curve of Figure 2-11 indicates the strong relationship between aperture diameter and a system's bit error rate. It should be noted that this curve considers the scintillation averaging effects of various aperture size, neglecting the greater radiation collecting ability of larger apertures. The bit error rate curve of Figure 2-11 would fall at a much greater slope if a constant detected power had not been maintained by attenuating the beam with neutral density filters as the aperture was increased.

2-30

REPRODUCIBILITY OF THE
ORIGINAL PAGE IS POOR

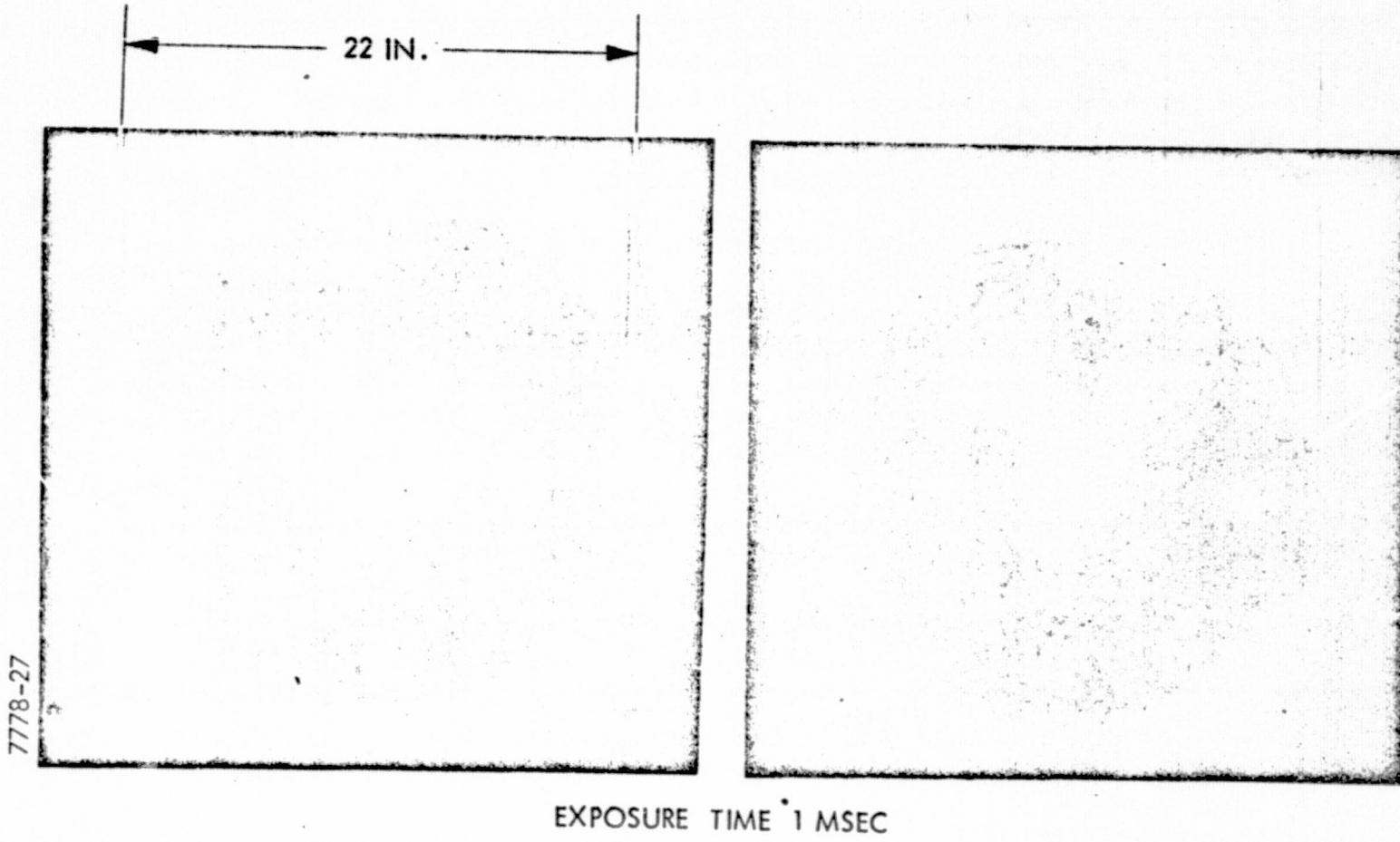
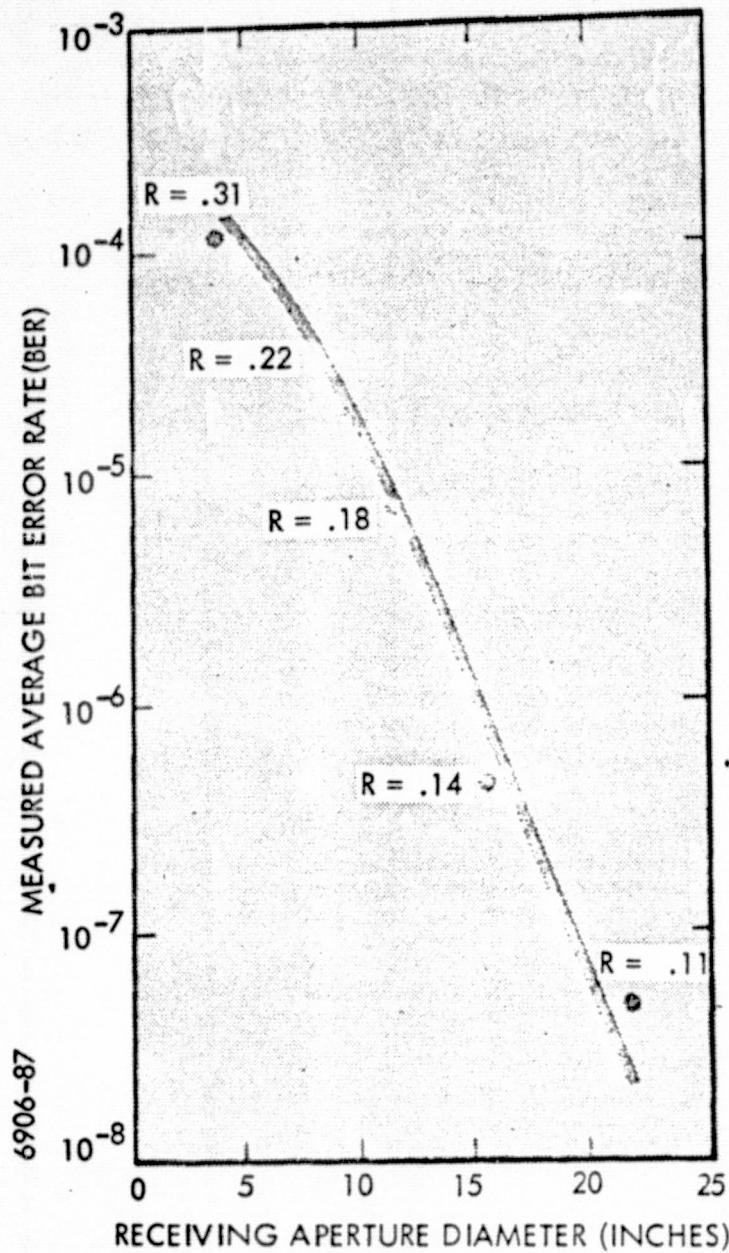


Figure 2-10. Atmospheric Scintillation



SIGNAL HELD
CONSTANT WITH
NEUTRAL DENSITY
FILTERS.

$\bar{N} \approx 500, N_S \approx 300$

MODULATION
INDEX = 0.3

TEMP: 48°F

WIND: 5 MPH FROM NE

RELATIVE HUM.: 33%

2000 HRS

Figure 2-11. Bit Error Rate vs Receiving Aperture

REPRODUCIBILITY OF THE
ORIGINAL PAGE IS POOR

Figure 2-12 shows the performance of the communications system in field tests under conditions of heavy turbulence. For comparison the theoretically predicted performance for $\rho = 0.35$ is represented as the solid curve on the right. Data runs with varying laser radiation intensities were recorded, and the results are shown as horizontal bars. The term r is an estimate of the parameter ρ , calculated from experiment data. Since r is a statistic of the non-stationary atmosphere, its value is constantly changing and the use of the Δr interval is appropriate. The fit of theoretical predictions to the tested performance of the system is seen to be quite close.

2.4 Radiometric Analysis

This section presents a system performance analysis for the tracking and communication functions. Since the end-to-end link analysis involves the ground terminal as well as the AOCP, certain assumptions are made regarding the parameter values and specifications for the ground terminal hardware. The radiometric analyses are presented as uplink and downlink. The uplink analysis implies radiometry from the ground terminal transmitter to the AOCP receiver and includes atmospheric propagation considerations. The transmitted beamwidth are assumed to be large compared to the pointing noise, therefore, dynamic pointing error effects are not included. Transmitted beam profiles are assumed to be gaussian and the performance is evaluated at the beam half-power point. Also, the beam cross section is assumed to be large compared to the collection aperture.

Derivation of the fine tracking noise equivalent angle is presented and applied to determine the theoretical blocking accuracy. In the communications performance analysis, the detection threshold is assumed to be ideal and the optimized level is defined. Although this hardware does not utilize an adaptive detection threshold circuit, the merits of such a circuit have been analyzed and a possible implementation for such a circuit is presented.

The analysis presented here was aided by an IBM 360/65 computer available through an APL telephone terminal which also plotted the results given in Figures 2-13 through 2-16.

Figures 2-13, 2-14, and 2-15 were given by the algorithm PDUP presented in Figure 2-17. Figure 2-16, however, was generated by a program SCINT. The subroutines it calls are not presented in this report in the interest of brevity and were given to NASA/MSFC previously.

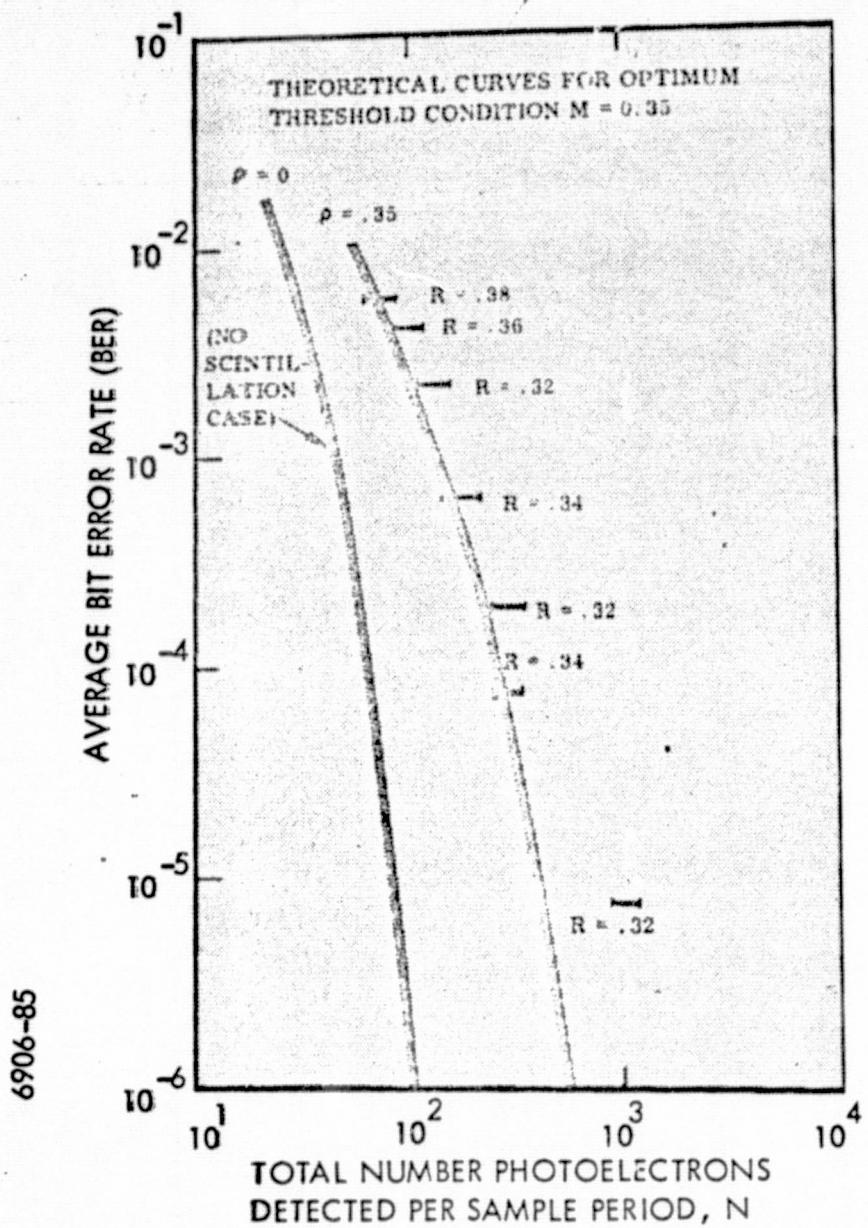


Figure 2-12. Comparison of Experimental Data with Log-Normal Atmospheric Model for Single Channel System

REPRODUCIBILITY OF THE
ORIGINAL PAGE IS POOR

2.4.1 Selection of Parameter Values. - Although the parameters chosen for the several links are printed out on the curves they are presented in Table 2-2 with some explanation where required.

TABLE 2-2

UPLINK PARAMETERS

Laser Max Power (Watts)	0.2
Laser Ave Power (Watts)	0.1
Transmitter Transmittance	0.01
Atmospheric Transmittance	0.1
Range (Feet)	84,853
Background Radiance $\omega/\text{cm}^2 \cdot \mu\text{-ster}$	0, 0.014
Optical Filter Width (microns)	0.002
Receiver FOV (arc-secs)	18.0
Collector Diameter (inches)	3.71
Photo-cathode Sens. (including mesh) (amps/watt)	0.025
Multiplier Noise Figure	1.5
Receiver Transmittance (comm)	0.182
Scint Receiver Transmittance	0.034
Track Bandwidth (hz)	1,000.0
Comm. Bandwidth (hz)	50,000.0

The maximum power of 0.2 watts is the ground station laser power radiated in the absence of modulation, P_M . The laser average power, \bar{P} has been set at $P_M/2$ for Figures 2-13, 2-14, and 2-15.

Thus, the power radiated by the intensity modulated laser is:

$$P_R = \bar{P}(1 + \mu \cos \omega_s t) = \frac{P_M}{2} (1 + \mu \cos \omega_s t)$$

where

P_R = modulated laser power

μ = modulation index

ω_s = subcarrier radian frequency.

The transmitter transmittance of 0.01 is a perhaps conservative estimate of the ground transmitter transmittance. The atmospheric transmittance of 0.1, however, is the transmittance of a very clear atmosphere for the range of close to 85,000 feet used.

The range used, ~85 Kft, is the 45° slant range to an aircraft 60 Kft above the ground station.

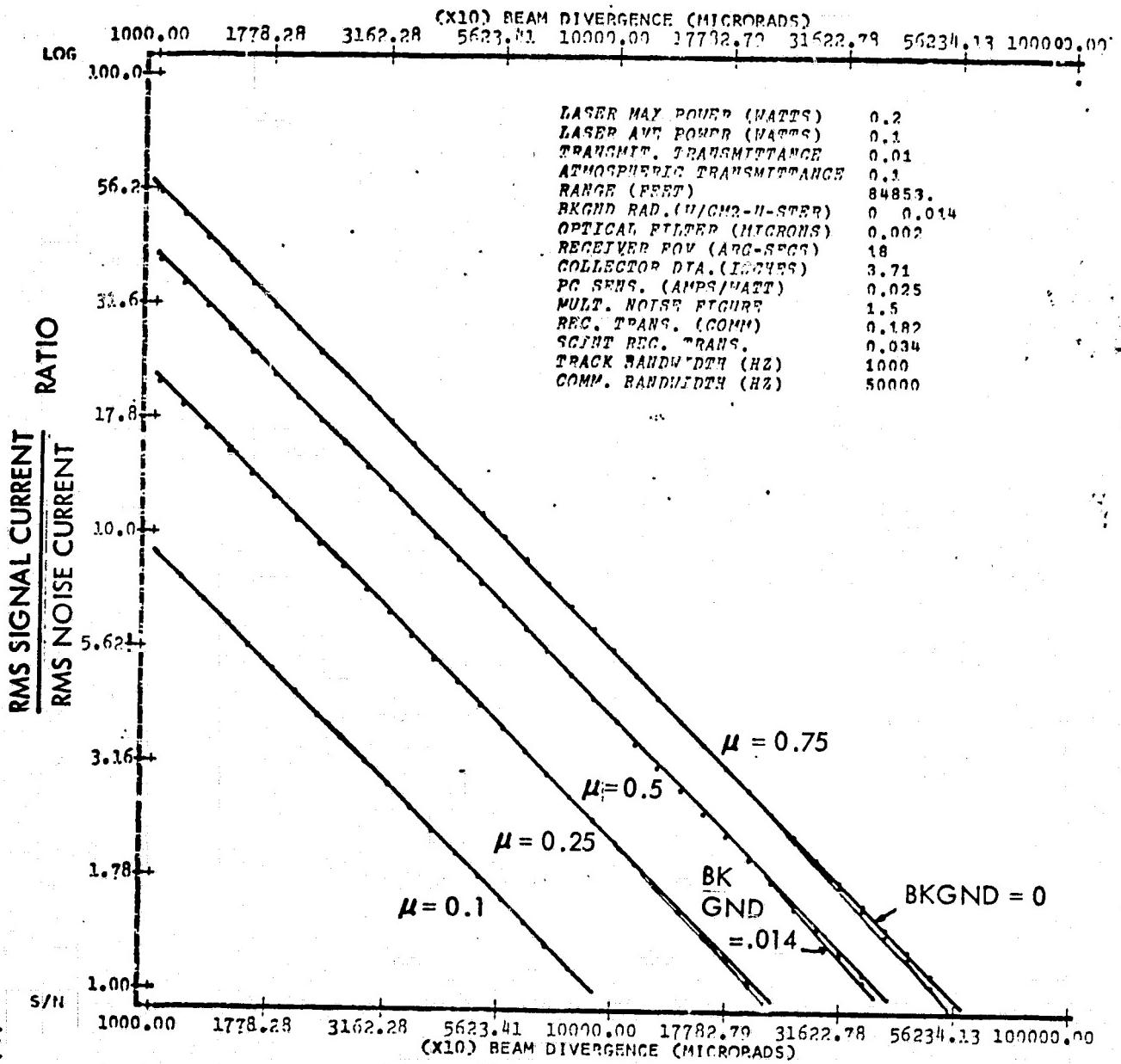
Background radiances of 0 and $0.014 \text{ w/cm}^2 \cdot \mu\text{-ster}$ bracket all the backgrounds to be encountered. The higher value is that for sunlit clouds. As can be seen from the curves, the sunlit background is used. The optical filter of 20 \AA serves only to limit the background power to the receiver. The receiver field of view of 18 arc seconds serves the same purpose although it is more intimately associated with design considerations of aperture size in the image dissector and the focal length of the telescope.

The collector diameter is the effective unobscured diameter of a collector which is 3.88 inches in diameter with 1.13 inches of central obscuration.

The photocathode sensitivity is taken from the standard S-20 photocathode curve and divided by 2 to allow for losses in the mesh following the photocathode in the image dissector. The multiplier noise figure of 1.5 is a realistic value based on experience which agrees with analyses.

The communications receiver transmittance of 0.182 is the result of multiplying the transmittances and reflectances of the several elements in the light path of the receiver optics. The value of 0.034 for the scintillation monitor was obtained in the same way. Table 2-3 lists the elements and the effective transmittances used for both paths.

S/N VS BEAM DIVERGENCE FOR AVLOC UPLINK COMM. MU=0.1,0.25,0.5,0.75



6906-141

Figure 2-13. Signal-to-Noise vs Beam Divergence for AVLOC Uplink (MU=0.1, 0.25, 0.5, 0.75)

SCINT MONITOR POWER VS BEAM DIVERGENCE, AVLOC UPLINK COMM.

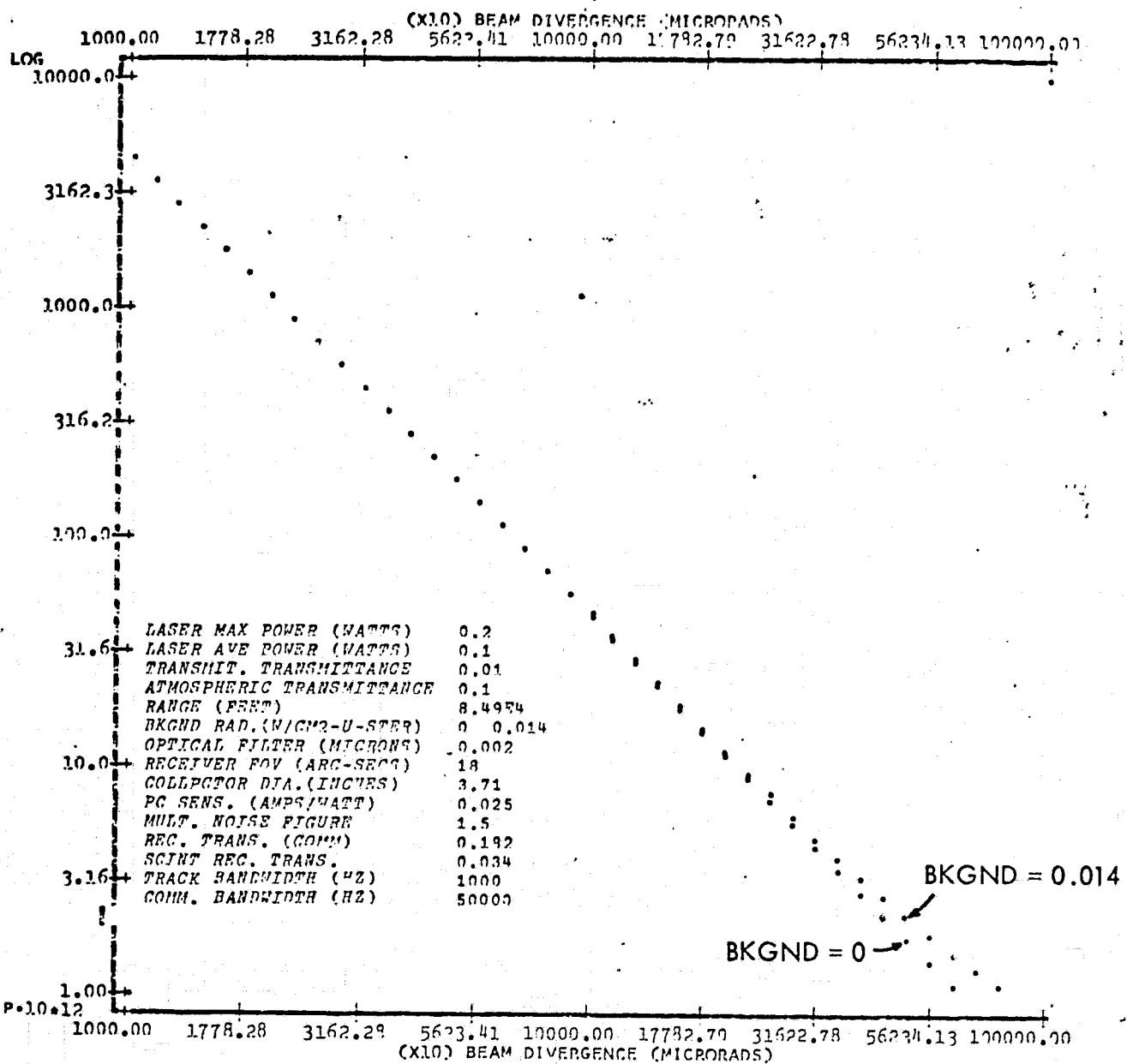


Figure 2-14. Scintillation Monitor Power vs Beam Divergence,
AVLOC U link Comm.

CHANGE TYPE-BALL

6906-142

6906-143

S/N VS BEAM DIVERGENCE, AVLOC UPLINK TRACK, MU=0.1, 0.25, 0.5, 0.75

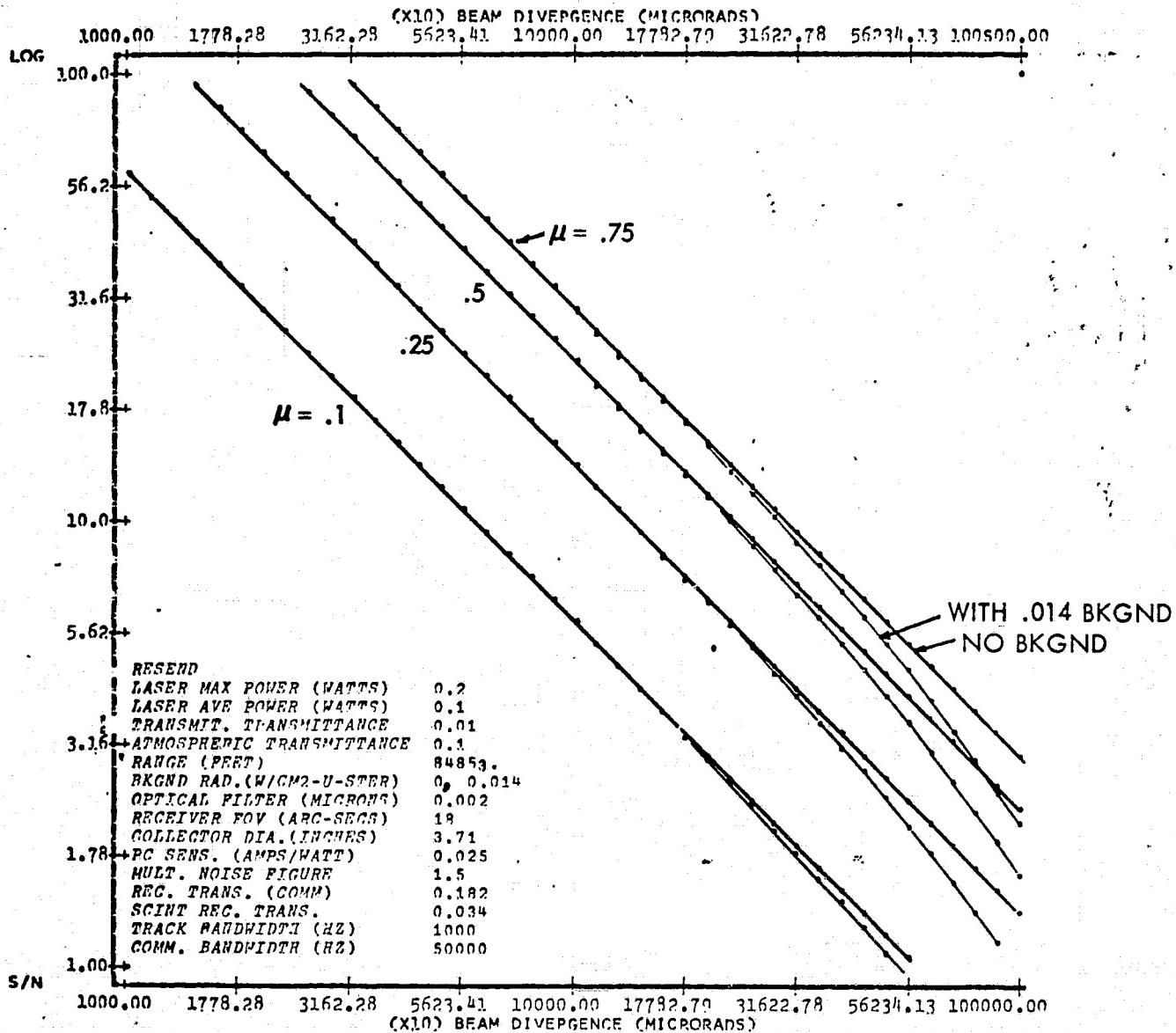
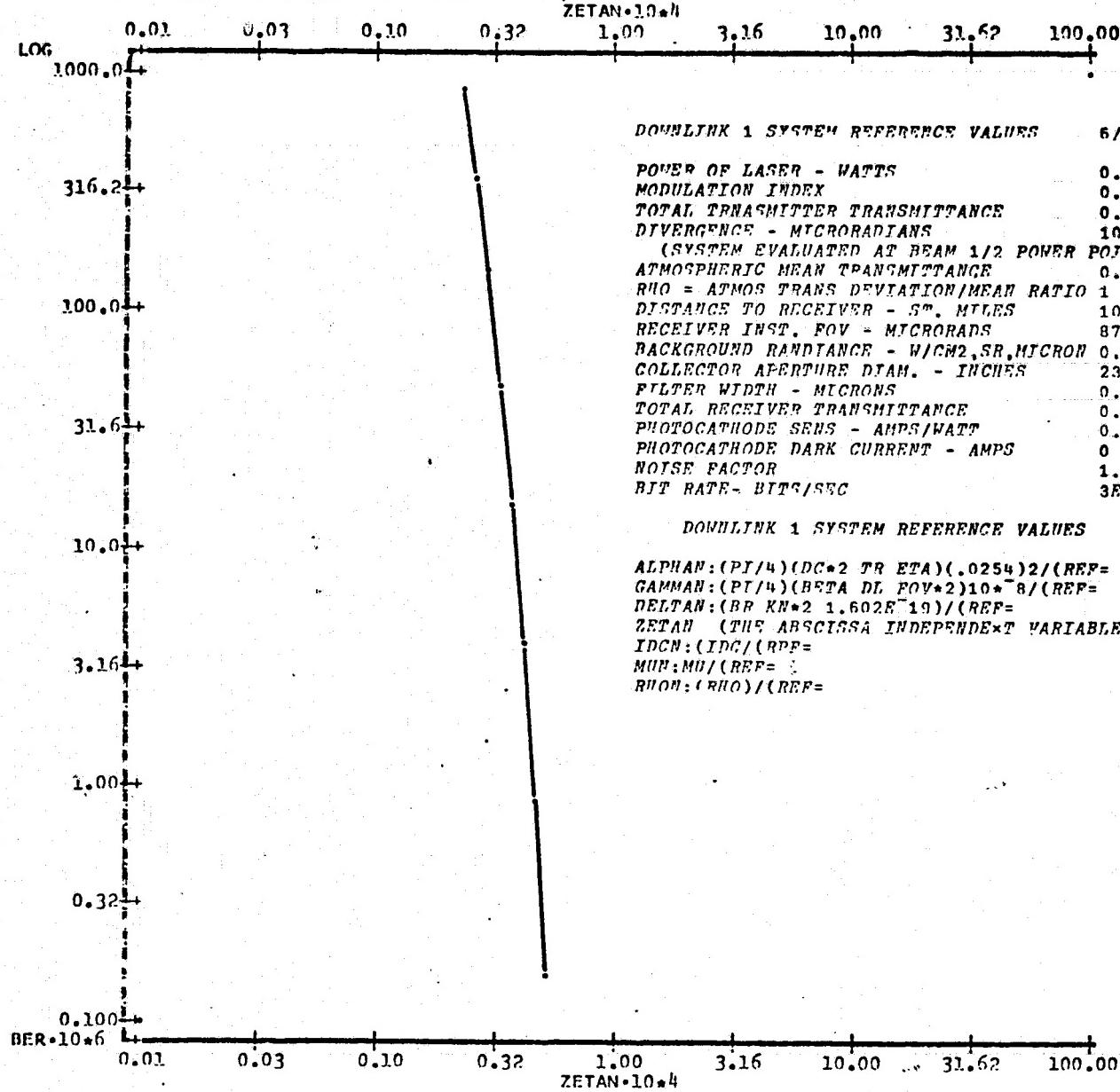


Figure 2-15. Signal-to-Noise vs Beam Divergence, AVLOC Uplink Track (MU=0.1, 0.25, 0.5, 0.75)

CHANGE TYPE=RALL

LEGIBILITY OF THE
ORIGINAL PAGE IS POOR

AVLOC DOWNLINK 1 COMMUNICATIONS, BER VS ZETAN



DOWNLINK 1 SYSTEM REFERENCE VALUES 6/08/73

POWER OF LASER - WATTS	0.005
MODULATION INDEX	0.749
TOTAL TRANSMITTER TRANSMITTANCE	0.25
DIVERGENCE - MICRORADIANS	10
(SYSTEM EVALUATED AT BEAM 1/2 POWER POINTS)	
ATMOSPHERIC MEAN TRANSMITTANCE	0.8
RHO = ATMOS TRANS DEVIATION/MEAN RATIO	1
DISTANCE TO RECEIVER - FT. MILES	10
RECEIVER INST. FOV - MICRORADS	873
BACKGROUND RADIANCE - W/CM ² , SR, MICRON	0.014
COLLECTOR APERTURE DIAM. - INCHES	23.2
FILTER WIDTH - MICRONS	0.001
TOTAL RECEIVER TRANSMITTANCE	0.1
PHOTOCATHODE SENS - AMPS/WATT	0.025
PHOTOCATHODE DARK CURRENT - AMPS	0
NOISE FACTOR	1.5
BIT RATE - BITS/SEC	3E7

DOWNLINK 1 SYSTEM REFERENCE VALUES 6/08/73

ALPHAN: (PI/4)(DC/2 TR ETA)(.0254)2/(REF=	0.000684) = 1
GAMMAN: (PI/4)(BETA DL FOV*2)10 ⁻⁸ /(REF=	8.37E ⁻⁸) = 1
DELTAN: (BR KN*2 1.602E ⁻¹⁹)/(REF=	1.08E ⁻¹¹) = 1
ZETAN (THE ABSCISSA INDEPENDENT VARIABLE)	
IDCN: (IDC/(RPF=	0) = 1
MUH: MU/(REF=	0.749) = 1
RHON: (RHO)/(REF=	1) = 0

Figure 2-16. AVLOC Downlink 1 Communications, BER vs ZETAN

CHANGE TYPE-BALL

▼PDPUP[0]▼

▼ PDPUP

[1] $BPP \leftarrow 0,0$
 [2] $PTA \leftarrow 0,2$
 [3] $PTAA \leftarrow PTA + 2$
 [4] $TTA \leftarrow 0,01$
 [5] $TA \leftarrow 0,1$
 [6] $RX \leftarrow (60000) \times (2 * 0,5)$
 [7] $RM \leftarrow RX \times 12 + 39,37$
 [8] $DIVMIN \leftarrow 0,0001$
 [9] $DIVN \leftarrow ((DIVMIN) \times (10 * 0,05) * (140)), (DIVMIN)$
 [10] $NB \leftarrow 0,0,014$
 [11] $NBE \leftarrow NB \times (10000000000)$
 [12] $DLG \leftarrow 0,002$
 [13] $DLGN \leftarrow DLG \times (1E-6)$
 [14] $FOV \leftarrow 18$
 [15] $FOVN \leftarrow FOV \div (3600 \times 57,3)$
 [16] ' $MU =$ ' ; MU
 [17] $N \leftarrow 0$
 [18] $A1 : N \leftarrow N + 1$
 [19] $NRNA \leftarrow NRBN[N]$
 [20] $RPD[N] \leftarrow NRNA \times DLGN \times ((FOVN \times 2) \times 3,142 + 4)$
 [21] $\rightarrow A1 \times 1 (N < 2)$
 [22] $SPDA \leftarrow PTAA \times TTA \times TA \div (((RM \times DIVN) \times 2) \times 3,142 + 4)$
 [23] $DIVNX \leftarrow DIVN$
 [24] $DIVN \leftarrow DIVN, DIVN$
 [25] $DC \leftarrow ((3,88 \times 2) - (1,129 \times 2)) \times 0,5$
 [26] $DCN \leftarrow DC \times 0,0254$
 [27] $ETAN \leftarrow 0,05 + 2$
 [28] $KN \leftarrow 1,5$
 [29] $TR \leftarrow 0,182$
 [30] $BRT \leftarrow 1000$
 [31] $BRC \leftarrow 50000$
 [32] $TRS \leftarrow 0,034$
 [33] $PSC \leftarrow ((RPD[1] + SPDA), (RPD[2] + SPDA)) \times TRS \times ((DCN \times 2) \times 3,142 + 4)$
 [34] $KS \leftarrow ((PSC \geq 1E-12) \times (PSC \leq 1E-8))$
 [35] $PSC \leftarrow (KS / PSC), 1E-12, 1E-8$
 [36] $IOPD \leftarrow ETAN \times (DCN \times 2) \times (3,142 + 4) \times TR$
 [37] $JAVC \leftarrow SPDA \times (1 + (MU \div (2 * 0,5)))$
 [38] $JAVC \leftarrow ((JAVC + RPD[1]), (JAVC + RPD[2])) \times IOPD$
 [39] $INC \leftarrow (((3,2E-19) \times BRC \times JAVC) \times 0,5) \times KN$
 [40] $ISC \leftarrow (SPDA, SPDA) \times MU \div (2 * 0,5) \times IOPD$
 [41] $SNC \leftarrow ISC + INC$
 [42] $JAVT \leftarrow (SPDA \div (1 + MU)) \times (1 + (MU \div (2 * 0,5)))$
 [43] $JAVT \leftarrow ((JAVT + RPD[1]), (JAVT + RPD[2])) \times IOPD$
 [44] $INT \leftarrow (((3,2E-19) \times BRT \times JAVT) \times 0,5) \times KN$
 [45] $IST \leftarrow ((SPDA, SPDA) \div (1 + MU)) \times IOPD \times MU \div (2 * 0,5)$
 [46] $SPT \leftarrow IST + INT$
 [47] $KC \leftarrow (SNC \geq 1) \times (SNC \leq 100)$
 [48] $STHCP \leftarrow (KC / SNC), 1,100$
 [49] $KT \leftarrow (SNT \geq 1) \times (SNT \leq 100)$
 [50] $STHTP \leftarrow (KT / SNT), 1,100$
 [51] $DIVCP \leftarrow ((KC / DIVN), DIVMIN, (DIVMIN \times 100)) \times (1000000)$
 [52] $DIVTP \leftarrow ((KT / DIVN), DIVMIN, (DIVMIN \times 100)) \times (1000000)$
 [53] ~~• PSC IS THE SCINT MONITOR POWER RAD IN MICRO-MICROWATTS~~
 [54] ~~• DIVSC IS THE BEAM DIV. IN MICRORADS. (PSC AND DIVSC ARE READY FOR PLOTTING)~~
 [55] ~~• STHCP AND DIVCP GIVE THE PLOT OF TRACK SIGNAL/NOISE RATIO VS DIV IN MICRORADS~~
 [56] ~~• STHTP AND DIVTP GIVE THE PLOT OF COUNTS. SIGNAL/NOISE RATIO VS DIV IN MICRORADS~~
 [57] ~~• STHSC AND DIVSC WILL PLOT SCINT MONITOR S/X VS DIV IN MICRORADS~~

Figure 2-17. AVLOC Radiometric Analysis Program

TABLE 2-3

	<u>Comm. Receiver Path</u>	<u>Scint Monitor Path</u>
Afocal Telescope	0.60	0.60
Z Steerer	.96	.96
Y Steerer	.96	.96
Beam Combiner	.90	.90
Narrow Band Filter	.6	.6
Beam Splitter	.82	.14
Lens	.80	.85
Neutral Density Filter	.96	-
Mirror	.97	.97
	<hr/> 0.182	<hr/> 0.034

The uplink tracker receiver is, of course, common with the communications receiver until the output of the image dissector is reached where the 10.7 megahertz subcarrier tone is separated from the low frequency components which really contain the tracking information.

The tracker scan generates a 1 kc modulation of the I. D. output current.

Although the tracker modulation index is self imposed by the tracker and is unrelated to the sub-carrier modulation index, it will affect the communications S/N ratio. This cross-coupling was not done on the computer simulation because of the many possible combinations.

In fact, the S/N current ratios of the uplink communications channel assume the tracker modulation is zero. However, during the track modulation the communications S/N will range between the maximum given by Figure 2-13 and $\sqrt{1-\mu_T}$ times that value. Thus, if the tracker imposes a 50 percent modulation index on the average incoming power, the S/N current ratio of Figure 2-13 will vary at a 1 kc rate from the values given by the curves to $\sqrt{1-0.5} = 0.7$ of those values.

The "signal current" used for the track channel is its own modulation signal. The "signal current" used for the communications receiver is the 10.7 megahertz tone with a noise bandwidth of 50 kc.

Note also that the signal to noise ratios given are defined as:

$$S/N \equiv \frac{\text{rms signal current}}{\text{rms noise current}}$$

(These values must be squared to obtain power S/N.)

In the case of the scintillation monitor, total power to the photomultiplier only is plotted against the transmitted beam divergence.

2.4.2 Downlink Parameters. - The downlink system maximum laser power used is 5 milliwatts. The modulation index of 0.749 was calculated based on supplying 0 to 46 volts to the intensity modulator and using the actual wave shapes resulting when square waves were applied. Under those conditions it was found that the maximum transmittance of the modulator was 0.29 and an extinction ratio of 7 was achieved.

The plot of the downlink analysis, although more complex than was done for the uplink, is far more useful because tradeoff analyses can be done with it.

The abscissa variable is actually the normalized power density of the signal at the receiver on the ground. It has been labeled "zetan" for "normalized zeta".

$$\zeta_N = \frac{(P_T/P_{TO})(T_T/T_{TO})(T_A/T_{AO})}{(R/R_O)^2 (\phi_B/\phi_{BO})^2}$$

where

P_T = Laser Power

T_T = Transmitter Transmittance

T_A = Atmospheric Transmittance

R = Range

ϕ_B = Beam Divergence Angle

The "O" subscript represents the reference value used for that particular parameter - i.e., $P_{TO} = 0.005$ watts, etc.

If all parameters are at their reference values, $\zeta_N = 1$. From the results of Figure 2-16 however, we note that $\zeta_N = 10^{-4}$ or even less gives acceptable bit error rates.

We can therefore state that:

$$\left(\frac{P_T}{P_{TO}} \right) \left(\frac{T_T}{T_{TO}} \right) \left(\frac{T_A}{T_{AO}} \right) \left(\frac{\phi_{BO}^2}{\phi_B^2} \right) \left(\frac{R_O^2}{R^2} \right) \geq 10^{-4}$$

and a tradeoff analysis between these parameters, which satisfy the above inequality, can be made.

For example, the reference beam divergence of 10 microradians allows the beam divergence to be increased to 1000 microradians as long as the other parameters are at their reference values. Similarly, if the beam divergence of 10 microradians is used along with the reference values for the other parameters, the laser power could be dropped four orders of magnitude from its reference of 5 milliwatts without noticeable system performance degradation. Alternatively, the atmospheric transmittance can drop to 0.00008 from 0.8 etc.

The reference values are chosen rather arbitrarily because of the above. It is important to know only what the reference values are not whether they are accurate at the time. For example, although the transmitter transmittance was referenced at 0.25, it has since been determined that a value 1/2 as great is more accurate. Also the range of 52,800 feet is inconsistent for comparison with the uplink where 84,900 feet was used along with an atmospheric transmittance of 0.1 instead of 0.8 Using these values:

$$1 = \frac{1}{2} \times \frac{1}{8} \times \left(\frac{\phi_{BO}^2}{\phi_B^2} \right) \times \left(\frac{528}{849} \right)^2 \geq 10^{-4}$$

we find that

$$\sigma_B \geq 156 \text{ microradiars}$$

to get bit error rates of the order of 10^{-9} errors/sec or

$$\phi_B \geq 220 \text{ microrads}$$

for a bit error rate of 10^{-7} sec.

The slope of BER vs ζ_N shown in Figure 2-16 means that actually using $\phi_B = 220$ microrads does not allow for atmospheric transmittance degradation unless the range is reduced.

To tradeoff other parameters, it is necessary to generate other curves to be perfectly general, but the same curve applies if

$$\alpha_N \equiv \left(\frac{D_C^2}{D_{CO}^2} \right) \left(\frac{T_R}{T_{RO}} \right) \left(\frac{\eta}{\eta_O} \right) = 1$$

$$\gamma_N \equiv \left(\frac{N}{N_O} \right) \left(\frac{\Delta\lambda}{\Delta\lambda_O} \right) \left(\frac{fov}{fov_O} \right)^2 = 1$$

$$\delta_N \equiv \left(\frac{B_R}{B_{RO}} \right) \left(\frac{K_N}{K_{NO}} \right)^2 = 1$$

$$M_{UN} \equiv \frac{M_U}{M_{UO}} = 1$$

where:

- D_C = collector aperture diameter
- T_R = receiver transmittance
- η = photocathode sensitivity
- Δ_λ = optical filter width
- fov = field of view of receiver
- B_R = bit rate
- K_N = receiver noise figure
- M_U = modulation index

That is: If the receiver transmittance is reduced by 50 percent, the collector effective diameter must be increased by 40 percent ($\sqrt{1/2-1}$) to maintain the performance curve given.

Figure 2-18 is a plot of the beam dimension between 1/2 power points for some ranges vs the beam angular dimensions to relate to the collector aperture diameter.

2.4.3 Tracking S/N

Noise Equivalent Angle - A scanning tracker for which the signal spot diameter, d_s , is smaller than the scanning aperture diameter, d_a , yields signal electrons proportional to the approximate area, $d_a d_s$. (See Figure 2-19.)

The noise equivalent area, or the area d_N^2 which receives an average of one electron, is then:

$$d_N^2 = \frac{1}{K_T} \quad (2)$$

2-46

6906-156

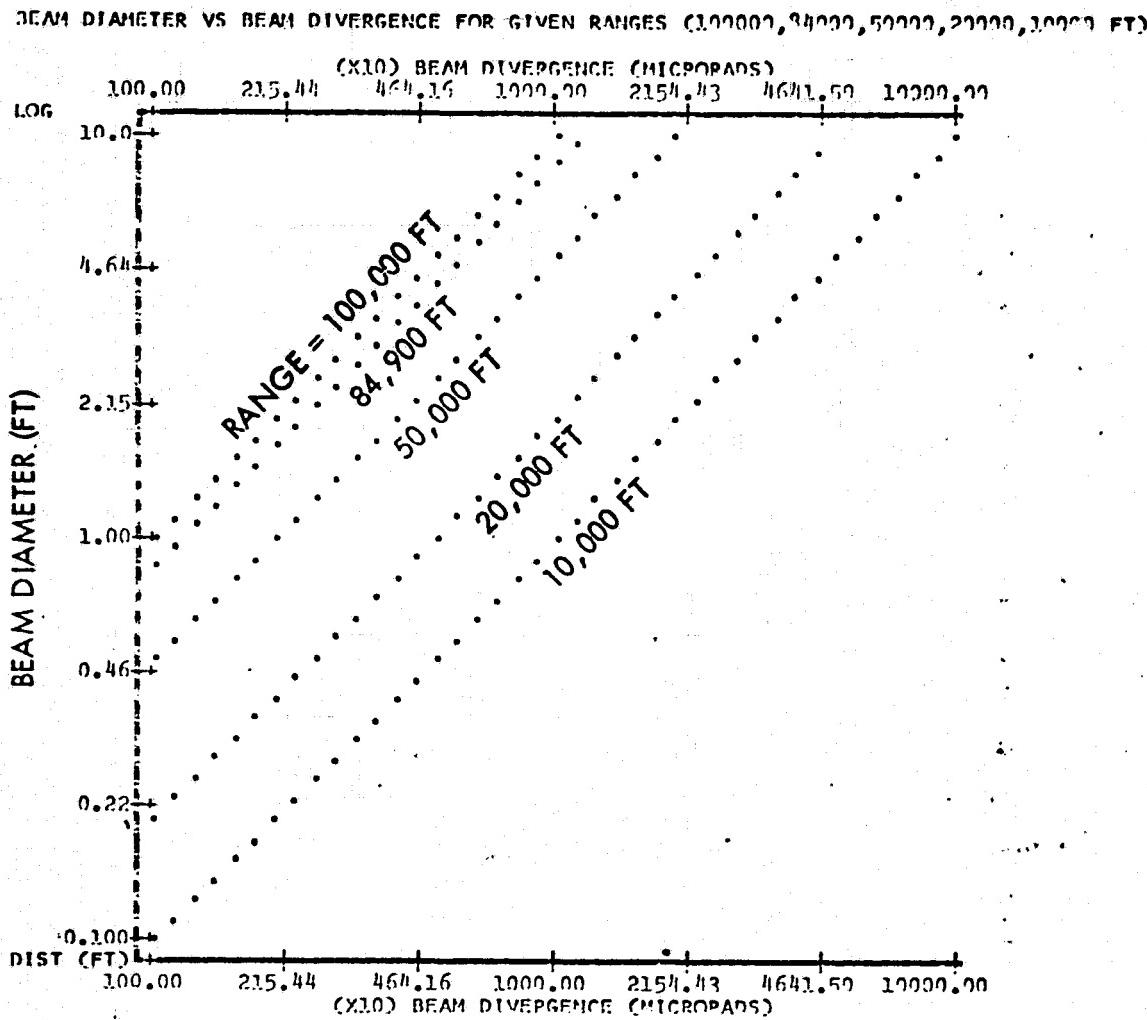
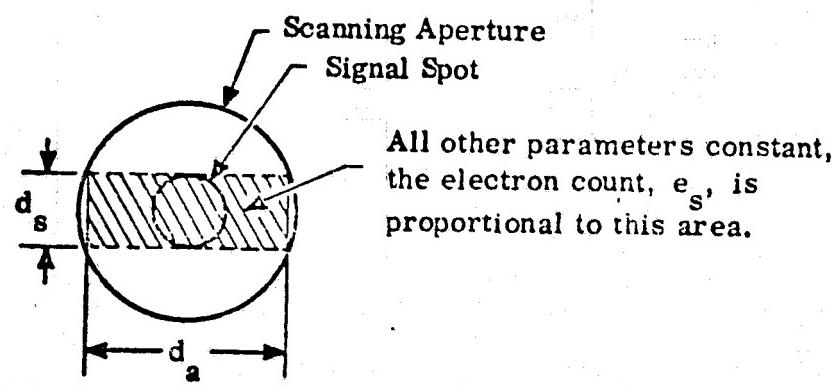


Figure 2-18. Beam Diameter vs Beam Divergence for Given Ranges (100000, 84000, 50000, 20000, 10000 Feet)



$$e_s = K_T \left(\frac{d_a}{d_s} \right) \quad (1)$$

Figure 2-19

Substituting (2) into (1) gives:

$$e_s = \frac{d_a d_s}{d_N^2} \quad \text{or} \quad (3)$$

$$d_N^2 = \frac{d_a d_s}{e_s} \quad (4)$$

Dividing both sides of equation (4) by the square of the focal length restates the equation in terms of angles.

$$\alpha_N^2 = \frac{1}{e_s} (\alpha_a \alpha_s) \quad (5)$$

Finally, the equation for the tracker noise equivalent angle is:

$$\alpha_N = \sqrt{\frac{\alpha_a \alpha_s}{e_s}} \quad (6)$$

Tracker noise equivalent angle, α_N , versus aperture angle, α_a ; spot size angle, α_s ; and electron count per bit, e_s .

Electron Count for Reliable Tracking. - Track lock - The ability of the tracker to maintain track - becomes relatively unreliable if the equivalent noise angle exceeds about 1/4 the aperture angle (empirically determined).

$$\alpha_N \leq \frac{\alpha_a}{4} \quad (7)$$

Substituting (5) into (6) and solving for e_s gives the number of electrons per bit, e_{ST} required to maintain track, as:

$$ST \geq 16 \frac{\alpha_s}{\alpha_a} \quad (8)$$

Electron count per bit for reliable tracking.

Noise Equivalent Pointing Angle. - The derivation of α_N (equation 6) gives the accuracy for the tracker itself. The tracker is used to point a transceiver or receiver by means of beam steering devices which generally increase the bit integration time. Although this factor is generally 10, we shall maintain generality and call it n.

Noise equivalent pointing angle, α_p .

$$\alpha_p = \sqrt{\frac{\alpha_a \alpha_s}{n e s}} = \frac{1}{\sqrt{n}} \alpha_N \quad (9)$$

SNR Degradation. - It should be noted that SNR degradations such as will occur in the detector photomultiplier and elsewhere in the system makes it necessary that the electron counts derived be increased by a factor of about 6 when the electron counts at the detector photocathode are being considered.

2.5 Adaptive Signal Processing Threshold Analysis

First, the adaptive threshold concept as applied to analyses using normally distributed noise density functions as an approximation to Poisson statistics is briefly described. The adaptive threshold concept using Poisson statistics for the noise density function is then developed. The optimum threshold value is derived in equation form. This form is then manipulated into a form which minimizes the equipment accuracy requirements. An alternate concept leading to a practical circuit is also developed and described in detail.

2.5.1 Ideal - Threshold Circuit. - Table 2-4 lists the parameters of interest to this subject. Figure 2-20 illustrates the continuous probability density curves associated with the assumption of a normal distribution of the probability of achieving a particular count during an integration time. If the Laser transmits at full power continuously, then the average count per integration time will be $D + B + LM = P$, and the area under the mark curve will be unity since the probability that a mark is being sent is 100 percent. If, for example, the probability that a mark (one) is being sent during any randomly chosen integration time is $P(M)$, then the area under the mark curve will be equal to $P(M)$. Since the Laser contribution to the count during the actual reception of a mark is still LM , the value of P is unchanged by a variation in $P(M)$, and only the height of every point on the mark curve is scaled by $P(M)$.

TABLE 2-4. PARAMETER LIST

- B** = Background*
- D** = Dark*
- L** = Laser*
- LM** = Laser transmitting a Mark (one)*
- LS** = Laser transmitting a Space (zero)*
- P** = Peak (maximum value)*
- V** = Valley (minimum value)*
- T** = Threshold*
- N** = A general counting parameter*
- τ** = Integration time
- M** = $(P-V)/(L+V)$ = modulation index at the receiver
- G_M** = Current gain of the photomultiplier
- R** = Photomultiplier load resistance
- G_{PA}** = Preamplifier voltage gain
- R_{PA}** = Transresistance amplifier gain, if used is equivalent to $(R)(G_{PA})$
- G_{AGC}** = Gain of the gain-controlled section. May be greater, equal to, or less than unity
- G_A** = Gain of the amplifier from the AGC section to the threshold comparator
- G** = $(G_M)(R)(G_{PA})(G_{AGC})(G_A)$
- Q** = Electronic charge in coulombs

*All of the above parameters are photoelectron counts accumulated during one integration time.

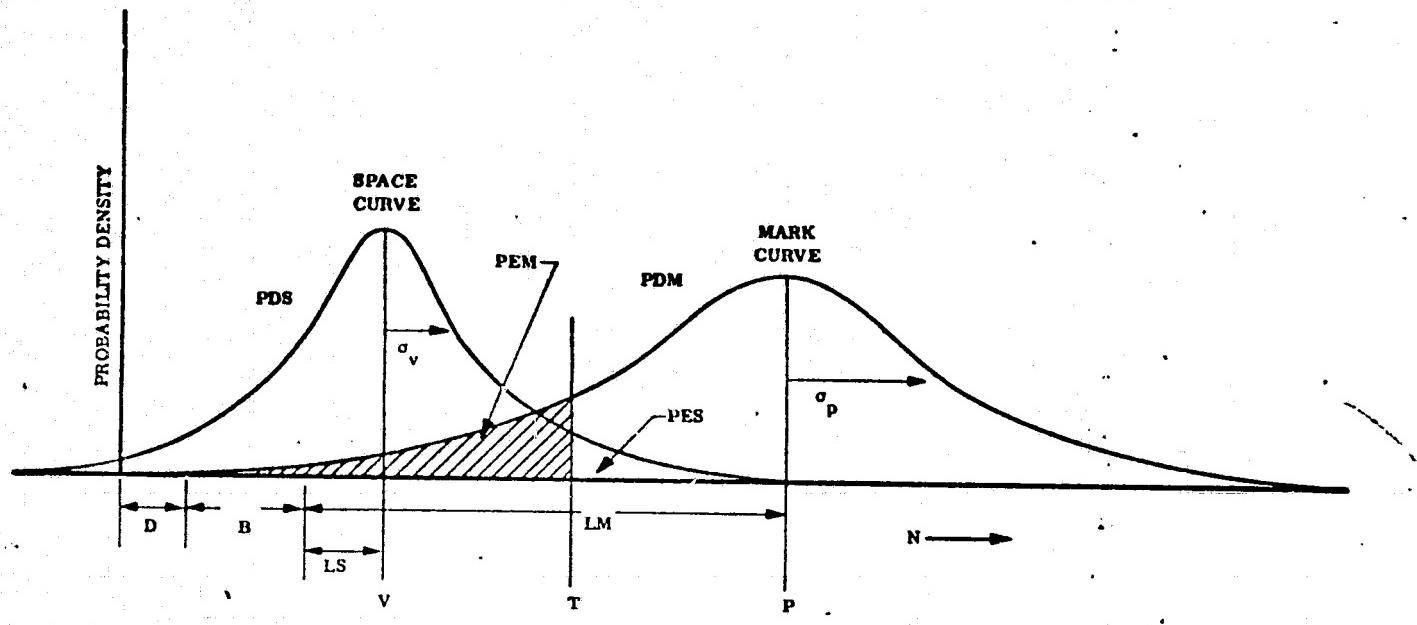


Figure 2-20. Space and Mark Normal Probability Distribution

Considering first, only the intervals in which a mark is actually received. $P(M) = 1$, the mean count is P and the value of the normal probability density curve at any count N is

$$PD = \frac{1}{\sigma_p (2\pi)^{1/2}} \exp(-0.5(|N - P|/\sigma_p)^2)$$

In general, however, the probability density curve height is scaled by the probability of occurrence of the case it represents so that the value of PDM at an arbitrary count of N will be

$$(PDM) = \frac{P(M)}{\sigma_p (2\pi)^{1/2}} \exp(-0.5 n_p^2)$$

where $n_p = \frac{|N - P|}{\sigma_p}$, the number of σ that T is from P

$$\text{and } \sigma_p = (\text{variance of } P)^{1/2}$$

Since the normal curve is intended to simulate a Poisson distribution for which the variance is equal to the mean, let $\sigma_p = \sqrt{P}$. Also, typically, but not always, $P(M) = P(S) = 0.5$ where $P(S)$ is the probability that a space occupies a randomly chosen integration time. Similarly the value of the "space curve" PDS at any count N is then

$$(PDS) = \frac{P(S)}{\sigma_v (2\pi)^{1/2}} \exp(-0.5 n_v^2)$$

$$\text{where } n_v = \frac{|N - V|}{\sigma_v}$$

$$\text{and } \sigma_v = \sqrt{V}$$

Now if τ represents an arbitrary threshold for making a mark versus space decision, the area under PDS to the left of τ is the probability that a received space (zero) will be decided to be a space, and the area PES under PDS to the right of τ is the probability that a space will be incorrectly counted as a mark. Similarly, the area under PDM to the right of τ is the probability of correctly calling a mark as a mark, and the area PEM is the probability of an error when receiving a mark.

Then the total probability of error is

$$PE = PEM + PES = \int_{-\infty}^{\tau} (PDM) dN + \int_{\tau}^{\infty} (PDS) dN$$

It may be seen from Figure 2-20 that moving τ up from V, toward P, increases PEM and decreases PES. It may also be anticipated that PE can be minimized by choosing an appropriate value for τ .

Let us find the value of τ which minimizes PE.

$$\frac{d}{dT} (PE) = (PDM) - (PDS) = 0$$

$$(PDM) = (PDS)$$

Thus the intersection of the "mark curve" and the "space curve" is the location of the optimum threshold. Note that these curves cannot simply be the tabulated probability density curves but must include the a priori $P(M)$ or $P(S)$ scaling factors. Note also that if more than one intersection occurs, the intersection at which the slopes of the curves are of opposite sign must be chosen.

It may be readily shown by equating PDM and PDS that the minimum error rate occurs for the following value of threshold count T .

$$T = \sqrt{PV} \left(1 + \frac{\ln P/V - 2\ln F(M)/P(S)}{P - V} \right)$$

For the typical case of $P(M) = P(S) = 0.5$,

$$T = \sqrt{PV} \left(1 + \frac{\ln P/V}{P - V} \right)$$

Note that for any given P/V ratio, as the values of P and V are both scaled upward, the $\ln P/V$ is divided by an increasing $P-V$. Thus in general for large counts T is closely approximated by

$$T = \sqrt{PV}$$

Consequently

$$\frac{n_p}{\sigma_p} = \frac{|P - T|}{\sigma_p} = \frac{|P - \sqrt{PV}|}{\sqrt{P}} = \sqrt{P} - \sqrt{V}$$

$$\text{also } \frac{n_v}{\sigma_v} = \frac{|T - V|}{\sigma_v} = \frac{|\sqrt{PV} - V|}{\sqrt{V}} = \sqrt{P} - \sqrt{V}$$

The threshold distance from the peak or from the valley is the same number of σ_p or σ_v for the large-count case. One may say the mark signal-to-noise ratio (SNR) is equal to the space SNR and we may speak of the SNR of the system without being ambiguous.

In the truly general and accurate normal approximation, the optimum threshold is somewhat different from \sqrt{PV} and the mark SNR is not exactly equal to the space SNR. In order to avoid ambiguity then, one must either speak of the mark and space SNR separately or must define "the SNR". A convenient definition of an unambiguous SNR is: $\sqrt{P} - \sqrt{V}_{10}$, in general, it will not by itself specify the bit error rate.

Consider now the implication of the integration from $-\infty$. A normal probability density curve is symmetrical about the mean value and extends to infinity in both directions. Obviously, in the case under consideration, a negative count N has no physical meaning. The normal curve therefore cannot be correct. It is simply used as an approximation to the Poisson distribution because of its convenient symmetry.

The Poisson probability density distribution yields the discrete (discontinuous) probability of counting any integral number of equally-probable independent events during a given time duration located arbitrarily in time. It provides, therefore, a good model for the counting of photo-electrons during any randomly located time interval of known duration.

Applying our previously defined parameters to the discrete Poisson distribution we have:

$$(PDS) = \frac{P(S) \times V^N e^{-V}}{N!}$$

and $(PDM) = \frac{P(M) \times P^N e^{-P}}{N!}$

where, in this case, N is defined to be the integral number of photoelectrons which has the probability of occurring during any arbitrarily chosen integration time for which the mean is P for a mark and V for a space. To enhance the similarity to the normal distribution case, let us plot the discrete probability of a given integer count of N occurring as an equal probability density value extending from $N-1/2$ to $N+1/2$. For the actual Poisson distribution of photoelectrons, the curves of Figure 2-20 will be replaced by curves of similar overall shape. The curves will be made up in detail of unit width vertical flat-topped bars whose heights obey the Poisson expressions given above. If we attempt to set the stepped PDS and PDM Poisson "curves" equal to each other to find the optimum threshold, it would be an extraordinary coincidence if an integer count would exist for which the two bars would be of equal height. The expected situation would be for PDS to exceed PDM at one integer value of N , and for PDM to exceed PDS for the next highest integer value of N . The optimum value of threshold would then be midway between the two integer values. Consequently, if we allow N to vary continuously and then set PDS = PDM and solve for N , we can

determine a threshold value which will lie between the proper two integer values. Theoretically, the threshold should be set midway between these integer values. Practically, it is anticipated that the precision with which T can be evaluated in a working system would not justify the additional circuit complexity necessary to approximate a threshold voltage lying midway between the two highly magnified counts existing at the point in the system where thresholding is to be applied.

The optimum threshold count (as defined above) will now be determined at the integer counting level, recognizing that the non-integer value so determined will actually be used at the high-level thresholding point in the system. Equating (PDS) and (PDM) yields

$$\frac{P(S) \times V^T e^{-P}}{T!} = \frac{P(M) \times P^T e^{-P}}{T!}$$

in which T is assumed to vary continuously, and all functions of T are assumed to be continuously defined.

$$P(S) V^T e^{-V} = P(M) V^T e^{-P}$$

$$e^{P-V} = \left(\frac{P}{V}\right)^T \left(\frac{P(M)}{P(S)}\right)$$

$$P-V = T \ln P/V + \ln P(M)/P(S)$$

$$T \ln P/V = (P-V) - \ln P(M)/P(S)$$

$$T = \frac{P-V}{\ln P/V} - \frac{\ln P(M)/P(S)}{\ln P/V}$$

For the typical case of $P(M) = P(S) = 0.5$,

$$T = \frac{P-V}{\ln P/V}$$

This then is the threshold count which, when referred up from its present photocathode level (or aperture level in the case of an image dissector) to the actual thresholding point in the system, will yield the minimum bit error rate for the typical case of $P(M) = P(S) = 0.5$.

If the signal were to be dc coupled through all intermediate circuitry, then the actual threshold voltage would be QTG/τ less any dc biases accrued by passage through the circuit elements. For practical reasons the signal will not be dc coupled through all stages. Moreover, the customary threshold, T_C , midway between the amplified peak and amplified valley is readily achieved. Thus

$$T_C = \frac{P+V}{2} \frac{QG}{\tau}$$

may be achieved without regard to the numerical values of G , τ , or Q by means of two suitably connected peak detectors.

It would therefore be desirable to manipulate the expression for the ideal Poisson threshold into a form in which the mean of the peak and valley would constitute the primary component of the threshold and the remainder of the expression would represent an adaptive adjustment. The required manipulation is displayed below:

For $x > 0$, $\ln(x) = 2 \left[\frac{y}{1} + \frac{y^3}{3} + \frac{y^5}{5} + \dots \right]$

where $y = \frac{x-1}{x+1}$

If $x = (P/V)$

$$\text{then } y = \frac{(P/V) - 1}{(P/V) + 1} = \frac{P-V}{P+V} = M$$

where M equals the modulation index apparent at the receiver.

So for $(P/V) > 0$,

$$\ln(P/V) = 2 \left[\frac{M}{1} + \frac{M^3}{3} + \frac{M^5}{5} + \dots \right]$$

$$\ln(P/V) = 2 \left(\frac{P-V}{P+V} \right) \left[1 + \frac{M^2}{3} + \frac{M^4}{5} + \dots \right]$$

Then

$$T = \frac{P+V}{2} \left[\frac{1}{1 + \frac{M^2}{3} + \frac{M^4}{5} + \dots} \right]$$

$$T = \frac{P+V}{2} \left[1 - \frac{M^2}{3} - \frac{14M^4}{45} - \frac{36M^6}{14175} - \frac{80M^8}{42525} - \dots \right]$$

$$T = \frac{P+V}{2} - \frac{P+V}{2} \left[\frac{M^2}{3} + \frac{14M^4}{45} + \frac{36M^6}{14175} + \frac{80M^8}{42525} + \dots \right]$$

$$T = \frac{P+V}{2} - (P-V) \left[\frac{M}{6} + \frac{14M^3}{90} + \frac{36M^5}{28350} + \frac{80M^7}{85050} + \dots \right]$$

$$T = \frac{P+V}{2} - (P-V) \left[0.166667M + 0.155556M^3 + 0.001270M^5 + 0.000941M^7 + 0.00019M^9 + \dots \right]$$

$$T = \frac{P+V}{2} - (P-V) [f(M)]$$

This last expression may be referenced to the actual thresholding point in the circuit by multiplying, as previously, by the factor QG/τ .

$$QTG/\tau = \left(\frac{P+V}{2} \right) \left(\frac{QG}{\tau} \right) - \left(\frac{QG}{\tau} \right) (P-V) [f(M)]$$

The first term represents the potential midway between the mark and space potentials delivered to the thresholding circuit and can be "delivered" by a circuit similar to Figure 2-21 in which the adaptive component is set to zero.

The circuit consists basically of two peak detectors of opposite polarity, such that the potential difference between their filter capacitors is equal to the peak-to-peak swing between the amplified mark and space levels. This whole circuit is referenced to ground by a center-tap on a resistor connecting the two filter capacitors. Thus the potential midway between the mark and space potentials applied to the comparator is forced to be equal to zero. Referencing the comparator to zero, then also puts the threshold at the average mark and space potentials.

Now consider the adaptive portion V_A of the previous expression for high-level threshold.

$$V_A = - \frac{QG}{\tau} (P-V) \left[0.166667M + 0.155556M^3 + 0.001270M^5 \right. \\ \left. + 0.000941M^7 + 0.00019M^9 + \dots \right]$$

Now recognize again the $(QG/\tau)(P-V)$ is the actual difference between the mark and space levels (peak-to-peak voltage) as measured at the thresholding point in the circuitry. Note also that this quantity is tightly controlled by the AGC circuit and may be considered constant. Thus the only variable component of the expression for the adaptive portion of the threshold voltage is the infinite series representing the function of M , the apparent modulation index. Since this function is precalculable, it can be stored in a function generator. Thus the only variable parameter whose value must be known, to set the adaptive threshold, is M . Measurement of M is ideally possible by combining $0.5(P+V)(QG_M R_L / \tau)$ available at the photomultiplier output with $(QG/\tau)(P-V)$ available at the AGC detector output. The practical difficulty lies in determining $G/G_M R_L$, the gain between the photomultiplier output and the thresholding point in the circuit. The practical difficulties involved in evaluating M , due to determining this gain to the required accuracy, appear to render this approach unreliable.

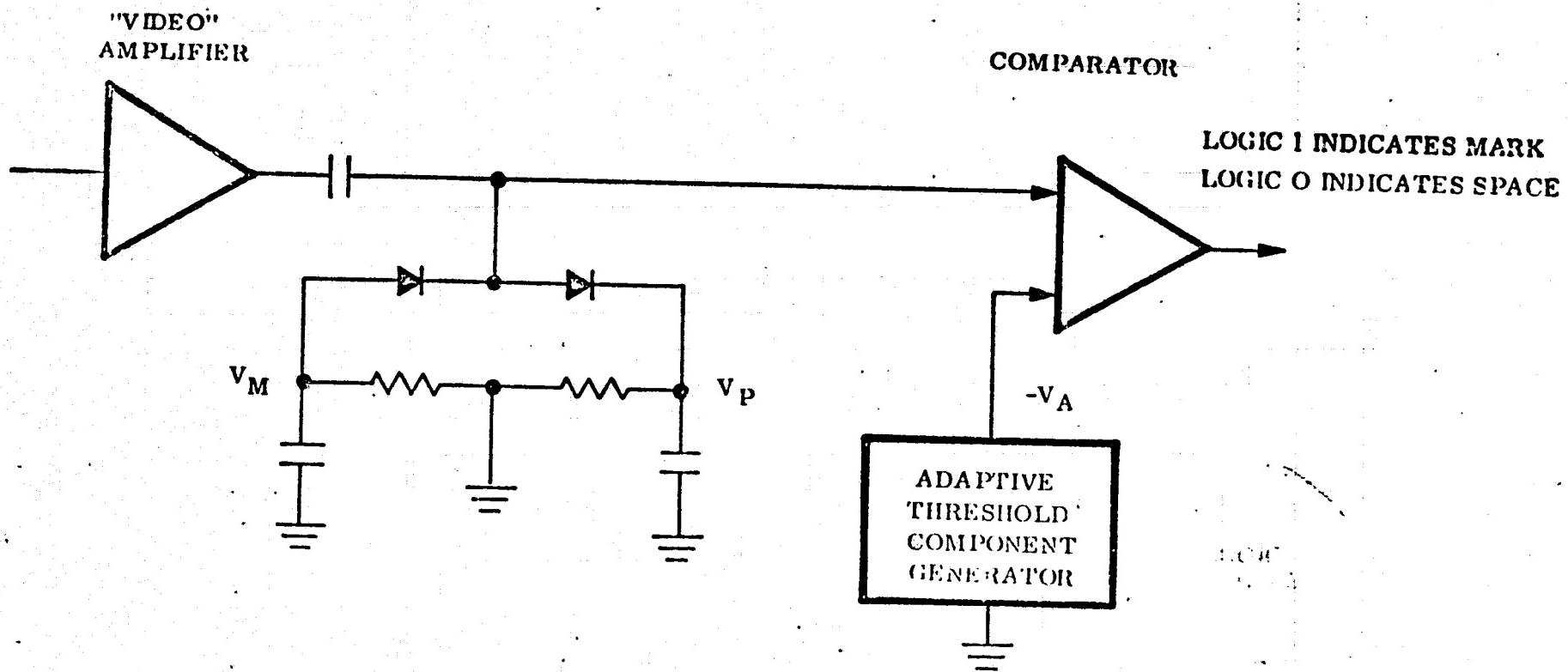


Figure 2-21. Implementation of Threshold Equation

2.5.2 Practical Threshold-Circuit. - In the search for a realizable adaptive threshold circuit, the following concept evolved. It was recognized by a numerical investigation that, at the level of electron counts involved, little difference occurs in the signal-to-noise ratio, whether a Poisson distribution or its normal approximation is chosen. Accordingly the situation of primary interest was recognized to be the attainment of signal-to-noise ratios (SNR's) during mark intervals and during space intervals which are proportional to the probability of occurrence of marks and spaces. In the typical case of $P(M) = P(S) = 0.5$, the Mark SNR should equal the Space SNR in order to minimize the sum of the mark and space bit error rates. Equal SNR's will be attained when the mark-to-threshold distance bears the same ratio to the mark noise as the space-to-threshold distance bears to the space noise. A circuit was devised which will yield a measure of the mark noise on one wire and a measure of the space noise on a second wire. Figure 2-22 includes enough detail to indicate the theory of operation of this adaptive threshold method.

The two center diodes and two capacitors form two peak detectors whose detection efficiencies are adjusted such that the upper capacitor floats at the average space level. Note that during a space, the upper capacitor remains at the mark level, and during a mark, the lower capacitor remains at the space level. The capacitors thus act both as a reference voltage for their respective differential amplifiers as well as a bias source for the diode feeding of the other differential amplifier input terminal. The net result is that the upper differential amplifier yields an output waveform consisting of a zero baseline which rises only to follow the excursions of the mark noise above the average mark level. Similarly the lower differential amplifier output waveform consists of a zero baseline which rises to follow the excursions of the space noise below the average space level. The peak detectors following the differential amplifiers then yield dc voltages proportional to the mark and space noises, respectively. These dc voltages are summed, amplified and gain controlled to a level equal to half the peak-to-peak voltage of the input bit stream. The dc output of the lower peak detector is put onto a carrier and passed through the same gain controlled channel and then demodulated back to a dc voltage. The summing resistor R2 from the modulator to the amplifier is adjusted so that the gain from D to C is twice the gain from A to C (assuming the MOD and DEMOD gains are unity). The reference voltage R is one half the peak-to-peak signal voltage and

$$\frac{P-V}{2} = K \sigma_P G_{BC} + K \sigma_V G_{DC}$$

since $G_{BC} = G_{DC}$

then $\frac{P-V}{2} = K(\sigma_P + \sigma_V)G_{DC}$

Also the threshold voltage (above ground) is

$$T = K\sigma_V G_{AC}$$

$$\frac{T}{(P-V)/2} = \frac{K\sigma_V G_{AC}}{K(\sigma_P + \sigma_V)G_{DC}}$$

$$\frac{T}{P-V} = \left(\frac{2G_{AC}}{G_{DC}} \right) \left(\frac{\sigma_V}{\sigma_P + \sigma_V} \right)$$

Since we have set $G_{DC} = 2G_{AC}$

$$\frac{T}{P-V} = \frac{\sigma_V}{\sigma_P + \sigma_V}$$

Since the signal waveform into the comparator has its negative peak (valley) clamped to zero, we can write:

$$\frac{T-V}{P-V} = \frac{(T-V)}{(P-T) + (T-V)} = \frac{\sigma_V}{\sigma_P + \sigma_V}$$

or $\frac{T-V}{P-T} \approx \frac{\sigma_V}{\sigma_P}$

Thus the circuit sets the threshold such that its distances from P and from V are proportional to the respective noise levels, and the bit error rate is thus minimized.

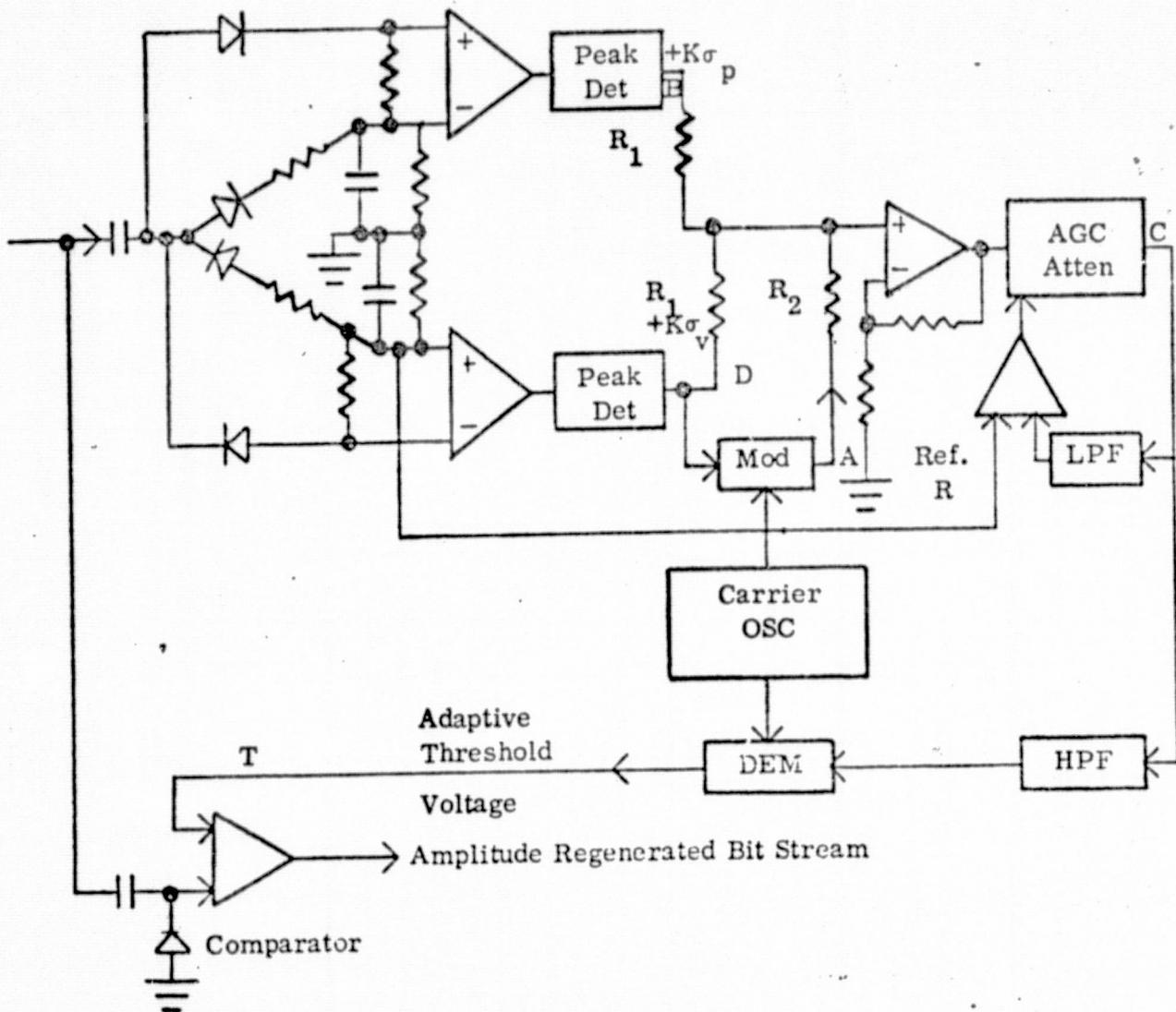


Figure 2-22. Theory Schematic of Adaptive Threshold Generator

2.6 Analysis of the Ground Based Acquisition System

The purpose of this section is to briefly state the analytic approach and results obtained on examining the requirements and performance of an active ground based acquisition system. This system utilizes a pulsed laser transmitter, and retroreflective (cubecorner) targets on a cooperative aircraft. The laser is scanned in space over the expected aircraft path, and when the aircraft enters the beam, the reflected signal is detected by an image dissector phototube camera.

The relationships between the ground equipment characteristics (laser power, pulse repetition rate, wavelength, optics aperture, detector sensitivity), target characteristics (size and number of retroreflectors), aircraft parameters (altitude, velocity), and predicted system performance (detection probability, false alarm rate) are examined, and specific cases of interest are discussed.

Developed in the following paragraphs are the relationships between the scan geometry of the laser transmitter, the aircraft velocity and altitude, the pulse repetition rate of the laser, and the beam divergence of the laser transmitter (i.e., the scan element angular size).

The geometry of the system is shown in Figure 2-22. The aircraft is flying at velocity v and altitude H , and is at range R from the ground based acquisition system. The line of sight from the ground station to the aircraft is at an angle θ with the local vertical. The angular velocity of the aircraft with respect to the ground station is $\dot{\theta}$. The acquisition system transmits laser pulses of angular width $\Delta\phi$, using n such pulses to sweep out the search scan angle Ψ . Successive pulses overlap by the fraction ρ_x .

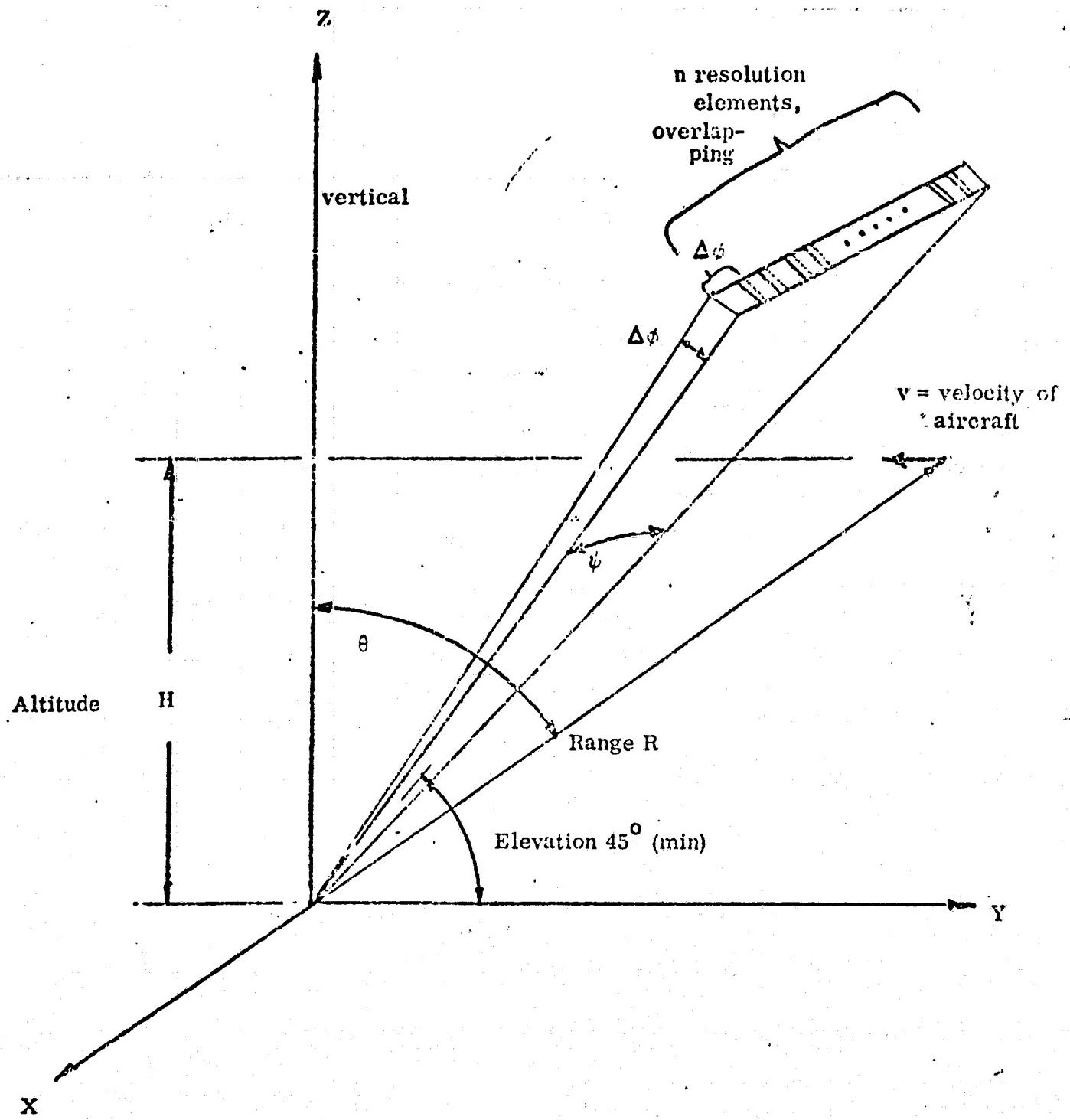


Figure 2-22. System Geometry

REPRODUCIBILITY OF THE
COPYRIGHT PAGE IS POOR

The image dissector camera is effectively inactive during its retrace, which requires some fraction ϵ of the trace scan period.

In order to allow some time, T_{acq} , to change mode of operation of the ID Camera from "search" to "acquisition and track", an effective overlap in the scanning scheme is provided in the direction of the aircraft velocity. The overlap factor is ρ_y .

The target aircraft is known to be flying a course that will pass within the search scan angle ψ , and is traveling with an angular velocity θ ; therefore, its possible position sweeps out a solid angle at a time rate of

$$\Omega_a = \psi \theta \quad (1)$$

(The subscript a refers to "aircraft".)

The ground acquisition system operating in the search mode must sweep out or scan its search field of view at a somewhat faster rate, because of the overlap factors and ID tube retrace factor previously mentioned. The search sweep rate of the system is

$$\Omega_s = \Omega_a (1 + \epsilon) (1 + \rho_x) (1 + \rho_y), \quad (2)$$

or, from (1) and (2),

$$\Omega_s = \psi \theta (1 + \epsilon) (1 + \rho_x) (1 + \rho_y) \quad (3)$$

A diagram illustrating the above relationship is shown in Figure 2-23.

Let the laser pulse repetition rate be f pulses per second, the time between pulses be t seconds, and the laser beam have a square cross section of angular dimension $\Delta\phi$.

ϵ = retrace factor

ρ_x = overlap factor, x

ρ_y = overlap factor, y

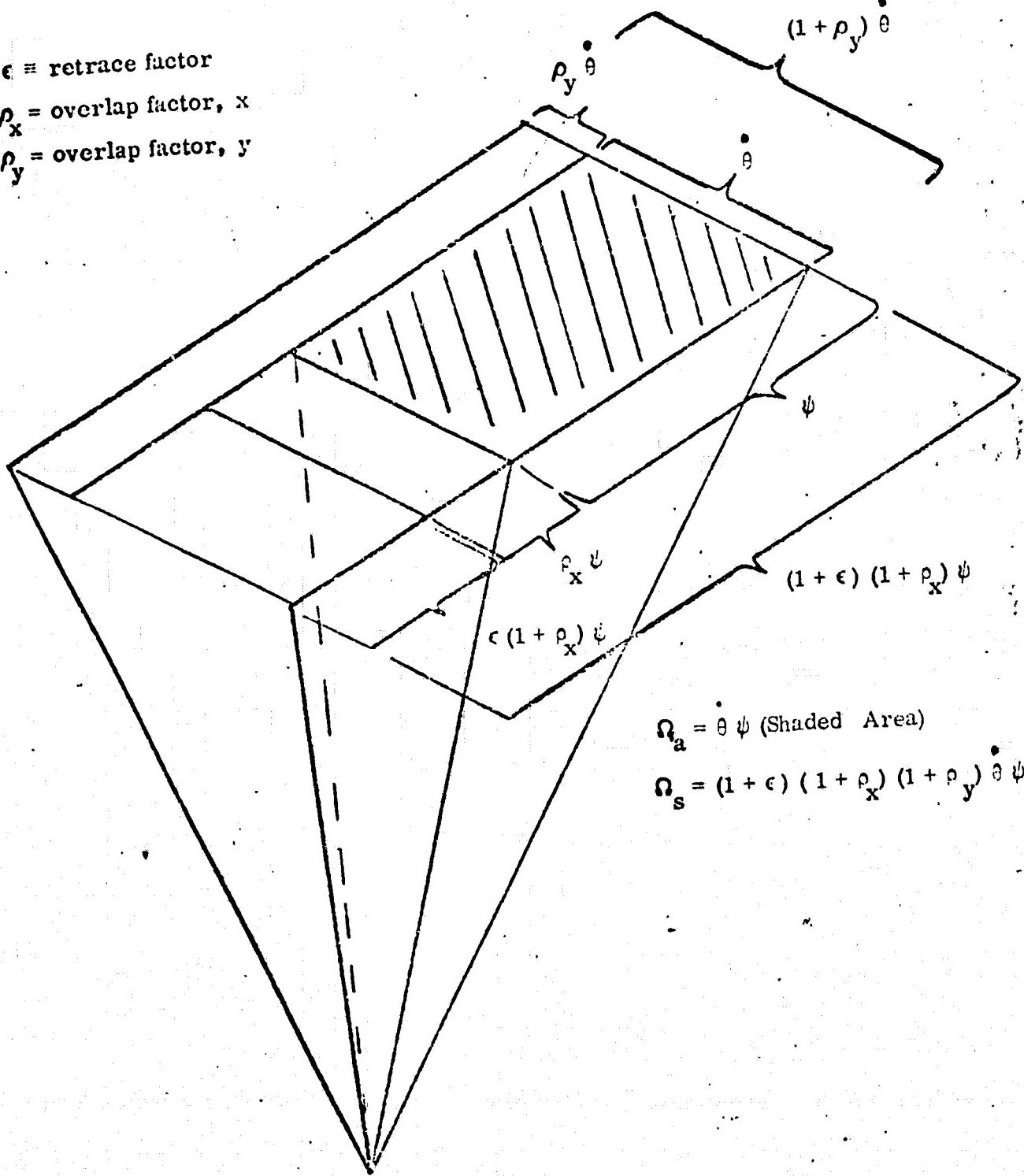


Figure 2-23. Representation of Solid Angle scan rate (steradians/sec)
for aircraft (Ω_a) and search system (Ω_s).

The pulse repetition rate is the reciprocal of the time between pulses, i.e.,

$$f = \frac{1}{\tau} \quad (4)$$

The solid angle of the laser beam must be

$$(\Delta\phi)^2 = \frac{\Omega_s}{f} = \frac{\Omega_s}{s} \tau \quad (5)$$

The number of elements per search scan line, n , is then

$$n = \frac{\psi(1 + \rho_x)}{\Delta\phi} \quad (6)$$

Taking the square root of equation (5), and substituting in (6), one obtains

$$n = \frac{\psi(1 + \rho_x)}{[\Omega_s \tau]^{1/2}} \quad (7)$$

Substituting (3) into (7),

$$n = \frac{\psi(1 + \rho_x)}{[\psi \theta (1 + \epsilon) (1 + \rho_x) (1 + \rho_y)]^{1/2}} \quad (8)$$

This simplifies to:

$$n = \left[\frac{\psi(1 + \rho_x)}{\theta(1 + \epsilon)(1 + \rho_y)\tau} \right]^{1/2} \quad (9)$$

The time T_ϕ for the aircraft to pass through the beamwidth $\Delta\phi$ is

$$T_\phi = \frac{\Delta\phi}{\dot{\theta}} \quad (10)$$

The minimum (worst case) time the system will have to perform the mode change from "search" to "acquisition and track" is

$$T_{\text{acq}} = \rho_y T_\phi = \frac{\rho_y \Delta\phi}{\dot{\theta}} \quad (11)$$

The search line scan period, τ_ψ , is

$$T_\psi = n \tau (1 + \epsilon) \quad (12)$$

Also,

$$T_\psi = T_\phi (1 - \rho_y) \quad (13)$$

It should be noted that

$$T_\phi = T_\psi + T_{\text{acq.}} \quad (14)$$

Application to Specific Cases

The relationships derived in Section 2.1 are now applied to specific cases of interest, and the results presented in tabular form. These results are utilized later in radiometric calculations.

The following values are assumed:

$$\psi = 10 \text{ degrees}$$

$$\dot{\theta} = 0.5 \text{ degree/second}$$

$$\epsilon = 0.2$$

$$\rho_x = 0.1$$

$$\rho_y = 0.2$$

It is noted that θ , in radians/sec, is

$$\dot{\theta} = -\frac{v}{H} \cos^2 \theta, \text{ where } v \text{ is the aircraft velocity and } H \text{ its altitude.}$$

The assumed value of 0.5 deg/sec, is appropriate for acquisition at $\theta = 45$ degrees for an aircraft of velocity 675 ft/sec (400 nautical miles/hour) at an altitude of 40,000 feet or greater.

Several pulse repetition rates are of interest, corresponding to the ranges available from Gallium Arsenide semiconductor diode lasers and pulsed Argon ion gas lasers.

The specific values chosen for f are:

200; 400; 1,000; 2,000; 4,750.

Using the above assumed values in Equation (4) and (9), one can calculate n , the number of laser pulses (or resolution elements) per scan. This result is substituted into Equation (6), which is solved for $\Delta\phi$.

Also, T_ϕ , T_{acq} , and T_ψ are calculated from Equations (10), (11), and (12).

The results are tabulated in Table I.

2.7 System Performance Prediction

The purpose of this discussion is to determine the relationships among the GBAA system parameters and to predict the system performance in a specified environment. The procedure to determine performance will be to establish the required signal power level required to achieve a specified detection and false alarm probability during a laser radar pulse period.

The required photoelectron current is determined, based on an assumed background radiation level. This required photoelectron current is then used as a basis for computing the required radiant flux density at the ground station, with specific values assumed for the optical collector area, optical efficiency, and photocathode sensitivity. The radiant flux density at the ground is then used to compute the required radiant flux density at the ground station, with specific values assumed for the optical collector area, optical efficiency, and photocathode sensitivity. The radiant flux density at the ground is then used to compute the required radiant flux density at the aircraft, for assumed values of atmospheric transmittance, number of retroreflectors and area of each. Finally, the required laser power for various ranges is calculated, based on the required flux density at the aircraft, assumed value of atmospheric transmittance, and solid angle of the laser beam.

2.7.1 Required Photoelectron Current. - The average current \bar{i}_b (in electrons/sec) due to background in the image dissector phototube receiver is

$$\bar{i}_b = N_b \Delta_\lambda T_F T_R K_{\Delta\lambda} A_R W_R e^{-1}, \quad (15)$$

where:

N_b is the background spectral brightness, in $\frac{\text{watts}}{\text{cm}^2 \text{-steradian-}\mu}$, evaluated at

the laser wavelength.

Δ_λ is the width of the spectral filter in the receiver, in microns.

T_F is the optical filter transmittance

T_R is the optical transmittance of the receiver

$K_{\Delta\lambda}$ is the image dissector photocathode spectral sensitivity at the laser wavelength, in amps/watt, or equivalently, in coulombs/sec-watt.

A_R is the area of the receiver optics, in cm^2

W_R is the solid angle of the instantaneous field of view of the receiver, in steradians.

e is the electronic charge, in coulombs/electron.

Dimensional analysis of Equation (15) shows consistency, i.e.,

$$\frac{\text{watts}}{\text{cm}^2 \cdot \text{ster} \cdot \mu} \cdot \mu \cdot \frac{\text{coul}}{\text{sec-watt}} \cdot \frac{\text{cm}^2}{\text{ster}} \cdot \frac{\text{electrons}}{\text{coul}} = \frac{\text{electrons}}{\text{sec}}$$

A convenient approximation in working with small solid angles is that a solid angle expressed in degrees² can be converted to steradians by multiplying by 3.046×10^{-4} steradian/degree². The solid angle field of view of the image dissector receiver must be somewhat larger than the solid angle of the transmitted laser beam, to account for the tolerance in the mutual alignment of the transmitter and receiver under dynamic search conditions. (For tracking, it may be desirable to have the laser beam solid angle larger than the instantaneous field of view of the receiver, so that the image dissector can "dither" without "dithering" the laser beam.)

Assuming that an overlap of 0.17 in each dimension is adequate, then the receiver field of view solid angle must be $(1.17)^2$ or 1.40 times as large as the transmitted beam solid angle, or

$$W_R = 1.4 (\Delta\phi)^2 \quad (16A)$$

for $\Delta\phi$ in radians, and

$$W_R = 1.4 (\Delta\phi)^2 \times 3.046 \times 10^{-4} \quad (16B)$$

for $\Delta\phi$ in degrees

The following values are used for the quantities in Equation (15), and are applicable to a Gallium Arsenide Laser operating at a wavelength of 0.9μ .

$$N_b = 8 \times 10^{-4} \quad (\text{Blue sky, at } 0.9 \mu)$$

$$\Delta_\lambda = 0.2$$

$$T_F = 0.8$$

$$T_R = 0.7$$

$$K_{\Delta\lambda} = 3 \times 10^{-3} \quad (\text{S-25 photocathode, at } 0.9 \mu)$$

$$A_R = 55 \quad (\text{lens dia. approx. } 8.3 \text{ cm})$$

$$e = 1.6 \times 10^{-19}$$

The result is,

$$\bar{i}_b = 9.24 \times 10^{12} (W_R) \text{ electrons/sec} \quad (17)$$

For the Argon laser operating at 0.514 micron, the appropriate values for use in Equation 15 are $N_b = 3 \times 10^{-3}$, and $\Delta_\lambda = 2 \times 10^{-3}$, and $K_{\Delta\lambda} = 6 \times 10^{-2}$, and the result is:

$$\bar{i}_b = 6.93 \times 10^{13} (W_R) \text{ electrons/sec} \quad (18)$$

It is noted that the assumption of a blue sky background is appropriate for a cooperative high altitude aircraft, since no clouds are likely at the high altitude, and any clouds present at lower levels will probably obscure the aircraft completely.

The required signal current for a given probability of detection, PD, and time between false alarms, TFA, is dependent on the background current, and the electronic bandwidth Δf of the system. The bandwidth may be set based on the laser pulse width at 1/2 power, t .

$$\Delta f = \frac{1}{2t} \quad (19)$$

Using Gaussian statistics, which approximate the more exact Poisson approach at higher current levels, one can obtain the following relationships:

$$i_t = \bar{i}_b + \sqrt{\pi k (\Delta f) \bar{i}_b \log_e \left[\frac{TFA (\Delta f)}{2} \right]} \quad (20)$$

$$i^2 + i [\pi k (\Delta f) \log_e 4(1-PD) - 2 i_t] + i_t^2 = 0 \quad (21)$$

$$i_s = i - \bar{i}_b \quad (22)$$

The total current i is the sum of the background current and signal current, and i_t is the threshold current. The factor k is a noise factor associated with the dynode gain in a photomultiplier, and is approximately equal to 1.6.

The method for determining the required signal current is to compute \bar{i}_b from Equation 17 or 18, as appropriate; next, compute Δf from Equation 19; select a probability of detection and time between false alarms, and solve Equation (20) for threshold current, i_t ; use this result in Equation (21), and solve for i ; finally, solve Equation (22) for the signal current required.

A computer program for implementing the above method was written. It was utilized for the Gallium Arsenide analysis, which requires $\Delta f = 5 \times 10^6$ Hz, based on a 100 nanosecond pulse duration. The output data is i_s for various \bar{i}_b values, for a specified PD (0.990) and TFA (100 seconds). The data is shown in Table 2-5 and plotted in the graph of Figure 2-24.

From Table 2-6, the angle of the laser beam, $\Delta\alpha$, for the various pulse repetition rates of interest, can be determined. This is used to determine W_R , the solid angle of the receiver, from Equation (16 b), which is substituted into Equation (17) to determine \bar{i}_b . Then, i_s is determined from the graph of Figure 2-24. The results are tabulated in Table 2-7, along with other related data.

TABLE 2-5. SIGNAL CURRENT CALCULATION FOR GALLIUM ARSENIDE LASER

INPUT DATA

K = 1.60
PD = 0.9900
IFA = 0.10000E 03

I _B BAR	F _D LTA	I _T	I _S	S/N
0.10000E 07	0.50000E 07	0.23045E 08	0.12165E 09	0.49125E 01
0.10000E 08	0.50000E 07	0.79713E 08	0.20007E 09	0.61733E 01
0.10000E 09	0.50000E 07	0.32045E 09	0.42691E 09	0.83173E 01
0.10000E 10	0.50000E 07	0.16971E 10	0.11103E 10	0.10809E 02

REPRODUCIBILITY OF THE
ORIGINAL PAGE IS POOR

2-76

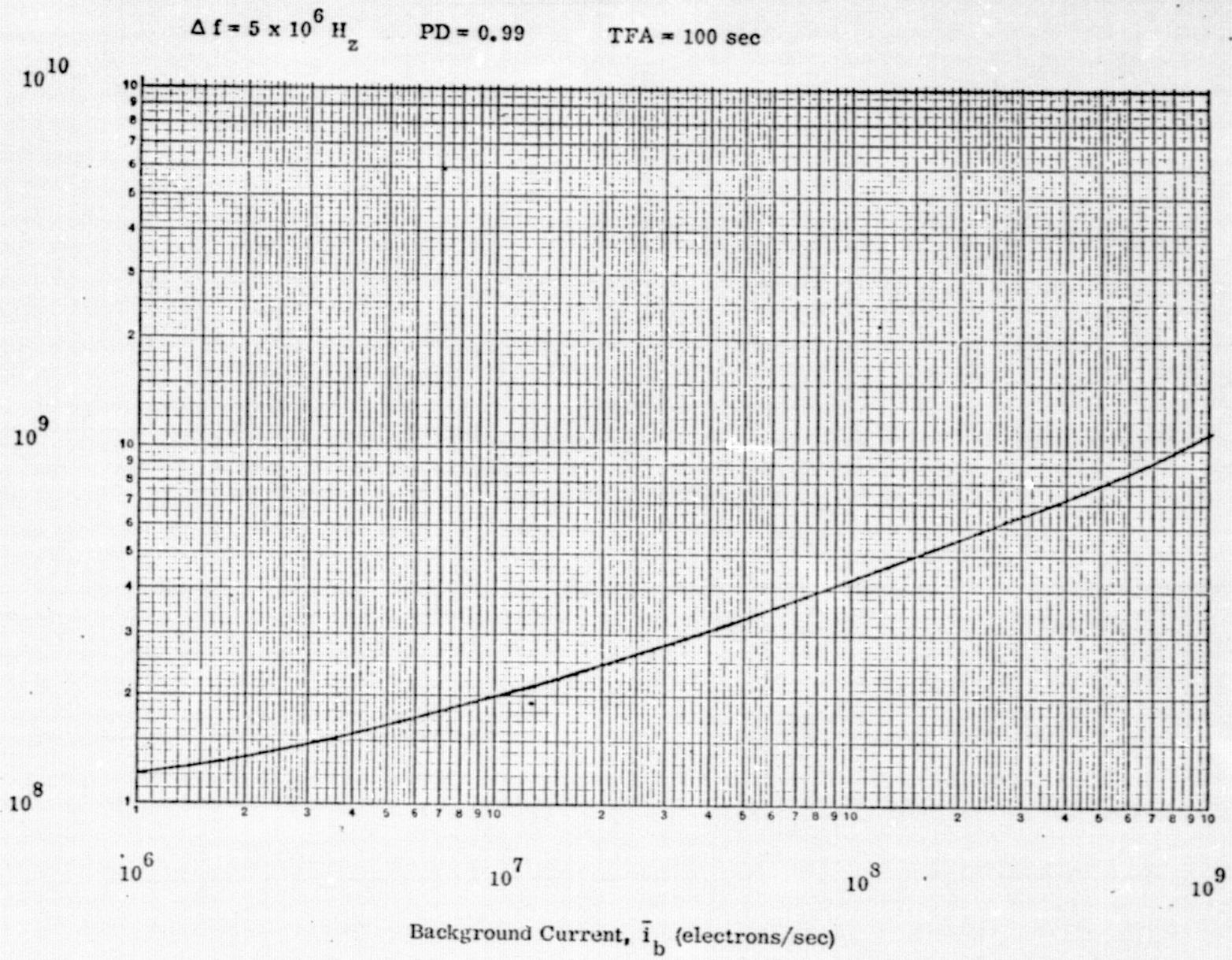


Figure 2-24. Required Signal Current Versus Background Current for Gallium Arsenide System

TABLE 2-6

f (sec^{-1})	τ (sec)	n	$\Delta\phi$ (deg)	T_ψ (sec)	T_ψ (sec)	T_{acq} (sec)
200	0.0050	58	0.1897	0.3793	0.3161	0.063
400	0.0025	82	0.1342	0.26832	0.2236	0.045
1,000	0.0010	129	0.08527	0.1705	0.1421	0.028
2,000	0.0005	183	0.06011	0.1202	0.1002	0.020
4,750	0.00021	281	0.03915	0.0783	0.0652	0.013

TABLE 2-7

f (sec $^{-1}$)	w_T steradian	w_R steradian	i_b electrons/ sec	i_s electrons/ sec	FDG watts/cm 2	FDG watts/ft 2
1000	2.215×10^{-6}	3.101×10^{-6}	2.865×10^8	2.75×10^8	4.76×10^{-10}	4.42×10^{-7}
2000	1.101×10^{-6}	1.54×10^{-6}	1.423×10^7	2.22×10^8	3.84×10^{-10}	3.57×10^{-7}
4750	4.67×10^{-7}	6.54×10^{-7}	6.041×10^6	1.75×10^8	3.03×10^{-10}	2.81×10^{-7}

2.7.2 Flux Density at the Ground Terminal. - The required retroreflected irradiance (flux density) from the cooperative cubecorner targets returning to the receiver, FDG, is derivable from the following equation:

$$\frac{i_s \text{ electrons}}{\text{s scc}} = \frac{(FDG) A_R T_F T_R K \Delta\lambda}{e} \quad (23)$$

Thus,

$$(FDG) = \frac{i_s e}{A_R T_F T_R k \Delta\lambda} \quad (\text{watts/cm}^2) \quad (24)*$$

For the Gallium Arsenide laser,

$$(FDG) = i_s \left[\frac{1.6 \times 10^{-19}}{(55)(.8)(.7)(3 \times 10^{-3})} \right] = i_s \left[1.73 \times 10^{-18} \right] \quad (25)*$$

For the Argon laser,

$$\begin{aligned} (FDG) &= i_s \left[\frac{1.6 \times 10^{-19}}{(55)(.8)(.7)(6 \times 10^{-2})} \right] \\ &= i_s \left[8.66 \times 10^{-20} \right] \end{aligned} \quad (26)*$$

2.7.3 Flux Density at Aircraft. - The dimension of flux density at the aircraft, FDA, is taken as watts/ ft^2 , for convenience, i.e., so the range R from the ground to the aircraft can be in feet. The area A_c of each of the N cubecorners is 0.0278 ft^2 . Because of atmospheric scintillation, the cubecorners will not be illuminated uniformly during any particular laser pulse. Some may not be illuminated at all. Therefore, to include this effect in the analysis, a scintillation efficiency factor, n , is introduced.

* Multiply by $929 \text{ cm}^2/\text{ft}^2$ to convert to watts/ ft^2

The flux density at the aircraft, for a peak laser power of P watts, is:

$$FDA = \frac{PT_A T_T}{R^2 W_T} \text{ watts/ft}^2 \quad (27)$$

2.7.4 Required Laser Power. - The flux density on the ground (watts/ft²), resulting from the retroreflection of the laser beam producing the flux density at the aircraft is

$$\begin{aligned} FDG &= \frac{\eta N A_c (FDA) T_c T_A}{R^2 W_c} \\ &= \eta N A_c P T_A^2 T_c T_T / R^4 W_c W_T \end{aligned} \quad (28)$$

$$\text{or } P = \frac{R^4 W_T W_c (FDG)}{\eta N A_c T_A^2 T_T T_c} \quad (29)$$

The symbol W_c is the solid angle of the beam from the retroreflecting cubecorners, and is assumed to be 4×10^{-10} steradians, corresponding to a 4 sec beam spread.

T_c is the cubecorner transmittance.

Substituting for (FDG) from Equation (24) into Equation (29)

$$P = \frac{R^4 W_T W_c i_s e}{\eta N A_c T_A^2 T_c T_T A_R T_F T_R k \Delta \lambda} \quad (30)$$

This equation states that for a given required signal current, the laser power required increases directly as the solid angle of the transmitter and cubecorner beams; increases with range to the fourth power; and is inversely proportional to the square of the atmospheric transmission; is inversely proportional to the optical transmission of transmitter, cubecorner, and receiver; the area of the N cubecorners and of the receiver; and inversely proportional to the spectral sensitivity. All of these factors are in the right direction, which serves as a check on the correctness of the derivation.

Equation (29) is solved for P , using the various values of W_T previously listed in Table 2-5, for several ranges.

Assume $\eta = 0.5$ (i.e., half the cubecorners are unilluminated due to scintillation effects). Assume $N = 16$, $T_A = 0.1$, $T_C = 0.9$, $T_T = 0.5$. Substituting into Equation (29), one obtains

$$P = 4.0 \times 10^{-7} [R^4 W_T (\text{FDG})] \quad (31)$$

Table 2-8 lists the results for the Gallium Arsenide laser.

All the parameter values used for the Gallium Arsenide case are listed below.

Calculations on a pulsed Argon laser system were performed manually. Assumptions, calculation method, and results are summarized below.

The Argon laser operates at $f = 400$ pulses per second, and the pulse width (1/2 power), t , is 1 microsec. From Equation (19), $\Delta f = 10^5$ Hz. From Equation (9), $n = 82$. From Equation (6), $\Delta\phi = 0.134$ degrees, which makes the solid angle $(\Delta\phi)^2$ equivalent to $W_T = 5.48 \times 10^{-6}$ steradians. Substituting this into Equation (18) gives $i_b = 3.79 \times 10^8$ electrons/sec. From Equation (20), $i_t = 4.33 \times 10^8$ electrons/sec. From Equation (21), $i_s = 4.553 \times 10^8$ electrons/sec, giving $i_s = 7.63 \times 10^7$ electrons/sec, from Equation (22). From Equation (26), $\text{FDG} = 6.61 \times 10^{-12}$ watts/cm², or 6.16×10^{-9} watts/ft². Substituting into Equation (31), using the desired range R , the required laser power P is obtained. Results are tabulated in the lower portion of table 2-8.

TABLE 2-8

<u>f sec⁻¹</u>	<u>FDG watts/ft²</u>	<u>W_T steradian</u>	<u>R feet</u>	<u>R⁴ ft⁴</u>	<u>P watts</u>
1000	4.42×10^{-7}	2.22×10^{-6}	10^5	10^{20}	39.2
			$.7 \times 10^5$	$.24 \times 10^{20}$	9.42
			$.5 \times 10^5$	$.62 \times 10^{19}$	2.42
2000	3.57×10^{-7}	1.10×10^{-6}	10^5	10^{20}	15.7
			$.7 \times 10^5$	$.24 \times 10^{20}$	3.76
			$.5 \times 10^5$	$.62 \times 10^{19}$.973
4750	2.81×10^{-7}	4.67×10^{-7}	10^5	10^{20}	5.25
			$.7 \times 10^5$	$.24 \times 10^{20}$	1.26
			$.5 \times 10^5$	$.62 \times 10^{19}$.326
400	6.16×10^{-9}	5.48×10^{-6}	10^5	10^{20}	1.36
			$.7 \times 10^5$	$.24 \times 10^{20}$.325
			$.5 \times 10^5$	$.62 \times 10^{19}$.084

Gallium
Arsenide

Argon

GaAs Laser Peak Power (Watts)

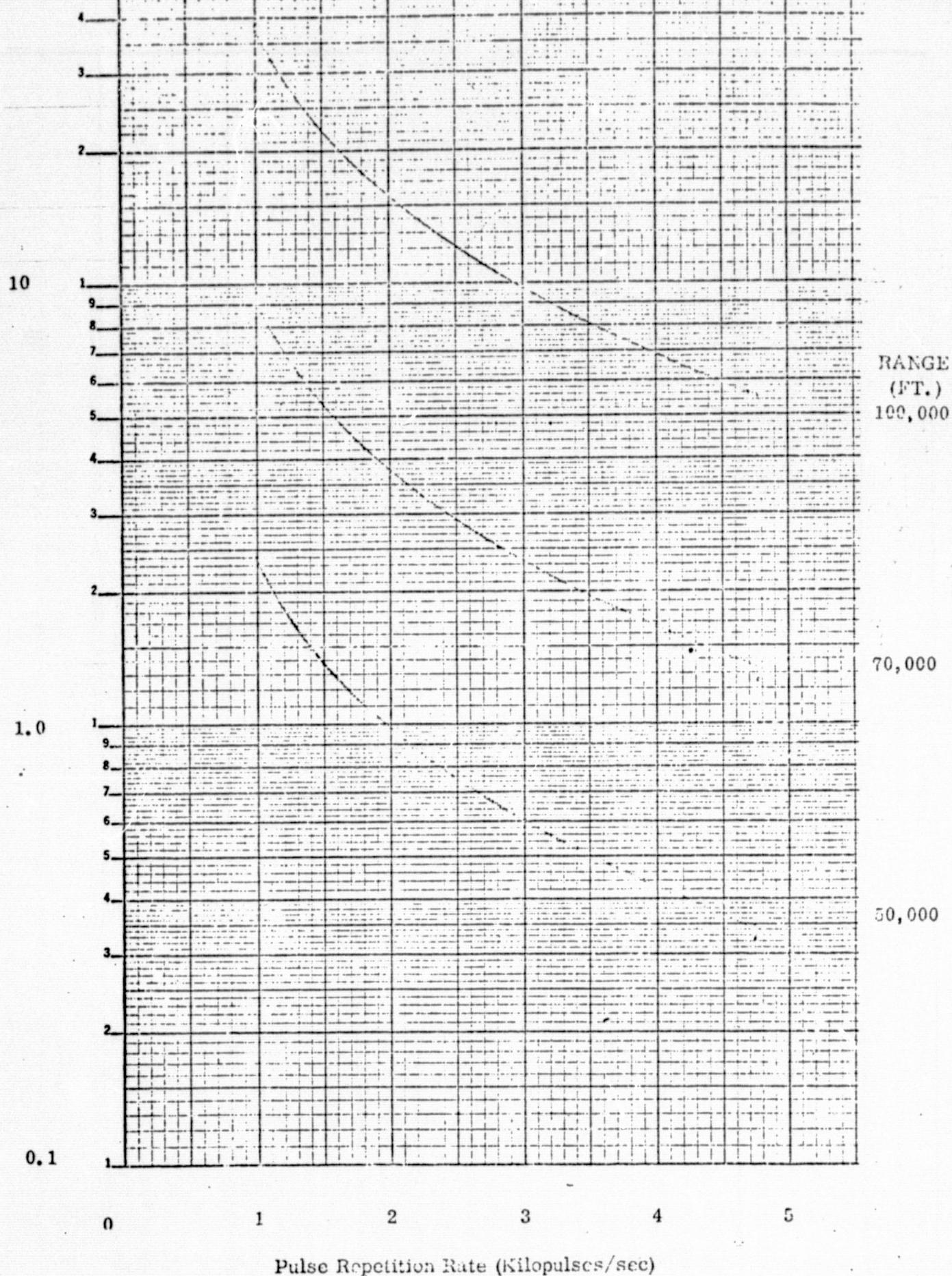


Figure 2-25. Required Peak Laser Power Versus Pulse Repetition Rate
for Gallium Arsenide System

REPRODUCIBILITY OF THE
ORIGINAL PAGE IS POOR

TABLE 2-8. CONDITIONS FOR CALCULATION ON GaAs SYSTEM

Laser pulse length 100 nanosec

Wavelength 0.9μ

$\Delta \lambda = .02\mu$ (200A)

$\Delta f = 5$ Megahertz

16 cube corners, 4 in² area each

Atmospheric transmission 0.1

ψ = search scan angle = 10°

$\dot{\theta}_{max} = 0.5$ deg. sec, at acquisition

K = 1.6 (dynode noise factor)

PD = 0.99 TFA = 100 sec.

Retrace factor 0.2

Overlap factor, parallel to scan 0.1

Overlap factor, normal to scan 0.2

$N_b = 8 \times 10^{-4}$ watt/cm²/ster/ μ @ $.9\mu$ (blue sky)

Overlap factor of receiver aperture edge over transmitter beam

OF = 0.17. This implies 40% solid \angle overlap since $(1.17)^2 = 1.4$

Gaussian approximation assumed

Cube corner transmittance = 0.9

Cube corner beam spread = 4 sec

Scintillation factor = 0.5

Laser transmitter transmittance = 0.5

Receiver optics 3.2 in. dia.

The result of these radiometric calculations will be a statement of system performance, expressed as the worst-case atmospheric transmission and scintillation which will allow a system probability of detection, $PD = 0.9$, with a time between false alarms, $TBF = 100$ seconds.

2.7.5 Power Distribution in the Gaussian Beam. - By inspection of the Gaussian distribution, the beam width at the half-power points is $2.4/4 = 0.6$ of the beam width at $1/e^2$ points.¹ Skolnik's² derivation for $A(z) = \cos^2(\pi z/2)$ is applicable to the Gaussian distribution to a close approximation, and will be used.

Let P_t = the total power in the Gaussian beam,

ϕ_t = angular diameter of the laser beam at the $1/e^2$ power density points in radians,

Ψ_t = corresponding solid angle of the laser beam = $\pi \phi_t^2/4$,

.6 ϕ_t = angular diameter of the laser beam at the half-power points in radians, and

.36 Ψ_t = corresponding solid angle of the half-power laser beam.

Then the peak power density at the center of the Gaussian beam, according to Skolnik is

$$\frac{.667 \times P_t}{\frac{\pi}{4} (.6 \phi_t)^2} = \frac{2.358 P_t}{\phi_t^2} \text{ watt steradians}^{-1},$$

or
$$\frac{.667 \times P_t}{.36 \Psi_t} = \frac{1.852 P_t}{I_t} \text{ watt steradians}^{-1}.$$

¹ ITT Reference Data for Radio Engineers; fifth edition, pg 39-4, or fourth edition, pg 988

² M.I. Skolnik, Introduction to Radar Systems, McGraw-Hill, 1962, pg 267

Also, by inspection of the Gaussian distribution, at a diameter one-half that at the $1/e^2$ points, the power density is 0.6 of the peak power density, as noted in paragraph 2.1, above. Therefore, the power density at the corners of any individual scan spot is

$$\frac{.6 \times 1.852 P_t}{\Psi_t} = \frac{1.111 P_t}{\Psi_t} \text{ watt steradian}^{-1}$$

Similarly, the peak power density at the center of the beam returned by the corner cube retroreflector array, in watts steradian⁻¹, will be $\frac{1.852}{\Psi_{cr}}$ times the total power (watts) in the retroreflected beam. Since the transit time of a laser pulse from transmitter to retroreflector to receiver is much smaller than atmospheric scintillation cycle times, the retroreflected beam may be presumed to travel the same path as its actual energy traveled from the transmitter, and the receiver will be at or near the center of the retroreflected beam.

2.7.6 Scintillation Effects. - The total transmission of radiant energy over any relatively long path through the earth's atmosphere fluctuates with time, but the energy received is always less than the energy transmitted. For convenience, the attenuating influences are separated into two concepts, (1) a steady-state transmission factor, T_a , and (2) a fluctuating "efficiency" factor to account for atmospheric scintillation effects

over the path, K_{sc} . It is unnecessary, here, to discuss the mechanisms involved in producing these effects, other than to point out that both factors are pure numbers less than one. The worst-case minimum allowable value of the product of those two factors will be a result of the following calculations.

2.7.7 Calculation of Signal and Background Currents. - The symbols, definitions, and numerical values of terms used in the radiometric equations are summarized for convenience in Table 4-3.

The signal current available at the ITT F4012 Vidissector tube photocathode, in electrons per second, produced in the GBAA system, when the retroreflector array on the aircraft is at the corner of one of the square acquisition scan spots, is

$$i_s = \frac{1.111 P_t T_t}{\Psi_t} \cdot \frac{T_a K_{sc}}{R^2} \cdot \frac{1.852 N_{cr} A_{cr} T_{cr}}{\Psi_{cr}} \cdot \frac{T_a K_{sc}}{R^2} \cdot A_r T_f T_r K_{\Delta\lambda} \times 1.6 \times 10^{19}$$

$$= \frac{3.292 \times 10^{19} P_t N_{cr} A_{cr} A_r K_{\Delta\lambda}}{\Psi_t \Psi_{cr} R^4} \frac{T_t T_{cr} T_f T_r (T_a K_{sc})^2}{(T_a K_{sc})^2} \text{ electrons sec}^{-1}.$$

The average photocathode current, in electrons per second, due to blue sky background within the receiver instantaneous field-of-view is

$$\bar{i}_b = 1.6 \times 10^{19} N_b A_r T_f T_r K_{\Delta\lambda} \text{ electrons sec}^{-1}.$$

As shown in ITT Technical Proposal 301530, dated 27 October 1969, for this system, the threshold photocathode current is

$$I_t = \bar{I}_b + \left(\pi K_{PMT} \Delta f \bar{I}_b \log_e \left[\frac{TFA \Delta f}{2} \right] \right)^{\frac{1}{2}} \text{ electrons sec}^{-1},$$

the total photocathode current, I_t , is the solution of the following quadratic equation,

$$I^2 + I \left[\pi K_{PMT} \Delta f \log_e 4(1-PD) - 2 I_t \right] + I_t^2 = 0,$$

and the minimum signal current, required for system operation with the probability of detection and time between false alarms used in the previous equations, is

$$I_s = I - \bar{I}_b.$$

This last quantity is to be compared with the available signal current, calculated by means of the first equation, above.

2.7.8 Evaluation of Optical Transmission. - The numerical values to be used in the calculations, as shown in Table 2-9 are taken generally from data furnished by the suppliers of the respective items. All transmitting glass optical surfaces, except the receiver filter and the Vidissector tube face, are assumed to have the OCLI HEA antireflection coating, optimized for the .5145 micron wavelength, for which the transmission factor is .997 per surface. The transmission of the filter, $T_f = .45$, includes surface effects, and the tube face (two surfaces) is assumed uncoated, with 4.4% loss per surface. The receiver lens manufacturer quotes its transmission as 81%.

Folding mirrors will have optimized interference-type reflection coatings, whose reflection factor is 99.5%. The beam deflector mirrors are assumed aluminized, with reflection factor of 88%, each. The efficiency of total reflection, such as in the corner retroreflectors, is taken as 99.9% per reflection. Transmission through glass is taken as 1% loss per 10 cm length of path.

The laser output used in the calculations is the minimum of 1.7 watts peak, stated by the manufacturer. However, the manufacturer's measurements on the actual laser furnished showed 2.1 watts for the .5145 micron TEM_{00} operation. Its beam divergence was taken from catalog information; if tests indicate a worse case, the beam deflector optics can be changed appropriately.

The ITT-published data for cathode sensitivity is conservative, and cathodes are consistently made with considerably higher sensitivities. Since the published data for S-20 photocathodes show $0.05 \text{ amperes watt}^{-1}$, no difficulty is expected in obtaining $K_i \lambda = 0.065 \text{ amperes watt}^{-1}$ for the GBAA application.

The scan aperture in the ITT FW 4012 Vidissector on order for the GBAA project is .004 inches square. In calculating the receiver instantaneous field-of-view, ϕ_r and Ψ_r , a 10% allowance was made for electronic focusing of this aperture at the photocathode, and scan spot .0044 inches square was used.

The value of N_b , the radiance of a clear daytime sky at .5145 microns is cited in the Journal of the Optical Society of America, Volume 50, December 1960, page 1314 as approximately 3×10^{-3} watts cm^{-2} ster $^{-1}$ micron $^{-1}$.

2.7.9 Calculations. - Substituting the values from Table 3-1 into the equations of paragraph 3.3, the following results are obtained.

The available signal photocathode current is

$$i_s = 4.584 \times 10^{10} (T_a K_{sc})^2 \text{ electrons sec}^{-1}.$$

The average background photocathode current is

$$\bar{i}_b = 3.039 \times 10^8 \text{ electrons sec}^{-1}$$

The threshold photocathode current is

$$i_t = 3.375 \times 10^8 \text{ electrons sec}^{-1}.$$

The total photocathode current is

$$i = 3.468 \times 10^8 \text{ electrons sec}^{-1}.$$

The minimum required signal current is

$$i_s = i - \bar{i}_b = 4.285 \times 10^7 \text{ electrons sec}^{-1}.$$

Setting the available equal to the minimum required signal current,

$$4.285 \times 10^7 = 4.584 \times 10^{10} (T_a K_{sc})^2$$

then the minimum product of atmospheric transmission and atmospheric scintillation efficiency factor is

$$T_a K_{sc} = .031.$$

If we assume minimum $T_a = 0.1$, then the minimum $K_{sc} = 0.31$ for probability of detection of 0.9 with average time between false alarms of 100 seconds.

The calculations show that the system will operate satisfactorily under a worst-case condition, as follows:

1. Probability of detection, 0.9;
 2. Average time between false alarms, 100 seconds.
 3. Retroreflector at the extreme corner of an acquisition scan spot.
 4. Retroreflector at extreme range of 100,000 feet.
 5. Atmospheric transmission and scintillation effects combined,
- $T_a K_{sc} = 0.031$. That is, for an atmospheric transmission, T_a , as low as 0.1, the transmission can be degraded by scintillation effects by an additional factor of $K_{sc} = 0.31$

TABLE 2-9. DEFINITIONS AND VALUES

<u>SYMBOL</u>	<u>DEFINITION</u>	<u>VALUE</u>
P_t	Peak power in transmitted laser beam	1.7 watts
N_{cr}	Number of corner retroreflectors	$N_{cr} A_{cr} = .33 \text{ ft.}^2$
A_{cr}	Active area per corner retroreflector	
A_r	Receiver optical collector area	.053 ft.^2 or 49.5 cm^2
K_r	Photocathode response at .5145 microns	.065 amperes watt ⁻¹
N_b	Radiance of background at filter passband, taken as clear daytime sky	$3 \times 10^{-3} \text{ watt cm}^{-2} \text{ ster}^{-1} \text{ micron}^{-1}$
	Receiver optical filter passband at .5145 microns	.002 microns
T_t	Transmitter optical transmission	.749
T_{cr}	Corner retroreflector optical transmission	.99
T_f	Receiver optical filter transmission	.45
T_r	Receiver lens and tube face optical transmission	.74
T_a	Atmospheric optical transmission (one way)	TBD
K_{sc}	Efficiency factor to account for atmospheric scintillation effects (one way)	TBD
ϕ_t	Angular diameter of transmitted laser beam at $1/e^2$ power density points	3.86 milliradians
ν_t	Solid angle subtended by ϕ_t	1.17×10^{-5} steradian
ϕ_{cr}	Angular diameter of retroreflected laser beam at $1/e^2$ power density points	.02 milliradian
ν_{cr}	Solid angle subtended by ϕ_{cr}	2.95×10^{-10} steradian
ϕ_r	Angle of one side of square receiver instantaneous field-of-view	1.7 milliradians

TABLE 2-9. DEFINITIONS AND VALUES (Continued)

<u>SYMBOL</u>	<u>DESCRIPTION</u>	<u>VALUE</u>
Ψ_r	Solid angle of square receiver instantaneous field-of-view	2.96×10^{-6} steradians
R	Maximum distance from transmitter and receiver to corner retroreflector	10^5 feet
λ	Laser wavelength (TEM_{00} mode)	.5145 micron
t	Transmitted pulse duration	15×10^{-6} second
f_r	Receiver system bandwidth	5×10^4 Hertz
π	Pi	3.14159
K _{PMT}	Photomultiplier dynode noise factor	1.6
TFA	Time between false alarms	100 seconds
PD	Probability of detection	0.9
i_s	Signal photocathode current, electrons sec ⁻¹	TBD
i_b	Background photocathode current, electrons sec ⁻¹	TBD
i_t	Threshold photocathode current, electrons sec ⁻¹	TBD
i	Total photocathode current, electrons sec ⁻¹	TBD

2.7.10 Radiometric Equations. - The factors of interest are N_b , the radiance of the background, T_a , the transmission of the air-path between the GBAA and the aircraft-mounted retroreflector, and K_{sc} , an additional multiplying factor to account for the minima reached in energy transferred along this air path, due to atmospheric scintillation alone. The controllable factors of interest are the range, R , the probability of detection, PD , the time between false alarms, TFA , and the characteristics of the retro-reflector array, as represented by N_{cr} , the number of retroreflectors, A_{cr} , the effective area of a single retroreflector, and T_{cr} , the optical transmission of the retroreflector. The quantity, $N_{cr} A_{cr} T_{cr}$, is treated as a single variable herein; diffraction of the retroreflector is a function of A_{cr} and is considered constant.

The radiometric equations reduce to the following, when all items considered constant are combined and designated C_1 , C_2 , C_3 , and C_4 .

$$\text{Available } \iota_s = \frac{C_1 N_{cr} A_{cr} T_{cr} (T_a K_{sc})^2}{R^4} \text{ electrons sec}^{-1} \quad (1)$$

$$\bar{\iota}_b = C_2 N_b \text{ electrons sec}^{-1} \quad (2)$$

$$\iota_t = \bar{\iota}_b + (C_3 \bar{\iota}_b \log_e [C_4 TFA])^{1/2} \text{ electrons sec}^{-1} \quad (3)$$

$$\iota^2 + \iota [C_3 (\log_e 4(1-PD)) - 2 \iota_t] + \iota_t^2 = 0. \quad (4)$$

$$\text{Required } \iota_s = \iota - \bar{\iota}_b \quad (5)$$

$$\text{Now, let } G = \frac{N_{cr} A_{cr} T_{cr} (T_a K_{sc})^2}{R^4}. \quad (6)$$

$$\text{Then } \tau_s = C_1 G. \quad (7)$$

$$\text{Let } Z = C_3 [\log_e 4(1 - PD)] - 2 \tau_t. \quad (8)$$

$$\text{Then } \tau = \frac{-Z + \sqrt{Z^2 - 4\tau_t^2}}{2} \quad (\text{Use positive root only}). \quad (9)$$

Setting available τ_s equal to required τ_s ,

$$G = \frac{\tau - \tau_b}{C_1}. \quad (10)$$

The four constants are evaluated as:

$$C_1 = 1.3932 \times 10^{31},$$

$$C_2 = 1.013 \times 10^{11},$$

$$C_3 = 2.513 \times 10^5,$$

and $C_4 = 2.5 \times 10^4$. The appropriate units have been used in this evaluation.

Equations (2), (3), (8), (9), and (10) were entered into a computer, and computations were made for various values of probability of detection and time between false alarms, and for background radiances ranging from daytime blue sky to sunlit clouds. The results are plotted on Figure 2-26, sheet 1, of the attached graphs, which show the probability of detection versus the "G" factor defined in equation (6). To aid in interpretation of these results, the relations between the factors comprising "G" are plotted on sheet 2 of the figure.

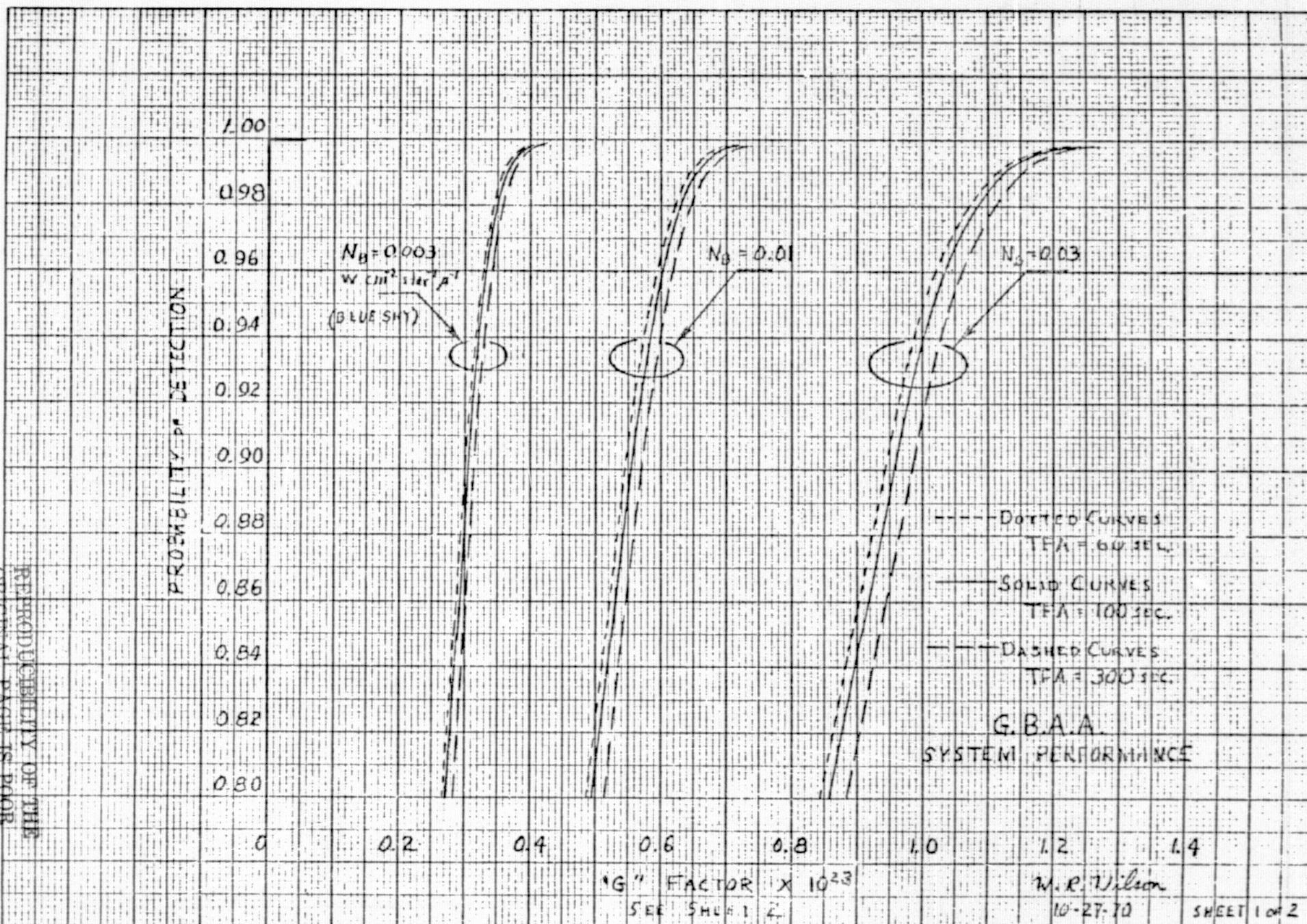


Figure 4-68 (Sheet 1 of 2)

REPRODUCIBILITY OF THE
ORIGINAL PAGE IS POOR

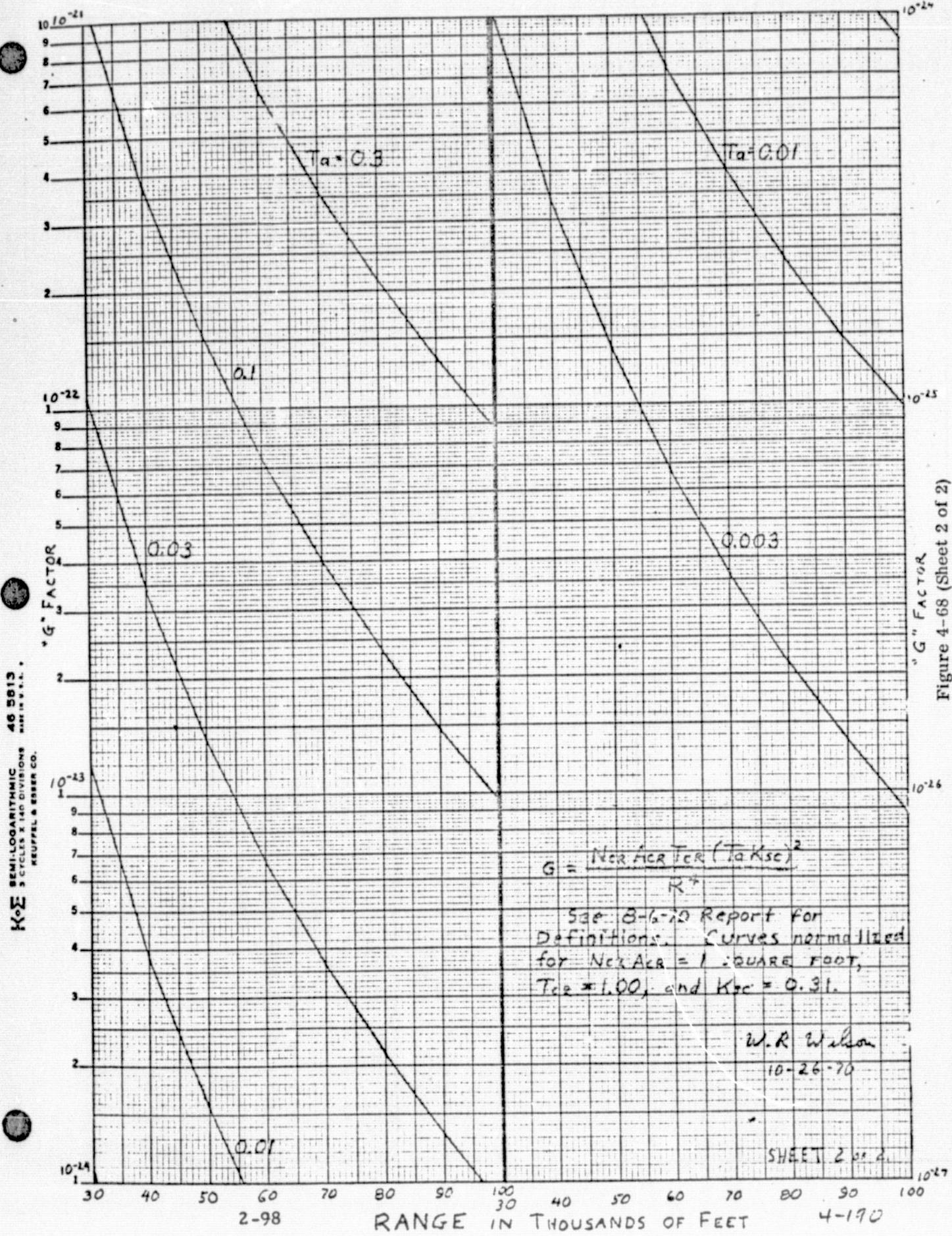


Figure 4-68 (Sheet 2 of 2)

As an example of the use of these results, consider the case calculated in the 8-6-70 report. The conditions of this case are as follows:

$$R = 10^5 \text{ ft. (maximum range)}$$

$$N_{cr} A_{cr} = 0.33 \text{ ft}^2$$

$$T_{cr} = 0.99$$

$$N_b = 0.003 \text{ w cm}^{-2} \text{ ster}^{-1} \mu^{-1}$$

at 0.5145 microns (blue sky)

$$T_a = 0.1$$

$$K_{sc} = 0.31$$

$$\text{TFA} = 100 \text{ seconds}$$

Enter sheet 2 at 100,000 ft. range. The curve for $T_a = 0.1$ intersects this at the normalized value $G = 9.61 \times 10^{-24}$. This value must be multiplied by the retro-reflector characteristics $N_{cr} A_{cr} T_{cr} = .3267$, resulting in

$$G = 3.14 \times 10^{-24}$$

Now, enter sheet 1 at this value of G. This intersects the curve for $N_b = 0.003$ and $\text{TFA} = 100$ at a probability of detection slightly higher than 0.90.

The curves plotted on the attached graphs can facilitate predictions of the operation of the BGAA system for many other conditions. In general, and as expected, factors which increase the "G" factor increase the probability of detection. The system, as designed, has low sensitivity to relatively large changes in time between false alarms. Decreasing the sky background radiance, enhances the probability of detection greatly.

It is pointed out that the curves are calculated for the case where the scintillation factor is $K_{sc} = 0.31$, a rather pessimistic value. This factor is mathematically identical in effect to the atmospheric optical transmission in equation (6), and will shift the curves of sheet 2 in the same manner. Thus, when other conditions are marginal, scintillation can aid or inhibit target acquisition, its effect depending upon the statistics of the percentage of time its value drops below 0.31.

2.8 GBAA System Design.

Many system design decisions have been made in the previous work, as shown in Table 2-10. These are the starting points for the present work, and the justification for these parameters is not included herein.

The purposes of the present work are to update the optical design of the laser transmitter, including its beam deflector, and to calculate the radiometric performance of the GBAA system. Transmitter optics are shown in Figure 2-27.

TABLE 2-10. GBAA SYSTEM PARAMETERS

Transmitter

Laser, Britt Model 2000A Burst Argon Laser

TEM_{oo} 0.5145 micron wavelength

Pulse width: 15 microseconds

Repetition rate: 1000 Hertz

Minimum peak power: 1.7 watts

Beam diameter at $1/e^2$ intensity points: 0.079 inch

Beam divergence (before deflector optics): 0.75 milliradian

TABLE 2-10. GBAA SYSTEM PARAMETERS (Continued)

Receiver

ITT F 4012 Vidissector Tube with S-20 photocathode

Cathode minimum sensitivity (selected) at 0.5145 microns, $K_{\Delta\lambda} = .065$ amperes per watt

Tube scanning aperture, square, .004 inch per side

Lens, DeOude Delft "Rayxar" E 65/0.75, serial No. L09172, efl 65 mm, f/0.75, measured entrance pupil 3.125 inches diameter

System bandwidth, $\Delta f = 5 \times 10^4$ Hertz

Optical filter bandpass at 0.5145 microns, $\Delta\lambda = 0.0020$ microns

Retroreflector Array

Glass "corner reflectors," mounted on aircraft

Total effective area, $A_{cr} = 0.33 \text{ ft}^2$.

Beam spread after retroreflection, $\phi_{cr} = 4 \text{ arc sec included angle}$,
or $0.02 \text{ milliradian diameter or } 2.95 \times 10^{-10} \text{ steradian solid angle}$

Operating Parameters

Acquisition and tracking total field-of-view, square $10^\circ \times 10^\circ$

Scan lines per raster: 128

Scan steps per scan line: 128

Scan fly-back time: 12.5% of line time

Distance, transmitter and receiver to aircraft, $3 \times 10^4 < R < 10^5$ feet

2-103

6906-203

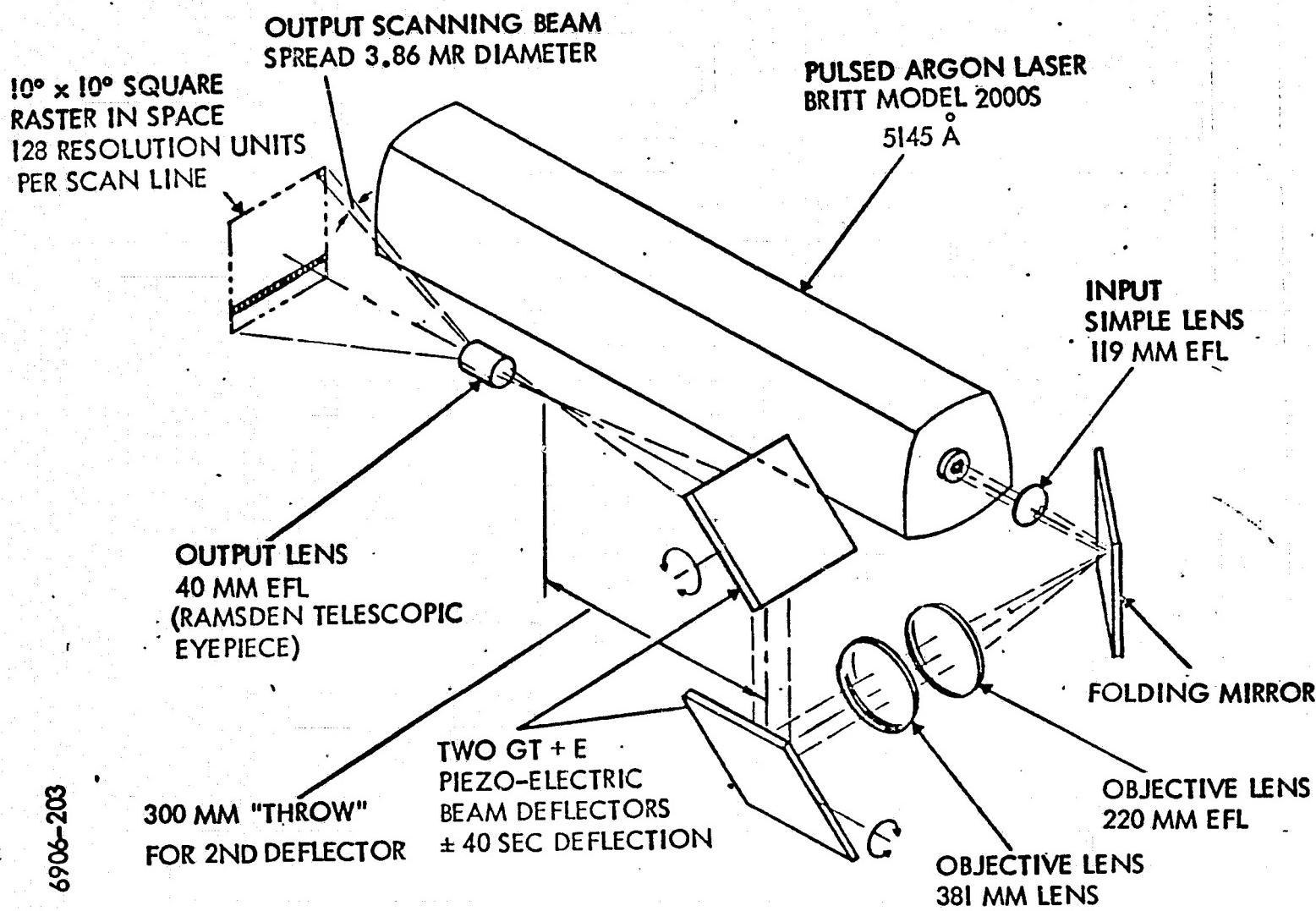


Figure 2-27. GBAA Transmitter Optics

2.8.1 Transmitter Optical Design.

2.8.1.1 Transmitter Output Beam Divergence. - In the TEM_{∞} mode, the distribution of laser beam power across the beam follows the Gaussian curve, and the beam diameter is defined as the diameter at which the power density falls to $1/e^2$ or 13.5% of the maximum power density in the beam, as shown in Figure 2-28.

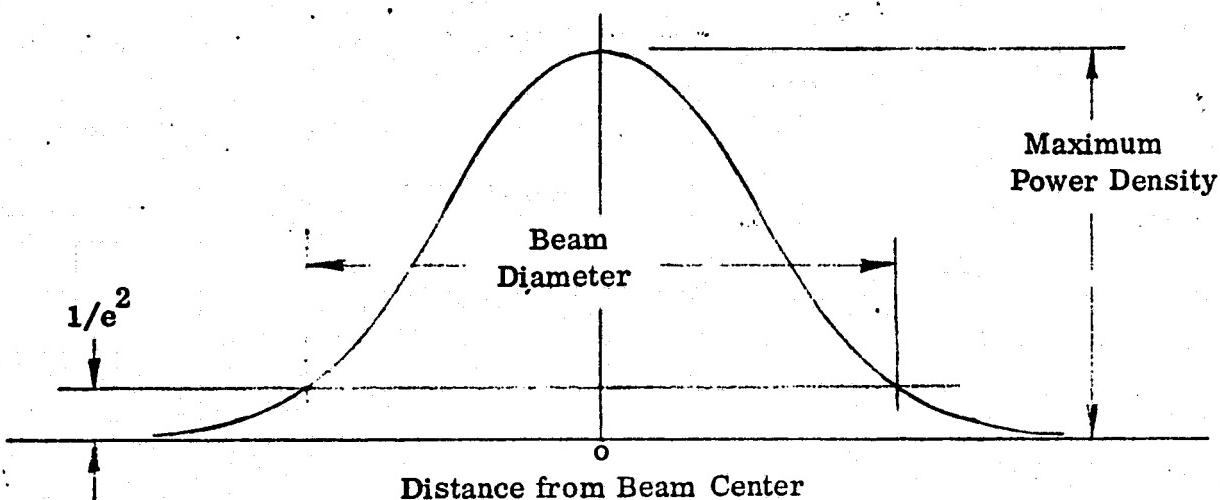


Figure 2-28. Gaussian Beam

Note that the beam diameter at the half-power-density points is approximately .6 of that at the $1/e^2$ points, and that the power density corresponding to a diameter of one half that at the $1/e^2$ points is approximately .6 of the maximum power density. These two approximations are used later in this discussion. See ITT "Reference Data for Radio Engineers," fifth edition, page 39-4, for information on the Gaussian distribution. If atmosphere turbulence is absent, the Gaussian distribution of beam power holds at any appreciable distance from the transmitter. Turbulence effects will be discussed later.

Since the $10^{\circ} \times 10^{\circ}$ raster contains 128 lines of 128 scan spots each, each scan spot will be a square 0.0781° or 1.364 milliradians on a side. (Note that both the transmitter beam and the receiver instantaneous field-of-view are larger than this.) The diagonal of each individual scan spot is 1.928 milliradians. In the worst case, the corner reflector will be located at one corner of the square scan spot. Since the transmitter beam is non-uniform over its cross-section, it is reasonable (but arbitrary) to decide that the power density at the spot corner must be not less than 0.6 of the power density of the control maximum. As shown above, this diameter is one-half the beam diameter at the $1/e^2$ points. Therefore, the transmitter beam diameter shall be

$$\phi_t = 2 \times 1.928 = 3.856 \text{ milliradian included angle}$$

$$\text{or } \Psi_t = \frac{\pi}{4} (3.856 \times 10^{-3})^2 = 1.168 \times 10^{-5} \text{ steradian solid angle.}$$

2.8.1.2 Beam Deflector Optics. - The piezoelectric-driven beam deflector, with an associated optical system, has been furnished as Government-Furnished Equipment (GFE) to the GBAA project. It is shown schematically in Figure 2-29.

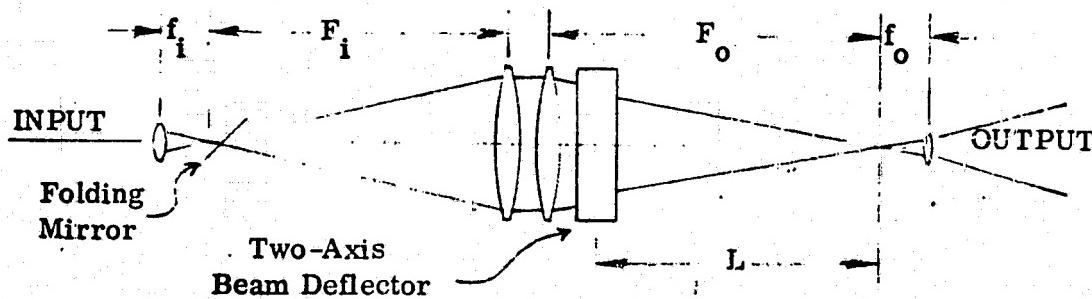


Figure 2-29. Beam Deflector Optics

The output beam deflection is determined by the beam deflector movement and the ratio L/f_o . The beam deflector mirrors move ± 20 arc minutes, and the laser beam in the location of "L" moves ± 40 arc minutes. It is required that the output beam deflect ± 5 degrees. Therefore,

$$\frac{L}{f_o} = \frac{5 \times 60}{40} = 7.5, \text{ which determines the focal length of the output lens, } f_o, \text{ other factors being set.}$$

NOTE: The two deflector mirrors are near each other, but at different distances "L" on the optical axis. Use the shorter "L" in the calculations. This implies that slightly less drive voltage is required for the deflector having the larger distance, inversely as the ratio of the respective distances.

The optical system is essentially two telescopes, back-to-back, and the output laser beam's divergence, ϕ_o , will be the divergence of the input beam, ϕ_i , multiplied by the magnification of the system.

$$\phi_o = \phi_i \cdot \frac{f_1}{F_1} \cdot \frac{F_o}{f_o}$$

From construction, $F_1 = 220$ mm

$F_o = 381$ mm

$L = 312$ mm

Calculating,

$$f_o = \frac{L}{7.5} = \frac{312}{7.5} = 41.6 \text{ mm}$$

Use a 40 mm Ramsden telescope eyepiece for this lens, since it has less aberrations than a Huygens eyepiece, and is readily available. Therefore,

$$f_o = 40 \text{ mm.}$$

From Table 1-1, $\phi_i = 0.75$ milliradian, and from paragraph 2.1

$$\phi_o = \phi_t = 3.856 \text{ milliradians.}$$

$$f_1 = \frac{3.856 \times 220 \times 40}{0.75 \times 381} = 119 \text{ mm.}$$

This lens can be a simple bi-convex lens, such as Edmund Scientific Company No. 94388, which has 114 mm focal length and 29 mm diameter. Only the central 2 or 3 mm of this lens would be used. Note that the beam deflection scale factor is set by the output lens, f_o , and that the beam divergence is set by the input lens, f_1 , after the output lens has been selected.

2.9 Additional Laser Candidate Consideration

The purpose of this discussion is to extend the consideration of candidate lasers to include an analysis of the applicability of a neodymium doped yttrium aluminum garnet (Nd:YAG).

The equations previously developed will be utilized. The parameters of optical system size, filter and atmospheric transmission, number of retroreflectors, etc., remain the same. New parameter values are listed below:

1. $N_b = 7 \times 10^{-4} \frac{\text{watts}}{\text{cm}^2 - \text{ster} - \mu}$ (Blue sky @ 1.06 μ)
2. $\Delta_\lambda = 0.002 \mu$ (20 Å bandpass filter)
3. $K_{\Delta\lambda} = 4 \times 10^{-4}$ amp/watt (S-1 photocathode)
4. $P_y = 0$ (i. e., no overlap in y direction - overlap will be provided by increasing the transmitted beam size, as part of a trade-off, as discussed later).

Using equation (9) from the original report,

$N = 142$. From Eq. (6), $\Delta\phi = \frac{11^\circ}{142} = 0.0774$ deg. Then, $(\Delta\phi)^2 = 5.99 \times 10^{-3} \text{ deg}^2$ or 1.825×10^{-6} steradians. From Eq. (19), $\Delta f = 5 \times 10^5$ Hz. From Eq. (15), $i_b = 1.97 \times 10^5$ electrons/sec. Substituting Eq. (20), $i_t = 3.10 \times 10^6$ electrons/sec. From Eq. (21), $i = 1.36 \times 10^7$ electrons/sec, and from Eq. (22), i_s is equal to 1.34×10^7 electrons/sec.

Note that the background current is very small compared to the required signal current. From Eq. (26), the required flux density at the ground $FDG = 1.74 \times 10^{-10}$ watts/cm², or 1.62×10^{-7} watts/ft². Substituting in Eq. (31), using range $R = 10^5$ ft, $P = 4 \times 10^{-7} \times 10^{20} \times 1.825 \times 10^{-6} \times 1.62 \times 10^{-7} = 11.8$ watts.

The use of a commercially available Nd:YAG laser in the Ground Based Acquisition Aid is now discussed.

The Coherent Radiation Laboratories Model 60 Nd: YAG, with Model 460 Q-switch, is specified to produce 400 watts (Peak) pulses of nominal 1 μ sec, duration at 1000 pps. The price for the laser without the Q-switch is about \$10,000. The head is 8 in. wide, 6 in. high, and 30 in. long, and weighs 50 lbs.

Considering the results of the analysis above, 11.8 watts peak power were required for the 10^5 ft. range, so 400 watts available from the Model 60 laser gives a factor of 34 to trade-off. The number of cube corners could be reduced to 4 from 16, requiring 4 times as much power. Also, the transmitter solid angle could be expanded 4 times to facilitate tracking, i. e., permit "dithering" the image dissector without requiring "dithering" of the laser beam deflectors. This reduction of excess power by 4X for fewer cube corners and 4X for larger transmitter angle thus leaves an excess power factor of 34/16 or 2.1. This permits operation under slightly lower atmospheric transmission conditions, or slightly lower performance of any of the system component.

The above analysis indicates that a Nd:YAG laser could be used for the Ground Based Acquisition Aid.

It should be noted that the high power requirements at 1.06 microns are caused by the low quantum efficiency of available detectors.

Frequency doubling of the 1.06μ radiation (to permit operation where detectors are much more sensitive) by non-linear effects in certain crystals, with high efficiency in the intracavity configuration, has been achieved. One such system which will soon be available commercially is the Chromatix Model 1000D Nd:YAG laser with Acoustic Q-switch and $LiIO_3$ frequency doubler, using the Model 1090-1 current regulator. This unit uses continuous operation of the krypton arc lamp for pumping, and Q-switching at between 360 and 3,600 pps. The peak output is about 360 watts (TEM_{00}), and pulse length about 200 nanoseconds. Price is about \$23,000, with delivery estimated at 120 days. The laser head dimensions are 10.25×6.31

x 27.25 inch, and its weight is 40 pounds. Cables and moderately stiff coolant carrying tubing are attached to the head and may put excess torque on a telescope mount designed for arc second tracking accuracy.

Cost and delivery schedule prevented use of this laser approach.

3. AIRBORNE OPTICAL COMMUNICATIONS PACKAGE (AOCP)

3.1 General

3.1.1 Functional Description. - The AOCP is a laser transceiver system providing the capability of duplex communications and includes acquisition, tracking, pointing, and atmospheric scintillation monitoring subsystems. Figure 3-1 is the AOCP hardware tree showing the various system elements and their relationships. Included is a cescription of the TV acquisition aid subsystem which utilizes an ITT owned TV camera and tracking system.

The AOCP design specifications were determined early in the program as a result of several planning meetings held at NASA/MSFC between ITTG technical personnel and the AVLOC principal investigation team.

Table 3-1 gives a complete list of the AOCP specifications. These final system specifications did not vary appreciably from those set forth initially, although some were made more complete or more stringent as the operational environment became better defined.

Figure 3-2 shows the AOCP unit mounted in its test fixture. This equipment view shows the receiver collection aperture and the concentric folding mirror and periscope path to the TV acquisition aid. The coordinate reference frame is also defined in this view. The x-axis is directed along the line of sight and the position sensing is in the orthogonal y, z plane. It should be noted that the transmitter aperture is offset from the center of the cassegranian receiver collector and located in the center of the annulus. The reason for this is to avoid a central obscuration in the transmitted beam.

TABLE 3-1 AOCP SUMMARY SPECIFICATIONS

COARSE ACQUISITION TV TRACKER

Acquisition Field-of-View	$5^\circ \times 7^\circ$ (87.2 mr x 122 mr)
Linearity	< 10 percent
Frame Rate	60 per second
Probability of detection	> 0.99
Track accuracy	< 1.5 mrad.
Detection Sensitivity	1×10^{-10} watt/cm ²
OPTICAL APERTURE, AOCP	3.88 inch diameter (9.85 cm)

RECEIVER-TRACK/COMMUNICATIONS

Detector Type	ITT 4012
Spectral Response	S-20
Minimum Detectable Power	1×10^{-12} watt at photocathode
Fine Acquisition FOV	0.5 x 0.5 degree (8.7 mr x 8.7 mr)
Instantaneous FOV	18 x 18 arc sec (87.3 µrad x 87.3 µrad)
Effective Focal Length	1.13 meters
Acquisition Frame Rate	1 Frame/sec.
Scan Format	128 x 128 element digital raster

TABLE 3-1 - (Continued)

Track Scan Type	partial scan-cruciform
Track Scan Rate	16 kiloHertz
Track Bandwidth	up to 1000 Hz
Tracking Accuracy	0.2 arc seconds rms
Receiver Attenuation	30/1 variable
Communications Bandwidth	50 kiloHertz
Modulation Type	10.7 MHz subcarrier FM
Optical Wavelength	0.488 micrometer
Optical Bandpass	± 1.0 nmeter
Tracker Signal Dynamic	
Range	60 db
Tracker AGC Bandwidth	300 Hz
Optical Transmission	.15

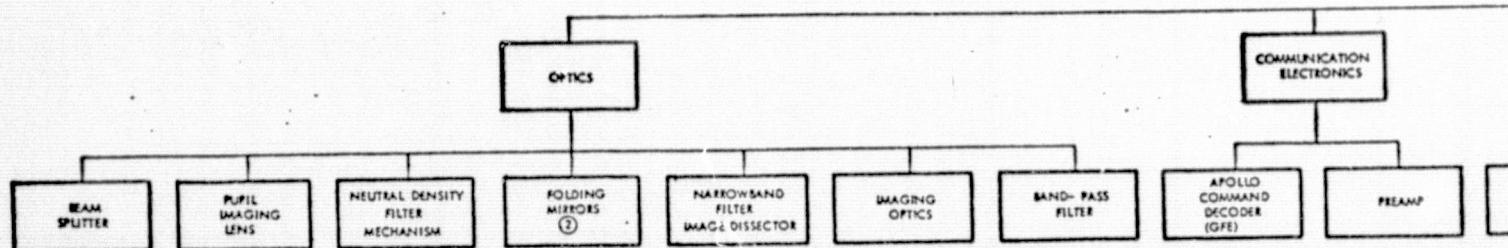
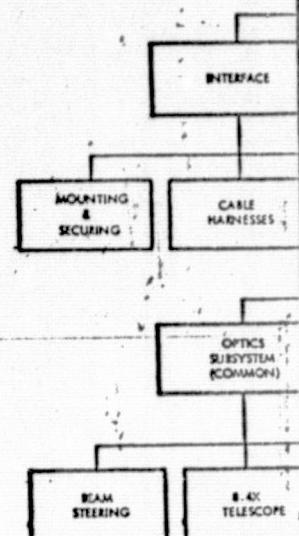
RECEIVER-SCINTILLATION MONITOR

Detector Type	Photomultiplier RCA 8644
Field of View	0.5 x 0.5 degree (8.7 mr x 8.7 mr)
Dynamic Range	60 db
Bandwidth	5 kHz
Outputs	<ol style="list-style-type: none"> 1. baseband linear 2. 10.7 MHz linear 3. 10.7 MHz log

TABLE 3-1 - (Continued)

Effective Aperture	3.8 inch diameter (9.85 cm)
Ratio of Aperture Variation	100/ \pm in area
Optical Bandwidth	± 1 nmeter
Optical Wavelength	0.488 micrometer
Optical Transmission	0.2
PAINTING SUBSYSTEM	
Beam Steerer Type	Torquer driven mirror-Flex
Bandwidth	pivot mounted
Steering Angle Range	240 Hz
Closed Loop Painting	± 0.5 degree two axes
TRANSMITTER	
Laser Type	HeNe
Laser Power	5 mw. TEM ₀₀
Wavelength	0.6328 micrometer
Beam Divergence	5 to 120 arc seconds variable
Modulator Type	Transverse field-electro-optical KD*P
Modulation Format	OOK
Modulation Index	75 percent-variable operating point
Data Rate	30 Mega bits/second
Weight	167 pounds (excluding RER)
Power Consumption	200 watts

REPRODUCIBILITY OF THE
ORIGINAL PAGE IS POOR



004-41

FOLDOUT FRAME

AOCP HARDWARE TREE

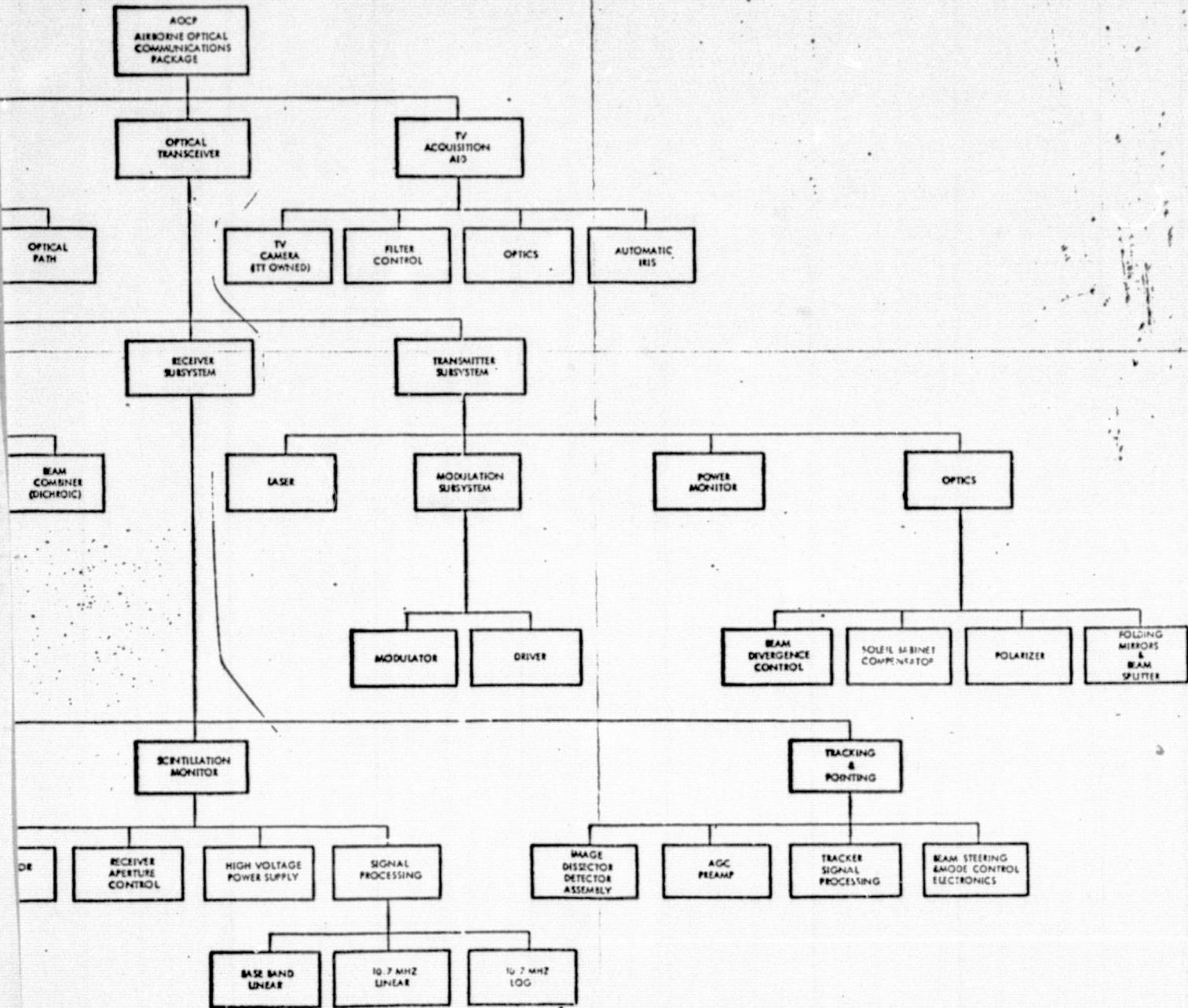


Figure 3-1. AOCP Hardware Tree

3-5/6

FOLDOUT FRAME

6906 - 31

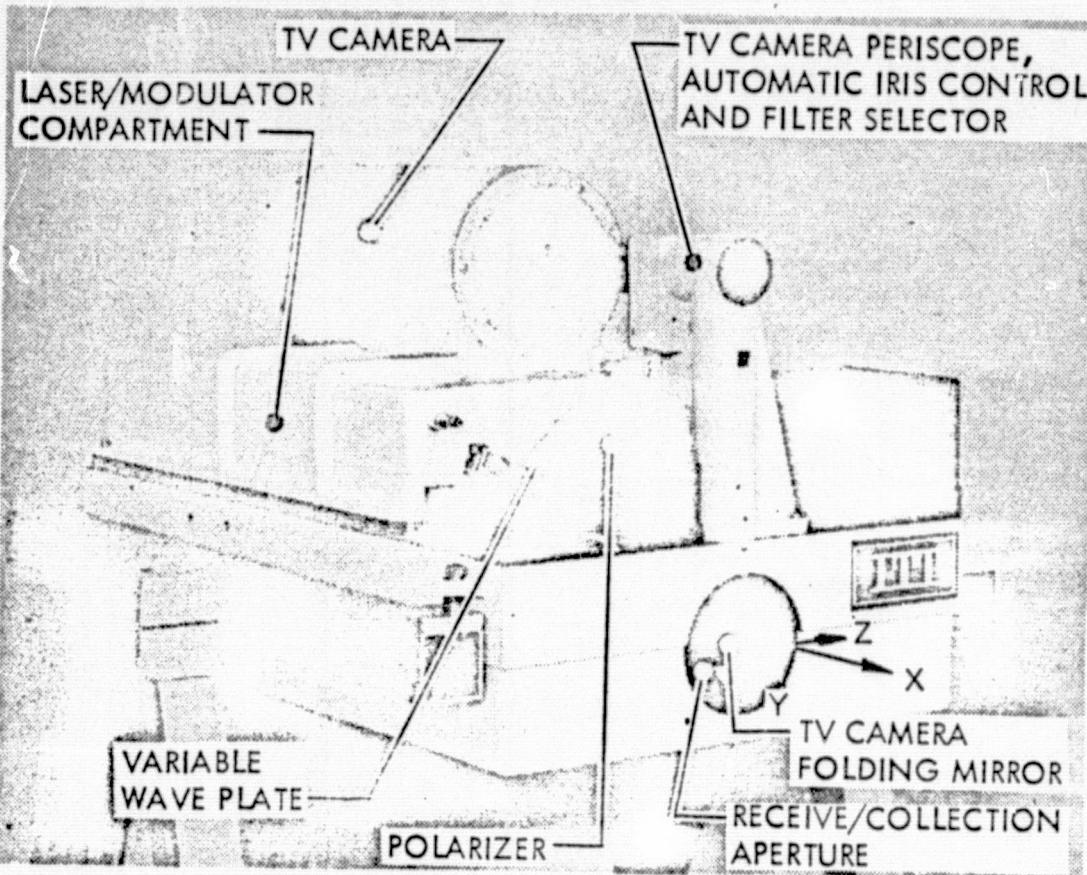


Figure 3-2. AOCP Flight Package in Test Fixture

REPRODUCIBILITY OF THE
ORIGINAL PAGE IS POOR

A more thorough analysis of this effect is given in a latter section of this report.

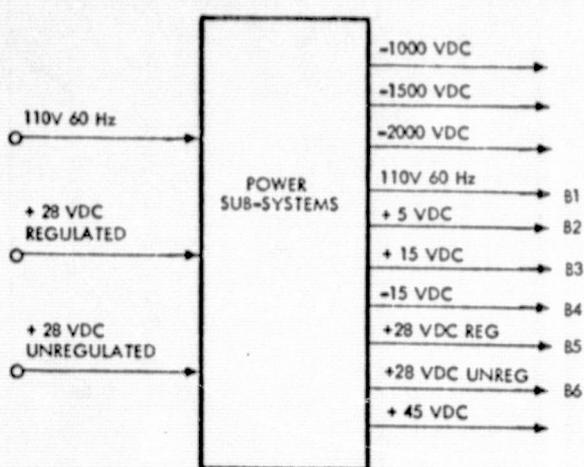
The operation of the AOCP can be understood by reference to Figure 3-3 which shows the system functional block diagram.

3.1.2 Mechanical Packaging of AOCP. - The Aircraft Optical Communications Package (AOCP) is subjected to operating in an environment that is most hostile to precision electro/optical devices. The altitude, which causes wide pressure variations; temperature variations; and vibration are the three main enemies of any precision E-O device. All three of these factors are present in the AOCP operating environment and have established the packaging rationale. Figures 3-4, 3-5, and 3-6 show the layout of components of the AOCP.

The two basic assemblies most affected by the operating environment are the Laser/Modulator package, and the basic optical package. The packaging rationale for each of these shall be discussed in turn.

The AOCP mechanical structure is formed from a hogged-out ribbed aluminum block to maximize strength and alignment stability. All optical elements are mounted directly to the main plate on either the top or bottom levels. The laser compartment was designed so that a 15 pound/square inch pressure loading would not deform the laser/modulator mounting plate and cause a boresight error between the transmitter and receiver. Figure 3-4 shows a view of the AOCP top level with the laser compartment cover removed and indicates the location of the various system components and assemblies.

REPRODUCIBILITY OF THE
ORIGINAL PAGE IS POOR



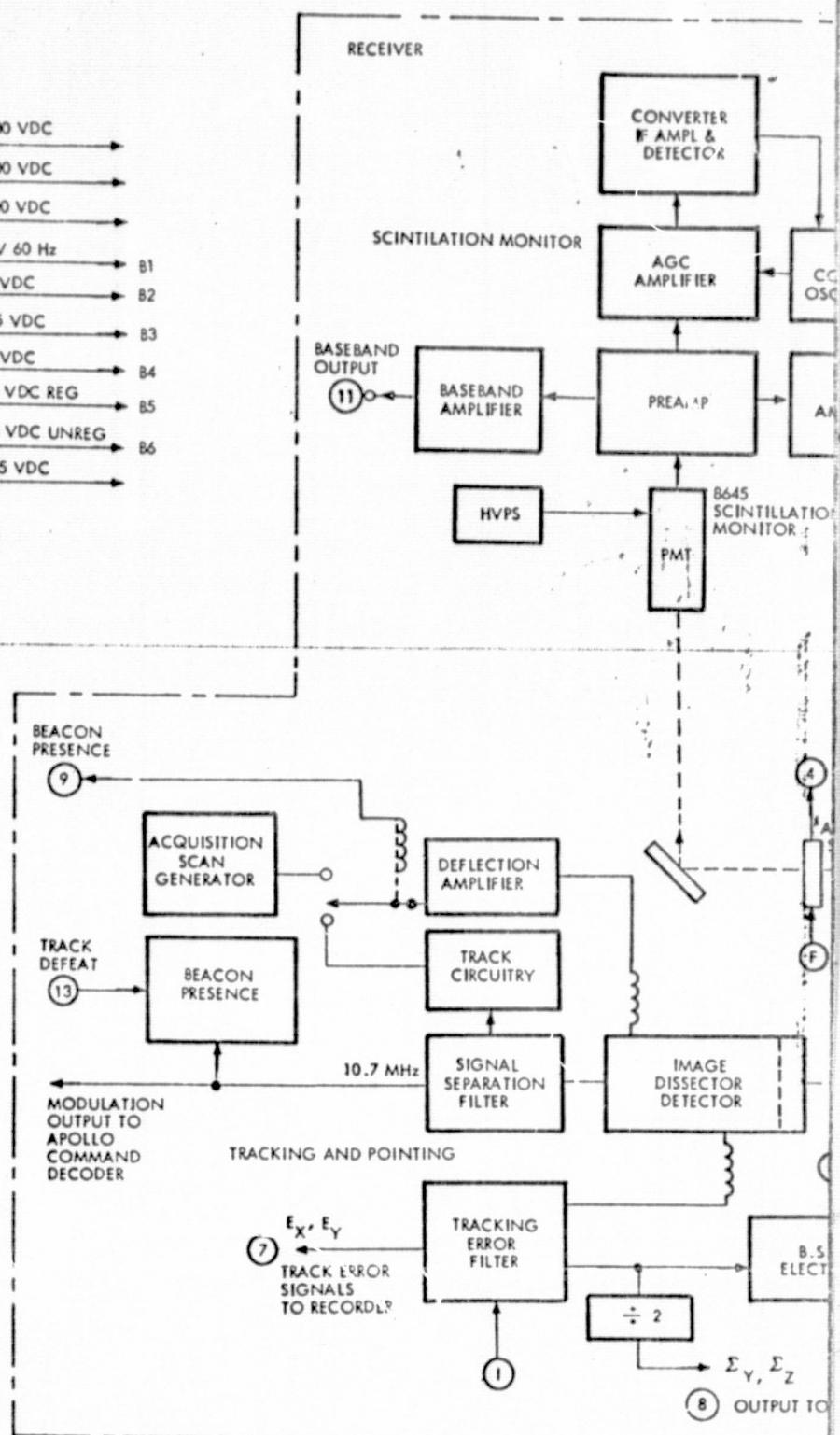
OUTPUTS

- 1 BEAM DIVERGENCE POSITION
- 2 TV TRACKER FILTER POSITION
- 3 RECEIVER ATTENUATION POSITION
- 4 SCINTILLATION MONITOR APERTURE POSITION
- 5 LASER SHUTTER POSITION
- 6 TV CAMERA VIDEO
- 7 E_Y, E_Z TRACKER SIGNALS TO RECORDER
- 8 E_Y, E_Z TRACKER SIGNALS TO CCSD GIMBAL DRIVE
- 9 BEACON PRESENCE SIGNAL
- 10 BEAM STEERER HOLD SIGNAL
- 11 SCINTILLATION MONITOR BASEBAND SIGNAL
- 12 SCINTILLATION MONITOR 10.7 MHz LOG SIGNAL
- 13 SCINTILLATION MONITOR 10.7 MHz LINEAR SIGNAL
- 14 LASER POWER MONITOR SIGNAL

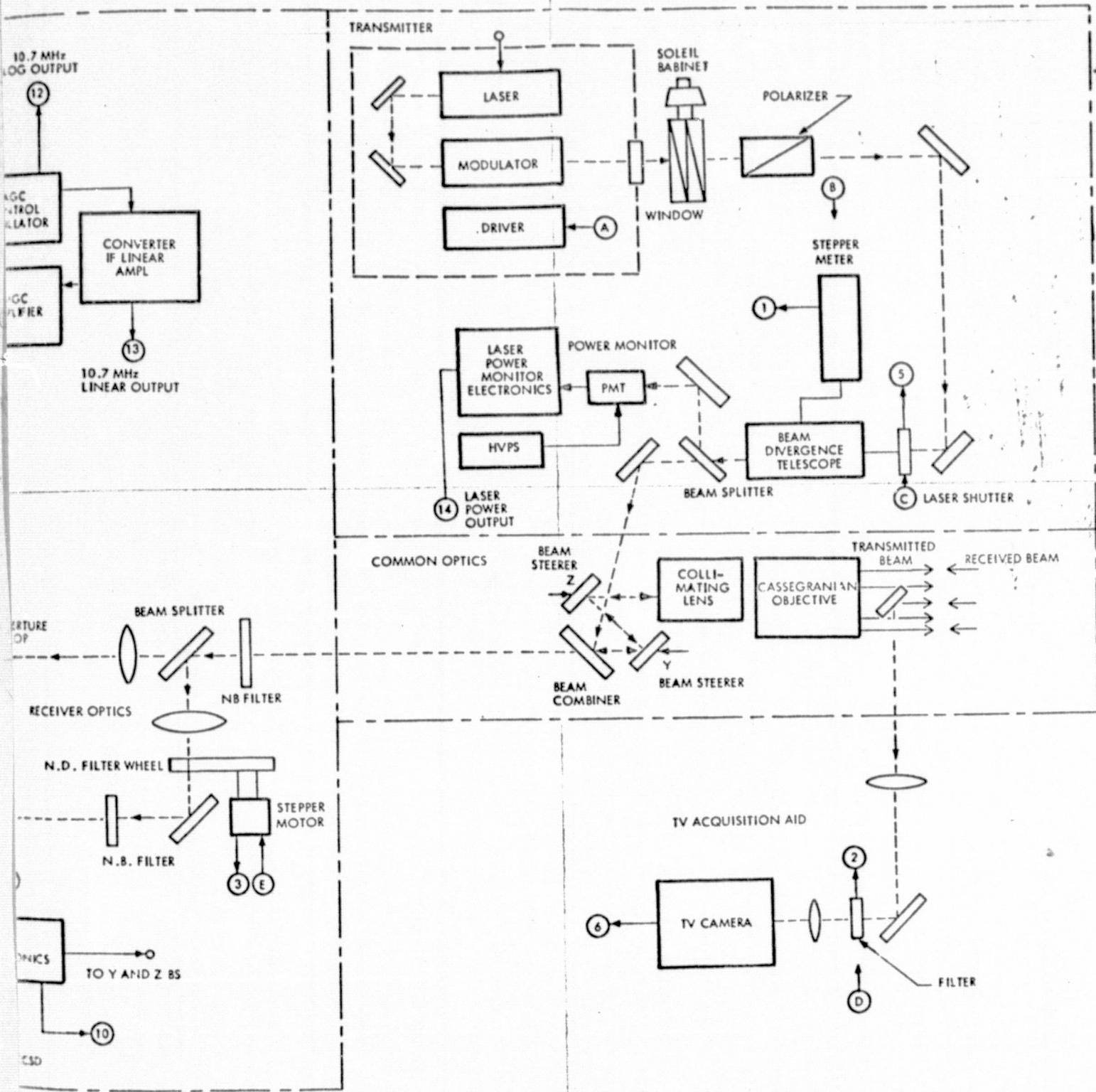
COMMAND INPUTS

- A DIGITALLY CODED MODULATION
- B BEAM DIVERGENCE COMMAND (1-6)
- C LASER SHUTTER OPEN/CLOSE
- D TV TRACKER FILTER IN/OUT
- E RECEIVER ATTENUATION (1-4)
- F SCINTILLATION MONITOR APERTURE STOP IN/OUT
- G TRACK DEFEAT
- H BEAM STEERER ON/OFF
- I BORESIGHT ADJUST Σ_Y, Σ_Z

6906-118
REV 1



FOLDOUT FRAME



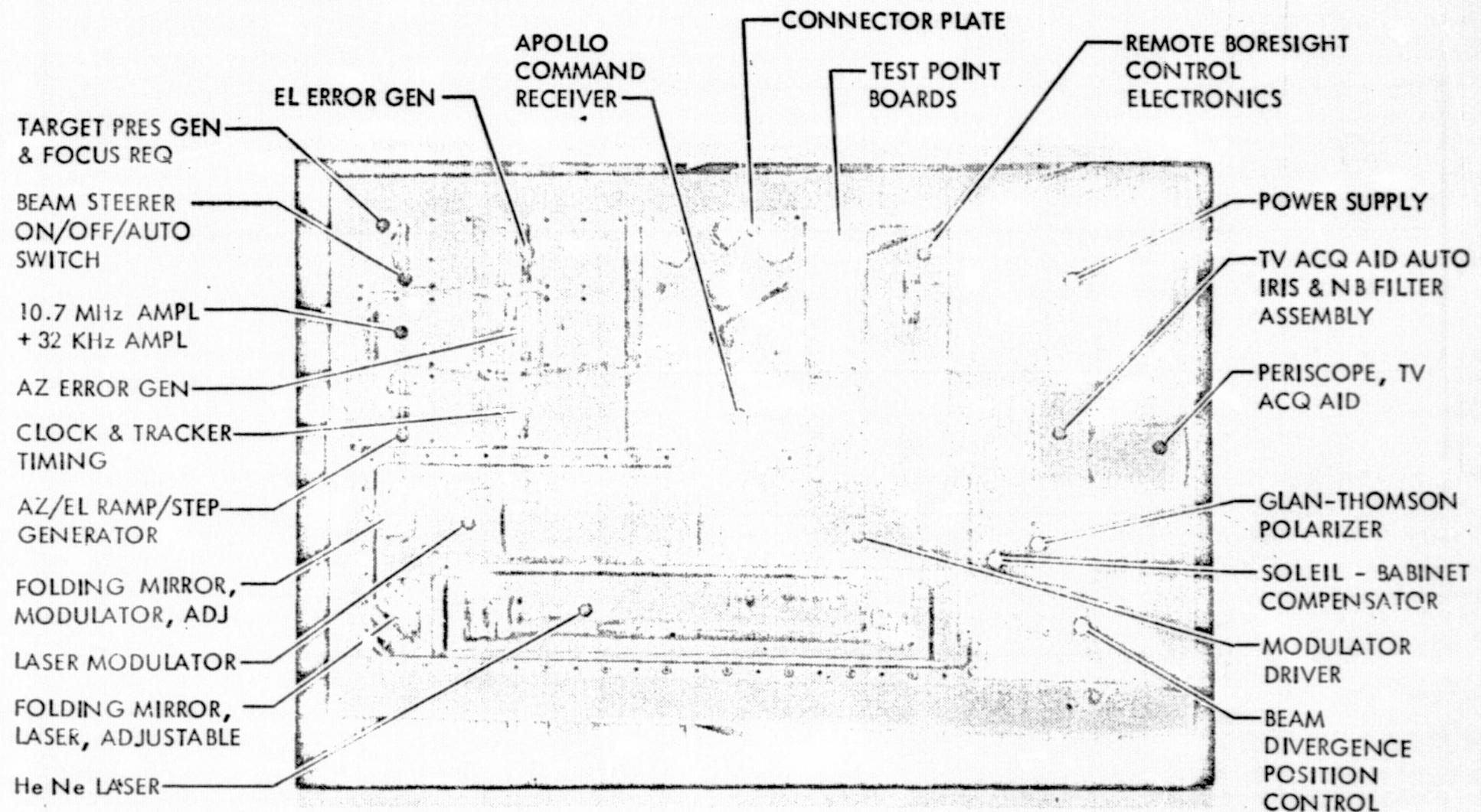


Figure 3-4. AVLOC Flight Package Top View (Cover Removed)

34
-
6

REPRODUCIBILITY OF THE
ORIGINAL PAGE IS POOR

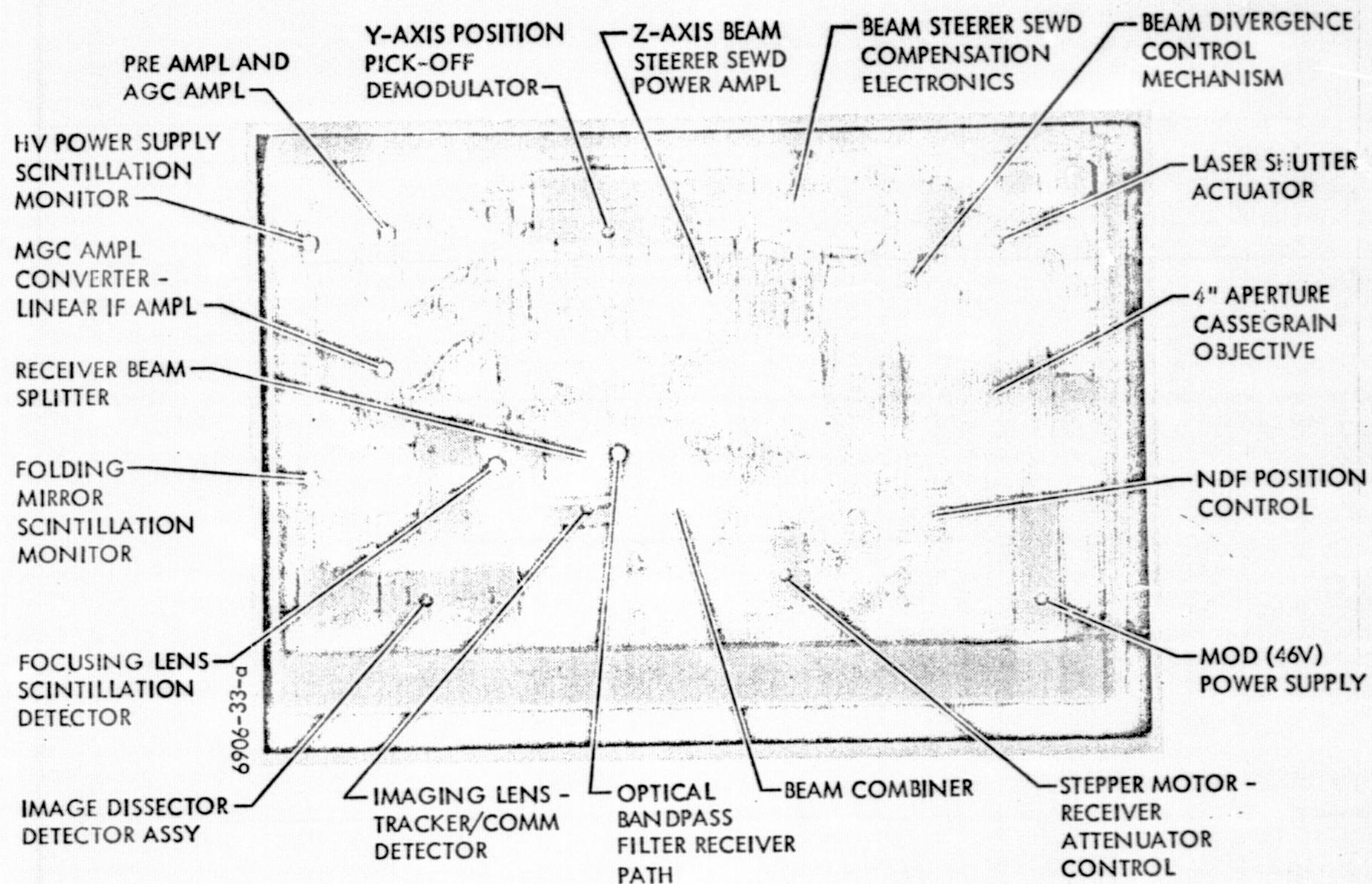


Figure 3-5. AVLOC Flight Package Bottom View (Cover Removed)

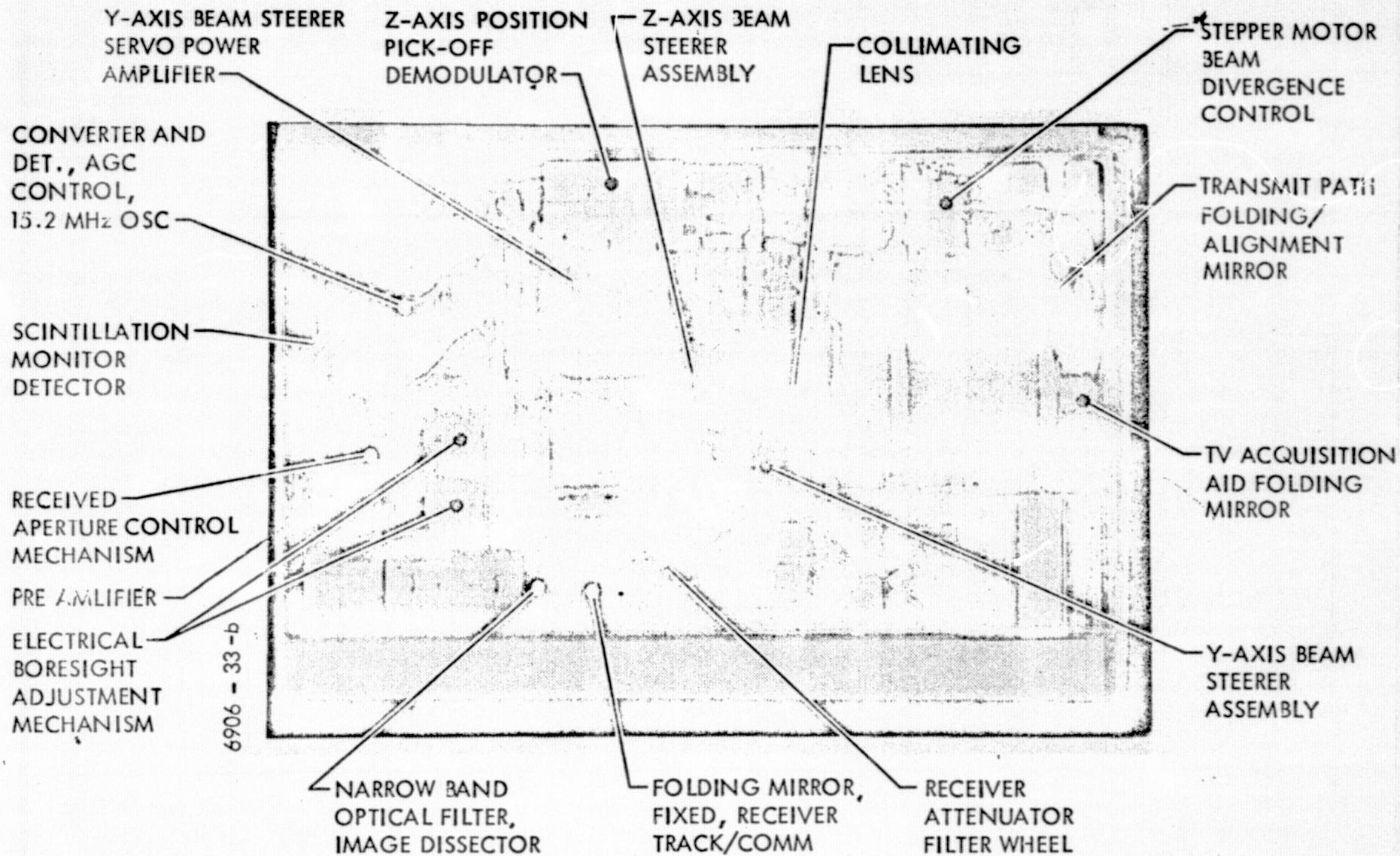


Figure 3-6. AVLOC Flight Package Bottom View (Cover Removed)

A more detailed description of the mechanical design of the transmitter compartment will be given in a later section of this report.

3.2.1 Laser/Modulator Package. - The laser itself is a commercial unit adapted to the AOCP and as such is not designed to withstand any of the deformations caused by pressure variations. These pressure variations introduce misalignment in the laser itself and severely degrade performance. To eliminate these deformations, an approach was necessary that would maintain a stable environment for the laser.

The approach taken in the laser modulator package is to have the laser, the laser modulator, and associated optics all mounted on a rigid baseplate. This baseplate has large openings machined through it and the bottom of the package is closed via a steel diaphragm. The remainder of the package is enclosed in an aluminum container which is ribbed to preserve its structural shape and to ensure that the O-ring sealing surfaces are not distorted. In operation, the entire package is pressurized at 1 atmosphere constantly. Any pressure variations are compensated for by the diaphragm. Thus the volume of the Laser/Modulator package is constantly changing as a function of external pressure changes causing the diaphragm to flex the net result is a constant pressure environment for these critical components.

Since the temperature variations also cause pressure changes, compensation for these temperature induced pressure variations are also compensated for by the diaphragm technique.

This entire package has been tested in a vacuum environment (10^{-5} TORR) and has demonstrated the soundness of this approach.

3.2.2 Optical Package. - The optical package itself, to which the laser/modulator package is affixed, is a complex and densely packaged unit.

The constraints of the program in terms of time and costs predicated a "Building Block" approach to the design. Rather than fabricate an intricately machined housing with a multiplicity of integrated optical devices, a baseplate design was utilized which permitted all other devices to be fastened to it as discrete components. This is a very cost and time effective method of packaging an engineering type of unit as it permits concurrent discrete parts fabrication and also lends itself well to the myriad modifications necessary on an engineering unit. It was possible to modify an individual element without completely disassembling the entire unit.

The basic concept then required a rigid, reasonably light baseplate or "Optical Bench", if you will, to which all other components were attached. A wrought aluminum billet was procured for the baseplate and was extensively machined on both top and bottom.

The net result was a light yet rigid baseplace with high webbed walls around its periphery and with considerable internal webbing. This yielded a light, rigid structure that was not too difficult to fabricate and yet had the high degree of torsional rigidity so vital in any optical system. The billet was rough machined, stress relieved, and then finish machined. This ensured the long term stability required. The baseplate could have been fabricated out of a weldment of brazement but the fabrication of the weldment pieces, welding, heat-treating and subsequent finish machining and stress relieving would constitute a longer fabrication cycle without the dimensional stability inherent in a homogeneous billet.

Once the base plate was fabricated, all of the other elements of the electro/optical train, which had been fabricated concurrently, were fastened to it as completed subassemblies. These subassemblies mount via precision interface and have sufficient adjustment capability built into them to facilitate accurate system alignment.

The entire optical baseplate is then enclosed top and bottom. Mounting ears are provided to interface with the carrying vehicle. These ears provide a three-point suspension in the vehicle.

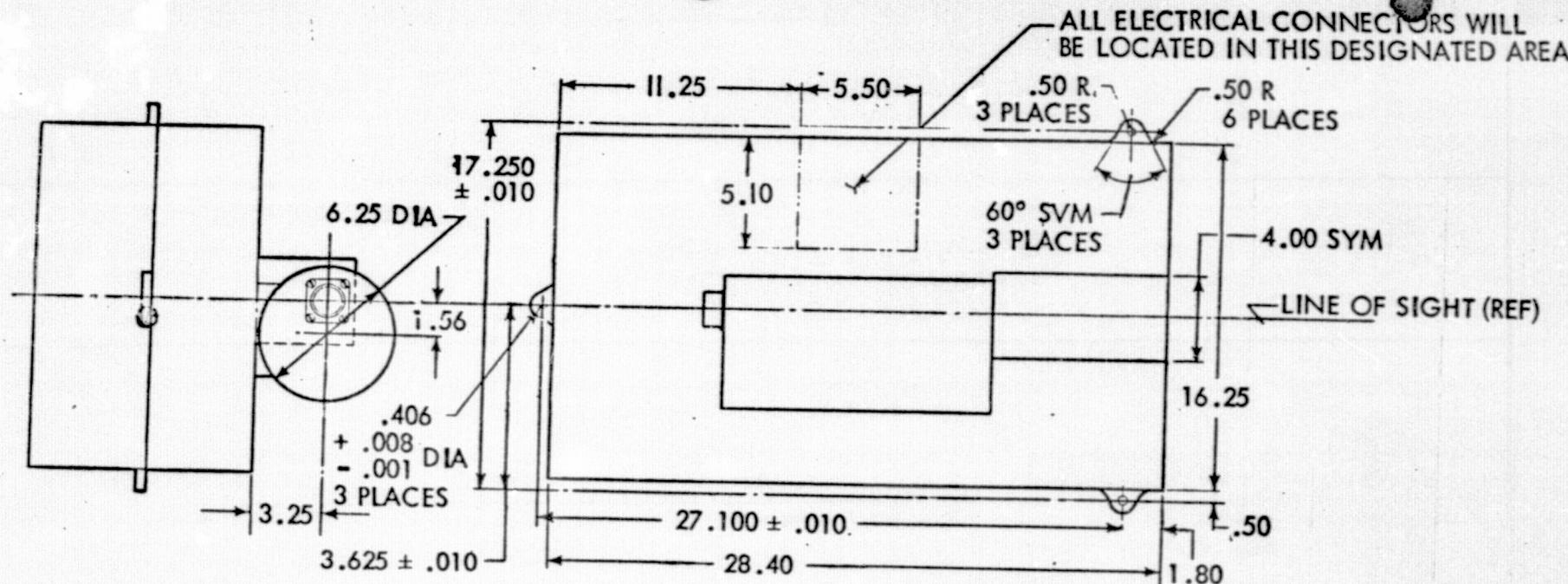
Figure 3-7 shows the AOCD mechanical package configuration with the outline dimensions and approximate cg location.

3.2 Common Optics Subsystem

The common optics subsystem includes the cassegranian-cataadioptric objective lens, the collimating lens, the beam steerer mirror, and the dichroic beam combiner. (See Figure 3-8.)

The catadioptric objective lens serves as the system "antenna." This lens system was manufactured by Wiley Optical Co. from a design for NASA/GSFC. The initial design specifications were for a compact (short length) 0.2 degree (0.035 radians) field of view with resolution defined by the Rayleigh criteria of better than 2 arc seconds (10×10^{-6} radian). The objective lens focal length is nominally 25 inches (63.5 cm) and clear aperture of 3.88 inch (9.85 cm), giving a numerical aperture ratio of f/6. The objective lens is a modified Schmidt design shown schematically in Figure 3-9. The total system length was 6 inches (15.24 cm) which made an unusually compact design. The focal length was variable over a considerable range by adjustment of the secondary mirror. Another feature was the prime focus location inside the primary mirror which permitted the collimating lens to be mounted directly into the objective housing. This provides a substantial reduction in the size of the AOCP common optics section over an earlier design around a Questor objective.

The second unit proved to be unacceptable in a Facult test because of a cusp peak in the corrector plate in the center of the entrance pupil annulus. The objective lens was reworked a second time and the performance was greatly improved. This latter lens



NOTES: UNLESS OTHERWISE SPECIFIED

\triangle MOUNTING PADS (3) TO BE FLAT
WITHIN .005 IN. AND PARALLEL
TO EACH OTHER WITHIN .005 IN.

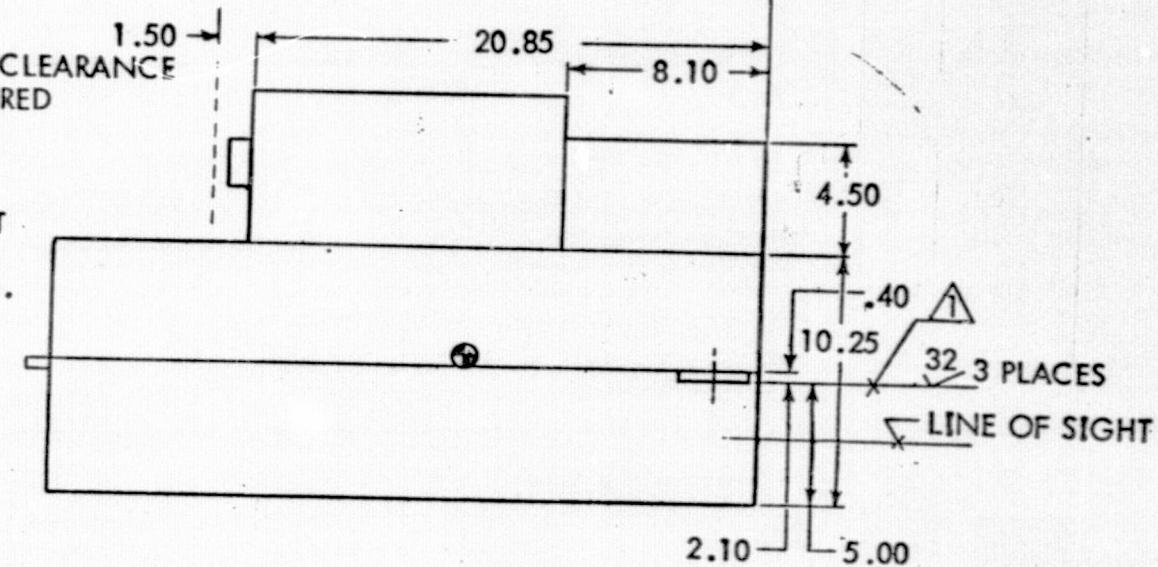


Figure 3-7. Aircraft Optical Communications Package

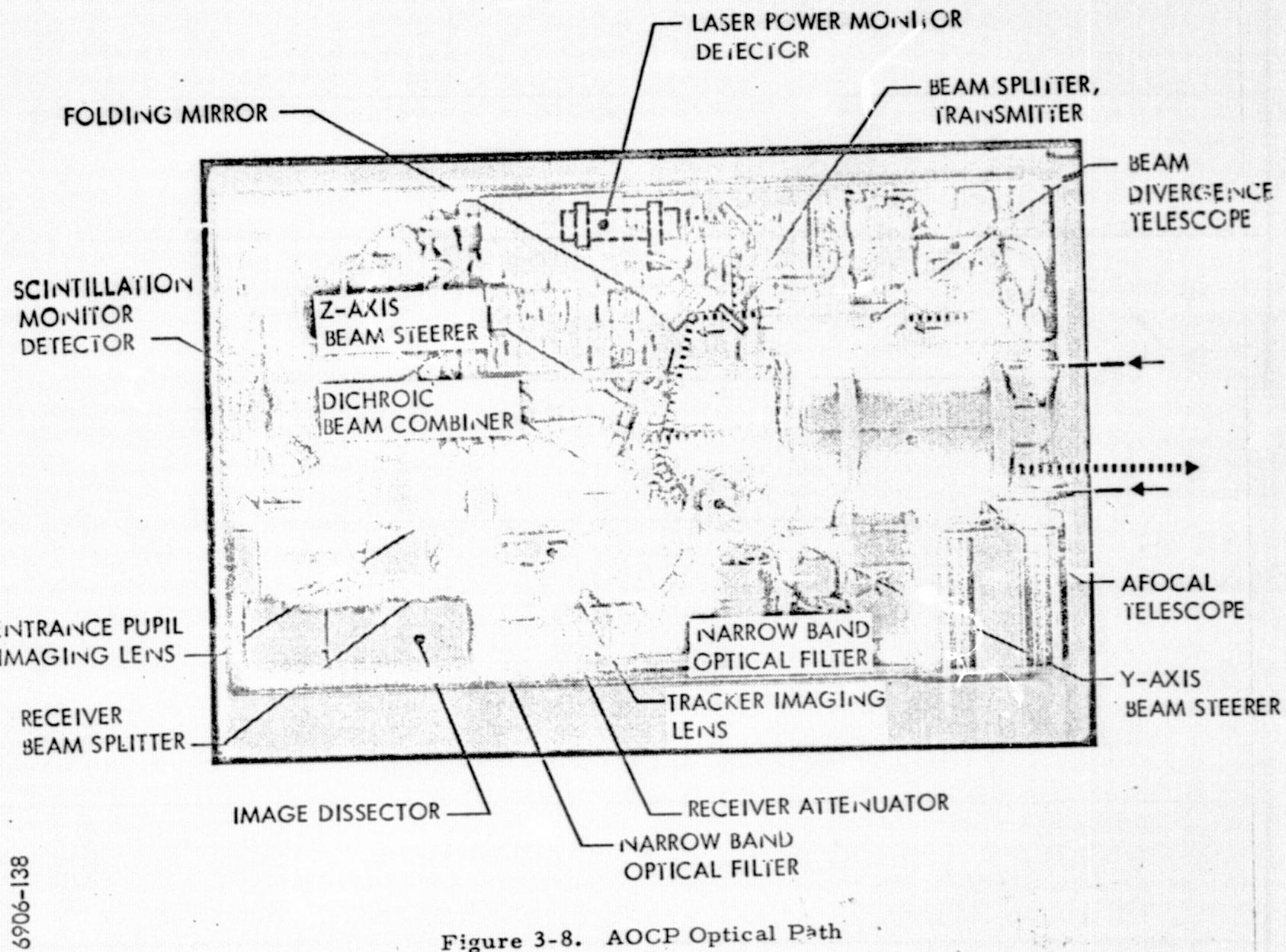


Figure 3-8. AOCP Optical Path

6906-138

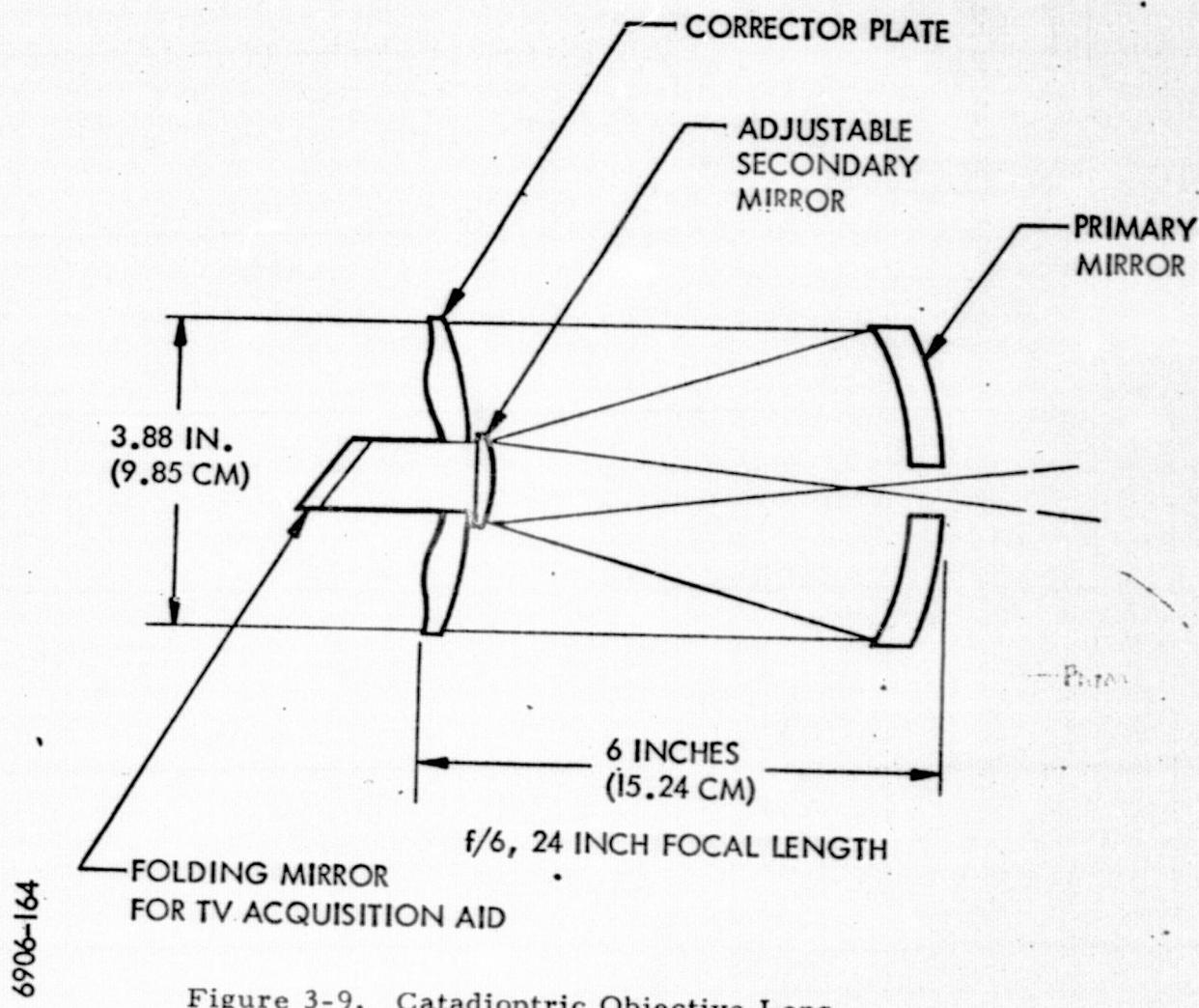


Figure 3-9. Catadioptric Objective Lens

system was installed in the field after the system had been delivered to NASA/MSFC.

The collimating lens is a multielement NIKON objective having a focal length of 75 mm. An adapter plate was made to interface the collimating lens to the catadioptric objective and form an afocal telescope as shown schematically in Figure 3-10. The afocal telescope power was determined by a careful measurement of the system entrance and exit pupils and determined to be 8.398. The exit pupil is located approximately 4.5 inches (11.4 cm) from the vortex of the collimating lens rear element. This permits the pupil to be located between the beam steerer mirror to minimize vignetting due to mirror motion.

The beam steerer mirror size is determined by the size of the exit ray bundle and the field of view divergence as illustrated in Figure 3-11. The distance of beam steerer mirror from the system exit pupil is made as short as possible to reduce the mirror size and improve its dynamic characteristics. The beam steerer mirror diameter, D_M , normal to the optical axis is given by.

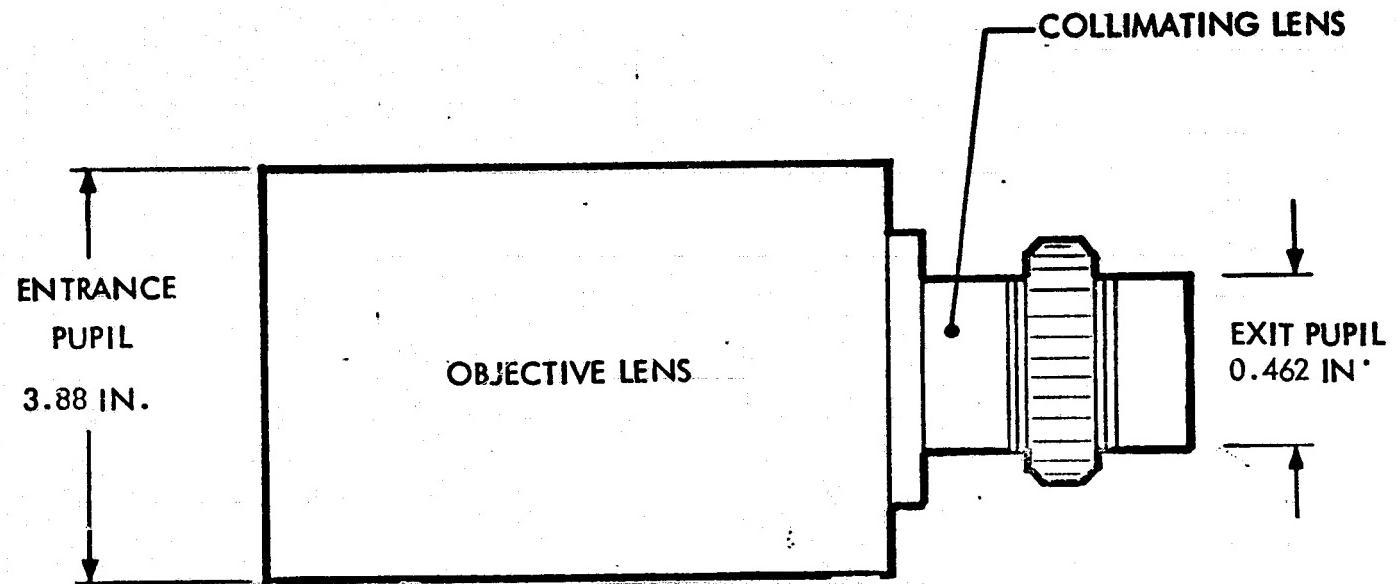
$$D_M \approx D_e + 2X_M \tan \frac{\theta'}{2}$$

where

θ' = (System field of view) x (afocal magnification)

X_M = distance from exit pupil to mirror

D_e = Diameter of afocal system exit pupil.



$$M = \text{POWER OF TELESCOPE} = \frac{3.88}{0.462} = 8.398$$

Figure 3-10. Afocal Telescope System

6906-65

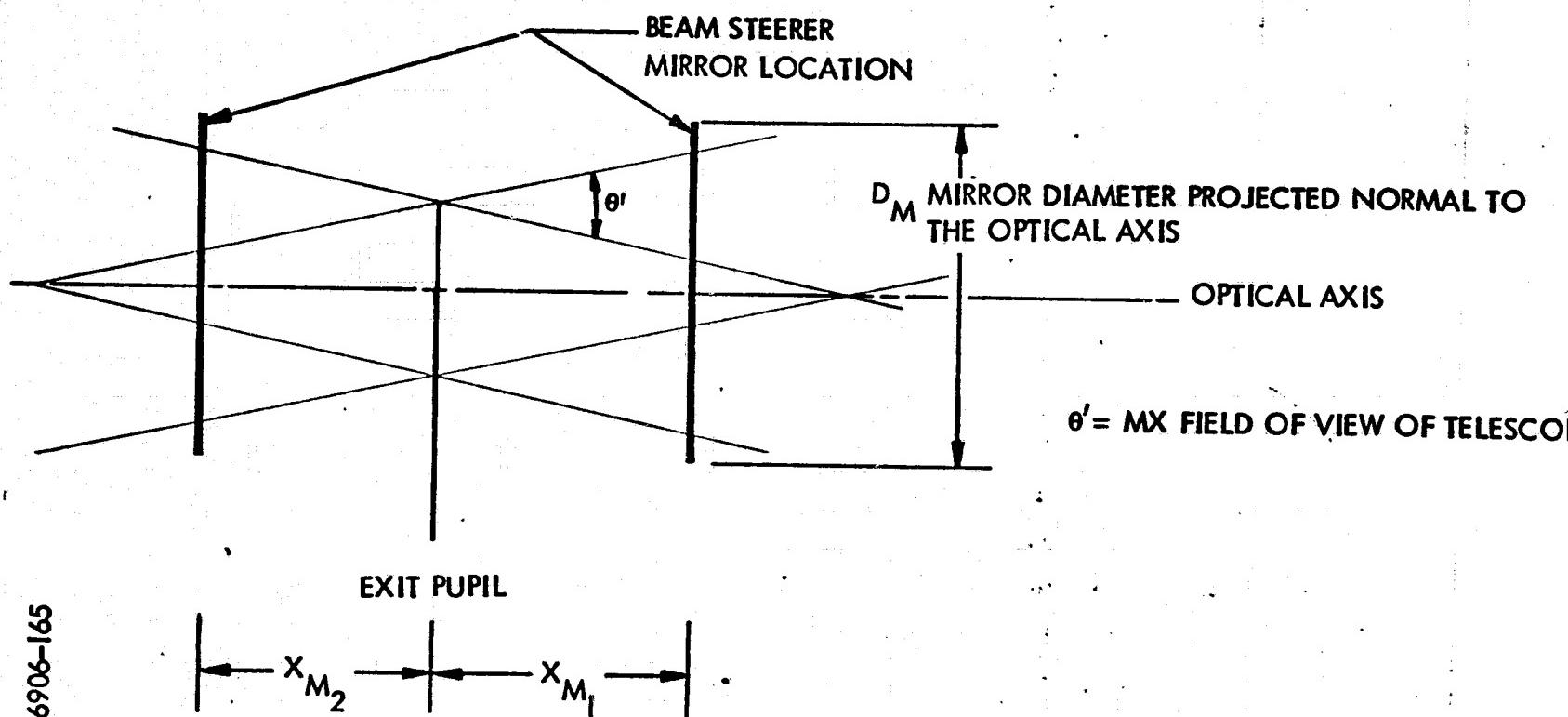


Figure 3-11. Beam Steerer Size Determination

For a 10.5 mrad (0.6 degree) field of view, a magnification of 8.4, an exit pupil diameter of 0.462 inches (1.17 cm) and a mirror separation of 1.5 under (3.81 cm) from the pupil, the mirror diameter projected onto the normal to the optical axis is 0.56 inch (1.42 cm). To allow for a 45° mirror tilt and a ±2 degree mirror rotation, the mirror size was set at 1 inch (2.54 cm).

The last element in the common optics train is the dichroic beam combiner. This element was designed for a nominal 40 degree incidence angle. The 0.633 micrometer reflectance is 0.8 or greater and the 0.488 micrometer transmission is 0.95 or greater. The beam combiner is gimbal mounted with spring loaded retention to permit coarse mechanical boresighting of the transmitted and received paths. The precision boresight is achieved electronically by offset tracking bias.

The first lens was manufactured to ITT wavefront deformation tolerances of better than $\lambda/20$ but was broken in shipment. In the interest of schedules, the lens was replaced by Wiley from stock with a rework of the corrector plate.

3.3 Receiver Subsystem

The AOCP receiver section comprises the receiver optics, tracking/communications sensor, tracking electronics, communications electronics, scintillation monitor, and the beam steering subsystem. Although beam-steering is a common element with the transmitter, it is controlled by the receiver tracker and will be described as a receiver subsystem. Location of the various receiver elements to be discussed in this section can be determined by referring to the Figures 3-4, 3-5, and 3-6.

The primary functions of the ACOP receiver subsystem are:

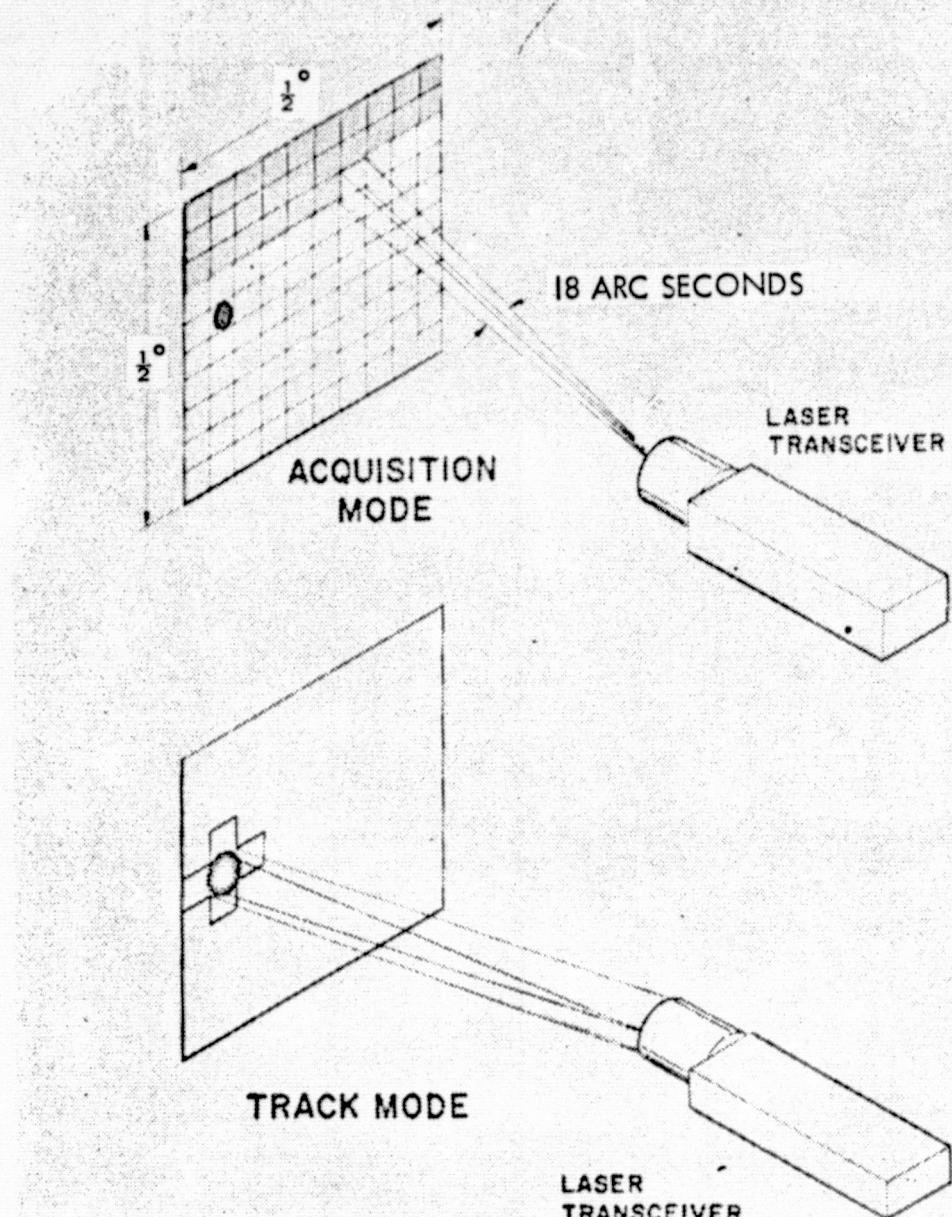
- a) Acquisition of a micrometer laser beacon within a 0.5×0.5 degree 0.488 field of view.
- b) Lock-on and auto track of the laser beacon with precision of a few microradians with a 1 kHz tracking bandwidth; providing two-axis output signals proportional to the position of the beacon relative to the sensor electrical null position.
- c) Closed-loop pointing of the transmitter laser beam through the beam steering elements to a precision of a few microradians rms in a 300 Hz bandwidth.

- d) Monitor atmospherically induced signal fading over a wide dynamic range both at baseband and at a 10.7 MHz subcarrier frequency with a bandwidth of 5 kHz.
- e) Detect modulation on the up-link laser beam for command of the AOCP status and
- f) Provide electronic boresight correction between the transmitter and receiver subsystems.

3.1.1 Receiver Subsystem. - A modulated (10.7 MHz subcarrier) Argon laser beam (0.488 micron) from the ground station (or ground checkout equipment, GCE) is guided by the coarse gimballed mirror onto the relatively wide-field-of-view TV acquistion aid. The TV acquisition aid subsystem detects and tracks the position of the ground beacon within its $5^{\circ} \times 7^{\circ}$ field-of-view and provides pointing commands in two axes to control the gimballed mirror to within the fine acquisition field of view (0.5×0.5 degrees). The fine acquisition is accomplished by an all electronically scanned image dissector detector searching sequentially a 128×128 element raster with a frame time of 1 second. Each raster element is approximately 68 micro radians on a side, and the instantaneous field of view is 87 micro radians which provides better than a 20 percent scan overlap. For the fine tracking system to acquire, the optical signal must exceed a threshold level (approximately 1×10^{-12} watt) and be modulated with a 10.7 MHz signal. This latter condition prohibits false lock-on to bright objects in the background.

REPRODUCIBILITY OF THE
ORIGINAL PAGE IS POOR

ANGULAR COVERAGE & SCAN PATTERNS



6906 - 43

AEROSPACE **ITT**

Figure 3-12. AOCP Search and Track Mode Illustration

Upon identification of the beacon, the receiver tracker switches into a track scan mode (the mode control functions and circuitry is described in the beam steering section of this report). The track scan is of the cruciform type which effectively displaces the optical image of the beacon back and forth in two axes alternately about the detection aperture as illustrated in the lower illustration of Figure 3-12. This action places a scan modulation on the detected signal which when synchronously demodulated with the sweep drive signal provides a measure of the optical image position in the sampling aperture. A more complete design discussion of this technique is given in the tracker section of this report.

The tracker output is a measure of the position of the optical beacon image on the detector photo cathode relative to the detectors null axis. The output signals are in rectilinear coordinator in the YZ plane.

Referring to the block diagram of Figure 3-3 and the photograph of Figure 3-8, the receiver optical path can be traced and the physical components identified. Laser radiation from the ground beacon is collected by the 9.85 cm diameter catadioptic objective and passes through the collimating lens, reflects from the Z-axis beam steerer onto the Y-axis beam steerer and through the dichroic beam combiner. From the beam combiner, the received radiation passes through a

bandpass filter centered about 0.488 micrometers and is divided into two paths by a neutral beam-splitter providing 80 percent of the energy into the tracking receiver path and 20 percent (less absorption losses), into the scintillation monitor path. Considering the tracking receiver first, the received radiation is reflected from the splitter passes through the imaging lens and receiver attenuator N. D. filter and is folded onto the receiver narrow band optical filter and focused at the image dissector detector photo-cathode. The path to the scintillation monitor detector is from the splitter through a lens which forms an image of the system entrance pupil; through an aperture stop located in the pupil image plane, and folded onto the scintillation monitor photomultiplier detector. A detailed discussion and analysis of the receiver optical system is presented under the optical discussion heading.

The key element of the acquisition and tracking receiver is the image dissector detector. This device has the capability of effectively scanning a large search field of view with a smaller instantaneous field of view thereby providing a large measure of spatial filtering of the background scene. The image dissector detector construction is illustrated in Figure 3-13. An optical scene imaged on the photocathode produces an equivalent photoelectron image that is relayed onto the aperture plate by electromagnetic focus

coils surrounding the electron drift tube section. By applying a deflection field through a second set of coils, the electron image, corresponding to the optical scene can be swept about the small aperture. Only the photoelectrons passing through the sampling aperture enter the multiplier section of the detector and produce an output. Consequently, the image dissector detector effectively scans a large scene with a small sensing element all electronically.

Figure 3-14 defines the effective focal length of the AOCP receiver imaging system. The optical system comprises the 8.398 power afocal telescope and a 135 mm focal length Snyder lens resulting in an effective total system focal length of 1133.73 mm. Figure 3-15 illustrates the total search field of view obtained by the 12.7 mm square search area on the image dissector photocathode. Similarly, Figure 3-16 defines the angular size of the scan aperture corresponding to the 0.1 mm image dissector square aperture.

The image dissector tracker is caused to scan the search field of view in a sequentially stepped raster containing 128 x 128 elements with a 24 percent area overlap to insure complete field coverage. This mode provides considerable spatial filtering of the uniform background level. Additional background suppression is obtained by narrow band optical filtering centered around the 0.488 micrometer beacon wavelength.

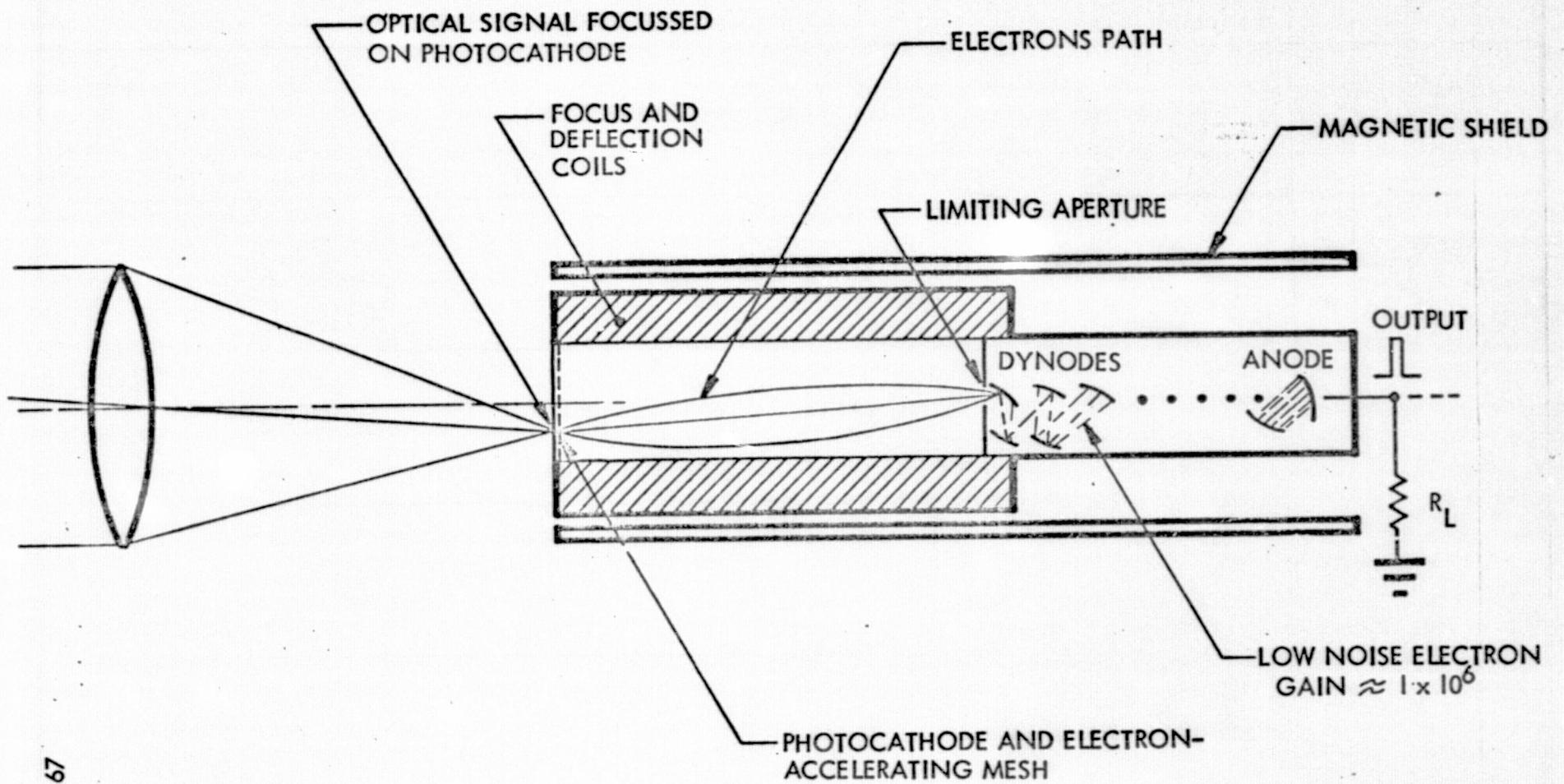
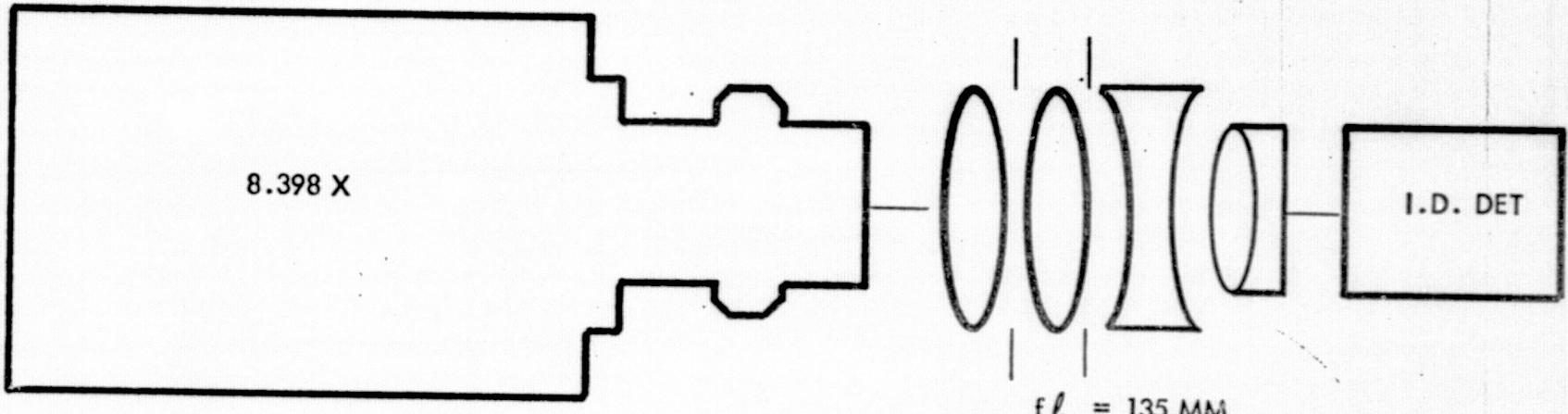


Figure 3-13. Image Dissector Assembly

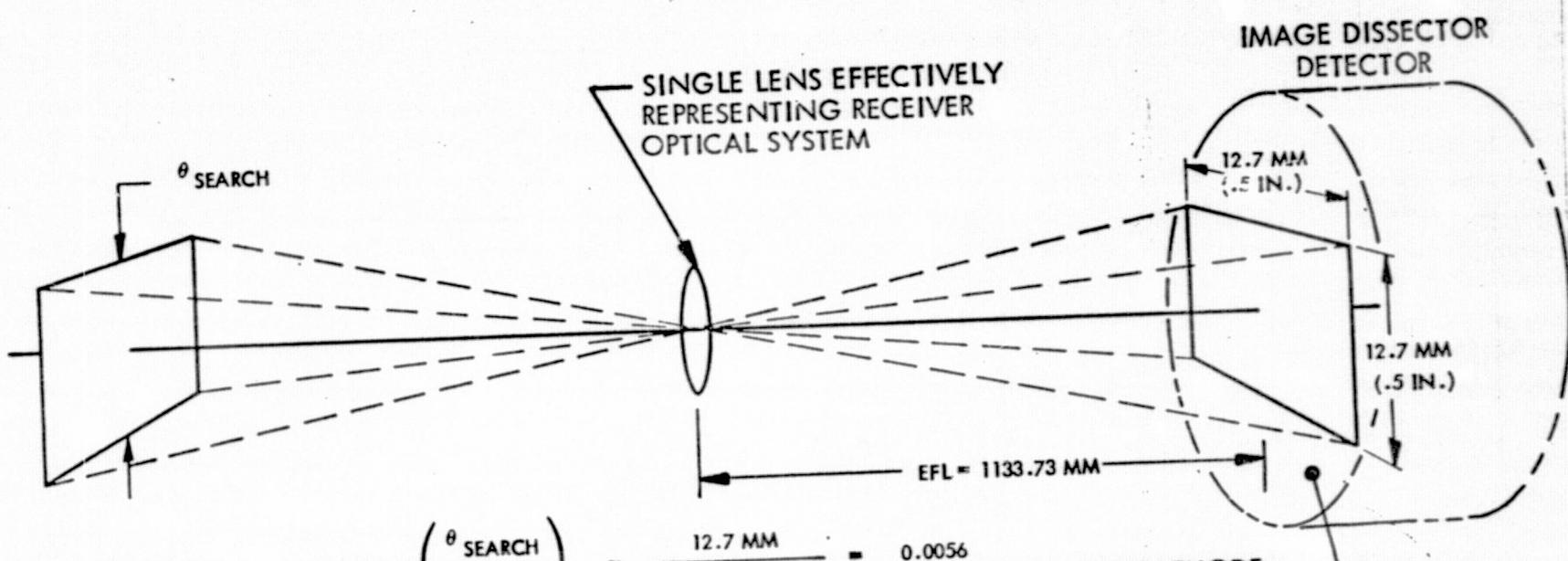
5-32

99 - 9069



EFL = EFFECTIVE FOCAL LENGTH OF IMAGING SYSTEM
= 135 MM X 8.398
= 1133.73 MM (44.635 IN.)

Figure 3-14. Imaging System



$$T_{\text{AN}} \left(\frac{\theta_{\text{SEARCH}}}{2} \right) = \frac{12.7 \text{ MM}}{2 \times 1133.73 \text{ MM}} = 0.0056$$

$$\theta_{\text{SEARCH}} = 2 \tan^{-1} (0.0056)$$

$$\approx 2 \times 0.0056 \text{ RAD} = 0.0112 \text{ RAD}$$

$$= 0.6417 \text{ DEG}$$

Figure 3-15. Fine Track Search Field of View

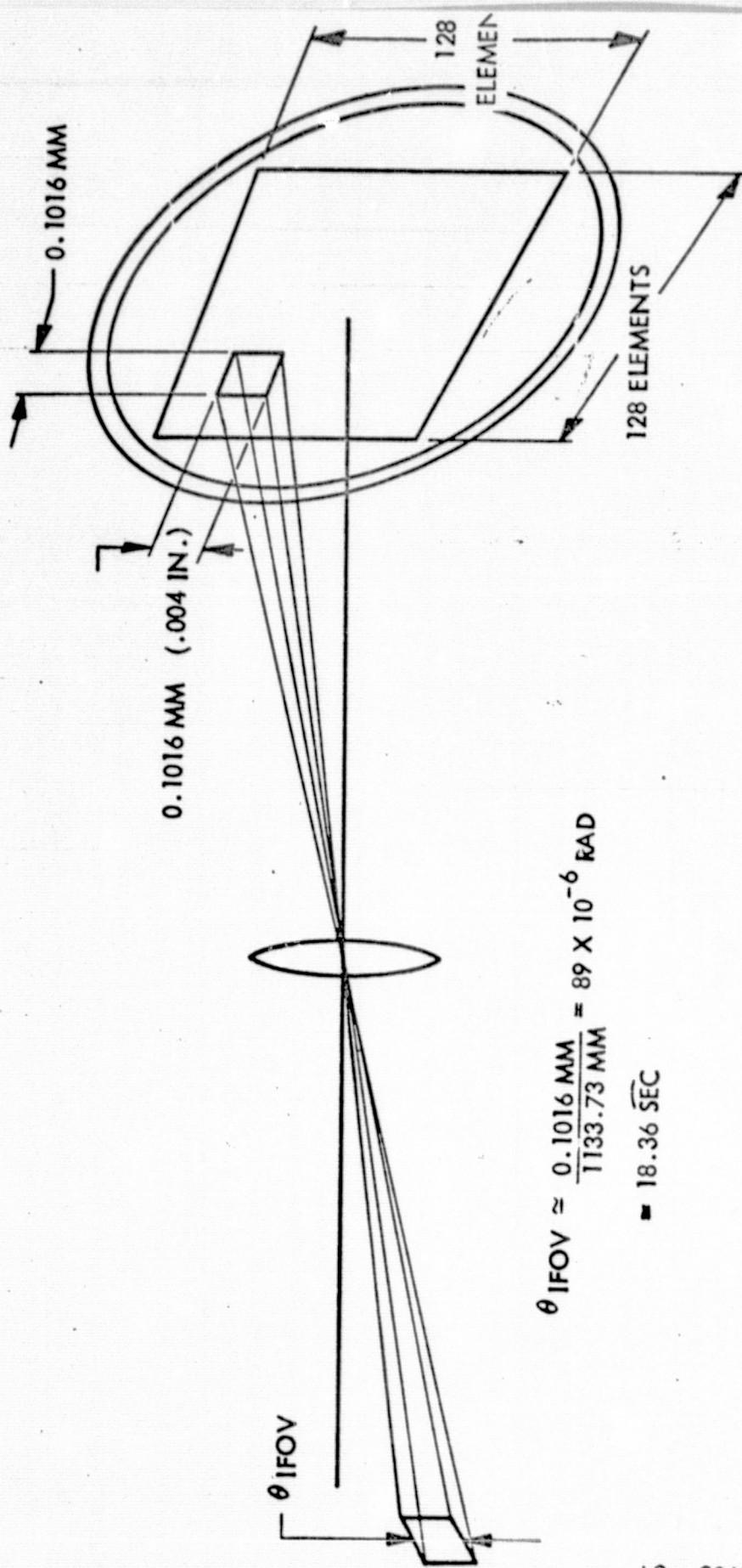


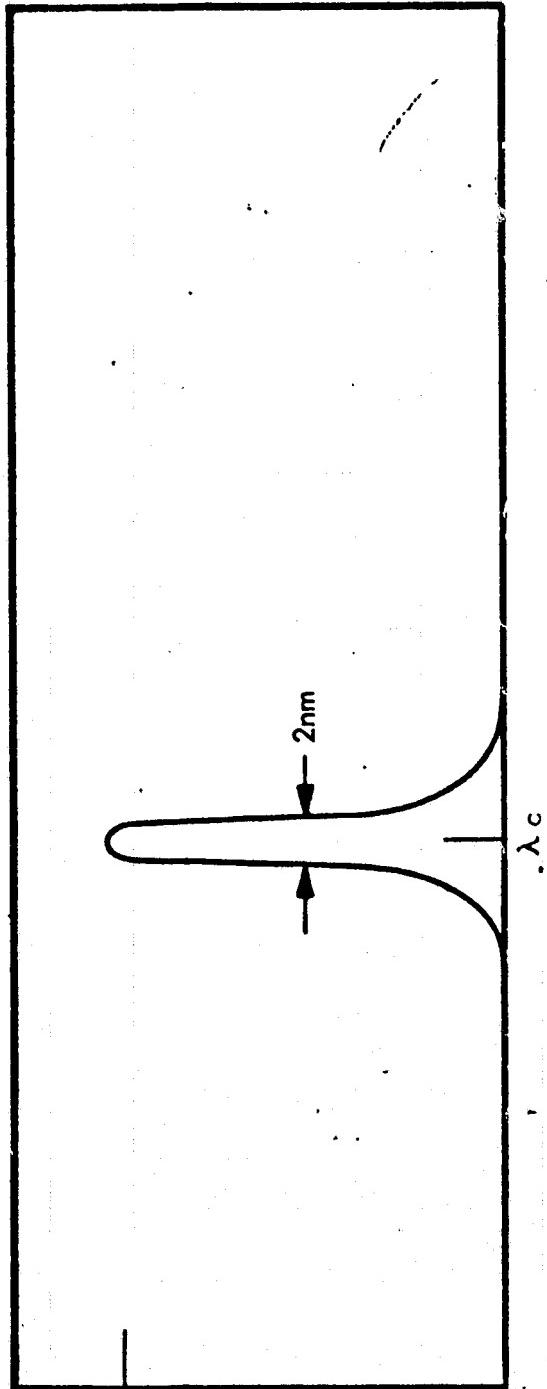
Figure 3-16. Fine Track Instantaneous Field of View

69 - 9096

Figure 3-17 illustrates the narrow band optical filter characteristics. Further background suppression is achieved by looking for the beacon modulation or signals exceeding the detection threshold. If a signal should exceed the detection threshold, the tracker would pause for a time at that element and determine whether or not it was due to the beacon by sensing the 10.7 MHz sub-carrier modulation presence. If the modulation was not present, the acquisition search would continue. It should be noted here that the switching between search and track modes is completely automatic. Any time track lock-on is lost, the system automatically reverts to a search mode.

3.3.2 AOCP Optical Tracker. - Figure 3-18 gives a functional block diagram of the AOCP image dissector. When a beacon image has been acquired and identified b the search mode, the circuitry automatically switches to the track scan mode. Sweep waveforms are generated by converting the outputs of a 14 stage synchronous counter to analog current. The first seven bits (highest frequency) are converted to generate the Y-axis staircase sweep and the last seven bits are converted to generate the Z-axis staircase sweep. The waveforms are shown in Figure 3-19.

The step reate is 16 kHz giving a dwell time of 62.5 microseconds per element and a frame time of 1 second.



65

68 - 9069

%T

3-36

Figure 3-17. Transmission Profile

A step size of 14.1 arc seconds covers the 0.5° dimension in 128 steps. With an IFOV of 18.5 arc seconds, a 24 percent overlap of elemental areas results throughout the scan.

In the acquisition mode, the IDT (image dissector tracker) is essentially in an open loop configuration as compared to the track mode in which the video information is processed for position. Offsets and/or drifts that might affect the acquisition sweep are prevented by use of solid state switches on the track loop and track sweep circuits.

Video from targets will be pulses of 62.5 microsecond duration with amplitude dependent upon source brightness. Selection of the uplink beam target is accomplished by detection of the 10.7 MHz modulation on the beam. As shown in the block diagram of Figure 3-18 the image dissector output is amplified in amplifier tuned to 10.7 MHz, rectified and level detected. Within one step time, a digital level hereafter referred to as VIDEO PRESENCE (VID PRES) is generated indicating that acquisition of the uplink beam has been completed and fine tracking can be commenced.

In this track mode, a modulation is placed on the optical signal (henceforth called the video) by partially deflecting the photo-electron image out of the detection aperture in two axes. A partial deflection scan implies that the photoelectron image is not completely

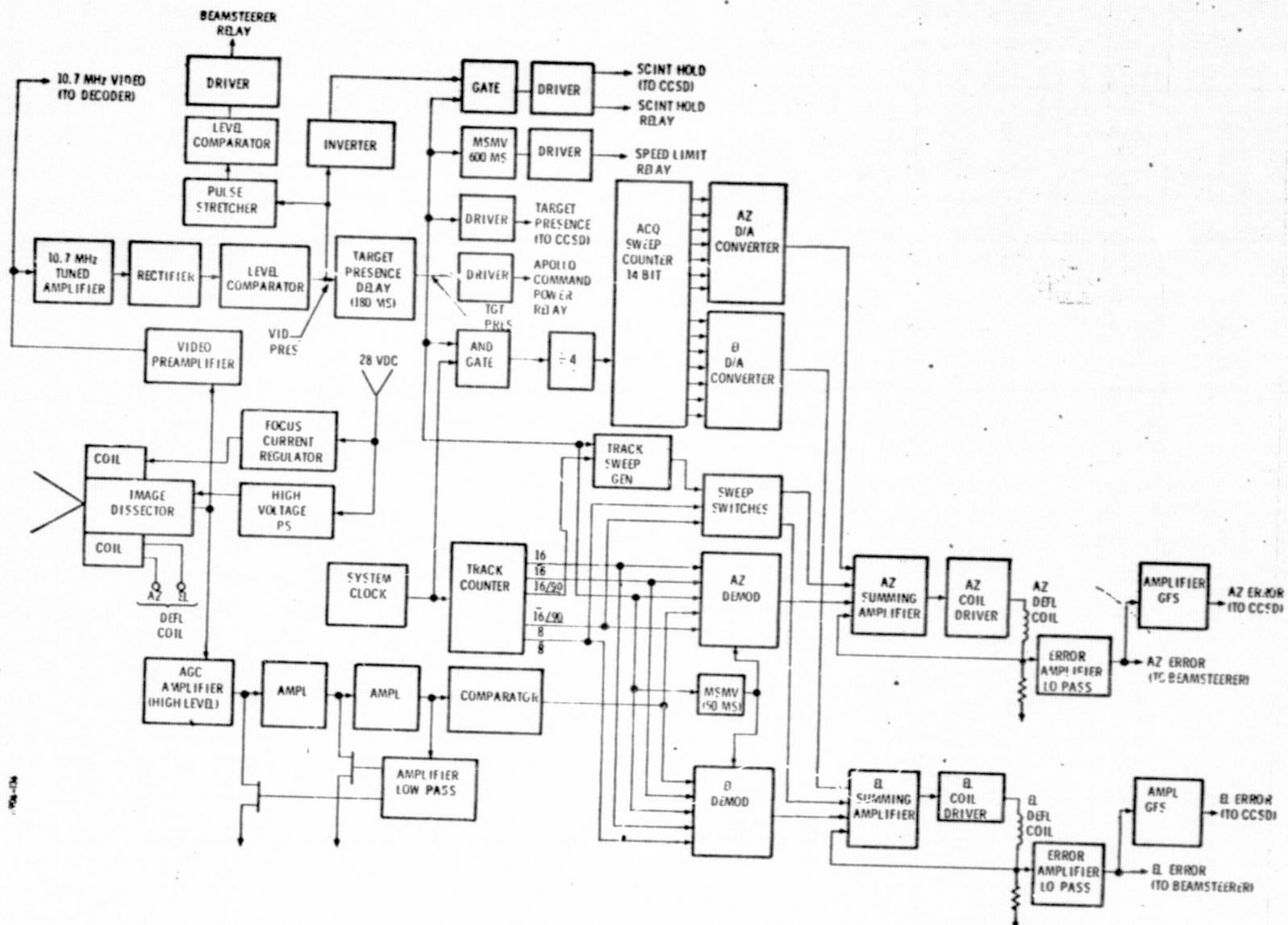


Figure 3-18. AOCP Optical Tracker

swept out of the aperture. The partial scan is employed so that some photoelectrons from the beacon image always enter the detector so that continuous communication is maintained. The amplitude modulation thus produced is demodulated synchronously with the deflection sweeps to determine the precise location of the photoelectron image centroid. A bias current is supplied to the deflection coils to exactly center the deflection sweep about the photoelectron image centroid. The bias current supplied to the deflection coils to effect the aperture scan centering is a measure of the beacon image position relative to the sensors null axis, i.e., zero bias position.

The video presence (VID PRES) logic level controls the Acquisition/Track mode status. When VID PRES is in a "1" state;

- 1) the clock input is removed from the acquisition sweep counter stopping the search scan.
- 2) the track sweep switches are enabled thereby commencing a cruciform scan at the immediate DC position
- 3) the demodulator steering gates are enabled thereby providing for closed loop tracking of the target image.

The track sweep is an analog cruciform of 8 kHz with individual Y and Z axis waveforms as shown in Figure 3-19. The scan amplitude is set so that the target electron is never completely deflected off the aperture. Although the sweep amplitude is dependent

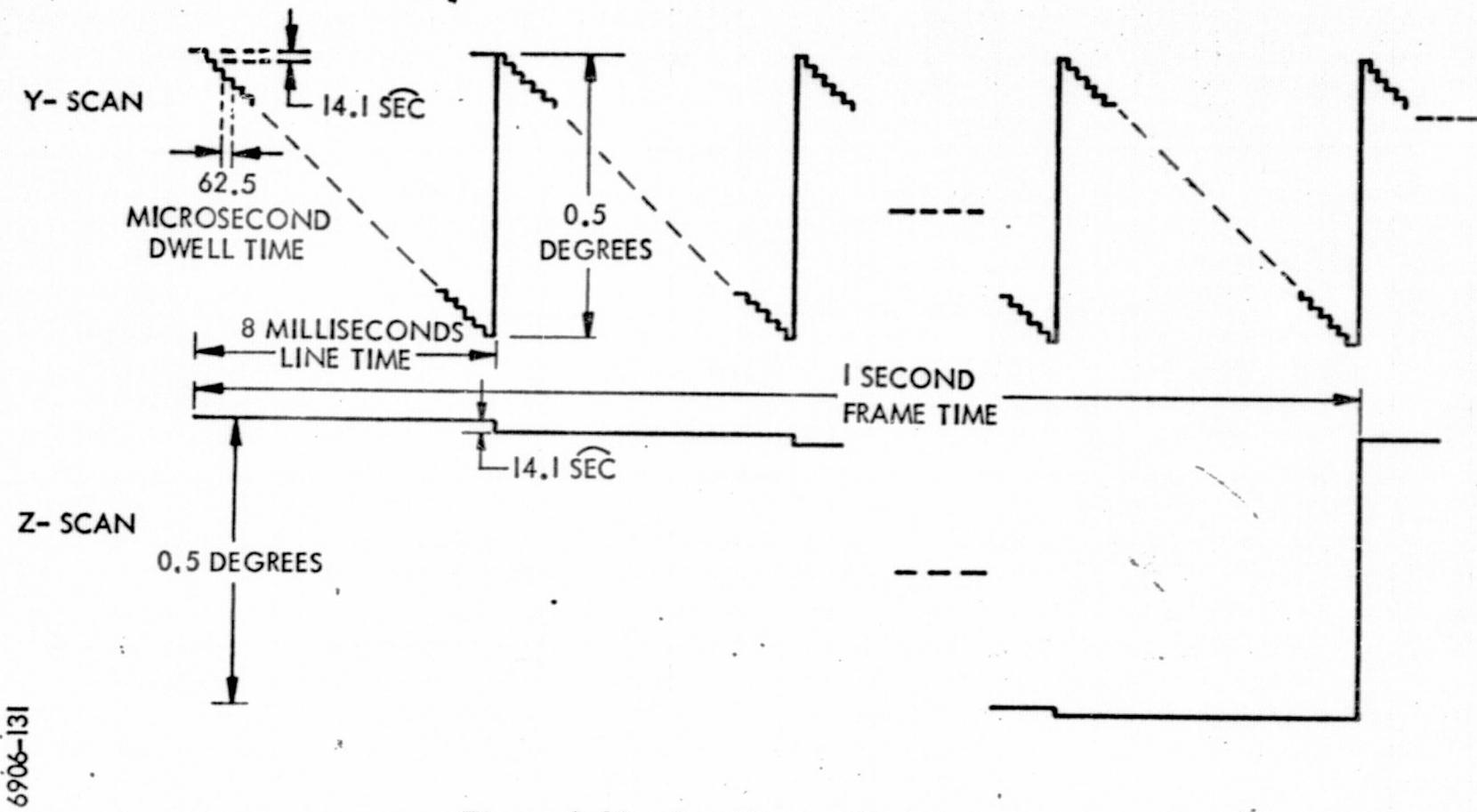


Figure 3-19. Search Scan Waveforms

6906-131

on the optical image size, it is nominally less than ± 1 IFOV for the AOCP IDT. The scan causes a pulse width and pulse duration modulation of the video signal.

The track video signal shown typically in Figure 3-20 has a frequency of 32 kHz (4 times the track scan frequency). The video is amplified and limited, thereby providing a position and duration pulse train to the demodulator. A three stage AGC is employed by the stages preceding limiting in order to minimize delays (phase shift) which result in an unstable track lock due to cross talk at the demodulator output. The AGC accommodates a 70 db input dynamic range in a 300 Hz bandwidth, which is typical of signal characteristics due to scintillation.

The video signal is synchronously demodulated with the output being an analog error signal proportional to the distance (the angle) between the center of the cross scan and the center of the target. It is noted that the transition from acquisition to track takes place when a TAR PRES is generated. The target image can be anywhere within the square 18.5 arc second IFOV and most probably not at the center.

The demodulator error signals are summed with the initial cross scan position to move the cross scan such that it becomes centered on the target image and the demodulator error voltage

approaches zero. The centered video waveform is shown in Figure 3-20. The track mode is characterized by a Type-O control loop where any movement within the acquisition field of view results in an automatic correction to the deflection coil current so that the cruciform remains centered on the target image. The track loop bandwidth is nominally 1 kHz.

While tracking, valid target position signals are generated by sampling the deflection coil currents. The target position signals, having a transfer function of 0.33 v/min. are applied to the beamsteerers. The beamsteerers position the uplink target image to a reference position and fine point the down link beam based on this reference.

Tracking is maintained as long as VID PRES is "1". The VID PRES status is relatively high bandwidth in that the status change occurs within tens of microseconds of applying or removing a 10.7 MHz signal at the preamp. Due to scintillation, signal fades of 100 milliseconds duration are common. Therefore the VID PRES changes states during these fades. Even with intervals of no signal, the track scan position is maintained within an IFOV. To prevent breaking lock during fades, the VID PRES loss is delayed approximately 180 milliseconds. The resultant digital level is referred to as TAR PRES and is the digital level used by the IDT to sequence between

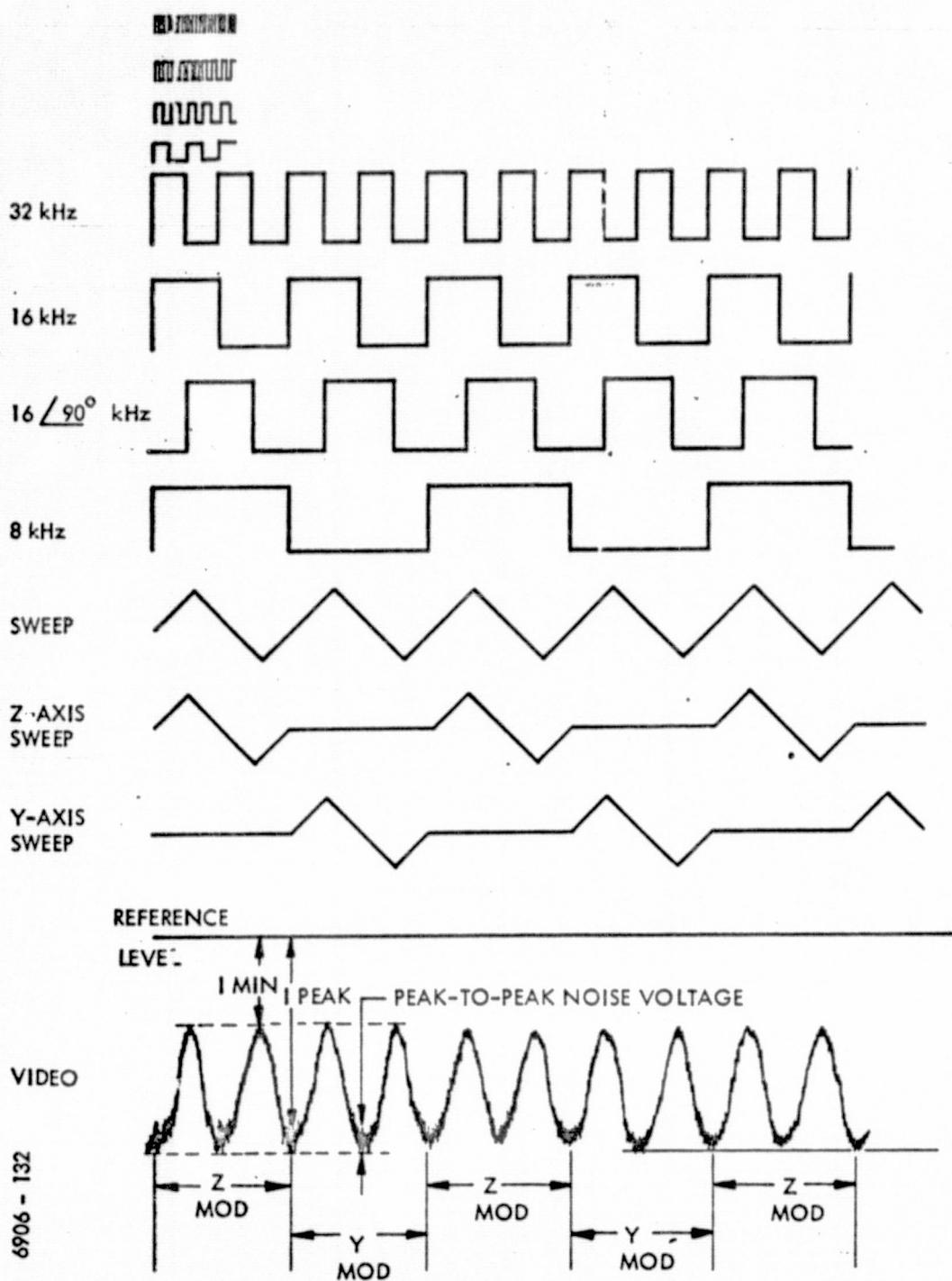


Figure 3-20. Track Mode Timing Diagram

acquisition and track. The return to acquisition occurs therefore, only if the 10.7 MHz signal is lost for greater than 180 milliseconds.

Loss of TAR PRES returns the IDT to the acquisition mode.

The transition is also used to place a 50 millisecond short on the tracking loop error demodulators as noted previously, the tracking functions are disabled during acquisition. However the error demodulator outputs which have a 2 second line constant can become high during tracking since they effect the closed loop operation. The outputs are shorted momentarily upon return to acquisition to prevent offset and drift of the acquisition scan.

The VID PRES signal is the primary AOCP mode control. A timing diagram of the various control signals derived from the VID PRES signal is shown in Figure 3-21.

Two of the control levels, namely TAR PRES and DEMOD SHORT are used internal to the IDT and were discussed in the previous section. The BEAMSTEERER RELAY level is delayed 120 milliseconds from the VID PRES signal. The BEAMSTEERER RELAY "1" level represents the time during which the pointing is under control of the IDT. The SPEED LIMITED level is derived from the TAR PRES signal, and provides a 600 millisecond delay during which the Beamsteerer Drive voltage is limited.

The SCINT HOLD is derived from the VID PRES and TAR PRES levels. It is used to insert a hold on the Beamsteerer Drive amplifier during times of signal fade. It essentially lowers the Beamsteerer loop bandwidth so that effects of IDT drift during times of no signal are minimized. Of course if the fade interval exceeds 120 milliseconds, the BEAMSTEERER RELAY becomes "O" and control of the loop is returned to the TV Tracker.

3.3.2.1 Track Loop Analysis. - The IDT is essentially a modification of previous ITTG tracker designs. In this respect, a significant amount of design analysis was not required. In the early design phases, a model of the target and variations thereof was not necessarily accurate. Therefore, design modifications to the initial tracker were made during field tests when actual targets and background were being encountered.

An important modification of the previous ITTG tracker design was the extension of the tracking loop bandwidth to 1 kHz. A block diagram of the loop components is shown in Figure 3-22.

3-46

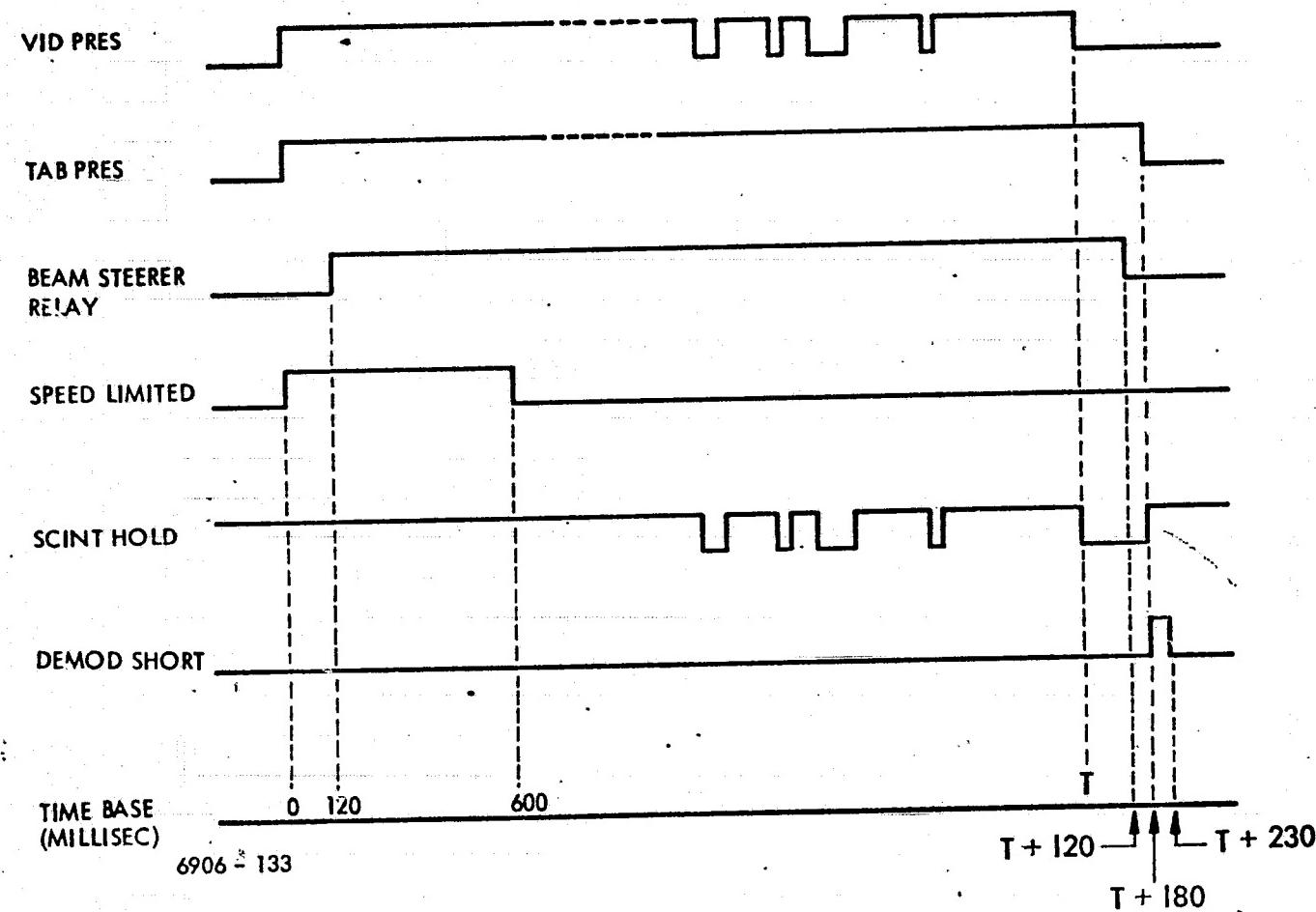


Figure 3-21. Control Signal Timing

6906 - 134

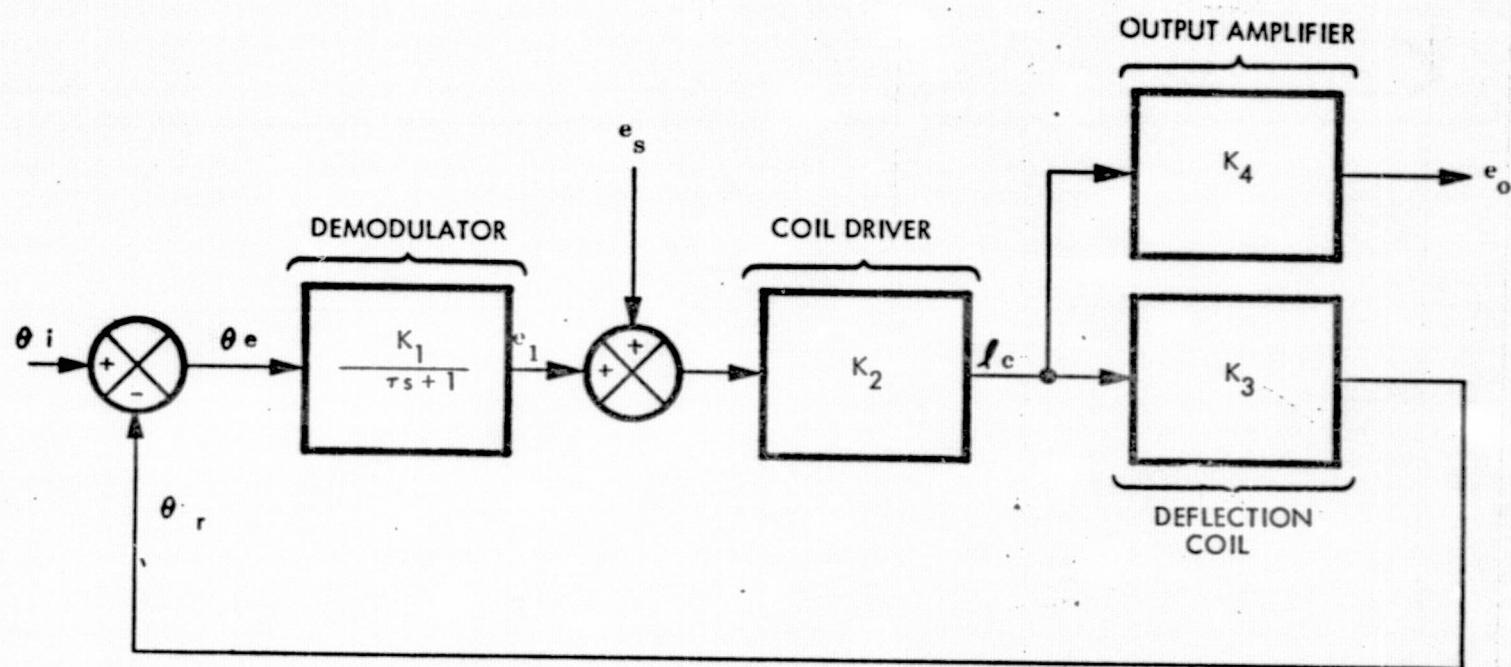


Figure 3-22. Tracking Loop (One Channel)

The closed loop gain of the loop is given by

$$\frac{C_o}{\theta_i} = \frac{K_1 K_2 K_4}{s + \frac{1 + K_1 K_2 K_3}{T}}$$

The bandwidth is

$$W_L = \frac{1 + K_1 K_2 K_3}{T}$$

The IDT constants have the following nominal value

$$K_1 = 2 \text{ volts/sec}$$

$$T = 2.2 \text{ sec}$$

$$K_2 = 254 \text{ ma/volt}$$

$$K_3 = 35 \text{ sec/ma}$$

Using these values

$$W_L = 8880 \text{ rad}$$

$$f_L = 1500 \text{ Hz}$$

It is noted that the demodulator gain K_1 is dependent on the signal strength. The value stated would be the maximum attainable. As the signal strength decreases, the value of K_1 decreases and the loop bandwidth decreases proportionately.

The maximum steady-state error would occur when initial acquisition of the target was at a field edge. For this case

$$E_{ss} = \frac{\theta_i}{K_1 K_2 K_3}$$

$$= \frac{30 \text{ min}}{17760}$$

$$= 0.1 \text{ sec}$$

3.3.2.2 Track Video Amplifier Test Results. - One major modification to the IDT was made as a result of field tests. Minor changes and additions were made with the VID PRES signal to facilitate the handover between the TV tracker and IDT.

During initial field tests between the Astrionics Laboratory and Madkin Mountain, apparent angular modulation was experienced which was excessive in both amplitude and frequency. Because of this effect it was impossible to close the beamsteerer loop and only intermittent tracking was possible with the IDT. This apparent angular modulation was traced to amplitude scintillation in the atmosphere causing dynamic phase changes in the IDT video amplifier.

Two separate problems existing in the ID tracker contributed to the tracking difficulties experienced in the initial field test. They were:

1. Excessive phase shift in the video signal over the input signal dynamic range.
2. Inadequate AGC bandwidth.

The phase shift problem existing in the video amplifier was a result of the gain controlling device working against the reactances of the image dissector and the input to the 10.7 MHz communication amplifier which is paralleled across the tube at this point. The resulting phase shift over the input dynamic range was in excess of 70°.

The initial AGC bandwidth was approximately 10 Hz which is below the normal frequency range of amplitude scintillation. The video amplifier low frequency cut off was approximately 100 Hz and limited the effective AGC bandwidth that could be incorporated.

Modifications were made to the amplifier. These changes brought about performance improvement and corroborated the fact that inability to track was due to the amplifier phase shift characteristics. However, it became apparent that a new amplifier design was needed to supply the AGC dynamic range and bandwidth.

A new amplifier was designed and tested. It replaced the original amplifier of the IDT and successful operation of the AOCP with Madkin Mountain was demonstrated on 2/10/72. The amplifier design is shown in Figure 3-23. Three attenuators are used to effect a dynamic range of greater than 60 db. The initial gain control is applied by the voltage divider of R_1 and the FET attenuator No. 1. As the signal increases the R_2 -FET attenuator No. 2 is added. Each divider is capable of 25 db attenuation. The bandwidth of the loop with these two attenuators was measured to be 120 Hz.

The input stage buffers the tube output from attenuator No. 1 thereby making the effect of attenuator capacity change negligible. However, the buffer stage must accommodate the dynamic range linearly. Attenuator No. 3 provides the necessary range. This third control becomes operative only for high input and can easily accommodate 15 dB.

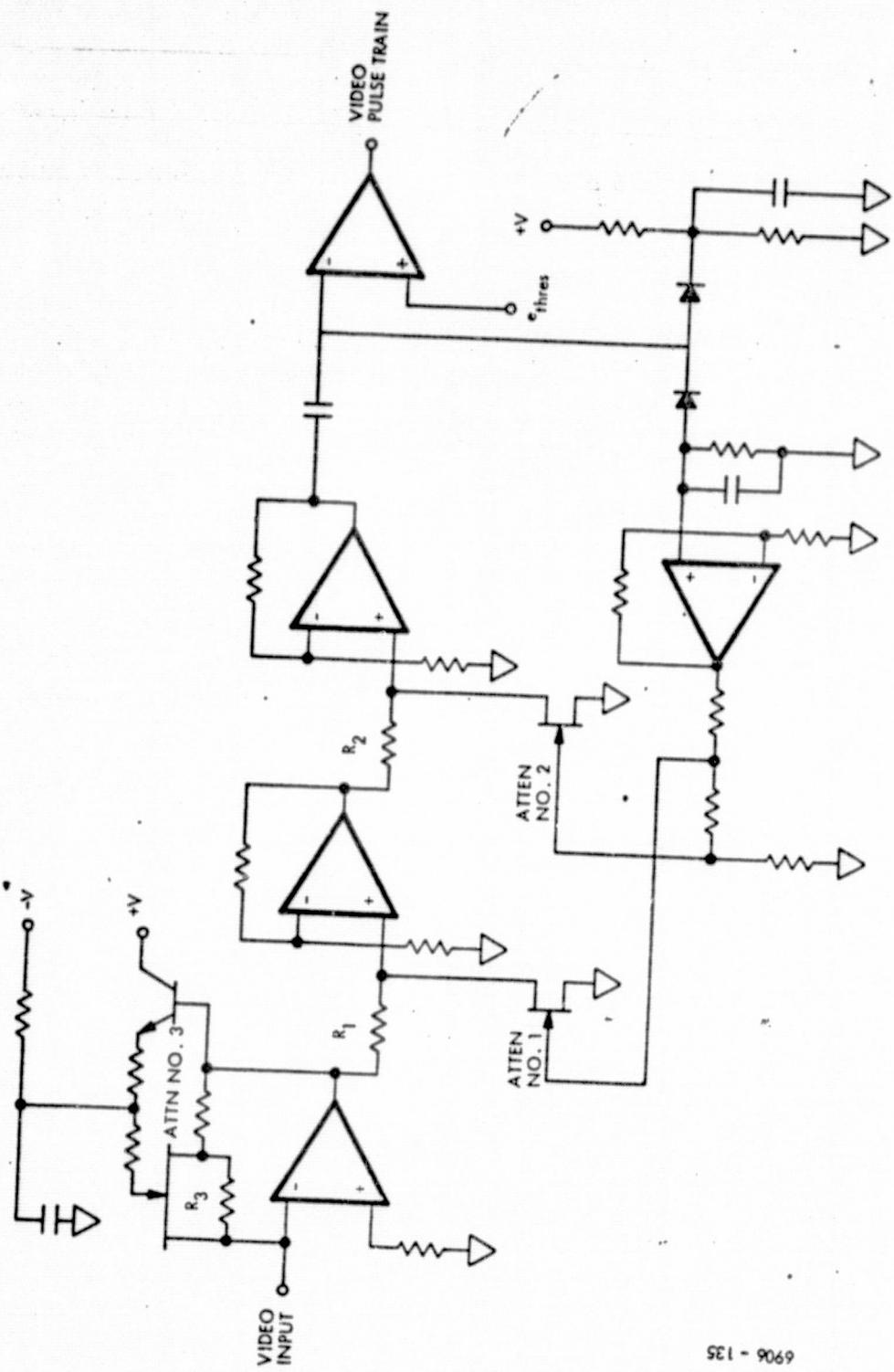


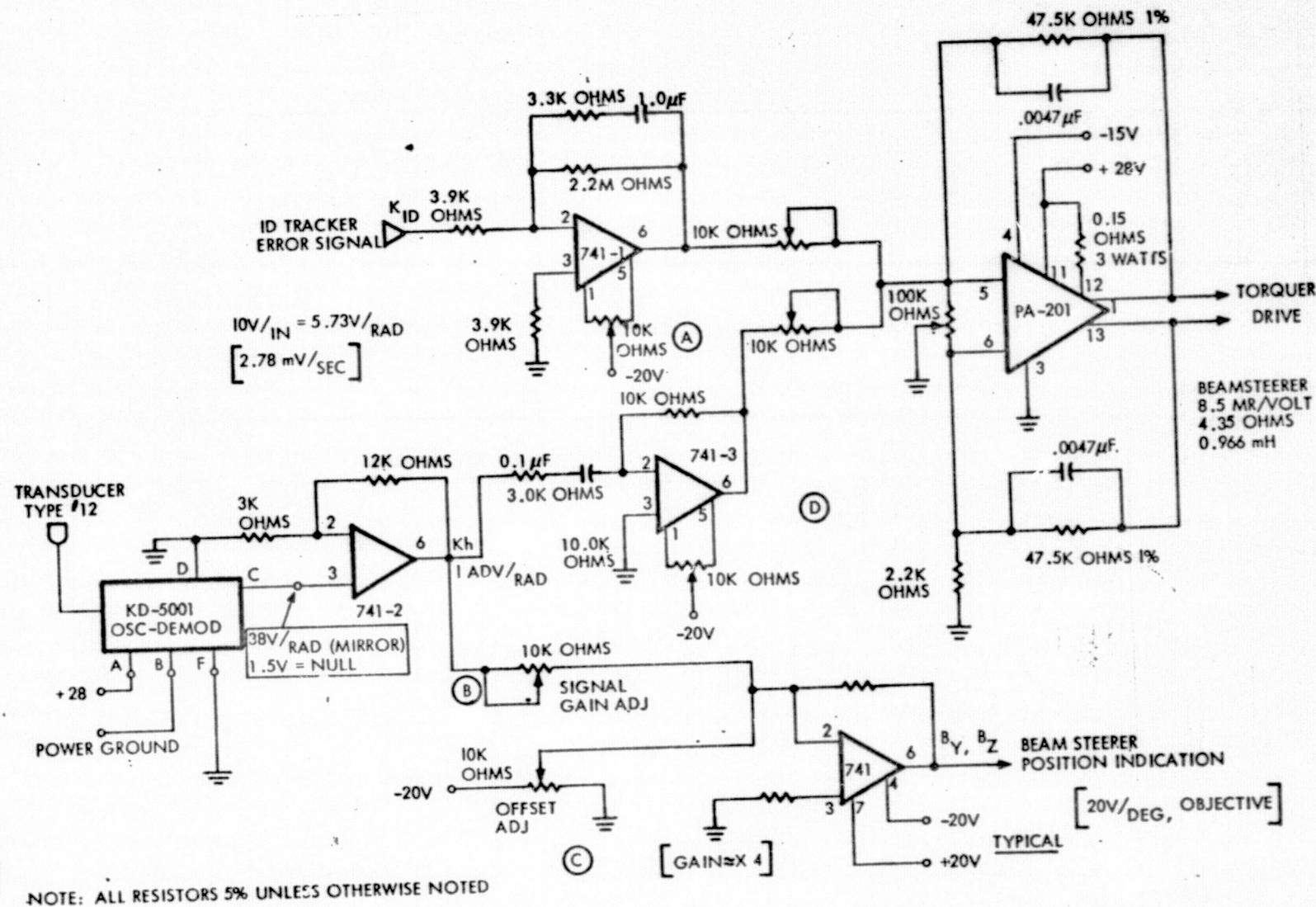
Figure 3-23. AGC Amplifier

6906 - 135

3.3.3 Beamsteerer Loop. - The keynote of beamsteerer design philosophy at onset of AOCP was flexibility. Fundamental to the selection of this course of design was the fact that little was known of the dynamics of the atmosphere for which the beamsteerers were to correct. Much has been learned during the course of the AVLOC Program regarding beamsteering that could and would be factored into later such designs. Notwithstanding the evolution of the beamsteering subsystem during the program the final iteration showed marked similarities to system originally shipped. The major differences are manifest in the very portions of the subsystem set aside to absorb those anticipated evolutionary changes, viz the loop compensation circuits. Figures 3-24 and 3-25 are presented to give an indication of those changes that ultimately took place during the life of the program. The final configuration shown in Figure 3-25 is that used in the final successful test flights.

The design analysis presented herein will accomplish the following purposes:

1. Present the final beamsteering subsystem configuration and brief operational description.
2. Define the characteristics and sources (when appropriate) of the elements making up the beamsteerer subsystem.
3. Present a complete servo block diagram of the subsystem (y-loop).



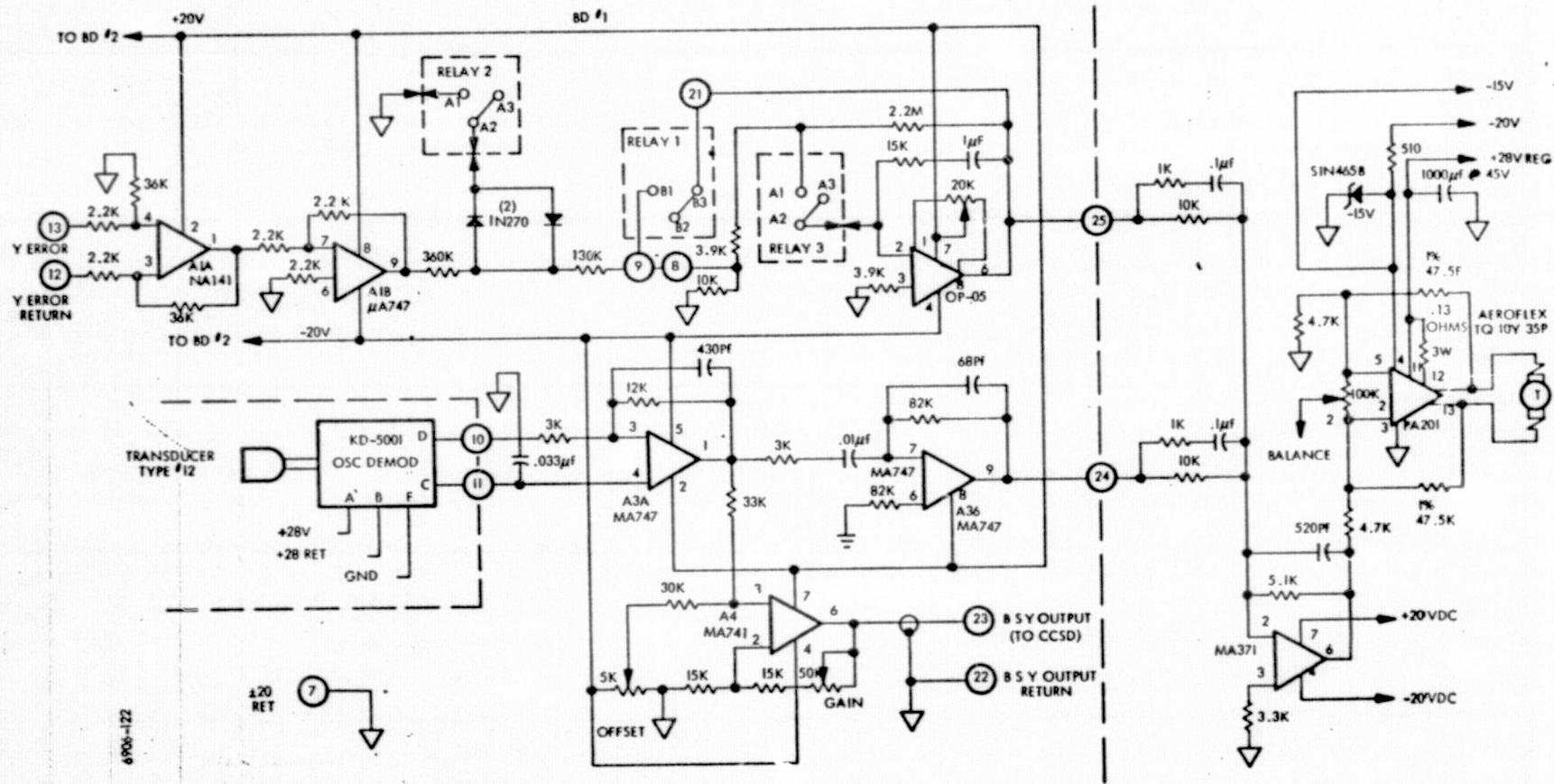


Figure 3-25. Final Compensation Configuration

4. Simplify the loop consistent with the bandwidth of the subsystem.
5. Develop a root locus of the simplified system, indentifying the location of the closed loop poles and zeros (p-z) for the appropriate loop gain.
6. Present the results of a frequency response taken from the p-z configuration and compare the analytical results with test measurements.

Operational Description. - One loop (or channel) of the beamsteerer subsystem is shown in Figure 3-26. This figure describes the basic elements from a functional viewpoint. The incoming laser beam is collected by a four-inch aperture afocal telescope. The beam emerging from the telescope is routed to beamsteering mirrors, one for each channel (y and z) then to another set of optics whose purpose is to focus the beam on the face of the image dissector tracker.

The tracker develops three sets of outputs that are of further use to the beamsteerer subsystem.

1. y and z error signals
2. video from the image dissector
3. 10.7 mHz target present signal

Image dissector video output and the 10.7 mHz target present signal control the mode of the beamsteerer subsystem. The error signals are appropriately routed to the remainder of the subsystem as called for in each mode.

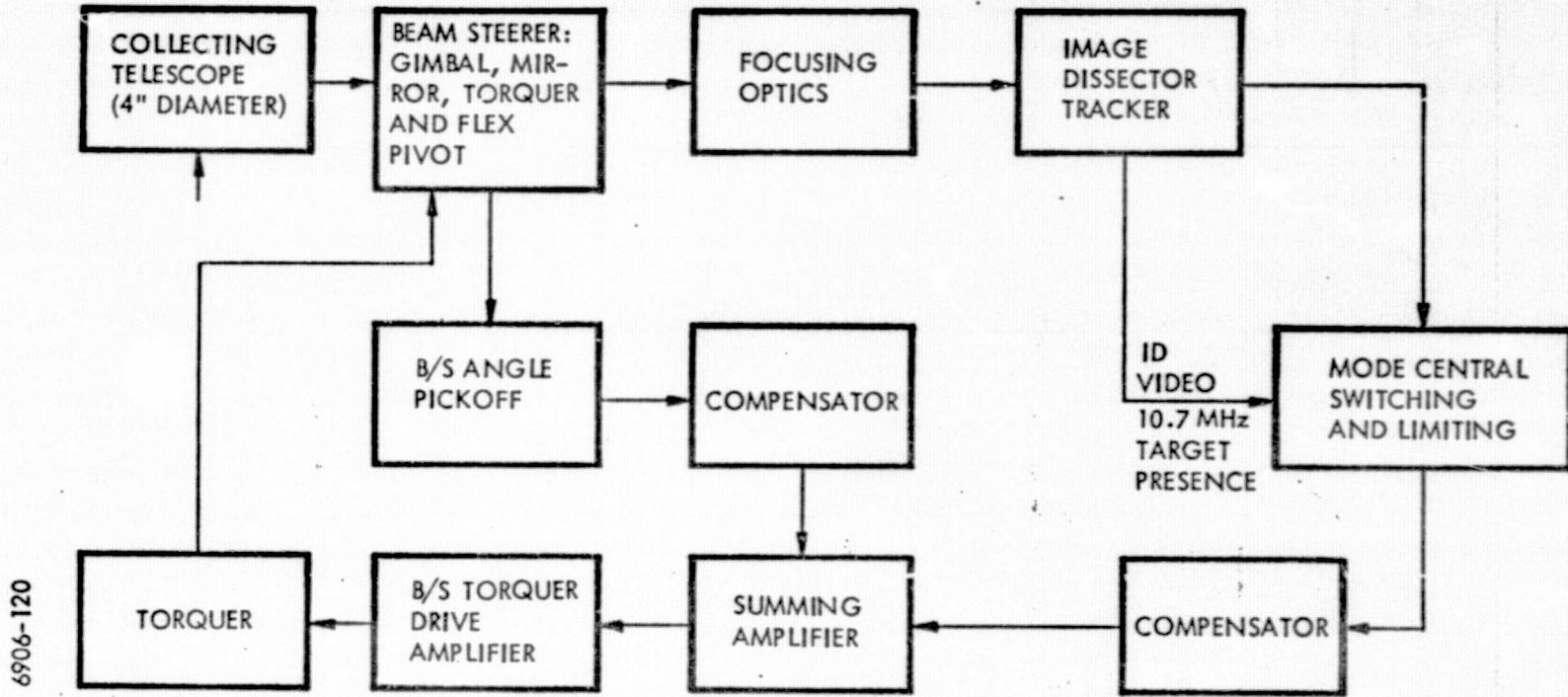


Figure 3-26. Function Configuration of the Beam Steering Subsystem.

The Collecting Telescope. - The first functional block of Figure 3-26 is the telescope. This device was purchased from Wiley Optical Corp. of Florida. Its principal characteristics are:

- a. 4" aperture
- b. 24" focal length
- c. 2 arc second resolution
- d. Magnification of 8.4 $\frac{\text{RAD}}{\text{RAD}}$

Beamsteering Gimbal, Mirror, Torquer, and Flexpivot. - This assembly was fabricated by ITTG per Drawing 5520160. The mirror and flex pivots were purchased from Precision Optics Company and Bendix, respectively. The mirror was manufactured to tight tolerances with a flatness of better than $\lambda/20$, and was mounted with a gimbal cell fabricated by ITTG. The gimbal cell was fashioned with tabs that worked in conjunction with a Karman Science Corp. position pickoff (Model KD-5001-12) so as to convert rotational to linear pickoff. The effective moment arm of the tabs was 0.65 inches. The electronics associated with the pickoff developed an output calibrated at 63 V/in over approximately 0.050 inch movements. The mirror and gimbal were mounted to the optical baseplate through the Bendix flex pivot. A set of two flex pivots were used, one on either side of the gimbal.

The flex pivots provided a no-power, return-to-zero capability as well as precluding use of bearings.

Torque was supplied the assembly by use of one Aeroflex Corp. direct drive brushless torquer TQ-10Y-35P, which was provided with a special order low resistance winding. A photograph of the fine beam steering assembly is shown in Figure 3-27.

A summary of the characteristics of these devices follows.

a. Mirror

- Flatness - $\lambda/20$
- Size - 25 mm diameter
- Angular gain - 2 rad/rad

b. Kaman Science Corp. Pickoff

- Gain 63 volts/inch (calibration curves on file)
- Moment arm (effective 0.65")

c. Bendix Flex pivots

- 1/4" pivot 5008-600
- 13.1 oz in/rad torque gradient

d. Teroflex torquer TQ-10Y-35P

- torque gradient 0.885 oz in/amp"
- resistance - 4.35Ω
- inductance - 0.966×10^{-3} h.
- back EMF - 5.53×10^{-3} v/rad/sec.

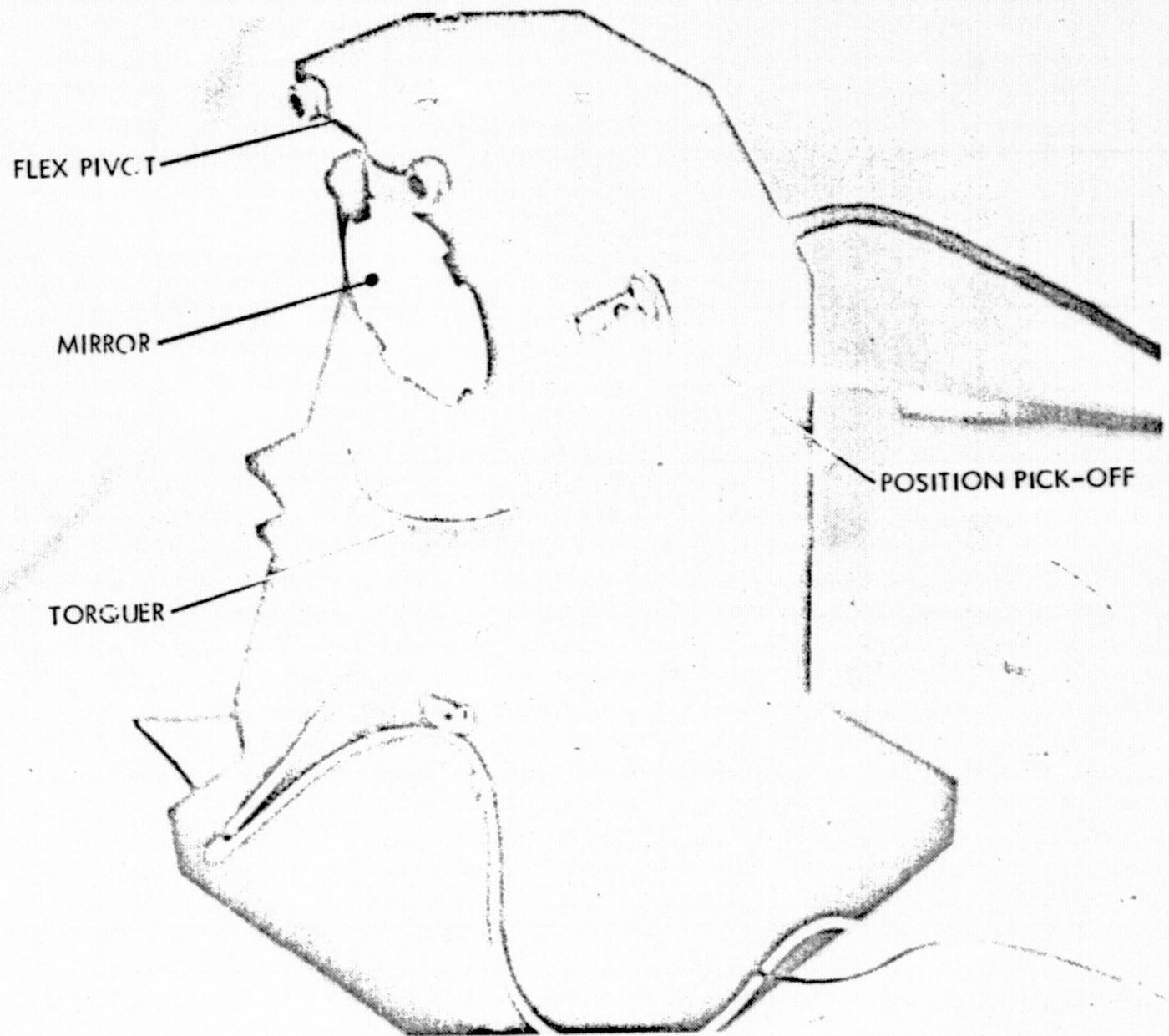


Figure 3-27. Beam Steerer Assembly

e. Polar moment inertia of rotating assembly. The rotating assembly includes

- mirror
- gimbal cell
- rotor of torquer
- outer shell of flexipivot

total polar moment of inertia

$$y \text{ loop } 19 \times 10^{-5} \text{ oz in sec}^2$$

$$z \text{ loop } 19 \times 10^{-5} \text{ oz in sec}^2$$

Focusing Optics. - The focusing optics (Schneider, refractive) have the following characteristics:

focal length - 135 mm (5.31 in)

f/3.5

Transmission 75 percent

Image Dissector (ID) Tracker. - The ID tracker was designed and fabricated by ITTG. It is described in detail elsewhere in this report. For our purposes its principal functional characteristics are sufficient. The output of the tracker is expressed as volts per inches of displacement of

the focused image from the electrical center of the tracker at the photocathode.

In addition, the tracker has a nominal 1 KHz bandwidth. Summarizing:

Tracker output gradient: 25.6 volts/inch

Tracker bandwidth: 1000 Hz

Mode Control. - The operating mode control is an important part of the acquisition process if operation in a signal fade environment is required. The function of the mode control subsystem is to provide switching signals to select the appropriate sensor controlling the system operation. For example, the mode control logic determines when the system should be in coarse or fine track, search or track, pointing system angular rate limit, pointing angle hold, or fine track search raster reset.

Figure 3-28 indicates the logic level condition for the control of the various modes indicated and the time associated with the delay intervals. The rate limit for instance limits the velocity of the optical image at the image dissector detector. This is necessary because acquisition near the edge of the field-of-view would cause the tracker to apply immediately a large rate command to zero the image position to the beam steerer subsystem. Such a rate would otherwise exceed the tracker's rate capacity. Other delays are built in to permit transients to damp out. The beam steerers hold command is provided so that, during periods of deep signal fades when the beacon presence is lost, the system will continue to remember the last target position for immediate reacquisition should the signal reappear. If, after a time, long compared with the expected signal fade period, the signal is not detected, the system reverts back to a fine acquisition search and then into a coarse acquisition.

Operationally the mode control aspects are critical, they however do not enter the closed loop dynamics of ordinary functioning.

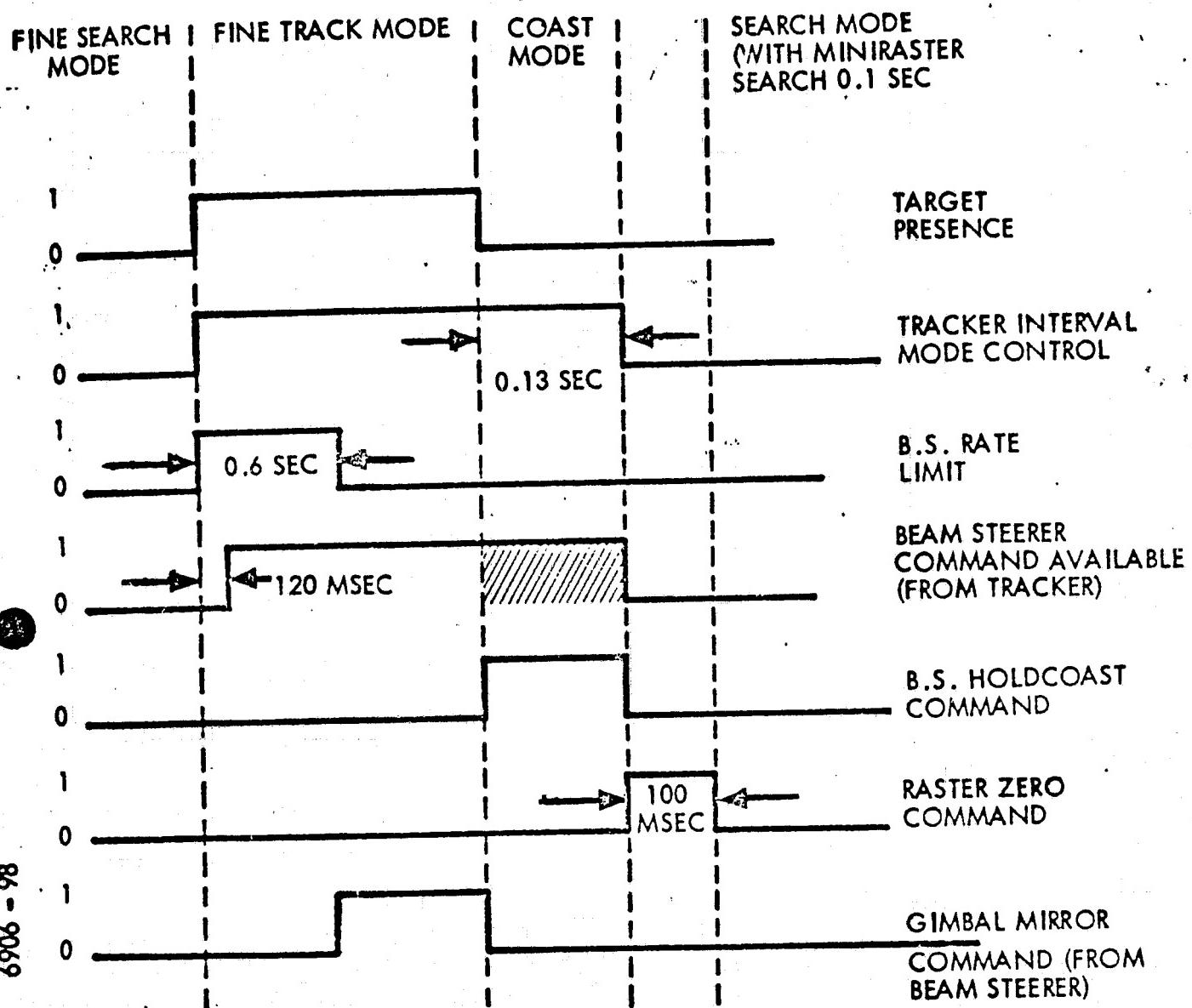


Figure 3-28. Mode Control Logic

Forward Path Compensation. - From Figure 3-25 we extract the circuits shown in Figure 3-29. Some simplification is also accomplished in that switching is not included. The circuit shown makes up the compensation block of Figure 3-26. The characteristics of each stage of the circuit are developed below and shown adjacent to the appropriate part of the circuit in Figure 3-29.

Figure 3-30 is the appropriate timing diagram for the modes.

These various modes of operation are necessary to allow the subsystem to handle transient conditions associated with target lock on and loss, and deep fades of the incoming laser signal.

When the beamsteerer subsystem is operating in its tracking mode, the tracker error signal is supplied to the forward loop compensation circuits.

The output on this circuit is summed with the compensated output of the beamsteerer mirror angle pickoff properly phased for negative feedback.

The resultant signal is utilized to drive the torquer which acts on the gimbal, mirror and flex pivot.

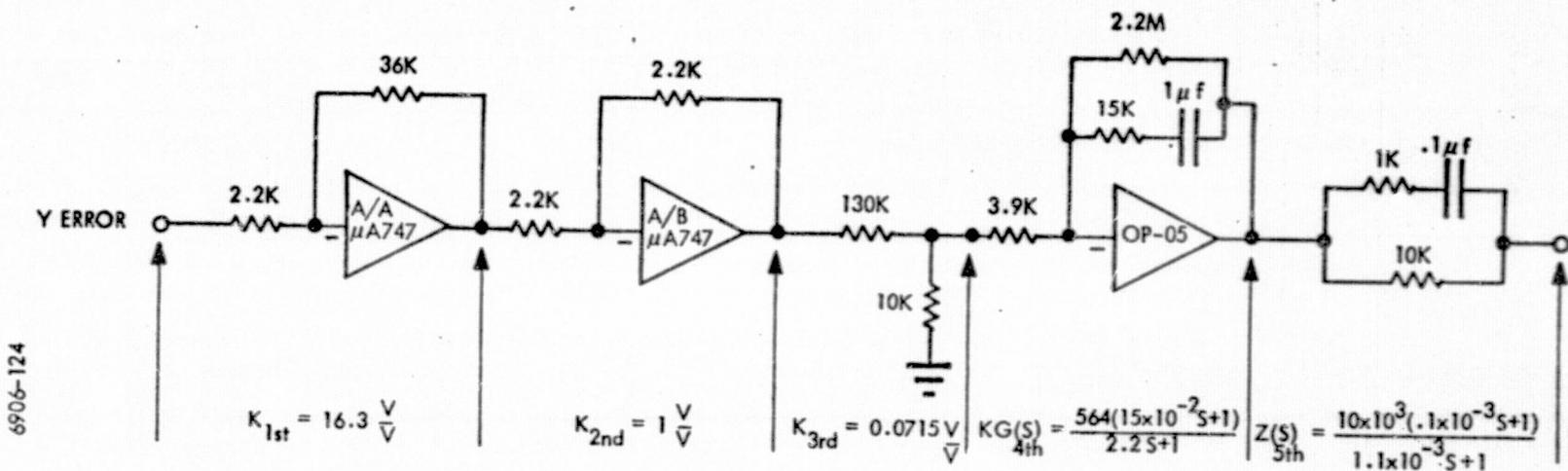
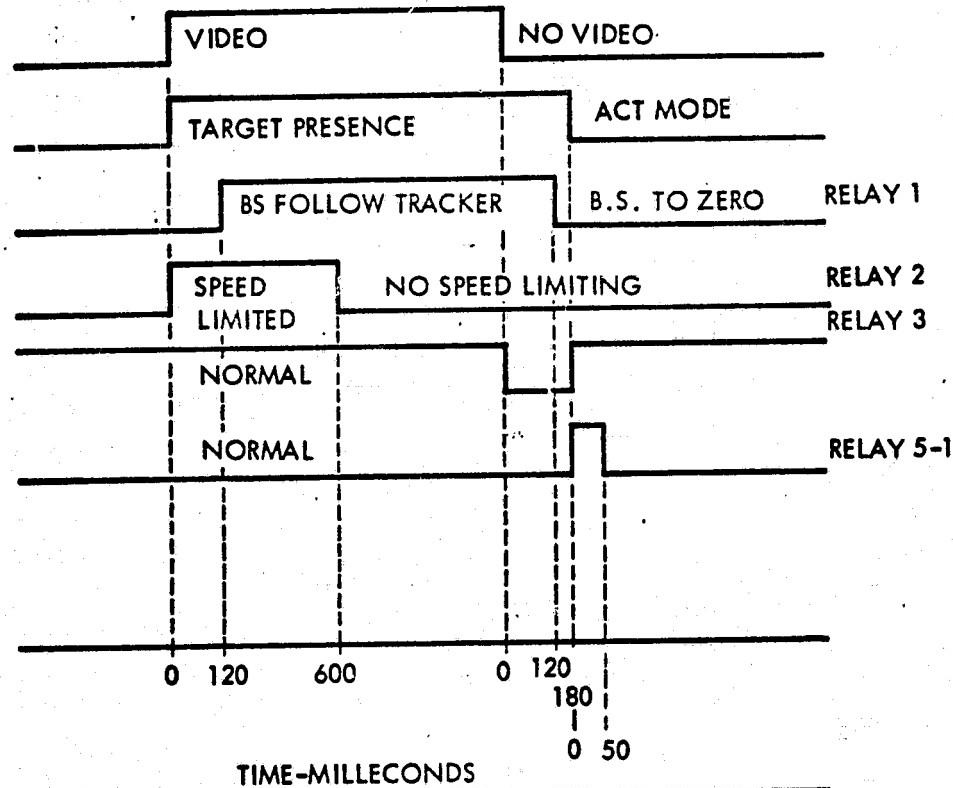
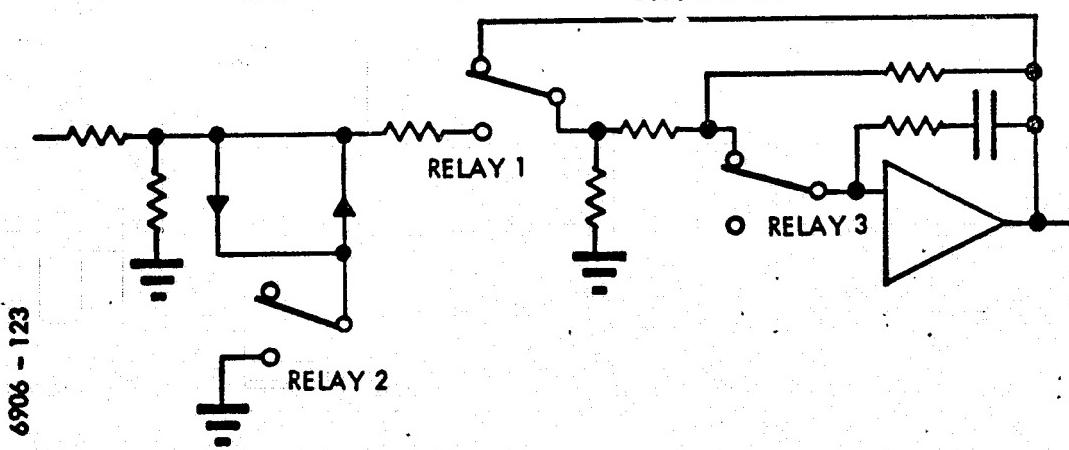


Figure 3-29. Forward Path Compensation Circuits

COIL CURRENT } RELAYS 1, 2, 3, 5-1
 NO COIL CURRENT



B.S. Y-Z CONTROL



6906 - 123

Figure 3-30. Mode Timing Diagram

1st State (AIA). - This is a simple feedback amplifier arrangement with the error supplied to the inverting input. The gain of this stage is: error supplied to the inverting input. The gain of this stage is:

$$G = \frac{R_{fb}}{R_{in}} = \frac{36K}{2.2K} = 16.3$$

2nd Stage (AIB). - This is a similar configuration to 1st stage that has a gain of unity.

$$G = \frac{R_{fb}}{R_{in}} = \frac{2.2K}{2.2K} = 1$$

3rd State. - This stage is merely a resistor divider that splits the signal in the ratio $\frac{10}{140} = 0.0715$.

4th State. - Stage 4 represents the first stage with frequency dependent terms that help shape the response of the subsystem. The transfer function for this stage is found in the usual manner: i.e. $\frac{Z_{fb}}{Z_{in}}$

$$GH = \frac{564 (15 \times 10^{-3} s + 1)}{2.25 + 1} \text{ volts/volt}$$

5th Stage. - This circuit is the summing impedance which interfaces with the summing impedance from the Feedback Path Compensation circuits. The circuit impedance will be necessary when the summation is made. It is therefore shown below

$$Z_5 = \frac{10 \times 10^3 (0.1 \times 10^{-3} S + 1)}{1.1 \times 10^{-3} S + 1}$$

Clearly this circuit provides additional frequency dependency and hence contributes to the compensation.

Feedback Path Compensation. - This block will be considered next since its contribution in a similar way to the B/S Torquer drive amplifier as does the forward path compensation. Figure 3-31 extracts from Figure 3-26 the portion of the subsystem concerned with feedback path compensation.

This will be handled as the forward path was.

1st Stage (A3A). - This stage acts as an amplifier for the signal emanating from the Kaman position pickoff. It should be noted that the signal is into the non-inverting input of the amplifier. As a result the expression for gain of the first stage is slightly different. Note

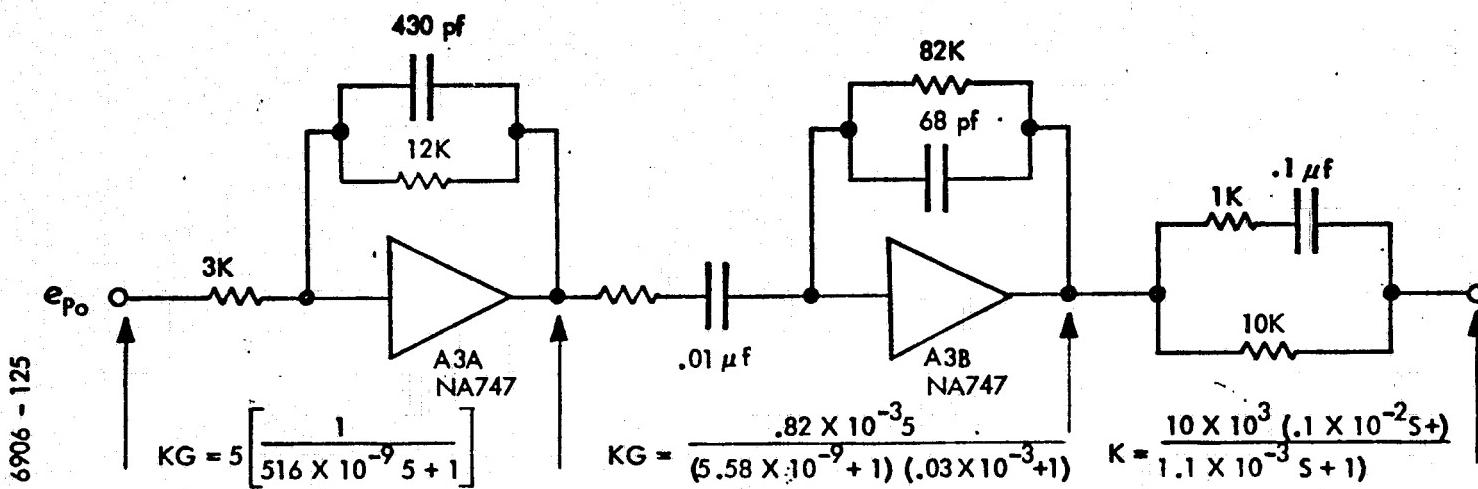


Figure 3-31. Feedback Path Compensation Circuits

also that while the transfer function developed has a frequency dependent term, its influence is not felt in the region of interest to the B/S subsystem. A simple gain is used when applying this stage to latter uses. The transfer function is:

$$KG = \frac{Z_{fb} + Z_{in}}{Z_{in}} = 5 \left[\frac{1}{5.16 \times 10^{-9} S + 1} \right] \text{volts/volt}$$

2nd Stage. - This stage provides a portion of the feedback path compensation by virtue of its input resistor/capacitor combination that is effective in the B/S frequency range. Its transfer functions:

$$KG = \frac{0.82 \times 10^{-3} S}{(5.58 \times 10^{-9} S + 1)(0.03 \times 10^{-3} S + 1)} \frac{\text{volt sec}}{\text{volt}}$$

3rd Stage. - The 3rd stage of the feedback compensation is the summing impedance that interfaces with the forward path. Its electrical characteristics are identical viz:

$$Z = \frac{10 \times 10^3 (0.1 \times 10^{-3} S + 1)}{1.1 \times 10^{-3} S + 1} \text{volts/volt}$$

Summing Amplifier. - The first point to deal with is the character of the summing process. For this the model shown in Figure 3-32 is used.

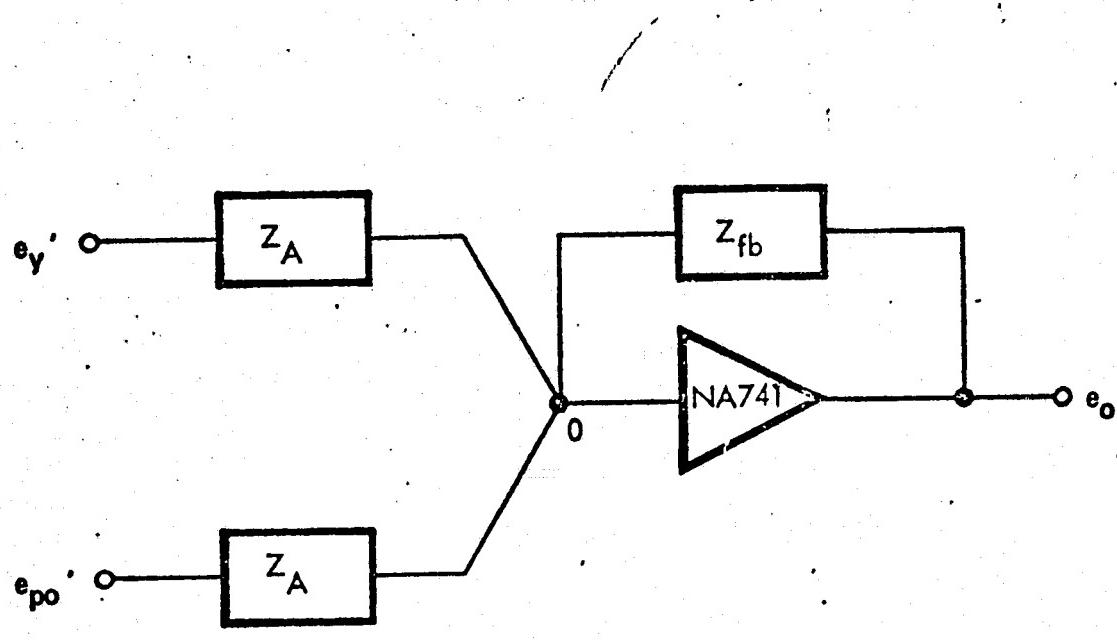


Figure 3-32. Model of Summing Amplifier

e_y' and e_{po}' represent the conditioned signals from the tracker and the pickoff. Z_A is the summing impedances previously derived. Using current summing at Node 0: $I_{ey'} + I_{po'} + I_{fb} = 0$

$$\frac{e_y'}{Z_A} + \frac{e_{po}'}{Z_A} + \frac{e_o}{Z_{fb}} = 0$$

giving $e_o = \frac{Z_{fb}}{Z_A} [e_y' + e_{po}']$

On this basis then we obtain:

$$\frac{Z_{fb}}{Z_A} = \frac{0.51 (1.1 \times 10^{-3} s + 1)}{0.1 \times 10^{-3} s + 1}$$

In this case the high frequency influence of the 520 pf capacitor has already been removed from the expression.

Beam Steerer Torquer Drive Amplifier. - The Torque Systems Inc. PA201 is used for torquer drive purposes. This amplifier has a bridge output configuration, and, as a result, even with the signal being delivered to the apparently non-inverting input, the gain for the device in the voltage mode is:

$$K = \frac{R_{fb}}{R_{in}} = \frac{47.5K}{4.7K} = 10 \text{ volts/volt}$$

The Y and Z axis drive amplifier balance adjustments and angle kickoff output centering and gain controller are located on the underside of the AOCP and shown in detail in Figure 3-33. This completes the subsystem description necessary before discussing the performance analysis.

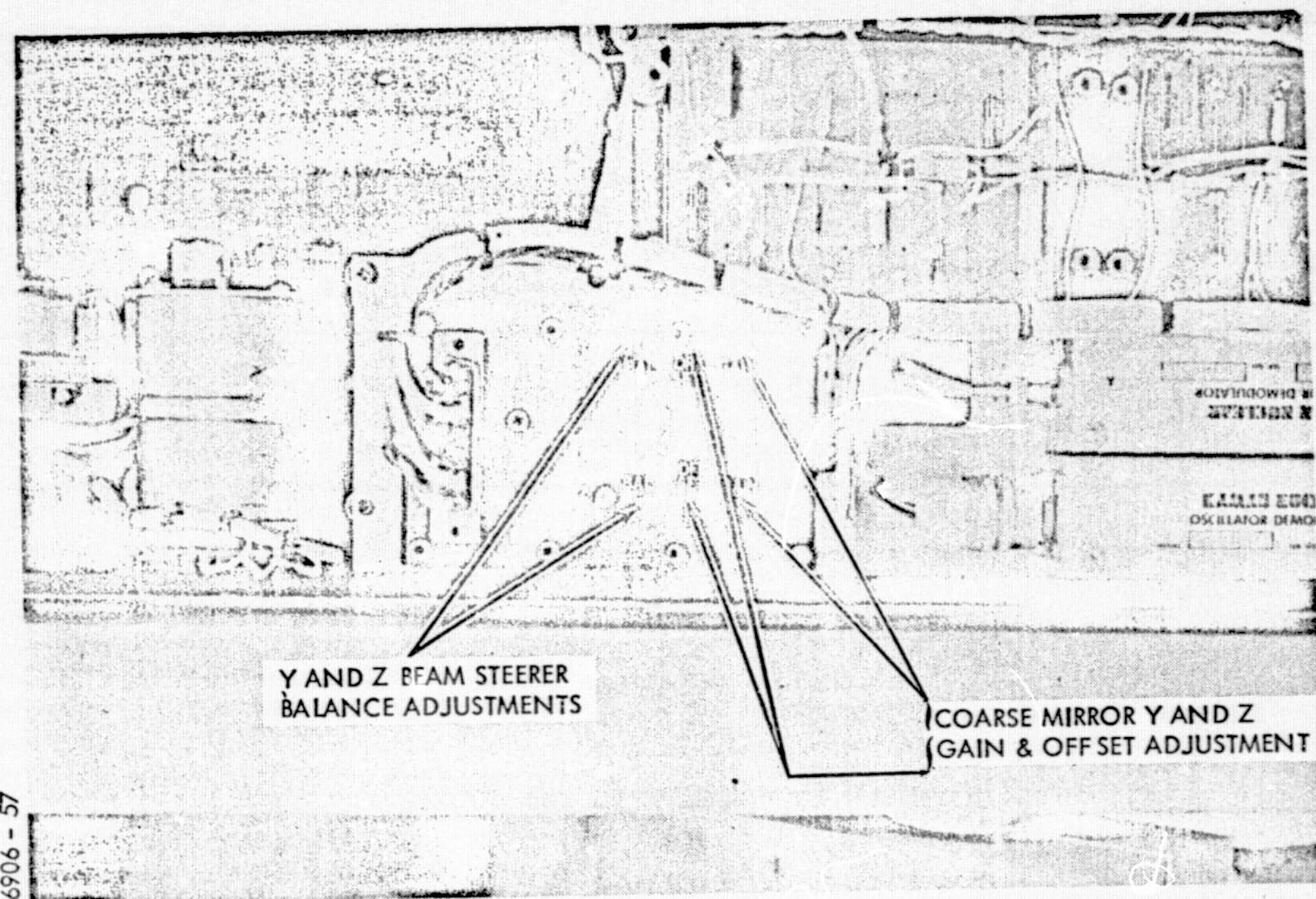


Figure 3-33. Beam Steerer and Coarse Mirror Servo Controls

• Performance Analysis

All of the information (except for high frequency terms) developed above is shown in the block diagram of Figure 3-34. In addition the figure is laid out in a fashion to facilitate analysis, i.e., each block has the transfer characteristic associated with it. Our analysis will start with the inner most loop - the gimbal and flex pivot loop - and continue expanding until an expression for the complete system is developed. Since earlier analyses have dealt with the relation θ_e / θ_i , we shall continue that approach. This means that the effect of the collecting telescope never enters the analysis.

1. Flex Pivot/Gimbal Cell Loop

Using the notation shown in Figure 3-34 we have

$$\frac{\theta_o}{T} = \frac{0.043}{7.25 \times 10^{-6} s^2 + 1} \text{ rad/oz in}$$

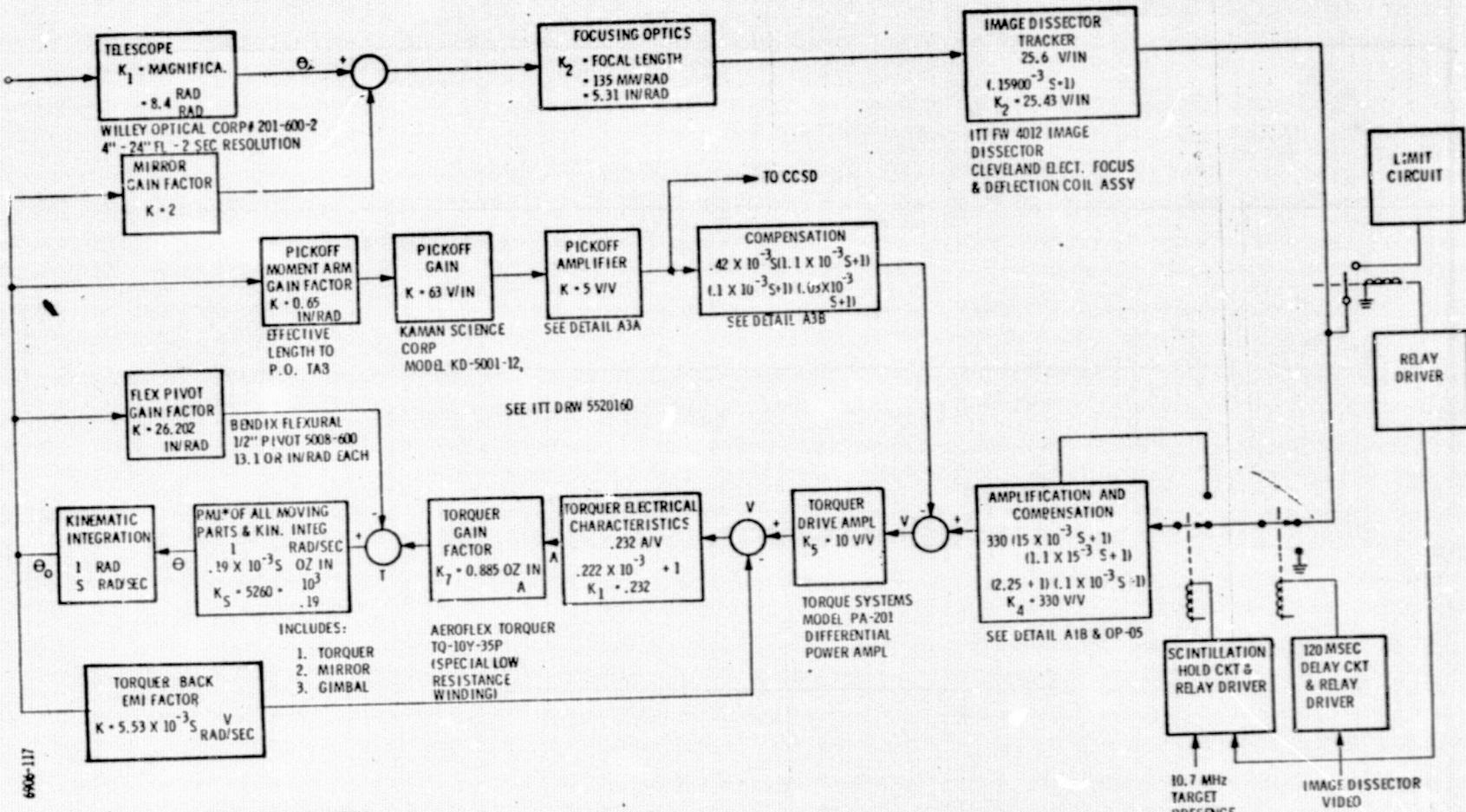
As expected this is a marginally unstable loop because of the undamped nature of the mass/springs of the flex pivot/gimbal cell.

2. Torquer/Gimbal Cell Back EMF Loop

Not a significant amount of damping is provided by the back EMF of the torquer, but this loop is included since earlier analysis considered it.

3-76

REPRODUCIBILITY OF THE
ORIGINAL PAGE IS POOR



*P.M.I. — POLAR MOMENT OF INERTIA

Figure 3-34. AOCP Beam Steerer Servo Diagram

$$\frac{\theta_o}{V_T} = \frac{0.00883 \text{ rad/volt}}{1.61 \times 10^{-9} S^3 + 7.2 \times 10^{-6} S^2 + 0.271 \times 10^{-3} S + 1}$$

when the denominator of this expression is investigated for roots, the following is obtained:

$$(S = 4.5 \times 10^3) (S^2 + 7S + 138 \times 10^3).$$

The very small coefficient of the S term in the quadratics indicates that damping, although small, is afforded by the back EMF of the torquer.

3. Gimbal Angle Pickoff/Compensation/Torque Drive Amplifier Loop

The characteristic equation of the B/S subsystem becomes more involved as more and more of the mechanism is encompassed by the expression. Applying the proper rule of combination we have:

$$\frac{\theta_o}{V_c} = \frac{0.0883 (0.1 \times 10^{-3} S + 1)(0.03 \times 10^{-3} S + 1) \text{ rad/volt}}{4.85 \times 10^{-18} S^5 + 0.232 \times 10^{-12} S^4 + 2.56 \times 10^{-9} S^3 + 15.7 \times 10^{-6} S^2 + 0.410 \times 10^{-3} S + 1}$$

We note at this point that the DC gain is precisely 10 times that of the previous loop. This is due to two factors: 1) The torque drive amplifier has a gain of 10, and 2) the DC gain of the feedback path is zero as a result of the free S in the numerator of the compensation that comes from the series capacitor in the feedback path. Clearly then the feedback loop of concern at this point of the analysis is

effective only so long as dynamics are in existence, i. e., when θ is not constant. Considering the very undamped nature of the gimbal/flexpivot situation, the kind of feedback provided is quite to the point; having its greatest effect in dynamic conditions.

4. Total Open Loop Expression θ_B / θ_e

At this point we're ready to look at the complete beam-steerer subsystem. First the total open loop expression for θ_B / θ_e will be written in the form of the previous relations to expose the D. C. gain of the open loop expression. Following this, the expression will be converted to the form used in Root Locus (R/L) work and the analyses carried on from that point. The significant steps in the following will be

- (1) Obtaining the total open loop expression.
- (2) Conversion of expression to R/L form.
- (3) Simplifying the expression on the basis of the pole and zeros in the open loop.
- (4) Drawing a R/L, locating the pole locations at the point called for by the existing loop gain values.
- (5) Using the pole locations from the R/L, develop the closed loop expression for the ratio θ_e / θ_i and plot the poles and zeros of this relationship.

(6) Perform a frequency response of the $\frac{\theta_B}{\theta_e}$ and compare it with the measurements taken on the system.

$$\frac{\theta_B}{\theta_e} = \frac{7907(15 \times 10^{-3} S + 1)(1.1 \times 10^{-3} S + 1)(0.1 \times 10^{-3} S + 1)(0.03 \times 10^{-3} S + 1) \text{ rad/rad}}{(0.159 \times 10^{-3} S + 1)(2.2 S + 1)(0.1 \times 10^{-3} S + 1)(4.85 \times 10^{-18} S^5)}$$

$$+ 0.232 \times 10^{-12} S^4$$

$$+ 2.56 \times 10^{-9} S^3$$

$$+ 15.7 \times 10^{-6} S^2$$

$$+ 0.410 \times 10^{-3} S + 1)$$

From this we see: 1) that the D. C. gain of the open loop is 7907 radians/radian, and 2) a pole and zero at $S = -10 \times 10^3$ rad/sec exists and hence cancel each other.

Continuing; the expression is now converted to R/L format.

$$\frac{\theta_B}{\theta_e} = \frac{2.32 \times 10^{12} (S + 33.3 \times 10^3)(S + 66.6)(S + 910)}{(S + 0.455)(S + 6.4 \times 10^3)(S^5 + 47.8 \times 10^3 S^4 + 528 \times 10^6 S^3 + 3234 \times 10^9 S^2 + \dots + 1658 \times 10^{12} S + 206 \times 10^{15})}$$

Synthetic division is used to factor the 5th order term, giving:

$$\frac{\theta_B}{\theta_e} = \frac{2.32 \times 10^{12} (S + 33.3 \times 10^3)(S + 66.6)(S + 910)}{(S + 0.455)(S + 6.4 \times 10^3)(S + 202)(S + 348)(S + 35.5 \times 10^3)}$$

$$(S + 5.9 \times 10^3 + 7 \times 10^3)(S + 5.9 \times 10^3 - 7 \times 10^3)$$

Note that two more simplifications are in order at this point: 1) The pole at $S = -35.5 \times 10^3$ rad/sec is very close to the zero at $S = -33.3 \times 10^3$; we shall consider these as cancelling each other; 2) three poles are so far out from the area of interest that their deletion would make but small change in the continuing analysis. Figure 3-35 shows the root locations for total θ_B/θ_e . Since our concern focuses in the region of $0 \rightarrow 3000$ radians per second, a good representation of the system can be achieved by eliminating the complex poles at $S = -5.9 \times 10^3 \pm j7 \times 10^3$ radians per sec, and the real pole at $S = 6.4 \times 10^3$ radians/sec. To properly eliminate these poles the "gain" value must also be modified. Carrying out the proper operations results in:

$$\frac{\theta_B}{\theta_c} = \frac{4090(S + 910)(S + 66.6)}{(S + 0.455)(S + 202)(S + 348)} = \frac{N}{D}$$

This set of poles and-zeros is shown in Figure 3-36 along with the locus of the poles of the closed loop expression for θ_e/θ_i as the open loop gain goes from $0 \rightarrow 4090$. The final location of the poles is that of the closed loop for gain 4090.

On the basis of the root locations and the fact that

$$\frac{\theta_e}{\theta_i} = \frac{1}{1 + \frac{\theta_B}{\theta_e}} = \frac{1}{1 + \frac{N}{D}}$$

18-E

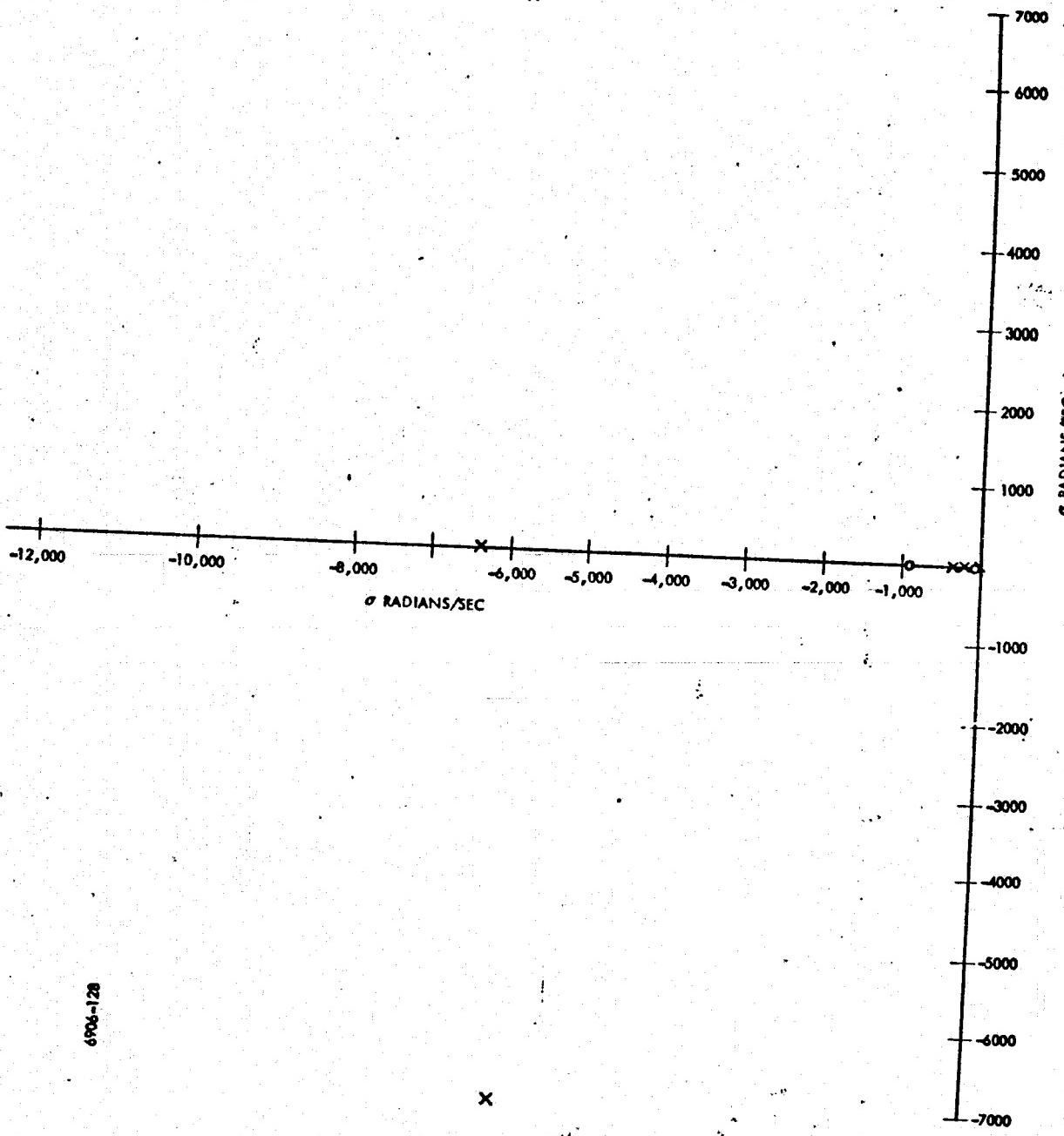


Figure 3-35. Root Locations of Total Open Loop Expression
(Cancelling Pole & Zero Near $S = -33.5 \times 10^3$ not shown)

6906-128

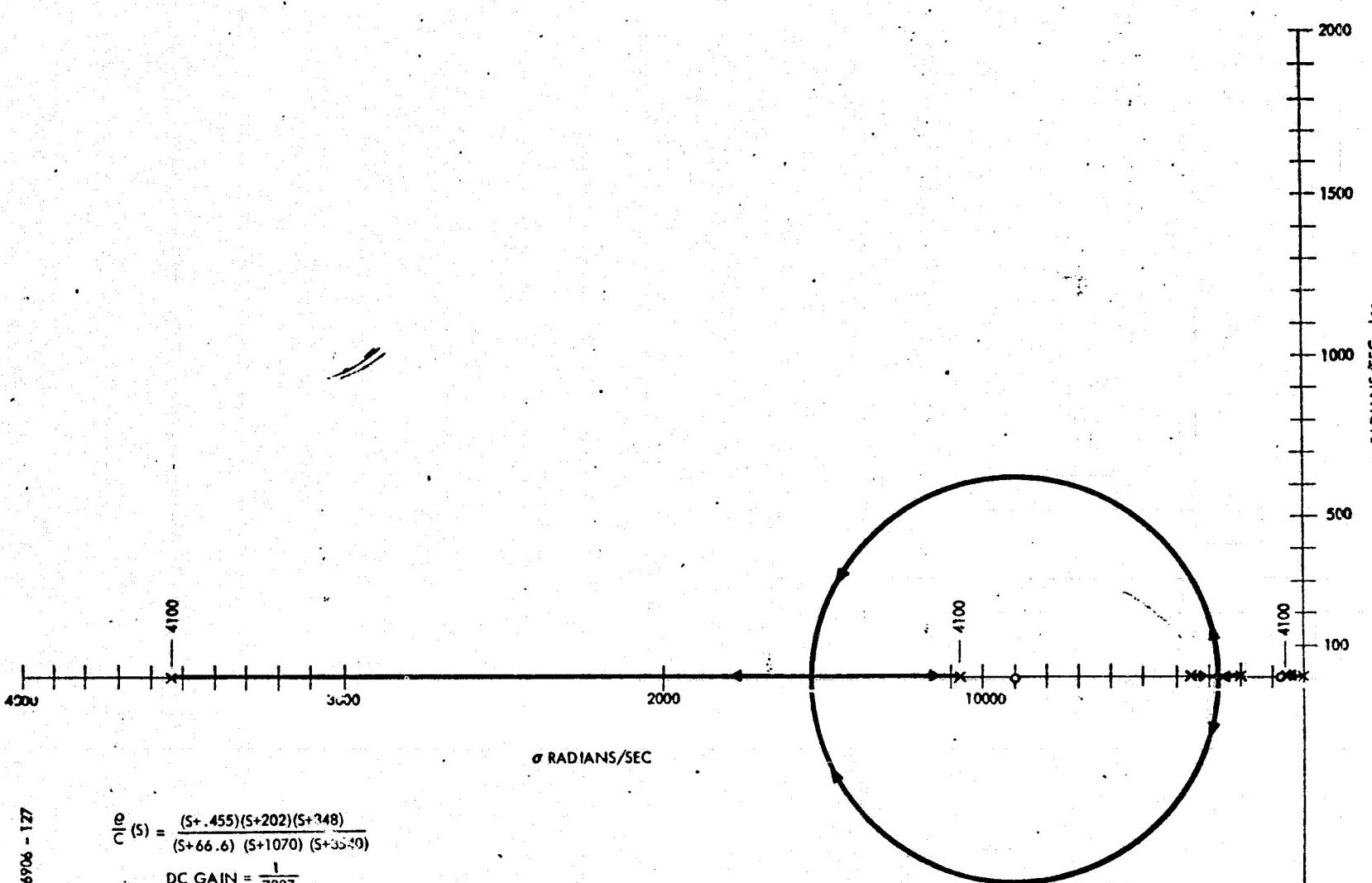


Figure 3-36. OPEN LOOP ROOT LOCATION/ROOT LOCUS/CLOSED LOOP ROOT LOCATION FOR SIMPLIFIED $\frac{\theta_B}{\theta_C}$ WITH "GAIN" OF 4090

$$\frac{\theta_e}{\theta_i} = \frac{D}{\text{poles location from Root Locus}}$$

$$= \frac{(S+0.455)(S+202)(S+348)}{(S+66.6)(S+1020)(S+3540)}$$

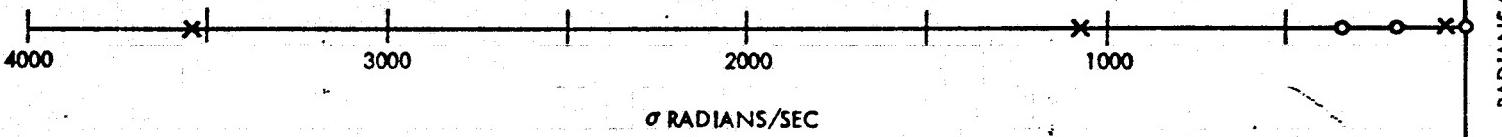
for which the DC value is $\frac{1}{7887}$, close to the reciprocal of the DC gain of 7907 developed earlier.

The pole/zero configuration of θ_e/θ_i is shown in Figure 3-37.

From this arrangement a frequency response was generated. The results of this is shown on Figure 3-38 along with test data.

Inspection of Figure 3-38 shows that the test data and analysis of the Y loop agree quite well to the vicinity of 100 radian/sec. The results diverge in the neighborhood of 100 radians/sec and pick up a somewhat parallel response after that point which seems to differ from the analytical results by a factor of 2. This difference is unexplained at this point in time.

3-84



6906 - 129

Figure 3-37. POLE/ZERO CONFIGURATION OF $\frac{\theta_e}{\theta_i}$ FOR BEAM STEERING SUBSYSTEM

3.3.4 Scintillation Monitor. - The scintillation monitor subsystem was added to the receiver later in the program and as a result of a PI meeting held at NASA/MSFC. The purpose of the scintillation monitor is to measure atmospherically induced intensity fades in the received signal. A functional block-diagram of the scintillation monitor is given in **Figure 3-39.**

The scintillation monitor is located in the AOCP receiver section and receives energy split from the tracking and communications channel by the beam splitter shown in Figure 3-8. The lens that follows the beam splitter images the entrance pupil of the AOCP afocal telescope onto an aperture stop and also serves as a field lens to converge the received radiation onto the scintillation monitor photomultiplier detector. The field of view of the scintillation monitor defector is approximately 0.6 degree diameter which assures that there is no vignetting edge modulation induced by the beam steerer pointing noise.

The radiation detected by the scintillation monitor photomultiplier is modulated by a 10 MHz (approximately) subcarrier. This subcarrier is amplitude modulated by variations in atmospheric transmission of the uplink path. The output of the photomultiplier passes through a matching network (bandpass filter) to a 10 MHz AGC controlled amplifier. The amplifier output is rectified,

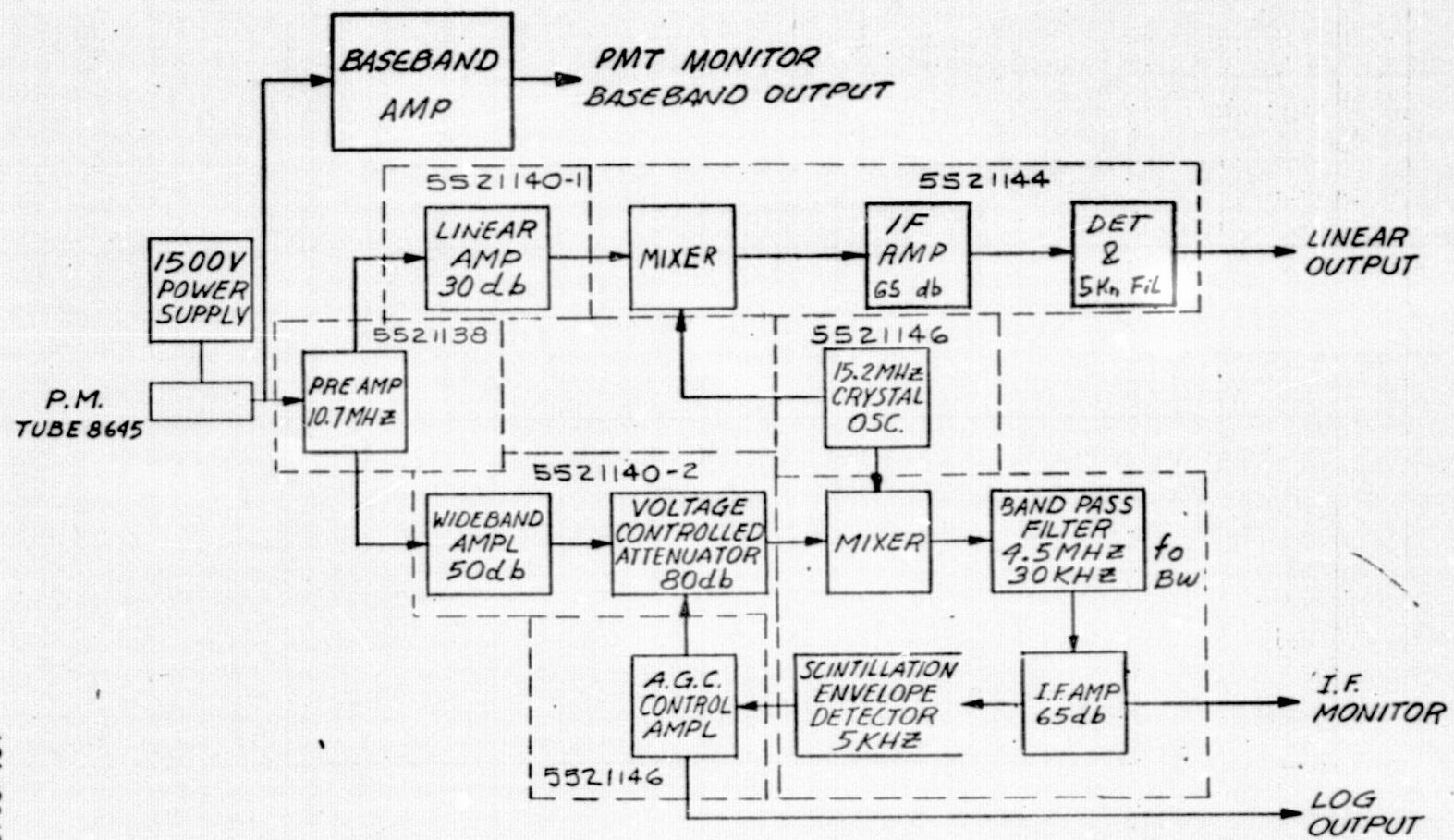


Figure 3-39. SCINTILLATION MONITOR FUNCTIONAL BLOCK DIAGRAM

filtered to 10 MHz, and utilized as the AGC control for the amplifier.

A dc control voltage varying from +0.5 to +4.5 volts supplies 80 db of control range to the amplifier. The circuit sensitivity is therefore 10 db/0.5 volt, linear in db/volt throughout the range. Since the AGC control loop bandwidth is 10 KHz, the AGC voltage is a direct logarithmic indication of the uplink optical scintillation.

A linear amplifier coupled out of the matching network also operates in the 10 MHz range. A manual gain control allows selection of a portion of the log amplifier range and will be especially useful for selecting high level signals that are compressed in the logarithmic output. A detector, filter, and amplifier after the linear amplifier permits utilization of the maximum dynamic range for a 10 KHz scintillation monitor bandwidth.

A third output is derived directly from the photomultiplier detector and is linear with received optical power over a baseband range (dc coupled) to 5 KHz.

Three calibratable signal outputs are provided in the scintillation monitor as follows;

1. A signal linearly proportional to the total power incident on the detector at baseband (0 to 5 KHz).

2. A signal linearly proportional to the fluctuations in power of the 10.7 MHz subcarrier modulated onto the ground station beacon, and
3. A signal proportional to the log of the power in the 10.7 MHz subcarrier on the received beam.

Calibration and techniques data are given in the calibration and test section of this report.

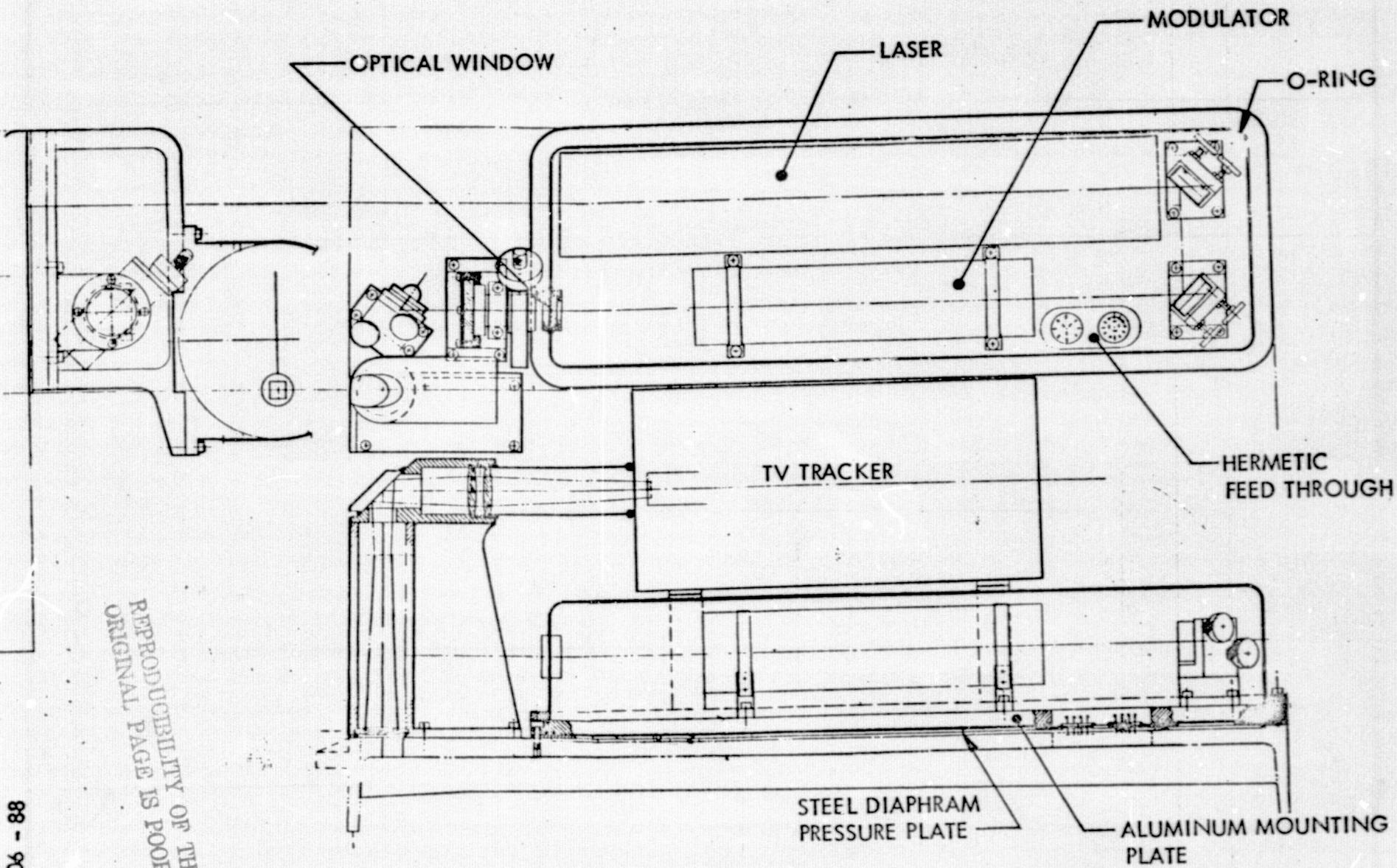
3.4 Transmitter Subsystem

The transmitter subsystem consists of the helium-neon laser, optical modulator, modulator driver, optical compensator and polarizer, beam divergence control telescope, and laser power monitor.

The laser, modulator, and modulator driver are housed in a hermetically sealed compartment under one atmosphere of dry nitrogen. The construction of the laser compartment is illustrated in Figure 3-40. The laser, folding mirrors, and optical modulator are mounted on a 0.5 inch thick aluminum plate hermetically sealed to the AOCP main frame. This mounting plate is pressure released to avoid flexing in reduced pressure environments. The compartment pressure seal is formed by a thin steel plate recessed into the AOCP main frame with hermetic feedthroughs for electrical power and modulator driver signals.

The source of optical radiation is a CW helium-neon laser, operating in a single mode (TEM_{00}) at 0.6328 micrometer wavelength with an output power of approximately 5 mw. The laser beam is directed through the optical modulator by finely adjustable folding mirrors providing both lateral and angular positioning of the beam in the modulator aperture.

Further description of this laser has been provided in the O&M manual and will not be repeated in this report. It has been



REPRODUCIBILITY OF THE
ORIGINAL PAGE IS POOR

Figure 3-40. Laser Transmitter Optical Layout

necessary to replace the laser plasma tube several times during the course of the system operation because of difficulty in start-up. At least one flight was made during which the laser failed to start. The specific problem identified with this characteristic was low voltage from the 110V power system on the A/C.

The transmitter path can be traced by referring to the Figure 3-41. Beginning with the laser, the 0.6328 micrometer laser beam is folded twice and directed through the electro-optical modulator and out of the laser compartment through the cover seal window. From the window, the polarization modulated beam is passed through a variable phase retardation plate (Soleil-Babinet compensator), a polarizer and reflected from a folding mirror and directed into the lower level. Referring again to Figure 3-41, the transmitter path enters the lower level and is directed past a cut-off shutter and through the beam divergence control telescope.

The transmitter beam emerges from the divergence control telescope and impinges onto a beam sampling splitter which reflects less than 1 percent of the power in the transmitted beam onto a power and modulation monitor photomultiplier detector. The primary beam passes through the beam sampling splitter and is reflected from a path folding mirror onto the dichroic beam combiner where the transmitted and received optical paths combine. The transmitter and receiver paths are made parallel, i.e., boresighted mechanically at the beam combiner and exits through the same path followed by the received beam, but offset to avoid the central obscuration of the cassegranian telescope.

When an electric field is applied to materials of this type, the crystal's symmetry changes to bi-axial, making the crystal birefringent.

In crystals of low symmetry, such as KDP, the optical dielectric property (or refractive index) of the crystal varies with the magnitude and direction of an applied electric field. For the case of the electric field applied along the crystal's optic axis, and for light propagating normal to the applied field, as illustrated in Figure 3-42, the difference in indices for the two principal planes of polarization is given by

$$n_z - n_x = n_e - n_0 + \frac{1}{2} n_0^3 r_{63} E_z$$

where

n_0 = ordinary refractive index

n_e = extraordinary refractive index

r_{63} = electro-optic coefficient in cm/volt

E_z = magnitude of the electric field applied in the z direction.

The signs depend upon the sign of the applied electric field. For a crystal of length L, a phase shift is induced between the two principal waves on propagation through the crystal, which is related to the magnitude of the applied electric field. The time, t, that light takes to traverse the crystal in the y direction, depends upon the presence or absence of the electric field, as well as the plane of polarization.

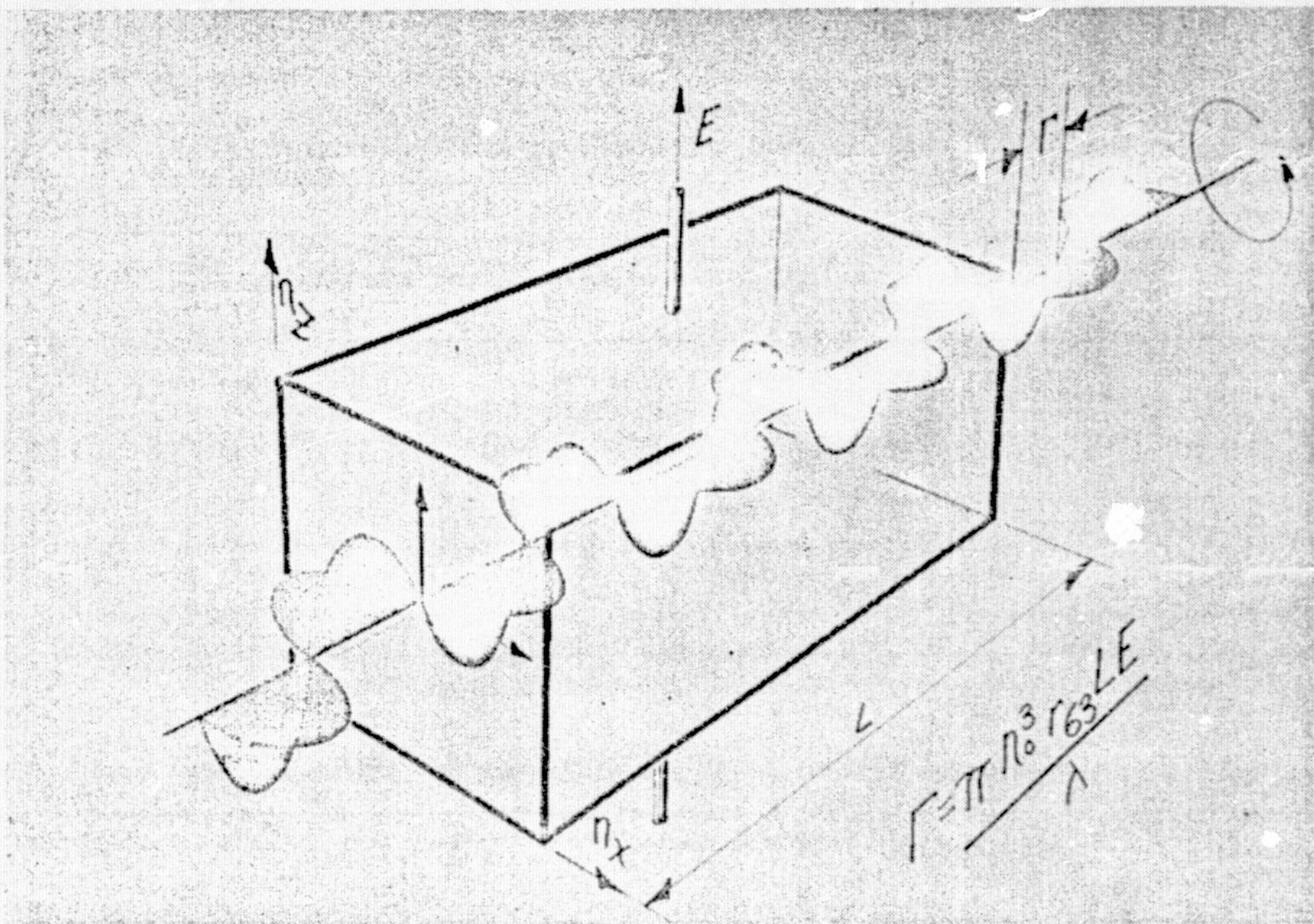


Figure 3-42. Transverse Field Electro-Optic Effect

The times of traversal of the two orthogonal polarizations directed along z and x, respectively, are given by the following equations:

$$t_z = \frac{L n_z}{c} = \frac{L n_z}{\nu \lambda}$$

and

$$t_x = \frac{L n_x}{c} = \frac{L n_x}{\nu \lambda},$$

where c is the speed of light in vacuum. The difference in the traversal time, Δt , between the two waves at the crystal's output is

$$\Delta t = t_z - t_y = \frac{L}{c} (n_z - n_x)$$

The phase difference, Γ , is related to the differential time by

$$\begin{aligned} \Gamma &= 2\pi\nu\Delta t \\ &= \frac{2\pi\nu L}{c} (n_z - n_x) \\ &= \frac{2\pi L}{\lambda} (n_z - n_x) \text{ radians.} \end{aligned}$$

Substituting equation (2-1) into equation (2-7) gives

$$\Gamma = \frac{2\pi L}{\lambda} (n_e - n_0) + \frac{\pi L}{\lambda} (n_0^3 r_{63} E_z).$$

The first term in the transverse field equation represents the natural birefringence, and the second term indicates the field dependent retardation. One of the more difficult problems with the transverse field modulator arises from the field independent term because of its sensitivity to environmental changes. It is possible to construct a modulator which is thermally compensated by cancelling

the natural birefringence terms. This is accomplished by arranging the electro-optic crystals in suitably oriented pairs.

The polarization state at the modulator's output is, in general, elliptical, with an ellipticity which depends upon the relative phase difference, Γ , between the two normal field components. By applying the correct electrical field magnitude, the output can be made either right or left circularly polarized. This occurs for an induced phase difference of $\pm \pi/2$ radians respectively. The voltage required to change the output polarization from one orthogonal state to another is defined as the modulation half-wave voltage, $V \lambda/2$; and corresponds to a unity modulation depth.

Since system performance is related to the information carrying power, rather than the total power in the transmitted beam, it becomes necessary to define a modulation depth parameter. Consider the transfer characteristics of the system's optical elements, shown schematically in Figure 3-43. Element number one is the optical modulator which is effectively a variable phase retardation plate, having axes denoted S_1 and F_1 , and produces a phase difference, Γ_1 , between polarization components directed in the S_1 and F_1 axes, of amount

$$\Gamma_1 = \frac{\pi n_0^3 r_{63} L}{\lambda} E_z$$

6906-201

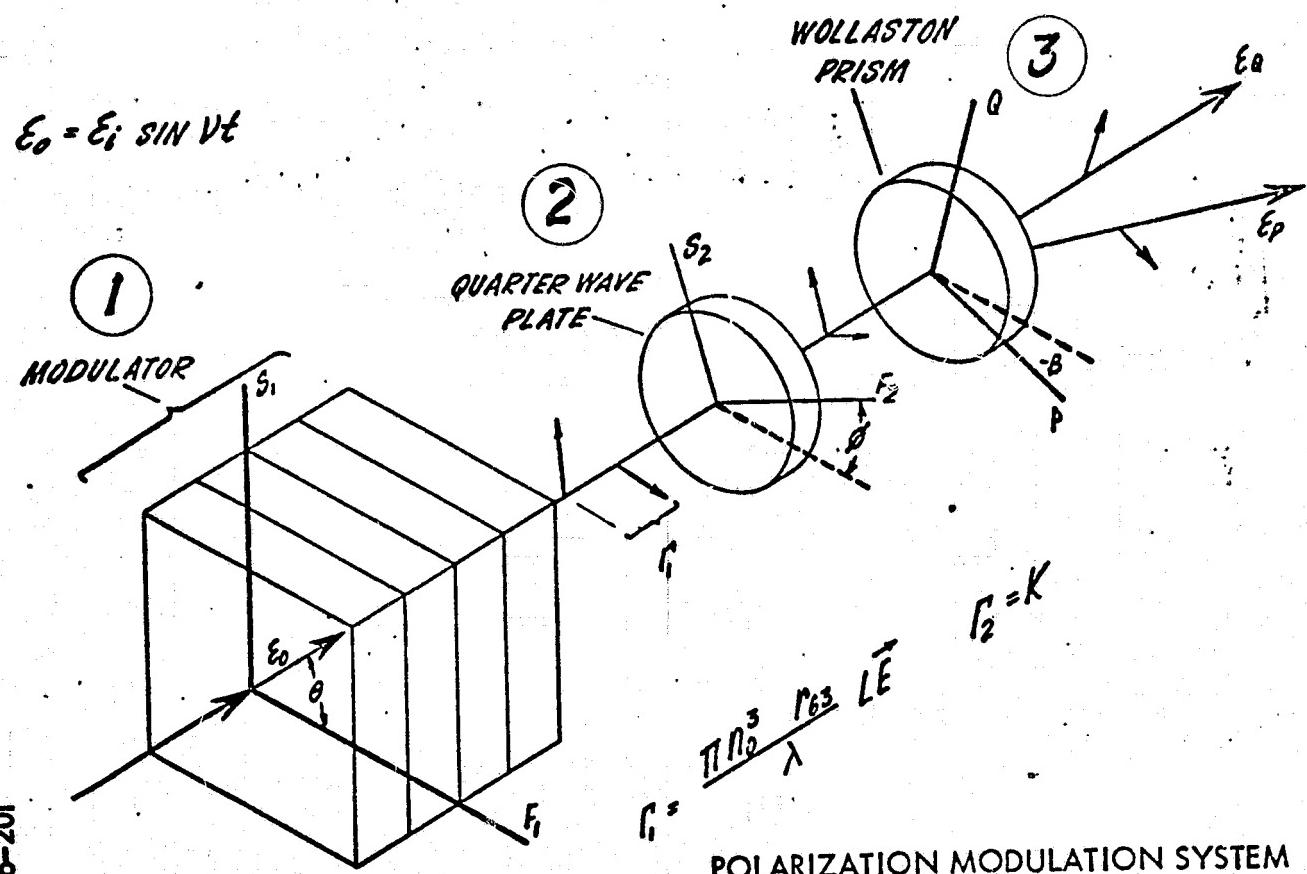


Figure 3-43. Optical Component Train in Polarization Modulation Mode

Element number two is a phase plate having axes S_2 and F_2 rotated through an angle ϕ with respect to the reference direction F_1 and which produces a phase retardation Γ_2 between components along S_2 and F_2 . The Saleil-Babinet compensator is a precisely variable phase retardation plate which permits a continuous adjustment of Γ_2 over several optical wavelengths. Element number three is the polarization prism which spatially separates the polarization components having directions along Q and P . The polarization prism has its P axis rotated through an angle β with respect to the reference direction F_1 . It can be shown by simple analysis that the transfer characteristics of this series of elements are given by equations in Figure 3-44, where E_P and E_Q denote the electric field amplitudes of the two spatially separated beams. Either the E_P or the E_Q field can be selected in an OOK communications system as employed in the AOCP. The trigonometric representation is used, rather than the Jones calculus in this analysis because it readily displays the cyclic nature of the component's orientation. A computer program has been written which gives the ratio of the output beam intensity to that at the input to the optical modulator with optical bias and component tolerances and orientations as parameters.

Figure 3-45 shows the transfer characteristics of the train of components illustrated in Figure 3-43 for ϕ of 0 and β of $\pi/4$ radians. The optimum operating point can be seen to occur at a

$$\begin{aligned} \epsilon_p = \epsilon_i & [\sin(\nu t) (\sin \theta \sin \beta \cos^2 \phi - \frac{1}{2} \sin \theta \cos \beta \sin 2\phi) \\ & + \sin(\nu t + \Gamma_1) (\cos \theta \cos \beta \sin^2 \phi - \frac{1}{2} \cos \theta \sin \beta \sin 2\phi) \\ & + \sin(\nu t + \Gamma_2) (\sin \theta \sin \beta \sin^2 \phi + \frac{1}{2} \sin \theta \cos \beta \sin 2\phi) \\ & + \sin(\nu t + \Gamma_1 + \Gamma_2) (\cos \theta \cos \beta \cos^2 \phi + \frac{1}{2} \cos \theta \sin \beta \sin 2\phi)] \end{aligned}$$

$$\begin{aligned} \epsilon_q = \epsilon_i & [\sin(\nu t) (\sin \theta \cos \beta \cos^2 \phi + \frac{1}{2} \sin \theta \sin \beta \sin 2\phi) \\ & - \sin(\nu t + \Gamma_1) (\cos \theta \sin \beta \sin^2 \phi + \frac{1}{2} \cos \theta \cos \beta \sin 2\phi) \\ & + \sin(\nu t + \Gamma_2) (\sin \theta \cos \beta \sin^2 \phi - \frac{1}{2} \sin \theta \sin \beta \sin 2\phi) \\ & - \sin(\nu t + \Gamma_1 + \Gamma_2) (\cos \theta \sin \beta \cos^2 \phi - \frac{1}{2} \cos \theta \cos \beta \sin 2\phi)] \end{aligned}$$

6906-200

Figure 3-44. Polarization Modulation Transfer Equations

6906-207

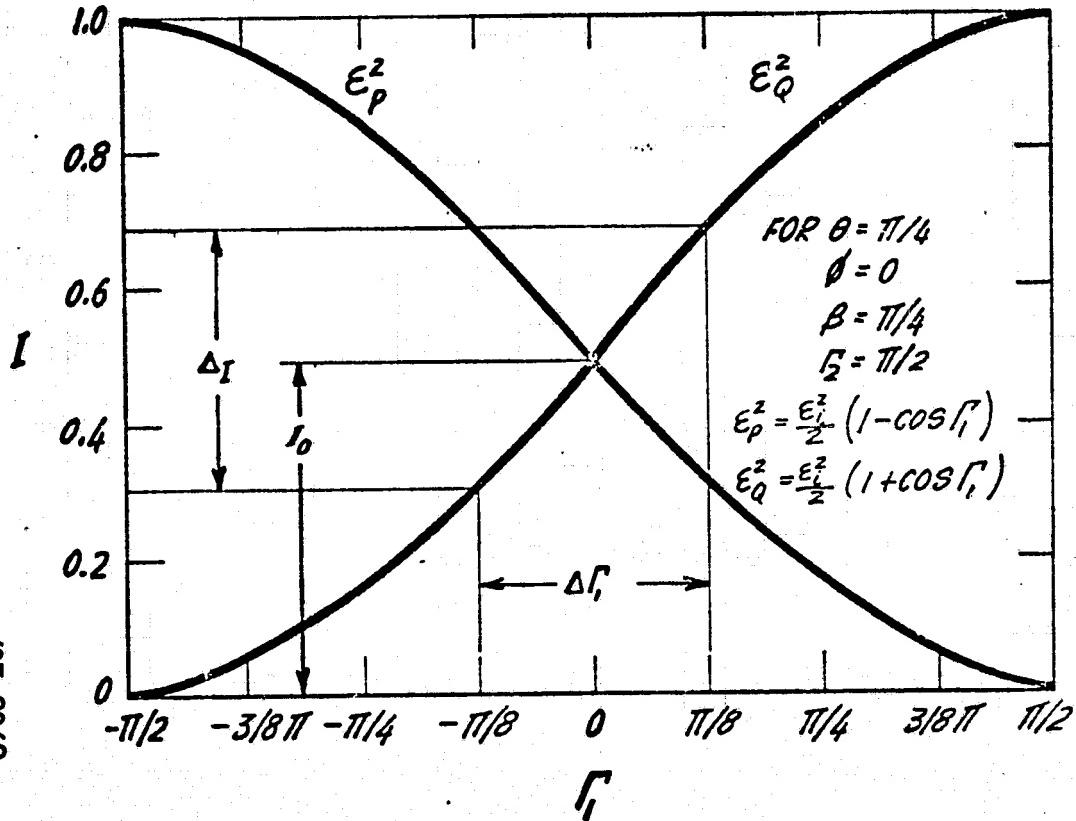


Figure 3-45. Optical Communication System Modulation Characteristics

modulator bias point of $\Gamma_1 = 0$ radian. It can be seen by inspection of equations of Figure 3-44 that the E_P and E_Q amplitudes vary in quadrature with Γ_1 for this operating point.

The outputs of the square-law photodetectors are proportional to the input beam intensities, or the square of the beam amplitudes.

The respective output photocurrents I_P and I_Q are given by

$$I_P \propto E_P^2 \propto \frac{1}{2} (1 - \cos \Gamma_1)$$

$$I_Q \propto E_Q^2 \propto \frac{1}{2} (1 + \cos \Gamma_1)$$

for

$$F_2 = \pi/2 \text{ radian}$$

$$\varphi = 0$$

$$\beta = \pi/4 \text{ radian.}$$

A modulation depth parameter, M , can be defined as

$$M = \frac{I_{\text{peak}} - I_0}{I_0}$$

for each channel, where I_{peak} is the peak intensity of the beam, and I_0 is the average beam intensity for $\Gamma_1 = 0$ for the operating point shown

in Figure 3-45. Note that, for this condition, the transfer characteristics are symmetrical for the two outputs and the modulation depths in the two channels are equal. Figure 3-46 shows a plot of modulation index M for the optimum operating point, and indicates the nonlinear nature of the transfer characteristics of the system with respect to phase retardation Γ_1 and the applied modulation voltage.

Another useful parameter for describing modulation in the dynamic extinction ratio, i.e., the ratio of the energy in off state to that of the on-state. Figure 3-47 illustrates the modulated waveform and gives the dynamic extinction ratio for various modulation waveform use and fall times.

Modulator Design

Modulator Design. - The optical modulator is shown in Figure 3-48, with the crystals exposed. The modulator consists of four, 90 percent deuterated KDP crystals having dimensions 3.5 mm x 3.5 mm x 50.8 mm. The crystals are arranged in pairs to cancel the natural birefringent terms. Two crystal orientations are employed in this construction as illustrated in Figure 3-49 (a) and (b), with the electric field applied along the crystallographic (001) axis in both

6906-202

PERCENT MODULATION

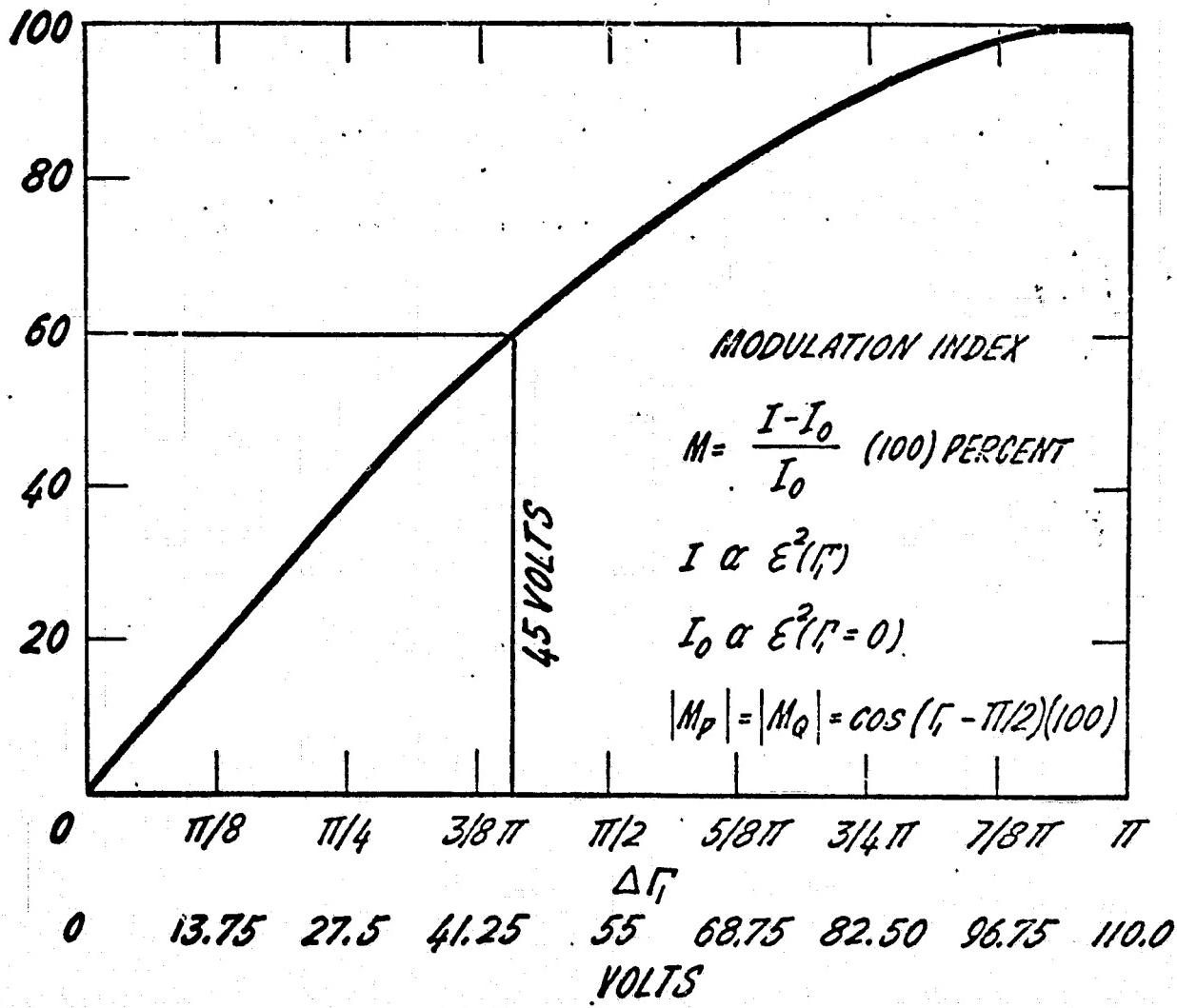


Figure 3-46. Modulation Index

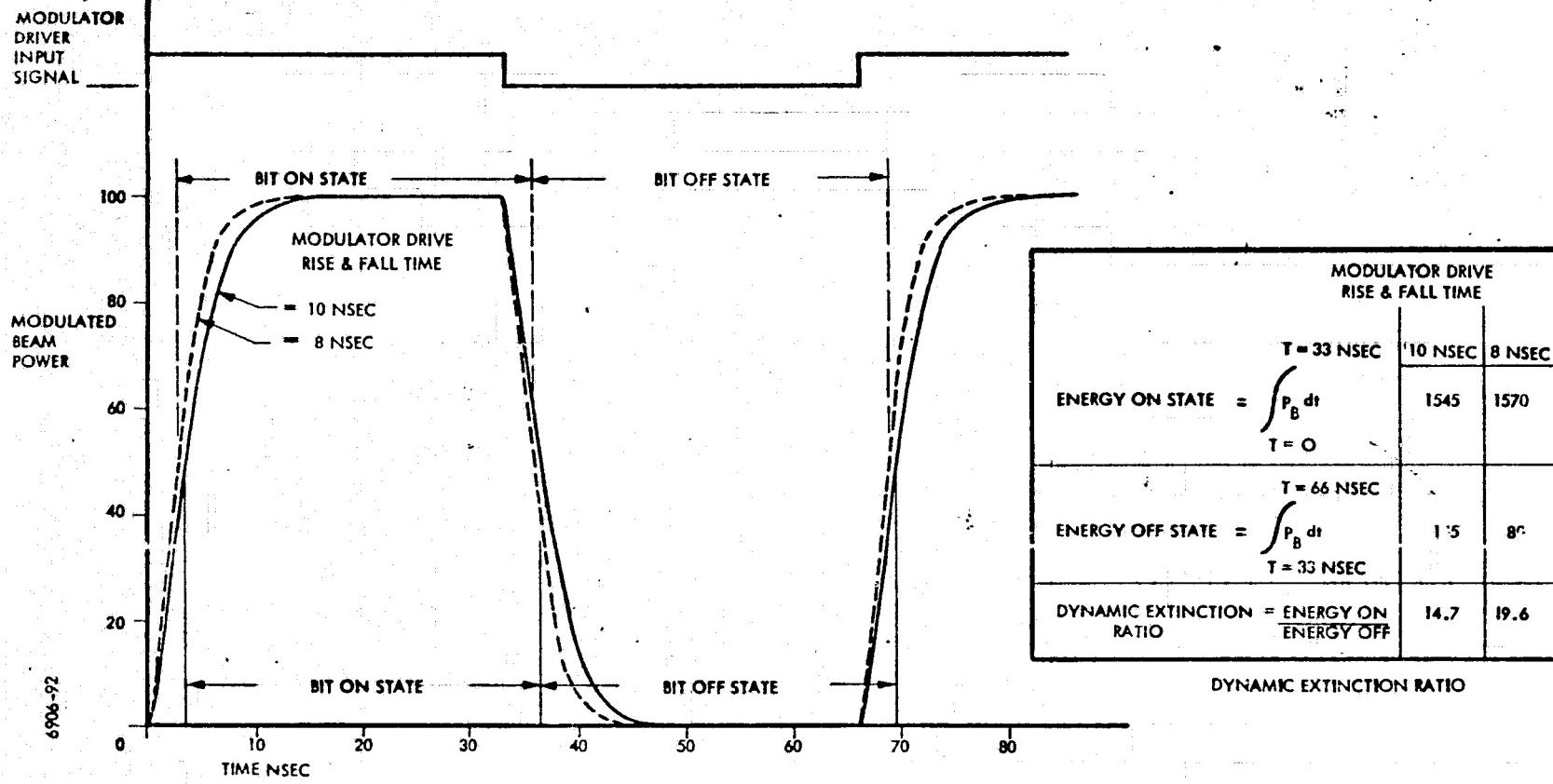
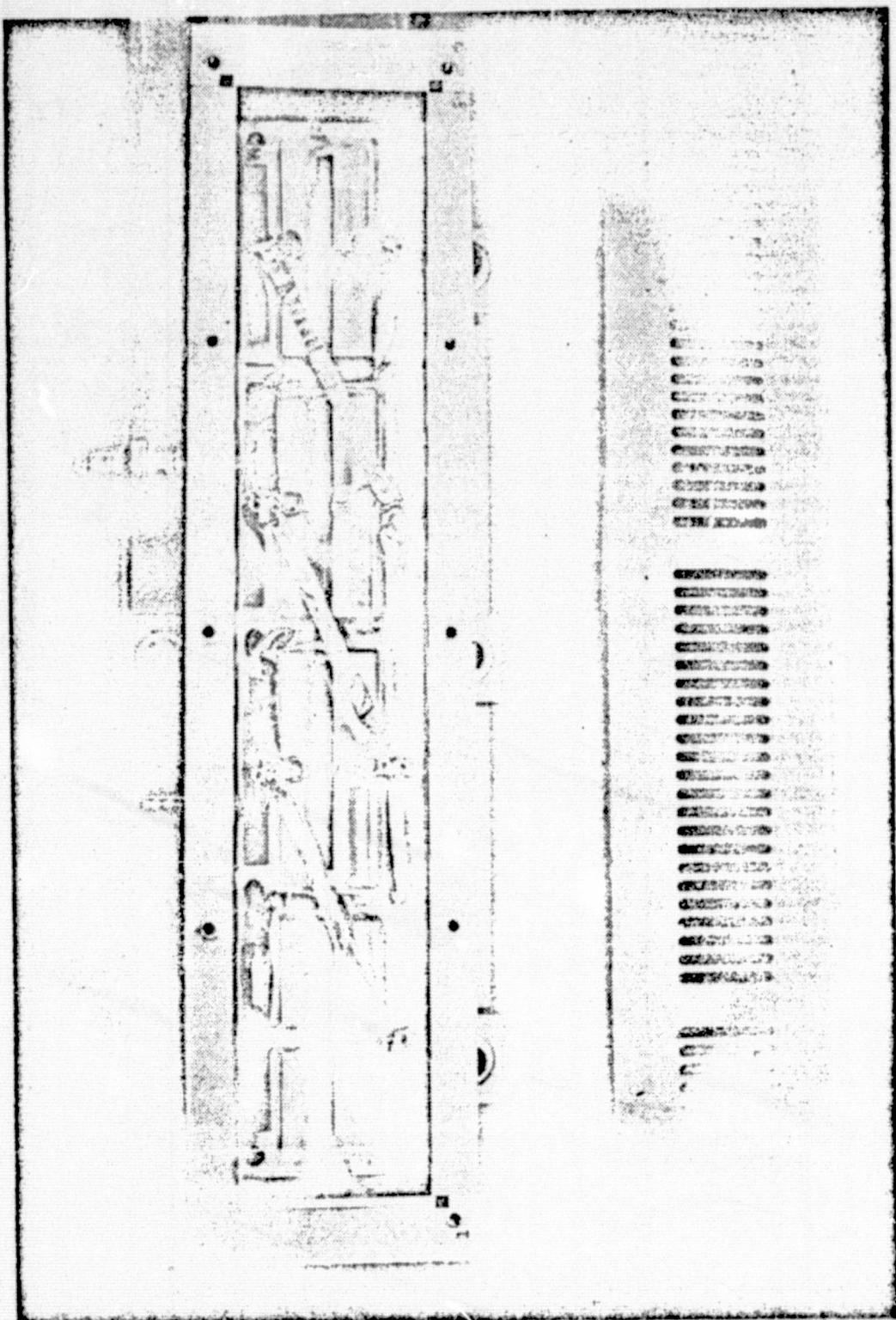


Figure 3-47. 30 Megabit Beam Modulation



88-9069

Figure 3-48. Transverse Field Optical Modulator

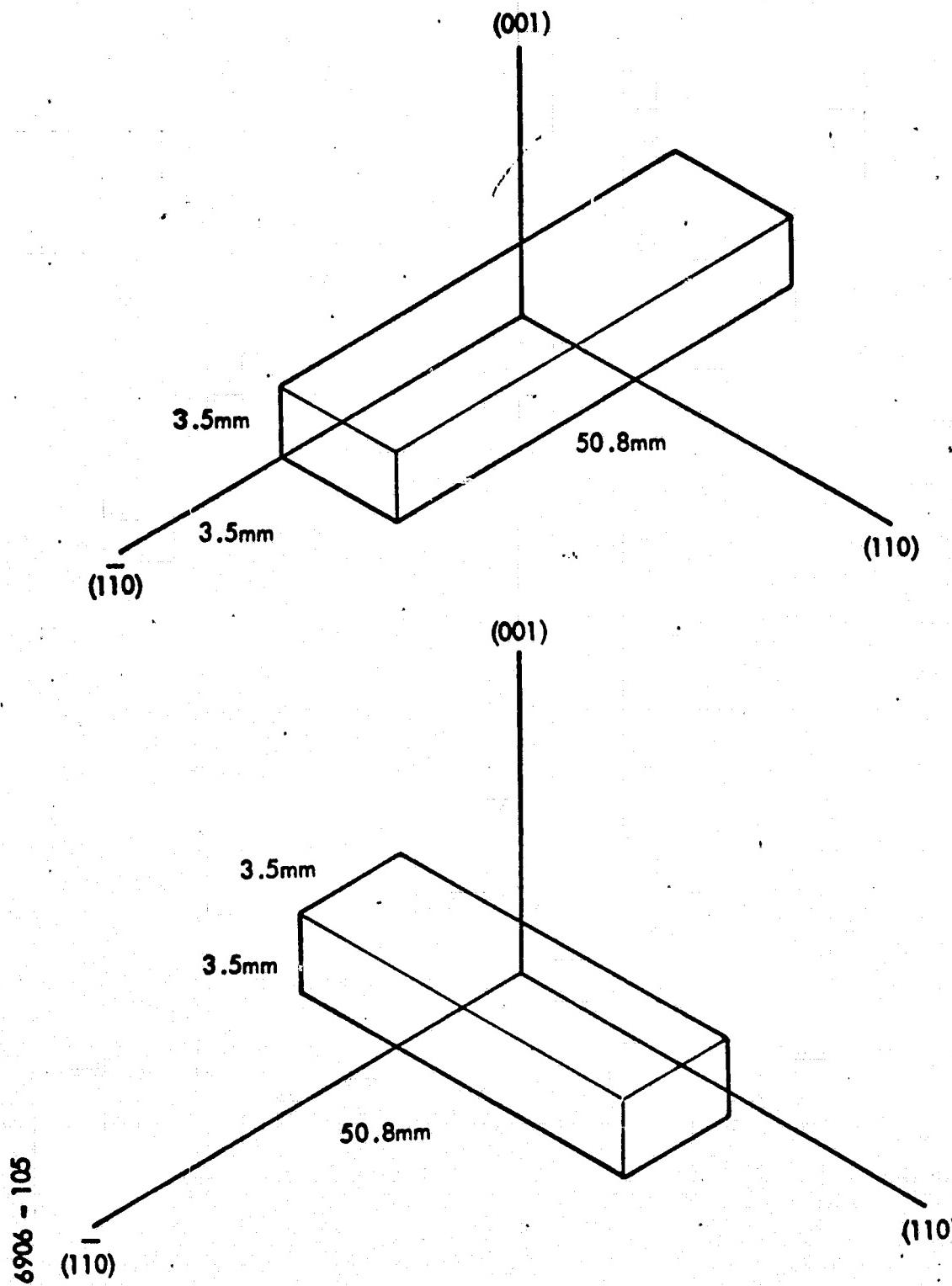


Figure 3-49. Crystal Orientation

orientations. Figure 3-50 shows the arrangement of the crystal pairs in the modulator. The crystals are alternately rotated 90° and the driving voltage polarity at each crystal is selected so that the electrically induced birefringence terms are additive, and the field independent terms cancel.

The modulator is filled with a lightweight, silicone oil (Dow Corning 550 Fluid) which provides both improved thermal stability and a good optical interface index matching.

The longitudinal half-wave voltage (i.e., voltage required to produce a π radian phase difference between two orthogonal polarizations propagating along the optical axis) has been measured for the deuterated KDP to be

$$\frac{V_{\lambda}}{2} \text{ (longitudinal)} = 3.2 \text{ Kv.}$$

The corresponding voltage for the same material used in the transverse mode (i.e., light propagating transverse to the optic axis and electric field direction) is given approximately by

$$\frac{V_{\lambda}}{2} \text{ (transverse)} = \frac{2d}{S_T} \frac{V_{\lambda}}{2} \text{ (longitudinal)},$$

where

d = crystal dimension in direction of electric field

= 3.5 mm

S_T = total crystal length

= $S_1 + S_2 + S_3 + S_4$

= 203.2 mm.

6906 - 106

3-108

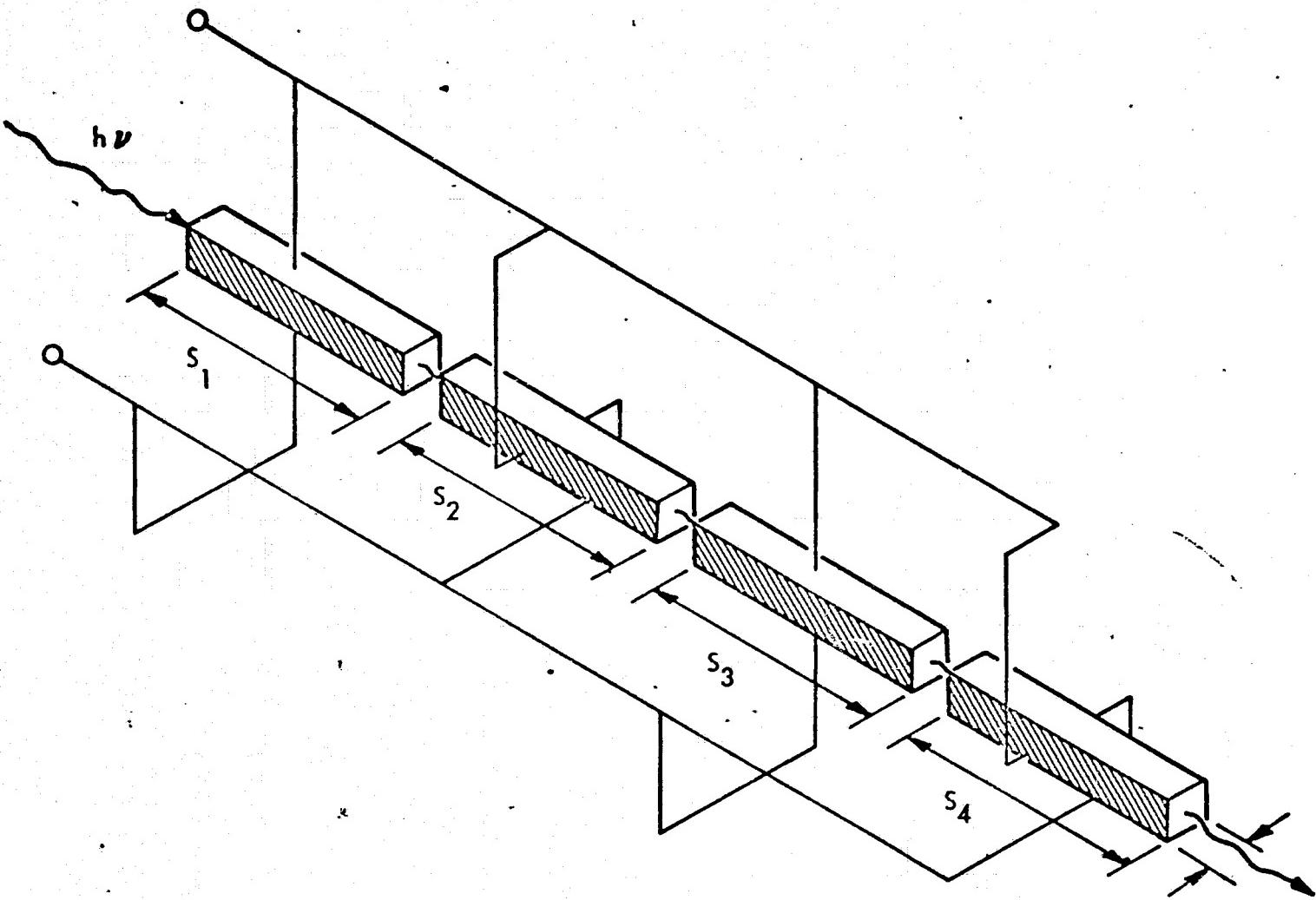


Figure 3-50. Electro-Optic Modulator Crystal Arrangement

The computed $V_{\frac{\lambda}{2}}$ for the transverse mode is

$$V_{\frac{\lambda}{2}} \text{ (transverse)} = 3.2 \times 10^3 \text{ volts} \left(\frac{2 \times 3.5 \text{ mm}}{203.2 \text{ mm}} \right)$$
$$= 110.2 \text{ volts.}$$

The measured transverse mode half-wave voltage is within 2 percent of the calculated value.

The modulator appears electrically as a parallel plate capacitor of square cross section with a capacitance given by

$$C = K \epsilon_0 S_T ,$$

where

$$\begin{aligned} S_T &= \text{total modulator crystal length} \\ K &= \text{dielectric constant} \\ &= 50 \\ \epsilon_0 &= \text{free space permittivity} \\ &= 8.854 \times 10^{-12} \text{ farad/meter.} \end{aligned}$$

The computed modulator capacitance is

$$\begin{aligned} C &= 50(8.854 \times 10^{-12} \text{ farad/meter}) (0.2023 \text{ meter}) \\ &= 80.95 \times 10^{-12} \text{ farad.} \end{aligned}$$

The measured capacitance is approximately 100 picofarad.

The difficulty with a modulator of this type arises from its relatively high capacitance and the concomitant problem of constructing a driver capable of providing

the required charging currents for fast rise time pulse operation. It can be shown that the capacitance, C, of the modulator is related to the half-wave voltage, $V_{\frac{\lambda}{2}}$, by

$$V_{\frac{\lambda}{2}} = \left(\frac{\epsilon'}{n_0^3 r_{63}} \right) \left(\frac{\lambda a}{C} \right)$$

where

ϵ' = permittivity of the electro-optic material

= $442.7 \text{ coul}^2/\text{n-t-m}^2$

n_0 = ordinary index of refraction

r_{63} = electro-optic coefficient

λ = laser wavelength

a = laser beam cross section diameter.

This equation shows simply that, for a given modulator, the half-wave voltage can be reduced only at the expense of increased modulator capacitance. The modulator/driver problem becomes one of effecting a suitable voltage/current compromise for a desired performance which is compatible with available electronic components and to devise a driver circuit which is conservative of driver power.

The present system has a modulator crystal length of 20 cm with an aperture of 3.5 mm, and has a half-wave voltage of 110 v. Modulator capacitance is approximately 100 pf. The charging current required for 10 nsec pulse rise time is

$$i \approx C \frac{v}{t} = \frac{(10^{-10} \text{ farad})(1.1 \times 10^2 \text{ volts})}{10^{-8} \text{ sec}}$$
$$= 1.21 \text{ amperes.}$$

This voltage/current requirement exceeds the rating of existing semiconductor components capable of the fast switching speeds; consequently, some compromise must be made. The present modulator/driver is capable of providing 50 v with the required rise time for a modulation depth of 65 percent.

The input power required of the modulator driver is given by:

$$P_{\max} = \frac{1}{2} C V_{\text{r/2}}^2 \frac{\lambda}{2} (\text{N}) \text{ watts}$$

where

C = modulator capacitance $\approx 170 \text{ pf.}$

$V_{\text{r/2}}$ = modulator half-wave voltage $\approx 55 \text{ volts (or voltage applied to modulator)}$

N = number of signal transitions per second

A 30 megabit/second data rate, assuming alternate ones and zeros gives approximately 3×10^7 transitions per second. Figure 3-51 shows the maximum drive power required for this modulator.

Modulator Driver

The modulator driver performs the function of interfacing the A/D converter with the optical modulator. The driver accepts a nominal 0 and 1 volt digital signal from a 75 ohm source and provides a 0 and 50 volt output at the necessary impedance match to drive the optical modulator. The driver employs an all solid state design and consists of three pulse amplifiers, two emitter followers, and a modified push-pull output stage as illustrated by the schematic diagram of Figure 3-52.

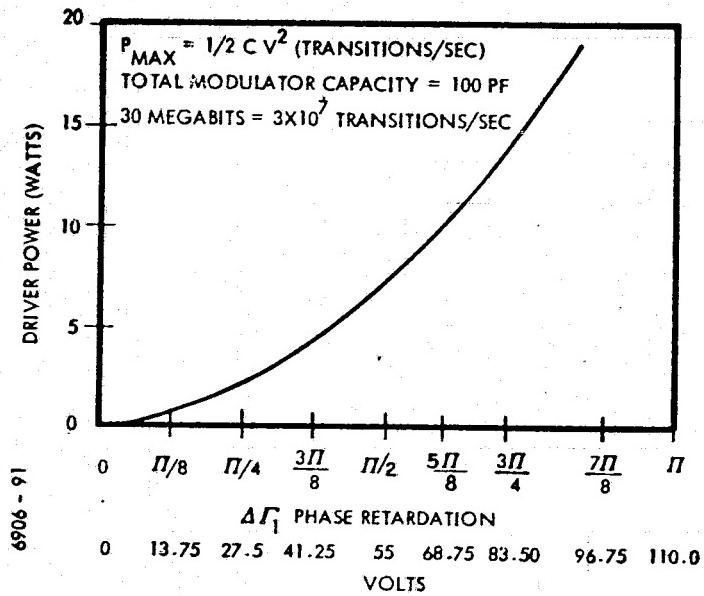


Figure 3-51. Maximum Power Requirements

751-9069

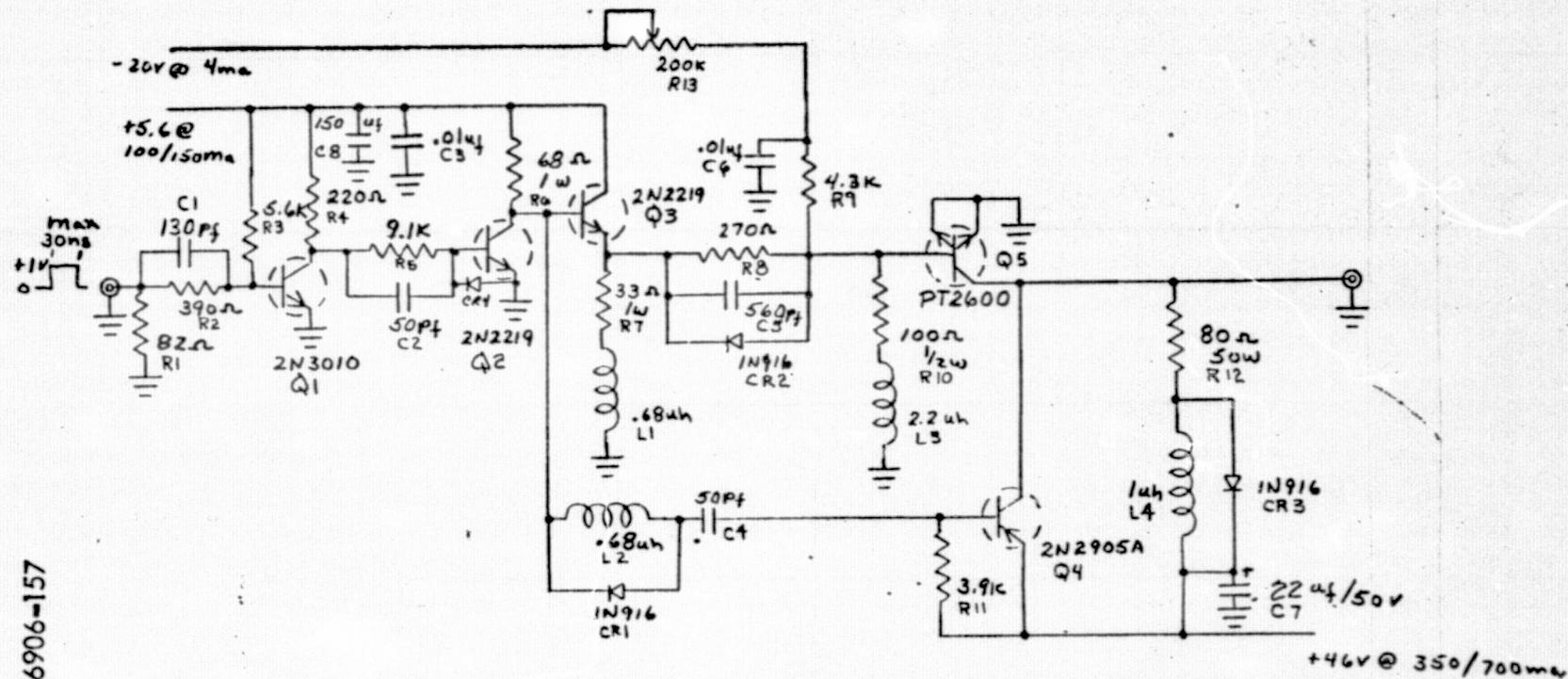


Figure 3-52. 30 M-Bit Modulator Driver

A 1.0 volt input pulse is received at the base of Q1. With a 1.0 volt input, the transistor is just turned on and yields little gain so the 6.8 K resistor was added in the base circuit to prebias the base, thereby allowing the input pulse to draw this transistor into full conduction. The second transistor is an emitter-follower which acts as a buffer for the first amplifier. The following amplifiers, Q3 and Q4 sharpen the pulse rise time and develop the power necessary to drive the output stage. The emitter-follower Q5 matches the pulse drive to the input of the final stage which is a PT 2600 high frequency power transistor. Since this device is capable of operating with amps of collector current, it requires a good base drive to deliver output power. To be an effective driver, the unit must operate at a 30 megabit rate which requires handling pulses of 33 nsec duration. The driver must deliver these high voltage pulses to a capacitive load of approximately 100 pf (the crystal modulator). The capacitive load tends to store a charge. Unlike a resistive load, it must be caused to discharge rapidly enough to reproduce the input pulse with reasonable accuracy. Discharging the load is relatively easy as Q6 is caused to conduct by a positive pulse on its base, it forms a very low resistance path to ground, rapidly discharging the load capacitor (the discharge time being 12-14 nsec).

If the required charge path for the capacitor was through the 5 watt load resistors which total 140 ohms it would take, considering 5 time constants for full charge, 70 nsec to charge the capacitor. Therefore, a different charge path is required. At the end of the input pulse, the negative going edge is coupled capacitively to Q7 causing Q7 to draw current during the negative transition and thereby charging the load capacitance in 18 nsec through the low resistance path of the emitter to collector of Q7. The input to Q7 is delayed a few nsec to allow Q6 to begin turning off. If Q6 were not turning off, it would supply a low resistance short through its collector to emitter junction which would draw a destructive current through Q7. Q7 is a relatively low current transistor compared to Q6. The unique push-pull method described above is made necessary by the lack of high power, high frequency PNP transistors on the market. The PT 2600 is a 5 watt amplifier

which has useable gain at 250 mc; no PNP complement could be found for this device. The PNP transistor, 2N2905, which is used dissipates less than 1.0 watt, but has the necessary frequency response for this circuit. In addition to the power and frequency requirements, the transistors must be capable of handling high collector-to-base voltages, the requirement here being a minimum of 50 volts. This made PNP transistors even more scarce for this application.

The modulator driver has been operated into dummy loads of up to 200 pf capacitance at a 30 megabit rate with a 45 volt output pulse amplitude. The pulse width and pulse repetition rate capabilities are from 30 nsec to 50 μ sec pulse width and 15 MHz to 4 KHz pulse repetition rate.

Figure 3-53 shows a comparison of the signal waveform at the driver input to that at the output of a PMT detector. The signal waveform is derived from the 31 bit pseudorandom generator in the RER.

The longest pulses anticipated in the nonreturn-to-zero system is 667 nsec. No pulse stretching should occur for a pulse of this duration. However, transistors which have been saturated for a considerable length of time tend to remain in a conduction state due to the base storage charge. The driver will operate better with digitized TV pictures of lower contract, i. e., no rapid transitions

6906 - 51

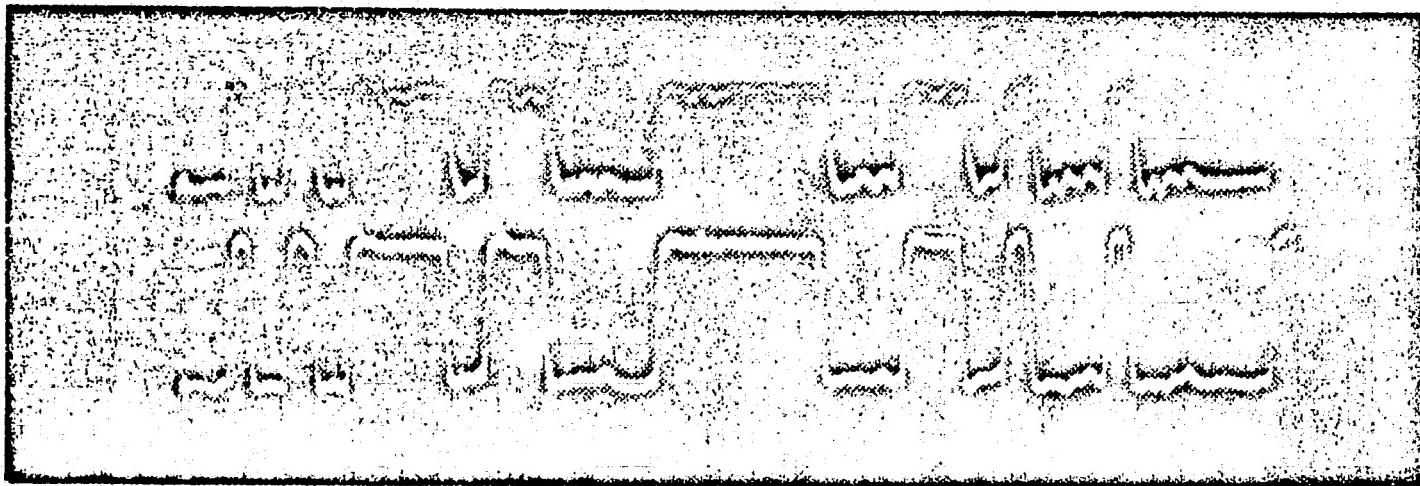


Figure 3-53. Optical Modulation Pseudo Random Word

A WAVEFORM AT INPUT TO DRIVER

B DETECTED WAVEFORM OUTPUT OF OPTICAL RECEIVER.

NARROW PULSE 27 NSEC WIDE.

from black to white, where there is the opportunity to generate long pulses. This is not to conclude that it will not operate with high contrast, but the error rate measured is higher, although picture quality appears good. For example, when the vidicon beam is turned down so there is no picture, the A/D converter transmits a 1:2 on-off ratio of 33 nsec pulses at a 100 nsec repetition rate. The measured error rate for this condition is much lower than for a high contrast picture.

The construction and operation of the driver is relatively simple, in that there are no variable components and, therefore, no need for tuning or adjusting to become operational. The unit is reliable, even when handling high power, fast rise time pulse information; no failures have been recorded throughout laboratory or field testing.

3.4.3 Laser Power Monitor. - The function of the laser power monitor is to measure the average modulated laser power and to monitor the noise on the output laser beam within a 5 kHz bandwidth. The noise measurement is made so that any noise existing within this bandwidth will not be interpreted as atmospherically induced. The laser power monitor

is an RCA type 8644 photomultiplier sampling less than 1 percent of the transmitted laser power. Narrowband and neutral density filters are located in the power monitor path to reduce the laser power and background power on the detector to an acceptable level ($\sim 10^{-10}$ watts).

The laser power monitor subsystem circuit diagram is given in Figure 3-54.

3.4.4 Beam Divergence Control. - The beam divergence control subsystem provides a continuously variable transmitted beam divergence control, i.e., without interruption of the transmitted beam. The divergence is made in

six discrete steps by displacement of one lens of a small telescope.

The range of adjustment is from near diffraction limit for the 1.5 inch (3.81 cm) output beam diameter to approximately 0.5 mrad.

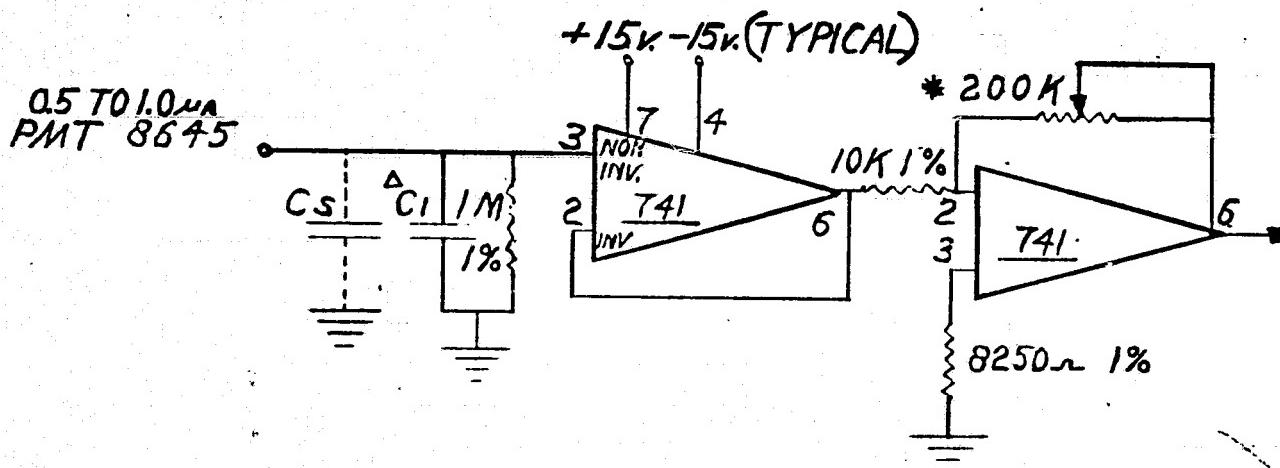
The calibration data for this device is presented in a later section.

This beam decollimation is achieved without loss due to vignetting and without substantial output beam diameter change in the design selected.

The beam divergence subsystem comprises a moveable paritive focal length lens, L_1 , and a fixed positive focal length relay lens, L_2 . Lens, L_1 provides a twofold function, 1) it produces a point image of the laser input beam which is moveable relative

3-119

651-9069



*BOURNS TRIMPOT MO.3059L - HI TEMP TRIMPOT
△ SELECT C_I AFTER PMT COAX LEAD LENGTH DETERMINED
C_I = 11PF C_S = 47PF

Figure 3-54. AOCP Laser Power Monitor 5 KC BW

to lens L_2 and 2) it permits a selection of the appropriate telescope power to control the exit beam diameter to ensure proper location and size of the transmitted beam in the primary optical system exit pupil.

Figure 3-55 shows the optical schematic for the beam divergence telescope. The basic equation describing the beam divergence subsystem operation are as follows:

$$\tan \frac{\theta}{2} = \frac{y(a-f_2)}{Mf_1 f_2}$$

or for small angles

$$\theta \approx \frac{2y(a-f_2)}{Mf_1 f_2}$$

where θ = beamwidth in object space from the system primary afocal telescope

y = radius of beam at input of beam divergence telescope

(at L_1)

a = distance between lens L_2 and point image formed by

L_1

f_1 = focal length of lens L_1

f_2 = focal length of lens L_2

M = Magnification of primary afocal telescope

6906-166

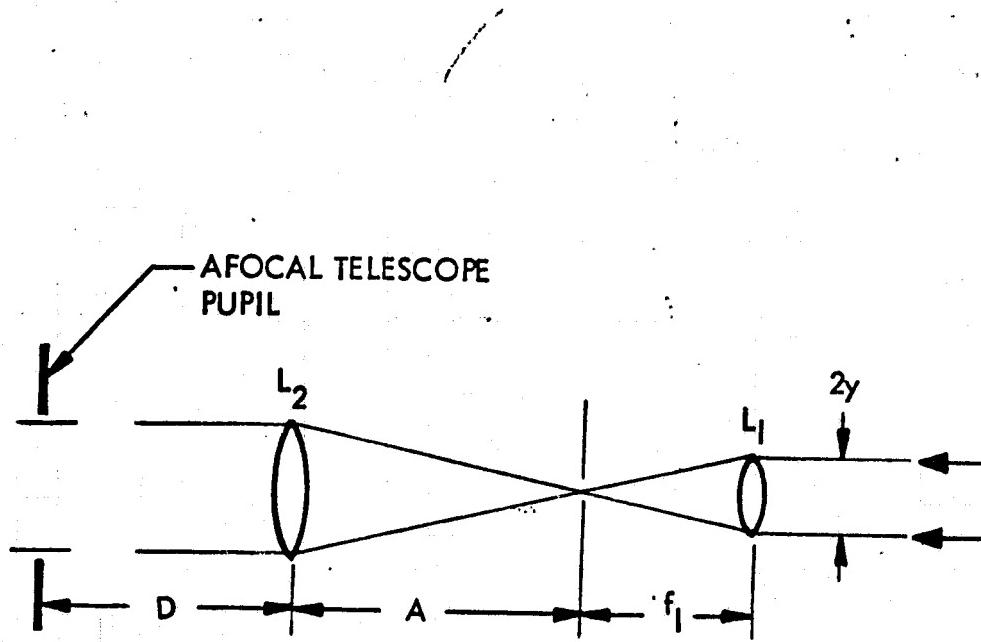


Figure 3-55. Beam Divergence Telescope Optical Schematic

Figure 3-56 shows the mechanism that controls the beam divergence. The actuator is a six position stepper motor controlled by an electronic logic circuit. Lens L₁ is mounted in a honed piston/cylinder for precise axial motion. The spring loaded piston assembly is driven by a precision cam and follower. The cam shape and position on the stepper motor shaft determines the range of the beam divergence adjustment. Calibration of the beam divergence control is described in the test and calibration section of this report.

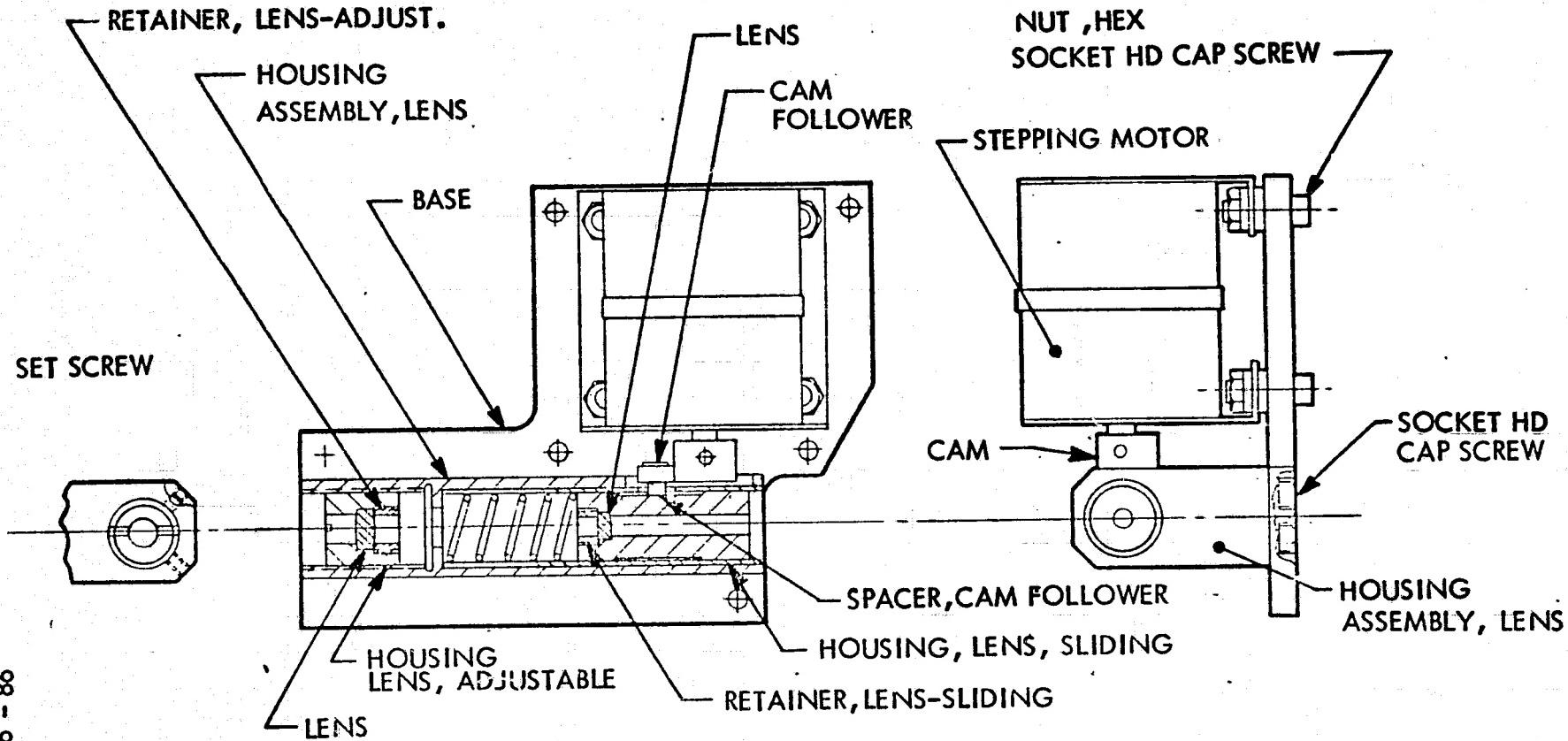


Figure 3-56. Telescope, Adjustable (AOCP)

TV Acquisition Aid

The TV coarse acquisition aid was adapted from an ITT Electro-Optical Sensor designed specifically for the Short Range Missile (SRM) application. Some of the outstanding features of the EO Sensor are: small physical size, fast acquisition, high tracking rates, proportional error outputs and adaptive gates.

The camera (video sensor) and all on gimbal components are packaged within a 4.25" diameter sphere. The off gimbal electronics occupies 48 cubic inches of space excluding power sources, converters and regulators.

Acquisition times are between 10 to 150 millisecond after a target has been detected. The initial error outputs are available within 10 msec; however depending on line of sight rates, target contrast and background clutter; the peak detector requires one or more video fields to complete target selection.

Tracking rates are a function of gate size, target range and contrast.

Continuous tracking is maintained if contrast smear due to relative motion between target and sensor does not lower the video level below system threshold; the target does not move out of the gated (window) area in a 10 msec field period; and the target video is found above threshold on a minimum of two video lines in the field of view. Line of sight rates on targets of 100% contrast that fill 10% of the field of view are in excess of 30 degrees per second if no pointing error corrections are made.

The azimuth and elevation error outputs are proportional to the position of the center of the target in the field of view accurate to within 5% over the entire field and less than $\pm 1\%$ over the inner 40% of the field of view.

Adaptive gates which are a function of target size and shape help reduce background clutter in the field of view by eliminating all video from the area outside of the tracking gates from the signal processing. The gates may be set at any ratio proportional to target width and height and in this tracker have been set to twice the target size so that the gates are 1/2 target dimension beyond each edge of the target.

The error outputs (azimuth and elevation) are accumulated at the camera field rate which is 60 fields per second. Since no smoothing is supplied in the sensor the data rate, 60 samples per second, is equal to the camera field rate and twice the frame rate (30 frames per second).

The $5^{\circ} \times 5^{\circ}$ F.O.V. (field of view), minimum target size (9 feet) at 3 n.mi. (nautical miles), acquisition times of less than 200 msec and tracking rates of 30 degrees per second were considered in arriving at the frame rate and number of television lines per field. These considerations include the minimum number of lines to achieve the required resolution, the MTF (modulation transfer function) of a 1/2" vidicon and the ease of converting standard television sweep and interlace circuits. At a range of 18,000 feet the 87.25×87.25 milliradian FOV is 1572 ft^2 . A 9 ft^2 target subtends $9/1572 = 1/175$ of the FOV. To obtain one bit of video information the target must subtend at least a portion of the width of a scanned line, preferably a complete line, each time the FOV is scanned. If a 50 frame/second rate with interlace is used the number of fields scanned is 100 per second and it is necessary to subtend a portion of the target on one line in each field to obtain X-Y information at a 100 sample/second rate. Therefore at 100 fields/second the number of lines/field must be at least 175 to assure having target information in each field for minimum target types. Since there are 2 fields/frame with retrace time it requires 350 plus lines/frame.

The sensor consists of two major subsystems which are the camera and the tracker. The camera is defined here as the vidicon and all peripheral components which cause it to operate in such a manner so as to produce usable electrical signals which are spatially referenced to the scene in time. It should be noted here that a standard 1-inch vidicon camera having conventional raster scans and frame rates has been substituted for the SRM camera for the AOCP application. The tracker consists of all circuits which are required to suppress clutter and convert the target signature into error voltages which may be used by the missile guidance system to ultimately direct the missile to the target. In addition, the tracker applies gates on itself through which only a minimum amount of video immediately surrounding the target is allowed to be processed in the tracking circuits. Simplified block diagrams for the camera and tracker electronics are given in Figure 3-57 and 3-58.

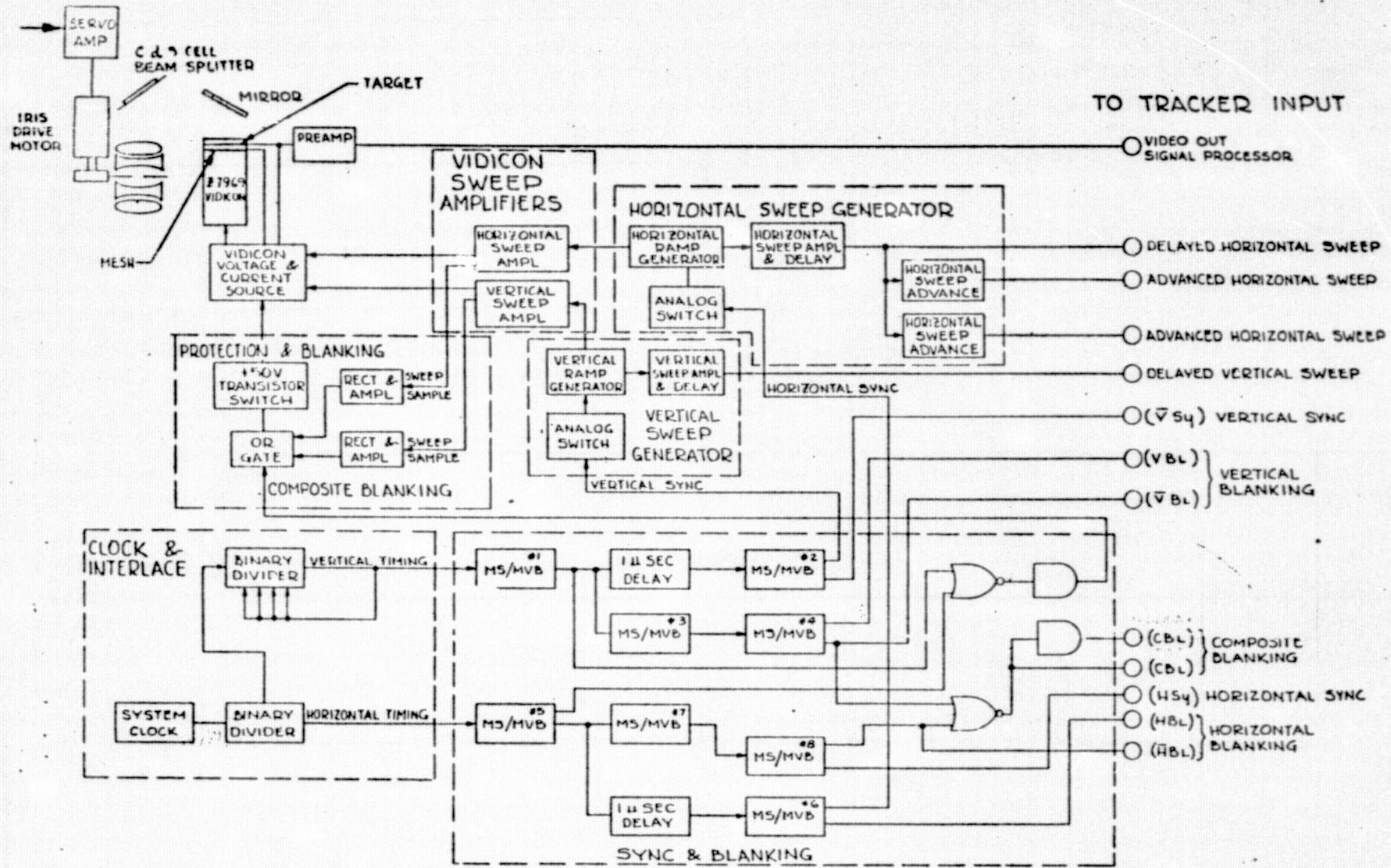


Figure 3-57. TV Tracker Camera Block Diagram

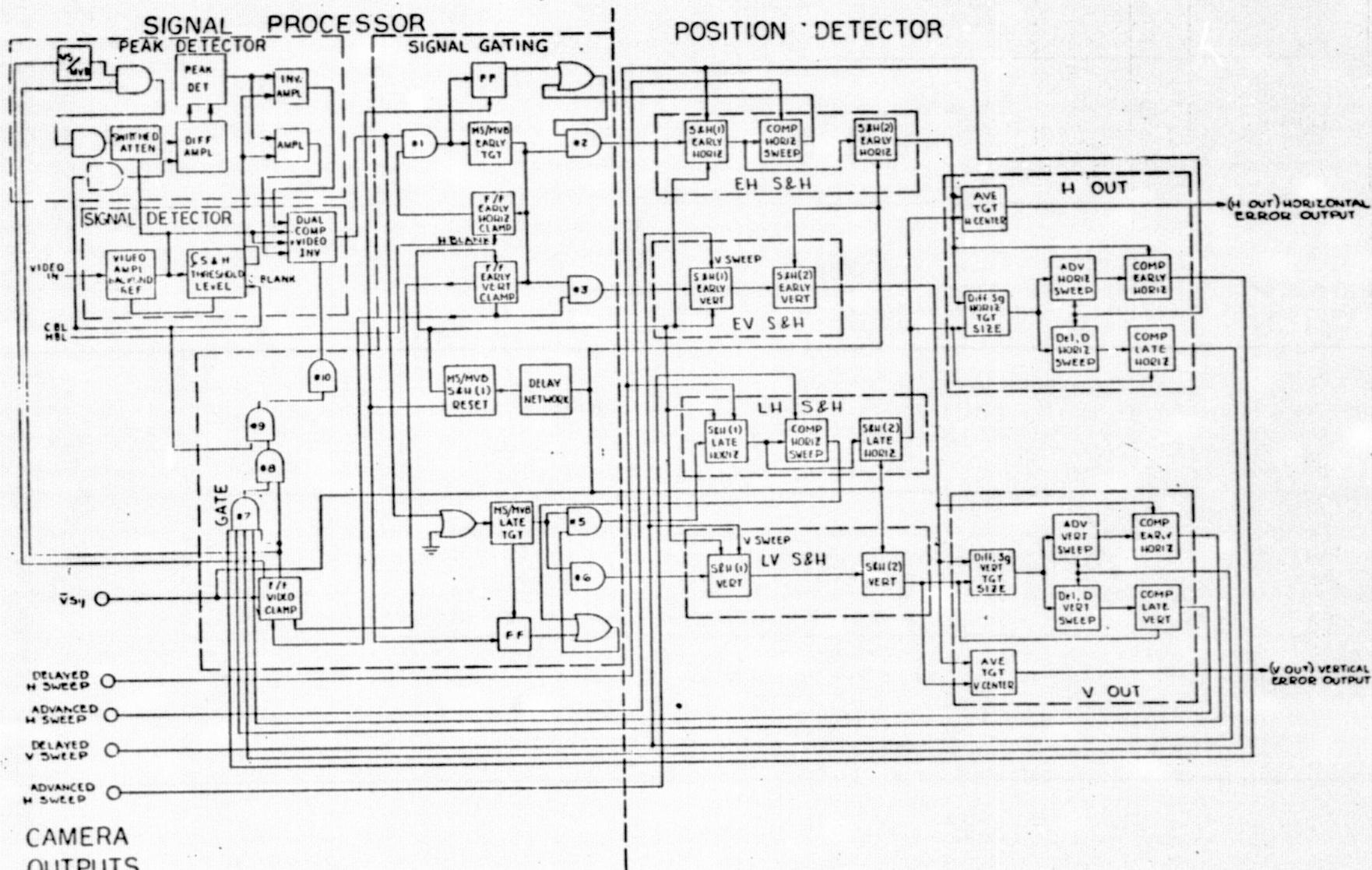
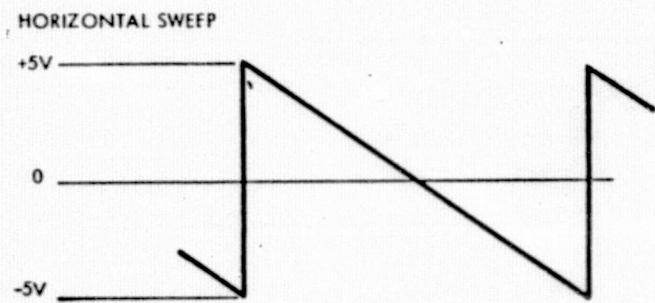
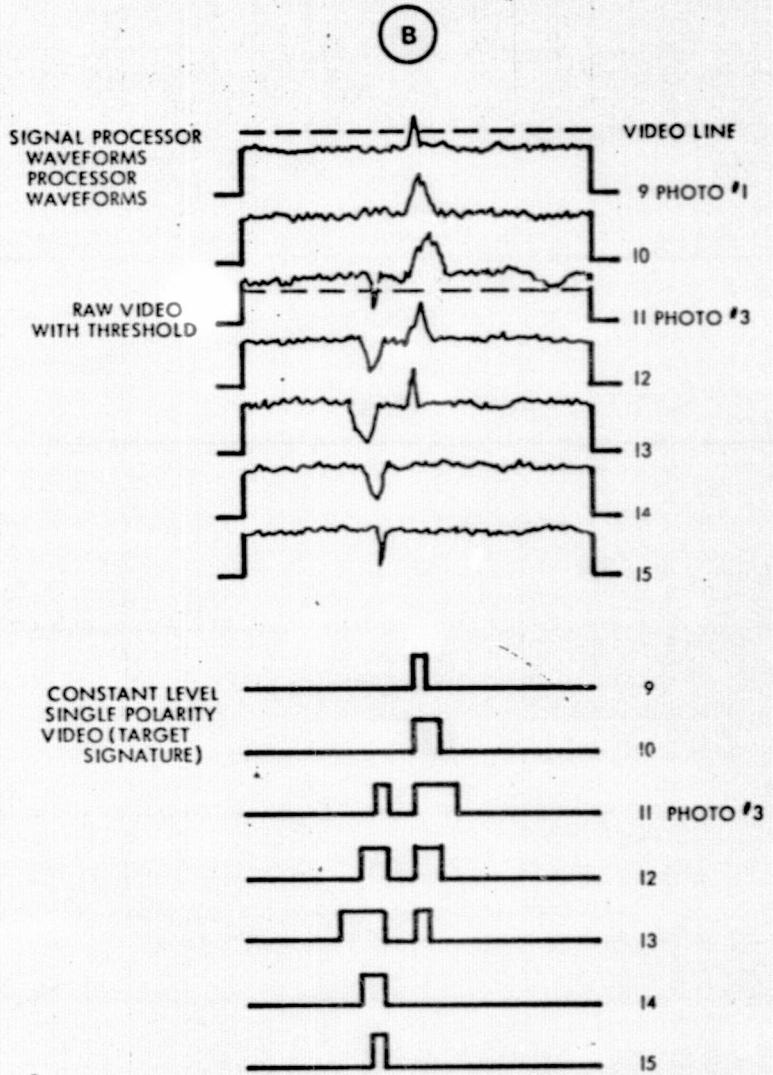
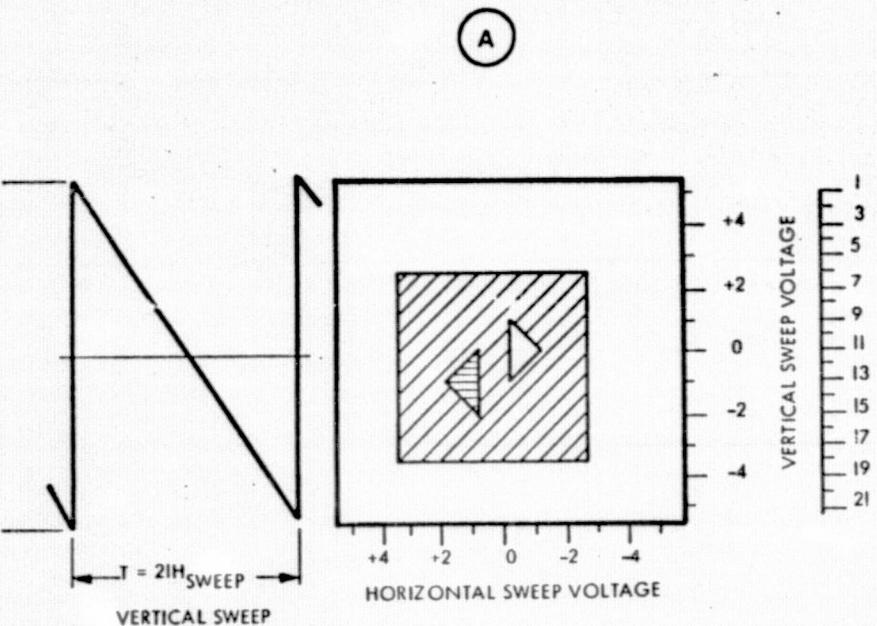


Figure 3-58. TV Tracker Signal Processor and Position Detector

Tracker Operation

To promote a better understanding of the TV acquisition aid sensor, a signal will be traced through the signal processor and position detector to show how error signals are derived from target information imaged on the vidicon. It is assumed that the reader understands the operation of a television camera and it will only be necessary here to establish a relationship between the target spatial position, time established by the sensor clock and the error voltage derived from these two. To facilitate ease of drawing waveforms and explanation we will use the simple target of Figure 3-59(A) with only 21 lines of video. This particular target is complex enough to demonstrate the functions of the signal processor and position detection circuits. The voltages, number of video lines and relative magnitudes are used only to simplify the explanation. It should be kept in mind that all of the operating principles described are applicable to the actual SRM sensor shown in the Camera and Tracker Block Diagrams. (Figures 3-57 and 3-58.)

The vidicon target is scanned by an electron beam which is deflected by the vertical and horizontal ramp functions as shown in A of Figure 3-59. For each elemental position on the vidicon target there is a time and voltage relationship with the system clock and the ramp functions generated by this clock, (see Figure 3-59). Therefore, if the signal processor and position detector obtain their reference from the same source as the vidicon we can obtain a set of error voltages which indicate the spatial position of the target center if it is anywhere within the field of view.



011-9069

Figure 3-59. Video Target-Time-Voltage Relationship

As the field of view is scanned line by line raw video is sequentially made available to the signal detector. The waveforms for video lines 9 through 15 are shown in B of Figure 3-59. The raw video has certain inherent information which is utilized in the signal processor. There is the background level which is due to the average scene brightness, the target and clutter may be lighter or darker than the background and portions of the scene may have more contrast than others which results in higher peak levels in the video. The raw video is first amplified in an operational amplifier. The amplified output is integrated to achieve a d.c. voltage proportional to the average scene brightness. This integrator input is opened by an analog switch during blanking time to eliminate blanking information from the integrated output. The d.c. output is differentially added to the video operational amplifier input so the output video is always referenced to the average background. The video output is positive or negative with respect to ground depending on whether it is brighter or darker than the background. In addition, the d.c. generated from the background is added as a portion of the threshold voltage which will ultimately determine if video is target or clutter. A portion of the background referenced operational amplifier output is further amplified in a differential amplifier. This integrated amplifier has a gate controlled input which is used to disable the amplifier during camera blanking. Both video polarities from the differential outputs are peak detected and the peak amplitude voltage is held in a memory circuit. The peak

detector is active at all times in the absence of video input. After video information is first detected a timing circuit is energized which holds the peak detector circuit at full gain for approximately 15 fields. During this period the field of view is tested by the peak detector for the highest contrast. After this selection is made and the gates are set around the detected contrast area the timing circuit reduces the peak detector gain to allow lower threshold control and consequently tracking of the entire target rather than the highest contrast in the target. The peak detector output is summed with the background reference level to establish threshold levels for the video comparator.

The video comparator is an integrated circuit dual comparator. The background referenced video which contains positive and negative outputs is compared to positive and negative threshold levels derived from the background level and peak detector. The positive and negative threshold may be adjusted for different dynamic slopes and ranges.

If the video input is more positive than the positive threshold or more negative than the negative threshold the comparator output switches state yielding a positive logic level output (B of Figure 3-59). The comparator has a strobing input also used to apply gates to the video signal. After acquisition the position detector locates early and late gates around the target. These gates are used to disable the comparator so that clutter which may appear in the field of view is not passed to the position detector if it is outside of the gated (window) area. The output from the comparator is logic level pulses which are proportional in width to the video which is above threshold.

3.6 Down Link Communications Equipment

3.6.1 Information Coding. - The video A/D converter uses a form of the delta modulation process which transmits, one bit at a time, the changes in the video analog signal.

The changes in the analog input signal are determined by comparing the input level with the level of a previously sampled portion of the input by means of a digital feedback loop. The difference between the levels of the reconstructed analog and the input video appears as an error signal from the comparator which feeds a binary decision circuit. In a conventional linear integration delta coder, positive or negative pulses are generated at the clock rate, depending upon whether or not the reconstructed output is greater or less than the input analog. The pulses generated are either positive or negative at each clock period, and their amplitudes are constant regardless of the magnitude of the error. The analog signal is reconstructed from the pulse train by an integrator whose output decreases or increases a fixed amount, depending upon the polarity of the pulse and its input. The feedback from the integrator to the comparator is degenerative, so that the reconstructed signal approaches the input signal, as shown in Figure 3-60. The digital signal coupled out of the analog-to-digital converter is the pulse train from the binary decision circuit. The analog signal can be reconstructed at the receiver by using an integrator identical to the analog-to-digital converter.

The A/D conversion employed in this equipment is a slight modification of the conventional process in that a pulse train of only one polarity is used to drive the integrator. A pulse either exists or does not exist at each clock period. The integrator circuit consists of an integrating capacitor and a resistor. The capacitor charges one step of voltage when there is an input pulse, and discharges through the resistor in the absence of a pulse. The integrator is nonlinear, since the leakage current is proportional to the voltage across the integrating capacitor, as shown in Figure 3-61.

3-133

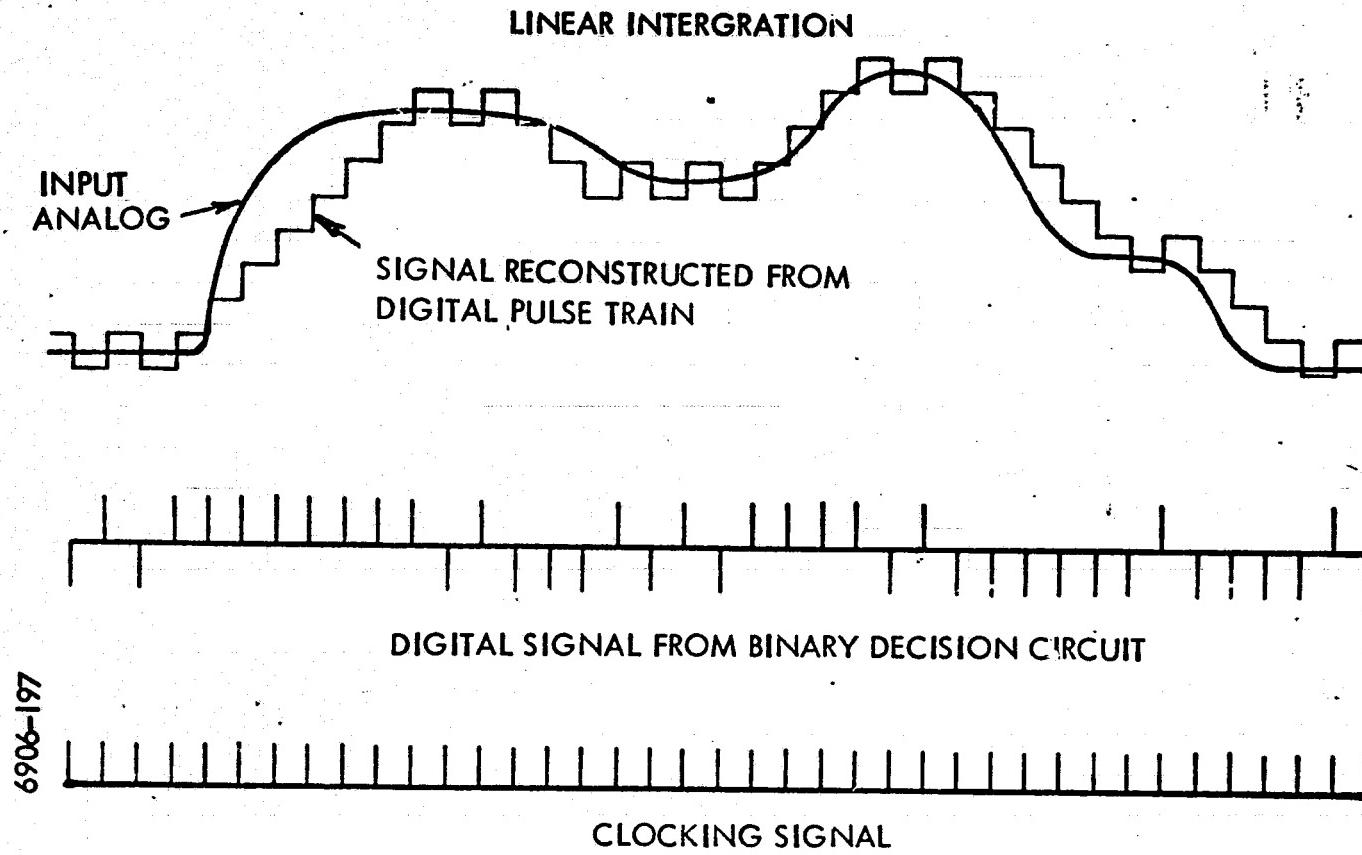


Figure 3-60. Delta Modulation Process

NONLINEAR INTEGRATION

INPUT ANALOG

**SIGNAL RECONSTRUCTED FROM
DIGITAL PULSE TRAIN**

DIGITAL SIGNAL FROM BINARY DECISION CIRCUIT

CLOCK SIGNAL

6906 - 107

Figure 3-61. Delta Modulation Process, Nonlinear

Figure 3-62 shows a block diagram of the analog-to-digital converter.

The input analog video is amplified and compared with the reconstructed analog at the summing junction. The difference voltage is fed to the first binary decision circuit, which samples the error signal at a rate determined by the system's clock generator. If the error voltage exceeds a prescribed threshold, a pulse appears at the output of the first decision circuit. The pulses appearing at the output of the first decision circuit have some leading and trailing edge jitter, which is proportional to the magnitude of the error signal. To remove this signal, a second decision circuit is used. The clock signal gating the second decision circuit is delayed slightly, so that it does not respond to the jittering edges on the pulses from the first decision circuit. The pulse train from the second decision circuit is fed to the integrator, which reconstructs an analog video signal from the pulses. The reconstructed analog is fed to the summing junction, and to an output which permits monitoring of the analog-to-digital conversion performance. The digital signal from the second decision circuit, which contains the video information, is of the return-to-zero form. The reclocker circuit converts the output to a nonreturn-to-zero signal at a nominal 0 and 1 volt level, which is accepted by the optical modulator's driver circuit.

A detailed description of the digital communications equipment has been supplied to NASA in a separate report.

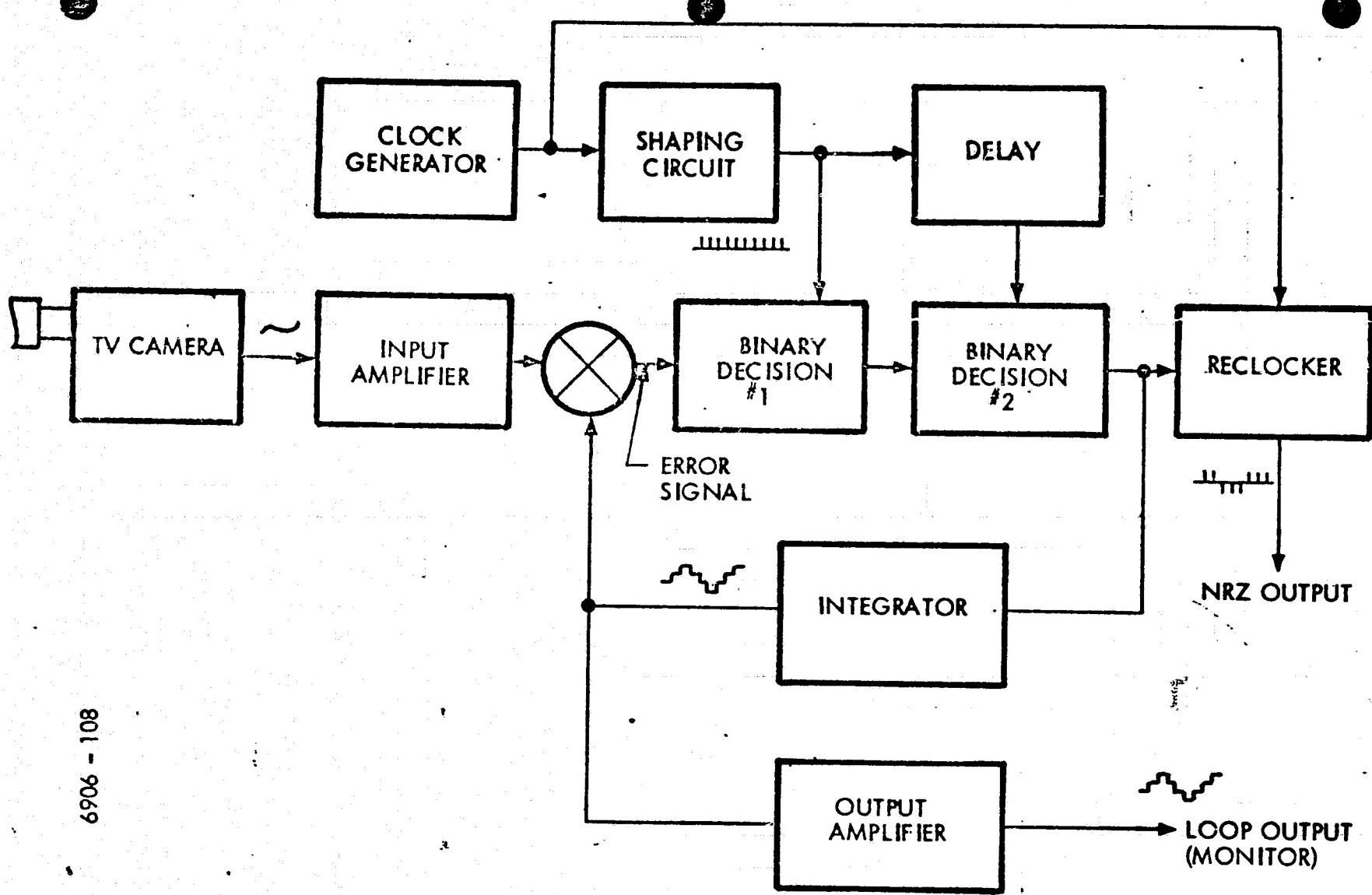


Figure 3-62. Analog to Digital Converter Block Diagram

3.6.2 Pseudo Random Generator. - A relatively short, 31 bit pseudo random pattern length, has been utilized in the communication experiment equipment for bit error rate measurement. This length is adequate for measuring error rate on the present wide-band laser link, and at the same time permits scintillation measurement by use of convenient low center frequency filters at the ground station.

For some communication channels, longer pattern lengths (on the order of 2^{11} to 2^{13}) are required to adequately measure error probability.

These channels are characterized by intersymbol interference extending over many adjacent bit intervals. A noise band telephone channel is an example. Here the interference is caused by phase distortion due to one or more sharp cutoff filters in tandem. In these cases, the error probability at a particular bit time depends on the particular combination of a number of the adjacent bits.

Measurement of average error probability requires a sufficiently long pattern to be sure all possible bit combinations are exercised during the measurement.

In the AVLOC system, however, the inherent channel bandwidth (optical carrier) is much broader than the signal bandwidth, even at the highest bit rate (30 mb/s). The intersymbol interference due to the channel is thus negligible. The pattern length only has to be sufficiently large so as to ensure that all combinations of the two bits immediately adjacent to the current bit are exercised. This could be ensured by a pattern as short as 15 bits. The

reason for considering the immediately adjacent bits is to ensure that any intersymbol interference caused by imperfectly matched filtering in the communication detector is properly measured.

Since the pattern is periodic, its spectrum consists of a number of discrete spectral lines, as shown in Figure 3-63 for the 30 MHz bit rate. The scintillation measurement made with data modulation can be achieved by filtering out one of the spectral lines (greatest amplitude component) and measuring its fluctuating amplitude. If the pattern is too long, the spacing between spectral lines will be too close to separate with simple filters. The selected length, 31 bits, permits this filtering with convenient values of center frequency. For example, extraction of the fundamental spectral line requires the following nominal center frequencies:

<u>BIT RATE</u>	<u>FUNDAMENTAL FREQUENCY</u>
30 kb/s	970 Hz
1 mb/s	32 kHz
5 mb/s	160 kHz
30 mb/s	970 kHz

For bit rates above 30 kb/s, extraction of the fundamental code frequency component readily enables measurement of scintillation within the entire 0 - 5 kHz band. At the 30 kb/s rate, the first five code components fall within the 5 kHz band. Consequently, extraction of only the 970 Hz component would limit the scintillation band to nominally 0 - 500 Hz. The PN spectrum or any intensity modulation, poses potential problems to the optical tracker. If the code components fall in the spectral region of the scan modulation or tracker bandwidth, erratic tracking or loss of track can result.

P-R SPECTRUM - 30 mHz RATE 6906 - 93

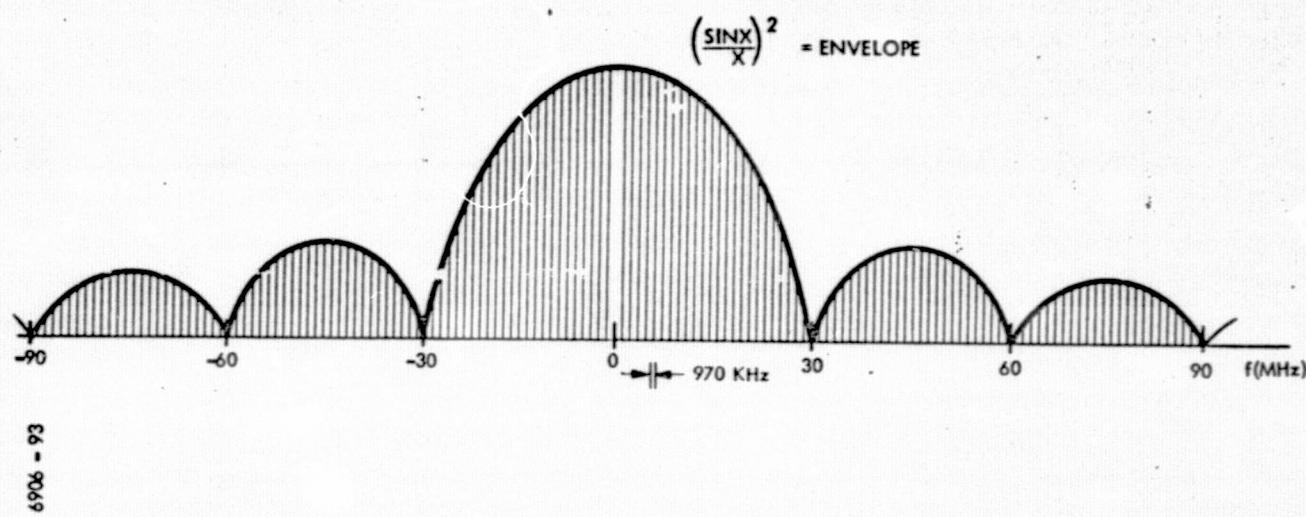


Figure 3-63. P-R Spectrum-30 MHz Rate

3.7 AOCP Calibration and Test

This section describes the calibration techniques for the various AOCP subsystems and presents calibration data acquired prior to shipment of the system hardware. Because of the schedule delays resulting from the earthquake damage, there was considerable pressure to ship to the integration contractor's facility to avoid further program delays and increased program costs. Consequently, the system tests prior to shipment were not as extensive as was desirable. Further, the dynamic environment was not defined and tests in that environment were planned to be conducted at the integration contractor's facility.

Calibration and acceptance test plans were prepared and the NASA/MSFC COTR witnessed tests prior to delivery. The primary test instrument was the GCE described in later sections of this report. The following paragraphs summarize the calibration tests performed at the time of acceptance.

3.7.1 Modulation Index. - Modulation index measurements were made using the pseudo random word input to the modulator driver. The modulation sensor in the GCE provided an output (dc coupled) to an oscilloscope from which the peak and minimum of the detected modulation waveform could be measured. Modulation index was maximized by adjustment of the modulation transfer characteristic operating point using the soleil-Babinet compensator as described in the Modulator section of this report. Modulation index can be varied over a range from zero to 75%. The voltage transfer characteristic for the modulator are given in the Modulator section of this report.

The AOCP modulation index can be readily and conveniently measured using the GCE and is a routine preflight procedure.

3.7.2 Transmitted Beam Divergence. - The transmitted beam divergence was measured by projecting the beam onto a scene at a long distance and determining the beam cross section diameter. Figure 3-64 illustrates the experimental setup. The beam diameter is measured at the exit aperture of the afocal telescope and at the screen at a distance of 36.58m (1440 inches). The beam diameter thus determined corresponds to approximately the $\frac{1}{e^2}$ intensity points.

The beam divergence angle, θ , is given by

$$\theta \approx \frac{\bar{B} - \bar{A}}{R}$$

where \bar{B} = beam cross-section diameter at the scene

\bar{A} = beam diameter at the exit pupil of the afocal telescope

R = distance to screen

Because of the initial poor quality of the afocal telescope corrector plate, considerable transmitted beam distortion was present causing fringes to appear in the beam cross-section. Figure 3-65 shows tracings of the beam profile at the screen for the various beam divergence positions. Estimates of the effective beam diameter were made by averaging many readings taken by several observers. Table summarizes the diameter averages for a given beam divergence control position and indicates the equivalent beam divergence angle. This data is plotted as the original calibration data in

TABLE BEAM-DIVERGENCE CALIBRATION DATA

Stepper Motor Position	A Avg. Diameter Transmit Beam (cm)	B Avg. Diameter Beam at Distance R (cm)	$\overline{\theta}$ Beamwidth (μ rad)	θ Beamwidth (Arc Sec)
1	1.91	2.16	66.4	13.7
2	1.60	1.65	16.48	3.4
3	2.29	2.74	123.6	25.5
4	3.07	4.32	337	69.5
5	2.74	5.21	674	139
6	3.00	6.10	848	175

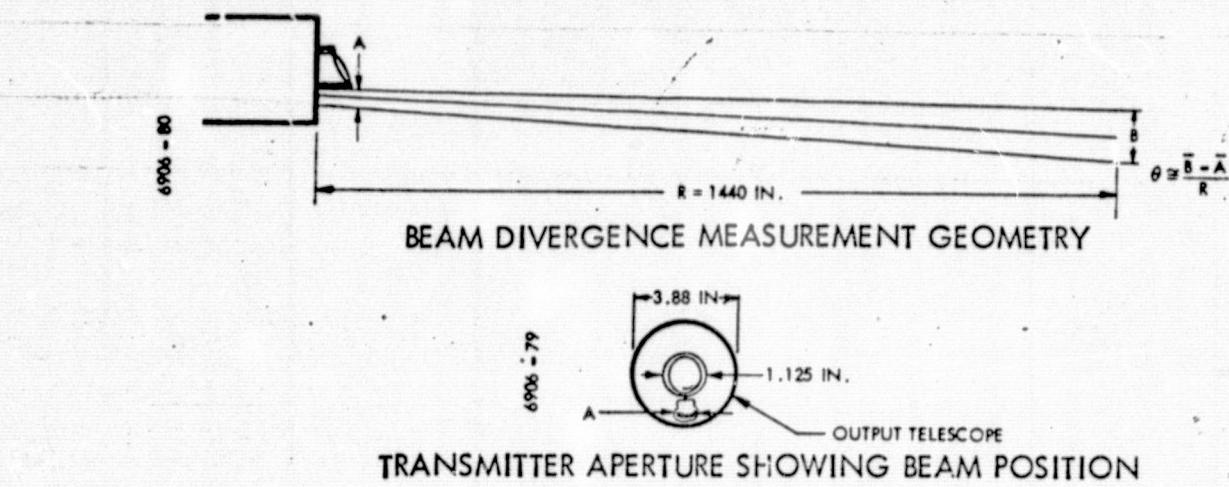


Figure 3-64

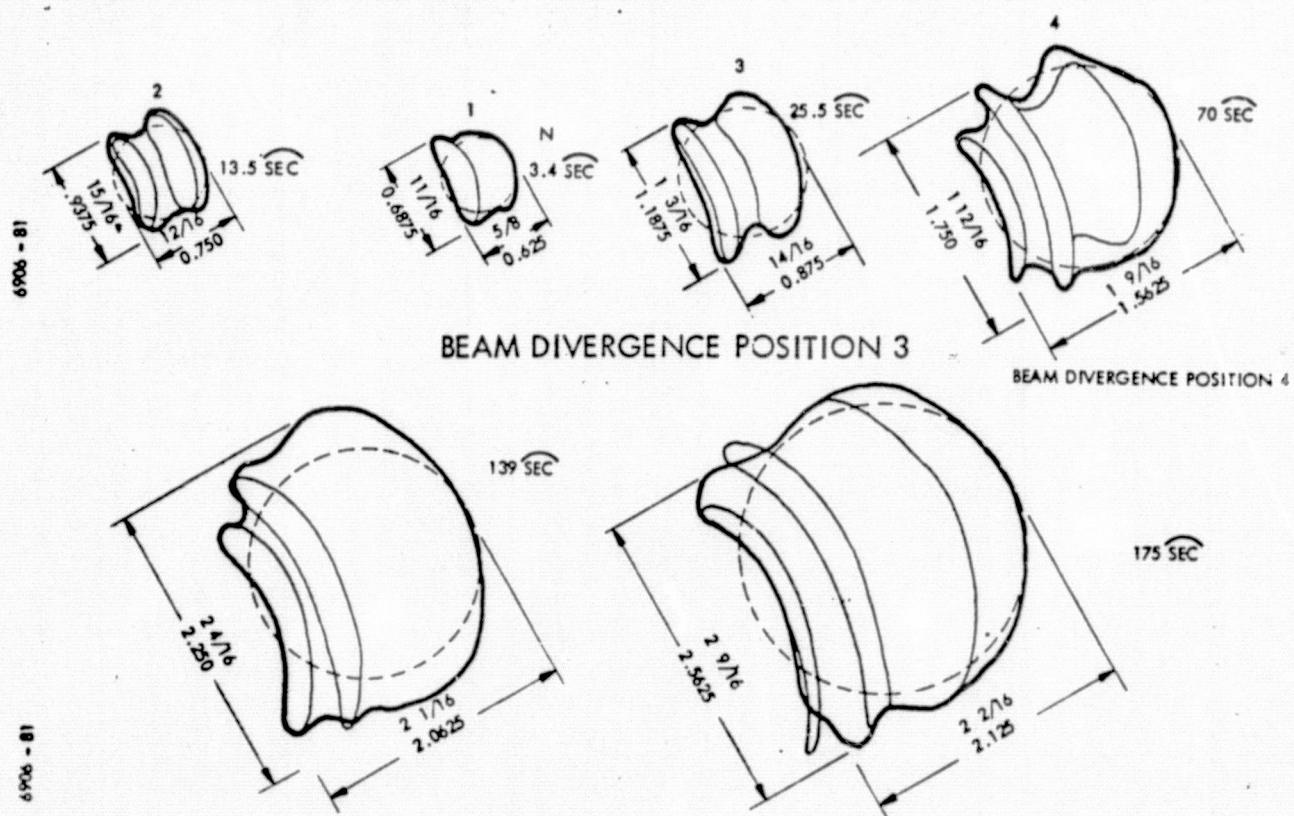


Figure 3-65. Transmitted Beam Pattern at 36.58M (1440 Inches) Range

Figure 3-66. Note that the beam divergence cam was positioned so that it was possible to move on either side of collimation and actually converge the beam somewhat at position 1. The beam divergence control was later adjusted at MSFC and the calibration was repeated by both ITT and NASA personnel. The revised calibrations for these two sets of measurements are plotted in Figure 3-67, with the original data.

3.7.3 Laser Power Monitor. - The function of the laser power monitor is to measure the average modulated power output of the AOCP HeNe laser. The laser power was measured at the output of the AOCP afocal telescope and compared to the voltage obtained from the power monitor output. The measurement stand was a precisely calibrated photo diode power detector and power level changes were made by inserting neutral density filters into the transmitter path prior to the laser power monitor location. Figure 3-68 is a plot of the laser power monitor calibration data.

3.7.4 Scintillation Monitor. - Calibration of the scintillation monitor, subsystem utilized the GCE modulated beacon laser as a source and an NBS traceable vacuum photo diode standard detector. Figure 3-69 illustrates the photo diode radiometer construction. Because of a nonuniform beam intensity profile from the GCE, a large area collector was used which simulated the AOCP entrance pupil in size and shape including the central obscuration. The GCE modulation index was adjusted to 70 per cent, and the power transmitted was measured with the calibrated photo diode radiometer in a darkened environment. Then

6906 - 71

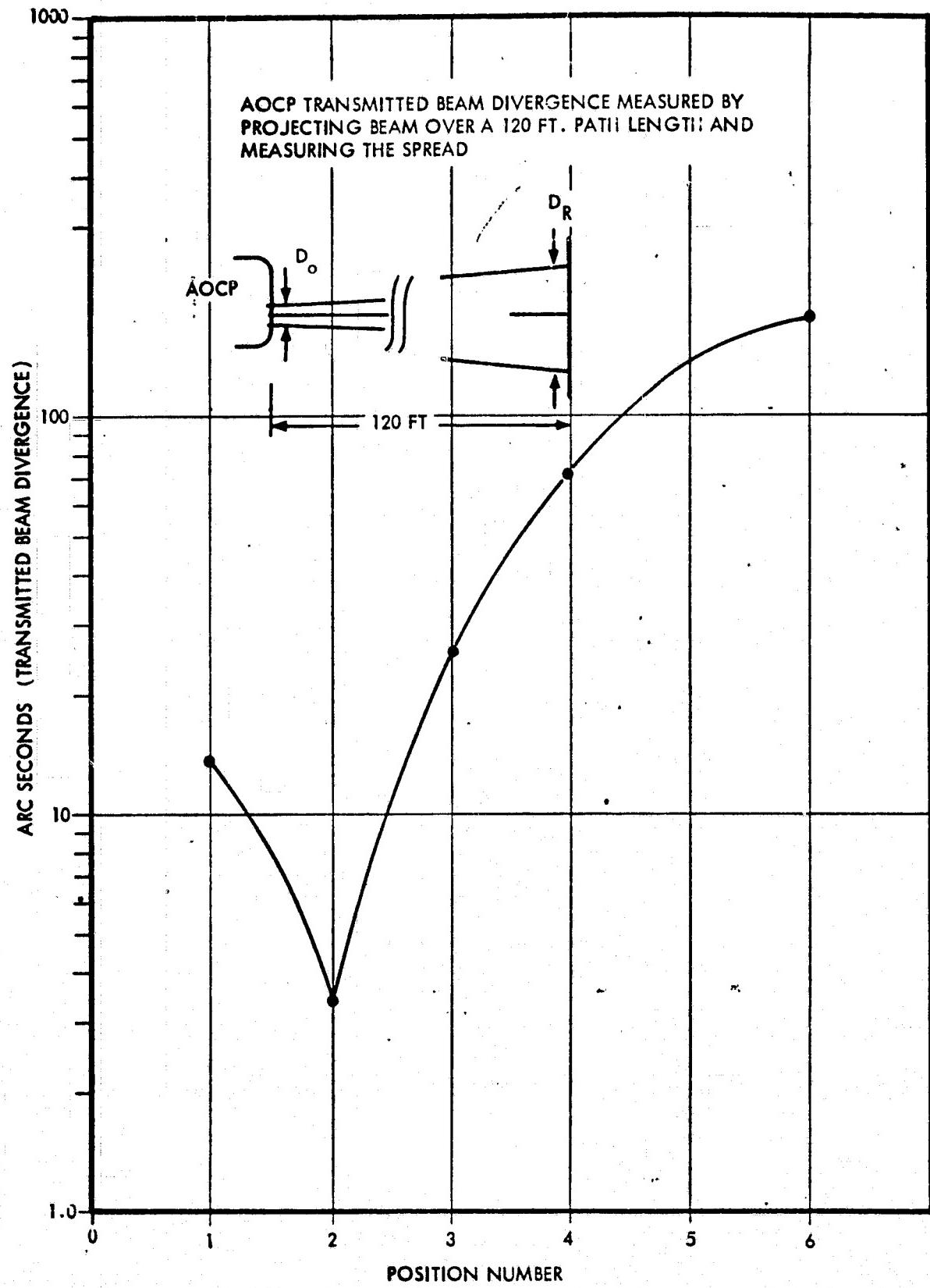


Figure 3-66. Beam Divergence Calibration

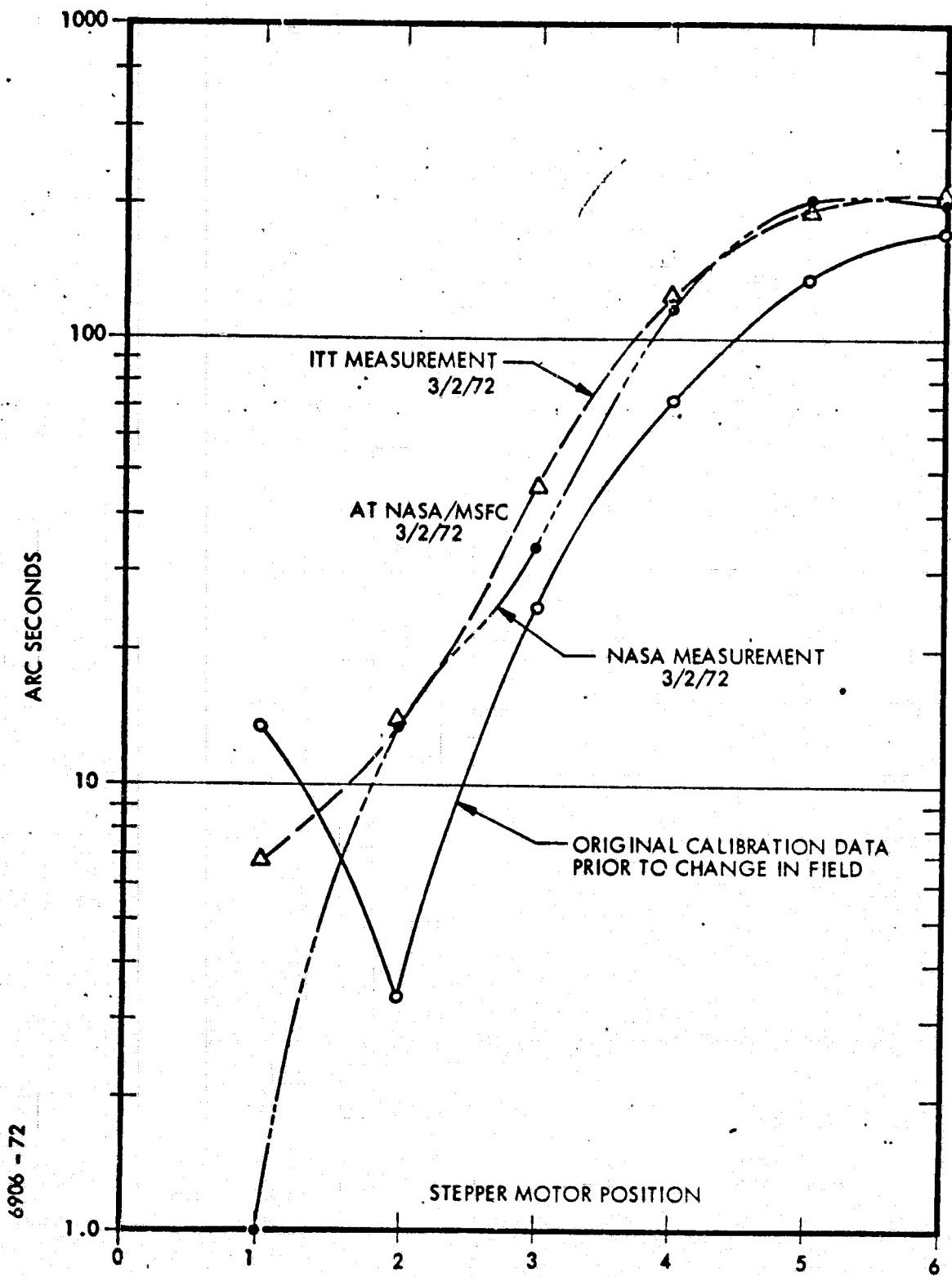


Figure 3-67. Beam Divergence Calibration

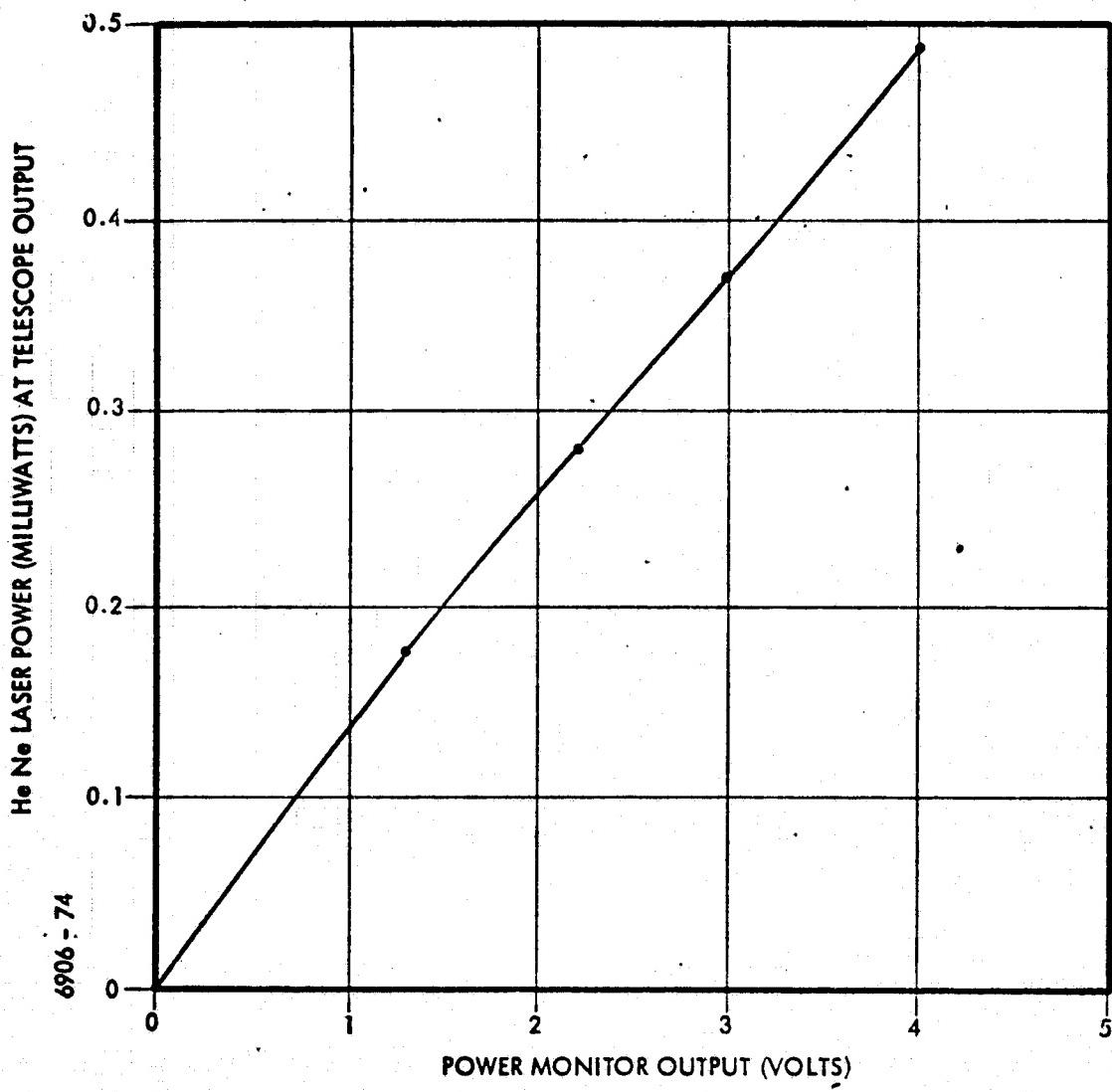


Figure 3-68. AOCP Laser Power Monitor Calibration

6906-70

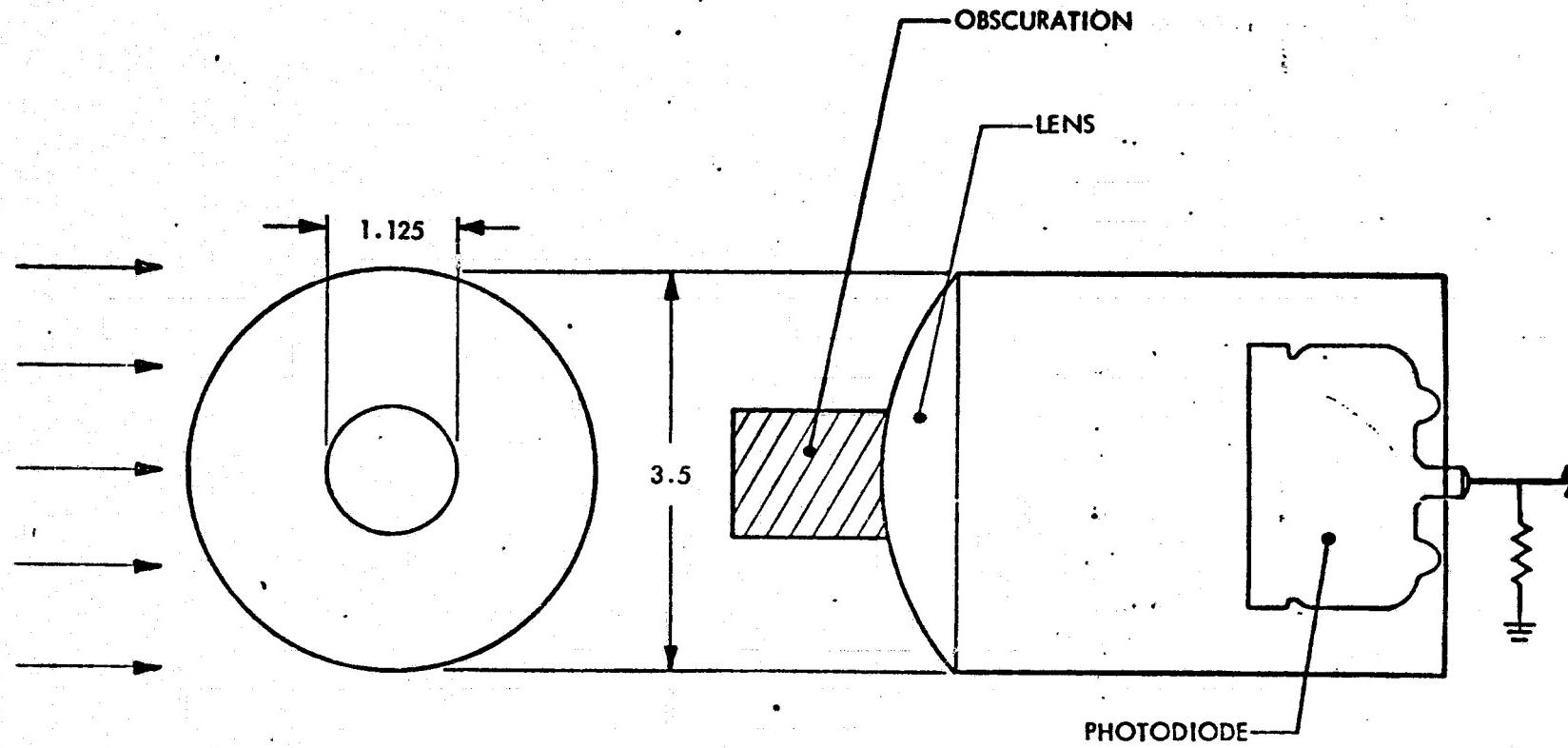
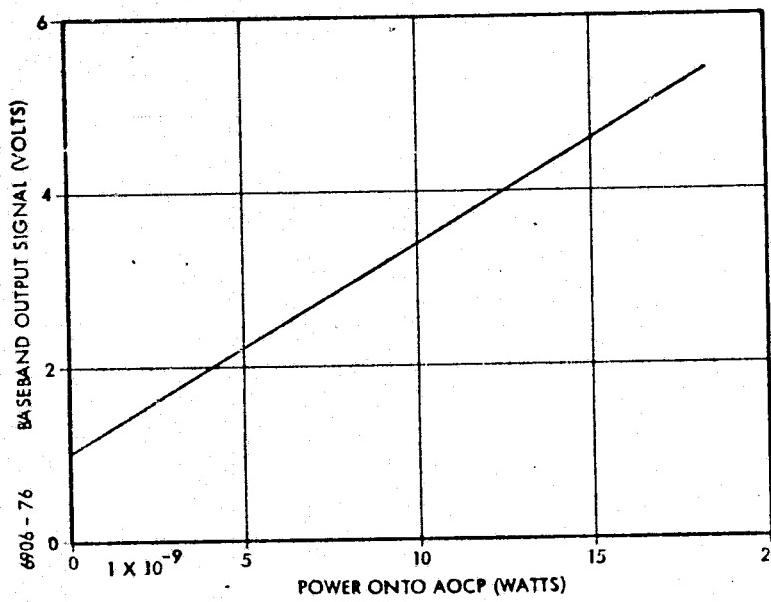
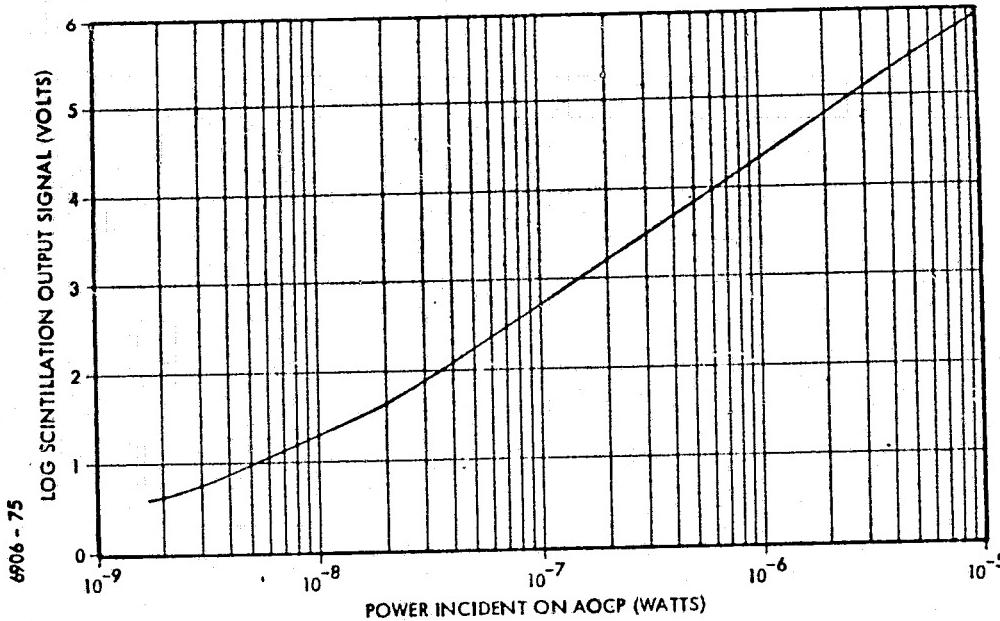


Figure 3-69. Scintillation Monitor Calibration Reference

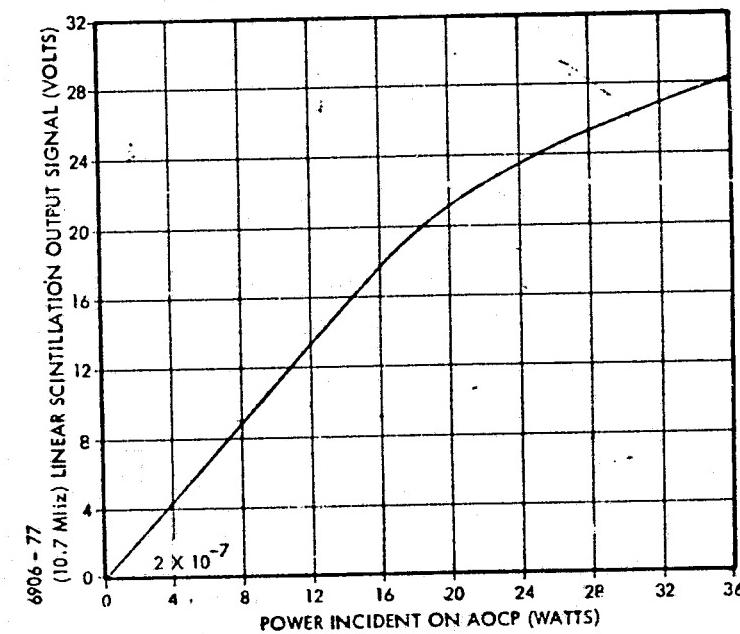
the beam from the GCE was permitted to impinge on the AOCP aperture and the scintillation monitor outputs were recorded. This was repeated for various power levels to obtain sufficient number of points for plotting. Note that the scintillation monitor outputs are related to the total power at the AOCP collection aperture rather than at the photo detector located within the AOCP. Plots of the scintillation monitor calibration for each of the three outputs are given in Figure 3-70. Outputs of the scintillation monitor can be obtained as a function of irradiance at the collection aperture for a uniformly illuminated aperture by dividing the power of the calibration curves by the collection area as shown in Figure 3-71.

3.7.5 Tracker Linearity. - The tracker subsystem transfer characteristic gain-slope and linearity was measured. The measurement procedure was to place the AOCP tracker into the five track operation mode on the GCE beacon and precisely deflect the GCE output beam using the GCE finely adjustable folding mirror. The beam deflection angle, as measured by autocollimator, was recorded and plotted with the corresponding tracker output voltage. The data taken was plotted on a six-foot graph and linearity and orthogonality was determined to be better than 0.5 per cent. A summary of this data is given in Figure 3-72. The tracker transfer characteristic gain is determined by the slopes of the z-axis and y-axis plots and are indicated on the graph.

10.7 MHz SCINTILLATION MONITOR LOG OUTPUT CALIBRATION



BASEBAND SCINTILLATION
MONITOR OUTPUT CALIBRATION



10.7 MHz SCINTILLATION MONITOR
LINEAR OUTPUT CALIBRATION

Figure 3-70

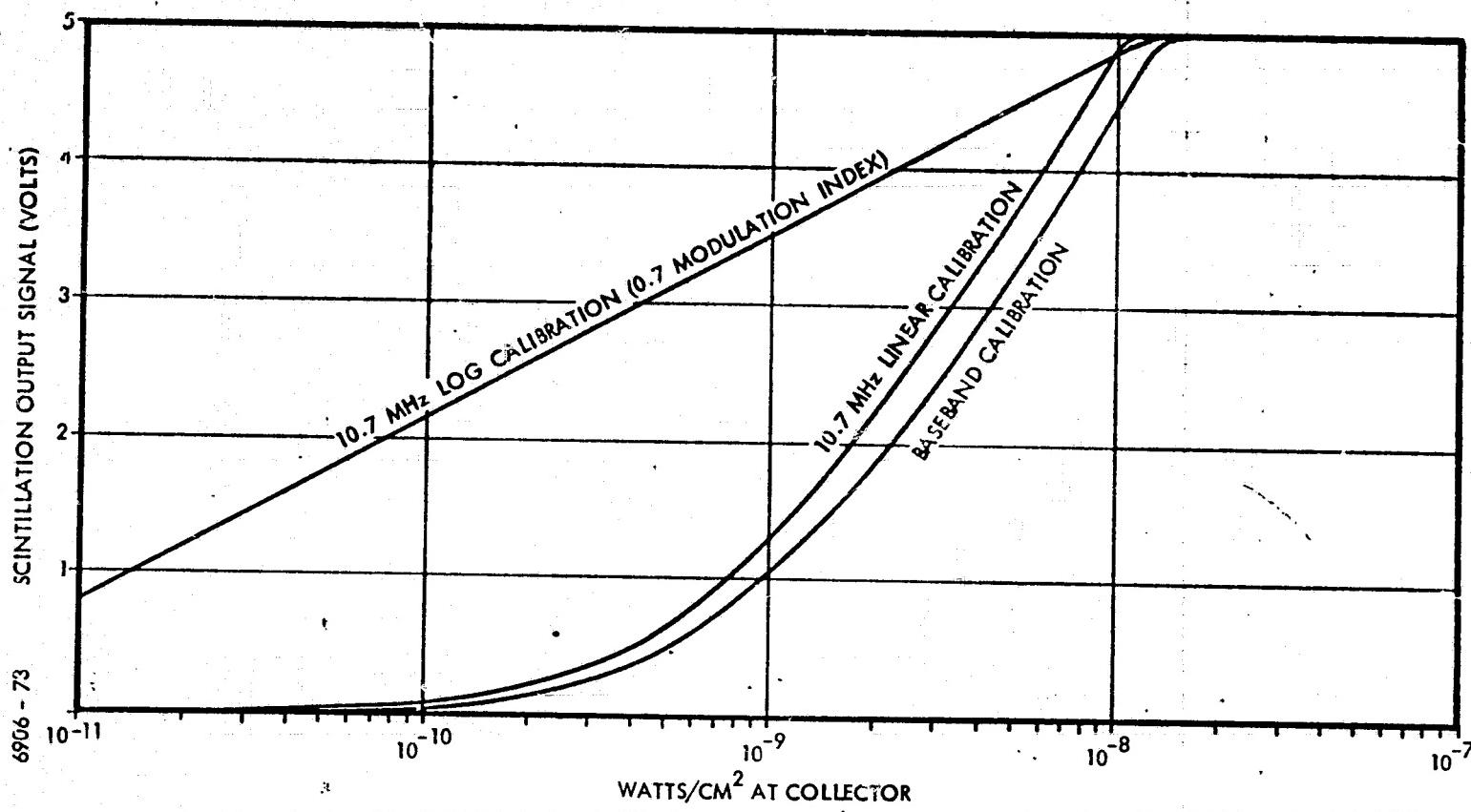


Figure 3-71. Scintillation Monitor Calibration

AOCP TRACKER OUTPUT
TRACK MODULATION \sim 30%
INSTANTANEOUS FOV 17.5 ARC SEC
OPTICAL POWER ON DETECTOR = 7×10^{-10} WATT

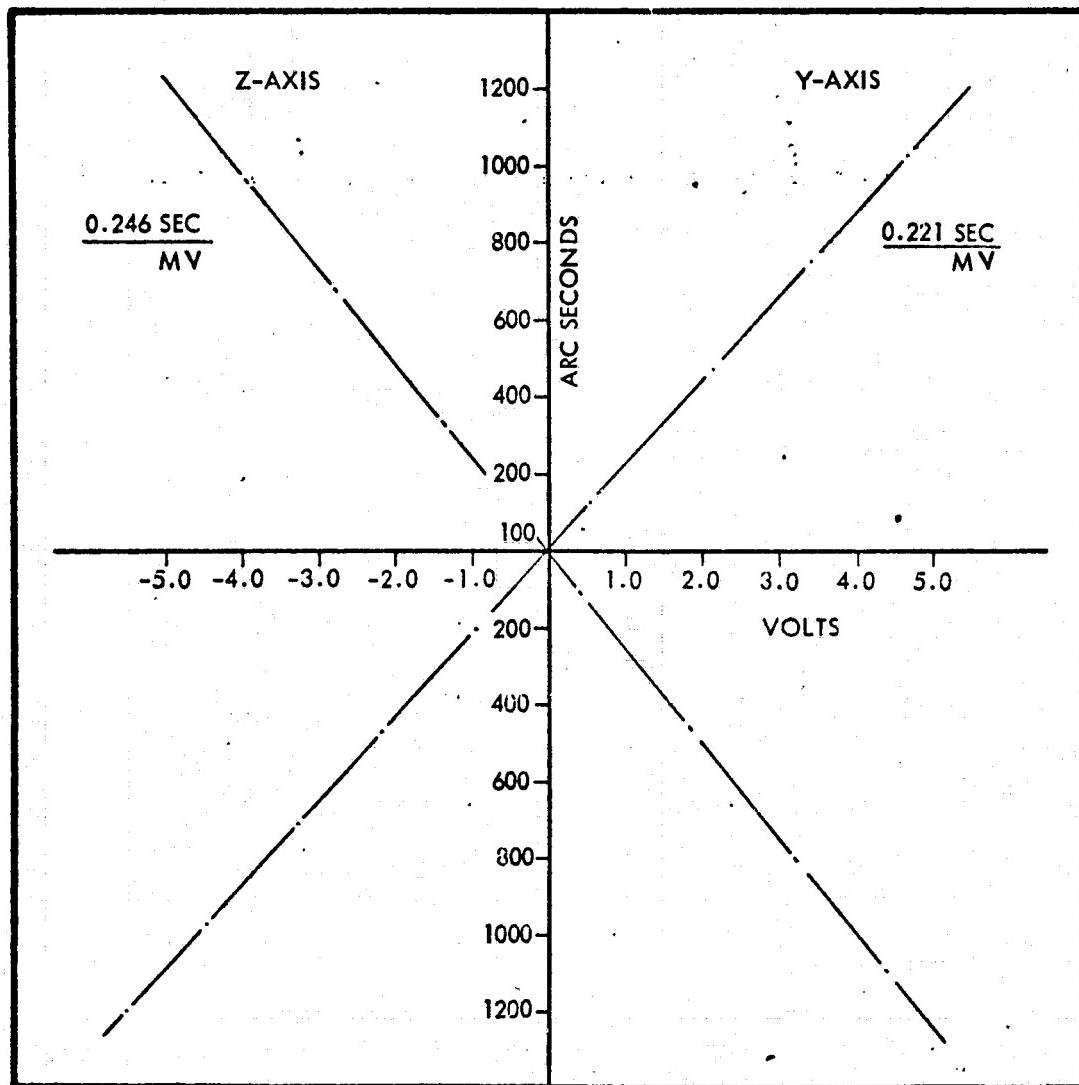


Figure 3-72. AOCP Tracker Linearity and Gain Calibration

6906 - 78

REPRODUCIBILITY OF THE
ORIGINAL PAGE IS POOR

Data was taken at various light levels covering a dynamic range of greater than 30 db in voltage. Figure 3-73 shows the optical image shape at the image dissector photocathode in terms of the aperture size as determined by scanning the image plane with the image dissector aperture. The plot indicates an optical image size to be very nearly the size of the aperture.

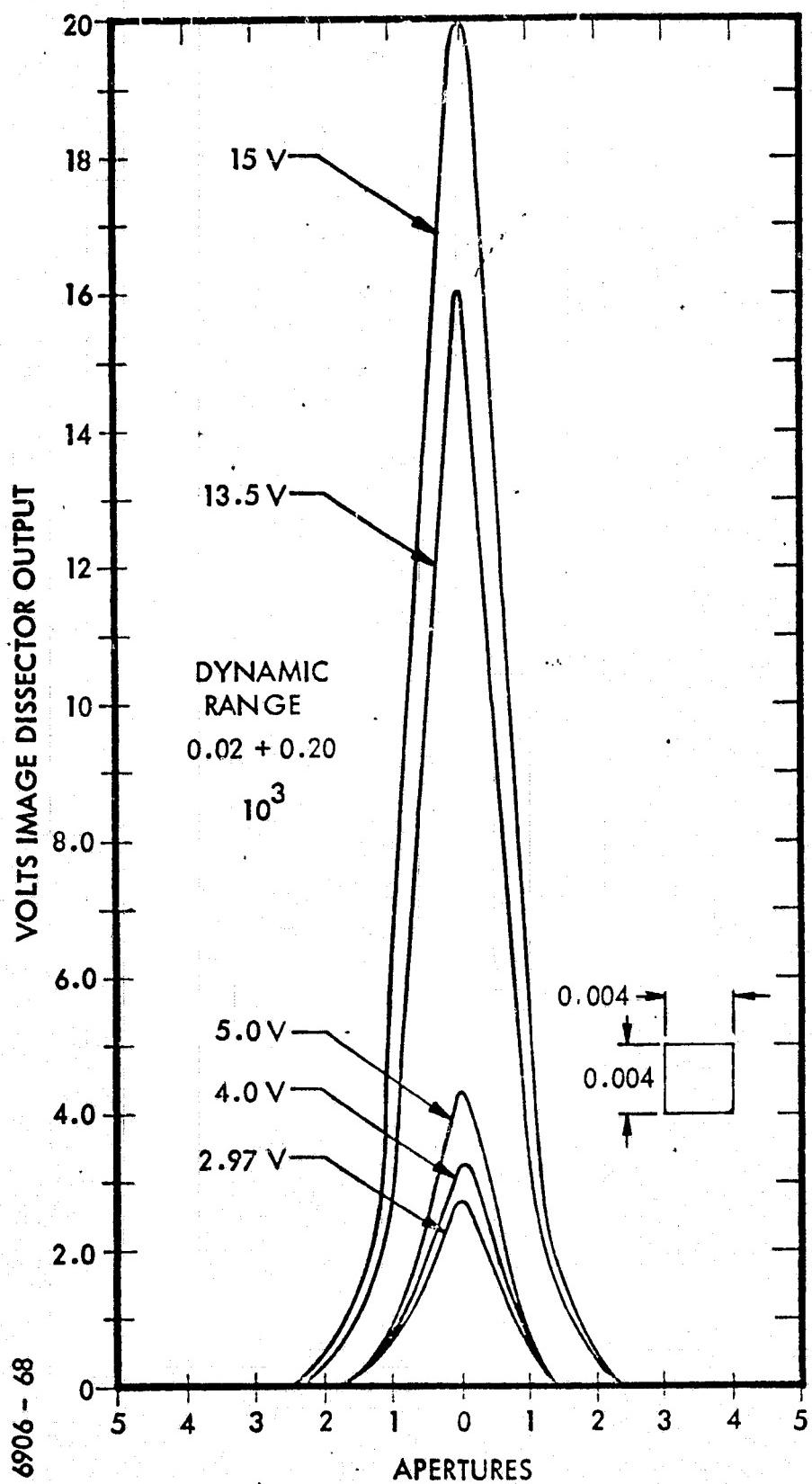


Figure 3-73. Optical Image Size at AOCP Image Dissector

3.7.6 Boresight Stability - The AOCP transmitter/receiver boresight alignment stability was measured at reduced pressure to demonstrate the integrity of the pressurized transmitter compartment and its ability to withstand the forces produced on the compartment.

Figure 3-74 shows the AOCP unit mounted in a vacuum test chamber that permitted the system to be operated and the output beam direction to be monitored or the pressure was reduced. The system was pumped down to 10^{-4} torr and held for 8 hours. No beam wander was observed nor was the pressure in the compartment reduced as a result of this test. Beam position was continually monitored during pump down by observing the position of the laser beam directly from the transmitter compartment impinging on a screen at a distance of 50 feet.

This test also verified the integrity of the high voltage components operating in a reduced pressure environment. Later in the flight test phase of the program, some problems occurred from high voltage breakdown at reduced pressure. This is believed to have been caused by the frequent subjection to moisture condensation resulting from faulty air conditioning during the flight tests. The problem was fixed by potting and additional high voltage insulation in the high voltage areas.

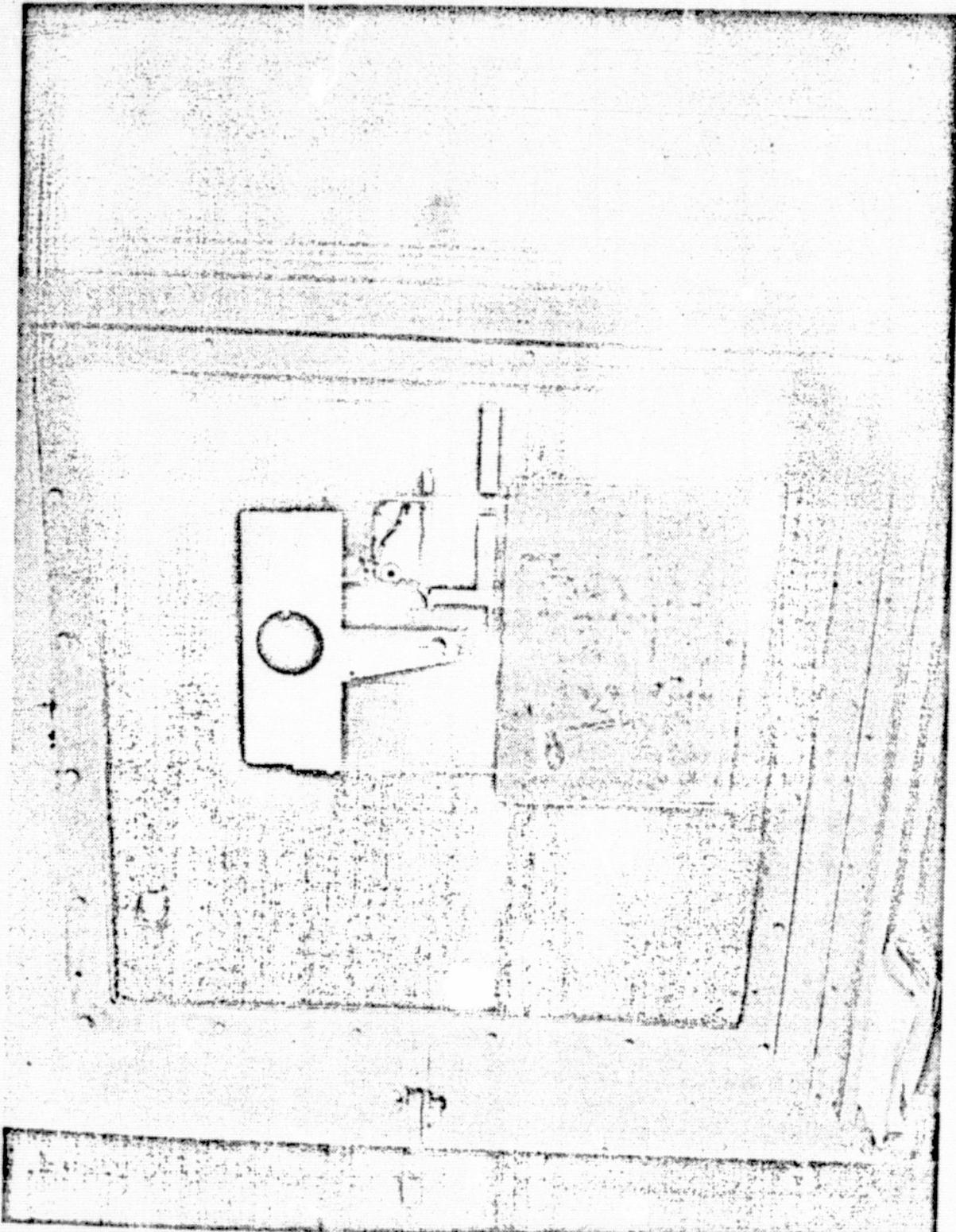


Figure 3-74. AOCP Environmental Test

6906 - 50

4. REMOTE EQUIPMENT RACK (RER)

The remote equipment rack (RER) hardware tree is illustrated in Figure 4-1. This unit comprises a connector panel for power distribution and housing the AOCP laser power supply, an ITT owned TV signal processor and tracker, and an analog-to-digital converter and pseudorandom word generator.

The power and connector panel shown in Figure 4-2 is typical mechanically of the three panels.

Figure 4-3 is a block diagram of the RER identifying the connector locations and listing the various inputs and outputs.

Detailed descriptions of the RER units are covered in the O & M manuals and elsewhere in this report.

4-2
6906 - 45

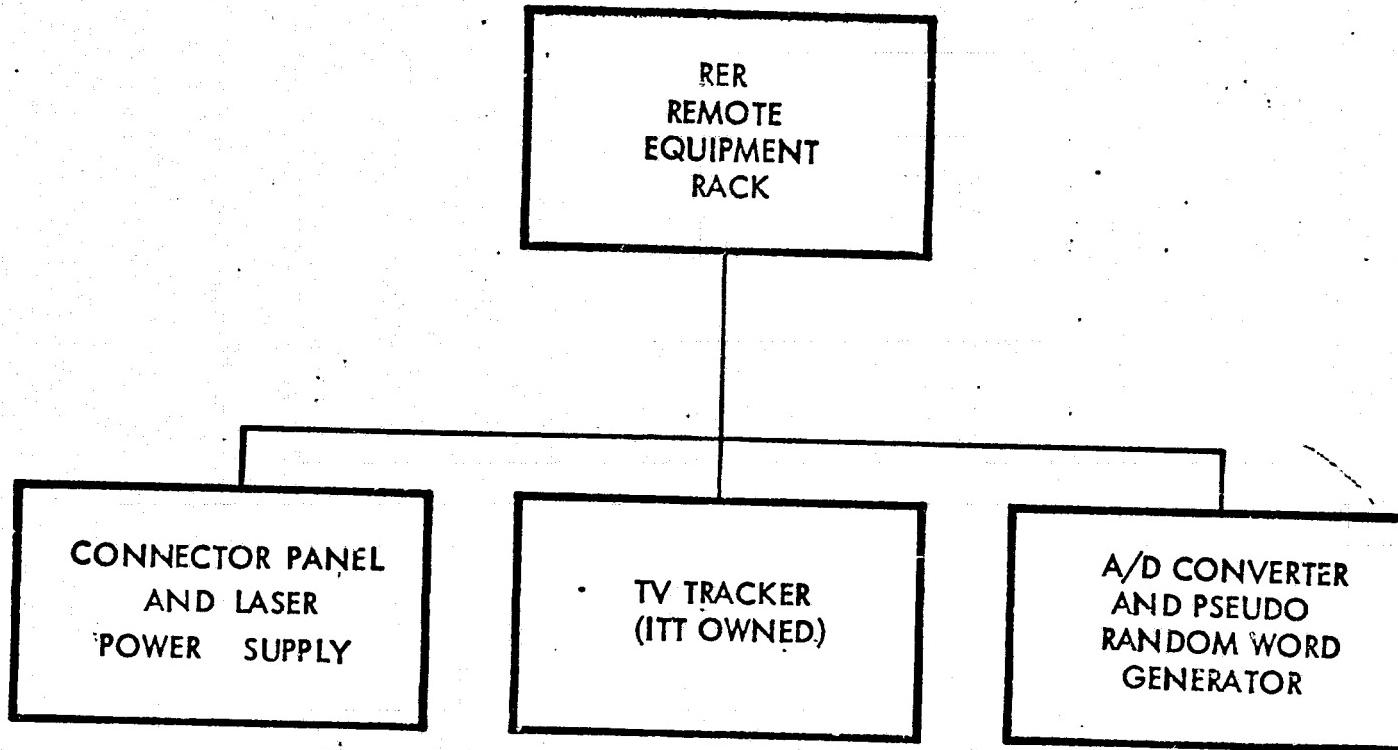


Figure 4-1. Remote Equipment Hardware Tree

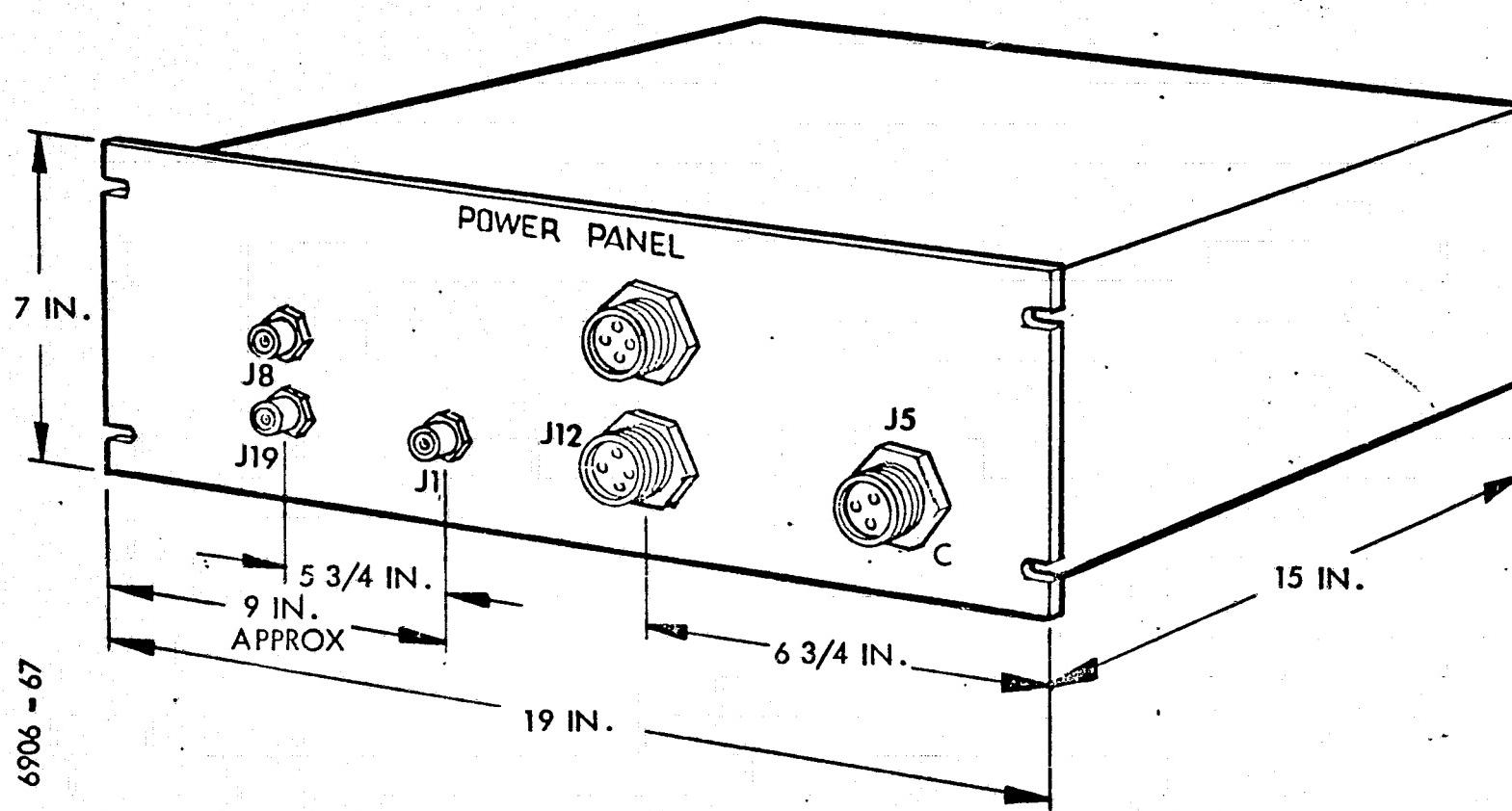


Figure 4-2. RER Connector Panel Layout

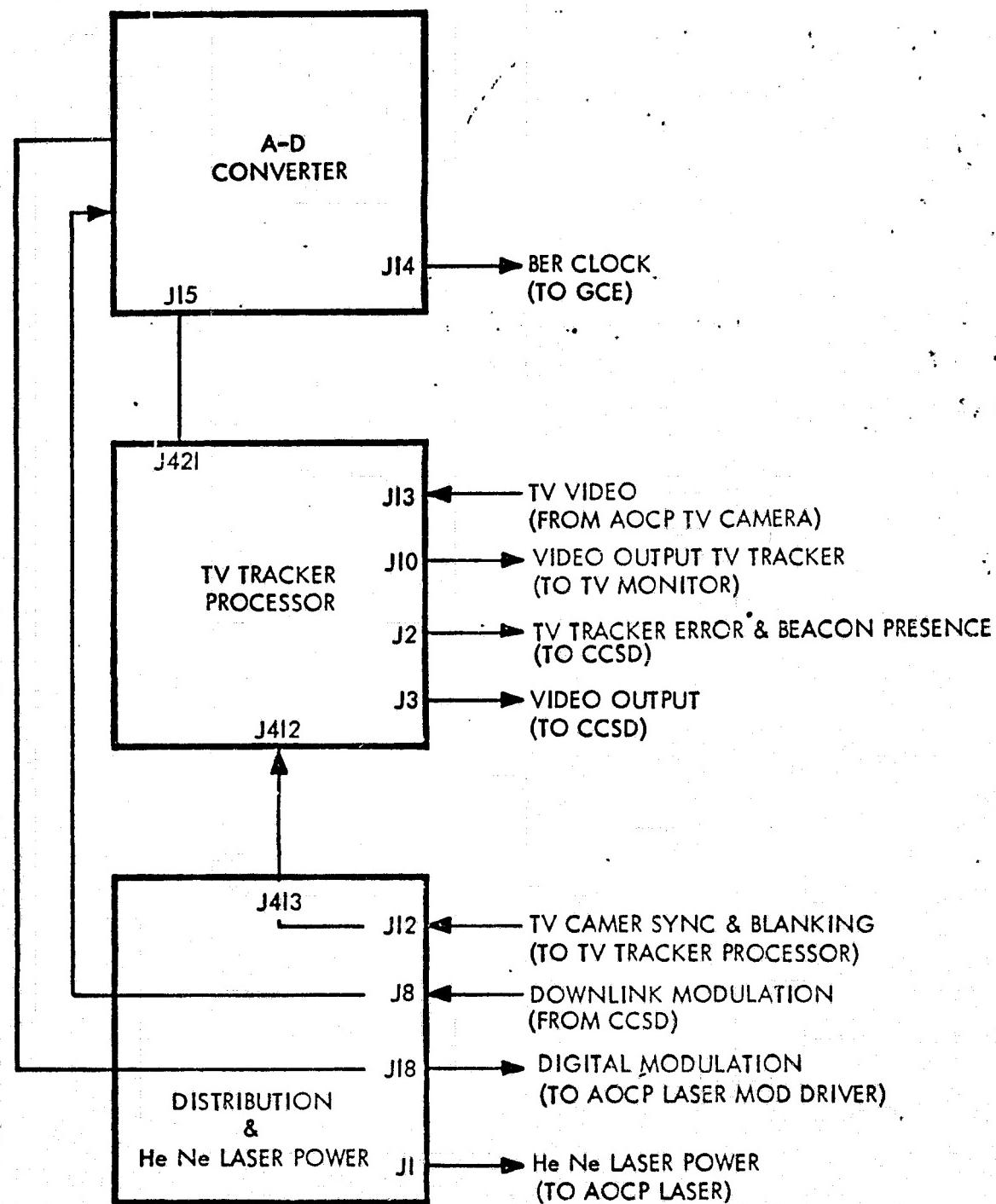


Figure 4-3. Remote Equipment Rack (RER) Block Diagram

6906-119

5. CUBE CORNER ASSEMBLY

The function of the cube corner assembly is to retro-reflect the GBAA laser radar energy at the aircraft and thereby greatly enhance the aircraft's apparent optical cross-section. The cube corner assembly comprises the optical element and its mechanical mount as indicated in the hardware tree of Figure 5-1. Two mechanical mount designs were made. The initial design was a three-point mount illustrated in the photograph of Figure 5-2. At the request of the integration contractor, the mechanical mount design was modified to a four-point mount as shown in the detailed drawing of Figure 5-3.

The optics were GFE items although the design was specified and acceptance tested by ITTG. The cube corner optical elements were procured from Precision Optical Company, Costa Mesa, California and proved to be of excellent quality near diffraction limited for the 2.75 inch usable aperture. The cube corner material was specified as fused silica so that the optical quality would be maintained over a large temperature range. Since the cube corner assemblies were to be mounted externally to the aircraft, they would experience the extremes of temperature variation from as high as +120°F on the ground to as low as -80°F at the higher altitudes.

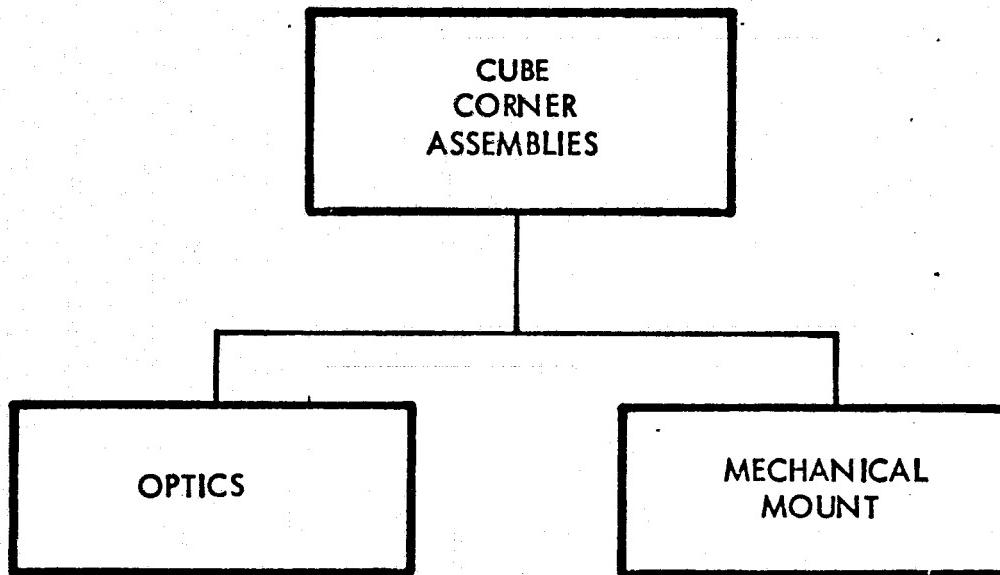


Figure 5-1. Cube Corner Assemblies Hardware Tree

6906 - 55

6906 - 26

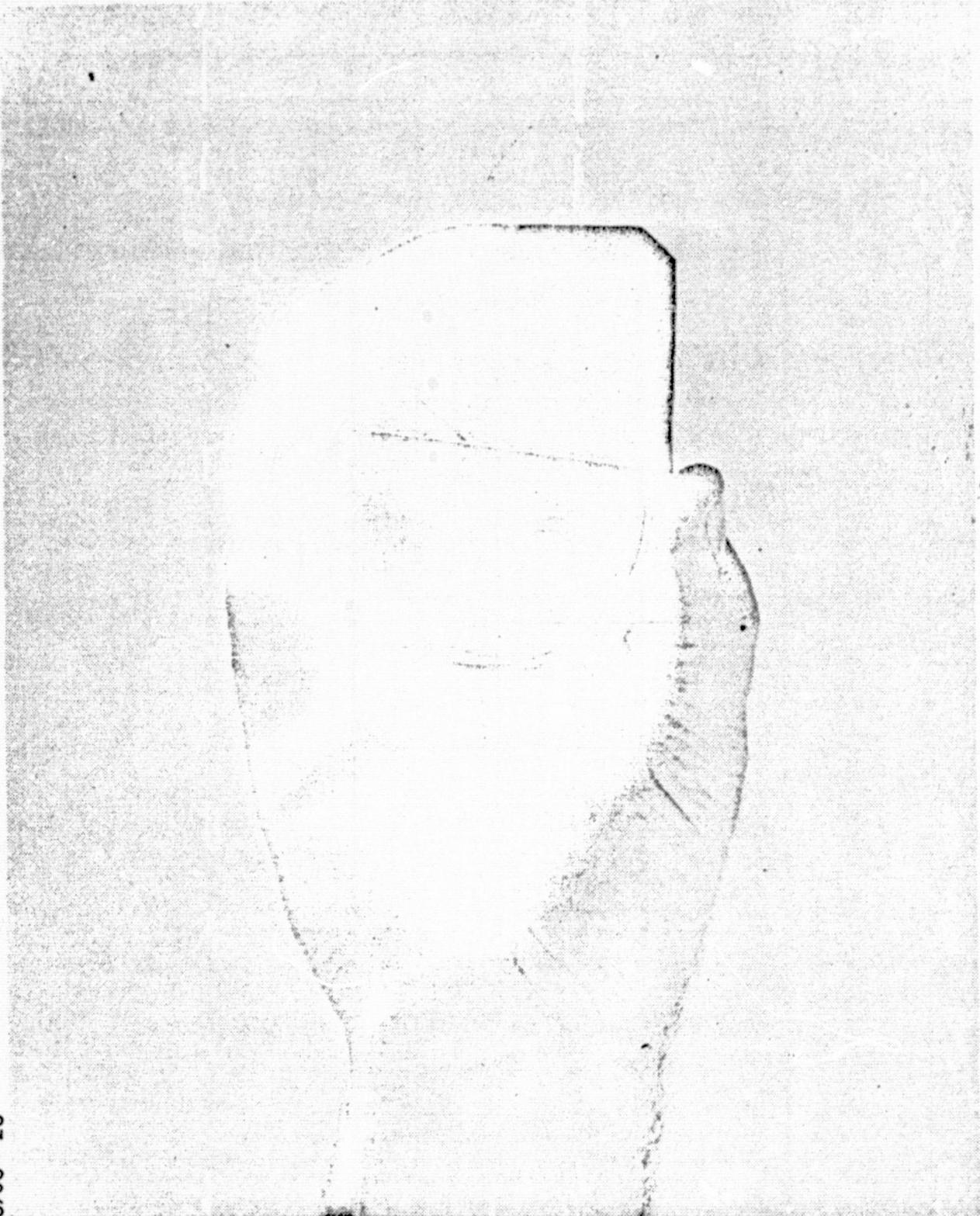


Figure 5-2. Cube corner Assembly

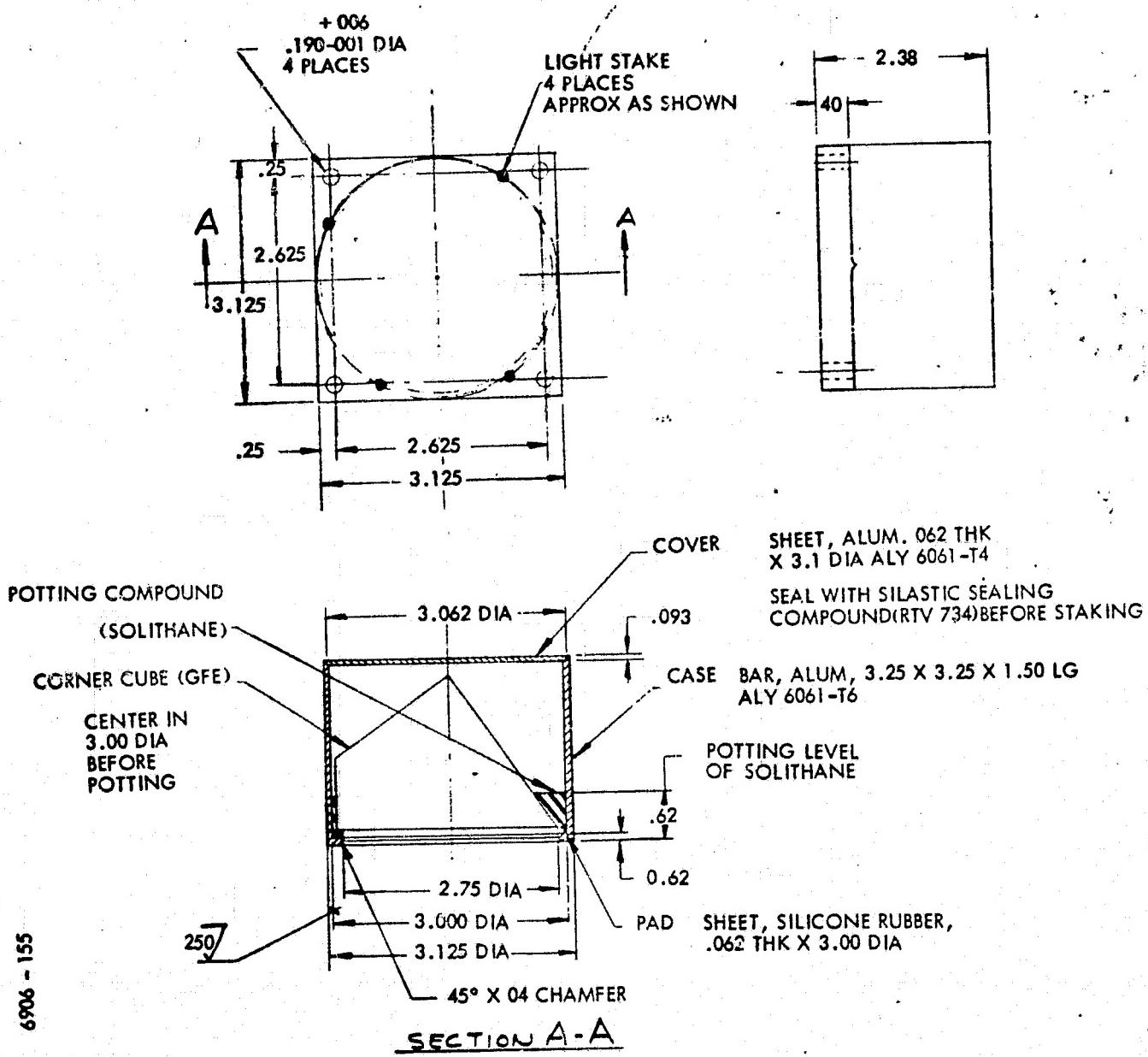


Figure 5-3. Corner Cube Assembly Optical Communications

Retro-Reflection Efficiency Factor - The radiometric analysis presented in the GBAA section of this report defined a factor:

$$G = \frac{N_{cr} A_{cr} T_{cr} (T_a K_{sc})^2}{R^4}$$

We now define a new factor

$$F = \frac{N_{cr} A_{cr} T_{cr}}{\psi_{cr}}$$

Using the definitions and values defined in the 8-6-70 report,

$$F = 1.1075 \times 10^9 \text{ ft}^2 \text{ ster}^{-1}$$

The quantity, ψ_{cr} , is the solid angle of the beam returned by the retro-flector toward the GBAA. This is affected by two phenomena, the diffraction of the beam by the aperture of each corner reflector, and the divergence caused by the pyramidal error (non-orthogonality of the reflecting faces) of each retro-flector.

These will be discussed separately, and then in combination.

Diffraction: Assuming perfect corner cubes, the reflected beam's divergence is a function of the shape and size of the effective area of the individual cornercube retroreflectors. The effective area, in turn, is a complicated function of the angle of incidence of the incoming beam from the GBAA transmitter. (The

incident angle is measured from the perpendicular to the retroreflector's entrance-exit surface.) A simplifying and "safe" assumption is that the effective area is the equivalent-area circle, with diameter, D.

The beam angular divergence (diameter) is, then,

$$\phi_{cr} = \frac{2.44\lambda}{D} \text{ radian.}$$

For $\lambda = 0.5145$ micron, and $\phi_{cr} = 4$ arcseconds, $D_{min} = 2.55$ inches.

This divergence corresponds to $\psi_{cr} = 2.95 \times 10^{-10}$ steradian, used in the previous calculations, referenced above.

Pyramidal Error: In the absence (assumed, but impossible) of diffraction effects, a beam from an infinitely-distant point source, filling the entrance-exit aperture of the cubecorner retroreflector, will emerge from the retroreflector in six distinct beams, of various shapes depending upon the angle of incidence. If pyramidal error exists, these emerging beams will not be exactly parallel to the entering beam nor to each other. For convenience, we define pyramidal error to be the angle between the incident beam and the worst-case emerging beam. As a consequence of a large enough pyramidal error, it is possible for all six sections of the returning beam to miss the GBAA receiver. The allowable pyramidal error must be specified for the cornercubes.

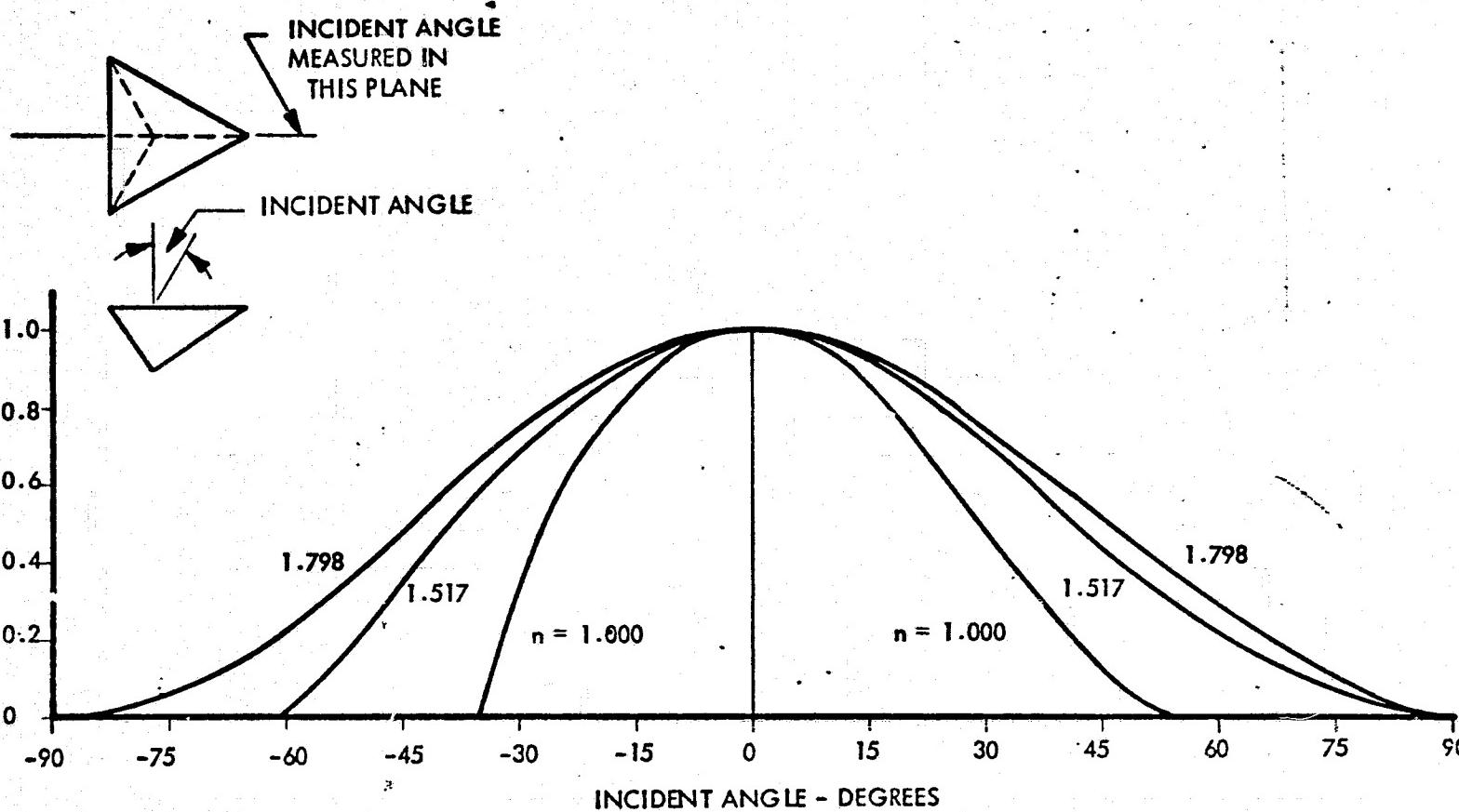
Pyramidal Error and Diffraction in Combination: In general, each of the six emerging (reflected) beams resulting from pyramidal error will have its own respective diffraction pattern, its exact form determined by the shape and size of its associated effective aperture, as indicated above. These diffraction patterns, of course, increase the angular "diameter" of their respective beams, and, if the diffraction angular semi-diameter is greater than the pyramidal error, the six retroflected beams will merge into a single pattern, essentially centered on the incident beam. The resulting pattern will be of more or less uniform intensity, depending upon the amount of pyramidal error and the incident angle at a particular time. The pattern in no case will be absolutely uniform.

Partial Specification of Cornercube Retroreflector: If the diffraction angular diameters of the six retroflected GBAA beams are each to be 4 arcseconds, then a pyramidal error of 2 arcseconds could theoretically result in zero intensity at the center of the composite retroflected beam pattern, and the total beamwidth could be 8 arcseconds. To assure better overlap, specify retroreflectors with 1 arcsecond maximum pyramidal error; in this case, the total beamwidth could be as large as 6 arcseconds.

Retroreflector Design:

Shape: Two common shapes are used for the cubecorner retroreflectors. One is like a cube, cut through on a diagonal between the opposite corners of three adjacent cube sides. The other is additionally cut to remove the three corners of the triangular diagonal face produced in the first shape, so that the diagonal face is then a regular hexagon. (These last 3 cuts are made perpendicular to the diagonal face.) This hexagonal shape (or circular when the edges are removed), is useful when the angle of incidence is always perpendicular to the entrance-exit face.

Effective Area: The effective area of the cubecorner is a rather complicated function of the angle of incidence and the index of refraction of the cubecorner material (glass). The graph of Figure 5-4 shows the relationships for a triangular cornercube, for indices of refraction of 1.000 (triangular mirror - not glass), 1.517 (Borosilicate glass-BSC2), and 1.798 (Schott Glass SF11 at 0.5145 microns wavelength). It is noted that the effective area drops off to 80 percent at incident angle of about 23° , for BSC2 glass. This angle rises to about 26° for the SF11 glass. The curves are unsymmetrical about zero incidence angle, in the plane for which calculations were made. The curve for fused silica ($n \approx 1.45$) lies intermediate to the curves for $n = 1.0$ and $n = 1.517$. There are three planes, at 120° degrees



8906-192

Figure 5-4. Cube Corner Reflector Effective Area as Function
of Refractive Index, η , and Incident Angle

intervals, where the same results are obtained. At all intermediate planes, the results are between those shown in the curves.

Transmission Losses: At 0.5145 microns wavelength, most optical glasses have from 1 percent to 3 percent loss per inch of optical path length. Use a nominal 2 percent per inch in this calculation, until the exact glass to be used is known.

The Fresnel loss at the entrance-exit surface, with proper anti-reflection coatings, will be between 0.5 percent and 1 percent, per pass through the surface. Use 1 percent in this calculation. A good silvered reflective surface, required in cornercube retroreflectors when the incidence angle is large enough to preclude use of total reflection, has a loss of about 10 percent per reflection. There are three such reflections in the cornercube. Thus, for a triangular corner prism, 4.33 inches on its longest side, whose optical path through the prism is 6.734 inches, the transmission will be

$$T_{cr} = (1 - 0.02)^{6.734} \times (1 - 0.01)^2 \times (1 - 0.1)^3 = 0.624$$

Summary: As shown above, the design criteria are expressed in the equation

$$\frac{N_{cr} A_{cr} T_{cr}}{\Psi_{cr}} = 1.1075 \times 10^9 \text{ ft}^2 \text{ ster}^{-1}$$

Any combination of factors which meets this requirement will permit the GBAA to operate in the assumed worst-case radiometric situation.

It can be shown that, where S is the length of a long side of the triangular cornercube in inches, the maximum effective area (at normal incidence angle) is

$$A_{cr} = \frac{0.28868 S^2}{144} \text{ ft.}^2, \text{ and that}$$

$$T_{cr} = (1 - 0.02)^{1.63304S} \times (1 - 0.01)^2 \times (1 - 0.1)^3,$$

and that

$$\psi_{cr} = \frac{\pi}{4} \left[\left(\frac{8.1518}{S} + 0.9696 \right) \times 10^{-5} \right]^2.$$

Note that A_{cr} must be multiplied by the factor obtained from the attached graphs, to obtain the effective area for a given case. For the GBAA, this must be correlated with the flight plan of the aircraft, to determine the geometry involved. Combining the above factors,

$$N_{cr} \times (\text{Factor from Graphs}) = 60.73 \frac{\left(\frac{8.1518}{S} + 0.9696 \right)^2}{S^2 \times (0.98)^{1.63304S}}$$

The results of this calculation are presented in the graph, shown in

Figure 5-5.

Although the triangular shape cube corner aperture provides the greater collection area with larger incidence angles, the circular cross-section was selected for convenience of mounting. The loss

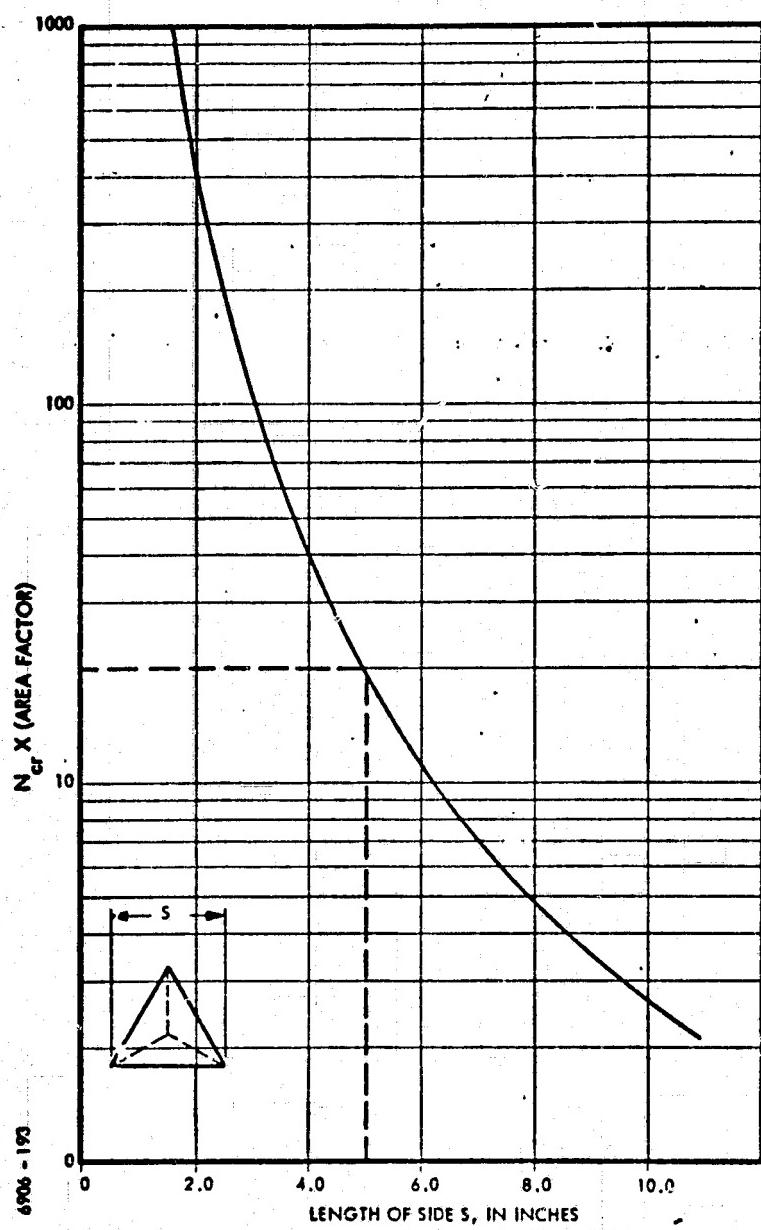


**Figure 5-5. GBAA Corner Cube Retroreflectors
Number Required Vs Size**

in collection efficiency was offset by the increase in the number of reflectors used in the arrays. The corner reflector arrays are separated on the aircraft to minimize the effects of atmospheric scintillation. An analysis of the required separation to minimize the scintillation effect is presented in the Appendix of this report.

The individual cube corners are aluminized and SiO_2 over-coated to maximize the reflection efficiency over large angles. The technique of assembly of the optical element into the mechanical mount shown in Figure 5-3, is to secure the glass into the aluminum cylinder with a flexible rolithane potting compound mixed to retain resiliency at the low temperatures so that the optical element is not stressed. The potting is used only in the region indicated in the assembly drawing to avoid abrasion of the coated surfaces that might be produced with expansion and contraction due to temperature changes. A small air bleed hold is placed in the cover to permit the enclosure to attain the ambient pressure.

The individual cube corner assemblies are mounted in five arrays of six assemblies each for attachment to the aircraft skin by the integration contractor. One of the six element arrays is shown mounted on the underside of the RB57 wing in Figure 5-6.

REPRODUCIBILITY OF THE
ORIGINAL PAGE IS POOR



Figure 5-6. Cube Corner Assembly Array (One of Five) Installed on RB-57 Wing

After several flights, some coating damage was observed on several of the cube corners as shown in the photographs of Figures 5-6 and 5-7. This coating flake was determined to have resulted from moisture condensation produced by returning to a very humid environment from the extremely cold high altitude environment. This moisture collected around the coating surface and probably froze on subsequent flights causing mechanical abrasions to the coatings. Once a fracture was produced in the hard overcoat, moisture could attack the aluminum coating producing the observed defect. The effect of this damage is to reduce the reflection efficiency of the affected unit by an amount proportional to the ratio of the damaged area to the full area of the entrance aperture. The maximum degradation for an affected unit was of the order of 15 percent and deemed to be an acceptable amount.

5-16

REPRODUCIBILITY OF THE
ORIGINAL PAGE IS POOR

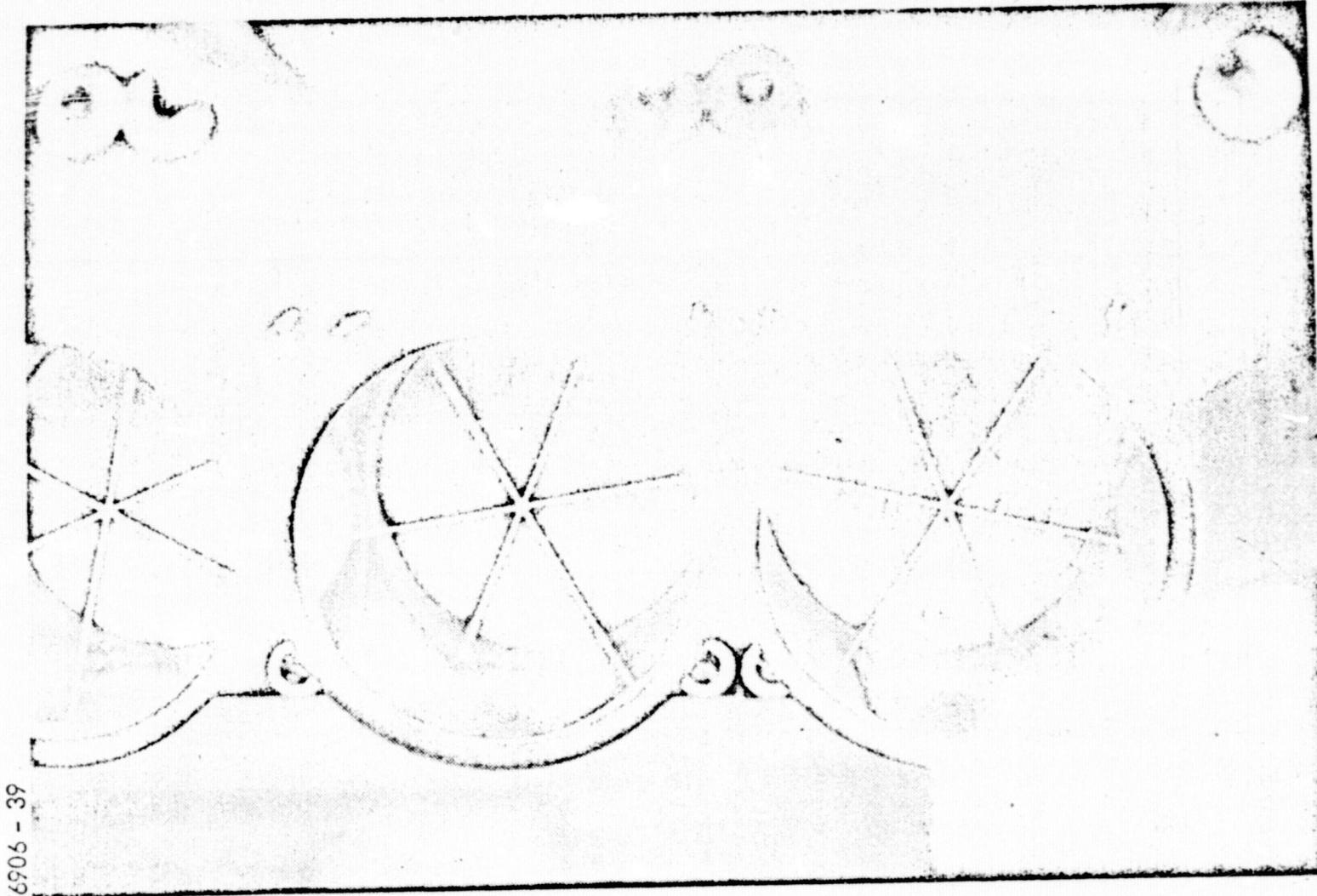


Figure 5-7. Cube Corner Assembly Showing Coating Damage

5-17

6906 - 140

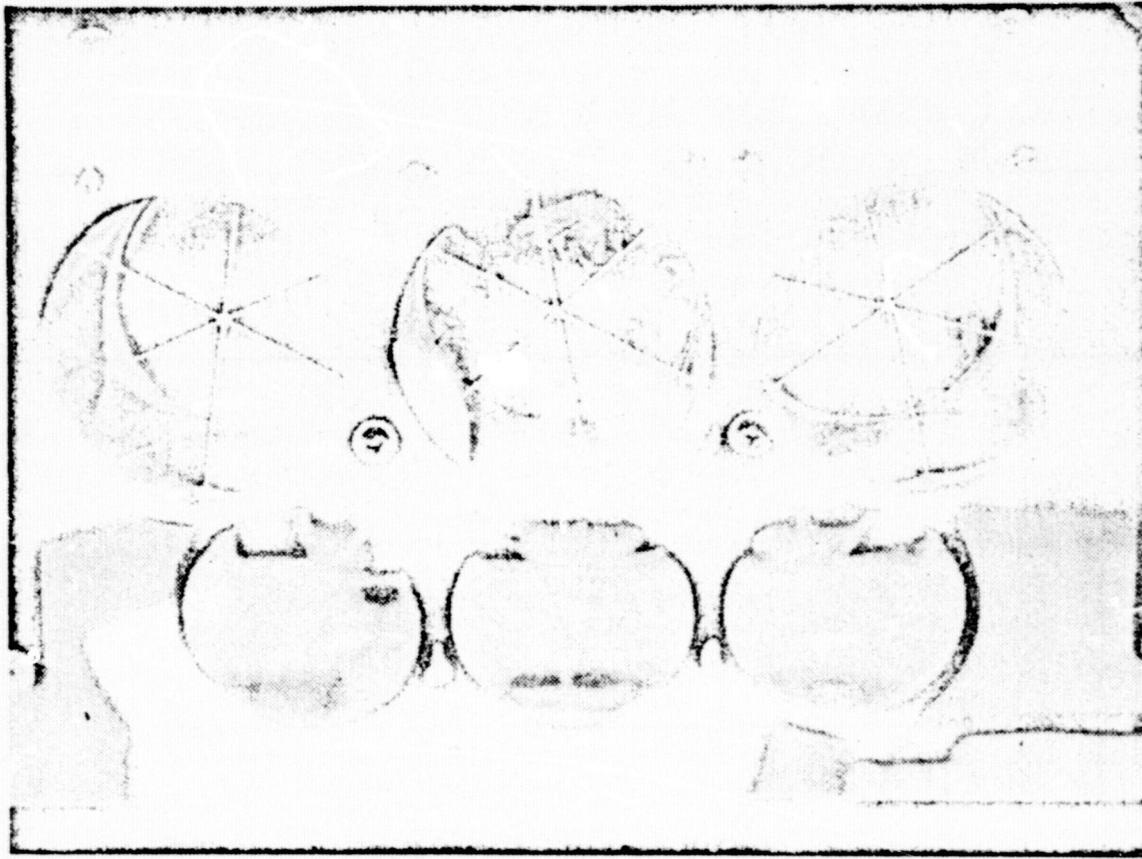


Figure 5-8. Cube Corner Assembly Showing Coating Damage

6. GROUND CHECKOUT EQUIPMENT (GCE)

The function of the GCE is to test the Airborne Optical Communications Package (AOCP), permit accurate optical alignment, and simulate the ground based portion of the optical communications link. The GCE also is capable of exercising the ancillary equipment (gimbal mirror, computer) furnished by the integrating contractor.

GCE capabilities include:

- self-checking of alignment, focusing, and optical modulator operation
- tests static and dynamic alignment of AOCP, with visual and electronic readout of alignment/tracking performance
- checks tracking capabilities of Image Dissector Tracker, Beamsteerers, and CCSD Gimbal Mirror
- Checks operation of Helium Neon laser and modulator on AOCP.
- Checks command decoder and command execution.

Figure 6-1 presents the GCE hardware tree showing the various subsystem relationships.

The GCE consists of two units, the Control Panel and the Optical Unit, which are linked by cables (not shown). The optical unit is mounted on a low-profile dolly, so that it can be positioned under the fuselage of the RB-57 Aircraft in which the AOCP is installed. Figure 6-2 is a photograph of the GCE equipment showing the cover open. The GCE control console is a rack of electronic equipment mounted on a four-wheel dolly shown in Figure 6-3 and consists of the following items:

- (1) Tone Generator (GFE), for controlling the modulation impressed on the Laser Modulator in the GCE Optical Unit.
- (2) High Frequency oscilloscope (Tektronix R454, GFE) for observing the modulation from the GCE and AOCP lasers, the outputs of the Y-Z Position Sensor, and for general utility.
- (3) Control Panel, which controls the variable speed nutating mirror motor, DC Power on the GCE optical Head, provides meter readout of the Y-Z Position sensors, controls flip mirror and shutter solenoids, and accepts BER clock and Video signals from the Aircraft mounted equipment.

GROUND CHECKOUT EQUIPMENT HARDWARE TREE

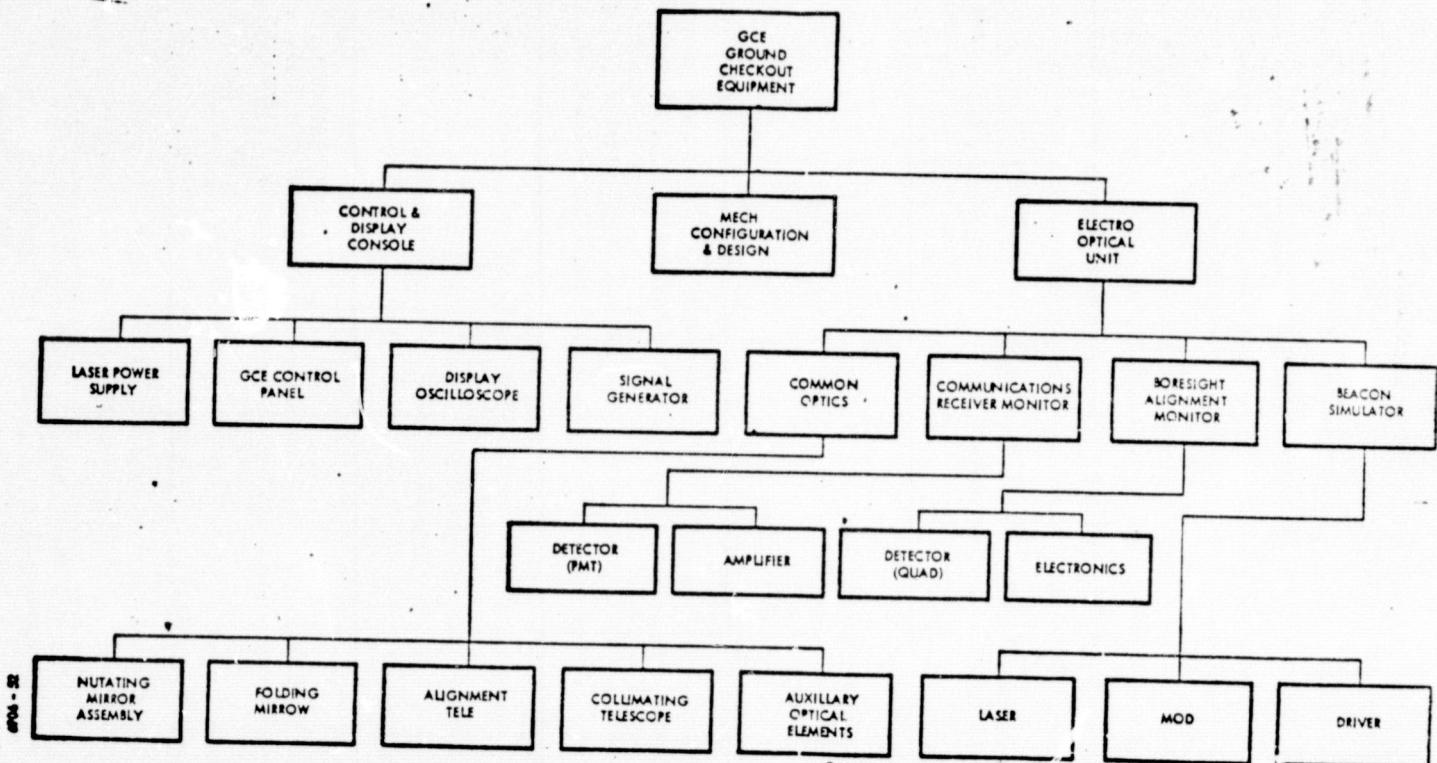


Figure 6-1.

6-3

REPRODUCIBILITY OF THE
ORIGINAL PAGE IS POOR

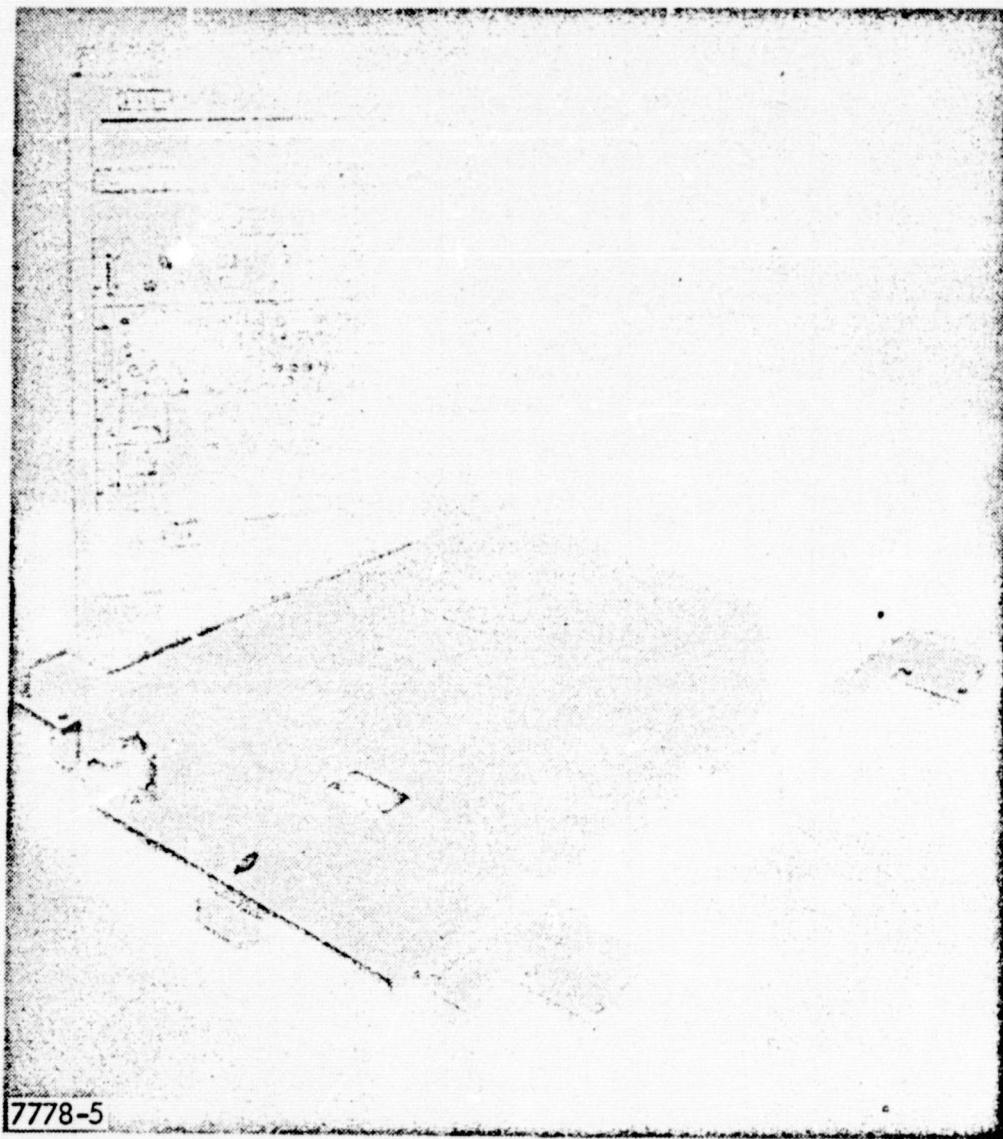


Figure 6-2. AVLOC System Ground Checkout Equipment

6906 - 25

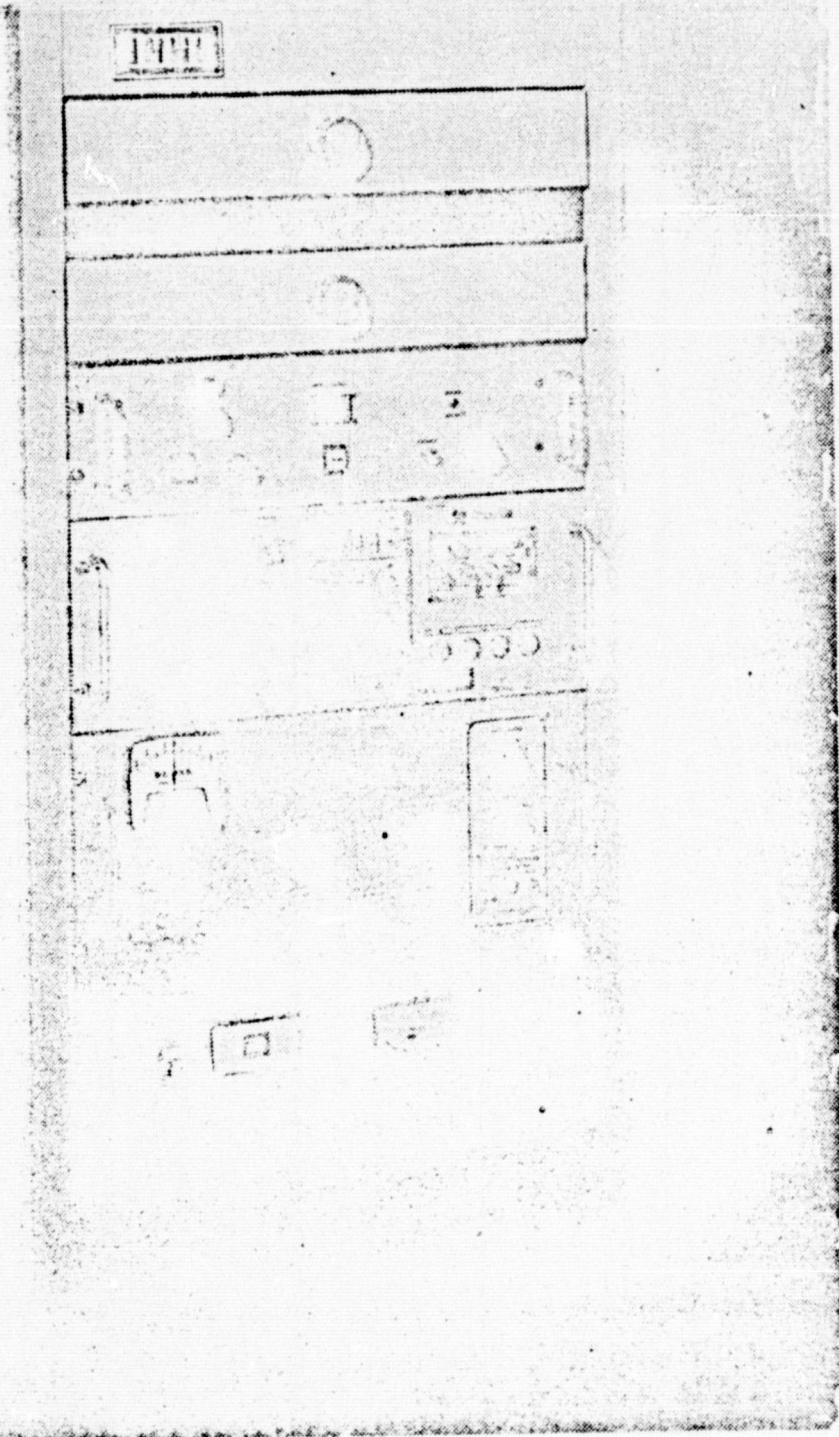


Figure 6-3. Ground Checkout Equipment (GCE) Control and Display Console

(4) Power Supply for RCA LD 2108 Argon Laser, which is mounted on the GCE optical Head. (Later replaced by Spectra Physics Model 162 laser.)

Also included in the rack are two drawers for storage of cables.

A small remote control box, which connects by cable to the Control Panel, is provided to permit actuation of the motorized potentiometers in the AOCP for adjustment of electronic boresight.

The GCE Optical Unit is an assembly of optical and electronic components and subsystems on an aluminum baseplate, mounted on a low-slung four-wheel dolly. The following items are included:

(1) An Argon Laser, with an output power of several milliwatts at 4880 Å to simulate the up-link beam to the optcom Receiver on the AOCP.

(2) A set of optical attenuators (density zero, three, five, and infinity), mounted on a rotary holder, and controlled by a knob on the bulkhead adjacent to the optical Viewer. These attenuators control the laser beam power.

(3) An electro-optical modulator (Lasermetrics EOM-704) and a modulator driver.

- (4) A 28 power laser beam expander (Spectra Physics).
- (5) An 8.3 power beam expander (4 inch diameter exit beam), with three "folding" mirrors, for projecting the collimated Argon laser beam, and for receiving the Helium-Neon laser beam from the AOCP.
- (6) Various beamsplitters, mirrors, and a cubecorner, for directing the beams to desired locations.
- (7) A Viewer (telescope), for visually observing the Argon and Helium-Neon laser beams and their mutual alignment, as well as for testing optical collimation.
- (8) A two-axis position sensor, with associated optics and nulling mirror, for electronic readout of boresight and tracking misalignment.
- (9) A photomultiplier detector and amplifier, for detecting the modulation on each of the laser beams, and providing signals for display on the oscilloscope in the GCE Control Panel.
- (10) A 6-inch diameter flat mirror, mounted in an adjustable holder on the shaft of a variable-speed motor, for providing a nutation of the projected argon laser beam

through various angles (nominally zero to six degrees) and at various rates.

- (11) A rectangular mirror mounted in an adjustable holder which rides on a track, for directing the projected beam upward into the Aircraft window at a variety of angles.

Figure 6-4 is a functional block diagram of the optical unit and Figure 6-5 shows the physical layout of this unit for easier identification of the components.

The beacon section includes an Argon laser operating at 0.488 micrometer followed by a neutral density filter wheel for controlling the beacon power. The initial design used an RCA laser model which proved to be unreliable and unstable in output beam direction. The laser plasma tube was short lived and replaced three times under warranty. The Argon laser was then replaced with a newly developed Spectra Physics model 162 which has demonstrated excellent stability and life characteristics and greatly improved the performance of the system. The laser is followed by an electro-optical modulator which places a 10.7 MHz rf subcarrier on the optical beam simulating the communications channel of the operational ground station. The 10.7 MHz subcarrier is FM modulated with the up-link command information to exercise the ACCP

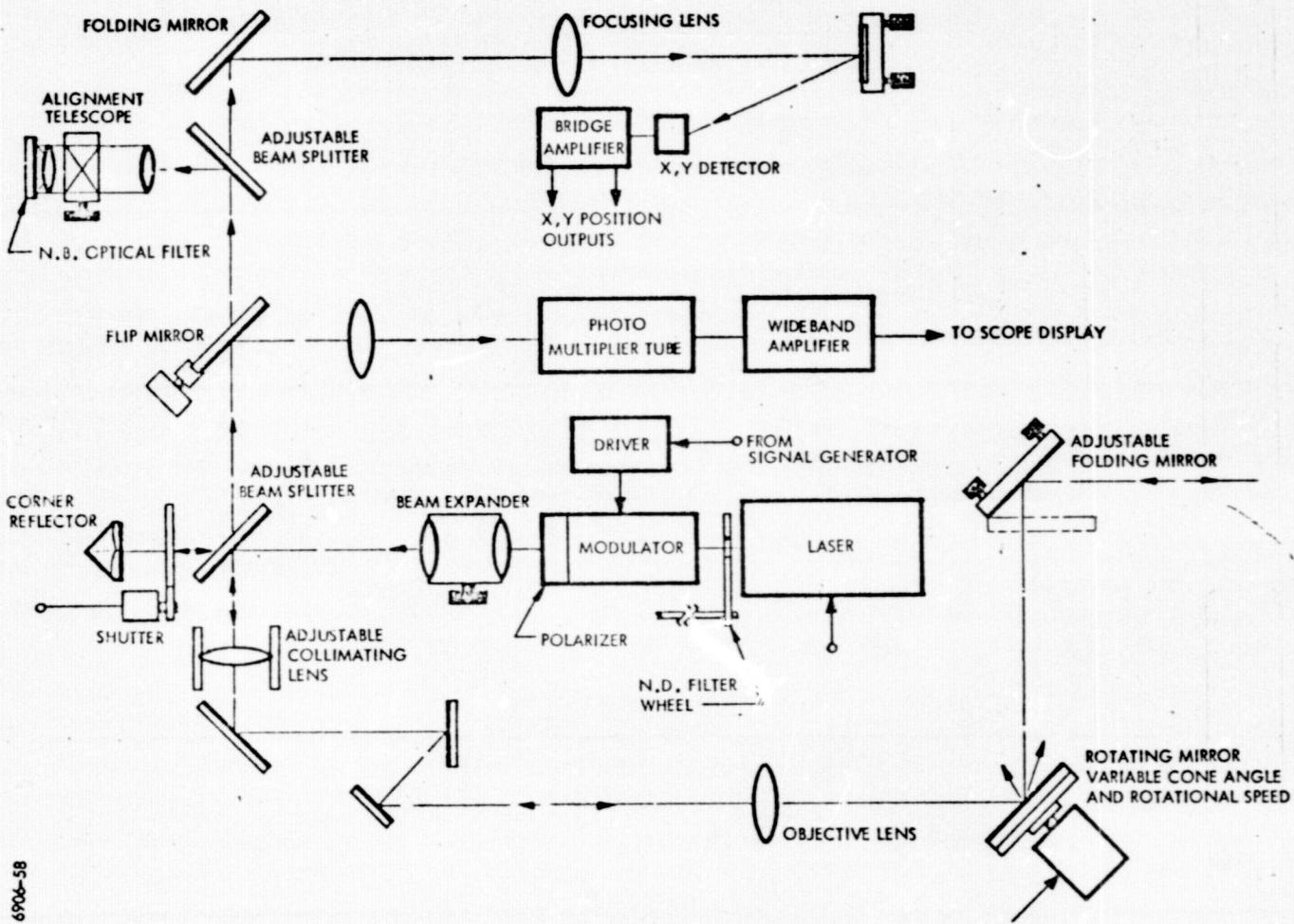


Figure 6-4. GCE Electro-Optical Unit Functional Block Diagram

6906-58

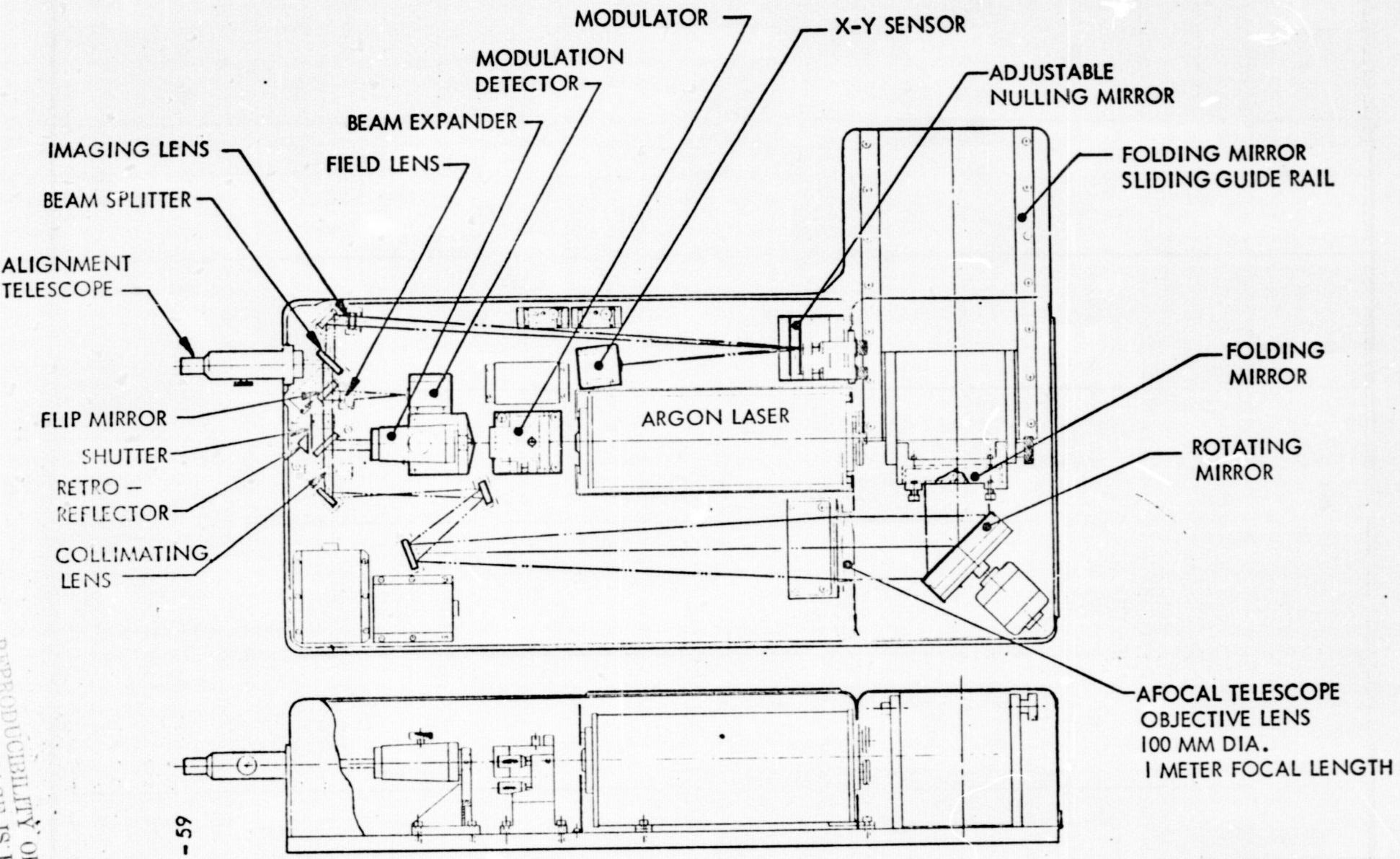


Figure 6-5. Ground Checkout Equipment

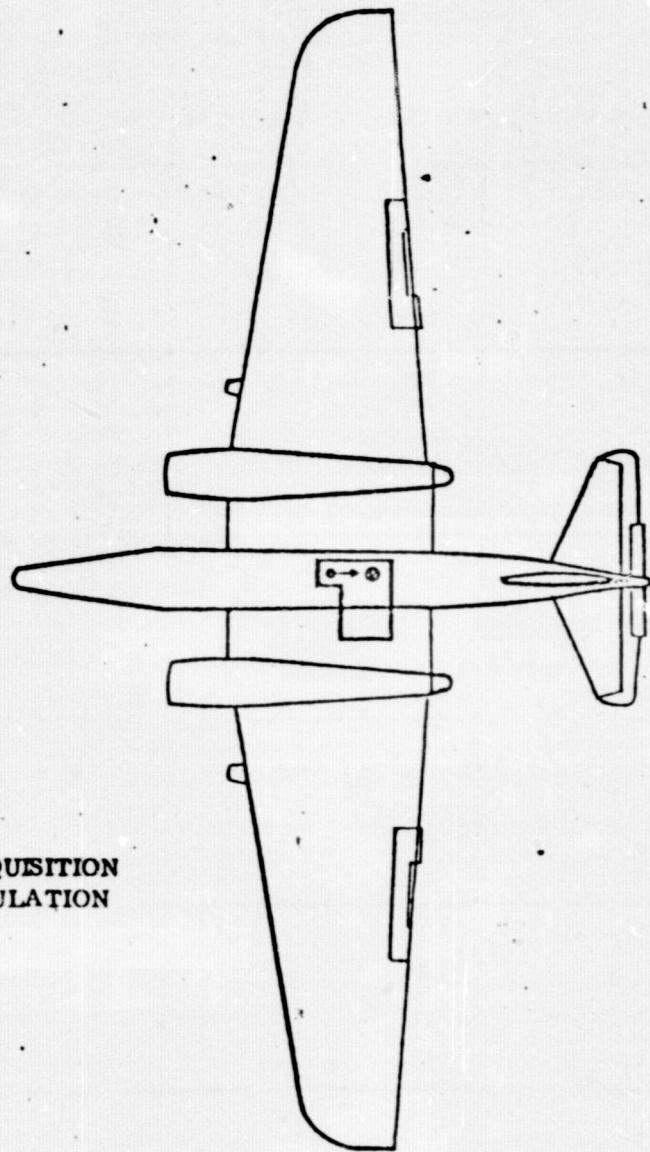
receiver system. A beam expander telescope (28X) expands the laser beam to fill the entrance pupil (0.48 inch diameter) of the output telescope. Most of the laser energy reflects from the beam splitter, shown in the functional block diagram, and exits the system through the afocal telescope (8.3X), rotating mirror and the adjustable folding mirror. The rotating mirror is included for the purpose of conically scanning the output beam direction through an adjustable cone angle and at an adjustable angular rate. This is accomplished by a dual wedge mirror mounting assembly which can be differentially rotated to provide deflection angle magnitudes from zero to approximately 10 degrees. The larger scan angles, which are beyond the field of view of the AOCP, are used to exercise the coarse acquisition system and the gimballed mirror. The folding mirror permits the GCE exit beam to be directed up into the aircraft window from various directions simulating different acquisition approach flight paths.

Figure 6-6 shows the orientation of the GCE beneath the RB57 aircraft for checkout in two different ground station approaches. In addition to the beam coarse direction control, the adjustable folding mirror provides a fine adjustment of the beam direction for quantitative calibration of the AOCP acquisition field and error signal gains. This mirror can also be positioned so as to autocollimate the GCE afocal telescope in its self alignment and calibration mode. (The

6-12

6906-172

A. ACQUISITION
SIMULATION



B. CIRCUIT FLIGHT
PATH SIMULATION

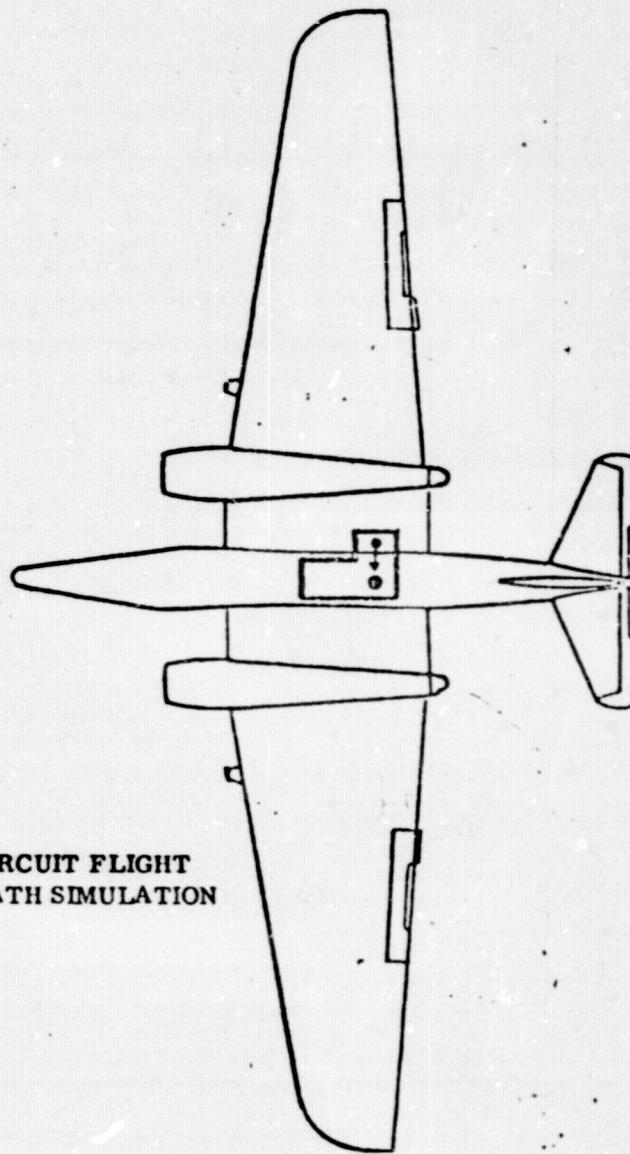


Figure 6-6. Ground Checkout Equipment Orientations

use of the GCE in its various calibration, alignment and test modes has been described in the O&M manual provided previously under this contract.)

A portion of the GCE laser energy passes through the adjustable beam splitter (coated to reflect 0.488 micrometer radiation and transmit 0.6328 micrometer radiation) and impinges on the corner reflector when the shutter is opened. The corner reflector returns the energy from the 0.488 micrometer laser to the beam splitter where it is reflected into the receiver portion of the optical unit for pointing direction reference and 10.7 MHz modulation index monitoring purposes. When the flip-mirror is in position, the GCE laser is deflected onto the photomultiplier detector and the 10.7 MHz subcarrier is detected and dc coupled through a wideband amplifier for display on the control console oscilloscope. This permits monitoring and control of the modulation depth of the laser subcarrier.

When the flip-mirror (controlled from the console) is removed from the optical path, the beam from the retro reflector continues onto the beam splitter element which reflects a portion of the energy into the alignment telescope to obtain a visual reference of the beam position and quality. The main part of the beam passes through the beam splitter and is imaged onto an X-Y position detector.

The X-Y sensor provides an output in two orthogonal axes indicating the beam position on the detector. An adjustable folding mirror is used to precisely center the 0.488 micrometer image on the X-Y sensor's null axis to establish the transmitted beam reference direction for later comparison with the received beams position from the AOCP. This then determines the magnitude and direction of any boresight error within the AOCP system. AOCP boresight correction is accomplished by commanding an offset track to the image director tracker from the GCE while nulling the received AOCP beam on the GCE X-Y sensor.

In operation, the collimated 4 inch diameter 0.488 micrometer beam is directed into the AOCP and acquired and tracked. The AOCP then points its 0.6328 micrometer beam back toward the GCE unit. The AOCP transmitted beam enters the GCE afocal telescope after reflection from the folding and rotating mirrors and passes through the beamsplitter into the GCE receiver section. When the flip-mirror is in position, the incoming beam is folded onto the photomultiplier detector for AOCP modulation index measurement. Removal of the flip-mirror permits the AOCP laser beam to be imaged onto the X-Y position sensor. Since the X-Y position sensor has previously been nulled with the GCE laser, the position read from the X-Y sensor from the AOCP beam is a measure of boresight.

error between the AOCP receiver and ACCP transmitter. When the rotating mirror is operated, causing the GCE beam to be deflected dynamically, the AOCP tracker will detect the input angle change and correct for this deflection by closed loop pointing of the beam steerer mirrors. Consequently, the AOCP transmitted beam direction exactly compensates for the GCE rotating mirrors deflection and the image on the X-Y sensor remain still. As the rotational rate of the GCE mirror is increased, the AOCP control system lag can be observed at the X-Y sensor output. The nulling sensitivity existing in the X-Y position sensor is better than one microradian.

Figure 6-7 is the electrical block diagram for the GCE. The dashed line represents the interface between the optical unit and the control console. The interface cabling and optical unit operation and mode selection occurs at the GCE control panel shown in Figure 6-8.

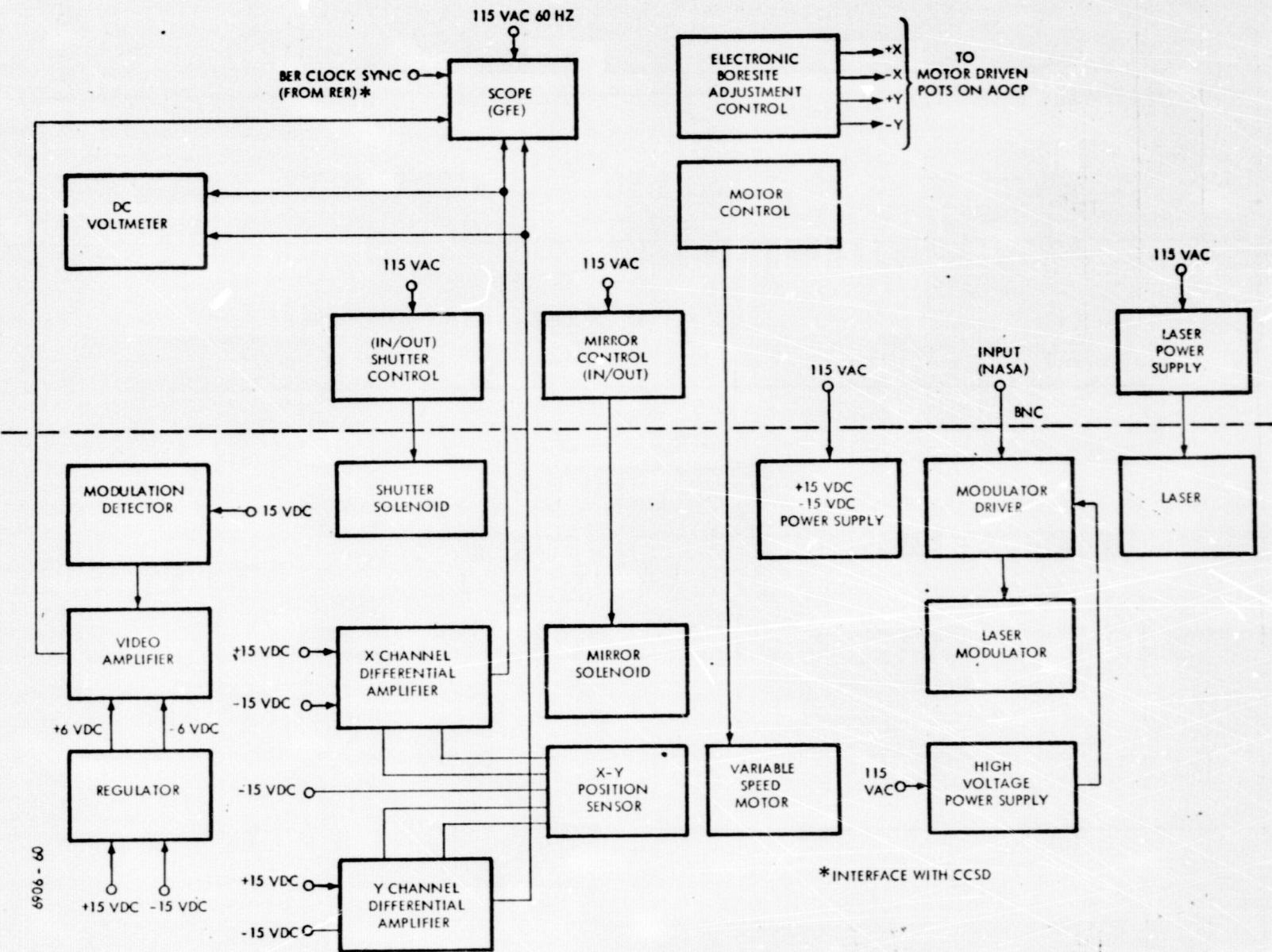


Figure 6-7. Electrical Block Diagram of Ground Checkout Equipment

95 - 9069

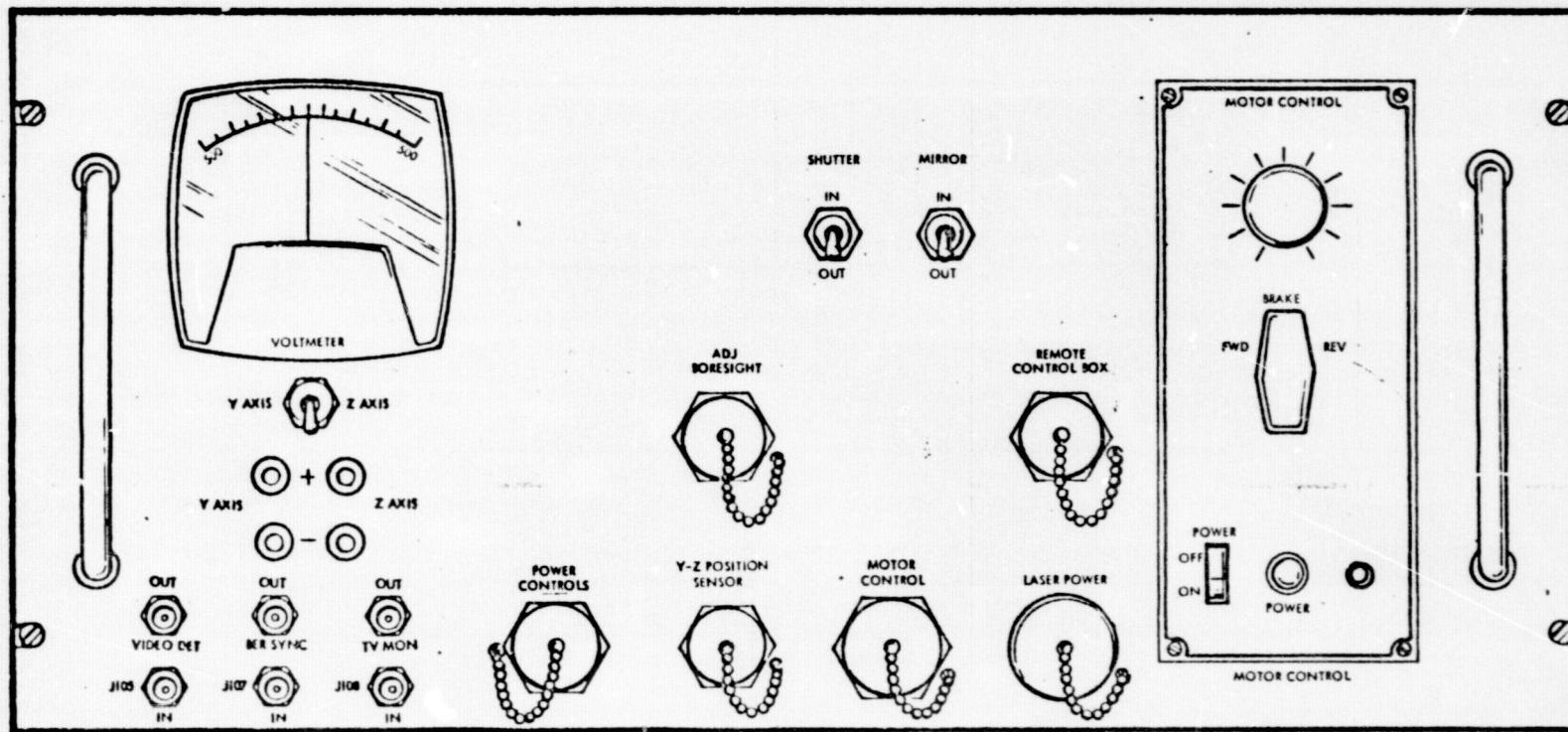


Figure 6-8. GCE Control Panel

7. GROUND BASED ACQUISITION AID (GBAA)

The GBAA portion of the High Altitude Optical Communication System is a Laser Radar and Ranging System for acquisition and tracking of high altitude aircraft. (See Figure 7-1.)

Design, development and preliminary testing of the complete system was accomplished in a time span of approximately two years. The majority of the system design was straightforward, utilizing ITT's vast knowledge in the field of star and vehicle trackers. Portions of the system, due to uniqueness of application, employed the use of either state-of-the-art equipment, or required unique modification of standard equipment. Final system performance dramatically demonstrated the worthiness of this extended design effort. Figure 7-2 shows the GBAA hardware tree to be discussed in this section.

7.1 Overall System Description

The GBAA has the capability of acquiring a cooperative target consisting of a high flying aircraft carrying a cube corner retroreflector array. The target will be acquired at a slant range of from 30,000 feet to 100,000 feet while traveling at an angular velocity $\leq 0.5^\circ/\text{second}$.

Target acquisition will be accomplished by the interception of the aircraft's retroreflectors by the GBAA search scan. (See Figure 7-3.) The search or fence scan is one in which a $10^\circ \times 0.09^\circ$ solid angle is scanned in the far field, simultaneously, by both transmitter and receiver. The 10° fence is scanned in 128 overlapping steps. As the aircraft passes through the search scan, a transmitter beam reflection from the cube corner's retroreflectors will be sensed by the CBAA receiver sensor. The laser radar will then automatically switch to TRACK mode. A cruciform track scan will be generated, continuously centered about the target aircraft by the receiver tracker. Declination and hour angle error outputs

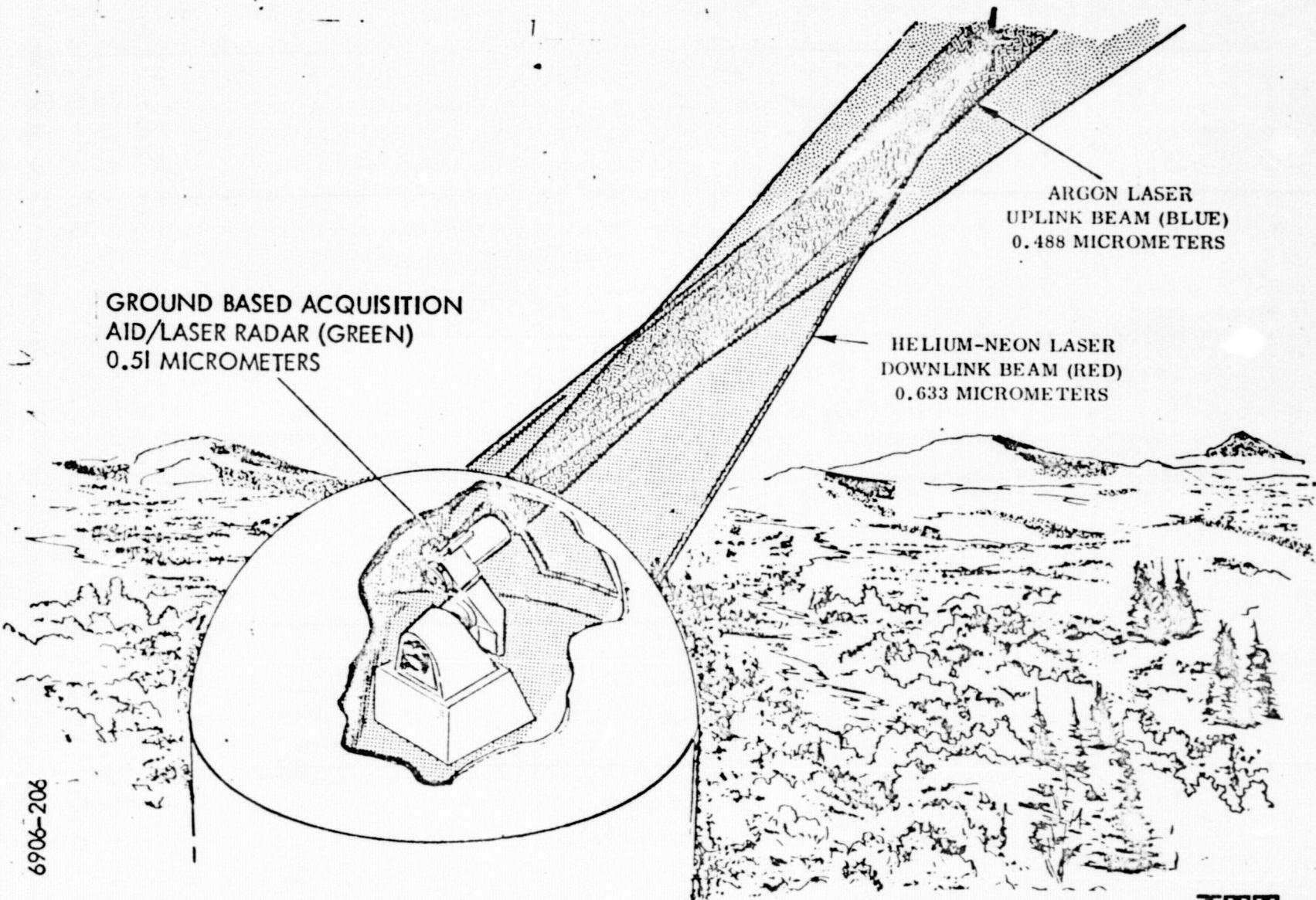
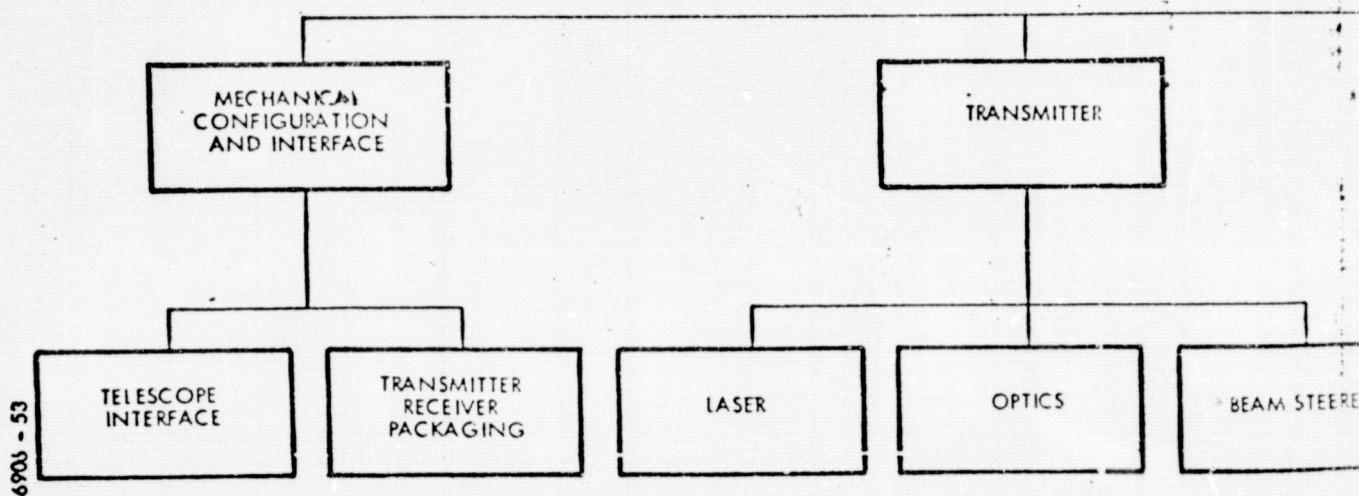


Figure 7-1. GBAA LASER RADAR AND RANGING SYSTEM

ITT

REPRODUCIBILITY OF THE
ORIGINAL PAGE IS POOR

GROUND BASED ACQU



6900 - 53

FOLDOUT FRAME

POSITION AID AND HARDWARE TREE

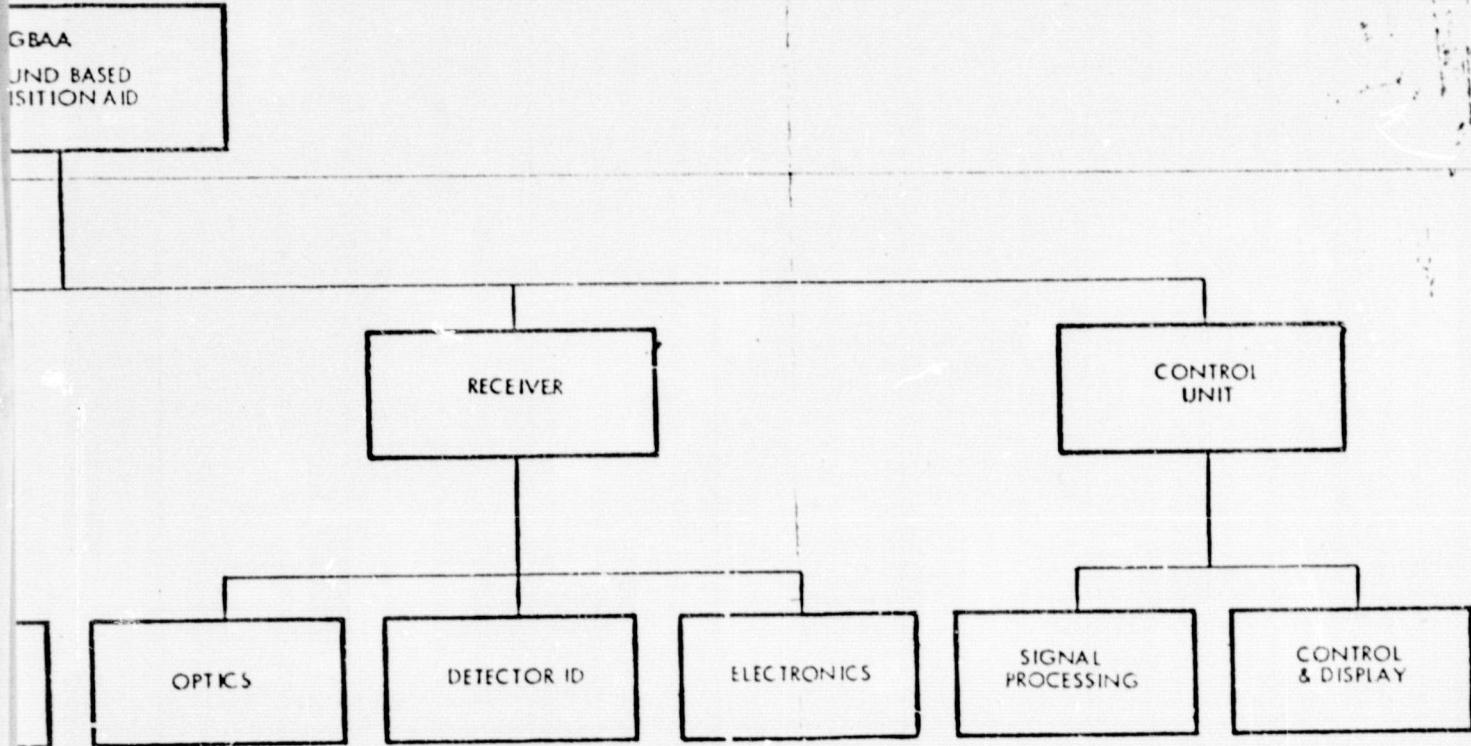


Figure 7-2. GBAA Hardware Tree

FOLDOUT FRAME 2

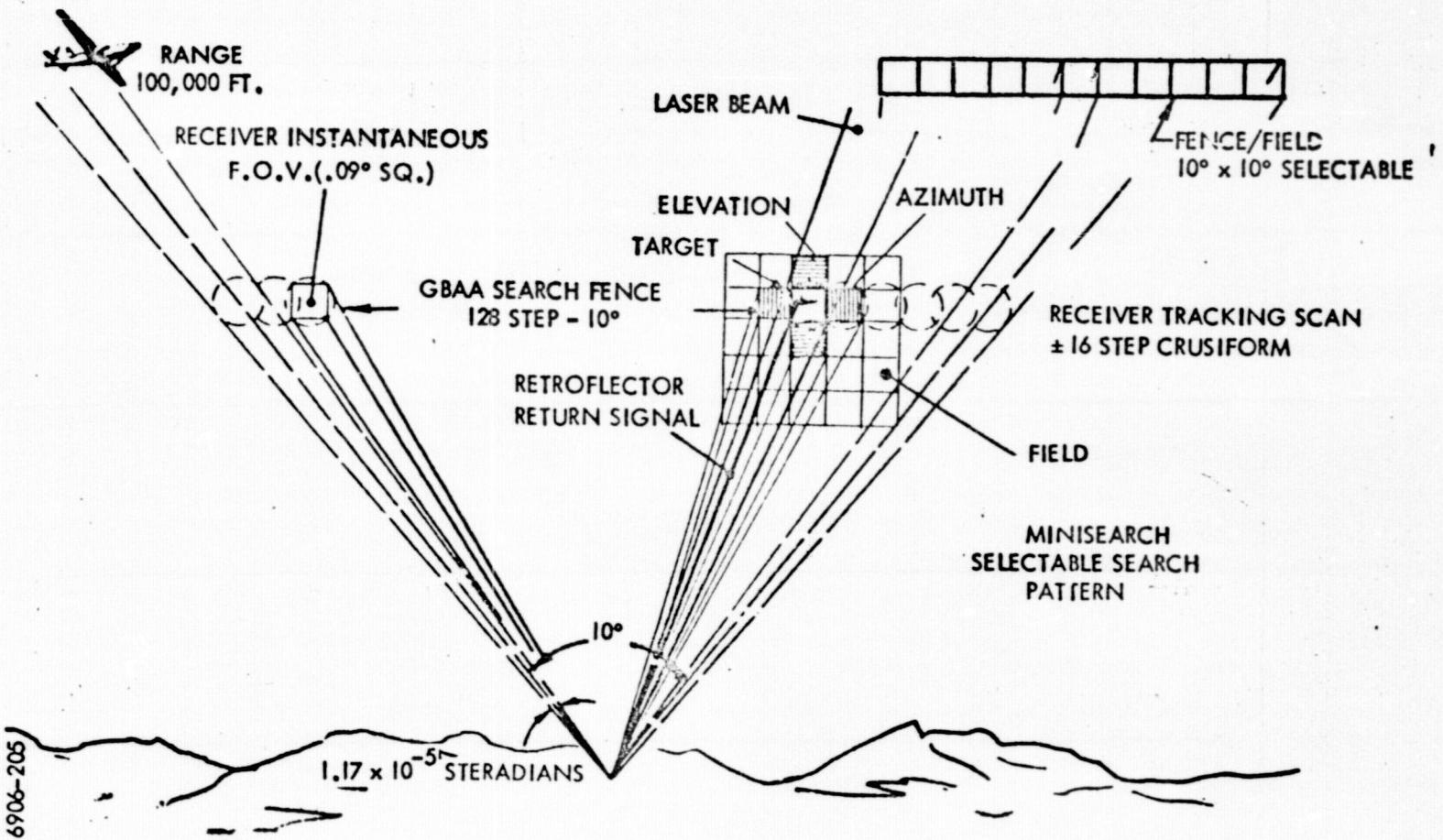


Figure 7-3. GROUND BASED ACQUISITION AID

will be available at the target tracker control unit to determine the target position relative to the GBAA boresight axis, accurate to $\pm 20\text{sec}$. Target RANGE will also be output in both digital and analog form with an accuracy equal to or better than ± 100 meters.

A star tracking mode has also been provided to affect an infinitely distant point source for mutual alignment of the GBAA laser radar and the optical communications telescope.

The GBAA operating parameters are listed in Table 7-1.

**TABLE 7-1. GROUND BASED ACQUISITION AID
SYSTEM PARAMETERS**

A. EQUIPMENT DESIGN SPEC.

1.0 Receiver Optics Assembly

1.1 Lens: De Old Delft, 65mm f.i., f/0.75, 21°E.O.V.

1.2 Band Pass Optical Filter:

Maximum on-axis transmittancy wavelength .5145 microns

Operating field of view $\pm 5^\circ$ incidence

Minimum transmittancy 60% at 0.5145 microns, on-axis

Maximum bandwidth (3db) 0.002 microns, on-axis

Blocking of 0.001 for S-20 photocathode

Diameter 3.0"

2.0 Receiver Sensor

2.1 Tube: ITTL F-4012, S-20 Photocathode, 4 mil square aperture,
nom. gain = 1×10^6 .

2.2 Deflection: Magnetic

2.3 Focus: Magnetic

2.4 Dynode-High Voltage Power Supply: DC to DC Converter.

3.0 Transmitter Beam Deflector & Power Driver

**3.1 Deflector type - G.T. & E PBM-5G, Deflection angle = ± 40 min
(Optical magnification to $\pm 5^\circ$ square field deflection)**

3.2 Power Driver: $\pm 2.5V$ input for full drive output.

4.0 Laser Transmitter

4.1 Type: Pulsed Argon Ion, nominal operating freq. = 1KHz, wavelength.
at maximum output = .5145 micron, single color, multimode.

5.0 Electronic Target Tracker and Ranging System

5.1 Angle tracker:

F.O.V. = 10° elevation $\times 10^\circ$ azimuth, I.F.O.V. = $.09^\circ$

Acquisition Scan = Singleline, 128 step, $\pm 5^\circ$.

Track Scan = ± 16 step cruciform = \pm one I.F.O.V.

Scan step rate = 1KHz.

Line Scan time = 150 millisec.

Tracking rate = $.5^\circ/\text{sec.}$

5.2 Laser Trigger:

P.R.F. = 1KHz

Ampl. = 2.5V

P.W. = 2 usec. Pulsewidth

Rise time = 150 n sec.

**TABLE 7-1. GROUND BASED ACQUISITION AID
SYSTEM PARAMETERS (cont'd)**

- 5.3 Beam deflector drive
 $\pm 2.5V$ for full deflection output
- 5.4 Angle error output:
1v/dg into 100 ohm load; source impedance 10 ohms max.
- 5.5 Ranging system:
Range outputs - Analog, Digital, Visual Display - > 33 KM
- 6.0 Power Supply Panel
- 6.1 Input 125VAC - 60 Hz
Output - DC Volts = $+5, \pm 15, +28, \pm 500$
- 7.0 Control & Display Panel
- 7.1 Readouts
Elev. & Azim. Angle Error - Metered
Target Presence - Indicator Lamp
- 7.2 Control:
Master Power on-off sw.
Tracker Control sw.
Laser transmitter power, sw.
Calibration & Test switching.

B. Input/Output Information

1.0 Input: 125VAC, 50-60 Hz, 15A

2.0 Error Output:

2.1 Angle Error output (elevation & Azimuth)
 $\pm 2.5V$ max into 100 load.

2.2 Crossover Gradient = $0.5 \pm .05$ Volt/deg
Gradient to be contained within \pm two assymptotic boundaries
with 10% slope differences. The boundaries shall intercept
the origin of the gradient plot. The gradient curve shall
be smooth & monotonic.

3.0 Search-Track, Re Acq, Status Indicator

3.1 Analogue or Visual (As Required)

4.0 Range Output:

kilometers/volt

kilometer's/volt

7.1.1 Modes of Operation. - To acquire and track a target, four basic modes of operation are required. These are: SEARCH, ACQUISITION, TRACK and MINISCAN. The SEARCH mode, as the term suggests, is used to scan the far field in the direction of the approaching target. The laser transmitter beam is deflected in small overlapping step increments to form a spatial "line of illumination" with which to intercept the approaching aircraft. In a similar fashion, the receiver sensors instantaneous field-of-view (IFOV) is scanned across the sensor photocathode in overlapping steps such as to be surrounded by the line being scanned by the transmitter in the far field. Once the transmitter beam has been intercepted by the aircraft, illumination of the retroreflector is seen by the receiver sensor in the form of a return pulse. The first return pulse stops search scanning and advances the mode to ACQUISITION. The next pulse is transmitted in the same angular direction. The second pulse is used to verify that the return signal was indeed energy returned by the target as opposed to "Noise." If a second pulse is received the mode is advanced to the TRACK mode. If not, the mode is returned to search and the search scan is continued until two successive return pulses are detected by the receiver. Once the target has been acquired it is necessary to determine its exact position, velocity, and direction of travel. To accomplish this, a cruciform tracking scan is generated. Target positions which deviate from the center of the tracking scan cause correction voltages to be generated which result in a repositioning of the track scan about the target. The absolute position of the track scan deflection is read out as an error voltage

representing the \pm deviation from center of the receiver field. The center being referred to as Boresight. The error signal is used by the telescope gimbal system to precisely align the telescope to the target. The tracking scan is continued so long as return pulses are being received by the receiver sensor. If return pulses should terminate due to scintillation for example, the miniscan mode of operation is initiated. In MINISCAN a small raster type field is scanned in order to relocate the target. It consists of a search pattern covering a field of approximately $.65^{\circ}$ square. The first return pulse received while in miniscan resets the mode control to the track mode and target tracking continues. If no return is received within twelve minifield scans, the mode control is recycled to the search mode where the field is once again searched in the original 10° line scan, or a $10^{\circ} \times 10^{\circ}$ raster type scan, as selected by the operator.

Search Mode. - In SEARCH mode, the transmitter and receiver searched the far field using a line scan consisting of 128 overlapping steps covering a 10° angle. The fence scan can be positioned anywhere in a $10^{\circ} \times 10^{\circ}$ total field-of-view (FOV).

The control unit provides selectable search scan options that will:

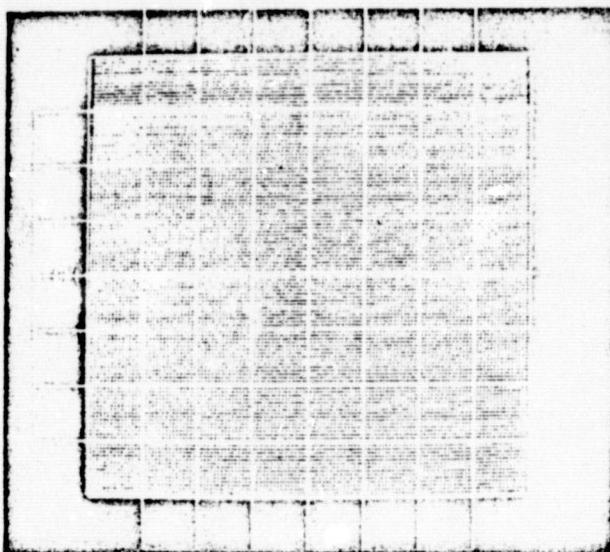
1. Search the total $10^{\circ} \times 10^{\circ}$ FOV - Raster Scan.
2. Search a single 10° line - Fence Scan.
3. Search a specific 10° line - Offset.
4. Search a 10° fence at elevation boresight - Position Scan.

All scans - ACQUISITION, TRACK, and MINI SCAN are digitally generated using TTL logic components. The acquisition scan generator is a 7 bit binary up-on counter which counts from 0 to a maximum count of 128 and back to zero. This produces a 128 step sawtooth waveform FENCE scan with a cycle rate of approximately 8 Hz. The fence scan searches the field from left to right at a stepping rate of 1 kHz. At the end of each search line the scan is rapid retraced at a rate of 8 KHz. The fence scan is positioned at a zero elevation angle by momentary depression of the POSITION SCAN button on the control unit. It may also be positioned to an elevation angle of -3.75° by selection of OFFSET. These two conditions are attained as the elevation acquisition counter is set to either logic #64 or logic #16, respectively. When in the FENCE mode, the elevation acquisition counter is held static subsequent to position selection.

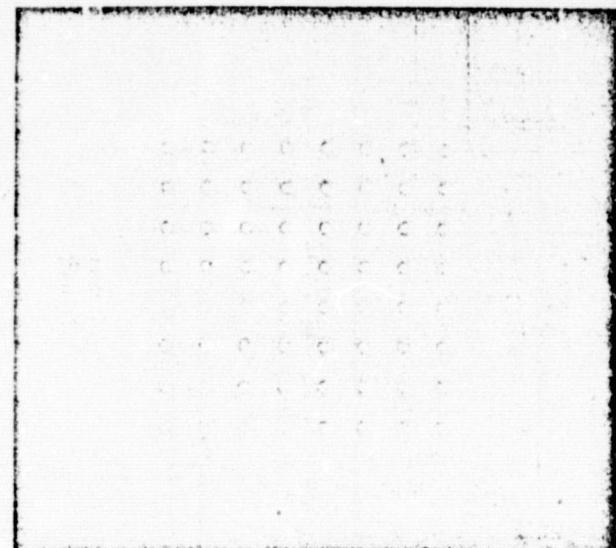
Raster Scan. - When RASTER is selected, the azimuth counter continues generating the 128 step fence scan. At the end of each azimuth line the elevation acquisition counter is advanced one count resulting in an elevation deflection of $.08^\circ$. This generates a RASTER type scan which searches the total $10^\circ \times 10^\circ$ FOV. At the end of each field scan the elevation counter is rapidly down counted to count #0. This produces an elevation sawtooth scan waveform of 128 steps which repeats at a rate of 16 sec/ \sim (See Figure 7-4.)

Figure 7-4. GBAA
TARGET TRACKER SCAN WAVEFORMS

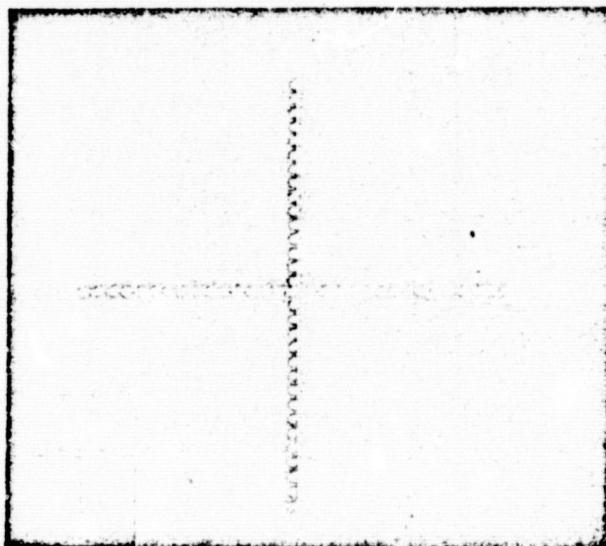
(Sheet 1 of 2)



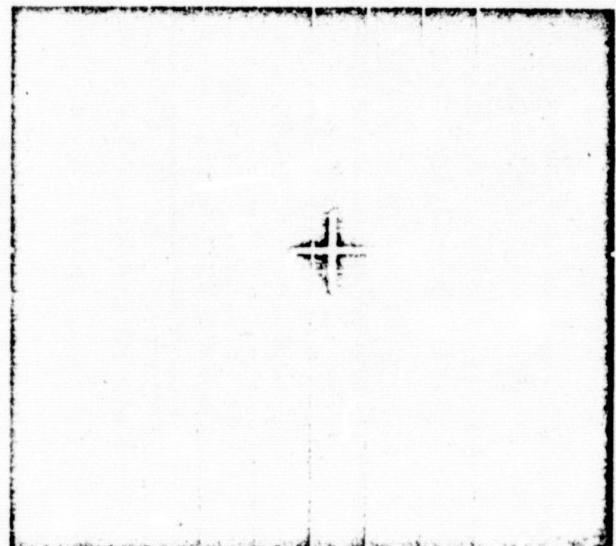
Search Scan
128 Step/ 10° Fence-W/ 10° x 10° Field Option



Mini-Search Scan
8x8 Steps/Field - $.08^{\circ}$ /Step



Tracking Scan
 ± 16 Step = $\pm .08^{\circ}$



Fence - Minifield & Track Scans
(Superimposed)

NOTE

Signals applied to oscilloscope inputs

Vertical: Voltage at Elevation coil current sampling resistor

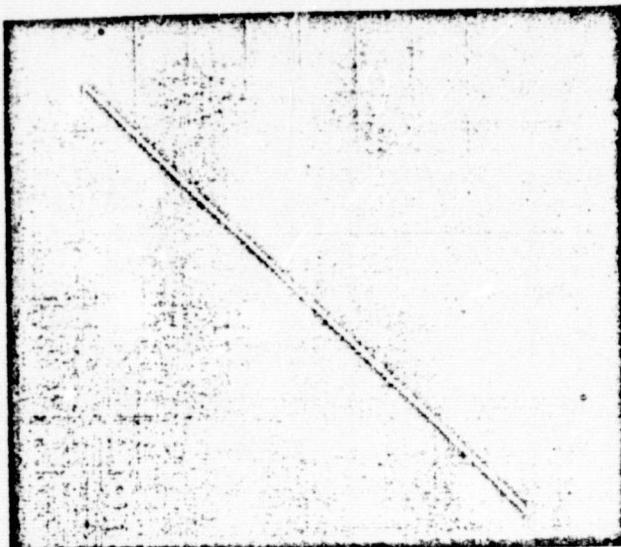
Horizontal: Voltage at Azimuth coil current sampling resistor

Figure 7-4

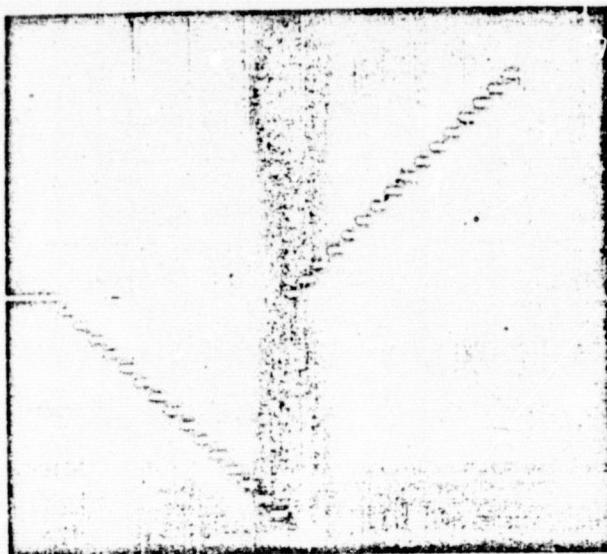
GBAA

(Sheet 2 of 2)

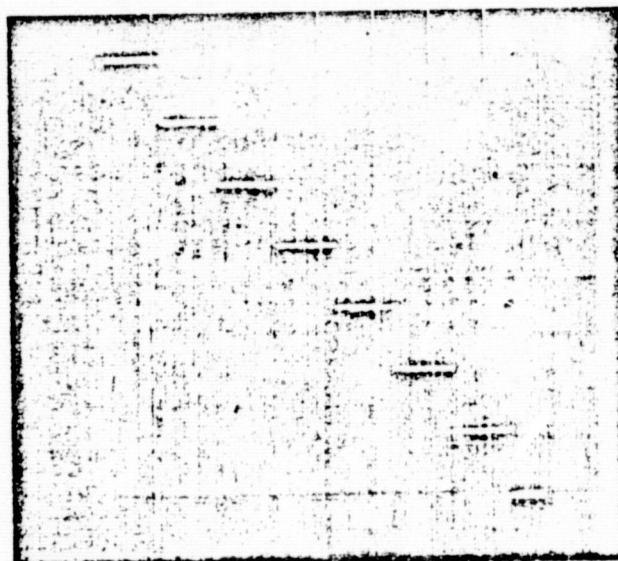
TARGET TRACKER SCAN WAVEFORMS



Search Fence
128 Step - 10° Azimuth Scan



Track Scan
 ± 16 Step - $.005^{\circ}$ /Step



Mini-Search
8 Step Elev. & Azim. - $.08^{\circ}$ /Step

NOTE

Signals applied to oscilloscope inputs

Vertical: Voltage at coil current sampling resistor

Horizontal: Internal Sweep

If, at any time during the RASTER scan, the FENCE mode is selected, the elevation drive will cease and the scan will continue in azimuth at that point in the FOV. In this manner, the FENCE scan can be positioned anywhere in the $10^{\circ} \times 10^{\circ}$ FOV by selection at the control unit.

Acquisition Mode. - When the first target return pulse is detected, the operating mode switches from SEARCH to ACQUISITION. In acquisition mode the clock pulse drive to all deflection scan generators is inhibited and a second pulse is transmitted. If the initial pulse was a false alarm (noise pulse) the mode automatically returns to search and the fence scan continues. When two successive return pulses are detected the mode switches from ACQUISITION to TRACK.

Track Mode. - In the TRACK mode, elevation and azimuth sawtooth scans are generated as pictured in Figure 7-4. The instantaneous field-of-view is deflected about the target by a track scan consisting of ± 16 steps. Each step equals 0.005° . The track scan alternately deflects in elevation and azimuth to produce the $\pm .08^{\circ}$ cruciform pattern. The track waveform initially positions the transmitter and receiver on the target and scans off the target. In this manner, the on target time (above and below and to the right and left) is weighed to determine the actual target position.

As previously mentioned, there are ± 13 track steps of 0.005° each which results in a total deflection equivalent to ± 1 acquisition step. This

deflection is obtained by preceding each acquisition counter with a 4 bit track counter. Sixteen track step increments are therefore necessary to advance the acquisition counters one step. The step rate remains at 1 kHz producing a complete cruciform scan at 15 \sim /sec. Subsequent to track scanning off the target the track scan is rapid retraced in 250 microseconds as it is driven with a 64 kHz retrace clock pulse. Track scanning continues providing the target remains in the FOV and appropriate signal-to-noise level is maintained. If the signal is interrupted for a period of two complete cruciform track scans, the mode switches from TRACK to MINISCAN.

Mini Search Scan. - The MINI SEARCH SCAN generator produces the pattern shown in Figure 7-4. It covers a far field area of $0.64^{\circ} \times 0.64^{\circ}$. Typical elevation and azimuth miniscan waveforms are also shown in Figure 7-4. The azimuth 8 step scan and retrace sawtooth waveform has a cycle rate of 120 Hz. The elevation scan cycles at 15 Hz. The 8 x 8 acq. step miniscan is generated as the 4 bit track counters are driven with 16 clock pulses per each acquisition step. Each acquisition step, for both transmitter beam deflector and receiver, is generated in sixteen .005 $^{\circ}$ increments. The finer stepping granularity reduces the beam deflector's tendency toward overshoot and ringing which might be encountered when using larger step increments.

The elevation and azimuth step sequencing is controlled by a flip flop with control counter synchronization as shown in the schematic diagram #4.

The first target return pulse received when in the miniscan mode switches the mode to track. If no target is sensed within 12 minifields the mode returns to SEARCH. When reverting to the SEARCH mode the scan is either FENCE or RASTER as determined by selection at the control unit.

Star Track Mode. - With slight modification the GBAA may be used for tracking stars. The change-over requires only two simple steps. First, the optical filter attached to the receiver sensor, must be removed. This is accomplished by loosening the three set screws in the periphery of the filter adapter. It is advisable to mark the filter adaptor alignment relative to the sensor housing for future register when re-installing the filter. The filter is then removed by a straight and constant pulling motion away from the sensor housing. A slight vacuum is created due to the close fit of the adaptor to the housing. This reluctance is to be expected during filter removal. Care must be taken when re-installing the filter to attain the same orientation as that prior to removal.

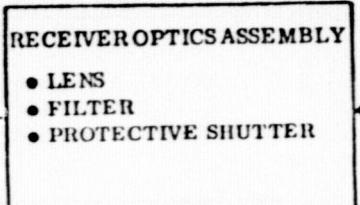
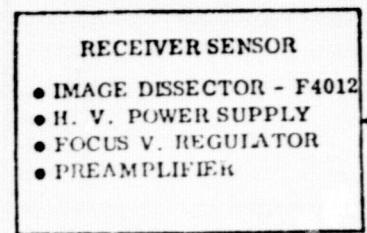
After removing the filter, caution should be used to protect the highly sensitive photo sensor from direct or excessive illumination. Step #2 is merely to actuate the Target Track - Star Track selector switch which is located inside the electronics chassis. This is a small single pole double-throw switch mounted on an adaptor socket (#4G) inside the tracker electronics chassis and may be located by removal of the chassis top cover. This switch may be relocated at a

more convenient position, such as the front panel, at the discrimination of the operator. After switching to Star Track, the M.G.C. (Manual Gain Control) may be zeroed, due to the absence of background illumination. All tracker systems will now operate in the conventional manner.

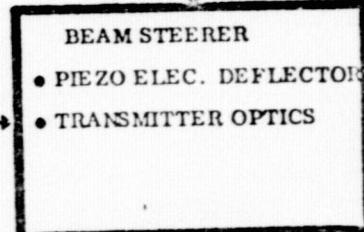
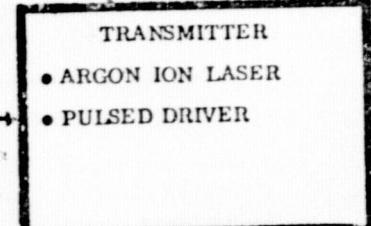
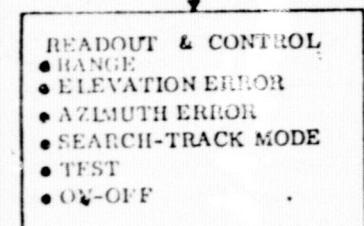
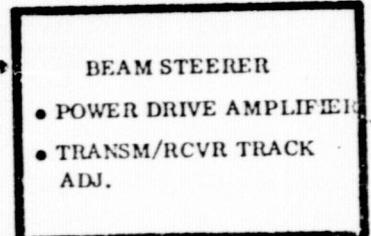
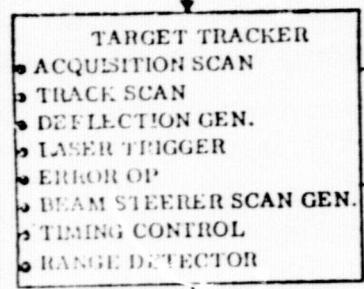
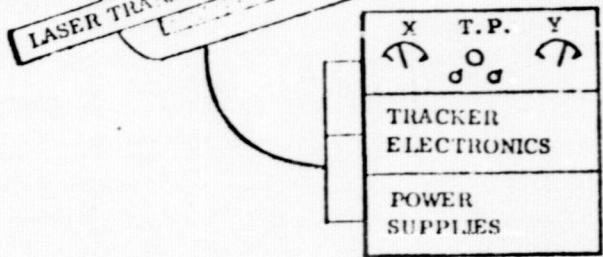
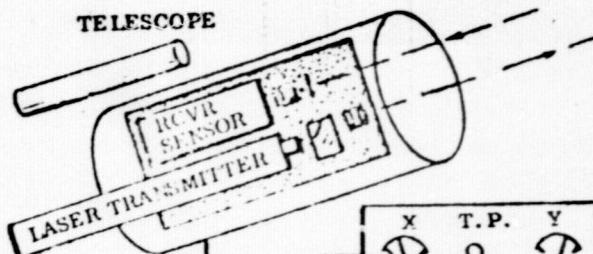
7.2 Transmitter Subsystem

Figure 7-5 shows an overall block diagram of the GBAA system with the transmitter subsystem indicated by the heavy block outlines. The transmitter subsystem comprises the following elements:

- **Laser System**
- **Beamsteerers**
- **Optics**



FROM
RETROREFLECTORS



2W PEAK
LIGHT SOURCE
 $\approx .08^\circ$ PENCIL
BEAM

ERROR OUTPUT
TO
TELESCOPE
GIMBAL

6906 - 146

Figure 7-5. GBAA Transmitter Block Diagram

7.2.2 Laser Performance Test. - To best understand the laser performance characteristics, a history of events which covers in-house testing and final systems operation, will be described.

In-house testing of the laser radar system required horizontal orientation of the transmitter test bed. A ground-based target was used for testing its pointing and tracking accuracy. The target consisted of a cube corner array positioned at a nominal range of 2 miles. The transmitter test bed was mounted atop a Leitz rotary table. The rotary table was used to vary the elevation and azimuth altitude of the test bed for testing the acquisition and tracking of the laser radar throughout its $10^{\circ} \times 10^{\circ}$ FOV. The pointing and tracking accuracy of the GBAA equipment was therefore restricted to a nominal horizontal orientation until installation at the MSFC/Madkin Mountain facility. Subsequent to mounting the GBAA to the gimballed telescope mount, rigorous tests were made to determine the transmitter's absolute pointing accuracy while operating over 360° of angular freedom.

A target was affixed to the end of the GBAA test bed for determining the transmitter's pointing stability while the entire test bed was subjected to nominal 360° of angular rotation. Dynamic testing revealed two serious problems. Both beam motion and intensity variations occurred while equipment attitude angle was varied. Laser transmitter power was observed to change from maximum rated power output to near extinction for certain

angular attitude orientations of the radar test bed. Test results including both beam motion and power changes were submitted to Britt Electronics, manufacturer of the Argon Laser. A subsequent Beam Motion Study was performed by Dr. Michael R. Smith of Britt Electronics Products Corp. The beam motion and power change study revealed the necessity of a laser mirror cavity structure redesign. (See Appendix C, Beam Motion Study - Final Report PO #29407, November 1971, and Appendix D, Investigation of Electro-optical Techniques for Controlling the Direction of a Laser Beam.) Following the redesign, two new laser tubes were fabricated, one of which was installed in the test bed laser. Laser operation subsequently proved excellent although further testing revealed beam motion contribution from sources other than the laser transmitter and are described in the Optics section.

7.2.1 Laser Description. - A pulsed Argon Ion laser is used as the primary light source in the laser radar transmitter system. The Britt Model 2000 pulsed laser was selected on the basis of size, weight, and peak power output consistent with single unit packaging. The laser is internally cooled and therefore requires no auxiliary plumbing. The Britt laser is pictured in Figure 7-6.

Laser operating specifications are (also see Figure 7-7):

1. Peak power output:	1.7 w (nominal)
2. Wavelength at maximum power output:	.5145 microns
3. TEM _{oo} , single color:	(5145 Å)
4. Pulse repetition rate:	1 kHz, adjustable
5. Pulse width:	15 µ s
6. Trigger mode:	Selectable, Internal/External
7. Operating position:	Any

The laser used is a model 2000 AN. Slight modifications were initially made to facilitate the specific requirements of the GBAA system.

The output pulse width and trigger rate, was changed from 50 microseconds @ 270 pps to 15 microseconds @ 1000 pps. A modification of the laser plasma tube was made to facilitate the vertical orientation operating requirement. A conical shaped particle deflector was installed in the plasma tube to prevent contamination of the mirror reflectors.

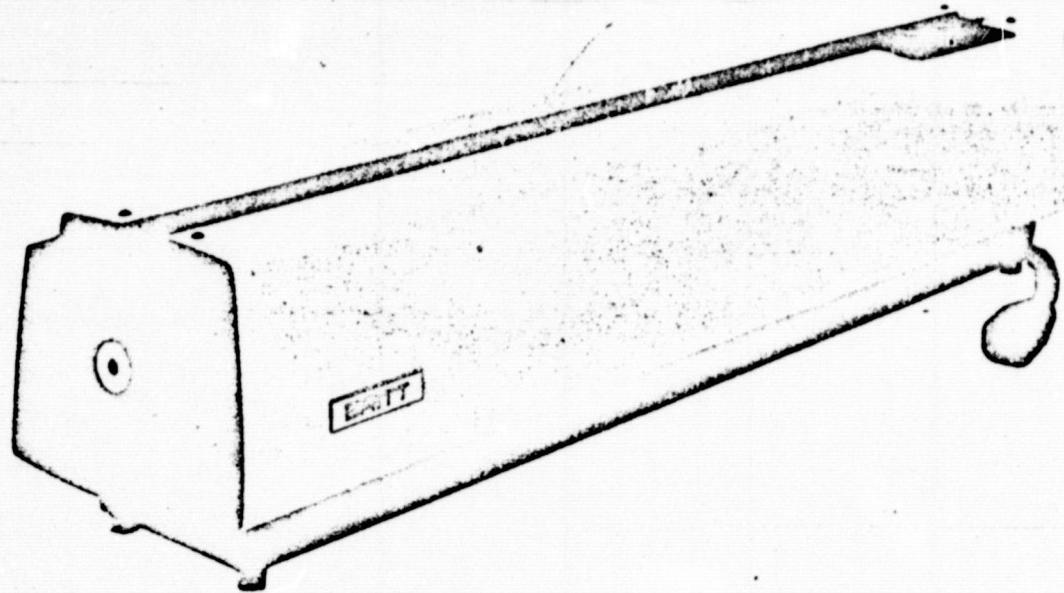


Figure 7-6.

THE MODEL 2000 ARGON LASER is a particular embodiment of the Burst Laser concept which is designed specifically for applications involving holography and other relatively high average power exposures. The Burst Laser concept is described in Bulletin No. 1. Other features which are common to all Britt ion lasers are described in Bulletin No. 2.

General Description

The Model 2000 is a high-duty (large percentage "on" time) repetitively pulsed ion laser which features unusually high average power output for a laser of its cost, size, and weight. Power specifications, selling price and physical characteristics are shown on the reverse of this sheet. Power supply and air cooling are included within the laser head and it operates from 115 Volt AC power. Other conveniences include internal timing and shuttering of exposures and interchangeable, permanently aligned mirror cells.

Functional Description

The Model 2000 laser offers two modes of operation. A continuous output beam of high average power consists of 50 microsecond pulses whose

repetition rate can be varied from 20 to 270 pulses per second. The Burst mode of operation produces timed bursts of pulses but at repetition rates over 1000 pps for .25 to 8 seconds, or over 1500 pps for .12 to 4 seconds. The burst is initiated by a hand-held pushbutton, which also disables the cooling fan to eliminate vibration during the burst. The burst duration is internally timed and is selected in half-stop increments ($\sqrt{2}$) by means of a rotary selector switch on the control panel.

Guarantee

The Model 2000 laser carries an unlimited gas fill life guarantee. See Bulletin No. 2 for detailed description. All other aspects of the laser are warranted for the first year against failures due to defects in material or workmanship.

Accessories

For holographic work the Model 2000 is offered with a Littrow prism wavelength selector and an internal etalon device for providing increased coherence. These accessories are described in Bulletin No. 2 but priced on the reverse of this sheet.

SUMMARY OF TENTATIVE SPECIFICATIONS
BRITT MODEL 2000 BURST ARGON LASER

FUNCTION BURST DURATION	Continuous	Burst	Short Burst
	Continuous	.25 to 8 sec	.12 sec to 4 sec
Minimum Average Power Output TEM ₀₀ -Etalon (5145Å) ¹ with Littrow and Etalon	15mW	50mW	90mW
TEM ₀₀ , Single Color (5145Å) ¹ with Littrow and Aperture	25mW	80mW	120mW
Multimode, Single color (5145Å) ¹ with Littrow only	30mW	100mW	150mW
Multimode, Multicolor Standard Mirrors	80mW	250mW	375mW
Description of Operation			
Burst Duration	Continuous	.25 to 2 sec	.12 to 4 sec
Burst Duty Cycle	100%	25%	25%
Pulse Repetition Rate	20-270 pps	150 pps	1650 pps
Pulse Width	50 μ sec	50 μ sec	50 μ sec
Pulse Amplitude Ripple	<5%	<10%	<20%
Minimum Peak Power			
TEM ₀₀ , Single Color (5145Å)	2.0W	1.8W	1.5W
Multimode, Multicolor	5.0W	4.5W	3.7W
Power Input			
Voltage Input		115 Volts AC 60Hz	
Current Input	5 amperes	14 amperes	20 amperes
Optical Characteristics, TEM₀₀			
Coherence length with etalon	>1 meter (see Bulletin No. 2)		
Beam Diameter	approx. 2 mm (at 1/e ² points)		
Beam Divergence (uncorrected mirror blank)	.75 mrad approx.		
Selling Price			
Standard Mirrors	\$4,250		
Wavelength Selector	\$4,600*		
Selector and Etalon	\$4,950*		

*These prices apply when the wavelength selector and etalon are substituted for standard mirrors. Extra standard mirror cells are priced at \$300 each. Prices subject to change without notice.

¹Power in other lines can be estimated by multiplying the 5145Å power by the following factors:

	5017Å	4965Å	4880Å	4765Å	4579Å
TEM ₀₀	.18	.30	.68	.31	.18
Multimode	.18	.31	.72	.33	.20

Weight: 62 pounds

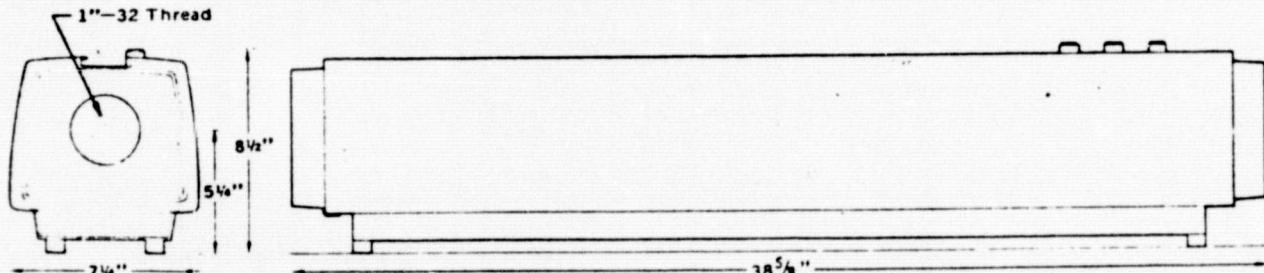
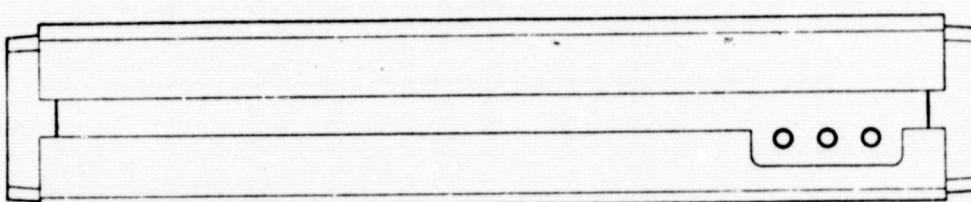


Figure 7-7.

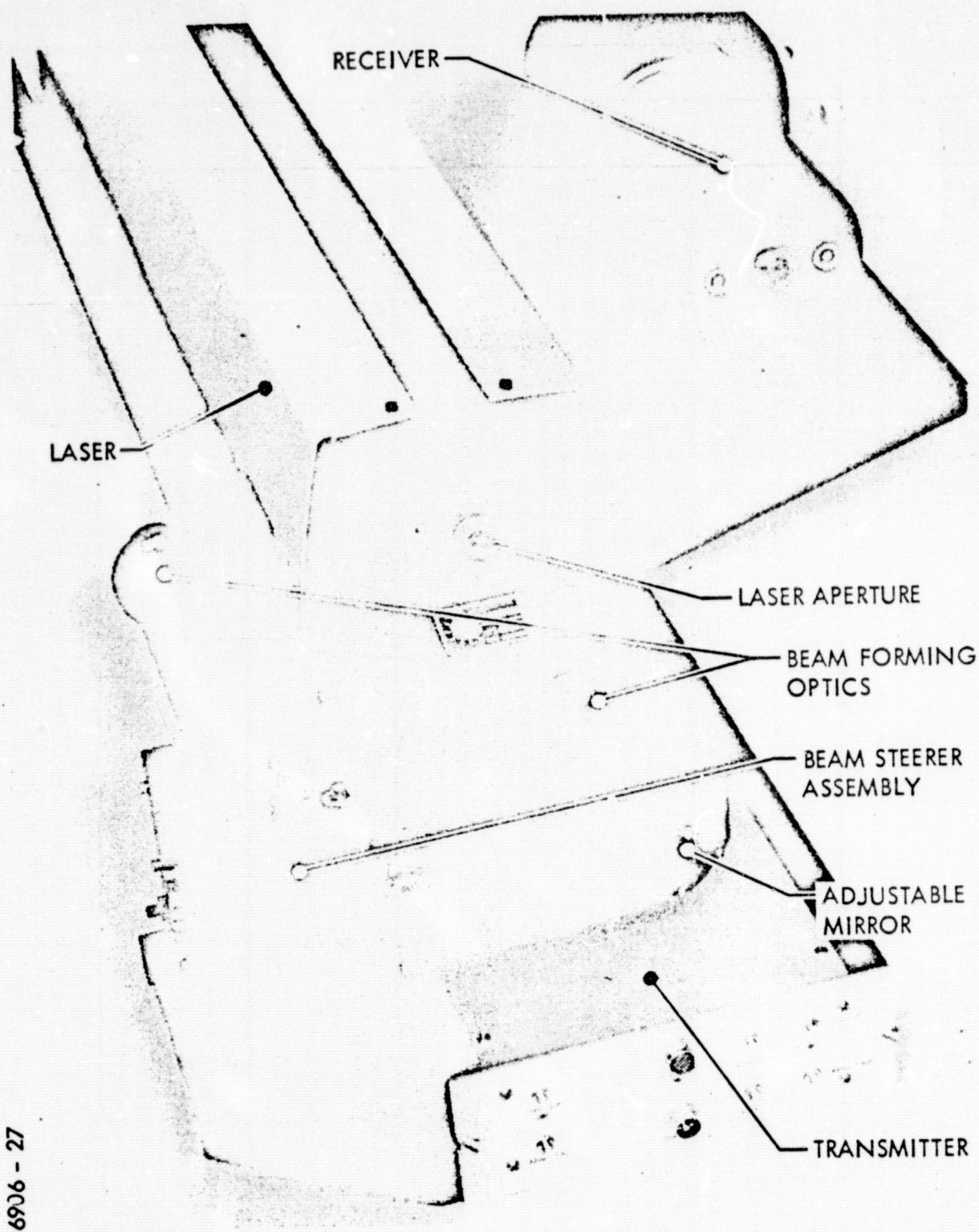
The laser was initially equipped with an internal, closed loop, gas-replenishing system which required liquid nitrogen cooling during the refill operation. An improved system was later installed which virtually eliminated the nitrogen cooling requirement. The new system, called BURP refill cycling, requires equipment down time in the order of minutes as opposed to the original hour..

The laser is equipped with a Littrow Prism wavelength selector. All principal visible Argon lines are selectable by knob control attached to the Littrow Prism. One revolution of the knob encompasses selection of all of the visible lines.

Total laser control is provided by the CONTROL UNIT. One power and two signal cables interconnect the laser to the control unit. One signal cable carries the 1 kHz laser triggering signal while the remaining signal cable contains the SENSED laser transmit pulse used by the ranging system. The 115 VAC laser primary power is supplied by the control unit through the remaining cable.

7.2.3 Beamsteerers. - The G. T. E. model PBM-5G dual axis, piezoelectric beamsteerers are packaged in a box structure. Six 1/4" plates form the four sides and the top and bottom covers. The two beamsteerers are mounted on the top cover while the horizontal or x axis deflector is mounted on the side plate, opposite the input optic arm. The plate mounted opposite the output optic arm is the back cover plate and is removed during the initial optical alignment. Alignment of the dual axis beamsteerers was performed at ITT Gilfillan prior to system shipment and requires no further adjustment. Realignment of the beamsteering assembly should only be necessary if the deflector adjustments have been changed or if the beamsteerers have been removed for replacement.

7.2.4 Electronic Control. - The two-axis beamsteerer control amplifier is shown in the photograph of Figure 7-8. The rear end of the GBAA main frame channel acts as an integral portion of the drive amplifier housing. The amplifier has been designed to be a portable, self-contained unit, capable of being removed from the transmitter main frame and remotely mounted, if desired. All cable connections and controls are located at the amplifier front panel. ConheX subminiature connectors are used for routing x and y deflection drive input signals, as well as the beam deflector's strain gauge and output drive cables. Deutsch connectors



6906 - 27

Figure 7-8. Ground Based Acquisition Aid (GBAA)
Transmitter and Receiver (Rear View)

carry the amplifier low voltage power and switching functions from the rack mounted CONTROL unit to the amplifier and beamsteerer units.

Fine trim BORESIGHTING controls are safety mounted behind the front panel and are adjusted through front panel access holes. Deflection sensitivity controls are also provided on the amplifier chassis. Chassis removal is required for deflection gain control access.

Dual axis beam deflection amplifier circuitry is mounted on a single circuit board. The y axis amplifier is mounted on the top of the board while the bottom of the board contains the x axis amplifier. Both amplifiers are electrically similar although not identical. The x axis amplifier has an additional unity gain phase inverter amplifier which corrects the beamsteerer's x axis deflection phase to that of the receiver sensor.

Major circuits contained in the beamsteerer drive amplifier are:

- Summing preamplifier
- Low pass filter
- Power drive amplifier
- Strain gauge sensor amplifier
- Differential amplifier
- Temperature compensation amplifier

Signal processing amplifiers are TO-5 can-type integrated circuit amplifiers. Beamsteerer signal amplification and drive is provided by transistor amplifiers. An operational description of the beamsteering drive amplification is as follows:

A beamsteering deflection drive signal voltage, at a transfer ratio of one volt per degree, is applied to the summing preamplifier. The preamplifier is driven by two sources, the input drive signal and the output of a summing differential amplifier. The differential amplifier's main function is to provide an additional transient drive voltage used to improve the amplifiers - step response - characteristics. Both input drive voltage and mirror position strain gauge voltages are applied to the differential amplifier. The differential amplifier senses a difference between the input drive voltage and the mirror position as sensed by the strain gauges. During the period of imbalance between a change in input voltage and mirror position response, the differential amplifier adds a voltage to the preamplifier which augments the initial drive signal. The combined effect is to increase the beamsteerer's transient or step function response. The bandpass characteristics of both the preamplifier and differential amplifier have been tailored to prevent overdriving the piezoelectric deflector at its resonant frequency. Voltage from the preamplifier is subsequently applied to the transistorized power amplifier. The high voltage power amplifier drives the piezoelectric effective .25 mfd load between voltage limits of \pm 500 volts. The resulting mirror motion is

sensed by attached strain gauges, amplified and applied to the differential amplifier as aforementioned. When the input drive voltage is balanced by the strain gauge voltage (at the differential amplifier input), transient drive voltage diminishes to zero and the mirror position becomes static.

Early testing of the beamsteering assembly revealed the existence of a beam position drift, which is related to temperature change. (See Figure 7-9.) Temperature changes which affected mirror position not sensed by the respective strain gauge sensors were subsequently corrected for by the addition of temperature-compensation circuitry. Drive, strain gauge, temperature compensation, and beam positioning voltages are all summed at the differential amplifier's input terminals. Auxiliary beam positioning controls are also mounted in the beamsteerer housing.

7-29

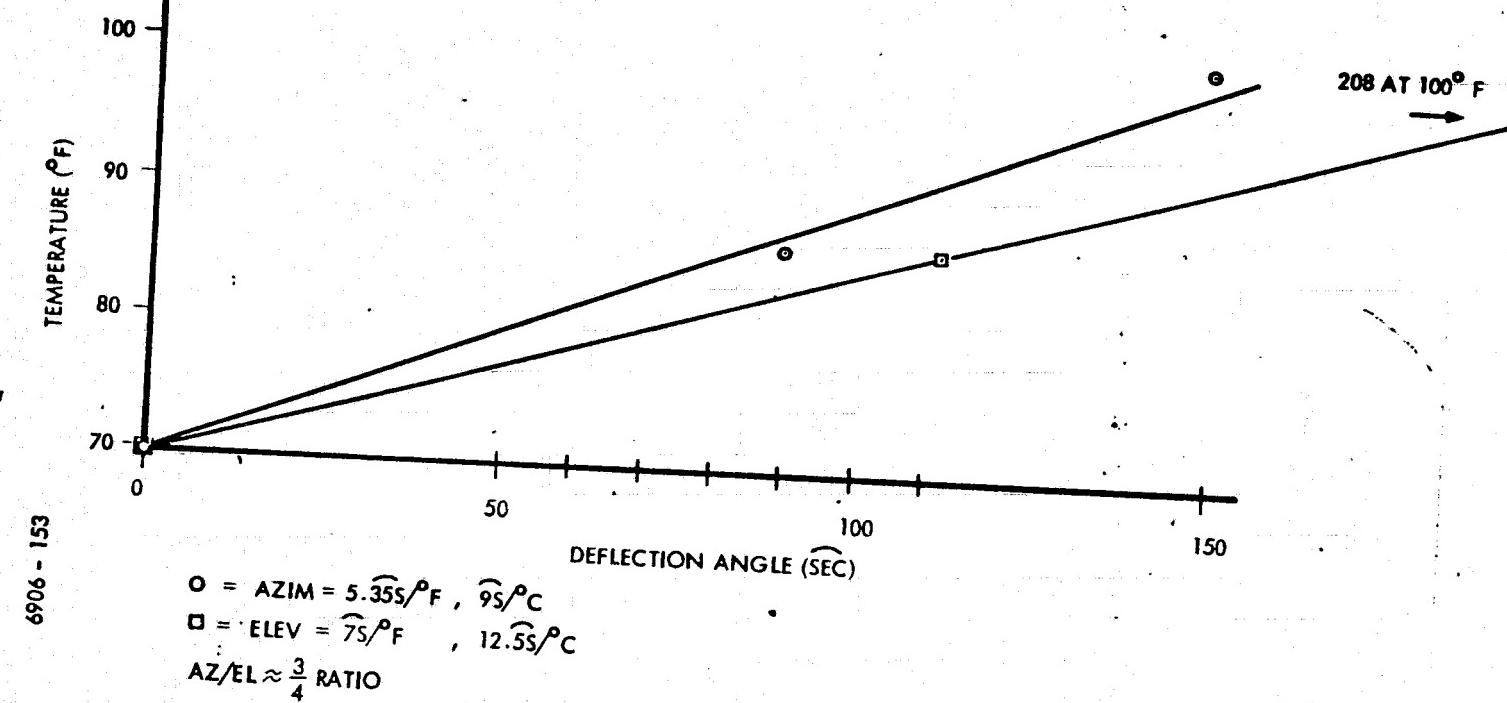
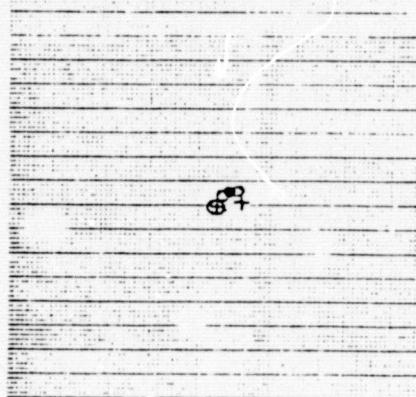
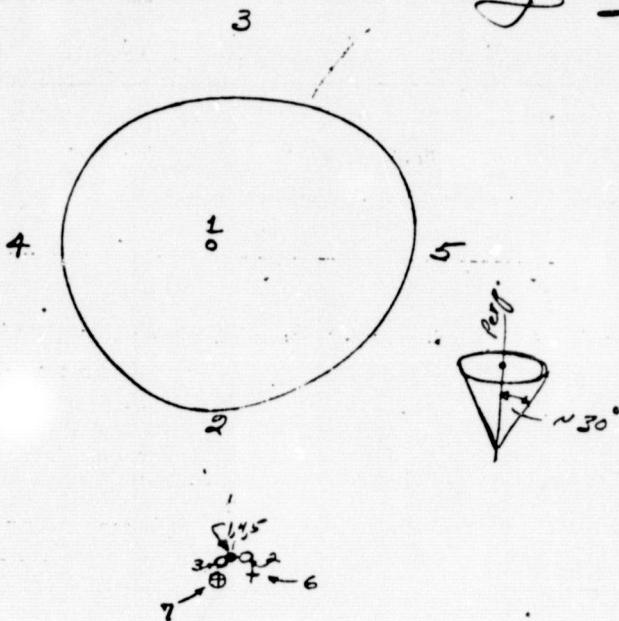


Figure 7-9. Beam Deflector Angle Vs Temperature

7.2.5 Transmitter Optics. - The transmitter optical system is rigidly mounted to the beamsteerer housing to form a compact modular optical unit. The optical path is folded 180° to facilitate packaging compactness. Excellent mechanical rigidity is obtained by the use of cylindrical supporting arms used to attach the input and output optics to the beam steerer housing. During system testing however, a transmitter beam motion was observed. As the GBAA was being operated in a static (non-tracking) boresighted mode, the transmitter beam was positioned on a target fixed to the transmitter mainframe. The gimballed telescope mount was then driven to impart a conical rotation of the transmitter assembly of approximately 30° off verticle. A plot of the transmitter beam position was recorded on the fixed target, at various angular positions. A transmitter beam wander of approximately two beam diameters ($\pm 0.1^\circ$) was noted (see Figure 7-10, Transmitter Beam Stability test). A program was henceforth initiated to rigidize the entire transmitter assembly consisting of the laser, beam steerer, receiver sensor and mounting plate mainframe. Subsequent tests revealed a reduction in beam motion, however, the primary motion source was later found to be a loose optics supporting cylinder within the input optics arm. The loose assembly was that of a cylindrical lens assembly, threaded for optical adjustment,

9-22-71
Ron George
R. George



Mirror defl. magnification by o.p. lens $\approx x9$.

Laser

10mm input lens

12mm lens

15mm lens

13mm lens

35mm lens

Target fixed to main frame

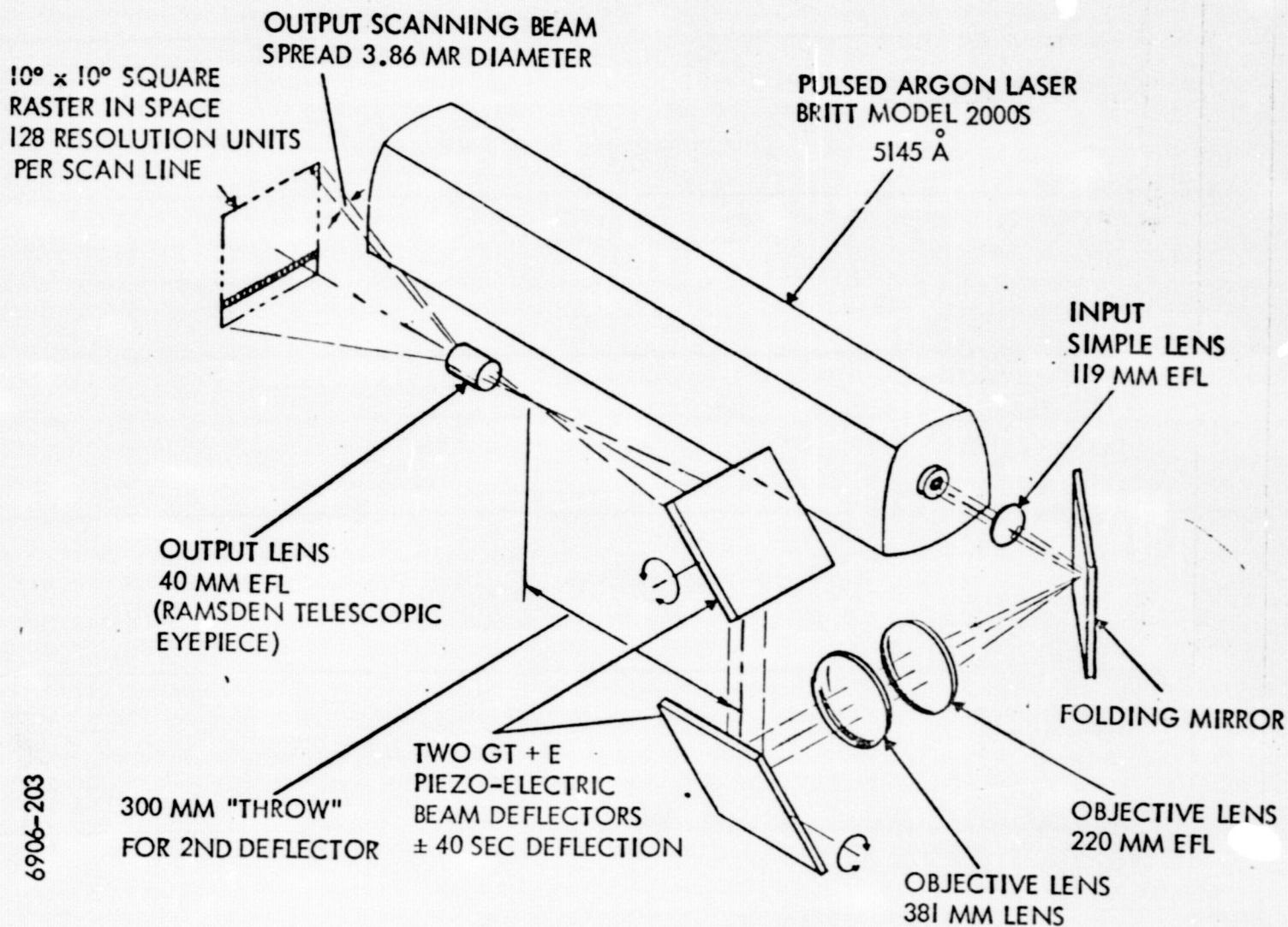
For simplicity - opt. sys. shown unfolded.
Dimensions are approx

Figure 7-10. GBAA Transmit Beam Stability Test

mounted inside the optics support arm. The motion involved was that of a cylinder rolling within a cylinder. A single set screw had apparently been jarred loose or left loose from a previous lens adjustment. A second set screw was installed at right angles to the original and both screws tightened to preclude further mechanical shift.

Future tests revealed excellent pointing and tracking stability of the transmitter and receiver sensor during actual air-craft tracking operation.

The transmitter beam steering and optics package is shown in Figure 7-11.



6906-203

Figure 7-11. GBAA Transmitter Optics

7.3 Receiver Subsystem

The general system block diagram is again used to indicate the relationship of the receiver subsystem to the other elements in Figure 7-12.

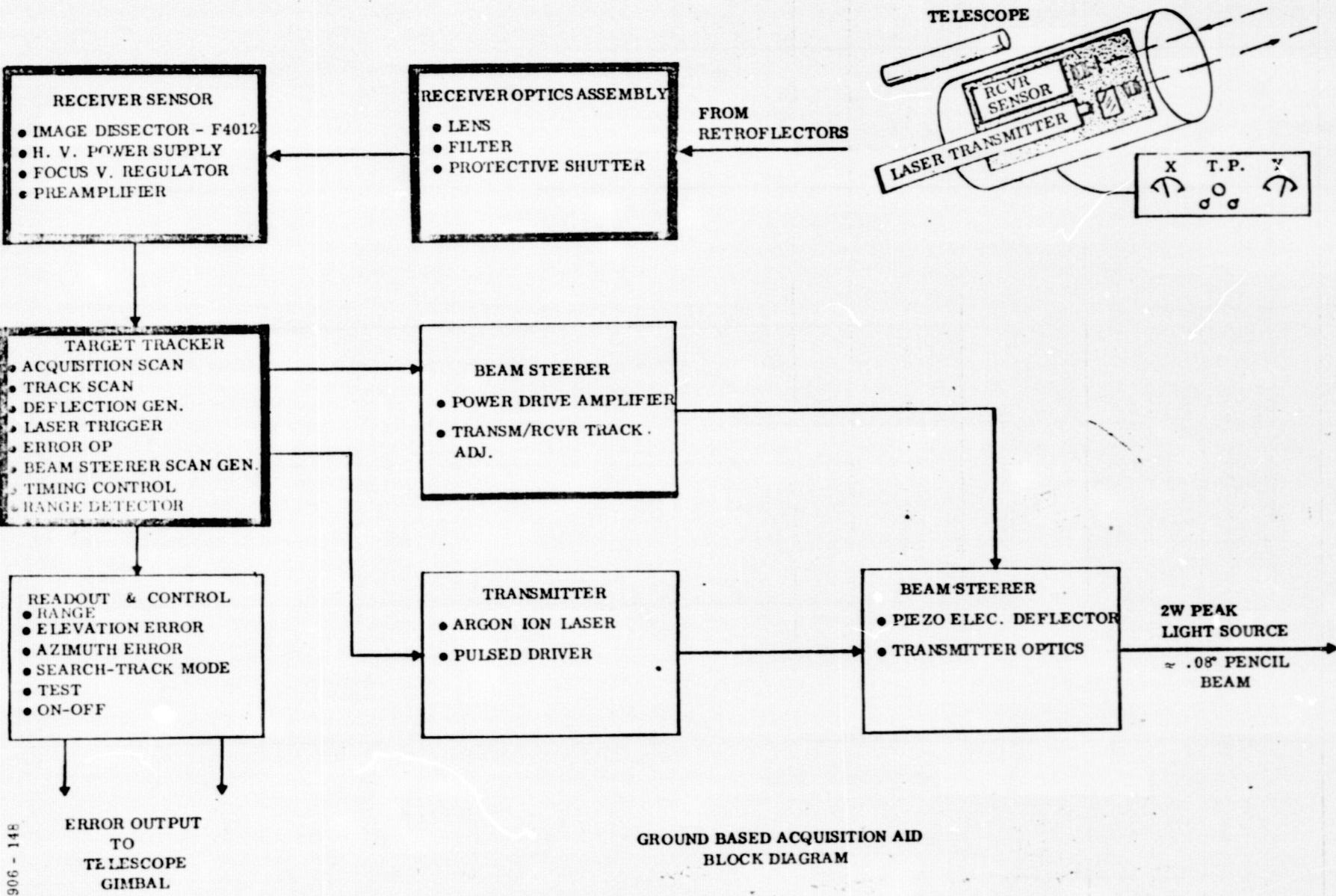


Figure 7-12. GBAA-Receiver

7.3.1 Receiver Sensor Optics. - The GBAA optical system consists of a high speed lens and spectral trimming filter. The lens is a De Old Delft, 65 mm f.1., f/0.75. The lens 21° total field-of-view more than adequately covers the GBAA 10° FOV requirement. The image size produced at the image dissector tube photo-cathode is determined by the angular field coverage and the lens focal length. With a lens focal length of 65 mm and a sensor field-of-view coverage of 10° square, the maximum image size as projected onto the photocathode of the image dissector tube is $0.448"$ square, with a maximum diagonal dimension of $0.634"$. This image size fits well within the image dissectors useful photocathode area diagonal dimension of $0.7"$.

The lens's only mechanical constraint is that its back focal length is adequate to provide clearance between the rear element support and the image dissector photo tube. This region is used to position the protective sun shutter blade.

The lens resolving characteristics are such as to produce a target image that falls within the image dissector's instantaneous photocathode dimension of $0.004"$ square. A modulation transfer function plot of the De Old Delft lens is shown in Figure 7-13.

Attached to the front of the lens is a $3.5"$ spectral trimming filter designed for maximum transmittance at the Argon Ion laser wavelength of

7-37

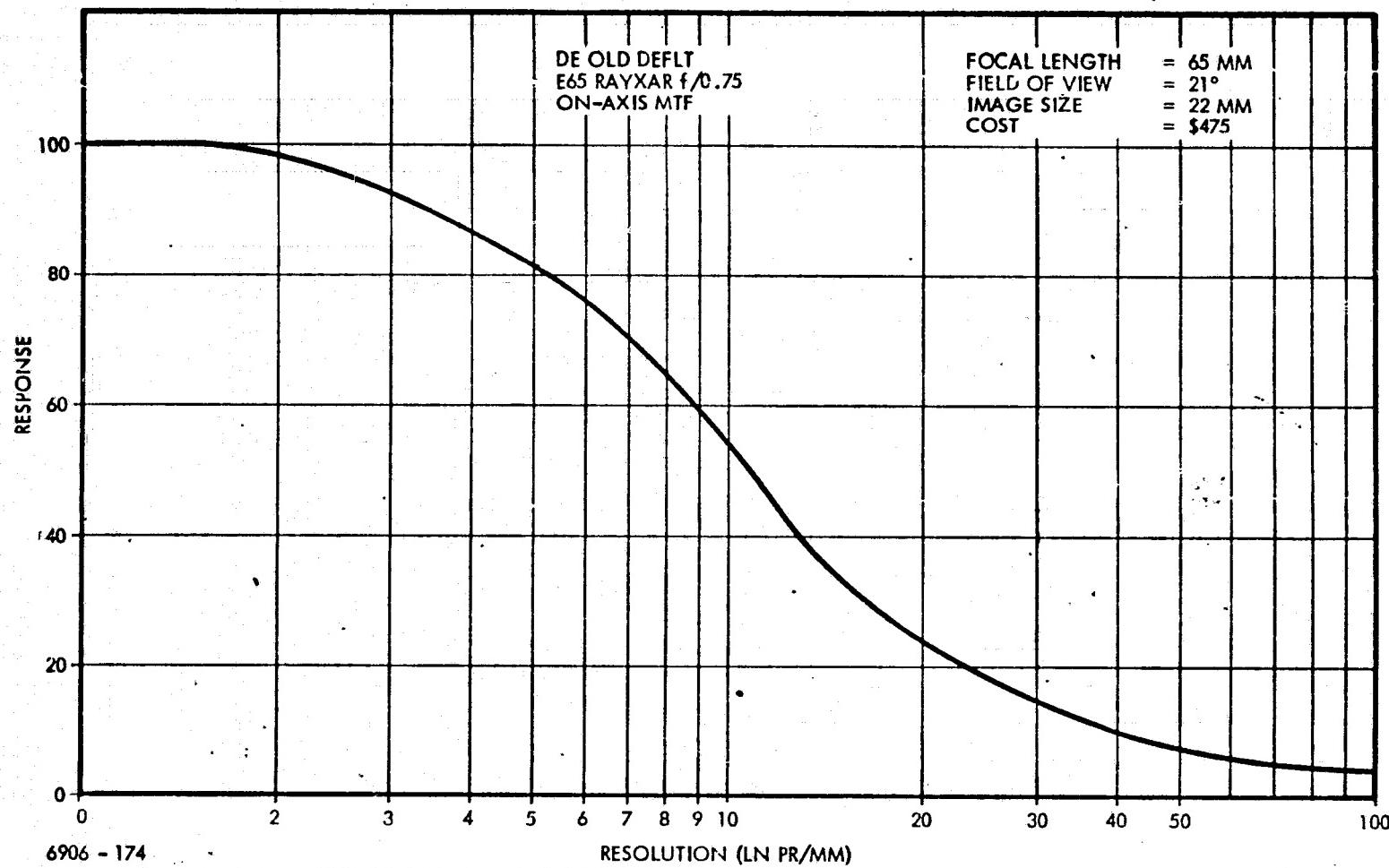


Figure 7-13. De Old Deflt E65 RAYXAR f/0.75 On-Axis MTF

.5145 microns. The on axis 3 db bandwidth is .002 microns. The maximum transmittance of 55% peaks at 5148.94 Ang. as shown in the spectral transmission curve of Figure 7-14. The filter is fabricated in the form of a glass sandwich.* Due to the cementing process, absolute flatness is no longer maintained. Local filter thickness variations result in minute optical aberrations. This condition requires that the filter rotation as mounted to the lens, be maintained consistent with that which occurred during sensor field mapping. Removal of the filter is made necessary due to the addition of a star tracking capability which is used to check the alignment and tracking of the GBAA to the communications telescope.

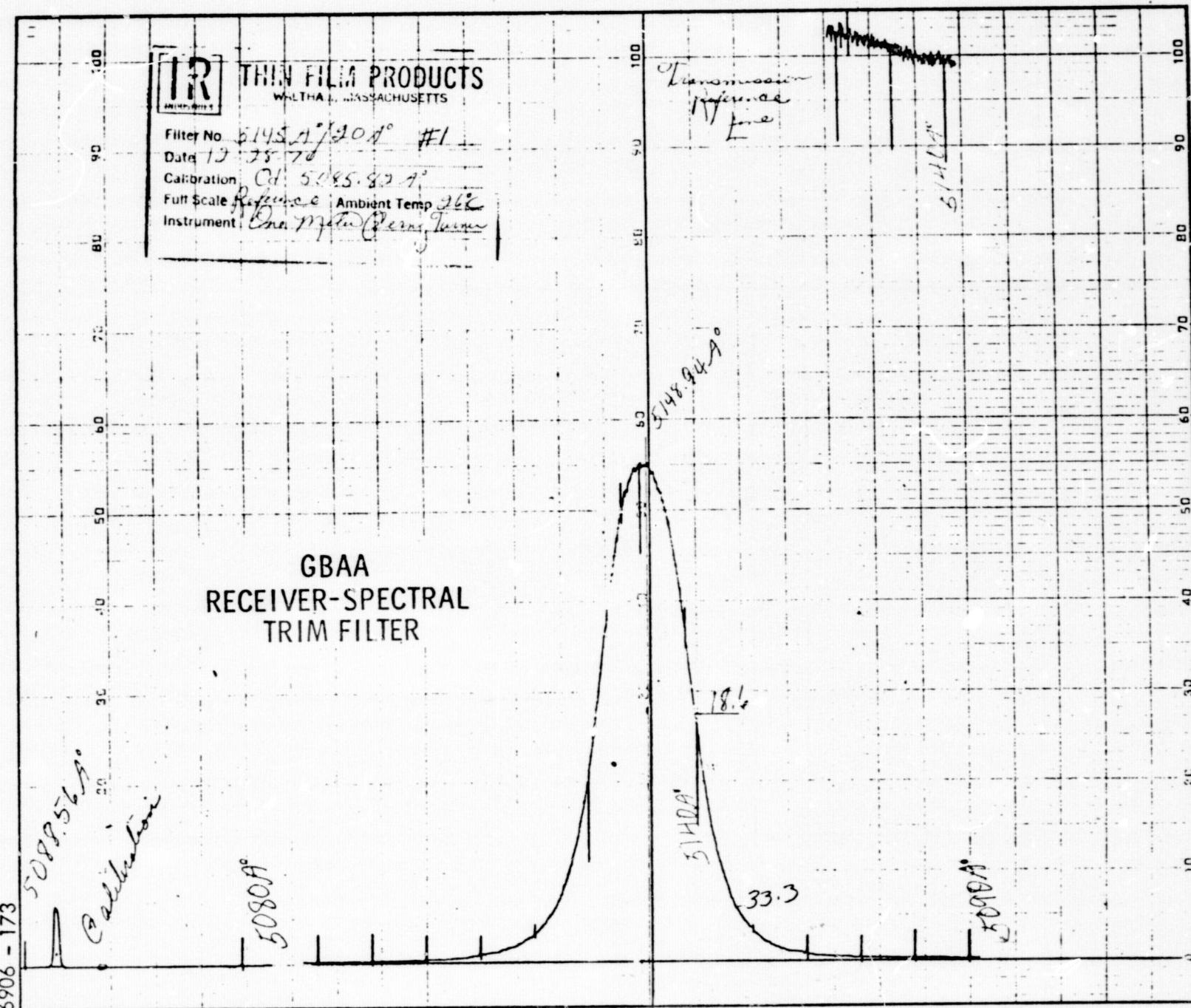


Figure 7-14. GBAA Receiver-Spectral Trim Filter

7.3.2 Detector-Image Dissector. - The heart of the GBAA receiver sensor is the photo detector. ITT image dissector photo sensors are used in a wide variety of tracking and camera applications. The photo sensor selected for use in the GBAA aircraft tracking application is the ITTL F-4012 remote processed image dissector tube, containing an S-20 photocathode, a 4 mil square internal limiting aperture and a nominal gain of 1×10^6 . The image dissector tube is used to analyze the total field-of-view (FOV) for the existence of a target, i.e., illumination of sensor by light reflected from the aircraft's cube corners. The unique characteristic of the image dissector tube is its capability of electro-optically sampling a very small area in its total FOV. Photon energy contained in the far field is optically focused onto the image dissector's photocathode. Photo current leaving the photocathode is magnetically focused and deflected past the dissector's internal limiting aperture. For any given deflection angle, only those electrons leaving a specific area of the photocathode will find their way through the limiting aperture. This area is defined by the projection of the limiting aperture onto the photocathode and is referred to as the instantaneous photocathode dimension (IPD). The IPD as projected by the optical system into the far field is referred to as the instantaneous field-of-view (IFOV). The IFOV, as produced by the 4 mil limiting aperture and the optical system, subtends a solid angle of 0.09° square. The IFOV is

magnetically deflected by the receiver electronics in a fan or fence pattern to search the 10° FOV. An overlapping step pattern is used to preclude missing the target. When the target is detected, the IFOV is deflected about the target in very small increments. This deflection is in the form of a cruciform pattern and is called TRACK SCAN. Deflection coil currents required to keep the IFOV centered about the target are a measure of the target's angular position relative to the optical boresight axis and are used to generate the Declination and Hour angle error output voltages. The error voltages are subsequently used to accurately align the communications telescope to the target aircraft.

Electrical and mechanical specifications of the image dissector used in the GBAA receiver sensor are shown in Appendix E, Vidissector-Image Dissector Test Data.

7.3.3 Sun Shutter. - Direct viewing of the sun or any other extremely bright source within the angular field of the receiver will damage its image dissector photosensor. To prevent this, a sun sensor and shutter system is described here. It is desirable in some applications to remove the high voltage from the tube in addition to closing the sun shutter as is done in the GBAA.

The thin metallic sun shutter is interposed when required between the lens and the tube face by the action of a small rotary solenoid. The tube is shielded from magnetic effects of the solenoid. The system is designed to be fail-safe. The shutter is spring-loaded to be normally in the closed position when the solenoid is not energized. The shutter will open when the GBAA is turned on, provided the sun sensor indicates the sun is not in the field of view.

A simple and small sun sensor is mounted on the receiver with its optical axis near and parallel to the GBAA axis. This sensor consists of a small photo-sensitive cell mounted within a short tube. Geometry of the assembly determines the angles through which the sun can illuminate the cell. As the output of the sun sensor rises above a present threshold, the associated circuitry triggers the closing of the sun shutter.

The sensor threshold level is set to trigger for sun positions within 30° of the optical axis. The shutter activation is latching and must be manually reset at the control unit for resumption of normal operation. The mechanical construction of the sun sensor is shown in Figure 7-15.

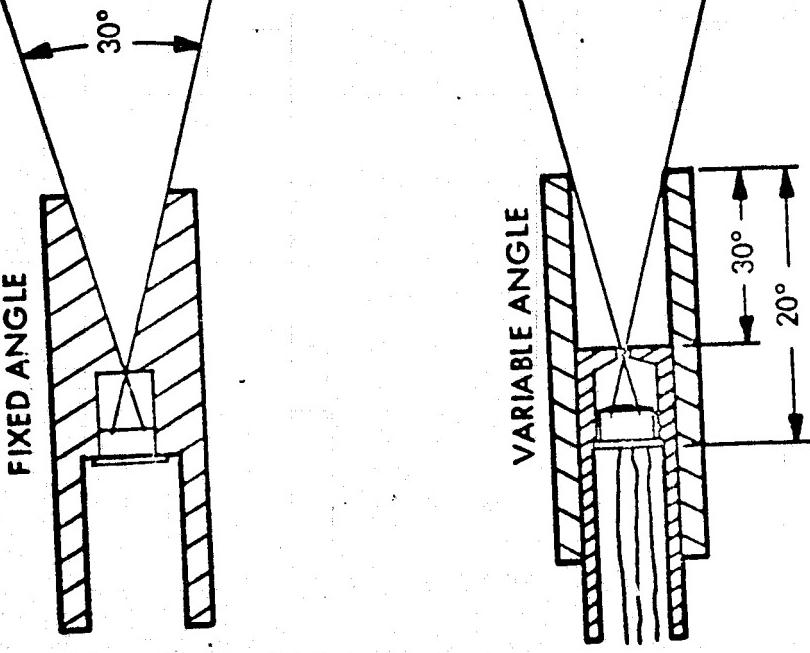


Figure 7-15. GBAA Sun Sensor Holder

6906-152

7.3.4 Ranging System. - The ranging system herein described is an add-on to the original contractual requirement of NAS8-20629. This inclusion of a ranging capability further enhances the versatility and usefulness of the GBAA as a data source. Both analog and digital range outputs provide aircraft position determination as a function of time, thereby aiding in the evaluation and correlation of atmospheric turbulence data.

Ranging characteristics are as follows:

1. Ranging granularity: 10 meters
2. Ranging accuracy: Better than 100 meters
3. Range: > 100,000 ft.
4. P.R.F.: 1 kHz
5. Transmit pulse width: 15 microseconds
6. Range smoothing: 32 samples
7. Range averaging time: 128 milliseconds
8. Range output: Visual display in kilometers
9. Range output for recording: Analog and Digital/Binary (12 bits)

The following ranging system is one which functions synchronously with the GBAA TRACK mode. It is unaffected by transmit pulse width or jitter and is desensitized to return signal fades. Gating is also used to optimize return signal characteristics. (See Figure 7-16.)

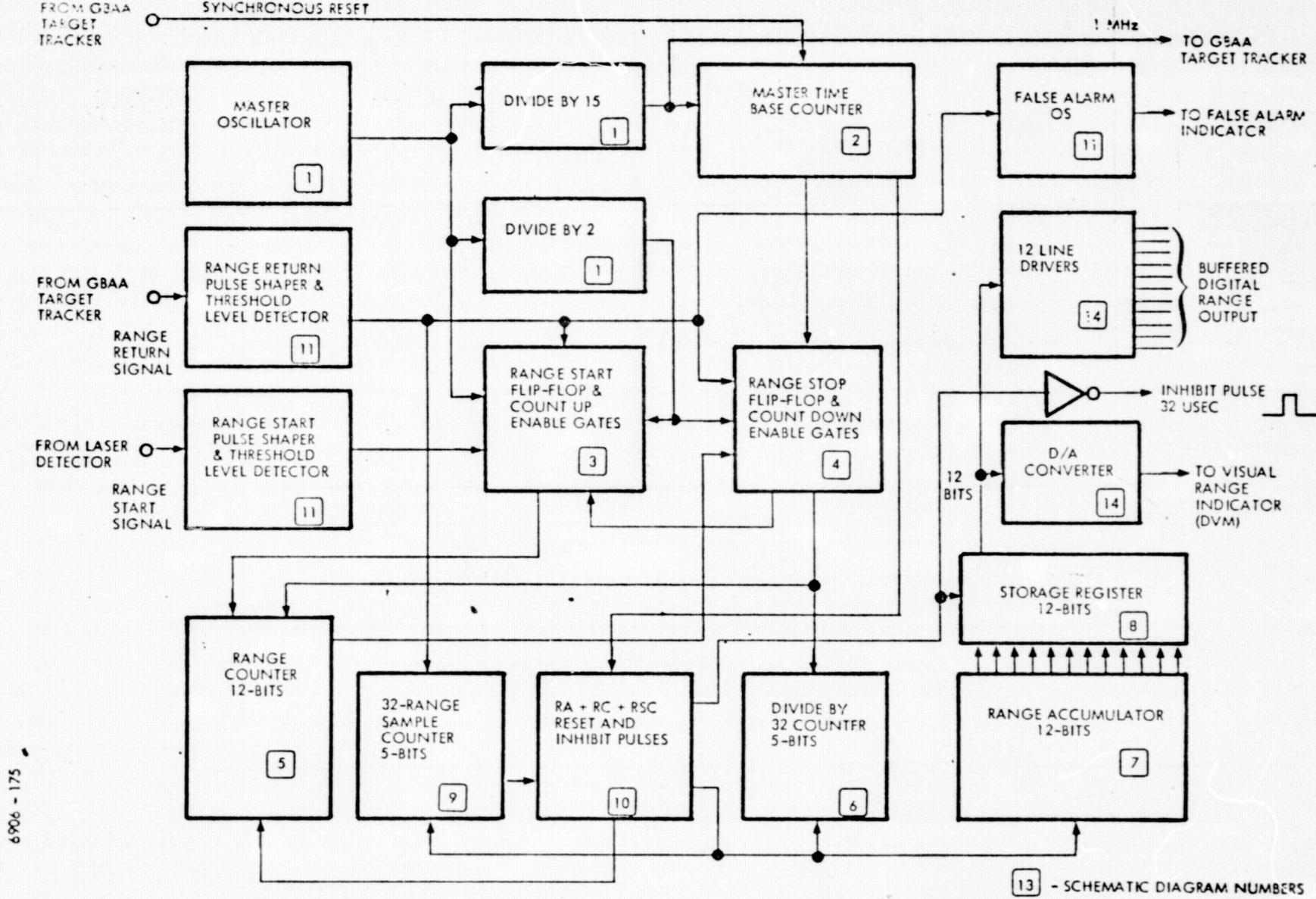


Figure 7-16. Ground Based Acquisition and Ranging System Block Diagram

Range is determined as a function of elapsed time between the center of the transmit pulse and the center of the return pulse. The pulse centers (in time) are determined by digitally measuring the width of each pulse and halving the result. Range measurement is therefore unaffected by laser pulse starting time or width variation. It is likewise unaffected by return pulse width variations due to scintillation but will be affected by pulse distortions.

If scintillation or noise should render the return pulse asymmetric, then the range readout will incur an error. To minimize this possibility, only those return pulses which occur when the GBAA track scan is closely centered on the target, are analyzed.

Major system circuits are:

1. Dual frequency clock
2. Transmit pulse sensor
3. Return signal discriminator/gate
4. Range counter
5. Range smoothing counter
6. Range accumulator
7. Storage register
8. Sample counter
9. Range digital to analog converter
10. Range readout

A typical ranging sequence is as follows:

The dual frequency clock pulse generator drives the range counter at a 15 mHz rate between the trailing edge of the transmit pulse and the leading edge of the return signal. The 15 mHz clock produces the basic 10 meter range granularity. The 7.5 mHz clock drives the range counter during the transmit and return pulse durations. This results in a range equivalent of one-half the transmit pulse plus one-half the return pulse. The total clock count is therefore the time equivalent of the range from the center of the transmit pulse to the center of the return pulse, in 10 meter increments.

The Range Counter is a binary UP/DN counter used to store individual range samples. It is driven by the aforementioned dual frequency clock for the period between transmit and return pulses. It is then DOWN counted as the Range Accumulator is simultaneously driven to accumulate 1/32 of the individual sample. The 5 bit smoothing counter is driven ahead of the range accumulator counter to provide the 32 sample smoothing. After 32 range samples have been accumulated, the count in the range accumulator is parallel transferred to a storage register. The register stores the binary equivalent range for each 32 sample period. The register outputs are connected to a 12 bit digital to analog converter. The converter output provides the voltage drive to the range buffer amplifiers. Two outputs are available with voltage to range transfer functions of 10 kilometers per volt and 4 kilometers per volt. The outputs are used to input both the external

computer and the visual display panel meter mounted in the control unit.

It is worth noting that only those range samples which occur during the first four steps of each cruciform scan lobe are used as range samples, and of those four, only those exceeding the return pulse discriminator threshold level are processed.

The range counter is cycled up and down at each transmit pulse.

In the absence of a return pulse the range smoothing counter is inhibited for that range sample period. When a return pulse is sensed, the smoothing counter is enabled and drives the range accumulator as the range counter is being down counted.

7.4 Control and Display

The GBAA control unit consists of a panel and chassis type unit in which all functional controls are housed. The unit is designed to mount in a standard 19" relay rack frame. All command controls and status monitors are mounted on the 7" x 19" front panel. Considerable design effort was exercised in producing a unit having a high degree of operational and testing flexibility while maintaining a basic simplicity for avoidance of operational error. Red/Green Go/no Go visual warning is incorporated in the control switching system to alert the operator of any control combination condition not required for normal operation.

The illuminated Power AC switch indicates a red TEST condition when the GBAA is initially energized and continuously thereafter until all control selectors have been set for normal operation. When the appropriate operating conditions have been selected, the Power AC indicator will switch to OPERATE green. Should the GBAA sensor be directed such as to intercept sun's rays, the sun shutter energizes and a red indicator will appear at the SHUTTER CLOSED push button. Conditions which allow normal tracking and ranging are as follows:

- 1. Power AC on.**
- 2. Tracker, beamsteerer and sensor power switches ON.**
- 3. Shutter open.**
- 4. Mode selector to OPERATE**

5. Readout Selector at RANGE
6. Scan selector - RASTER or FENCE, OFFSET or CENTER
7. Laser in OPERATE

Operating and test readout devices include:

1. A digital volt meter which provides readout of Target Range - in kilometers, elevation and azimuth errors - in degrees and tracker/ranging threshold levels - in volts.
2. A laser running time meter.
3. Declination and hour angle analog voltmeters

The declination and hour angle voltmeters are particularly useful during the transmitter-receiver aligning phase. Automatic meter sensitivity switching provides full scale sensitivities of 5° , 0.5° , 0.05° full scale with a minimum (low scale) resolution of $.002^{\circ}$ per division. The automatic switching provides the operator with - hands off - monitoring during the critical alignment phase.

The laser running time meter accumulates actual laser trigger time (as opposed to standby) and can be used as an aid in reference to a laser gas refill cycle schedule.

Dynamic operating mode status is indicated by three gallium phosphide light-emitting diodes positioned adjacent to the mode selector switch. Modes indicated are SEARCH, TRACK, and MINI SCAN.

Referring to the photograph of the GBAA control unit, Figure 7-17, the left hand row of push button switches are used to energize specific laser radar subsystems. The POWER AC switch is first energized. This operation distributes AC power to the +5 volts and ± 15 VDC power supplies as well as the laser transmitter and the cooling fan. The upper TRACKER pushbutton is next energized to distribute the low voltage DC power to the TARGET TRACKER and RANGING electronics. Operation of the BEAMSTEERER pushbutton energizes the ± 500 VDC supplies used to drive the piezoelectric beamsteerers. The SENSOR pushbutton applies high voltage (2 KV) to the receiver sensor image dissector tube. The SHUTTER OPEN switch has a momentary closure action and is normally energized when all other normal functions have been selected.

The right hand row of switches are used to select the type and field position of the required SEARCH scan.

Two rotary selector switches are located to the right and left of the center panel digital volt meter. The left hand switch selects the normal dynamic mode of operation when in the OPERATE position. Static mode, scan pattern tests are generated when TRACK or MINISCAN are selected. The READOUT SEL. switch provides a visual indication of TARGET RANGE (in kilometers) Elevation and Azimuth Angle Error outputs (in degrees) as well as sensor and ranging threshold voltages when in TEST.

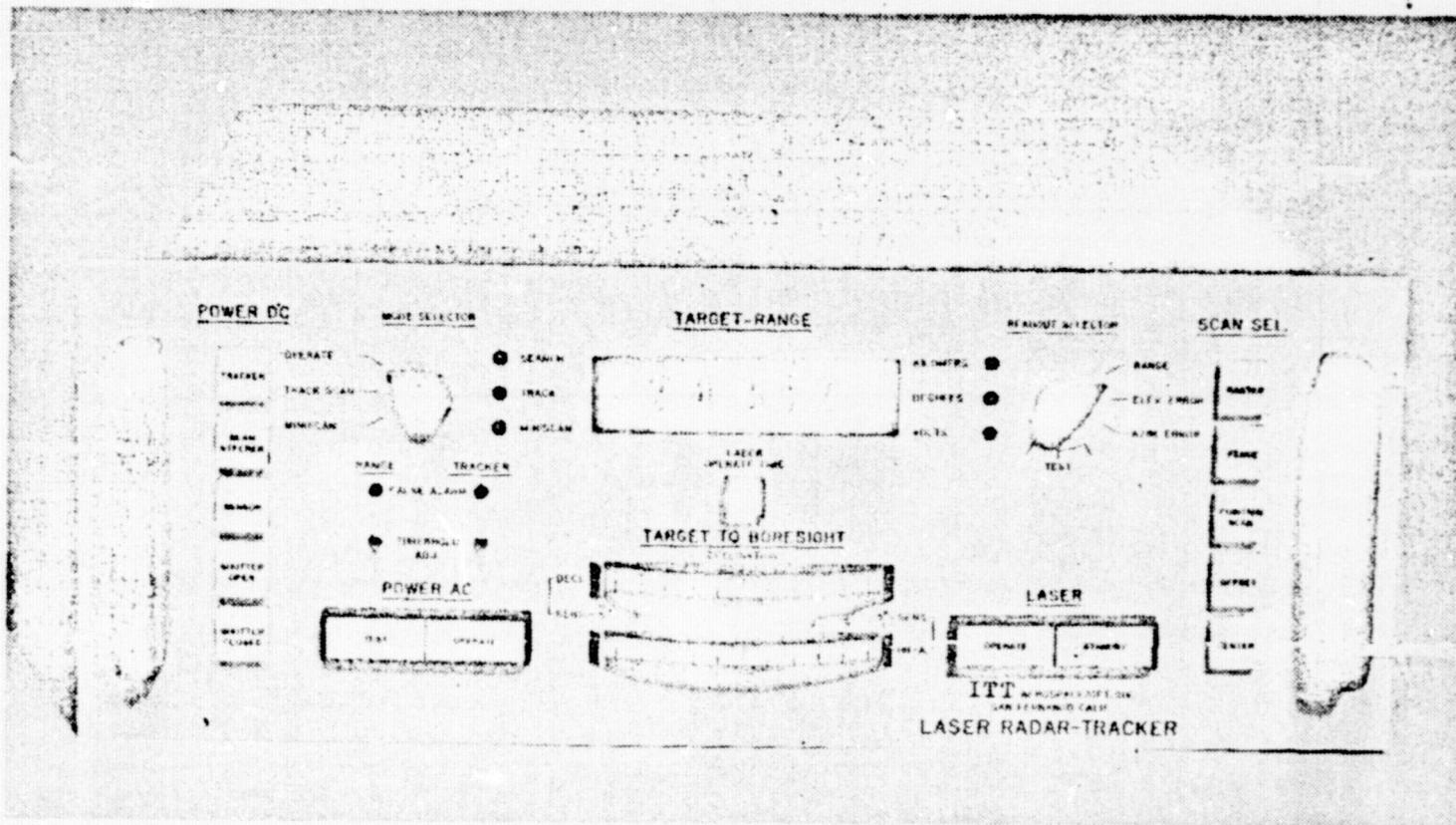


Figure 7-17. GBAA Control Unit

The TARGET to BORESIGHT analog meters readout tracking to boresight angle errors along the declination and hour angle axes. The meters have three scales of sensitivity - AUTOMATICALLY-switched between $\pm 5^\circ$, $\pm .5^\circ$ and $\pm .05^\circ$ full scale.

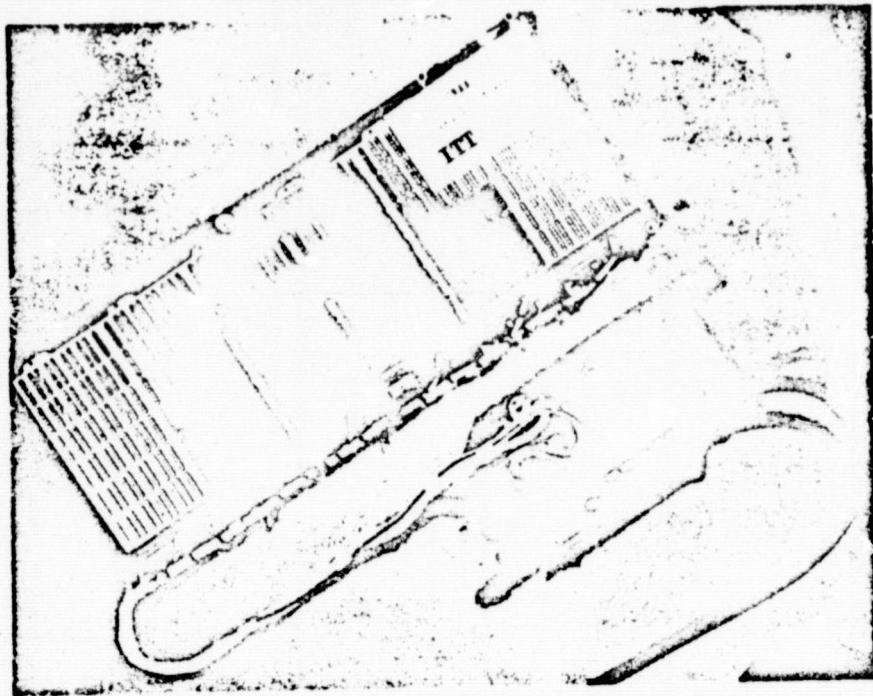
The LASER switch is operated in the red STANDBY mode awaiting approach of the target aircraft. Energizing the laser switch results in a green OPERATE mode coincident with triggering of the laser transmitter. A small running time meter is located immediately below the digital volt meter and is used to record actual laser trigger time.

Tracker and Ranging system threshold controls are located immediately above the power AC switch and can be adjusted by use of the adjacent visual false alarm indicators.

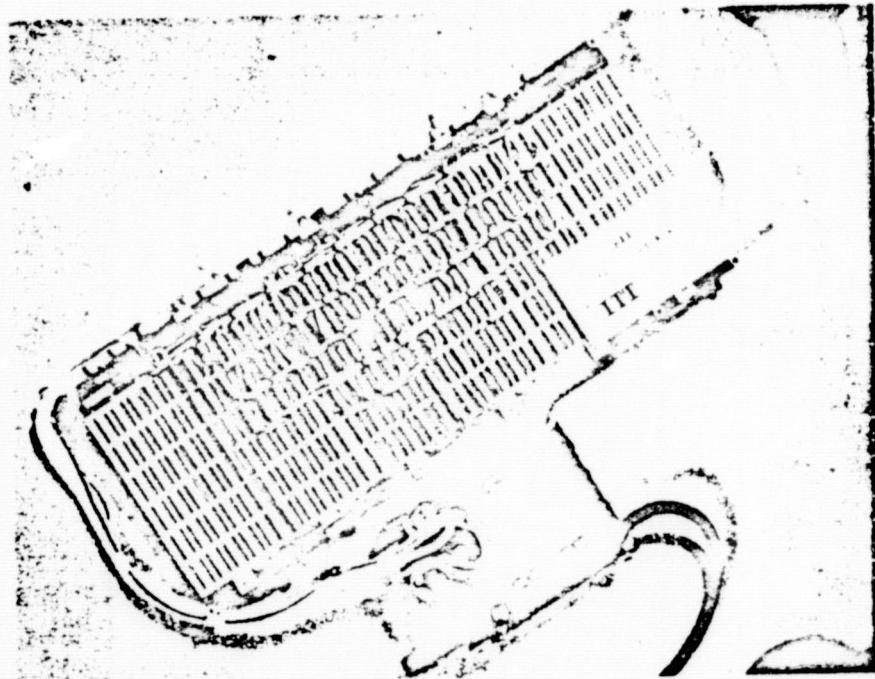
7.4.1 Signal Processing. - All signals for target tracking and ranging are processed within the control unit. All circuits are mounted in Augat type 8136-P integrated circuit chassis located at the bottom of the control unit. (See Figure 7-18.) Piano hinge mounting at the center of the control box provides accessibility to both wiring and component sides of the circuit boards. All socket interconnections are hard wired. Plug-in dual in line integrated circuit logic components are used throughout to facilitate ease of component test and replacement. Analog integrated circuit amplifiers and associated components are mounted on plug-in adapter sockets. Circuit board component and wiring sides are shown in the accompanying photographs.

Additional cooling for supplies and chassis components is provided for by a Rotron fan.

All signal and power connections are made at the control unit rear panel. Signal carrying connections are made with CONHEX subminiature connectors. Deutsch DM9600 series connectors are used to carry the sensor and beamsteerer deflection signals. Angle error and ranging signal outputs terminate in dual ELCO connectors. Power connections are made in standard 3 prong polarized cannon receptacles. An indicating type master fuse block is mounted immediately above the primary AC power connector. (See Figure 7-19.)



Component Side



Wiring Side

Figure 7-18. Target Tracker

6906 - 30

7-56

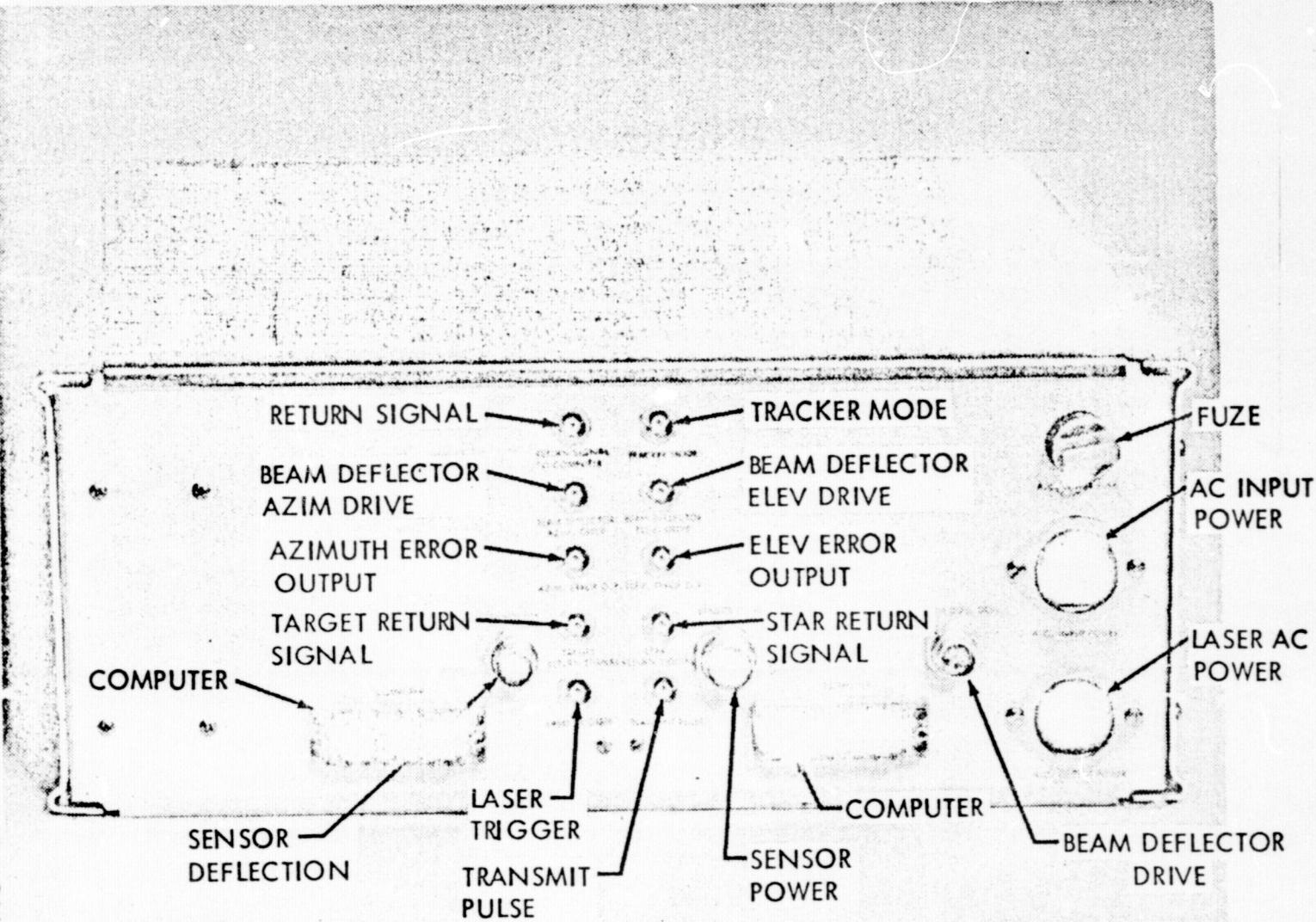


Figure 7-19. Ground Based Acquisition Aid (GBAA) Control Unit (Rear View)

7.5 GBAA Laser Radar Target Tracker

7.5.1 Start-Up and Operating Procedure. - To operate the tracker.

proceed as follows:

1. Operate the A. C. POWER switch. This energizes all dc power supplies and indicator lamps.
2. Operate the TRACKER switch. The TRACKER switch applies +5V and ± 15 Vdc to tracker logic, ranging system and transmitter and receiver amplifiers.
3. After a two to three minute warm-up period, the Britt Argon laser will automatically energize and be recognized audibly by the sound of the cooling fans. This warm-up cycle will repeat any time the ac power is interrupted. "Caution" is advised any time the laser is in operation. "NEVER" look directly into the laser beam." Refer to the laser manual for proper laser operation and maintenance.
4. All tracker functions should now be operable and individually selectable by the MODE SELECTOR switch. Cables may be tee connected to the beam deflector drive outputs (rear of electronics chassis) and connected to the respective horizontal and vertical inputs of an X-Y oscilloscope. The scope display may be used as visual verification of the proper operation of the mode selected. Proper operation of all drive modes should be obtained prior to application of power to the BEAM DEFLECTOR amplifier. A "first time" precaution can be obtained by selecting

boresight track scan mode. This is obtained by first selecting TRACK MODE then beam position center by momentarily depressing the CENTER pushbutton then the POSITION SCAN button (in and out). This set-up should produce a track scan centered at boresight. By attaching the removable metal target to the end of the laser bed, (mounted with a single 1/4 - 20 screw) operation of the beam deflector may be observed. Attenuation of the laser beam, by insertion of a 1.0 to 2.0 neutral density filter in the light path, may be desired for viewing ease.

5. Pressing the LASER OPERATE button should produce a green spot on the target in the vicinity of the pencilled square. If laser spot is not visible, check laser per instruction manual, until normal output is obtained. If spot is visible, depressing the BEAM DEFLECTOR button should cause a discernable wobble to the spot - this is Track Scan. Selecting a centered miniscan should produce a mini-field pattern 8 steps wide by 9 steps high ($\approx .4''$ sq.). Selection of FENCE & SEARCH will produce a single line scan of 128 step increments. RASTER-SEARCH will cause the 128 step line to search a $10^{\circ} \times 10^{\circ}$ field. ($\approx 6''$ sq.).
6. After all modes and scan patterns have been obtained, mutual alignment of the transmitter and receiver can be checked. Beam position should be observed on the portable target with the tracker at boresight (POSITION SCAN depressed). The tracker electronics should be stabilized in approximately 15 minutes. The laser transmitter and beam steering

system will have a slow migratory drift for a one to two hour period. The beam position error can be electrically compensated for by adjustment of the boresight controls on the front of the beam deflector amplifier chassis. First, the Britt laser wavelength selector X-Y controls should be adjusted to yield the brightest spot. Then, the boresight controls should be adjusted to center the beam in the target box.

7. Following the beam centering, the target may be removed. Full operation of the equipment may next be obtained by locating a passive target (such as a corner cube or group of cubes) at an approximate 2 mile range. Transmitter or receiver may require filter attenuation, at short range, to prevent receiver sensor overdrive. With SENSOR depressed and SHUTTER OPEN, the receiver is readied for normal operation. By depressing the RASTER SCAN button and selecting OPERATE, normal tracker operating mode should be indicated by all red lights out. Any red push button indicator remaining would indicate the equipment in the test mode only. With all green lights indicating system O, the mode should indicate SEARCH until the target is encountered at which time an automatic switch to track will occur. If the tracker threshold (front panel rt. hand pot) is set too sensitive, acquisition on noise pulses may occur. Normal adjustment is

made by cw rotation of theshold adjustment until acquisition just occurs on noise then backed off just slightly.

8. For daylight tracking, compensation for high background brightness may be desired. This is accomplished by adjustment of the left hand, front panel threshold control. This control varies the receiver preamplifier attenuation (manual gain control). Its voltage level can be read on the DVM by positioning the operate selector in the straight down (6 o'clock) position. Attenuation starts at about the 1 volt level. 1.25 volts produces a nominal 20 dB attenuation. This is usually adequate for horizon type daylight tracking. The DVM monitoring position one-step cw of the aforementioned position is used for all voltage test measurements which can be facilitated by use of the Q ball probe attached to the underside of the electronics chassis.
9. Test jacks have also been provided on the underside of the electronics chassis for monitoring tracker video, scope sync (track mode only) and discriminated range return.

7.6 Mechanical Configuration

The ground based acquisition aid is packaged in two separate units interconnected by power and control cables. Mounted as a unit on the optical communications telescope is the laser radar consisting of the laser transmitter, optical beam deflector and receiver sensor.

The unmounted laser radar and control unit is pictured in Figure 7-20.

The laser radar unit is cable connected to the control unit which is rack mounted at a location near the telescope computer control center. The control unit packaging is described in the receiver subsystem section.

A single "U" shaped channel mainframe is used as the main packaging platform. The receiver and beam steering assemblies are cantilever mounted to the side of the channel mainframe.

It should be noted that the receiver has been relocated subsequent to installation at the Madkin mountain site and is now located on the same side as the beam deflector assembly. The receiver modification was made to increase sensitivity by positioning it such as to intercept a more intense area of the reflected laser beam.

7-62

REPRODUCIBILITY OF THE
ORIGINAL, PAGE IS POOR

6906 - 28

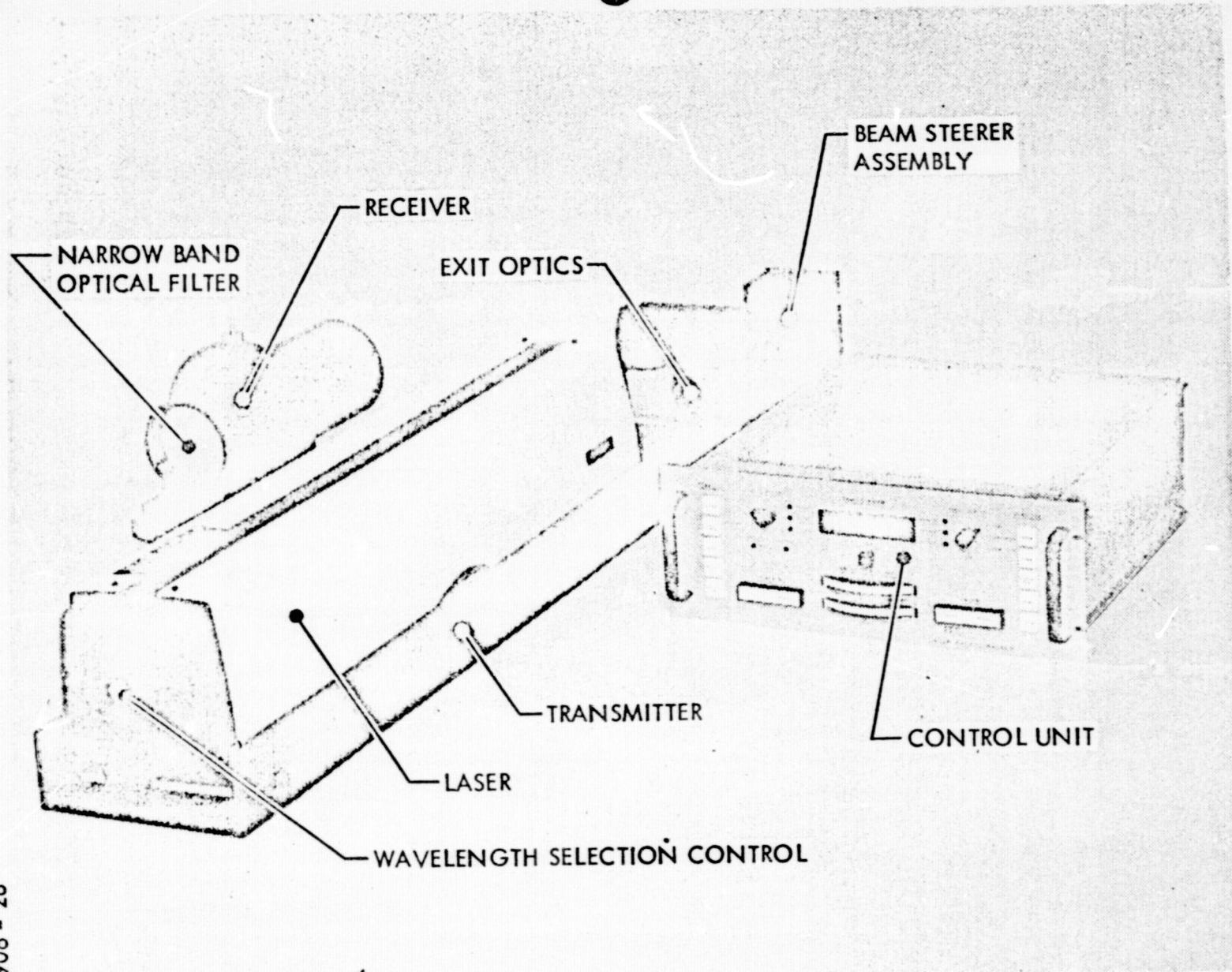


Figure 7-20. Ground Based Acquisition Aid (GBAA)

Modifications were made to the mainframe structure subsequent to preliminary testing. Early testing revealed a beam positioning instability coincident with a change in test bed platform orientation.

To eliminate any possible contribution of beam motion due to mechanical instability, the test bed mainframe was reinforced with a box type structure undergirding the entire U frame channel.

Additional supporting brackets were added to rigidize the transmitter input and output optics and the receiver sensor assembly. A brief description of the structural modifications is as follows.

7.6.1 Transmitter Test Bed - Structural Support Design. - The design approach was based on the fact that several units, laser beamsteerer, and receiver, were to be mounted individually on a mount system of sufficient rigidity to maintain inter-unit alignment in spite of overall system orientation throughout the tracking sequence.

Consequently, the structural mechanical mount was configured to provide rigidity; overall system deflections in the area of .0002 to .001 maximum when inverting or reorientating the system in a worst case condition. This was accomplished with a base mount constructed as follows. The basic structure is a 9" wide, 6" deep by 53" long box beam containing the basic telescope mount hole pattern. The box beam is built of 1/4" and

3/8" plates with **1/4"** shear panels as required with the top and bottom plates
(3/8) machined for flatness and parallelism. A second structural member,
a 9" x 53" long channel machined flat is attached to the box beam and contains
the appropriate attach bracketry for mounting and alignment of the laser
unit. This channel is fastened to the box beam in such a manner as to obtain
an overall box beam - channel composite structure. Next, two angle bracket
structural units are intertied to the box beam-channel assembly at required
locations to provide the necessary beamsteerer and receiver mount surfaces.
Inter related alignment set screws and bracket-saddle-strapping are provided
to stabilize the beamsteerer telescopic tube structure and the receiver container
for required alignment and overall unit stiffness.

The overall structural mechanical assembly is relatively simple in
concept but is of sufficient size structurally and configured mechanically to
achieve the required mounting configuration and overall laser optical align-
ments.

7.6.2 Telescope Interface. - The GBAA transmitter/receiver package is mounted to the 24" communications telescope main barrel. The telescope mounting surface consists of three raised pads or bosses. The bosses are located in a triangular arrangement. The boss at the apex of the triangle formation acts as the pivot point, about which, hour angle adjustment is made. The adjustment is made by use of a slotted interface bracket which couples the GBAA to the two remaining bosses and declination adjustment is made by shimming the adjustable mounting bracket. Figure 7-21 shows the laser radar telescope mounting interface prior to the addition of the box beam support.

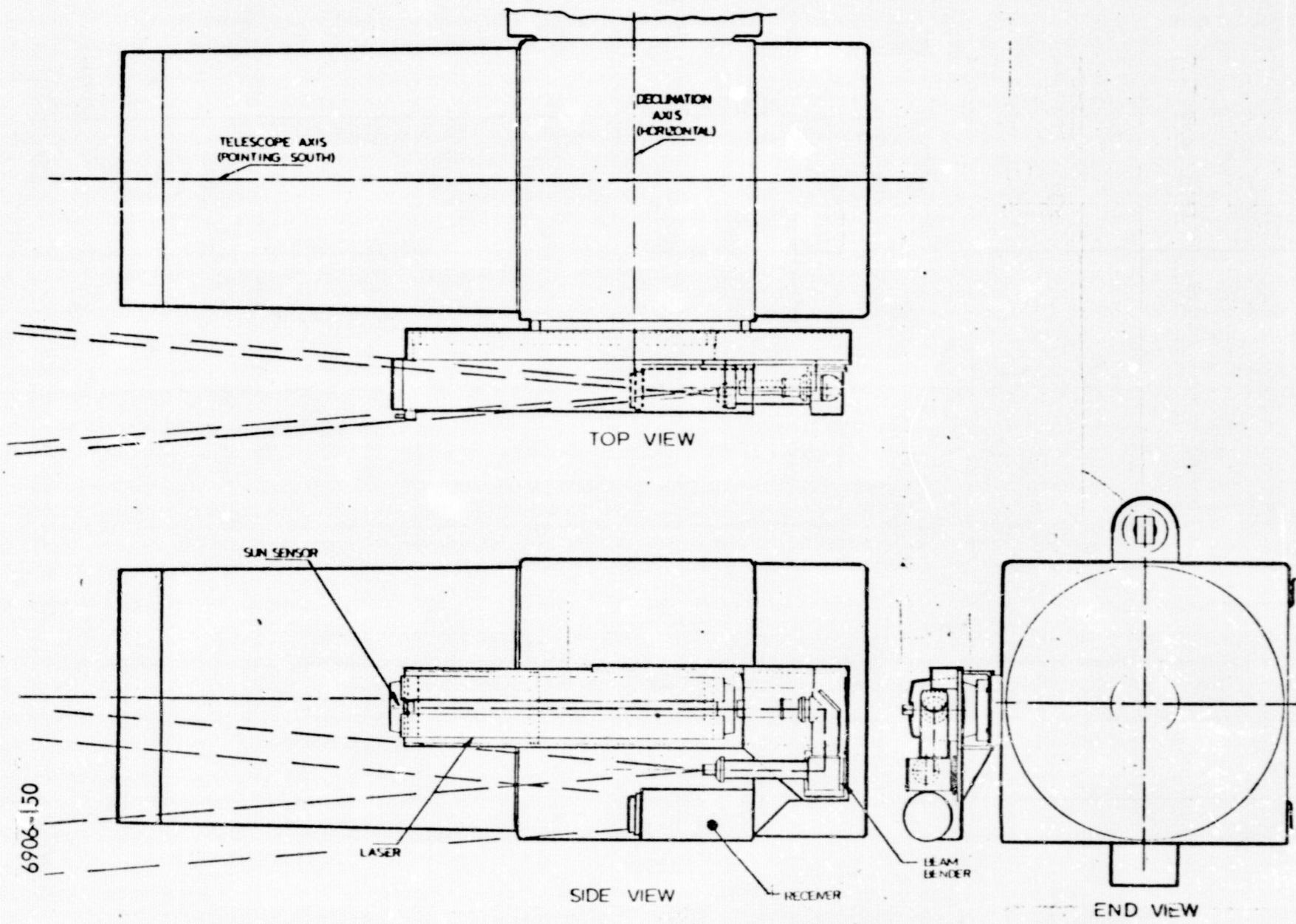


Figure 7-21. Mechanical Layout and Telescope Interface.

7.7 System Alignment and Calibration Test

The step-by-step procedure used to mutually align the GBAA transmitter and receiver is as follows:

Transmitter-Receiver BORESIGHT alignment setup - GBAA ON,
Position Scan, beam steerer ON, beam at BORESIGHT.

1. Attach the target plate to the GBAA test bed. This is used as a visual aid in aligning the transmitter beam to the test bed.
2. Mechanically position the laser such that its output beam enters the center of the beam steerer input optics.
3. Align laser to obtain beam at output optics, parallel to laser housing or to previously established target position if available.

NOTE: Laser horizontal adjustment moves output beam vertically and vertical adjustment moves the output beam horizontally - due to inversion through the beam steerer.

4. Release POSITION SCAN and select RASTER. Observe the $10^\circ \times 10^\circ$ full field raster scan to assure clearance of test bed.

5. Disconnect and terminate (100 Ω) the beam steerer input terminals. This is needed to immobilize the transmitter beam as positioned on a far field target, while allowing the receiver sensor to search.
 6. Position a reflective target, i.e., cube corner, at a convenient range (2 to 5 miles) and manually position the undeflected transmitter beam to the target.
- NOTE: Night time alignment operation vastly aids in the visual identification of the laser return beam.
7. Allow the receiver sensor to ACQUIRE and TRACK the target. The Declination and Hour Angle error outputs now indicate the misalignment between transmitter and receiver.
 8. While tracking the target, adjust the receiver sensor in elevation and azimuth to reduce to zero, the declination and hour angle error readouts. Accomplishing the above will result in the mutual, or boresight alignment of the transmitter and receiver.
 9. Reconnect the Beam Steerer input drives and lock the sensor adjusting screws. While monitoring the track video output signal, adjust the beam steerer Fine

Centering adjustments to obtain a balanced, elevation
and azimuth track scan output.

NOTE: During alignment procedures the return
signal amplitude should be attenuated such
that signal peaks can be observed.

Transmitter-Receiver ROLL Alignment. - Roll alignment is checked
in the AUTO/TRACK mode. The return signal is attenuated such that
the track video peaks can be monitored.

1. Rotate the GBAA test bed along one axis (plus and minus
from boresight), to produce an effective target motion
in declination or hour angle while monitoring the track
video signal. A degradation of the track video signal
occurs when misalignment exists in either ROLL or
deflection sensitivity between transmitter and receiver.

Roll alignment is most easily checked by nudging the
transmitter output optics in a direction to obtain a signal
improvement. When an improvement in signal return
is observed the sensor is then adjusted in roll to opti-
mize the signal return.

2. After each roll adjustment of the receiver sensor,
alignment should be rechecked at boresight.

7.7.1 Deflection Sensitivity Adjust. - The receiver deflection sensitivity is electronically set during fabrication and is therefore nonadjustable.

The beam deflector sensitivity is therefore adjusted to produce far field tracking between transmitter and receiver.

1. Generate effective target motion above and below and/or to the right and left of the target as described in the ROLL alignment. When video signal degradation is observed, vary the beam steerer gain of the appropriate axis. Increase or decrease the gain until signal amplitude is restored.
2. Check opposite angle from boresight and readjust.
3. Repeat 1 and 2 above to optimize transmitter and receiver alignment over the $10^\circ \times 10^\circ$ field of view. Transmitter and receiver alignment is now complete.

7.7.2 Calibration Test. - Declination and Hour angle outputs were calibrated using a LEITZ rotary table with which to generate very precise target angles (± 1 arc sec.). Final deflection and readout sensitivities are adjusted to the corresponding LEITZ table angular setting while target tracking in the AUTO TRACK mode. Both analog and digital angle error outputs are adjusted to a gradient of 1.0 volt per degree.

A range calibration adjustment is available in the Control Unit, however, due to the lack of a fixed target of known range, no absolute range calibration was made prior to equipment delivery.

8. SYSTEM INTEGRATION AND TEST

8.1 Introduction

The purpose of this section is to describe the interface between ITTG-delivered equipment and other GFE items, and to discuss the ITTG participants in the flight operations. ITTG technical personnel have been closely associated with the flight and ground equipment operations throughout the program, including equipment integration and test, field support of flight operation, and data review.

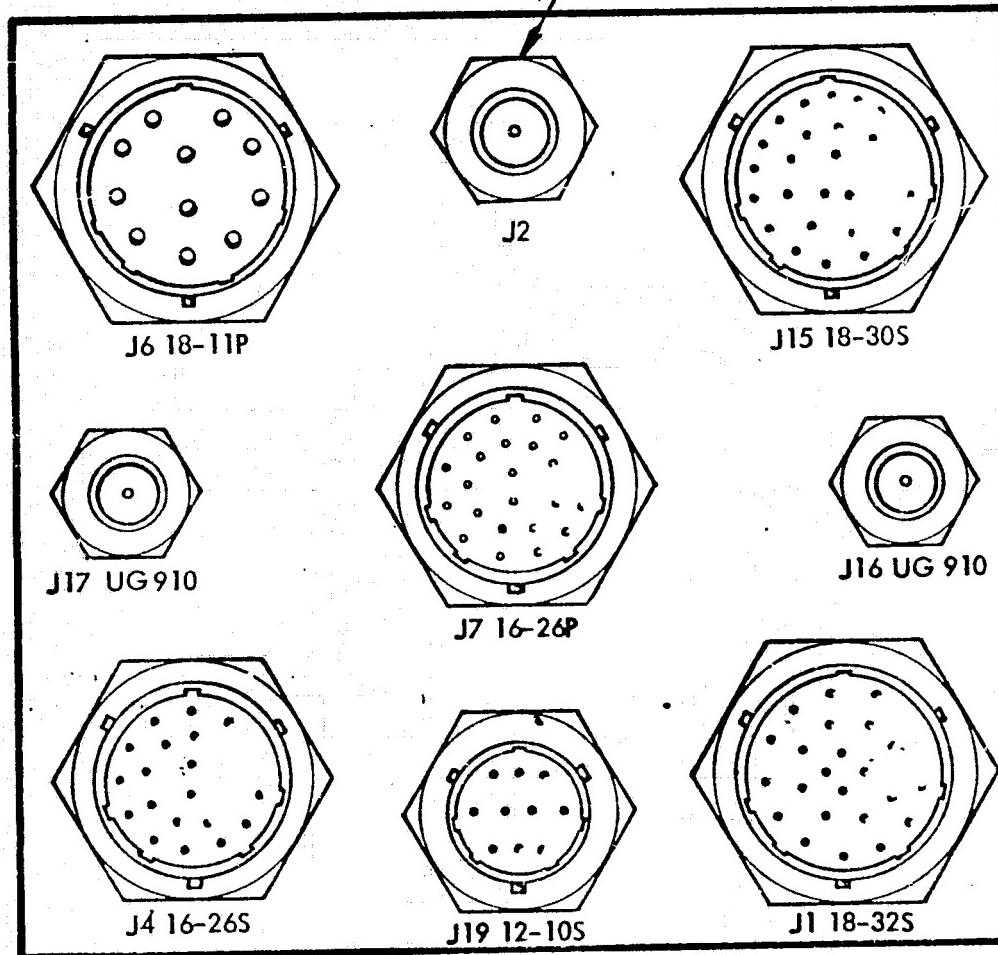
8.2 Interface

Detailed interface data (mechanical, electrical, cabling, etc.) and flight checkout operation procedures will not be incorporated in this final report. The interface data appears in the previously submitted interface control document prepared jointly by ITTG and CCSD. However, the locations of the interface connector plate with identifying connector numbers is shown in Figure 8-1.

The AOCP may be operated without being connected to the other Aircraft Equipment (power supplies, computer, etc.) by using a laboratory-type 28 VDC power supply, and a 117 VAC source. A power cable is supplied with the AOCP for this purpose so that lab test evaluation can be carried out independent of other equipment. Additional test cables have been provided to permit measurement and display of tracking signals, status signals, etc. Usually, for most tests, the Ground Checkout Equipment (GCE) is used with the AOCP. Operation of the GCE with the AOCP is described in the GCE Operation and Maintenance Manual.

19 - 999

REPRODUCIBILITY OF THE
ORIGINAL PAGE IS POOR



LASER POWER CABLE

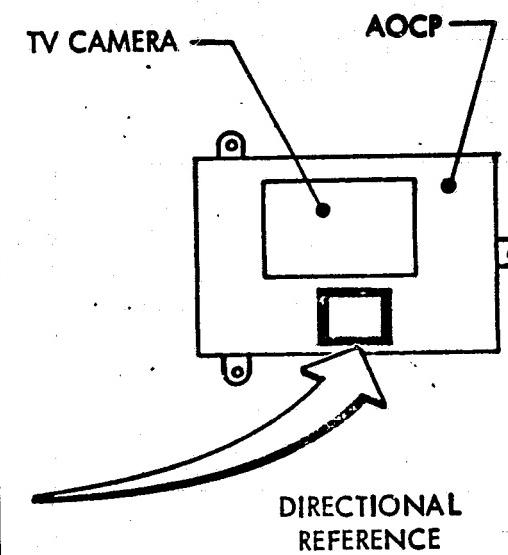


Figure 8-1. AOCP Connector Location

For actual flight tests and preflight checks, the AOCP is interconnected with the CCSD Aircraft and Ground Support Equipment (GSE), including the computer, data recorders, etc.

8.2.1 AOCP Interface with CCSD Platform. - The initial integration of the ACCP integration contractor facility (NASA/Mischoud Facility, Louisiana). This initial integration went extremely smooth by virtue of a very detailed IDC. After initial static alignment and functional tests were made on the integrated system with only minor adjustments in the control loop interface gains, etc., the dynamic tests began. The dynamic tests involved shaking of the AOCP and support frame containing the coarse steering mirror in an attempt to simulate (a yet undefined) aircraft environment. These dynamic tests uncovered several problems involving the tracking rate of the AOCP and various coarse gimballed mirror and support frame resonances. At this point, the two contractors (ITTG and CCSD) approached their equipment problems separately to improve performance in the dynamic environment. Detailed reports are available on this phase of the program and will not be repeated herein. Suffice it to say that substantial improvements were made in both ITTG and CCSD equipments and further quantitative tests of the integrated system in a more accurately simulated flight environment resulted in acceptable dynamic performance.

8.3 MSFC Field Tests

This section presents some data taken on the integrated AVLOC system at NASA/MSFC with the Madkin Mountain Ground Station. Some extensive tests were made of the AOCP controls subsystem at MSFC to improve the performance of the tracking and pointing required as a result of experiencing scintillation effects in the real atmospheric environment and obtaining a better knowledge of the aircraft platform vibration environment.

The MSFC field test range, illustrated in Figure 8-2, is between the Artrionics Laboratory (Bldg. 4487) and the Madkin Mountain Ground Station complex. During early tests over this range, the AOCP unit had difficulty maintaining lock-on with the ground terminal beacon and particularly when the atmospheric scintillation induced signal modes were deep and high in frequency (50 db, 100 Hz).

During initial field test between the Astrionics Laboratory and Madkin Mountain, apparent angular modulation was experienced which was excessive in both amplitude and frequency. Because of this effect it was difficult to close the beamsteerer loop and only intermittent tracking was possible with the ID tracker. This apparent angular modulation was traced to amplitude scintillation

8-5

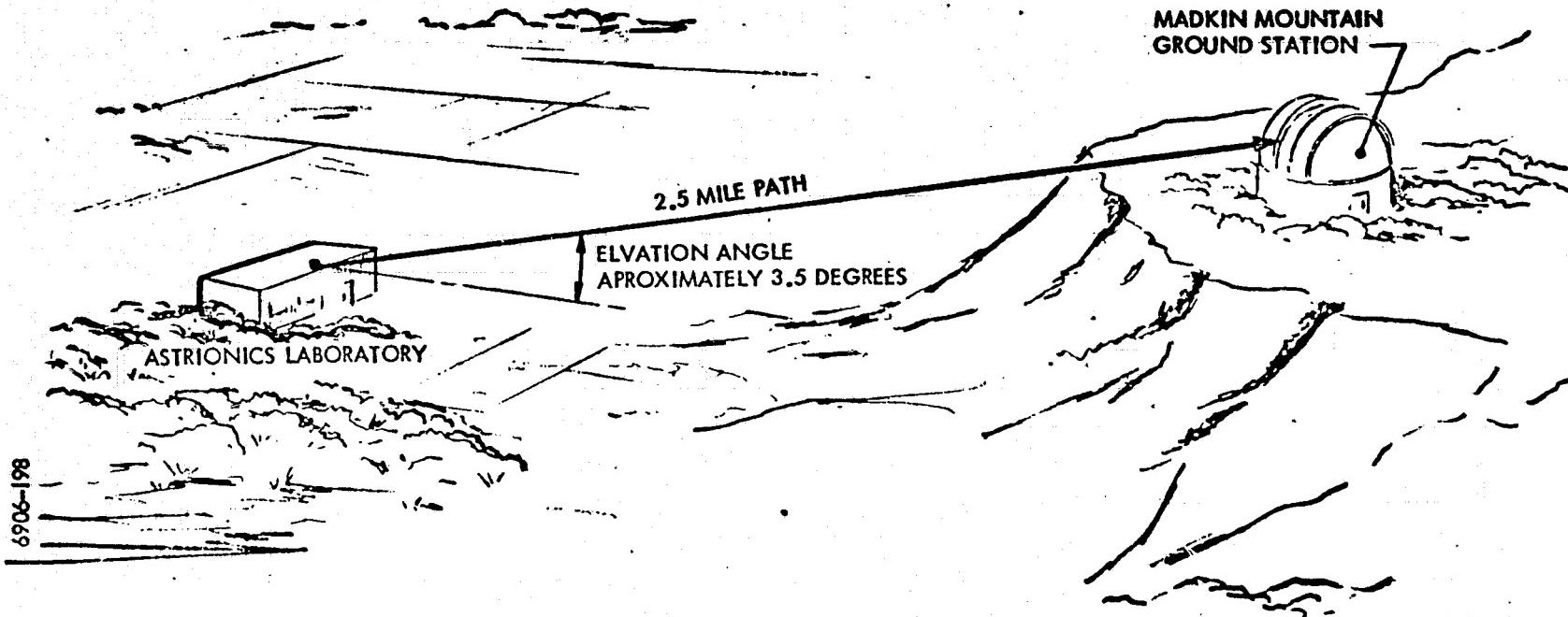


Figure 8-2. NASA/MSFC Field Test Range

in the atmosphere causing dynamic phase changes in the ID tracker video amplifier.

Two separate problems existing in the ID tracker contributed to the tracking difficulties experienced in the initial field test.

They were:

- 1) Excessive phase shift in the video signal over the input signal dynamic range.
- 2) Inadequate AGC bandwidth.

A field modification incorporated between 2/7/72 and 2/10/72 corrected the problems listed above. This modification resulted in successful operation of the AOCP with Madkin Mountain in a field test conducted 2/10/72. Data from this test was submitted to J. Randall. It is believed that further improvements are possible and a redesign is presently in process to replace the modified video amplifier in the ID tracker.

The phase shift problem existing in the video amplifier was a result of the gain controlling device working against the reactances of the ID photomultiplier tube and the input to the 10.7 MHz communication amplifier which is paralleled across the tube at this point. The resulting phase shift over the input dynamic range was in excess of 70° . The design modification isolated the tube output

reactance from the gain control device. This isolation amplifier converted the current output from the ID tube to a voltage. The gain controlling device (field effect transistor) was then allowed to operate against a resistive source as a voltage controlled attenuator. The resulting phase shift over the dynamic range was less than 2.5° . Phase data taken with an oscilloscope is difficult to determine accurately to small phase angles.

The AGC bandwidth was approximately 10 Hz which is below the normal frequency range of amplitude scintillation. The video amplifier low frequency cut off was approximately 100 Hz and limited the effective AGC bandwidth that could be incorporated. By adding additional low frequency breaks in the video amplifier the low frequency cutoff was moved to 1.5 KHz. The AGC control circuit was redesigned and the AGC bandwidth increased to 120 Hz.

The above modifications resulted in redesign of the video amplifier input stages, gain controlling circuits and the AGC amplifier. The proposed new design will replace the complete video amplifier resulting in increased dynamic range, AGC bandwidth, with the addition of adjustable gain and threshold controls to facilitate optimizing the tracker during field test between Madkin Mountain and the Astrionics Laboratory.

Figure 8-3 summarizes the before and after performance of the AGC amplifier. The AGC bandwidth was increased and the video bandwidth was narrowed to avoid overlap and central system instabilities. Some samples of the pointing performance are shown in Figures 8-4, 8-5 and 8-6 which are strip chart recordings of the tracker outputs. Each of these data show a region in time during which the beam steerers are turned off. When the beam steerers are off, the tracker outputs, E_x and E_y , indicate the amount of angular fluctuation of the arriving beacon laser. The angular fluctuations observed are partly due to atmospheric steering and partly due to system vibration (AOCP mount, gimballed mirror, etc.). The beam steerers are then manually turned on and the input fluctuations are steered out as indicated by the lower amplitude portions of the tracings in Figures 8-4, 8-5 and 8-6. The closed loop point d precision at this point can be seen to be between 1.4 and 1.8 arc recorder peak-to-peak in the presence of severe turbulence which corresponds to an rms accuracy of slightly over 1×10^{-6} radian.

Figure 8-7 shows a correlation of the received power fluctuations (lower trace), as determined from the linear baseband scintillation monitor output, and the closed-loop pointing accuracy of the AOCP in the upper trace.

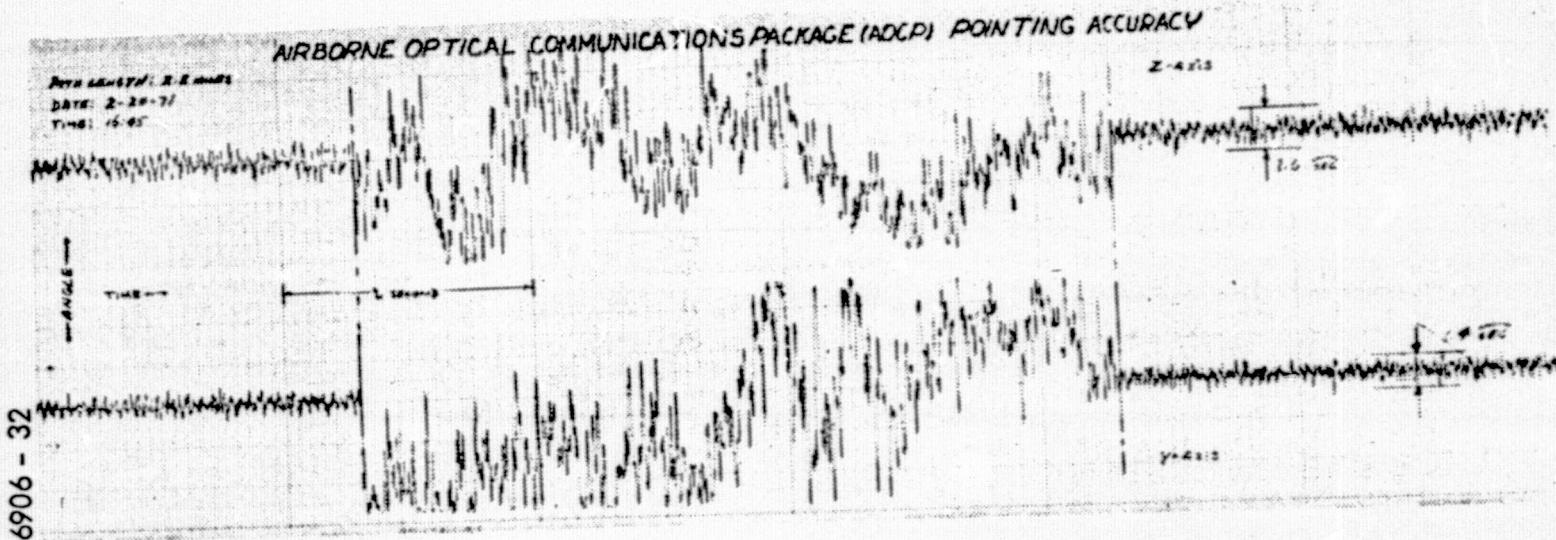


Figure 8-3. AVLOC Pointing Performance

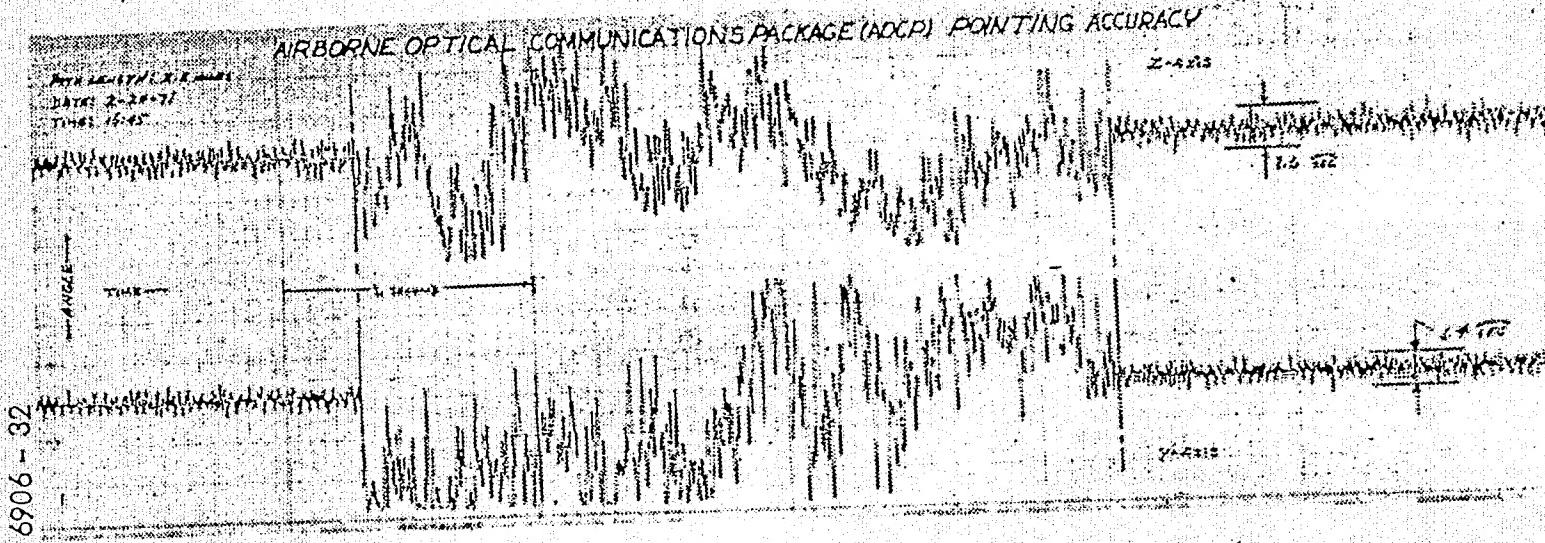


Figure 8-3. AVLOC Pointing Performance

AIRBORNE OPTICAL COMMUNICATIONS PACKAGE (AOCP) POINTING PERFORMANCE

7778 - 47

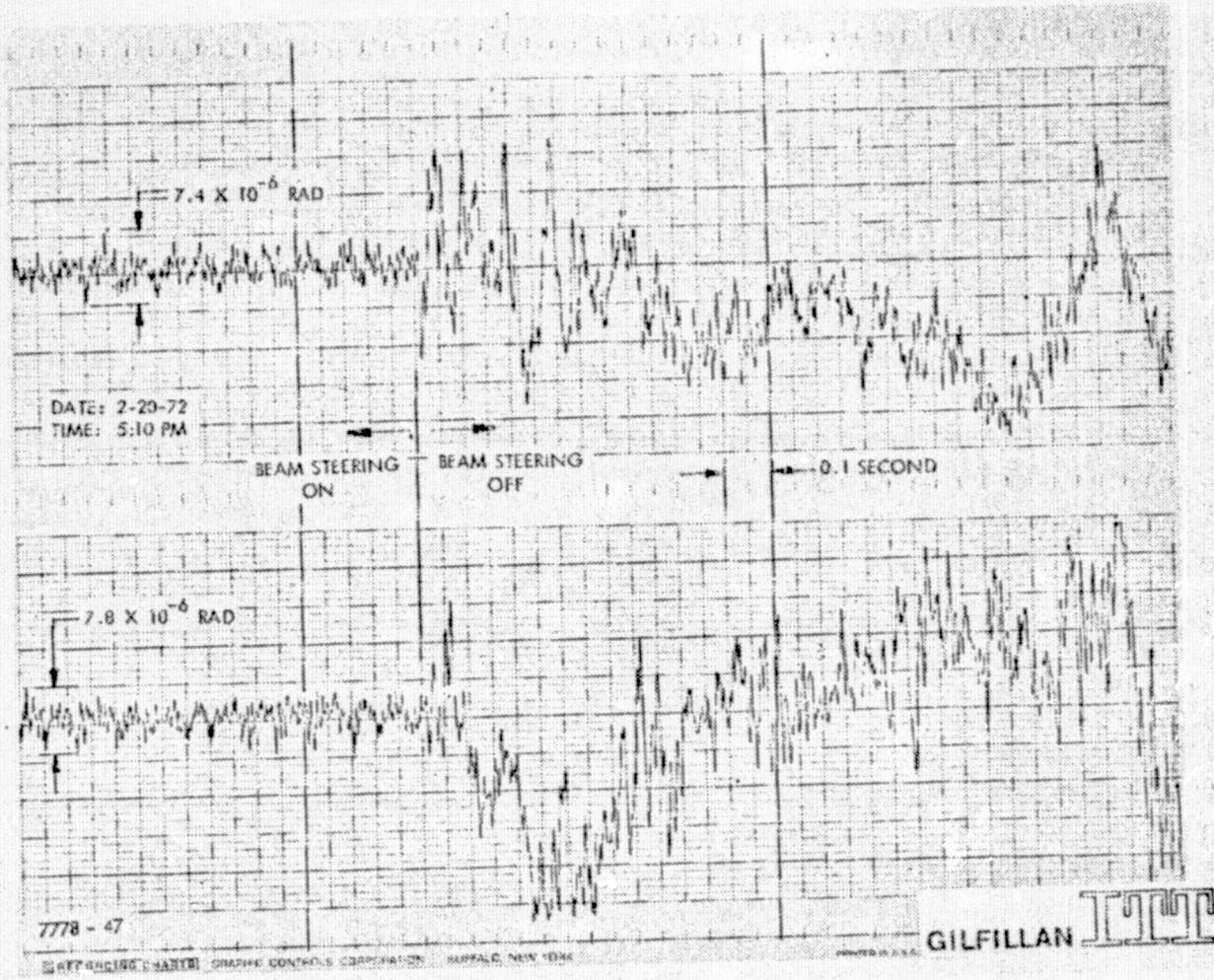


Figure 8-4. Data Sample B AOCP Field Test Tracking and Pointing

AIRBORNE OPTICAL COMMUNICATIONS PACKAGE POINTING ACCURACY

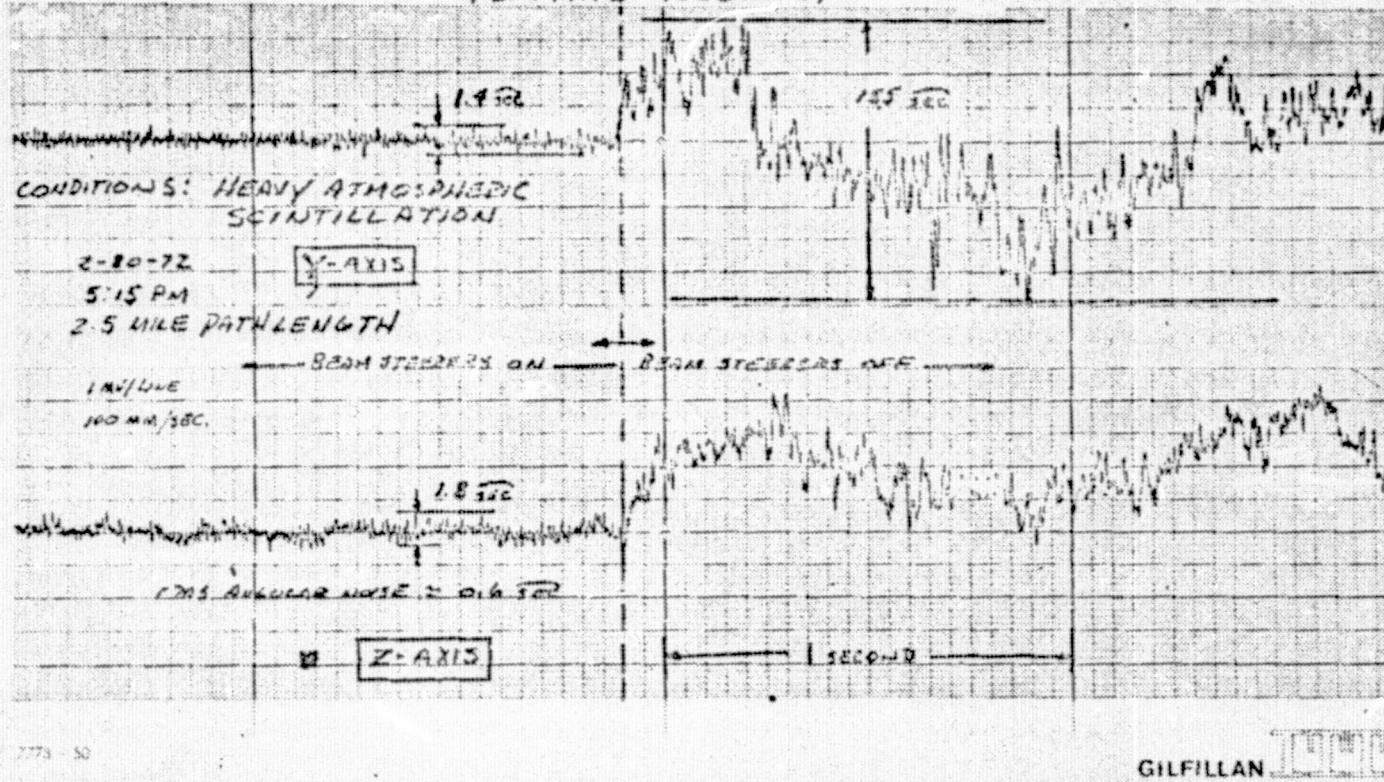


Figure 8-5. Data Sample A AOCP Field Test Tracking and Pointing

REPRODUCIBILITY OF THE
ORIGINAL PAGE IS POOR

8-11

6906 - 42

2-20-72

AOCP POINTING ACCURACY

DATE: 2-20-72
TIME: 15:00 hrs
PATH LENGTH: 2.5 MILES

100 mrad/sec
0.5 mrad

Z-AXIS
ANGLE OUTPUT

E_z

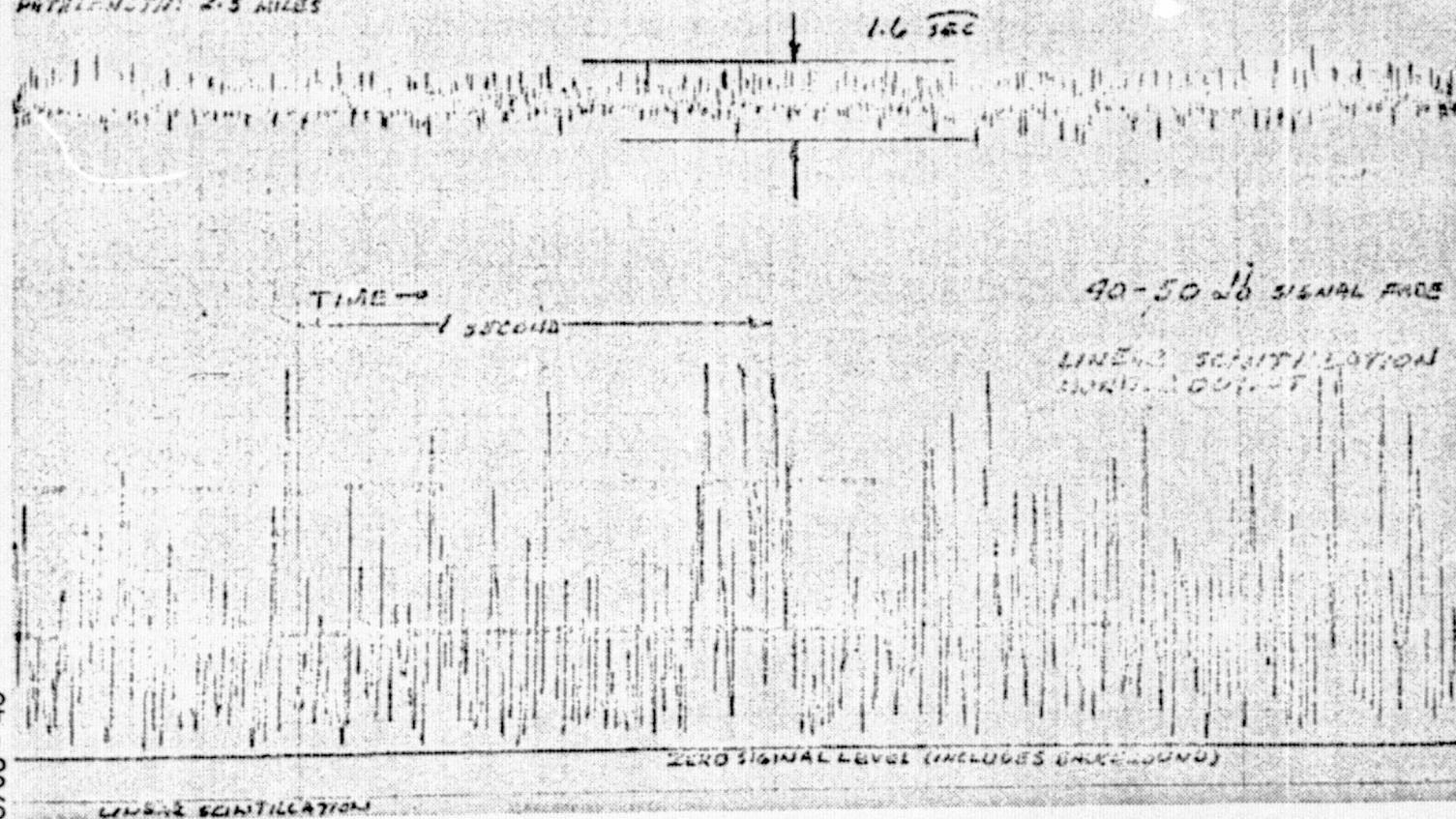


Figure 8-6. Field Test Data Sample Showing Scintillation Monitor Output and Pointing Accuracy

9.0

FLIGHT OPERATIONS

The purpose of this section is to describe the flight system as it is installed in the aircraft and to show the locations of the various equipments as used in the preflight and postflight tests. ITTG personnel were responsible for the operation of the AOCP and GCE in these tests, and participated in the overall flight readiness program. The tasks required in this field support were: a) routine maintenance of the hardware, including repair and cleaning, and b) incorporate system modifications resulting from flight operation experience. Examples of these modifications are provisions for aircraft backseat operator to control the coarse gimbal steering, fine beam steering (on/off) control, and remote in-flight boresight adjustment.

The initial AVLOC equipment interface with the RB57 aircraft took place at Kirtland Air Force Base in Albuquerque, New Mexico.

Figure 9-1 shows a view of the RB57 belly in which the AVLOC equipment is located. In this view, the AOCP support frame and experiment enclosure with air-conditioning duct work can be seen. On the right side of this view, is the connector that houses the RER, computer, and power system. Several non-operating test flights were conducted from Kirtland AFB to test the compatibility of the system with the aircraft environment. A number of problems were identified during this test phase - the most major being the temperature control of the experiment enclosure at high altitudes. The temperature control problem continued to plague the program throughout

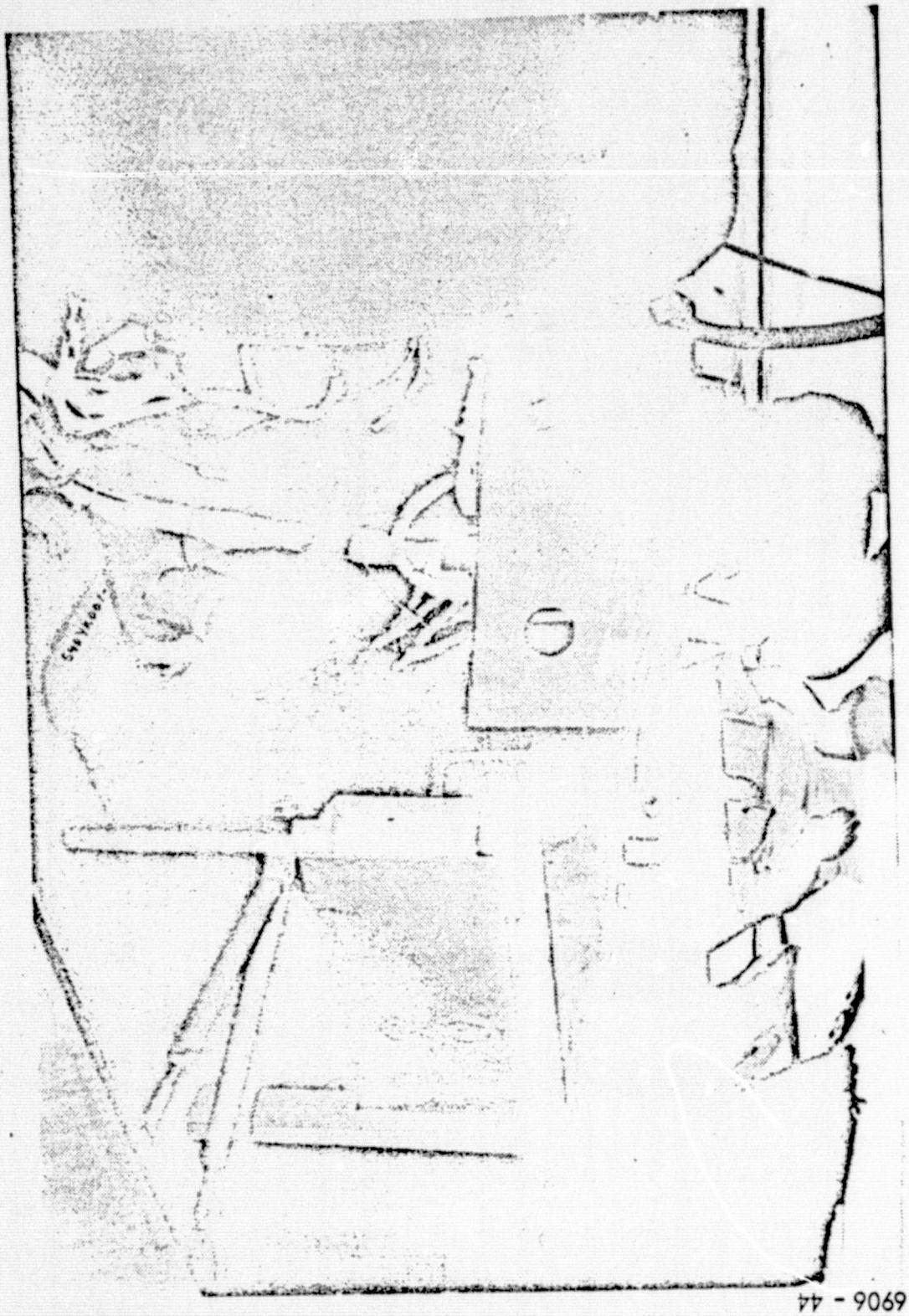
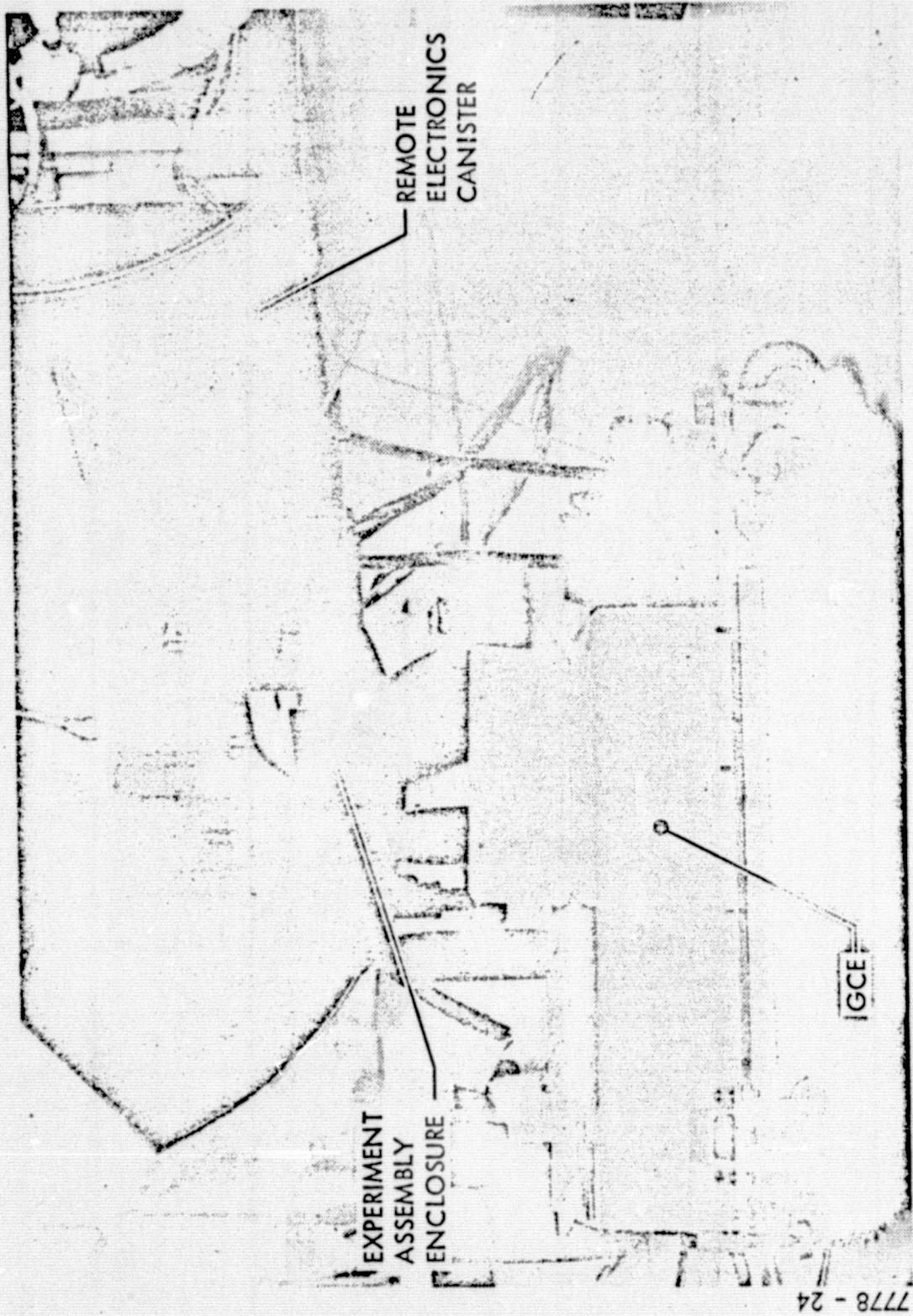


Figure 9-1. AOCP Installed in Aircraft Blue Frame

most of the flight series. The basic problem was the inability to raise the enclosure temperature which affected the AOCP performance and caused considerable moisture condensation throughout the system upon return to the higher temperature, high humidity ground environment. The transmitter power monitor beam splitter was cracked during an early checkout flight, probably because of extreme temperatures. Overall, the initial checkout phase went smoothly with only minor problems occurring at the interface.

The operational flight series was flown from Ellington Air Force Base, Houston, Texas. The preflight and postflight tests will be discussed briefly below. Details of the ground support of the flight tests are given in the AVLOC Aircraft Operations Plan, dated June 1972.

Preflight and postflight tests are conducted for each flight. The purpose of these tests was to determine the flight readiness of the system and to perform last minute calibration and alignment checks, and to set up any special test conditions that may be required. For these tests, the GCE is used to simulate the operational ground station. Figure 9-2 shows the GCE in position beneath the aircraft and lifted off the spring wheels by the lifting jacks so that it becomes a stable platform. The GCE is capable of completely exercising and calibrating the flight system, including the coarse acquisition and tracking subsystem. In operating sequence, the GCE illuminates the flight system coarse gimballed mirror with a wide angle scanning beam. The coarse acquisition subsystem TV tracker



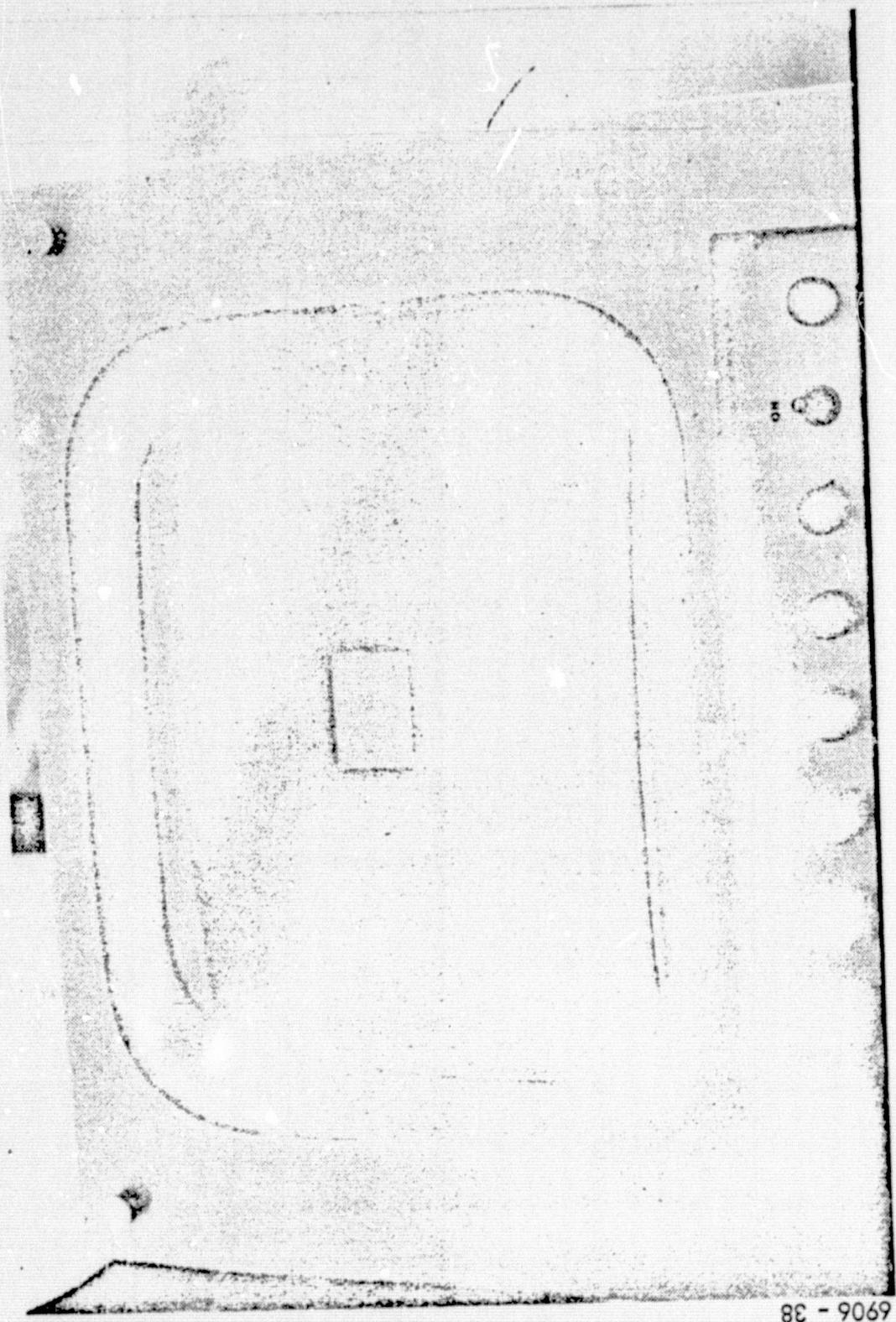
778 - 24

Figure 9-2. AVLOC Pre-Flight Test

detects and acquires the scanning beacon and causes the coarse gimballed mirror to dynamically slew to null the TV tracker outputs. Figure 9-3 shows a display of the TV tracker output on a monitor located on the GCE control console. The bright spot in the center of the grey square is the GCE beacon image. The TV tracker searches a field-of-view of approximately 5 degrees by 7 degrees and upon acquiring the beacon, establishes tracking gates, (indicated by the grey rectangle) about the target thereby marking the scene outside of the tracking gates from the signal processor. This reduces the probability of track error produced by sun glints and other bright objects that might appear in the scene after beacon acquisition. The TV display is calibrated and serves as a measure of the magnitude of the input beam scan when the coarse pointing gimbal is deactivated.

Following coarse acquisition, the gimballed mirror automatically pulls the beacon into the search field of the AOCP fine tracker where fine acquisition and auto tracking takes place. The track sweep amplitude, tracker noise, and errors are recorded for the closed loop system at this point. Figure 9-4 shows the monitoring and recording of dynamic tracking performance at test points during this test. The oscilloscope display is the cruciform track sweep indicating tracker noise and positional error magnitudes. Figures 9-5 and 9-6 show sample comparative data graphs for a tracking/pointing dynamic test for preflight and postflight

Figure 9-3. TV Acquisition Aid Display



88

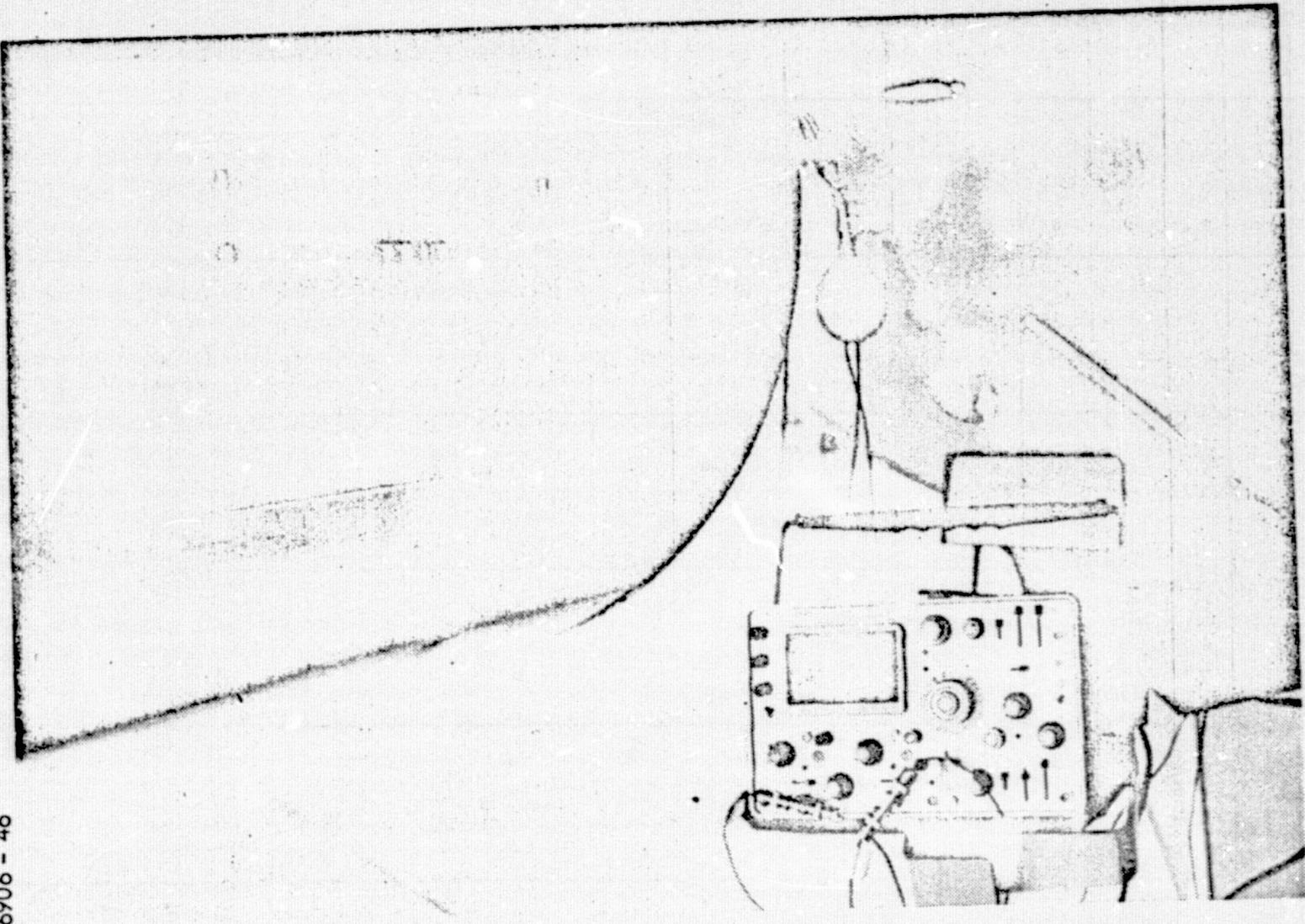


Figure 9-4. Track Scan Display Preflight Test

REPRODUCIBILITY OF THE
ORIGINAL PAGE IS POOR

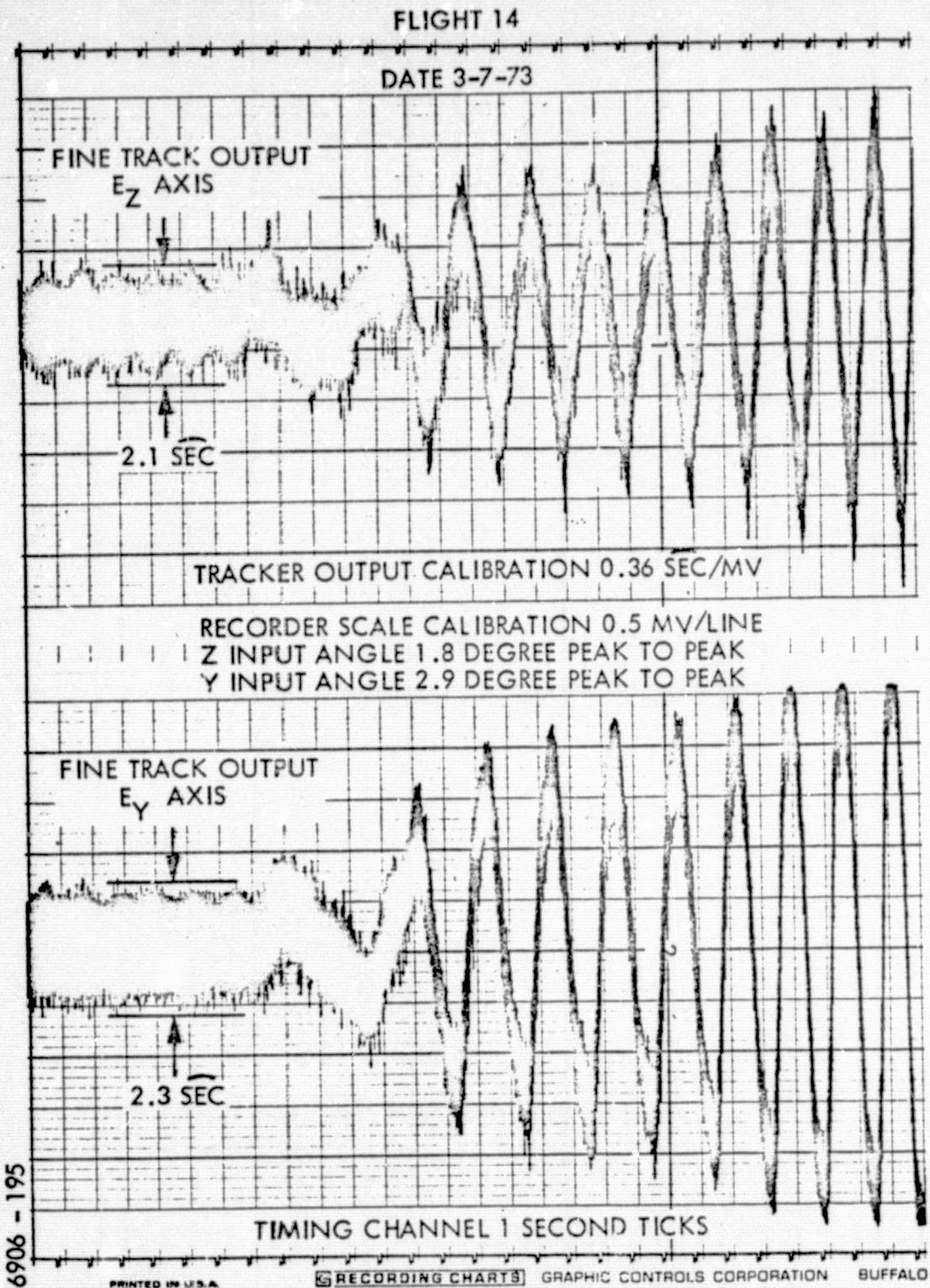


Figure 9-5. Preflight Closed Loop Pointing Test

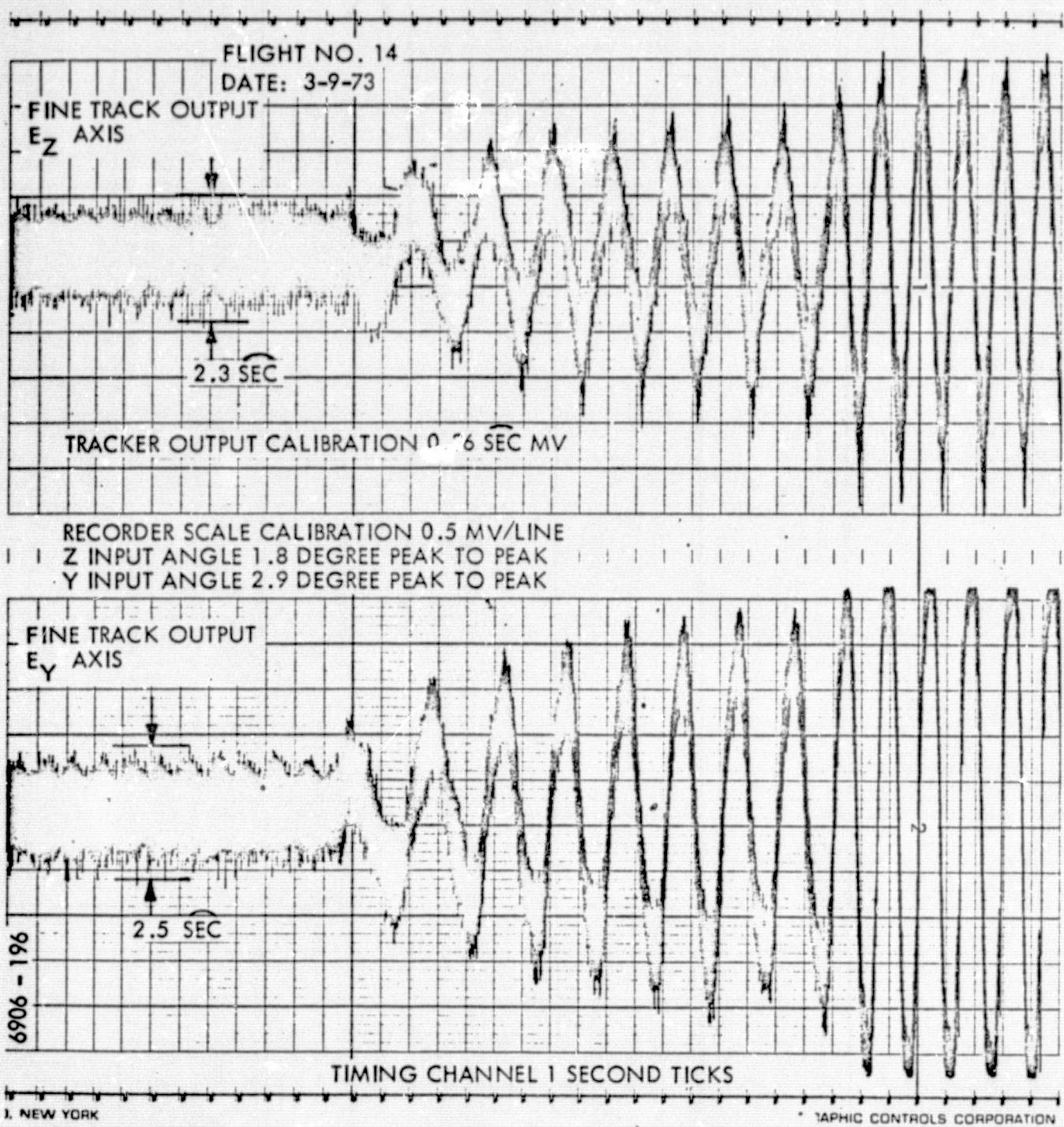


Figure 9-6. Post Flight Closed Loop Pointing Test

on flight number 14. Appendix B of this report is a preflight checklist and data summary for flight number 14 as an example of the type test performed.

In addition to the tracking and pointing tests, boresight alignment accuracy and modulation index are also set. The boresight alignment procedure is described in detail in the AVLOC Flight Operations Manual and will not be repeated here. Modulation index is monitored by the GCE sensor and displayed on the control console oscilloscope. Adjustments in the modulator operating point is made by adjusting the optical compensator on the AOCP. This requires the opening of the equipment enclosure cover as shown in Figure 9-7. This photograph also shows clearly the enclosure window and coarse mirror locations.

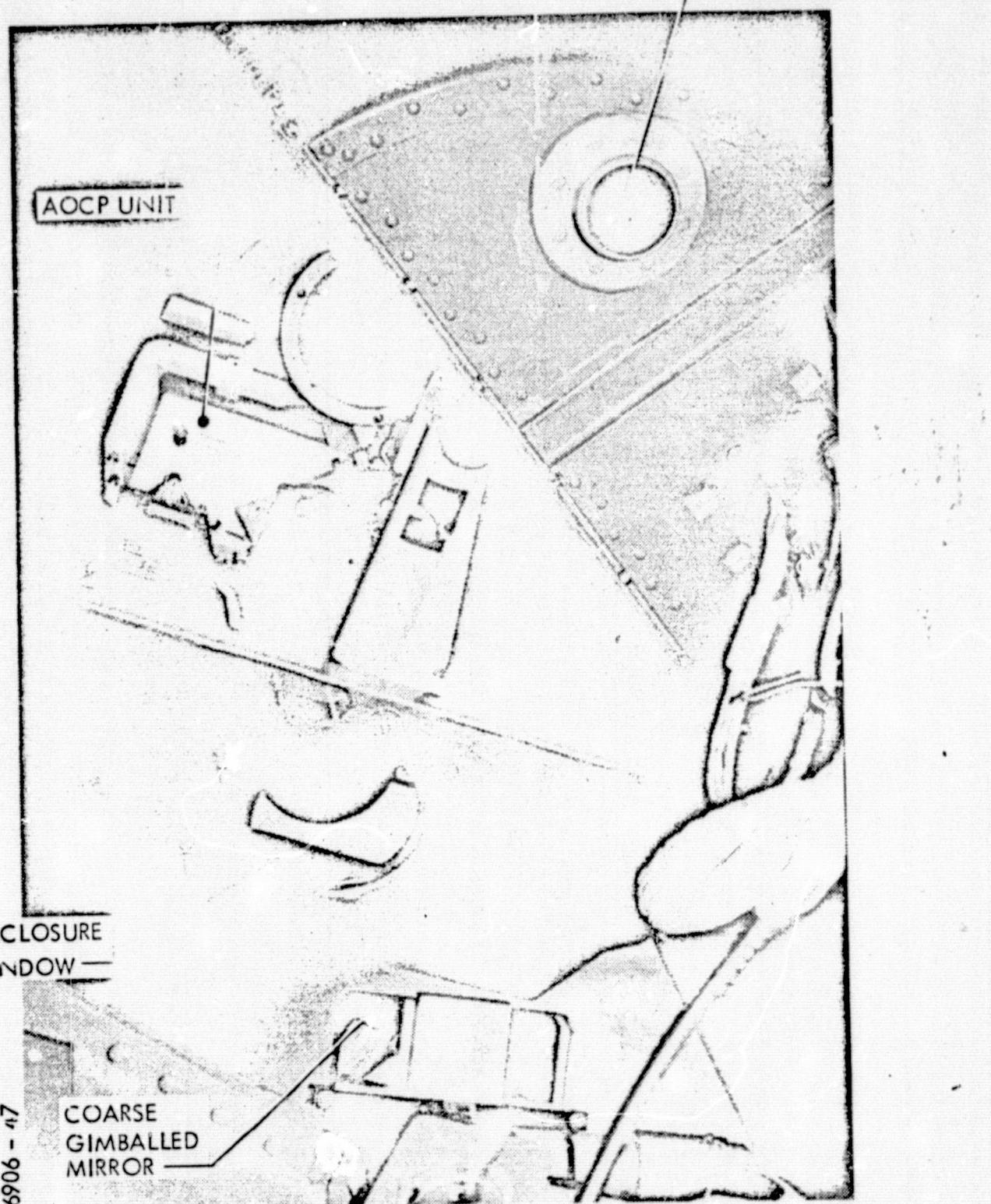
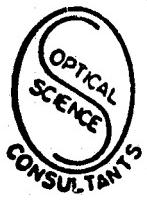


Figure 9-7. AOCP Mounted in Experiment Enclosure
Showing Aperture and Gimbal Mirror Configuration

APPENDIX A



OPTICAL SCIENCE CONSULTANTS
P.O. Box 388, Yorba Linda, California 92686 • Phone: (714) 524-3622.

Report No. TR-001

**Analysis of Propagation Loss Factors for the
Ground Based Acquisition Aid Portion of the
High Altitude Experiment**

Prepared by

D. L. Fried

for

J. Ward

**In Support of the ITT
Program on NASA Contract NAS8-20629**

August 1970

ABSTRACT AND SUMMARY

The statistics of optical propagation between a Ground Based Acquisition Aid pulsed laser transmitter-receiver and a corner reflector array on a high altitude aircraft are analyzed to determine the effects of system performance. It is shown that angular resolution/beam spread phenomena are of no significance for this system. A significant loss is predicted due to scintillation of the corner reflector array. It is shown that by separating the elements of the array by about 1.5 m between corner reflectors, this loss, which would approximately double the required power, can be reduced to the point where less than 25% more power is required. The magnitude of atmospheric turbulence induced scintillation is evaluated. It is found that without aperture averaging almost a factor of 4.0 power would be required for a 45° zenith angle, a 30 km altitude and nominal nighttime strength of turbulence. With aperture averaging, this factor of 4.0 reduces to 1.6 if the compact corner reflector array is considered, and only 1.35 if the dispersed array is used. For daytime conditions, with its stronger normal turbulence, the factor of 1.35 increases to 1.75. This, together with the factor of 1.25 for scintillation of the dispersed array, just pushes the combined loss to 2.2. Since this corresponds to a rather extreme condition, a design factor of 2.0 will probably yield acceptable performance. It does, however, use up some of the design conservatism contained in the rest of the design.

REPRODUCIBILITY OF THE
ORIGINAL PAGE IS POOR

1. INTRODUCTION

As part of a much larger program under Contract NAS8-20629, we are concerned with the performance of a Ground Based Acquisition Aid (GBAA) which will function as a ground based pulsed laser-radar to detect a corner reflector array mounted on the underside of a high altitude aircraft. The basic laser power, detector sensitivity, timing and scan geometry of the pointing have been worked out to assure an acceptably high probability of target detection, assuming that there are no propagation losses other than simple attenuation for which a worst case (round trip) factor of 10 has been allowed and some sort of atmospheric turbulence induced loss, for which a (round trip) factor of 2 has been allowed. It is the objective of this paper to more accurately evaluate the propagation loss factors other than the simple attenuation.

REPRODUCIBILITY OF THE
COPY IS POOR

2. EQUIPMENT DESCRIPTION

For the purposes of this analysis, the critical features of the equipment are the following. The GBAA utilizes a pulsed ionized Argon laser operating at 0.5145 microns. The pulses have a duration of 1.5×10^{-5} seconds. The laser beam is transmitted with a beam spread half-angle 1.74×10^{-3} radians. The target aircraft will be flying at an altitude of between 10^4 and 3×10^4 meters. It carries, on its underside, an array of 8 (3") 0.075 m aperture corner reflectors. The corner reflectors are nearly diffraction-limited with a half-angle return beam spread of 10^{-5} radians inherent in each of the units. The receiver is in immediate proximity to the transmitter. It has an (3") 0.075 m diameter aperture and a field-of-view half-angle of 8.7×10^{-4} radians.

The design objectives for the GBAA are a false alarm probability of 10^{-5} per pulse and a target detection probability, when the target is in the GBAA field-of-view, of 0.9, for a single laser pulse.

3. TYPES OF LOSS FACTORS

We are concerned with three distinct mechanisms by which propagation loss factors could be generated. The first of these has to do with angular resolution and beam spread. The second derives from the variability of the effective cross-section of the corner reflector array. The third loss factor originates in atmospheric turbulence induced scintillation on both the up link and the down link.

ANGULAR RESOLUTION/BEAM SPREAD -- Angular resolution and beam spread are opposite sides of the same coin, deriving from the same mechanism and having the same value over equivalent paths, as is shown in reference (1). If the atmospheric turbulence induced beam spread is greater than the designed transmitter beam spread, the transmitted beam will have a larger spread than intended and less of the laser radiation will reach the target. On the return path, if atmospheric turbulence makes the image of the received signal appear to be blurred to a size greater than the receiver field-of-view, then not all of the radiation collected will pass through the field-stop and be detected. This too will result in a loss factor.

We shall see in subsequent analysis, for the GBAA as presently contemplated, neither aspect of effect of angular resolution/beam spread will introduce any loss factor worth noting.

CORNER REFLECTOR ARRAY SCINTILLATION -- The variability of the corner reflector array cross-section is due to the fact that from different aspect angles the various corner reflectors in the array will send out return beams which will interfere with each other differently -- for each aspect, the interference pattern being different. The existence of this variable interference pattern is due to the fact that when the array is assembled, phase/position coherence between the corner reflectors is not obtained. The net effect is that examined at one time, the array may manifest a larger than normal cross-section, due to a favorable set of interferences, and return an extra strong signal. Examined at another time, with a slightly different viewing geometry, an unfavorable pattern of interferences can yield a very weak return. In fact, even a zero strength return is possible. Observed on a continuous basis with slowly changing viewing geometry, the cross-section of the array appears to scintillate. Considered from the point of view of a single sample (one pulse), we find that we can no longer count on some nominal return signal strength, as calculated from the average cross-section of the array. Instead, we must make allowance for the possibility that when we take the sample, the cross-section will be below average value. To counteract this, we have to send out more laser power in each pulse than the nominal case would seem to require, in order to maintain the desired detection probability. This increase in required transmitter power corresponds to a loss factor associated with scintillation of the cross-section of the corner reflector array.

In the analysis to follow, we shall present the statistics of this fluctuation and show that the scintillation can have a very substantial effect. We shall then show how, by changing the array from the initially contemplated compact pattern to a fairly widely spaced configuration, the effect of array scintillation can be suppressed for the GBAA.

TURBULENCE SCINTILLATION -- It is well known that atmospheric turbulence will introduce intensity variations into a laser beam so that what otherwise would appear to be a uniform intensity beam would be caused to become non-uniform and fluctuate at a rate of several to several tens of hertz. This manifests itself as scintillation. Scintillation is introduced on both the up-link, as a result of which the total amount of laser energy reaching the corner reflector array will vary, and on the down-link, as a result of which the fraction of the energy retrodirected by the array that reaches a point on the ground will vary -- quite independently of the corner reflector array scintillation referred to before. The atmospherically induced scintillation on both the up- and down-links has the same general effect as corner reflector array scintillation, as far as a loss factor is concerned. Because the more than average strength signal you get back sometimes isn't noticeably more useful than a just-above-threshold amount, while a less than average strength signal which we may receive is quite useless if it is below threshold, then to insure a useful signal at nearly all times, the average signal return has to be significantly above the threshold level. This extra power requirement, which is more than conventional photoelectric noise would require, corresponds to a propagation loss factor.

In subsequent detailed analysis, we shall see that although the basic atmospheric scintillation phenomena would seem capable of introducing a substantial loss factor in the GBAA, in fact there will be enough scintillation averaging due to extended aperture size so that the loss factor will be tolerably small.

4. ANGULAR RESOLUTION/BEAM SPREAD

To evaluate the effects of angular resolution and beam spread on the loss factor, we shall make the simplifying assumption that the target aircraft is well above the atmosphere, sufficiently so that it is valid to use angular resolution data associated with stellar observation. Our justification for making this assumption is that on the one hand, the angular resolution for an object well out of the atmosphere will be poorer than for the object at a lower altitude, while on the other hand we shall see that even with this pessimistic estimate of atmospheric limits on resolution, the effect on transmitter or receiver performance will be negligible.

In order to see that placing the object well above the atmosphere instead of just above or well inside the atmosphere will yield smaller atmospheric turbulence induced beam spread, we consider the expression

$$\delta\theta = (4\pi)^{1/2} / kr_o, \quad (1)$$

where $\delta\theta$ is a measure of the beam spread, k is the optical wave-number (i.e., $2\pi/\lambda$), and r_o is a measure of the coherence distance for an optical wavefront after propagation over the path in question. The value of r_o is given by the expression

$$r_o = 1.675 k^{-6/5} \sec^{3/5} \theta \left[\int_0^z dh C_N^2(h) \right]^{-3/5} \quad (2)$$

Here, θ is the zenith angle of the line-of-sight between the GBAA and the target object, z is the altitude of the target object, and $C_N^2(h)$ is a quantity called the refractive-index structure constant, which measures the optical strength of turbulence at an altitude h . A graph giving average values of C_N^2 , taken from reference (2), is presented in Fig. 1.

The point that we want to make is that obviously the larger the value of the integral in Eq. (2), the smaller r_o will be and the larger $\delta\theta$ will be. By considering the target altitude to be at an infinite altitude, instead of at the finite altitude z , we are making the value of the integral larger and so

making our estimate of $\delta\theta$ (slightly) more pessimistic than necessary. (A quick examination of Fig. 1 indicates that the principal part of the value of the integral is contributed by values of h in the vicinity of 1 km, and that we are not adding very much to the value of the integral by extending the upper limit from 30 km to infinity, or even from 10 km to infinity. Obviously, the degree of pessimism in the value of $\delta\theta$ we will come up with is not very significant.)

In order to evaluate $\delta\theta$, we could use Eq.'s (1) and (2) and the data of Fig. 1. However, now that we are considering the integral with its limit at infinity, we can get equivalent results by using astronomical observations of stars to give us $\delta\theta$. Good quantitative data has been obtained by Hoag³ and by Minel⁴, who measured the angular width of a pair of slits required to pass 68% of the available energy of a star's image. In Fig. 2, we show a cumulative probability distribution for Hoag's results. Minel's results are in substantial agreement. (The fact that the distribution is log-normal is interesting, but of no particular concern to us here.) The median value, at 50%, of about 1.6 arc seconds is in fair agreement with results calculated from Fig. 1. We, however, shall concern ourselves with the 99% value of about 4.0 arc seconds, with the assurance that almost never will the seeing be worse than this. Assuming a gaussian shape for the atmospherically spread image spot, the slit width for 68% transmission corresponds to plus and minus one standard deviation. Since the data of Fig. 2 is for near zenith, to correct for the worst case situation in which the line-of-sight has a 45° zenith angle, in accordance with Eq.'s (1) and (2), we introduce a factor of $[\sec(45^\circ)]^{3/2} = 1.23$. This gives us, as a very conservative upper (pessimistic) bound on $\delta\theta$ (the 2-standard deviation width of the atmospheric blur) 4.9 arc seconds, i.e., 24×10^{-6} radians.

The effect of this spread on the shape of the transmitted beam shape will be to smear out the edges of what otherwise would be a perfectly sharply defined beam. Nominally, if the target is anywhere in the 1.74×10^{-3} radian half-angle cone, it will receive full illumination. Because of the smear induced by turbulence, this half-angle should be reduced to about 1.72×10^{-3} radians for assurance that the target receives nearly full illumination. This is a sufficiently small correction that it can be ignored.

Similarly, in considering the receiver half-angle field-of-view of 8.7×10^{-4} radians, it is only if the image gets within two standard deviations of the edge of the nominal field-of-view that there will be as much as a few percent loss in received signal due to spill-over. This reduces the effective receiver field-of-view to a half-angle of about 8.5×10^{-4} radians, which is obviously a negligible correction.

Within these slightly reduced fields-of-view, the intensity of the transmitted beam and the efficiency of the receiver may be considered to be unchanged by the existence of atmospheric turbulence induced blur. There is then no loss factor correction required for this effect.

5. CORNER REFLECTOR ARRAY SCINTILLATION

When the corner reflector array is assembled, it is impossible to position the corner reflectors so that they have any common reference surface. As a consequence, the path length to any corner reflector will differ from the path length to any other corner reflector by some amount. The length will be small, i.e., probably less than a millimeter, but many wavelengths. This means that the return from the elements in the array will have a random phase relation to each other. As a consequence, the return signal will be of random amplitude due to the random nature of the interference between the returns. If there are N elements in the array and each produces a return of unit amplitude with a random phase ϕ_λ ($\lambda = 1, 2, \dots, N$), then the observed wave will be

$$u = \sum_{\lambda=1}^N \exp(i\phi_\lambda), \quad (1)$$

and the intensity will be

$$I = \frac{1}{2} u^* u = \frac{1}{2} \sum_{\lambda=1}^N \sum_{\lambda'=1}^N \exp[i(\phi_\lambda - \phi_{\lambda'})]. \quad (2)$$

The average intensity will be

$$\langle I \rangle = \frac{1}{2} \sum_{\lambda=1}^N \sum_{\lambda'=1}^N \langle \exp[i(\phi_\lambda - \phi_{\lambda'})] \rangle. \quad (3)$$

Since $\langle \exp[i(\phi_\lambda - \phi_{\lambda'})] \rangle = 0$, unless $\phi_\lambda = \phi_{\lambda'}$, i.e., unless $\lambda = \lambda'$, (because the random phase ϕ_λ (and $\phi_{\lambda'}$) is distributed more or less uniformly over 2π), it follows that

$$\langle I \rangle = \frac{1}{2} N. \quad (4)$$

This is just the average we would expect from a simplistic energy calculation and is what was considered in earlier signal-to-noise ratio calculations for detection. However, this average value is not the value we expect to observe at any instant. The instantaneous intensity will fluctuate due to the changing values of the ϕ 's.* The normalized variance of the intensity will be

$$\sigma_I^2 = \frac{\langle I^2 \rangle - \langle I \rangle^2}{\langle I \rangle^2} = \frac{\langle I^2 \rangle}{\frac{1}{4} N^2} - 1, \quad (5)$$

and

$$\langle I^2 \rangle = \frac{1}{4} \sum_{\ell=1}^N \sum_{\ell'=1}^N \sum_{\ell''=1}^N \sum_{\ell'''=1}^N \langle \exp[i(\phi_\ell - \phi_{\ell'} + \phi_{\ell''} - \phi_{\ell''''})] \rangle. \quad (6)$$

The average of the exponential will vanish unless either $\ell' = \ell$ and $\ell'' = \ell'''$, or $\ell' \neq \ell$ but $\ell'' = \ell'$ and $\ell''' = \ell$. Thus

$$\begin{aligned} \langle I^2 \rangle &= \frac{1}{4} \sum_{\ell=1}^N \left(\sum_{\ell''=1}^N + \sum_{\ell'''=\ell}^N \right) \\ &= \frac{1}{4} \sum_{\ell=1}^N (N + N-1) = \frac{1}{4} N (2N-1) \\ &= \frac{1}{4} (2N^2 - N). \end{aligned} \quad (7)$$

*The interrelationship of the ϕ 's will change as the angle between the line of sight to the array and the nominal surface normal of the array change. For the kinds of geometrics and aircraft speeds we are considering, this change will be very rapid.

Combining this with Eq. (5), we get

$$\sigma_I^2 = 1 - \frac{1}{N} \quad . \quad (8)$$

Apparently then, there is nearly 100% modulation associated with the corner reflector array scintillation. This raises a serious concern that at the instant a detection pulse sample is taken, the corner reflector array return may be substantially below the nominal average and the target may be missed.

To calculate exactly how serious the effect of this scintillation will be on target detection, we shall calculate target detection probabilities given this scintillation. We note that the sum of a large number of random phase components yields a mean square (intensity) which is distributed according to a Rayleigh distribution. (In this regard, see Middleton⁵.) The Rayleigh probability density (for intensity rather than amplitude) is

$$P_{Ray}(I) dI = e^{-I/\bar{I}} dI/\bar{I}, \quad 0 \leq I < \infty. \quad (9)$$
$$= 0 \quad I < 0$$

The mean value of I is

$$\langle I \rangle_{Ray} = \int_0^\infty I P_{Ray}(I) dI = \bar{I}, \quad (10)$$

and the second moment is

$$\langle I^2 \rangle_{Ray} = \int_0^\infty I^2 P_{Ray}(I) dI = 2\bar{I}^2. \quad (11)$$

This yields a normalized variance of

$$\sigma_{R_y}^2 = \frac{\langle I^2 \rangle_{R_y} - \langle I \rangle_{R_y}^2}{\langle I \rangle_{R_y}^2} = 1, \quad (12)$$

which, when compared with the results in Eq. (8), indicate that even with as few as eight corner reflectors in the array, the central limit theorem required to develop the Rayleigh distribution is quite accurate, yielding no more than a 12.5% error in the variance.

With the Rayleigh distribution in hand, we are in a position to calculate the target detection probability, considering the signal-to-noise ratio aspects of the problem. Although we shall be interested in the area under the tail of the gaussian distribution,

$$\begin{aligned} \Phi(x) &= (2\pi)^{-1/2} \int_x^\infty \exp(-\frac{1}{2}x^2) dx \\ &= (2\pi)^{-1/2} \int_{-\infty}^{-x} \exp(-\frac{1}{2}x^2) dx, \end{aligned} \quad (13)$$

we shall make use of the error-function

$$\text{erf}(x) = (\frac{4}{\pi})^{1/2} \int_0^x \exp(-t^2) dt, \quad (14)$$

in our calculations. We note that according to Abramowitz and Stegun⁶,

$$\Phi(x) = \frac{1}{2} [1 + \text{erf}(-x/\sqrt{2})], \quad (15)$$

and that to a very good approximation (error $\leq 1.5 \times 10^{-7}$)
for $x \geq 0$

$$\text{erf}(x) = 1 - \exp(-x^2) \sum_{m=1}^5 a_m t^m, \quad (16)$$

where

$$t = (1 + px)^{-1} \quad (17)$$

and

$$\begin{aligned} p &= .3275911, \quad a_1 = .254829592, \quad a_2 = -.284496736, \\ a_3 &= 1.421413741, \quad a_4 = -1.453152027, \quad a_5 = 1.061405429. \end{aligned} \quad (18)$$

Since

$$\text{erf}(-x) = -\text{erf}(x), \quad (19)$$

for $x \leq 0$, it is a very good approximation (error $\leq 1.5 \times 10^{-7}$)
to write

$$\text{erf}(x) = -1 + \exp(-x^2) \sum_{m=1}^5 a_m u^m, \quad (16')$$

where

$$u = (1 - px)^{-1}, \quad (17')$$

and the values of p, a_1, a_2, \dots, a_5 are as given in Eq. (18).

In order to achieve a false alarm probability of 10^{-5} per pulse, the detection threshold will have to be set at about $T\sigma_n$, where $T = 4.26$, and σ_n denotes the rms noise in the system. If the signal return is I , then the probability due to noise of missing the target when there is a return is

$$P_{M, \text{noise}}(I) = \int_{-\infty}^{T\sigma_n - I} (2\pi\sigma_n^2)^{-1/2} \exp(-x^2/2\sigma_n^2) dx$$

$$= \Phi\left(\frac{T\sigma_n - I}{\sigma_n}\right). \quad (20)$$

To achieve a 90% detection probability, we require that $(T\sigma_n - I)/\sigma_n = -1.28$, since $\Phi(-1.28) = 0.1$. This means that if $I = 5.54\sigma_n$, we will have our 90% detection probability.

However, because of the scintillation of the corner reflector, I is itself a random variable, and rather than discuss performance for a particular value of I , we should average over the expected values of I . Thus the target miss probability, given that I follows a Rayleigh distribution with mean value \bar{I} , is

$$P_M = \int_0^\infty P_{M, \text{noise}}(I) P_{R, \text{av}}(I) dI$$

$$= \int_0^\infty d\left(\frac{I}{\bar{I}}\right) \exp\left(-\frac{I}{\bar{I}}\right) \Phi\left(\frac{T\sigma_n - I}{\sigma_n}\right). \quad (21)$$

Substituting in Eq. (15), we get

$$P_M = \int_0^\infty d\left(\frac{I}{\bar{I}}\right) \exp\left(-\frac{I}{\bar{I}}\right) \frac{1}{2} \left[1 + \operatorname{erf}\left(\frac{I - T\sigma_n}{\sqrt{2}\sigma_n}\right) \right]$$

$$\begin{aligned}
&= \frac{1}{2} \left\{ \int_0^{x=\tau\sigma_n} d(x/\bar{x}) \exp(-x/\bar{x}) \left[1 + \operatorname{erf}\left(\frac{x-\tau\sigma_n}{\sqrt{2}\sigma_n}\right) \right] \right. \\
&\quad \left. + \int_{x=\tau\sigma_n}^{\infty} d(x/\bar{x}) \exp(-x/\bar{x}) \left[1 + \operatorname{erf}\left(\frac{x-\tau\sigma_n}{\sqrt{2}\sigma_n}\right) \right] \right\}. \tag{22}
\end{aligned}$$

We note that in the first integral, i.e., the one whose bounds are 0 to $\tau\sigma_n$, the argument of the error function is negative, so that we can replace the error function by its approximation in Eq. (16'). For the second integral, where the argument of the error function is positive, we use Eq. (16). We get

$$\begin{aligned}
P_H &= \frac{1}{2} \left\{ \int_0^{x=\tau\sigma_n} d(x/\bar{x}) \exp(-x/\bar{x}) \left[1 - 1 + \exp\left[-\frac{(x-\tau\sigma_n)^2}{2\sigma_n^2}\right] \right. \right. \\
&\quad \times \sum_{m=1}^5 a_m u^m \left. \right] + \int_{x=\tau\sigma_n}^{\infty} d(x/\bar{x}) \exp(-x/\bar{x}) \\
&\quad \times \left. \left[1 + 1 - \exp\left[-\frac{(x-\tau\sigma_n)^2}{2\sigma_n^2}\right] \sum_{m=1}^5 a_m t^m \right] \right\} \\
&= \int_{x=\tau\sigma_n}^{\infty} d(x/\bar{x}) \exp(-x/\bar{x}) + \frac{1}{2} \left\{ \int_0^{x=\tau\sigma_n} d(x/\bar{x}) \exp(-x/\bar{x}) \right. \\
&\quad \times \exp\left[-\frac{(x-\tau\sigma_n)^2}{2\sigma_n^2}\right] \sum_{m=1}^5 a_m u^m - \int_{x=\tau\sigma_n}^{\infty} d(x/\bar{x}) \\
&\quad \times \left. \exp(-x/\bar{x}) \exp\left[-\frac{(x-\tau\sigma_n)^2}{2\sigma_n^2}\right] \sum_{m=1}^5 a_m t^m \right\}, \tag{23}
\end{aligned}$$

where

$$u = \left[1 - \rho \left(\frac{x - T\sigma_n}{\sqrt{2}\sigma_n} \right) \right]^{-1}, \quad (24')$$

and

$$t = \left[1 + \rho \left(\frac{x - T\sigma_n}{\sqrt{2}\sigma_n} \right) \right]^{-1}. \quad (24)$$

We note that

$$\int_{x=T\sigma_n}^{\infty} d(x/\bar{x}) \exp(-x/\bar{x}) = -\exp(-x/\bar{x}) \Big|_{x=T\sigma_n}^{\infty}$$

$$= \exp(-T\sigma_n/\bar{x}).$$

(25)

To evaluate the two integrals in Eq. (23) inside the curly

brackets, we note that the dependence on $\exp\left[-\frac{(x-T\sigma_n)^2}{2\sigma_n^2}\right]$

is dominant. To a good approximation, $\exp(-x/\bar{x})$ can be considered to be constant with the value $\exp(-T\sigma_n/\bar{x})$. If we write,

$$N = \left[1 + \rho \left(\frac{x - T\sigma_n}{\sqrt{2}\sigma_n} \right) \right]^{-1} \quad (26)$$

then we see that

$$\begin{aligned}
 P_M = & \exp(-T\sigma_n/\bar{I}) + \frac{1}{2} \left\{ \int_0^{T\sigma_n} d(I/\bar{I}) \exp(-T\sigma_n/\bar{I}) \right. \\
 & \times \exp\left[-\frac{(I-T\sigma_n)^2}{2\sigma_n^2}\right] \sum_{m=1}^{\infty} a_m n^m - \int_{T\sigma_n}^{\infty} d(I/\bar{I}) \\
 & \left. \times \exp(-T\sigma_n/\bar{I}) \exp\left[-\frac{(I-T\sigma_n)^2}{2\sigma_n^2}\right] \sum_{m=1}^{\infty} a_m n^m \right\}. \quad (27)
 \end{aligned}$$

Because we will consider only values for I for which

$\exp\left[-\frac{(I-T\sigma_n)^2}{2\sigma_n^2}\right] \ll 1$, for $I < 0$, we can extend the lower

limit of the first integral from 0 to $-\infty$. Doing this, it

is now apparent that since the two integrands are identical and

symmetric about $I = T\sigma_n$, the two integrals cancel, and

$$P_M = \exp(-T\sigma_n/\bar{I}). \quad (28)$$

This is a very discouraging result, since it says that to achieve a 90% detection probability, we require that $\exp(-T\sigma_n/\bar{I}) = .1$, which means that we would require that $I = 2.30 T\sigma_n \approx 9.81 \sigma_n$. If our approximation in evaluating P_M had considered the variation in $\exp(-I/\bar{I})$ instead of holding it constant, the two integrals would not have exactly cancelled and there would have been an additional term in the answer

REPRODUCIBILITY OF THE
ORIGINAL PAGE IS POOR

which would require about another $0.1 \sigma_n$ in the value of \bar{I}^* , giving a required value of $\bar{I} \approx 9.9 \sigma_n$. Compared with the value of $5.54 \sigma_n$ that we would need if there were no corner reflector array scintillation, we see that there is a loss factor of 1.79:1. This uses up almost all of the allowed design factor of 2:1 intended for turbulence losses, without leaving anything for the turbulence effects themselves.

To avoid the effects of this corner reflector array scintillation, we can modify the design of the array from the compact pattern originally intended to an extended pattern with wide spacing between the elements. This will result in a very fine grained corner reflector array scintillation pattern at the GBAA collector, and in a reasonable amount of averaging. In fact, since the interference pattern between any two corner reflectors will vary sinusoidally, by making the aperture diameter several times the sinusoidal period, the averaging will be certain rather than statistical. If the diameter to sinusoidal period ratio is ρ , then the variance will be down by ρ^2 . The fact that there will be many interfering pairs of corner reflectors will confuse the pattern, but will not affect the averaging.

To compute ρ , we need to know the period of the interference pattern. In Fig. 3, we show a very simplified (and distorted scale) version of the geometry associated with the generation of the interference pattern. We consider the two corner reflectors denoted CR_1 and CR_2 located at position y_1 and y_2 in the nominal plane of the corner reflector array, with positioning errors Δ_1 and Δ_2 normal to the plane. The corner reflectors are located a height H above the GBAA, whose collector aperture plane contains the measurement points at x_1 and x_2 . The line of sight between the GBAA and the array makes an angle θ with the normal to the nominal plane of the array. (In our

* The missing term in the r.h.s. of Eq. (28) is approximately

$$\Delta = \exp(-\tau \sigma_n / \bar{I}) \frac{\sqrt{2} \sigma_n}{\bar{I}} \int_{\frac{I-\tau \sigma_n}{\sqrt{2} \sigma_n}}^{\infty} d\left(\frac{x}{\bar{I}}\right) \exp\left[-\left(\frac{x-\tau \sigma_n}{\sqrt{2} \sigma_n}\right)^2\right] \sum_{m=1}^5 a_m x^m \frac{(I-\tau \sigma_n)/\sqrt{2} \sigma_n}{\bar{I}}. \quad (*1)$$

Since

$$\sum_{m=1}^5 a_m = 1 \quad (*2)$$

$$\begin{aligned} \Delta &= \exp(-\tau \sigma_n / \bar{I}) 2 \left(\frac{\sigma_n}{\bar{I}}\right)^2 \int_{\frac{I-\tau \sigma_n}{\sqrt{2} \sigma_n}}^{\infty} d\left(\frac{x-\tau \sigma_n}{\sqrt{2} \sigma_n}\right) \exp\left[-\left(\frac{x-\tau \sigma_n}{\sqrt{2} \sigma_n}\right)^2\right] \left(\frac{I-\tau \sigma_n}{\sqrt{2} \sigma_n}\right) \sum_{m=1}^5 a_m \\ &= \exp(-\tau \sigma_n / \bar{I}) \left(\frac{\sigma_n}{\bar{I}}\right)^2 \int_{2x}^{\infty} dx \exp(-x^2) = \left(\frac{\sigma_n}{\bar{I}}\right)^2 \exp(-\tau \sigma_n / \bar{I}). \end{aligned} \quad (*3)$$

Since $(\sigma_n / \bar{I}) \approx 0.1$, the correction is about 1% in P_M and so also about 1% in \bar{I} .

analysis, we shall use Δ_1 and Δ_2 to denote not only the geometric positioning error of the corner reflector, but also a path length correction from the laser illuminator to the corner reflector, rather than to the center of the array. This, then, permits us to treat the corner reflectors as sources with the $z\pi A/\lambda$ treated as the phasing of the source.) The path length between x_i and y_j is

$$R_{i,j} = [(H \sec \theta + y_j \sin \theta)^2 + (x_i - y_j \cos \theta)^2]^{1/2}$$

$$\approx H \sec \theta + \frac{1}{2} \frac{y_j^2 \sin^2 \theta}{H \sec \theta} + \frac{1}{2} \frac{x_i^2}{H \sec \theta} + \frac{1}{2} \frac{y_j \cos^2 \theta}{H \sec \theta} - \frac{x_i y_j \cos \theta}{H \sec \theta}. \quad (29)$$

The phase difference observed between the return from the two corner reflectors, observed at x_1 is

$$\Delta \phi_1 = 2\pi \frac{(R_{1,1} + \Delta_1) - (R_{1,2} + \Delta_2)}{\lambda}, \quad (30a)$$

and at x_2 , it is

$$\Delta \phi_2 = 2\pi \frac{(R_{2,1} + \Delta_1) - (R_{2,2} + \Delta_2)}{\lambda}. \quad (30b)$$

Hence

$$\begin{aligned} \Delta \phi_1 - \Delta \phi_2 &= \left(\frac{2\pi}{\lambda}\right) \left(\frac{\cos \theta}{H \sec \theta}\right) (-x_1 y_1 + x_1 y_2 + x_2 y_1 - x_2 y_2) \\ &= \left(\frac{2\pi}{\lambda}\right) \left(\frac{\cos^2 \theta}{H}\right) (x_1 - x_2)(y_2 - y_1). \end{aligned} \quad (31)$$

The period of the sinusoidal interference pattern will be the value of $(x_1 - x_2)$ for which $\Delta\phi_1 - \Delta\phi_2 = 2\pi$. This occurs when $(x_1 - x_2)$ equals

$$\Delta = H \lambda / \cos^2 \theta (y_2 - y_1)$$

Under worst case conditions, $H = 3 \times 10^4$ m and $\theta = 45^\circ$. Since $\lambda = 5.145 \times 10^{-7}$ m, we see that the period, Δ is always less than or equal to $3.0 \times 10^{-2} / (y_2 - y_1)$ meters. If we choose a 1.5 m separation between corner reflectors, then the period of the interference pattern will be 2 cm or less. With a 7.6 cm diameter collector for the GBAA, we get $P = 3.8$ and a scintillation variance reduction of about 16.* The important point is that fades in intensity that are deeper than about 25% of average intensity are now impossible. We need only a negligible loss factor in the detection equation for the scintillation of the corner reflector array. The sort of corner reflector array pattern that would achieve this averaging is shown in Fig. 4.

* Since there are many interference patterns, (one for each of the $N^2 - N$ pairs of corner reflectors), we would expect a further reduction of the variance by not just 16, but $16(N^2 - N)$.

6. TURBULENCE SCINTILLATION

Just as scintillation of the corner reflector array could cause the target to be missed because at the instant when a strong return ought to have been observed, it was in a scintillation fade condition, likewise scintillation induced by atmospheric turbulence can cause a target to be missed. It, too, can result in an increase in the required transmitter power to assure target detection. This increase in the power requirement corresponds to a propagation loss factor. To determine the magnitude of this loss factor, we note that the statistics of the scintillation will be log-normal and that loss factor has been calculated in reference (7). It should be noted that the fact that the statistics are log-normal is a consequence not only of the log-normal nature of the basic propagation process, as first pointed out by Tatarski⁸, but also depends on Mitchell's result⁹ that the sum of log-normals is log-normal. We require this last fact since there is a substantial amount of aperture averaging, i.e., summation in making up the received signal.

Our first task is to evaluate the log-amplitude variances, σ_e^2 , for the up-link and for the down-link. It can be shown¹⁰ that for a point source, such as we can consider either the GBAA transmitter or the individual corner reflectors to be,

$$\sigma_e^2 \propto \int_0^z ds C_N^2(s) \left[\frac{(z-s)s}{z} \right]^{5/6}. \quad (1)$$

Here z is the length of the propagation path, s is position along the path, and $C_N^2(s)$ is the refractive-index structure constant at s . The first important thing to note about Eq. (1) is that when we consider the altitude dependence of C_N^2 , as shown in Fig. 1, and match it to the behavior of $[(z-s)s/z]^{5/6}$, we see that the value of the integral is almost independent of z for values of $z \approx 30$ km, and is apparently only slightly dependent on z for values between 10 km and 30 km. This means that we can consider the value of σ_e^2 for z approaching infinity. This justifies our intended use of measured stellar scintillation values.

The second important thing to note about Eq. (1) is that because of the symmetry of $[(z-s)s/z]^{5/6}$, we get the same result whether we take the ground level to correspond to $s = 0$ or to $s = z$. This means that σ_e^2 is the same for the up-link and the down-link. A good measured value for σ_e^2

is provided by Burkel¹¹, who obtained a value of 0.0511 at 0.55 microns, measured near the zenith. Using a $k^{7/6}$ correction for wavelength and noting the $\sec^{11/6} \theta$ dependence on zenith angle, we get as the nominal value we shall use

$$\sigma_s^2 = 0.0554 \sec^{11/6} \theta. \quad (2)$$

If this were the scintillation on a one-way path, then in the round trip we would expect a value of $0.1108 \sec^{11/6} \theta$. Referring to the results of reference (7), even at the zenith we would experience a loss factor of about 8 dB, or a laser power requirement increase of 2.5, while at $\theta = 45^\circ$, the log-amplitude variance would be 0.209 and the loss factor would be about 12 dB, or a laser power factor of 4.0, certainly more than was allowed for.

Fortunately, these calculated scintillation values do not apply because of averaging. First, the total amount of energy collected by the corner reflector array represents an average. According to whether we consider a compact array, or a widely spaced array as shown in Fig. 4, we may expect different averaging factors. For the 30 km altitude at the 45° zenith angle, which constitutes the worst case, the scintillation correlation distance for illumination on the array is $(4z/k)^{1/2} \approx 12$ cm. If we are dealing with the compact array, then from the results of reference (12), considering that the pattern of 8 corner reflectors, each about 7.5 cm in diameter, will have a diameter of about 22.5 cm, we see that the averaging factor will be

$$\Theta_{cr,c} = 0.13 \quad (3)$$

while if the array is dispersed, we get a factor of 0.60 for the individual corner reflector, and factor of 0.125 for the eight separate units. This gives an aperture averaging factor of

$$\Theta_{cr,d} = (0.60)(0.125) = 0.075 \quad (3')$$

The log-amplitude variance after averaging can be written as

$$\tilde{\sigma}_L^2 = \frac{1}{4} \ln \left\{ 1 + \Theta [\exp(4\sigma_L^2) - 1] \right\}. \quad (4)$$

According to whether or not the array is dispersed, we get for the worst case up-link (i.e., $z = 30 \text{ km}$, $\theta = 45^\circ$),

$$(\tilde{\sigma}_L^2)_{up; ce, c} = 0.0425, \quad (5)$$

$$(\tilde{\sigma}_L^2)_{up; CR, O} = 0.0234. \quad (5')$$

On the down-link, to determine the aperture averaging factor, we have to consider two separate factors. The first has to do with the angular range over which scintillation from separate sources may be considered to be coherent. The correlation angle has been found in reference (13) to be $(4/zk)^{\frac{1}{2}}$, which in terms of the source plane corresponds to the up-link scintillation correlation distance $z(4/zk)^{\frac{1}{2}} = (4z/k)^{\frac{1}{2}}$. This suggests that we can use the same aperture averaging factors on the down-link to account for the extended nature of the source.

There is also aperture averaging for the GBAA collector optics which is 7.5 cm in diameter. The correlation length for scintillation on the ground is $(4h_0 \sec \theta / k)^{\frac{1}{2}}$. Here h_0 corresponds to the nominal scale height of turbulence and is about $3 \times 10^3 \text{ m}$. Taking $\theta = 45^\circ$, we get for the correlation distance, 3.7 cm. The aperture averaging factor is found to be

$$\Theta_{GR} = 0.24 \quad (6)$$

for the ground receiver. Combining this with the results in Eq.'s (3) or (3'), we get for the down-link in the case of compact or dispersed corner reflectors

$$(\tilde{\sigma}_e^2)_{\text{down; CR,c}} = 0.0102 , \quad (7)$$

$$(\tilde{\sigma}_e^2)_{\text{down; CR,o}} = 0.0056 . \quad (7')$$

We get for the total up-link plus down-link scintillation

$$(\tilde{\sigma}_e^2)_{\text{total; CR,c}} = 0.0527 , \quad (8)$$

$$(\tilde{\sigma}_e^2)_{\text{total, CR,o}} = 0.0290 . \quad (8')$$

This gives rise to loss factors of

$$(L)_{\text{CR,c}} = 4.0 \text{ dB} = 1.60 , \quad (9)$$

$$(L)_{\text{CR,o}} = 2.6 \text{ dB} \equiv 1.35 . \quad (9')$$

These are equivalent to requirements for additional laser power of 60% or 35%, depending on the corner reflector array pattern.

7. CONCLUSIONS

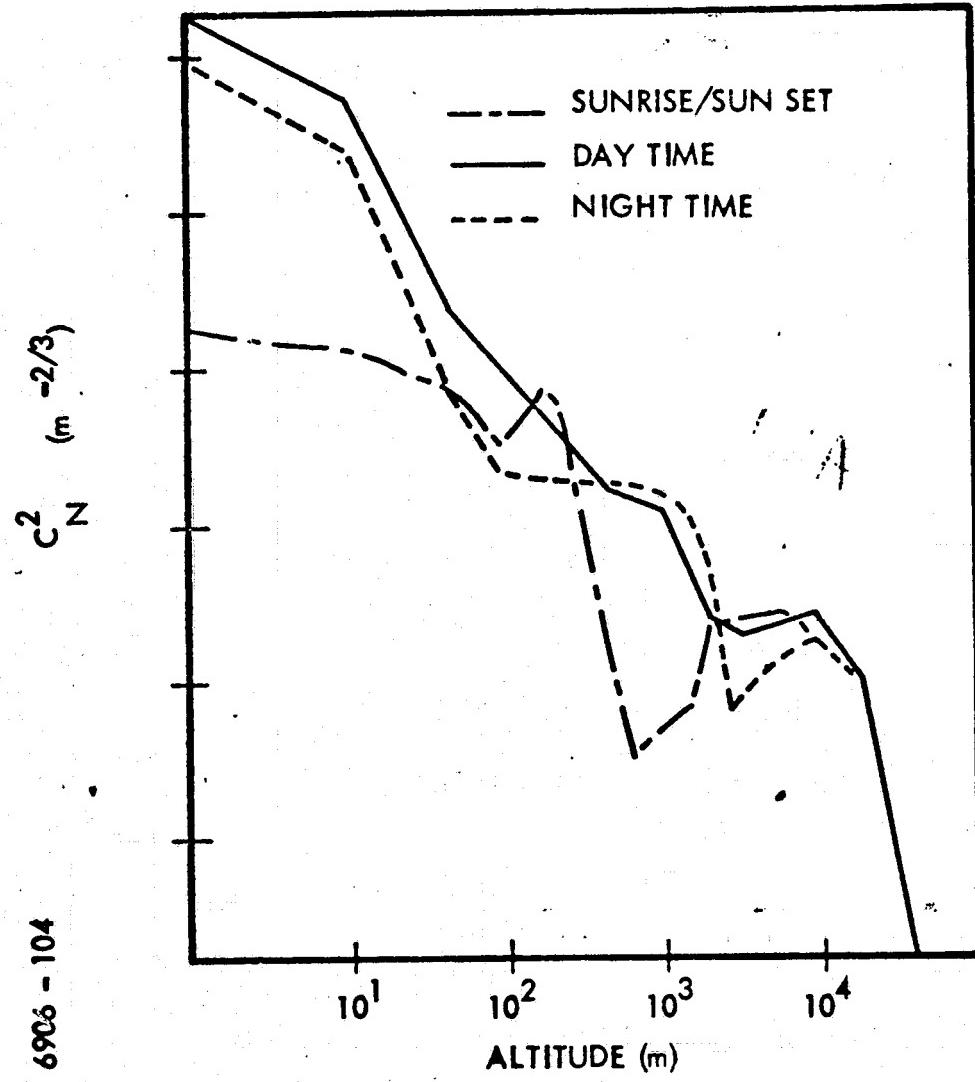
If we plan to use the compact array, the array scintillation requirement is for almost an additional 100% more power, meaning a total power increase of nearly $(1 + .6)(1 + 1) = 3.2$, i.e., an additional 220%. If we utilize the dispersed array pattern, then the array scintillation will require no more than about 25% additional laser power, for a total additional laser power requirement of about 70%. This falls well within the factor of two allowance made in the preliminary systems analysis. It is worth noting that estimates for daytime strength of turbulence, compared to the nighttime data which we have used may run a factor of two higher, which will result in almost a 5 dB loss, corresponding to a required 75% increase in required power for the dispersed corner reflector array. This, with the array scintillation requirement of about 25%, starts to push things just to the values which we have allowed for. If this is coupled with a further factor of two increase in the strength of turbulence for what is referred to in reference (2) as the worst 10% conditions, we have a 7.5 dB loss factor, or about a 2.4 increase required, so that it is apparent that even with the dispersed array, we have not allowed a sufficient safety factor in laser power.

We conclude that (1) a dispersed corner reflector array pattern of the type shown in Fig. 4 is required in place of a compact array; and (2) the factor of 0.5 allowance for propagation effects other than absorption is apparently adequate for all except the most extreme case, corresponding to 30 km altitude, 45° zenith angle and worst 10% strength of turbulence for daytime conditions.

RETROSCATTERING OF THE
REFLECTED FIELD IS POOR

REFERENCES

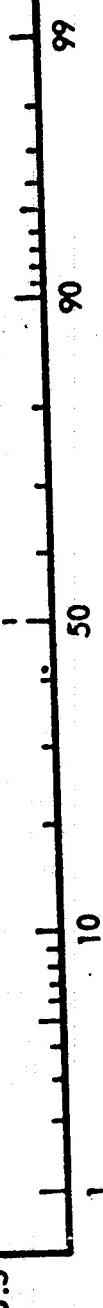
1. D. L. Fried, "Optical Space Communication," NASA SP-217, Appendix G, p.135, Aug. 1968.
2. D. L. Fried, G. E. Mevers, and R. P. Futrelle, Final Report on Contract No. DAHC60-69-C-0080.
3. A. A. Hoag, Bulletin Astronomique XXIV Part 2, 269 (1964)
4. A. B. Minel, "Final Report on the Site Selection Survey for the National Astronomical Observatory," Contributions from Kitt Peak National Observatory No. 45, Oct. 1963.
5. D. Middleton, "An Introduction to Statistical Communications Theory," McGraw-Hill Book Co., Inc., New York 1960, p.366.
6. M. Abramowitz and I. A. Stegun, "Handbook of Mathematical Functions," U. S. Government Printing Office, Wash., D.C. 20402, June 1964, Chapt. 7.
7. D. L. Fried and R. A. Schmeltzer, Appl. Opt. 6, 1729 (1967).
8. V. I. Tatarski, "Wave Propagation in a Turbulent Medium," McGraw-Hill Book Co., Inc., New York 1961.
9. R. L. Mitchell, J. Opt. Soc. Am. 58, 1267 (1968).
10. D. L. Fried, J. Opt. Soc. Am. 57, 980 (1967).
11. J. J. Burke, Optical Science News Letter (Univ. of Arizona) Apr.-May 1969, p.74.
12. D. L. Fried, J. Opt. Soc. Am. 57, 169 (1967).
13. D. L. Fried, "Spectral and Angular Covariance of Scintillation for Propagation in a Randomly Inhomogeneous Medium," in Final Report on Contract No. NAS8-18035, April 1967 - to be published in Applied Optics.



VERTICAL DISTRIBUTION OF THE OPTICAL STRENGTH
OF ATMOSPHERIC TURBULENCE

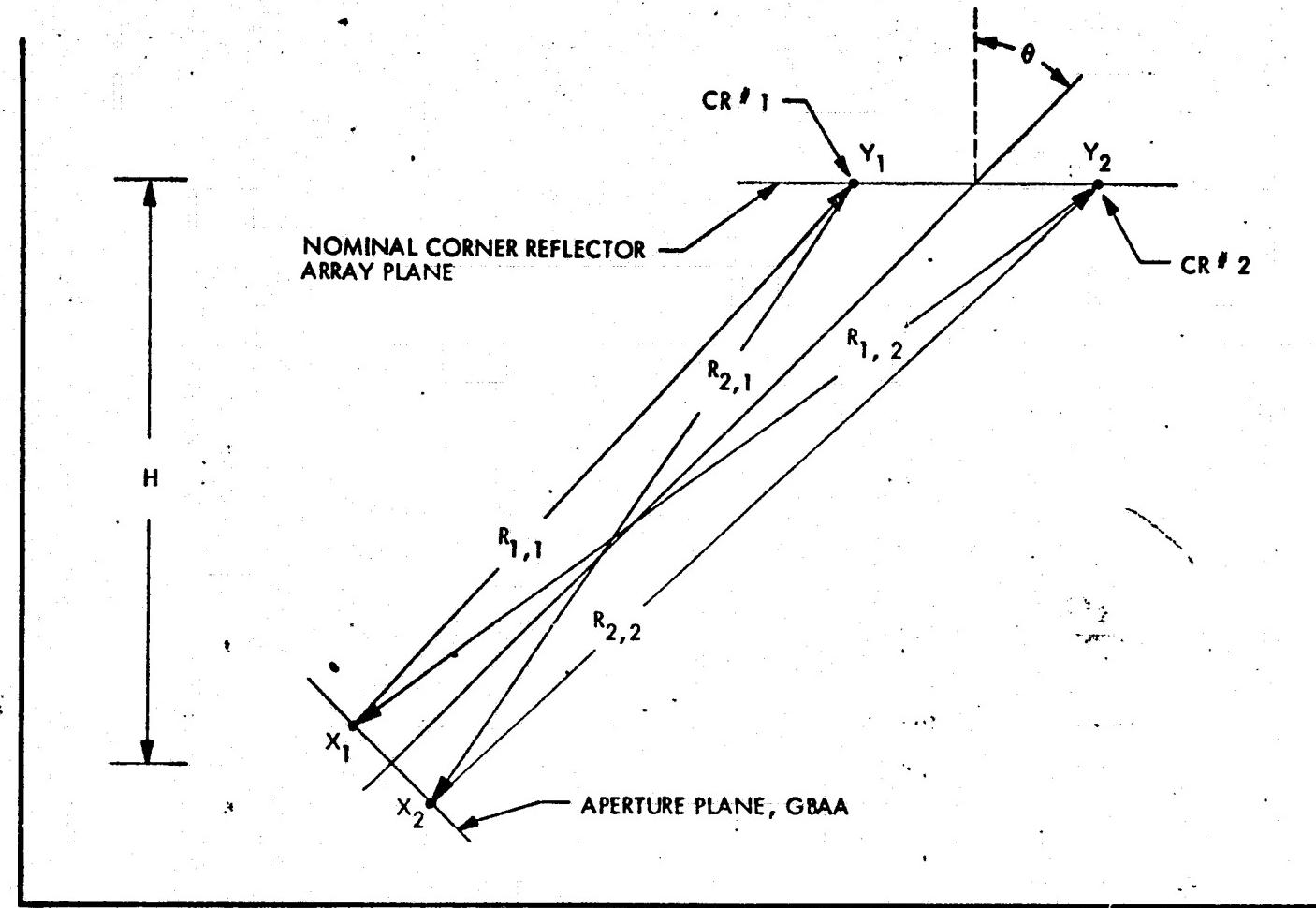
STELLAR IMAGE SIZE PROBABILITY DISTRIBUTION

CUMULATIVE PROBABILITY (%)



9069 - 103

101 - 9669



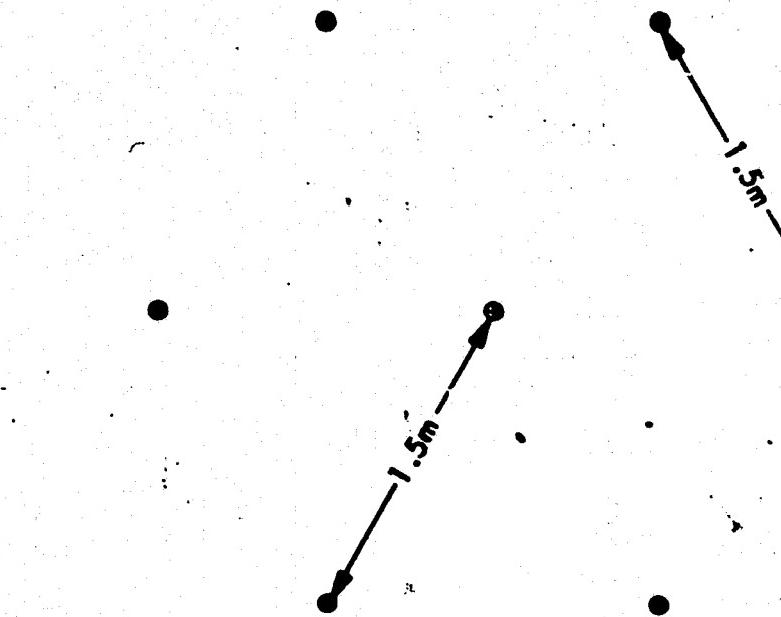
OBSERVATION GEOMETRY FOR CALCULATION OF CORNER REFLECTOR
ARRAY INTERFERENCE PATTERN IN GBAA APERTURE PLANE

REFLECTIVITY OF THE
ORIGINAL PAGE IS POOR

IC - 31

6906 - 102

PATTERN "A"



● 7.5cm DIA CORNER-REFLECTOR

POSSIBLE CORNER - REFLECTOR ARRAY PATTERNS

PATTERN "B"



APPENDIX B

AVLOC PREFLIGHT CHECK-OFF SHEETS

TEST PERSONNEL: CHRYSLER John Riles

ITT Virgil Hammock

OTHER _____

FL # 14

PRC 3-7-73

POST 3-7-73

3.3 O-Graph Setup ()

3.4 O-Graph Data Channels

STATUS "22"

<u>O-Graph Channel</u>	<u>Data Signal</u>	<u>Unity Line</u>	<u>Check Column</u>
1		.5v	(✓) ✓
2		.5v	(✓) ✓
3	B_y	36 sec	(✓) -
4	B_z	36 sec	(✓) ✓
5	Comp. Stat.	0.5v	(✓) ✓
6	Y-Accel.	0.1g	(✓) ✓
7	L-Accel.	0.1g	(✓) ✓
8	PAM Channels		
1.	"0-V"	0.5v	(✓) ✓
2.	"5-V"	0.5v	(✓) ✓
3.	f. Bea.	0.5v	(✓) ✓
4.	TV filt.	0.5v	(✓) ✓
5.	Col. Ap.	0.5v	(✓) ✓
6.	Rm. Div.	0.5v	(✓) ✓
7.	Las. Shut.	0.5v	(✓) ✓
8.	Lin. Scint.	0.5v	(✓) ✓
9.	Revr. Att.	0.5v	(✓) ✓
10.	TV Bea.	0.5v	(✓) ✓
11.	60 Hz Pwr.	13.5v	(✓) ✓
12.	400 Hz Pwr.	13.5v	(✓) ✓
13.	28v unreg.	3.2v	(✓) ✓
14.	28v reg.	3.2v	(✓) ✓
15.	5v DC	4.6v	(✓) ✓
16.	+15v DC	1.5v	(✓) ✓

<u>O-Graph Channel</u>	<u>Data Signal</u>	<u>Unity Line</u>	<u>Check Column</u>
	17. AOCP Temp	0.5v	(✓) ✓
	18. Can. Temp.	0.5v	(✓) ✓
9	E_y	2 sec	(✓) ✓
10	E_z	2 sec	(✓) ✓
11	P-Accel.	0.1g	(✓) ✓
12	Log. Scint.	1v	(✓) ✓
13	Pwr. Mon.	1v	(✓) ✓
14	Timing	1v	(✓) ✓

4.0 Preliminary Electrical Status

Record 60 Hz. voltage 123
122

Record 400 Hz. voltage 144
145

STATUS "22"

122

145

<u>Selector Switch Position</u>	<u>Data Identification</u>	<u>Preflight</u>	<u>Postflight</u>
1	28v Unreg.	<u>25.7</u>	<u>26.7</u>
2	+5v	<u>10.0</u>	<u>10.09</u>
3	28v Reg.	<u>28.0</u>	<u>28.05</u>
4	+5v	<u>5.23</u>	<u>5.24</u>
5	+15v	<u>14.68</u>	<u>14.65</u>
6	-15v	<u>14.10</u>	<u>14.17</u>
7	Timing	<u>2.64</u>	<u>2.63</u>
8	Ap. Sel.	<u>.06</u>	<u>.09</u>
9	Bm. Div.	<u>1.25</u>	<u>1.85</u>

Selector Switch Position

	<u>Data Identification</u>	<u>Preflight</u>	<u>Postflight</u>
10	Revr. Att.	.97	.97
11	TV Tilt	5.67	S.36
12	TV Drift	5.23	5.22
13	Shut	4.71	.05
14	Filt.	.07	.05
15	F. Bea.	.02	.02
16	He-He Pwr.	1.00	.91
17	Lin. Scint.	.10	.10
18	Log. Scint.	.64	.31
19	Comp. Stat.	.99	.02

5.0 GCE/AOCP AlignmentSTATUS "33"Task

Connect TV Monitor

Preflight

(✓)

(✓)

Set Tektronics Scope for monitoring
of Cruciform

(✓)

(✓)

Position GCE so as to align GCE and
aircraft

(✓)

(✓)

Check beam steerer operation and
systems alignment

(✓)

(✓)

Set Brush Recorder to record E_y and E_z

(✓)

(✓)

Record pitch gimbal angle 7.5°

(✓)

(✓)

Record azimuth gimbal angle 0

(✓)

(✓)

REPRODUCIBILITY OF THE
ORIGINAL PAGE IS POOR

6.0 Systems Operational Test**STATUS "33"****6.1 Acquisition System****Preflight****Postflight**

<u>Item</u>		
Coarse Beacon	(✓)	(✓)
Fine Beacon	(✓)	(✓)
Two-digit display "33" 25		
Sample data slice	(✓)	(✓)

STATUS RECORDINGS

<u>A. C. VOLTAGE</u>	MONITOR PANEL		O-GRAF		<u>CHAN #</u>
	<u>PRE</u>	<u>POST</u>	<u>PRE</u>	<u>POST</u>	
117 @ 400 Hz	<u>116</u>	<u>118</u>	—	—	COM 11
117 @ 60 Hz	<u>123</u>	<u>122</u>	—	—	COM 12
<u>SWITCH D.C. VOLTAGE</u>					
1 + 28 Unreg.	<u>25.74</u>	<u>26.35</u>	—	—	COM 13
2 ± 5	<u>9.96</u>	<u>10.23</u>	—	—	
3 + 28 Reg.	<u>27.96</u>	<u>28.03</u>	—	—	COM 14
4 + 5	<u>5.27</u>	<u>5.29</u>	—	—	COM 15
5 + 15	<u>14.66</u>	<u>14.66</u>	—	—	COM 16
6 - 15	<u>14.14</u>	<u>14.16</u>	—	—	
7 Timing	<u>2.66</u>	<u>2.69</u>	—	—	ST 14
8 AP Sel	<u>.08</u>	<u>.07</u>	—	—	
9 EM Div	<u>1.75</u>	<u>1.15</u>	—	—	COM 6
10 RCVR Att	<u>.97</u>	<u>.97</u>	—	—	COM 9
11 TV Tilt	<u>5.08</u>	<u>5.07</u>	—	—	
12 TV Drift	<u>5.24</u>	<u>5.22</u>	—	—	
13 Shut	<u>4.71</u>	<u>9.72</u>	—	—	COM 7
14 Filt.	<u>.08</u>	<u>.07</u>	—	—	COM 4
15 P. Bea.	<u>3.75</u>	<u>3.76</u>	—	—	COM 3
16 He-Ne Pwr.	<u>1.18</u>	<u>1.11</u>	—	—	CBW 12
17 Lin Scint	<u>.95</u>	<u>1.09</u>	—	—	COM 8
18 Log Scint	<u>1.63</u>	<u>2.15</u>	—	—	CBW 13
19 Com. Stat	<u>.94</u>	<u>.93</u>	—	—	ST 5

REPRODUCTION OF THE
ORIGINAL IS NOT TO PEAK
ORIGINAL

6.2 Uplink Commands

	<u>Master Tone</u>	<u>Command Code</u>	<u>Preflight</u>	<u>Postflight</u>
Track Mode Defeat		12	(✓)	(✓)
Increase/Decrease Aperture		13	(✓)	(✓)
Increase RCVR Att.	/	14	(✓)	(✓)
Decrease RCVR Att		15	(✓)	(✓)
Increase BM Div		23	(✓)	(✓)
Decrease BM Div		24	(✓)	(✓)
Remove/Install TV Filt.		25	(✓)	(✓)
Laser Shutter Open Overide		34	(✓)	(✓)
Select Video for Downlink		35	(✓)	(✓)
Select TM for Downlink		45	(✓)	(✓)
Select Rev. Mon. Downlink		21	(✓)	(✓)
Select Bit-Error Downlink		31	(✓)	(✓)
Enable/Disable Beam Deflector		41	(✓)	(✓)

6.3 AOCP Modulation Temp ()

	<u>Preflight</u>	<u>Postflight</u>
Record DC Max.	<u>14</u>	<u>10</u>
Record DC Min.	<u>5</u>	<u>3</u>
Record Calculated Mod. Index	<u>.98</u>	<u>MAX-MIN</u> <u>MAX+MIN</u>

6.4 Status Display

<u>Command Code</u>	<u>Two-Digit Display</u>	<u>Preflight</u>	<u>Postflight</u>
	33	(✓)	(✓)
23	41	(✓)	(✓)
13	91	(✓)	(✓)
13	41	(✓)	(✓)
24	33	(✓)	(✓)
24	25	(✓)	(✓)
24	17	(✓)	(✓)
24	09	(✓)	(✓)
24	01	(✓)	(✓)
14	02	(✓)	(✓)
14	03	(✓)	(✓)
14	04	(✓)	(✓)

6.5 Inflight Test

<u>Two Digit Display</u>	<u>Check Column</u>	
30	(✓)	✓
14	(✓)	✓
05	(✓)	✓
325	(✓)	✓

All lights reset

6.6 Pilot's Directional Indicator

<u>Item</u>	<u>Check Column</u>	<u>Meter Reading</u>	
No Signal	(✓)	Pegged	✓
0 Volts	(✓)	Center	✓
+10 Volts	(✓)	Right	✓
-10 Volts	(✓)	Left	✓

6.7 Dynamic Tracking Performance

	<u>Preflight</u>	<u>Postflight</u>
Record Video Circle diameter	<u>3 1/8"</u>	<u>3 1/8"</u>
Record rotation period	<u>1.5</u>	<u>1.5</u>
Record calculated rate	<u>3.6</u>	<u>1.82 Diameter Period</u>

<u>Channel</u>	<u>O-Graph Data</u>	<u>Preflight</u>	<u>Postflight</u>
1..		(✓)	(✓)
2		(✓)	(✓)
3	B _y	(✓)	(✓)
4	B _z	(✓)	(✓)
8	PAM Channels: 3 f. Bea.	(✓)	(✓)
	7 Laser shutter	(✓)	(✓)
	10 TV Bea.	(✓)	(✓)
9	E _y	(✓)	(✓)
10	E _z	(✓)	(✓)

6.8 Vibration Measurement

<u>Item</u>	<u>Preflight</u>	<u>Postflight</u>
Vib-pitch	(✓)	(✓)
Vib-yaw	(✓)	(✓)
Vib-long	(✓)	(✓)

6.9 Set Boresight

Status "09"

Draw Sketch

7.0 Scintillation Check

Log	Lin.	Base	
<u>1.12</u>	<u>.36</u>	<u>.15</u>	Threshold
<u>2.13</u>	<u>.93</u>	<u>.50</u>	
<u>2.53</u>	<u>1.70</u>	<u>1.00</u>	
<u>2.79</u>	<u>2.47</u>	<u>1.59</u>	
<u>3.03</u>	<u>3.19</u>	<u>2.32</u>	
<u>3.10</u>	<u>3.47</u>	<u>2.78</u>	
<u>3.27</u>	<u>3.91</u>	<u>3.44</u>	
<u>3.42</u>	<u>4.27</u>	<u>4.51</u>	
<u>3.82</u>	<u>4.84</u>	<u>5.24</u>	

8.0 Cockpit Check

	<u>Preflight</u>	<u>Postflight</u>
Tape Rec. On	(✓)	(✓)
TV Mon.	(✓)	(✓)
Calibration	(✓)	(✓)
Gimbal Scan	(✓)	(✓)
Fine Track	(✓)	(✓)
Status Lights	(✓)	(✓)
B. S. Disable	(✓)	(✓)
Scint. Hold	(✓)	(✓)
Tape Rec. Off	(✓)	(→)
<u>Tape Rec.</u>	(←)	(→)

9.0 Securing for Flight

9.1 Power Down Procedure	(✓)
9.2 Fairing Installation	(✓)
9.3 Retro Reflectors	(✓)
Mechanical Security	(✓)
Optical Surfaces	(✓)

REPRODUCIBILITY OF THE
ORIGINAL PAGE IS POOR.

APPENDIX C

**PULSED ARGON ION LASER
BEAM MOTION STUDY**

**Final Report PO #29407
November 1971**

**Michael R. Smith
Britt Electronic Products Corp.**

APPENDIX C

SECTION I: INTRODUCTION

This report summarizes the results of an experimental study of the angular and translational beam motion which occurs in the Britt Model 2000 laser, relative to the laser housing, when the laser is placed in an attitude similar to the extremes which are encountered in the NASA GBAA System.

This report contains a proposal for a program to design and construct a laser mirror cavity structure which will not be subject to any appreciable beam motion or cause any appreciable power output variation as a result of any particular orientation of the laser, such as is encountered in the NASA GBAA System. The proposal proposes the design and construction of two complete mirror cavity structures, one each for the original ITT laser and for the ITT spare discharge tube.

SECTION II: BEAM MOTION STUDY

The purpose of the beam motion study was to determine the amount and the cause of angular and translational motion which occurs in the Britt Model 2000 laser when the laser is placed in an attitude similar to that encountered in the NASA GBAA System.

A. Angular Deviation

A Britt Model 2000 laser (in house demo) was used to experimentally determine a maximum angular deviation of approximately .8 mrad, which is approximately equal to one beam diameter. The angular deviation was measured with the laser axis in a horizontal plane, while the laser was being subjected to a roll of 360 degrees about its axis. This was considered to be the worst case measurement.

The experimental apparatus which was used is described in figure 1. It consisted of a rigid optical rail to which were rigidly mounted a laser, a focussing lens (lens 1), an imaging lens (lens 2) and a viewing screen. Figure 2. illustrates that the displacement of the focussed spot at the focal plane of lens 1 is due only to angular deviation of the incident beam. A linear displacement of the incident beam does not result in a motion of the focussed spot. The angular deviation of the incident beam is related to the displacement of the focussed spot and the focal length of the lens.

$$\theta = \theta' \approx \frac{d}{f}$$

The imaging lens provides a magnification so that the displacement can be measured more readily.

B. Lateral Displacement.

The lateral displacement of the laser beam exiting from the laser was not measured directly. The lateral displacement of the laser mode selecting aperture (which determines the beam position) was measured. It is assumed that the displacement of the aperture is coincident with the displacement of the laser beam. A maximum displacement of .030 inches was measured for all laser orientations. Figure 3. shows the apparatus which was used to measure lateral displacement. The aperture inside the laser cavity was imaged onto a viewing screen by a lens. The displacement of the image is proportional to the motion of the aperture.

$$L = M \ell$$

where M is the magnification of the imaging system.

C. Power Variation

The laser power was measured simultaneously with the beam deflection measurements. The power varied from 100% with the laser upright along the horizontal axis, to approximately 0% with the laser rotated 180 degrees about the horizontal axis.

6906 - 160

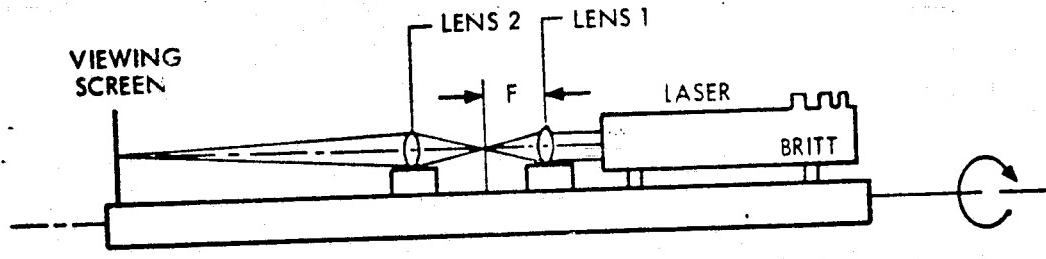
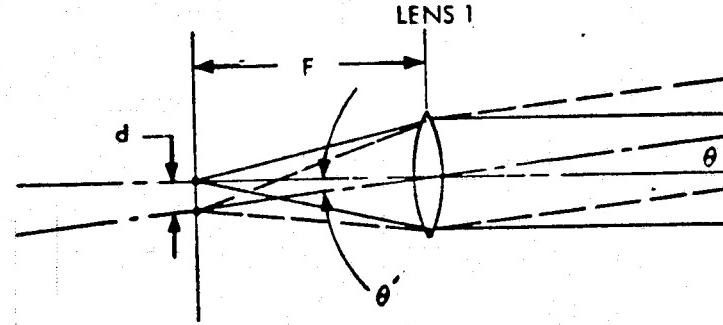


Figure 1.

6906 - 161



$$\theta = \theta' \approx \frac{d}{F}$$

Figure 2.

EXPERIMENTAL PROCEDURE

LINEAR DISPLACEMENT OF BEAM

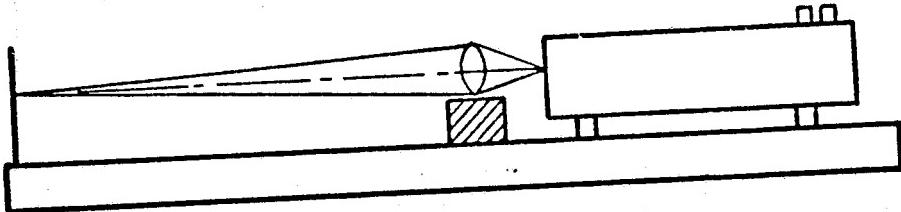
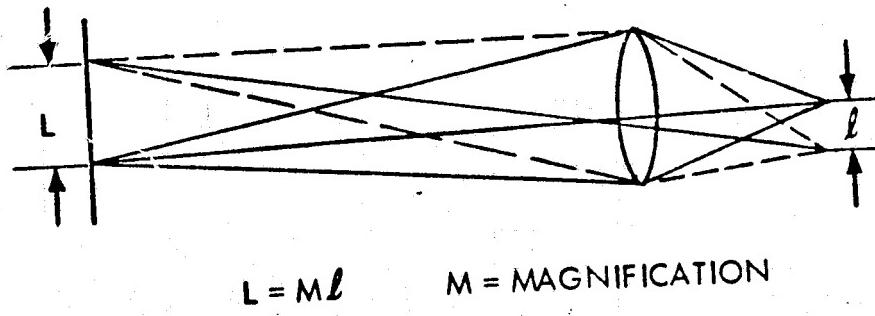


IMAGE OF LASER MODE SELECTING APERTURE ON
VIEWING SCREEN



6906 - 162

Figure 3.

REPRODUCIBILITY OF THE
ORIGINAL PAGE IS POOR

D. Analysis of Results

The observed angular deviation of the laser beam can adequately be accounted for by assuming that the laser mirror cavity structure is subject to bending under its own weight. A calculation of the magnitude of the bending adequately accounts for the amount of power variation which is observed. The lateral displacement of the beam is apparently caused by a wide tolerance in the gimble structure which allows the mirror yoke to rotate slightly as a function of roll orientation about the horizontal axis.

Figure 4. illustrates how the existing mirror cavity structure could cause the angular beam deflection and power detuning. The existing structure is supported near the ends so that a bending of the structure under its own weight will cause the mirror yoke to be oriented at an angle to the horizontal plane. In practice, the mirrors are adjusted to compensate for the angle α . However, when the structure is rotated 180 degrees, the bending is reversed resulting in a tilt of each mirror of twice α in the wrong direction.

The proposed mirror structure would have the support points located in such a position so that the bending angle is zero at the mirror plane. The penalty which must be paid is a displacement of the beam by a small amount. This displacement is in practice extremely small and can be made smaller by decreasing the weight of the entire structure. A rotation of the proposed structure will not cause an angular misalignment of the mirrors.

III PROPOSED MIRROR CAVITY STRUCTURE DESIGN

The results of the study indicate that a satisfactory mirror cavity structure would be designed. It would consist of a considerably lightened structure, with the gimbals positioned in such a way to provide a zero tilt angle at the mirror plane, and with a close tolerance gimble structure which will not be subject to rotation of the mirror yokes about the mirror support tube due to loose tolerances.

The proposed mirror cavity structure will be subject to the following specifications:

1. power variation due to orientation changes will be less than $\pm 10\%$

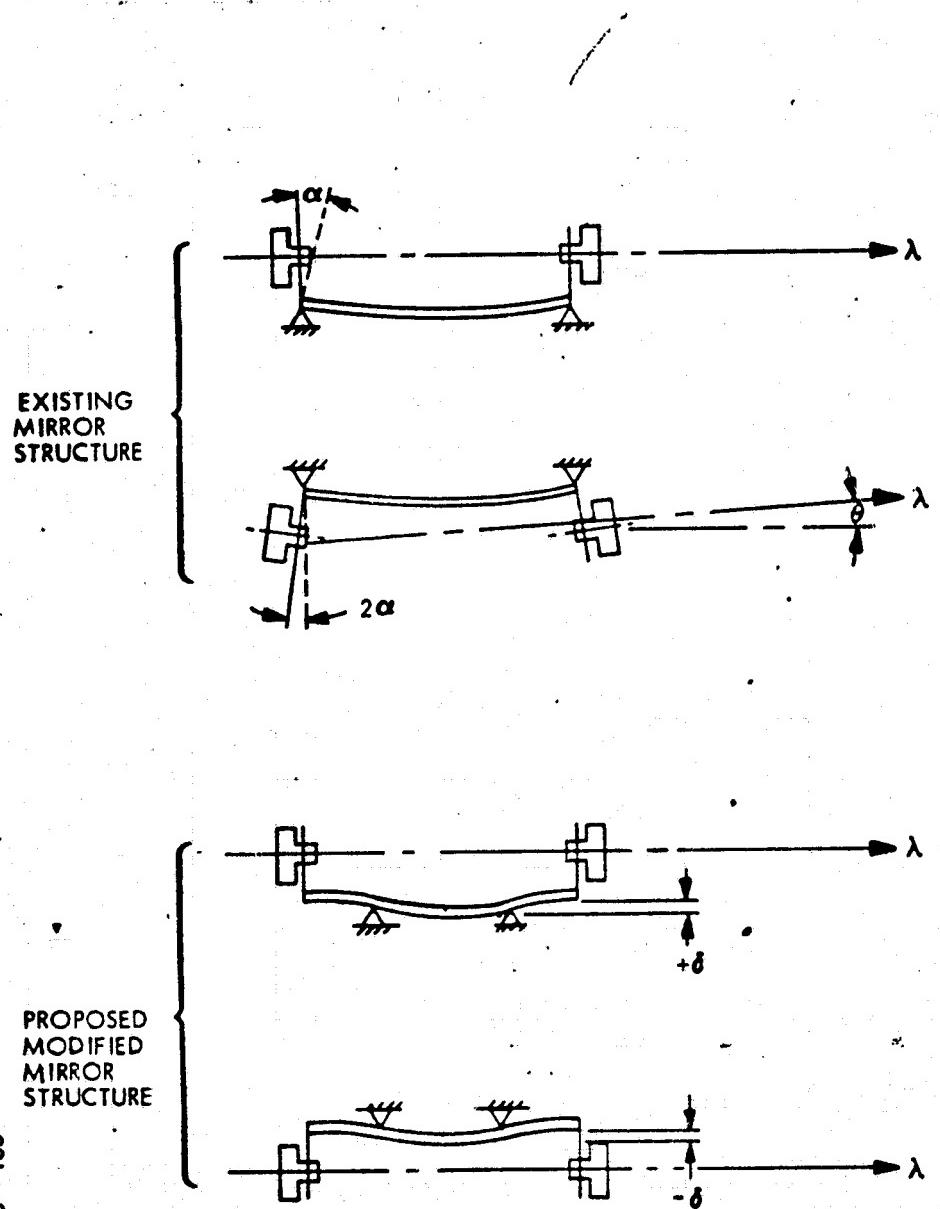


Figure 4.

6906 - 163

REPRODUCTION OF THE
ORIGINAL PAGE IS POOR

for all orientations

2. the angular deviation of the output beam with respect to the laser housing will be less than .3 mrad for all orientations
3. the linear displacement of the laser beam relative to the laser housing at the output mirror will be less than .2 mm

It is estimated that the price for designing the mirror cavity structure to meet the specifications described above, for constructing two structures, and for adapting the structures to the ITT laser and the ITT spare discharge tube is \$3,335 FOB Santa Monica, CA. The estimated completion date is 30 days after receipt of order.

APPENDIX D

**INVESTIGATION OF ELECTRO-OPTICAL TECHNIQUES
FOR
CONTROLLING THE DIRECTION OF A LASER BEAM**

INVESTIGATION OF ELECTRO-OPTICAL TECHNIQUES FOR CONTROLLING THE DIRECTION OF A LASER BEAM

The development of the piezoelectric-bender-mirror (PBM) deflector¹ has made available a lightweight, compact, low-power device for angular positioning of a laser beam. This report describes the design of such a deflector to meet the needs of a particular optical system and the incorporation of a strain gage sensing element and related circuitry in the deflector for precise monitoring of deflection. A complimentary solid-state high-voltage deflector drive amplifier has also been developed which will hold a static deflection with a minimum of standby power.

The objectives of this program called for the development of a two-dimensional optical deflector, deflection sensor and drive amplifier to be used in an optical radar acquisition and tracking system. Deflector performance specifications were generated in discussions with International Telephone & Telegraph Federal Laboratories, who were contracted by NASA to design and construct the optical radar system and attendant electronics. From these specifications the deflector design was evolved.

In the following sections an approach to the design of deflectors to meet specific performance requirements will be outlined. Implementation of strain gages for deflection sensing will be discussed, including techniques for applying gages to minimize hysteresis and nonlinearity effects. The circuit design and theory of operation of the deflector drive amplifier will be detailed and performance characteristics for each of the items will be given.

In previous programs^{1,2} the PBM deflector was analyzed in detail. Expressions were derived for mirror deflection, mechanical resonance frequency, mirror distortion and electrical equivalent circuit in terms of the material constants and deflector geometrical configuration. These expressions are used here to obtain a set of design curves for a particular deflector geometry. The curves permit a

-
1. "Investigation of Electro-Optical Techniques for Controlling the Direction of a Laser Beam," Interim Report, Contract NAS8-11459, GT&E Laboratories Inc., May 12, 1967.
 2. "Investigation of Electro-Optical Techniques for Controlling the Direction of a Laser Beam," Interim Report, Contract NAS8-11459, GT&E Laboratories Inc., February 28, 1968.

rapid determination of the deflector performance boundaries and what parameter tradeoffs may be made in integrating the deflector with the rest of the system.

Development of Design Curves

In choosing a deflector design the parameters normally specified are:

- Beam deflection angle
- Pupil size
- Resolution
- Useful bandwidth
- Maximum voltage requirements

Other secondary but important considerations are capacitance, mechanical strength, mirror flatness, and size. The formulas which define each of these quantities show that they are interrelated and that specifying certain ones also fixes the others. These formulas have been derived previously^{1,2} and are repeated here (see Fig. 1):

Peak-to-peak beam deflection:

$$\phi_{pp} = 12 bd_{31} \frac{\ell}{t} E \quad (1)$$

Number of resolvable spot positions peak-to-peak at wavelength λ :

$$N_{pp} = \frac{\phi_{pp} D}{1.27\lambda} \quad (2)$$

Mechanical resonance frequency:

$$f_r = 21.9 (10)^3 \frac{t/\ell^2}{\sqrt{1 + 1.46 (M'/m) (L/\ell)^2}} \quad (3)$$

$$M' = M [1 + (\pi/L)^2 + 12(h/L)^2]$$

Maximum drive voltage:

$$V_p = \frac{Et}{2} \quad (4)$$

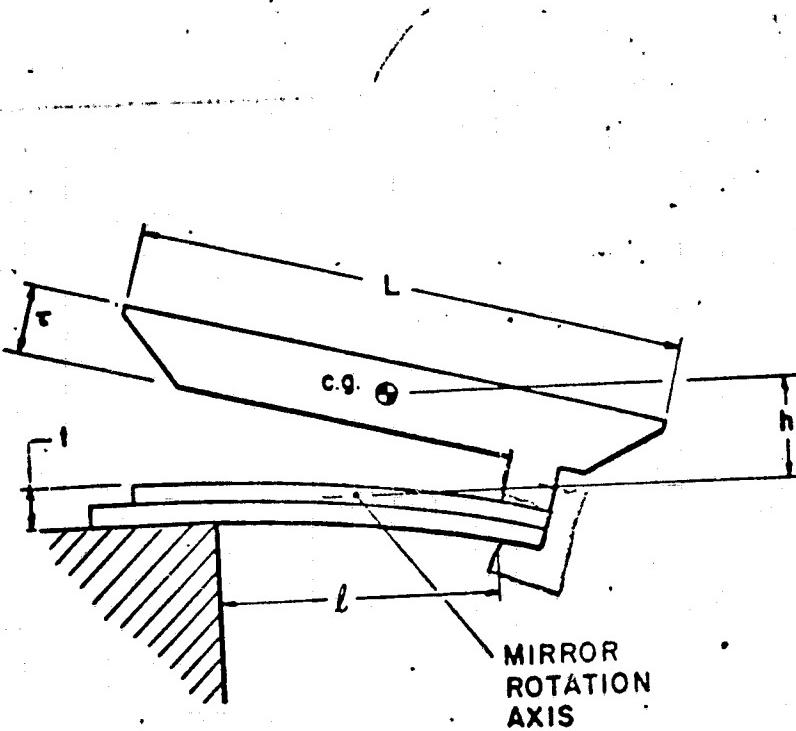


Fig. 1. Bender-driven-mirror deflector showing critical dimensions.

Pupil size for light beam incident at 45°:

$$D = \frac{L}{\sqrt{2}} \quad (5)$$

Capacitance of PZT-4 transducer :

$$C = 586 \frac{lw}{t} \text{ [pF]} \quad (6)$$

where (dimensions in inches)

E = depoling field of piezoelectric material

= $2.54(10)^4$ volts/inch for PZT-4*

d_{31} = pertinent electromechanical coupling factor

= $47(10)^{-10}$ inch/volt for PZT-4

b = factor varying with bender construction technique, determined
empirically = 1.44 for present deflectors

l = active length of transducer

t = thickness of transducer

w = width of transducer

m = mass of active portion of transducer

L = length of mirror

W = width of mirror

T = thickness of mirror

M = mass of mirror

M' = effective inertial mass of mirror

h = distance of mirror c.g. from mirror rotation axis

To simplify the design procedure, a basic deflector geometry has been chosen in which additional relationships between the deflector dimensions have been assumed. Some of these choices are based on practical experience as well as theoretical considerations.

*A piezoelectric ceramic material made by Clevite Corp.

The mirror thickness has been taken to be 1/8 its length and supported at a point about 0.6 of the distance from the center to its edge. Prior analysis² has shown that this thickness and support point will maintain the mirror flatness to better than $\lambda/10$ under all operating conditions. Consistent with this, the active transducer length will be approximately one-half the mirror length.

An important factor governing the mechanical resonance frequency is the ratio of mirror mass to transducer mass. This ratio may be adjusted to improve the resonance frequency without affecting the other parameters by making the transducer wider than the mirror. Beyond a factor of 2 difference in widths, however, this approach becomes ineffective because the transducer ends are weakly coupled to the center and begin to deflect independently.

Summarizing these assumed geometrical relations:

$$\tau = L/8$$

$$l = L/2$$

$$w = 2W$$

and as a practical nominal value the height of the mirror above the transducer is taken as:

$$h = 0.5\tau + 0.04L$$

Using these relations and the expressions for deflection angle, resolution, resonance frequency, maximum drive voltage, and pupil size a set of curves has been generated relating the different quantities. These are given in Figs. 2 and 3. The range of frequency extends only to 10 kHz because beyond this the equation for frequency becomes inaccurate. The curves are correct for a mirror substrate of fused silica and resolution is given for light of 0.5-micron wavelength.

Figures 2 and 3 contain the same information presented in different formats. Selecting any two of the variables automatically determines the others. One procedure for using the curves would be to select the resonance frequency and resolution thereby determining deflection angle, drive voltage and pupil size. If a square pupil is desired, then the mirror width and transducer capacitance are also determined.

The mechanical strength of a deflector tends to be proportional to its resonance frequency. Designs with a higher resonance will be less susceptible to

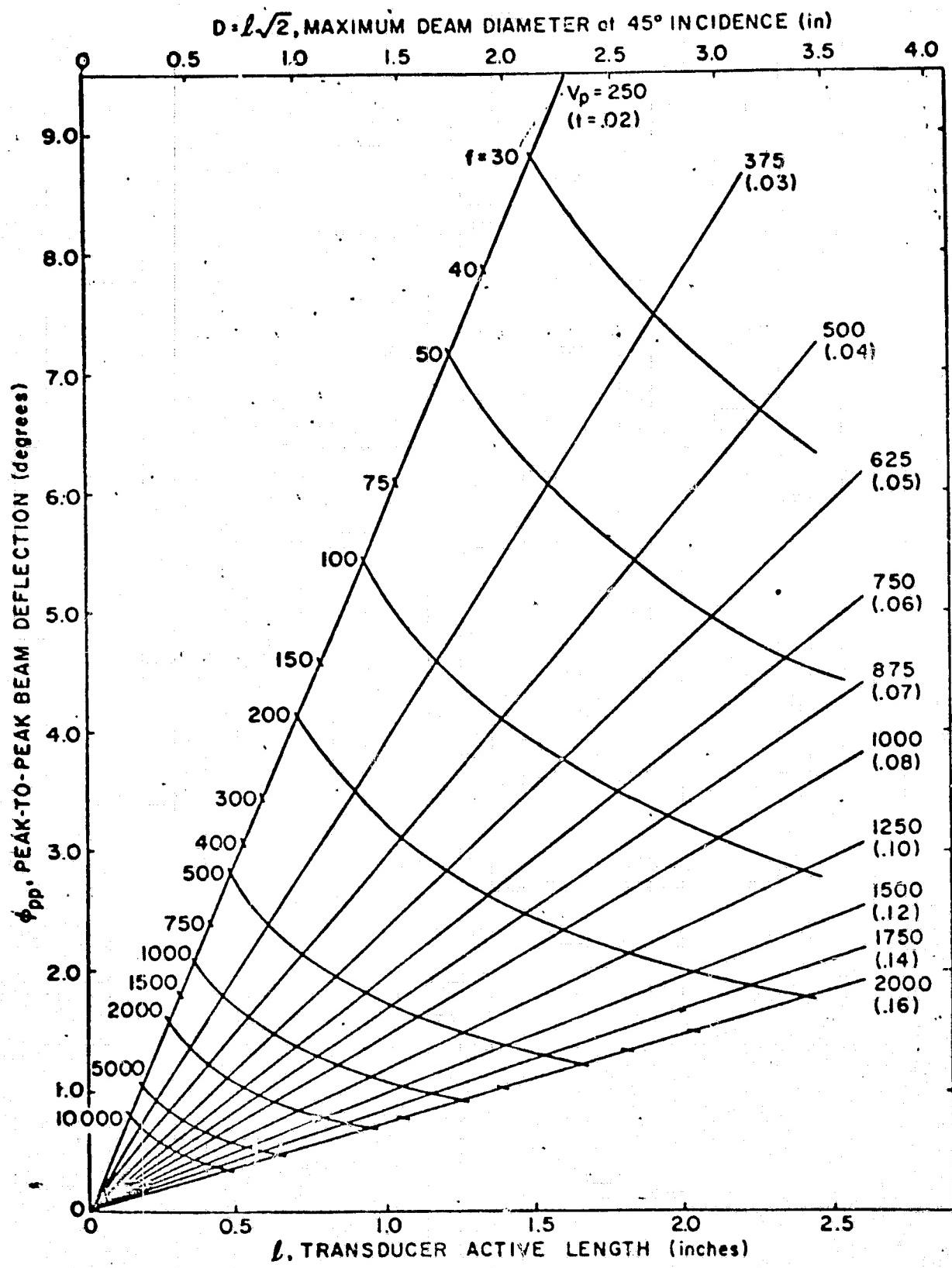


Fig. 2. Peak-to-peak beam deflection is plotted against bender active length or deflector aperture with resonance frequency and peak drive voltage as parameters.

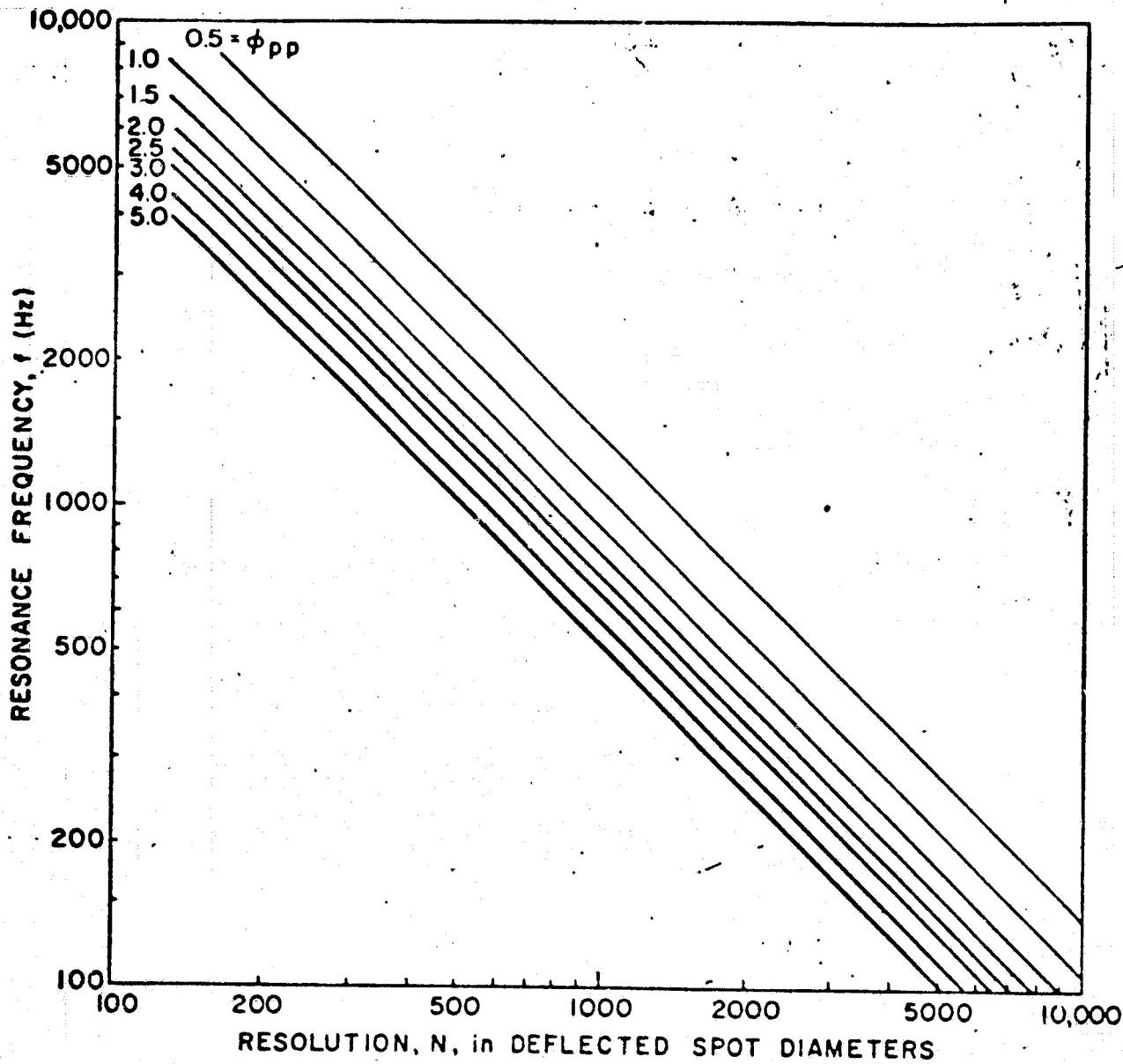


Fig. 3. Resonance frequency versus resolution with peak-to-peak deflection angle as a parameter. Resolution here is for a Gaussian beam of 0.5 micron wavelength incident at 45°.

mechanical shock, vibration, and electrical transients. Designing for resonance frequencies below a few hundred cycles is not recommended unless the structure incorporates a means for mechanical damping of the mirror vibration.

Deflector Design Meeting System Requirements

It was determined in a liaison meeting with ITT personnel that a two-dimensional deflector set was required which would deflect an f/10 cone of 0.9-micron laser light through at least 250 spot diameters in each dimension. The resonance frequency should be above 1000 Hz, since the deflector drive signal would have appreciable components at this frequency. An all-solid-state deflector drive amplifier was specified in keeping with the aim of eventual space qualifications of all of the system components. This set a limit of ± 500 volts on the maximum drive voltage which could be provided to the deflector with currently available high-voltage transistors.

With these restrictions the values $f = 1300$, $V = 500$ were used with Fig. 2 to determine a pupil size and deflection angle of 0.7 inch and 1.53 degrees respectively. If two deflectors such as this are arranged in an f/10 cone of 0.9 micron light, as in Fig. 4, the deflection resolution in each axis may be calculated by dividing the spot size at the focus, d , into the peak-to-peak deflection, S , at that point.

$$N_x = \frac{S_x}{d} = \frac{r \sin \omega_{pp}}{1.27\lambda f\text{-no.}} = \frac{(6 \cdot 2.54)(0.0266)}{(1.27)(0.9 \times 10^{-4})(10)} = 344 \text{ spot dia.}$$

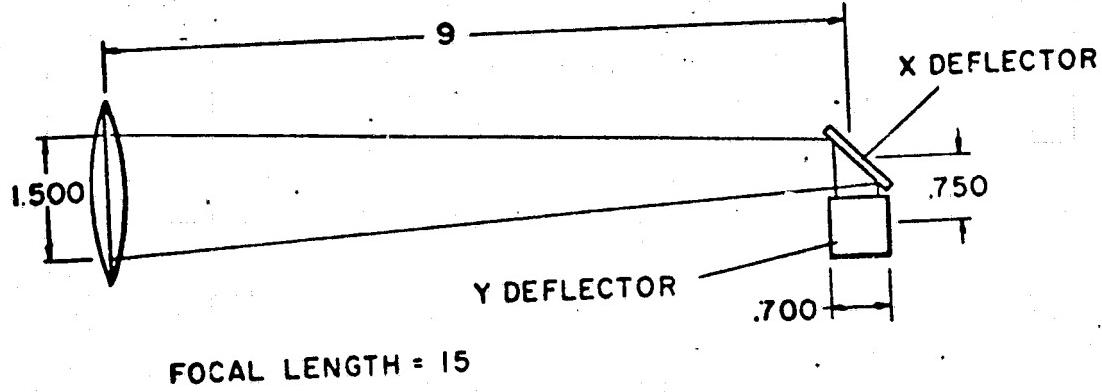
$$N_y = \frac{S_y}{d} = 300 \text{ spot dia.}$$

where r is the distance from the mirror to the focal plane.

Figure 5 shows a completed one-dimensional deflector mounted on a base which also houses the strain gage preamplifier. Below are listed typical characteristics for this deflector (Model PBM-5):

PBM-5 Deflector Characteristics

Maximum drive voltage	± 500 vclts peak
Beam deflection	± 0.8 deg
Mechanical resonance frequency	1300 Hz
Input pupil size at 45° incidence	0.7 x 0.7 inch



FOCAL LENGTH = 15

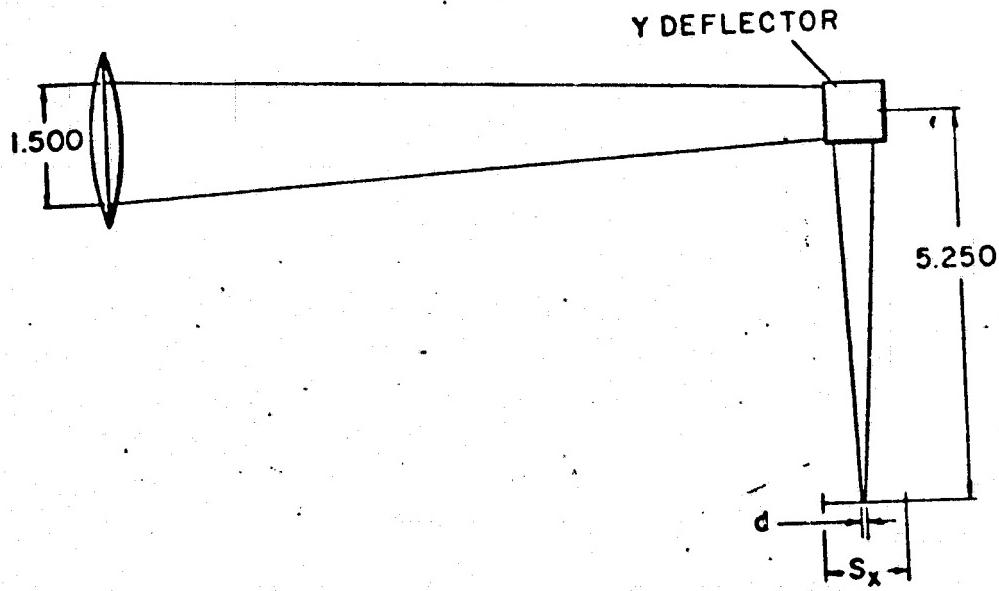


Fig. 4. Optical arrangement of two deflectors in an f/10 cone of light to give two-dimensional deflection.

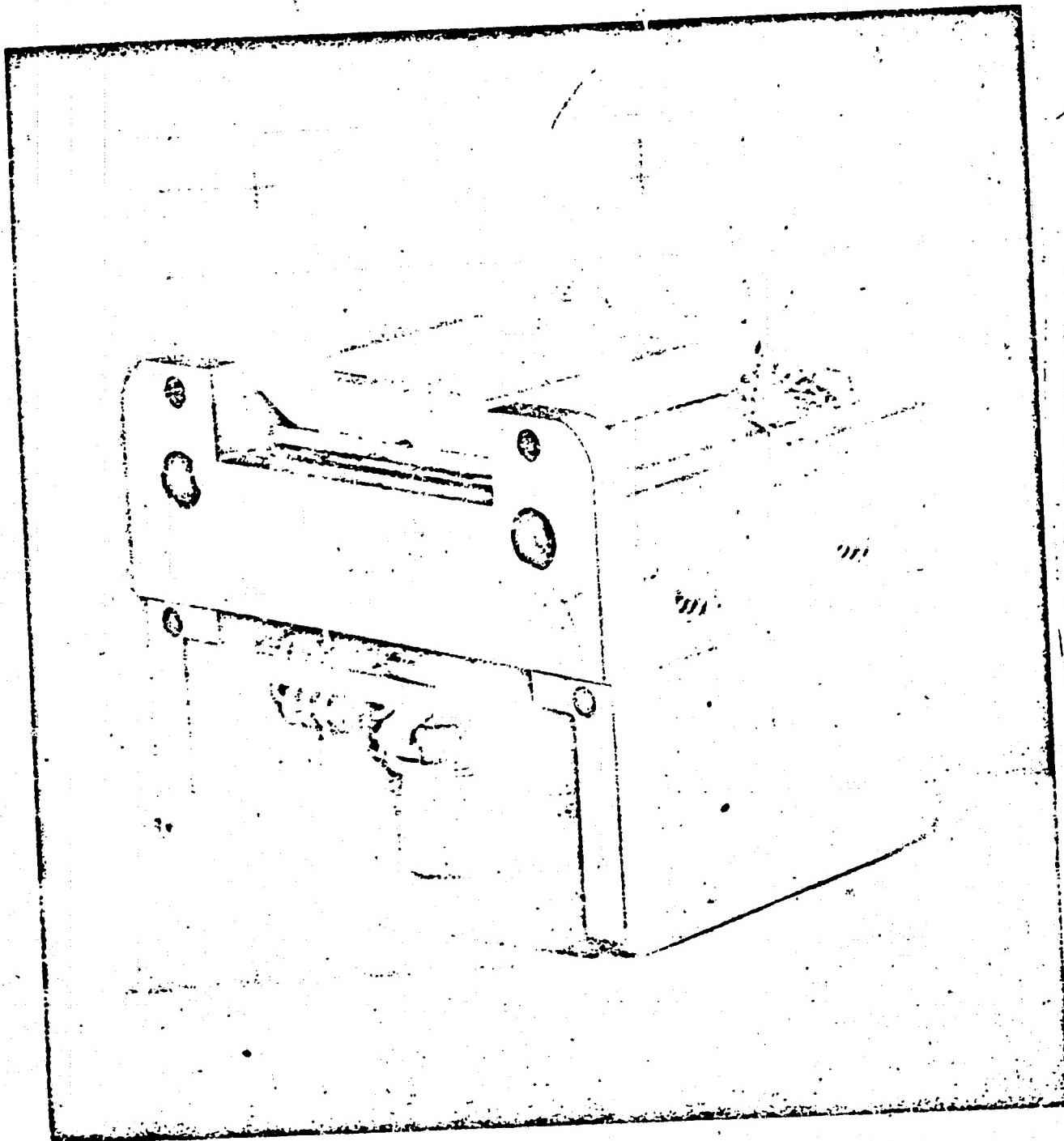


Fig. 5. Piezoelectrically driven mirror deflector PBM-5G with strain gage
deflection sensors and strain gage preamplifier (under base).

Capacitance	0.22 μF
Loss factor	<0.006
"Q" at resonance	10
Mirror distortion	< $\lambda/10$
Mirror reflectivity at 0.9 μ	99%
Overall size	1.5 x 1.25 x 1.187 inches
Weight with amplifier	4.6 oz.

Figure 6 shows beam deflection versus voltage for a typical PBM-5 deflector illustrating the inherent nonlinearity of the piezoelectric transducer material.

DEFLECTION SENSING WITH STRAIN GAGES

The investigation of various techniques for monitoring the angular position of the light beam from an optical beam deflector during previous phases of this contract has led to the consideration of strain gage sensors for use with PBM-type deflectors. The cantilevered piezoelectric bender which drives the mirror lends itself naturally to the use of strain gages for sensing the amount of bending which takes place with the application of deflection signals. These strain gages are resistive elements whose resistance is a function of strain. Since the angle made by the end of the cantilevered beam is proportional to the integral of the strain along either of its surfaces, a strain sensing element placed along this surface gives a direct reading of angular deflection. This technique offers the possibility of a simple, compact, reliable deflection sensing system with resolutions exceeding one part in 10^3 .

A typical installation uses two gages on each transducer, one for the upper surface and another on the lower surface of the bender, with the sensing signal derived from a bridge circuit, as shown in Fig. 7. As the transducer bends, the resistance of one gage increases while the other decreases, resulting in an output twice that of a single gage. An additional advantage in this type of circuit is that it may be manipulated somewhat to compensate for nonlinearity and temperature sensitivity in the gages.

Two basic types of strain gages exist, the wire or foil gage and the semiconductor gage. The greatest distinction between the two is that the semiconductor gage can have from 25 to 85 times the sensitivity of the metallic gage. When taken in relation to the strain sensitivity, nonlinearity and temperature coefficients for

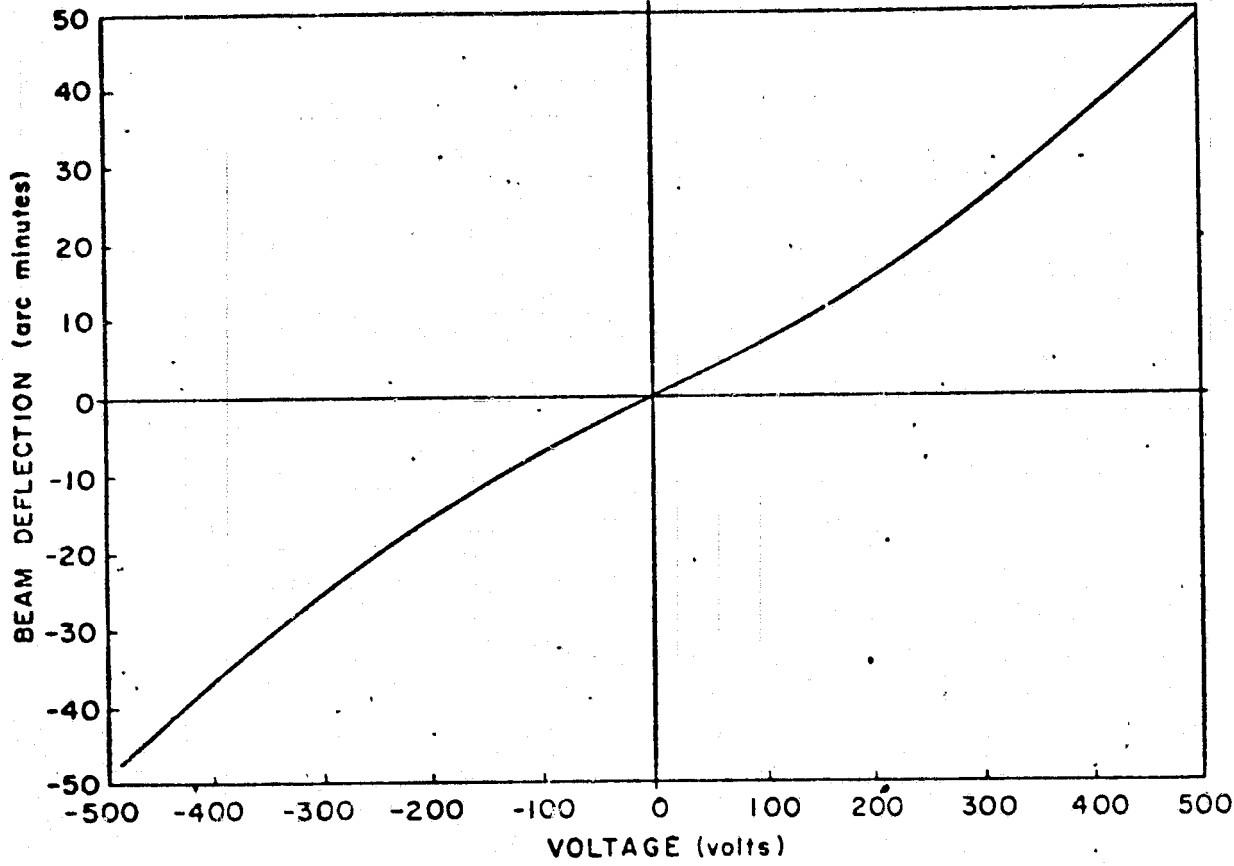


Fig. 6. Beam deflection as a function of drive voltage to show linearity. Hysteresis effects in the piezoelectric material have not been shown.

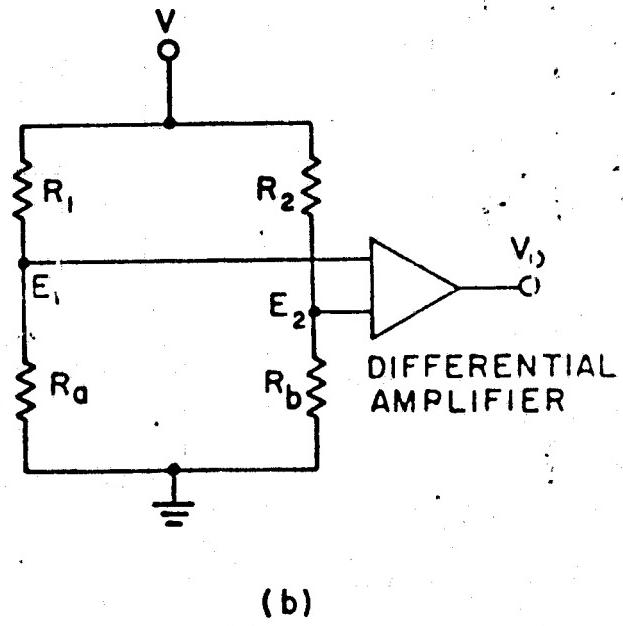
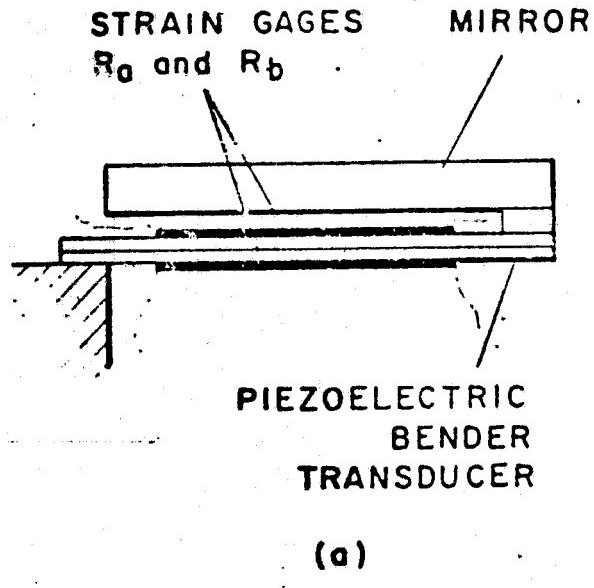


Fig. 7. Strain gages for sensing bender deflection (a) are located on two sides of the transducer and (b) use a bridge circuit to detect resistance changes.

both gages are comparable. This makes it advantageous to use the semiconductor gage for small strains where maximum resolution is desired, since its larger output yields a better signal-to-noise ratio. For this reason exclusive use of the semiconductor gage has been assumed in the following sections.

Certain problems exist, in attempting to use the strain gage as a precision strain transducer, which are associated with the basic characteristics of the gage itself and its relation to the substrate. The following may lead to inaccuracies in the strain measurement:

- Difference in the zero-strain resistance between gages
- Difference in the gage factor between gages
- Variation in gage resistance with temperature
- Variation in gage factor with temperature
- Prestressing gages during bonding operation
- Difference in thermal expansion coefficient between gage and substrate
- Nonlinearity in gage resistance as a function of strain
- Hysteresis and/or creep in the bonding material

The following sections outline some techniques for minimizing these problems to obtain the best possible accuracy and resolution from a strain gage installation of this type.

Analysis of Basic Strain Gage Circuit

It is useful to have a complete expression for the strain gage bridge output in which the interrelationship and function dependence of the various parameters is made explicit. The derivation of the output, $\Delta E = E_1 - E_2$, due to variations in the gage resistances R_a and R_b is a straightforward circuit calculation; it will, however, be complicated slightly here by taking into account the imperfect matching of the two gages in the mounted condition. After the gages are mounted, it is likely that there will be a residual strain or strain offset in each gage due to shrinkage in the bonding agent and to the difference in contraction between gage and the substrate upon cooling from the epoxy cure temperature. If the residual strain in each gage is not identical, the gage characteristics are no longer matched point for point. It

will be shown that the bridge output then contains extra nonlinear terms, which are a function of residual strain and non-matching gage factors, that must be kept small by careful mating and mounting of the gages.

The gage resistance R_a as a function of strain, ϵ , is approximated quite well by

$$R_a = R_{oa} (1 + F_a \epsilon_a + C_a \epsilon_a^2), \quad (7)$$

where F_a is normally given as the gage factor, C_a is the nonlinearity coefficient, and R_{oa} is the zero strain resistance.

The gages which are being used in this application have been chosen such that their temperature coefficient of gage factor is zero. This occurs in germanium gages at an impurity level of about 10^{20} . At this point, although the gage factor is down to 45, the nonlinearity of resistance with strain over a range of $\epsilon = \pm 10^{-3}$ has been decreased to 0.01 percent. Gages of this material with a resistance of 50 ohms have been acquired from Kulite Semiconductor Products, Inc.

Over the range of strain $\epsilon = \pm 10^{-4}$ which the gage will operate, this nonlinearity is at least an order of magnitude smaller and may be neglected in subsequent calculations. The resistance-strain relationship reduces to

$$R_a = R_{oa} (1 + F_a \epsilon_a). \quad (8)$$

The total strain seen by each gage is the sum of the bender induced strain, ϵ_0 , and the residual strains ϵ_1 and ϵ_2 , i.e.,

$$\begin{aligned} \epsilon_a &= \epsilon_1 + \epsilon_0 \\ \epsilon_b &= \epsilon_2 - \epsilon_0. \end{aligned} \quad (9)$$

From this the resistance of each gage may be written as

$$R_a = R_{oa} (1 + F_a \epsilon_1 + F_a \epsilon_0) = R_{oa} (r_1 + F_a \epsilon_0)$$

$$R_b = R_{ob} (1 + F_b \epsilon_2 - F_b \epsilon_0) = R_{ob} (r_2 - F_b \epsilon_0), \quad (10)$$

where r_1 and r_2 are factors which incorporate the effects of residual strain.

If the bridge circuit is to be balanced such that $E_1 = E_2$ for zero induced strain, R_1 and R_2 must be adjusted such that

$$\frac{R_1}{R_{oa} r_1} = k = \frac{R_2}{R_{ob} r_2}. \quad (11)$$

Referring to Fig. 7, the expression for the voltage across R_a may be written as

$$E_1 = \frac{V R_a}{R_1 + R_a} = V \frac{R_{oa} (r_1 + F_a \epsilon_0)}{R_1 + R_{oa} (r_1 + F_a \epsilon_0)} = \frac{1 + F_a \epsilon_0 / r_1}{k + 1 + F_a \epsilon_0 / r_1} \quad (12)$$

Since $F_a \epsilon_0 / r_1 \ll 1$, the expression for E_1 may be expanded in terms of ϵ_0 , neglecting terms beyond second order:

$$E_1 = \frac{V}{k+1} \left[1 + \epsilon_0 \frac{F_a k}{r_1 (k+1)} - \epsilon_0^2 \left(\frac{F_a}{r_1} \right)^2 \frac{k}{(k+1)^2} \right]. \quad (13)$$

Similarly for E_2

$$E_2 = \left[1 - \epsilon_0 \frac{F_a f k}{r_1 (k+1)} - \epsilon_0^2 \left(\frac{F_a f}{r_1} \right)^2 \frac{k}{(k+1)^2} \right], \quad (14)$$

where the difference in the two gage factors F_a and F_b due to manufacturing tolerances has been represented as

$$F_b = f F_a. \quad (15)$$

The bridge output, ΔE , may now be computed from

$$\Delta E = E_1 - E_2 = \epsilon_0 F_a \frac{Vk}{(k+1)^2} \left(\frac{f}{r_2} + \frac{1}{r_1} \right) \left[1 + \frac{\epsilon_0 F_a}{k+1} \left(\frac{f}{r_2} - \frac{1}{r_1} \right) \right]. \quad (16)$$

Nonlinearity in the output versus strain due to the last term in the brackets results when either r_1 , r_2 or f is not unity. In the present application the variations in gage factor and base resistance are set by manufacturing tolerances and the strain offset is a function of the gage bonding technique. Using the following values as typical, the percent nonlinearity may be calculated:

$$\begin{aligned} F_a &= 45 & r_1 &= 1.02 & \epsilon_0 &= \pm 10^{-4} \\ f &= 1.01 & r_2 &= 0.98 & k &= 1 \end{aligned}$$

$$\frac{\epsilon_0 F_a}{k+1} \left(\frac{f}{r_2} - \frac{1}{r_1} \right) = \pm 1.12 (10)^{-4} = \pm 0.0112\%.$$

This error is an order of magnitude less than the accuracy called for in this application. Therefore if reasonable tolerances on the gage factor and strain offset are maintained, these factors will contribute negligibly to strain gage readout error.

In Eq. (16) the temperature dependency of R_{oa} appears in the factor containing k . In terms of R_{oa} this factor becomes

$$\frac{k}{(k+1)^2} = \frac{R_{oa} R_1}{(R_{oa} + R_1)},$$

with a temperature dependency of the form

$$\frac{\partial}{\partial T} \left[\frac{k}{(k+1)^2} \right] = \frac{\partial R_{oa}}{\partial T} R_1 \left[\frac{R_1 - R_{oa}}{(R_1 + R_{oa})^3} \right]. \quad (17)$$

As can be seen when $R_1 = R_{oa}$ the temperature coefficient is zero.

Typically $R_1 - R_{oa} \leq 2$, $R_1 = 50$, $\partial R_{oa}/\partial T = 0.117 \text{ ohms/}^\circ\text{C}$ and

$$\frac{\partial}{\partial T} \left[\frac{k}{(k+1)^2} \right] = 11.7 (10)^{-6} / ^\circ\text{C}.$$

Although the gage temperature coefficient of resistance is quite large, the effect on bridge sensitivity is small. However, due to this large temperature coefficient, care must be taken to maintain the gages at the same temperature. A temperature difference of 0.002°C between the gages causes a bridge output equivalent to a strain difference of 10^{-7} . If the maximum strain is 10^{-4} , this is an error of one part in 10^3 . The minimizing of differential temperature between the gages is a problem which must be considered more thoroughly in subsequent work with strain gage sensors.

Practical Aspects of Deflector Strain Gage Instrumentation

One of the most important factors governing the ultimate performance of a strain gage transducer system is the quality of the gage installation on the stressed substrate. This is especially true for semiconductor gages. Since they are, ideally, monocrystalline filaments, the isolated gages behave in a perfectly elastic manner under stress, with no plastic region at temperatures below 500°C . Thus, any hystereses or creep in strain gage installation is generally a function of the gage bonding material or the stressed structure and is exhibited as a phase shift between the gage output and the mirror motion.

To minimize these effects, it is necessary to have the strain gage in as intimate contact as possible with the bender surface, while still maintaining good electrical insulation from the surface electrode. Use of gage types without (the sometimes incorporated) inert backing material is advisable for this reason as well as for the purpose of introducing the least amount of restraint on the piezoelectric bender. Isolation between the gage and the bender electrode may be obtained by initially coating the bender with a thin layer of the bonding agent or with an evaporated dielectric material. The gage is then attached over this layer and may be held as close as a few microns from the substrate.

The choice of bonding cements for the gage, as well as for the bender assembly, must be carefully considered in the light of the foregoing requirements. The cement should have low viscosity at room temperature to promote the formation of thin films and allow maximum squeeze-out under pressure. If filled, the particle size should be less than a few microns. A thermo-setting cement of the epoxy family is preferred, where nearly complete polymerization can be obtained. It is then that the most stable reaction products are formed and maintained over the working temperature range of the bond. A cement has been found which appears to meet these requirements, and with it acceptable gage installations have been made.

Experiments have shown that the strain along the entire length of the bender element must be sensed with gages to obtain a true measure of deflection. In some experimental models driven at below-resonance frequencies commensurate with the first mechanical resonance of the bender, deflections of the mirror were taking place which were not being registered by strain gages covering only 30 percent of the bender length. Evidently a small component of deflection at the resonance frequency was being excited by harmonics of the drive signal. At natural resonance the curvature of the deflected bender is slightly different from that of an electrically driven bender below resonance. This change in curvature is only partially registered by the less-than-full-length strain gage, and this results in anomalous behavior of the sensor output compared with actual deflection. When the gage runs the full length of the bender, the inactive ends of the gage (where the leads are attached) fall on inactive (unelectroded) portions of the bender. With this arrangement, full strain is transferred to the gage, end effects are minimized, and the bender experiences a uniform load along its length. The gages used on the PBM-5G deflector are 25 percent longer than the electroded portion of the transducer.

Any angular motion of the mirror not directly associated with bending of the piezoelectric transducer will cause a deflection of the light beam which is not registered by the strain gages. This can occur if the mirror is not rigidly attached to the bender or if the bender anchoring structure either is too compliant or has structural resonances below the deflector resonance frequency. It was found necessary to cement the end of the transducer in a slot in the mirror to obtain rigid coupling between the mirror and transducer to eliminate this source of deflection readout error in the PBM-5G design.

Gage installation on the PBM-5G deflector has evolved to the following procedure: The piezoelectric transducer is prepared by lapping the surfaces with a 0.9 micron abrasive before evaporating on nickel electrodes. Two stripes of sapphire 2 microns thick are evaporated, one on each side, down the center of the transducer perpendicular to the deflection axis. These isolate the gage from the nickel electrode. A gage is then cemented to each side of the transducer, on the sapphire stripe, with BR610* cement under a pressure of 15 lb/in^2 , following the cure recommendations of the manufacturer.

*W. T. Bean, Inc., Detroit, Mich.

Strain Gage Performance Characteristics

The foregoing procedure has led to successful gage installations in which creep and hysteresis phase shift error were less than one part in 10^3 to beyond 300 Hz. This is illustrated in Fig. 8, where phase shift error is shown in conjunction with the deflector resonance curve. A small anomalous resonance appears at 411 Hz. However, many gage assemblies were found to have leakage paths between the gage and nickel ground electrode beneath. Although the leakage path does not affect the hysteresis, it causes a shift in the gage resistance which affects the balance of the strain gage bridge. Introduction of 700 kilohms leakage resistance between the gage and ground shifts the bridge balance by about one resolution element. This is important because the leakage varies with time, temperature and operating conditions, leading to a continual shift of the bridge balance. Several new techniques are now being pursued for mounting the gages which should maintain the low hysteresis already achieved and eliminate leakage.

Because of problems encountered initially in obtaining hysteresis-free deflection sensing and then in maintaining a balanced bridge with gage leakage, no detailed measurements were made on strain gage linearity or temperature sensitivity. There is good reason to expect quite linear operation due to the inherent linearity of the gages themselves and the small range of strains encountered. Maximum strain generated in the gage by the transducer was measured at $\pm 100 (10^{-6}$ inch/inch.

Strain Gage Preamplifier

The strain gage preamplifier is a general-purpose operational amplifier designed for low quiescent power and low noise. A functional schematic diagram is shown in Fig. 9. The differential input to the amplifier is developed across the bridge circuit made up of $R_1 R_2$ and the two strain gages. Resistors R_3 , R_4 and R_5 provide an adjustment to obtain a balanced bridge since the gage zero strain resistance can vary by as much as ± 2 percent. The bridge circuit is designed to operate with 20 mA current in each gage. Resistors R_1 and R_2 are larger than the gage balancing resistors and thus would be most sensitive to temperature effects. These resistors are ultra stable cermat types matched to 0.5 ppm/ $^{\circ}\text{C}$ over a wide temperature range. Gage currents in the range of 20 mA are used to minimize heating of the strain gages. For the 50-ohm gages used, this current is developed for 2.2 volts on the bridge circuit, resulting in a dissipation of about 1.6 watts per square inch of gage surface.

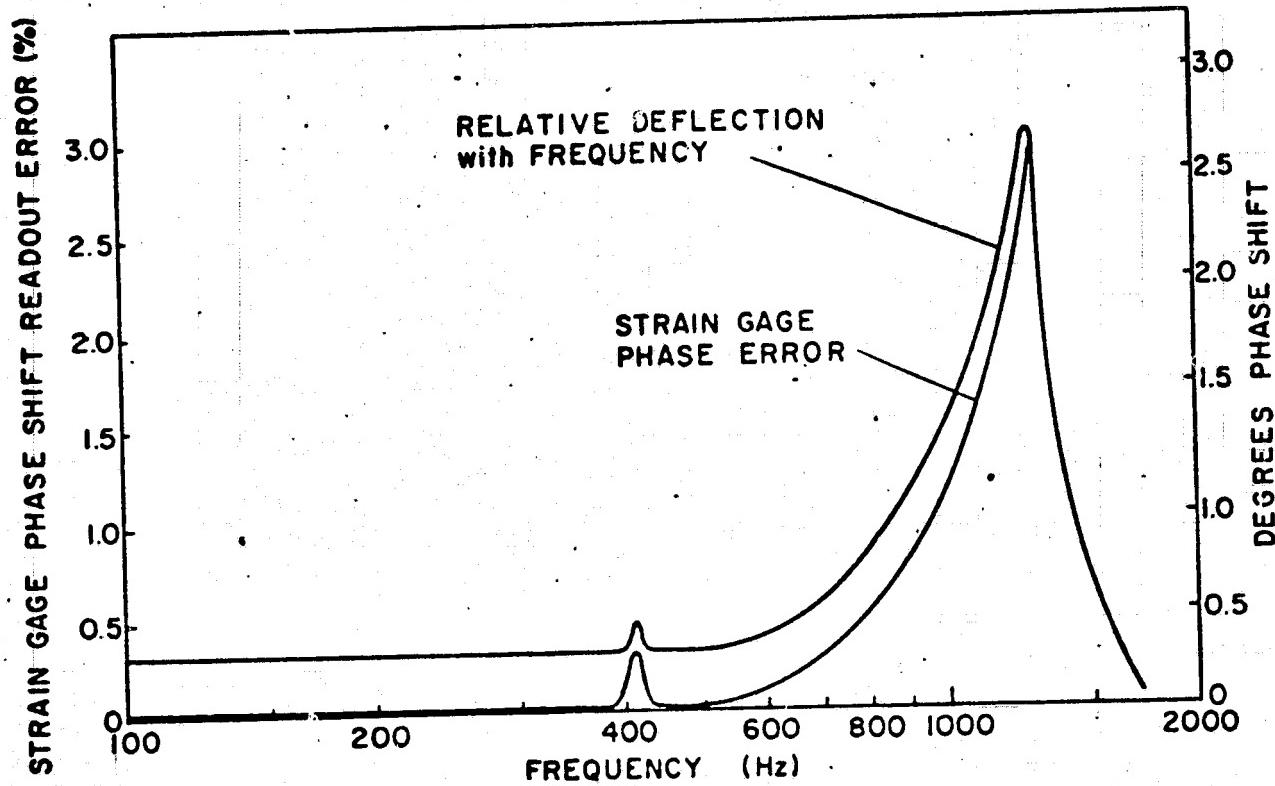


Fig. 8. Phase shift between strain gage output and mirror deflection is plotted against drive frequency . Relative deflection is also shown.

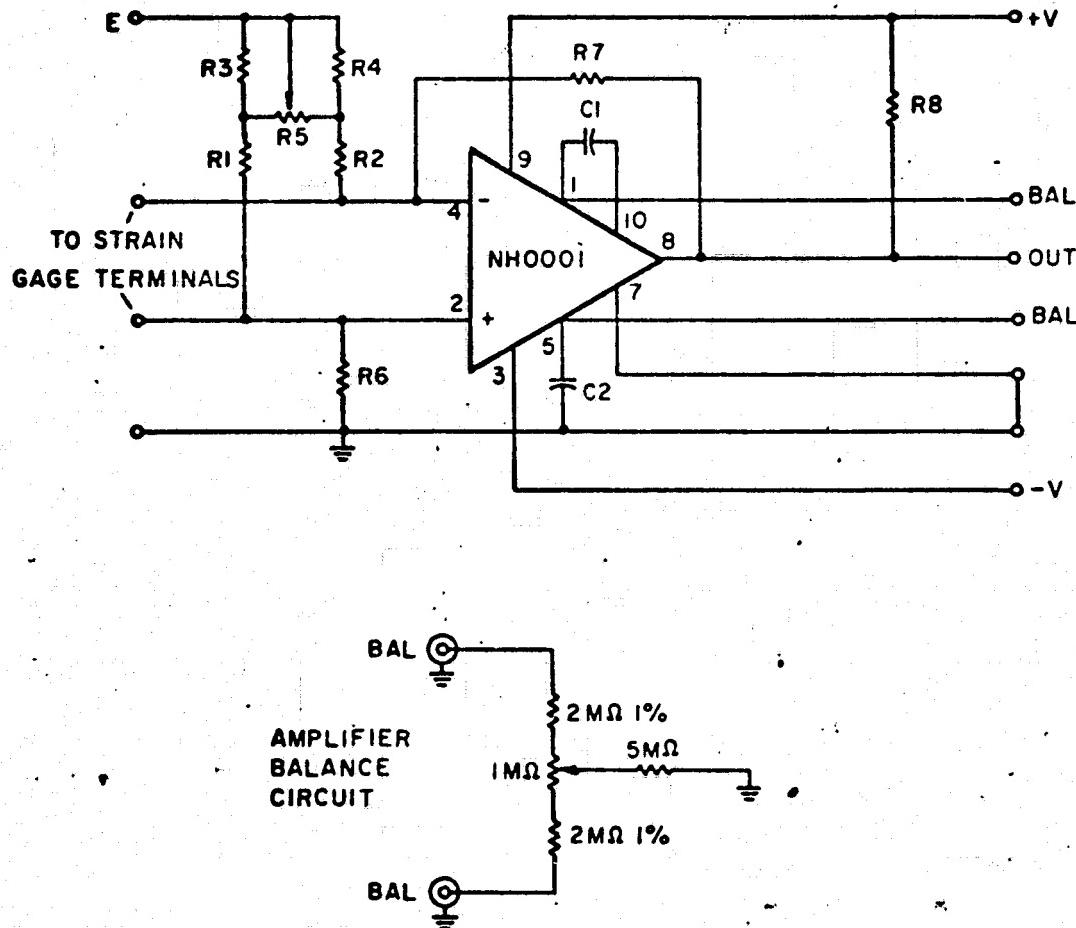


Fig. 9. Schematic diagram of strain gage preamplifier circuit.

The amplifier has a nominal gain of 137.5 and a nominal bandwidth of 38 kHz. Under no-load conditions, it can deliver 3.6 volts, p-p or 2.8 volts, p-p, with a 10-kilohm load provided the amplifier is biased with a 1-volt common mode voltage. For a peak strain in the order of 10^{-4} inch/inch, the output of the amplifier will not exceed 1 volt so that a load of somewhat less than 10 kilohms could probably be used. Since the output swing is small, the power supply voltage can be kept low (± 5 volts) to improve stability and maintain low dissipation. Although each amplifier and strain gage readout must be calibrated as a unit, the nominal output per resolvable spot for the system at 0.9 micron is 11.5 mv.

CONCLUSIONS

Enough is now known theoretically and practically about the PBM-type deflector to allow a deflector to be designed on paper with a fair degree of confidence that the predicted characteristics can be achieved. This is especially true for resonance frequencies no greater than a few thousand hertz, above which the approximations made in the mathematical model become increasingly crude.

The concept of using strain gages to accurately measure the induced strain in a bender transducer and thus monitor mirror deflection has been shown feasible. Sensing of deflection to an accuracy of one part in 10^3 , up to 300 Hz without hysteresis has been accomplished with a PBM-5G deflector. With its integral preamplifier, the strain gage sensor provides a simple and rugged means for deriving a signal proportional to beam deflection. Certain problems related to the gage bonding technique have made it difficult to produce consistently good gage installations, free of leakage to the underlying electrode. It is expected that these will be remedied in the near future.

With the proper choice of peak deflector drive voltage it has been possible to design a completely transistorized direct coupled deflector drive amplifier. A unique circuit approach to the problem of driving a capacitive load has reduced the quiescent power consumption of the amplifier without sacrificing frequency response or maximum power output. These features will be most important in space-borne applications of this unit.

Combined with strain gage deflection sensing the PBM-type deflector system appears to be the most compact, versatile and efficient way of deflecting a laser beam at frequencies within the audio-frequency range.

APPENDIX E
VIDISSECTOR - IMAGE DISSECTOR
TEST DATA

GRIFFITH

Page 1

**VIDISSECTOR - IMAGE DISSECTOR
TEST DATA.**

TUBE TYPE F4012 CATHODE TYPE RP WINDOW X SERIAL NO. 097001

APERTURE SIZE .004" x .004" PROJECT NUMBER 14-41000 DATE 9/23/70

PHOTOCATHODE SENSITIVITY.

RADIANT 1.

LUMINOUS 2.

	Sensitivity μA/lumen
Luminous	297 μA
5113 (5-58)	6.4
2540 (5-59)	
2418 (2-62)	152
2036 (2-64)	

UNIFORMITY

PHOTOCATHODE

The uniformity is $\pm 3.3\%$ over .56 inch diameter.

NOTE:

1. Radiant Sensitivity plotted on page 3
 2. Explanation of Luminous Sensitivity given on reverse side of page 3

ANODE OUTPUT

The uniformity is $\pm 15\%$
over .56 inch diameter

ELECTRON TUBE DIVISION

3700 East Pender Street, Fort Wayne, Indiana 46803

TUBE OPERATING VOLTAGES AT 1×10^5 GAIN

(With respect to Drift Tube)

Photocathode	<u>400VDC</u>	Separate Aperture	<u>N/A</u>
Dynode 1	<u>-15</u>	Separate Mesh	<u>N/A</u>
Dynode 2	<u>42</u>	Anode	<u>1378</u>
Dynode 3	<u>223</u>	Anode, in respect to Dynode <u>9</u>	<u>43</u>

See Voltage Divider Schematic, page 4

RESOLUTION

(Taken near cathode center)

TVL/ Inch	Modulation Amplitude Percent
100	<u>100</u>
200	<u>94</u>
300	<u>54</u>
400	<u>17</u>
500	<u>-</u>
600	
700	
800	

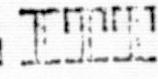
TVL/ Inch	Modulation Amplitude Percent
900	
1000	
1200	
1400	
1600	
1800	
2000	

MULTIPLIER GAIN AND LEAKAGE

Multiplier (Drift tube to Anode) Potential Volts	Gain	Leakage (ampères)
754	2×10^4	-
873	5×10^4	$.015 \times 10^{-9}$
978	1×10^5	$.028 \times 10^{-9}$
1090	2×10^5	$.05 \times 10^{-9}$
1265	5×10^5	$.15 \times 10^{-9}$
1419	1×10^6	$.30 \times 10^{-9}$

NOTES:-

1. D1 and D2 potentials, with respect to the Drift tube, affect the output uniformity. The values listed are for best uniformity.
2. Dynode 9 is adjusted for maximum gain or for gain calibration.

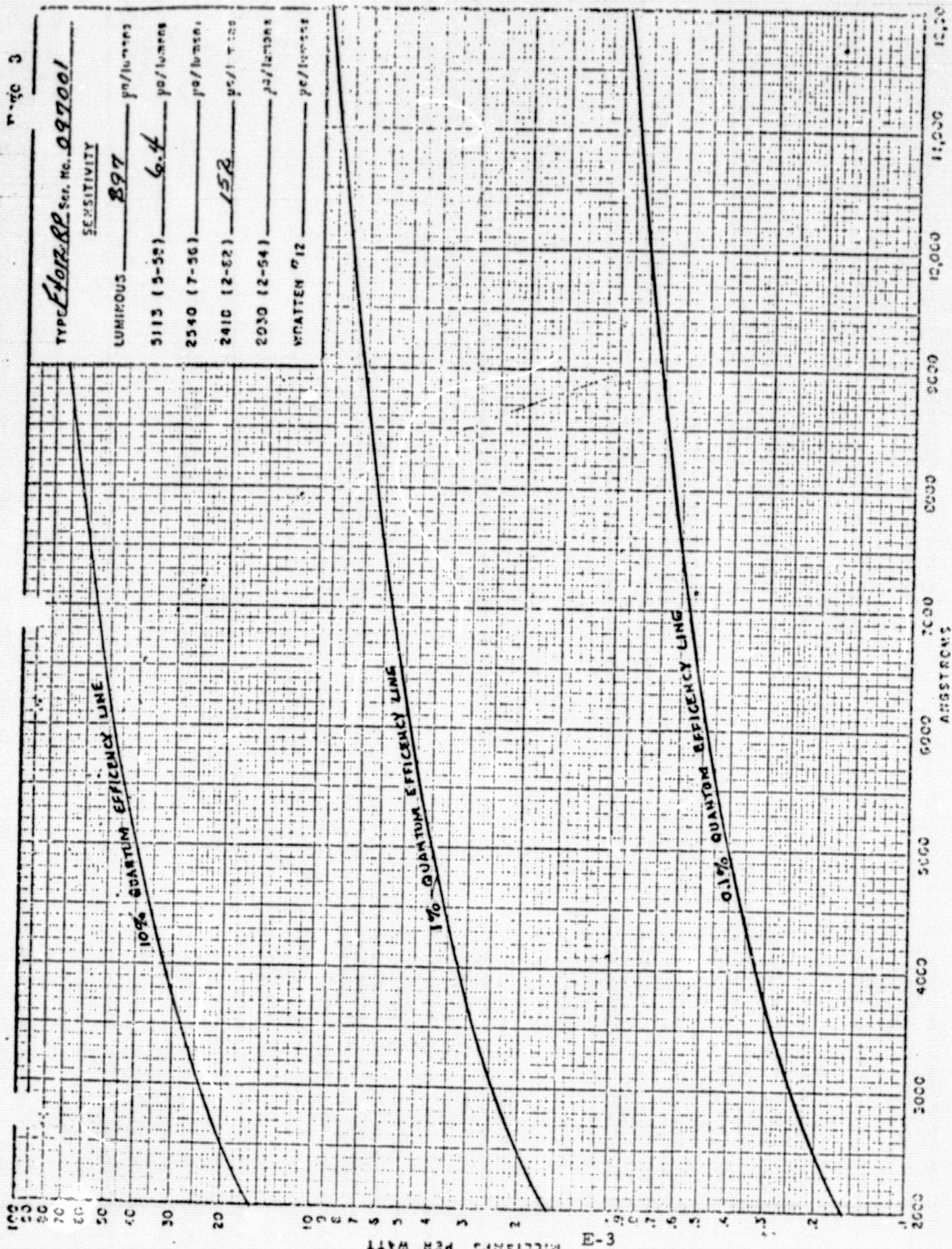
REPRODUCIBILITY OF THE
ORIGINAL PAGE IS POORELECTRON TUBE DIVISION 

3

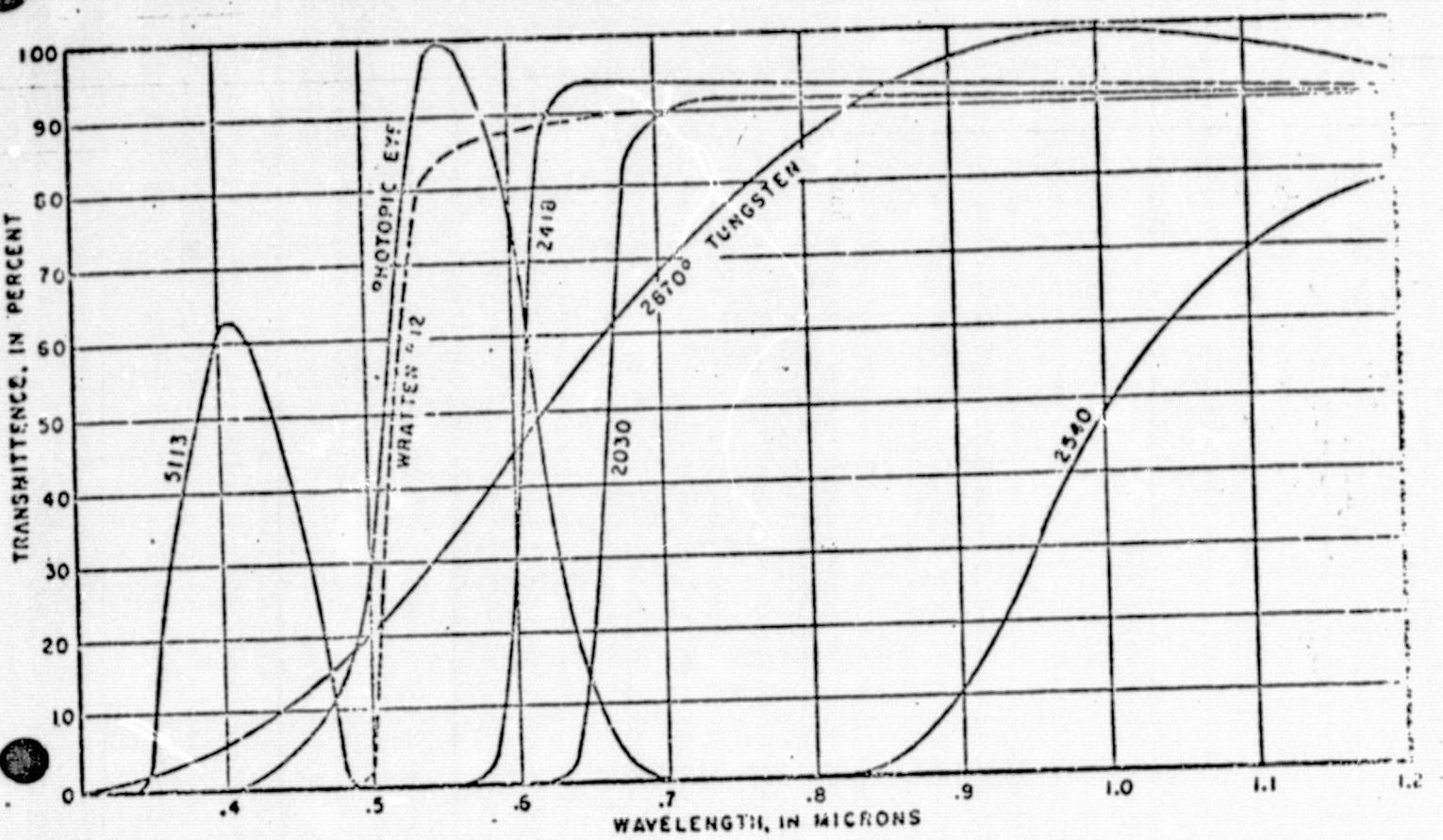
Typewriter No. 88 Serial No. 897001

ESTIMATES

LUMINOUS	<u>897</u>	17/10/1963
5113 (3-59)	<u>6.44</u>	10/10/1963
2540 (7-56)		10/10/1963
2410 (2-52)	<u>152</u>	15/10/1963
2030 (2-54)		22/10/1963
WATTEN "12		26/10/1963

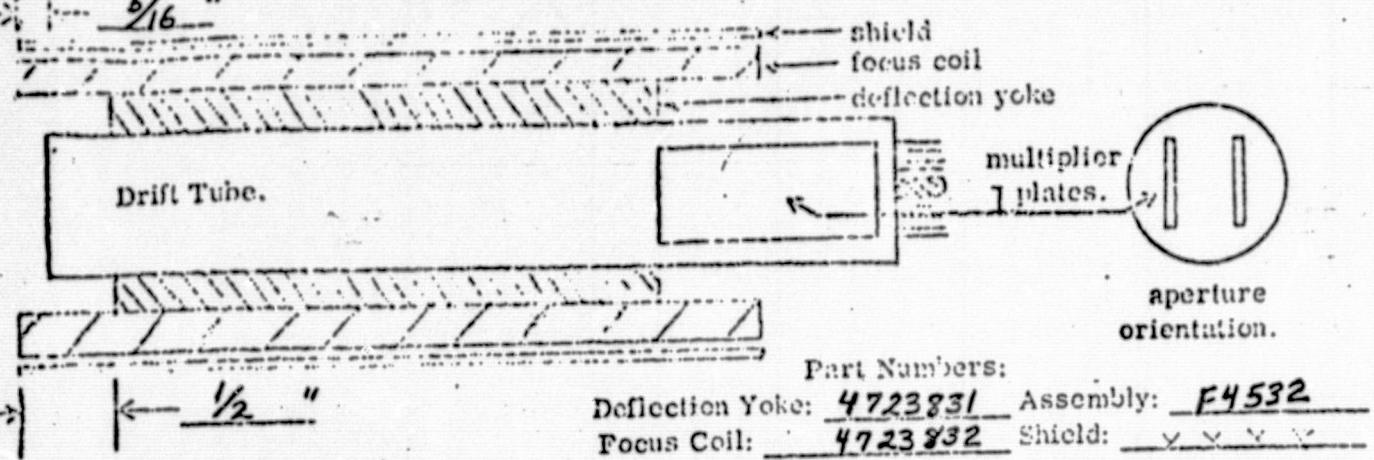


REPRODUCIBILITY OF THE ORIGINAL PAGE IS POOR

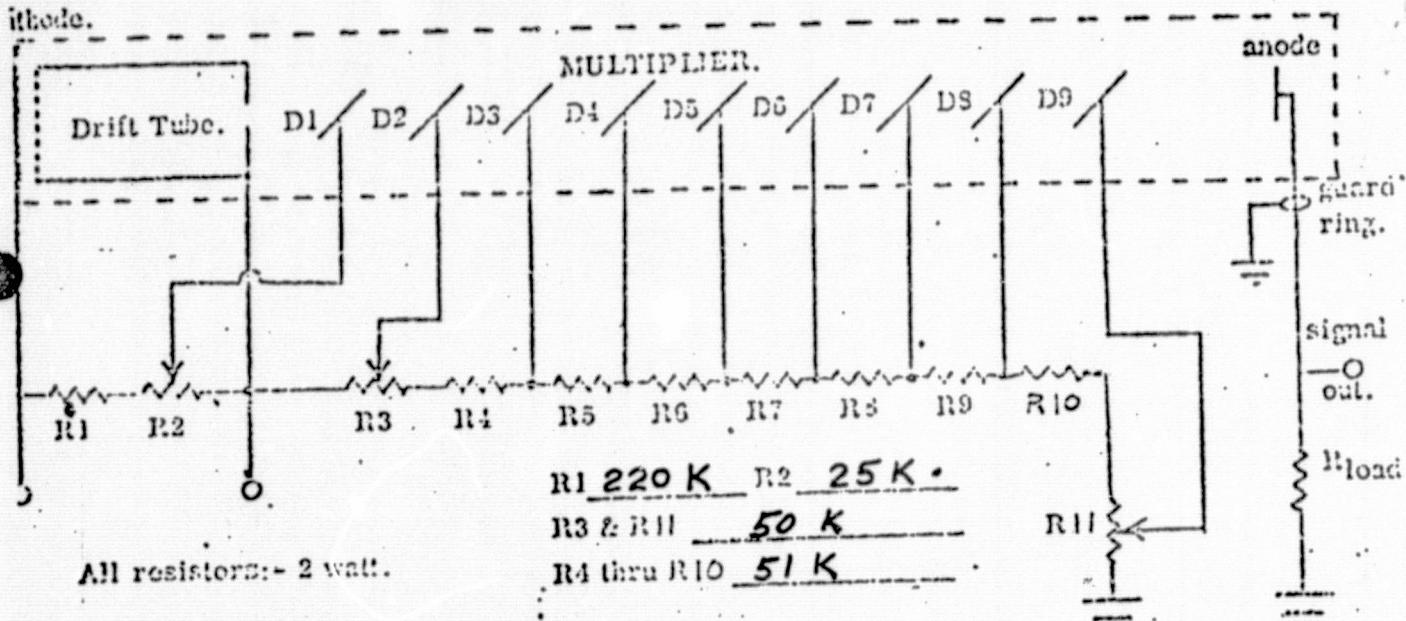


The standard luminous sensitivity is the response of the photocathode (in microamperes per lumen) to a tungsten lamp operating at 2870°K. The various numbered sensitivities are the response of the photocathode when Corning filters (filter numbers are four digits; dashed, three digit numbers in parentheses are a color specification number) of half stock thickness are interposed between the 2870°K lamp and the photocathode. Plotted above are the transmittance, in percent, of the filters, and the spectral distribution, in relative units, of 2870°K tungsten. Also shown are the photopic eye response and the transmission of a Wratten #12 filter.

TEST DIVIDER SCHEMATIC

Photo-
diode.

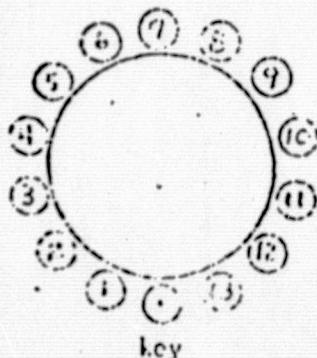
TEST DIVIDER SCHEMATIC



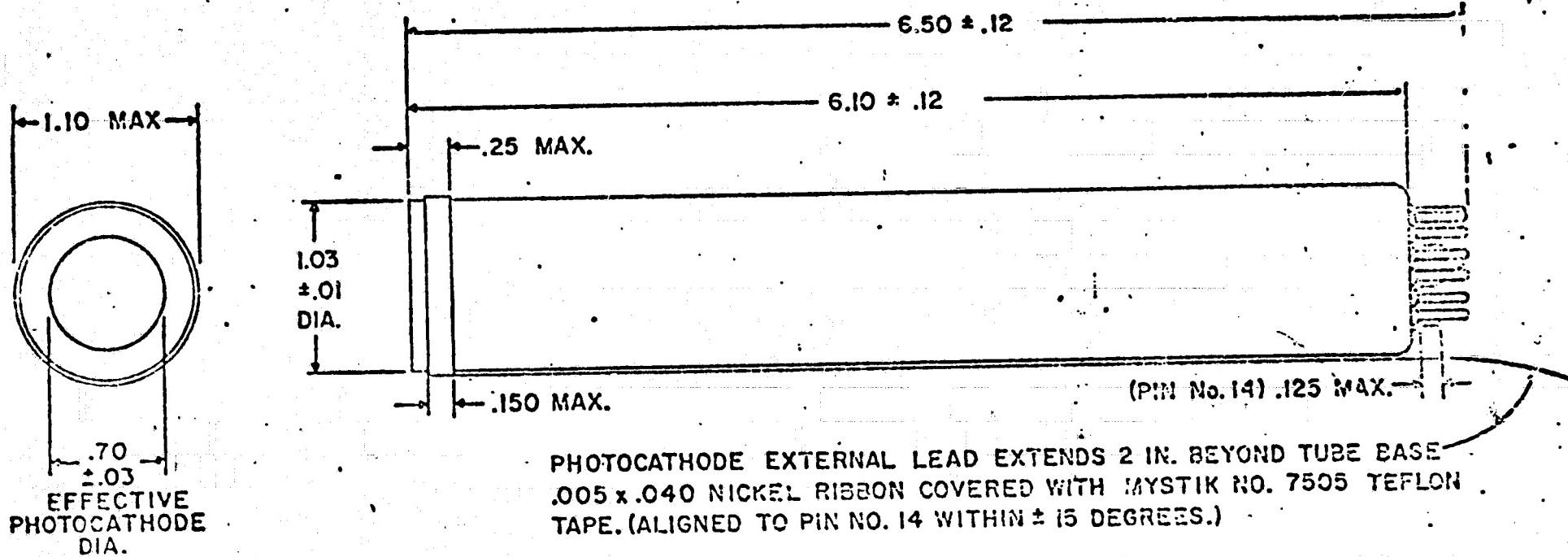
STANDING FLYING CATHODE

Pin	Element	Pin	Element
1	Dynode 1	8	Guard Ring
2	Dynode 3	9	Anode
3	Dynode 5	10	Dynode 4
4	Dynode 7	11	Dynode 8
5	Dynode 9	12	Dynode 6
6	Dynode 2	13	Drift tube
7	Dynode 11	14	Flying Lead Electro-Cathode

FLYING LEAD ELECTRO-CATHODE



F4012(S20RP)



APPENDIX F

APPENDIX F

ANALYSIS OF WINDOW SAG EFFECTS

This section presents a brief analysis for the optical tolerance requirements on components external to the AOCP.

The effects of external windows and mirrors on the resolution of the aircraft carried AOCP system will be discussed here. The present plan is to include two windows and a mirror in the optical train between the AOCP and the atmosphere, as illustrated in Figure F-1. The first window is 5 inches in diameter. This component is used as a pressure seal for the experiment enclosure containing the AOCP. The mirror (about 10" x 4.5") is mounted in a gimbal, and is used to direct the field-of-view of the AOCP. The second window (27" diameter) serves as an aperture and wind seal in the aircraft skin. An optical tolerance budget must be shared by all three of these components.

Tolerance Budget. - ITT intends that the AOCP system have better than 2 arc second resolution, and consequently, the upper limit on the optical tolerance budget is quite small. It is unreasonable to expect that this budget be shared equally by all three components. The fine-inch window can and should be constructed to more exacting tolerances so as to relieve the performance requirements on the mirror and larger wind seal window.

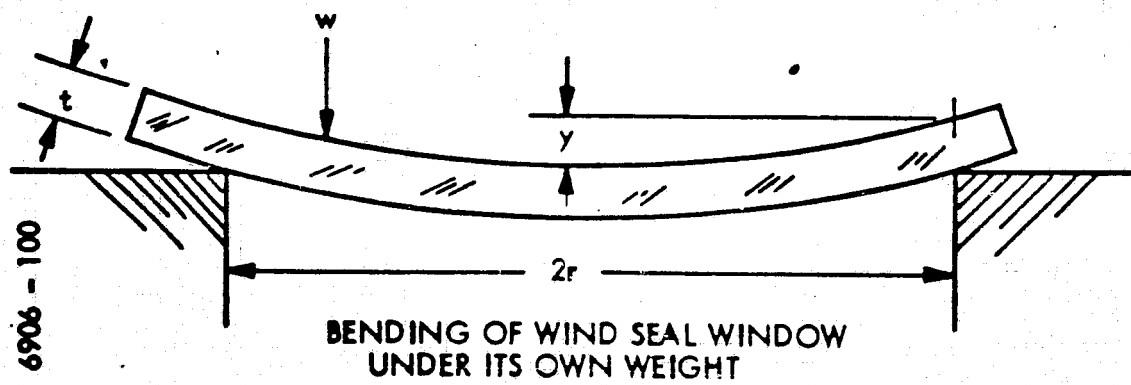
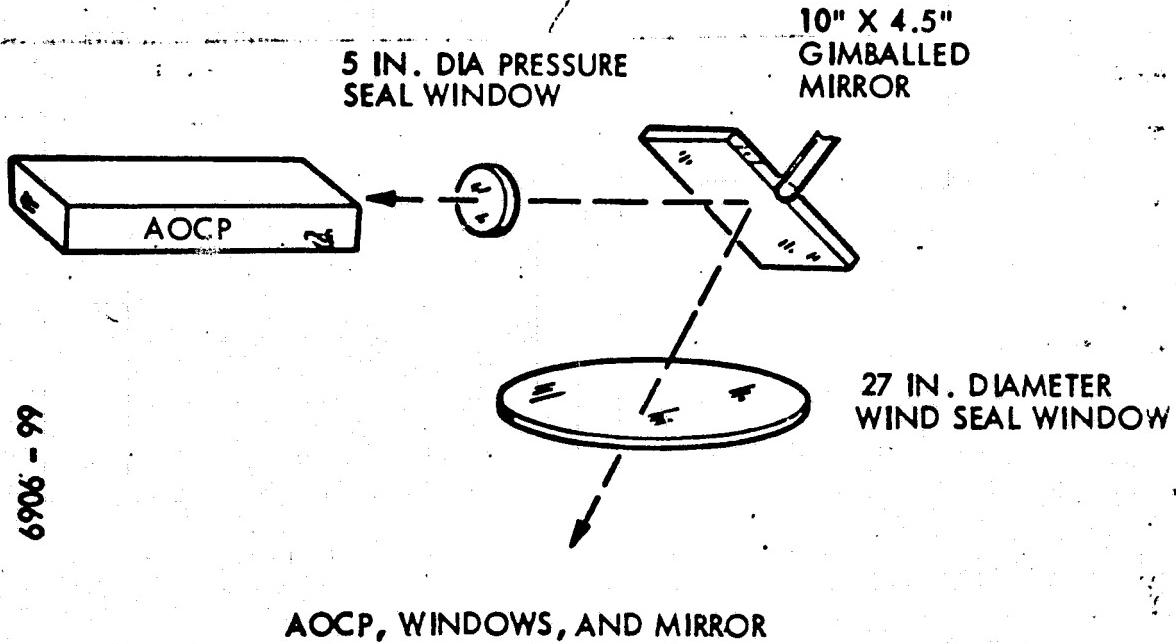


Figure F-1. AOCP, Windows, and Mirror

REPRODUCIBILITY OF THE
ORIGINAL PAGE IS POOR

We establish here a total tolerance budget, e_t , based on the deviation from a plane that a lightwave (4 inch diameter, 0.5 micron) will suffer in passing through the three elements. This tolerance (peak-to-peak) is set at

$$e_t < \frac{\lambda}{2} = 0.25 \text{ microns.}$$

Since tolerance errors are of a statistical nature, we will accept here a vector sum for establishing the error budget. Consequently,

$$e_t^2 = e_1^2 + e_2^2 + e_3^2 \quad (1)$$

Each of the terms above represents peak-to-peak wavefront distortion i.e. deviations from a plane wave.

- e_1 is the distortion caused by the 5 inch window,
- e_2 is the distortion caused by the gimballed mirror,
- e_3 is the distortion caused by the wind seal window in the aircraft skin.

Distortion in a wavefront is of course caused by both inhomogeneities in refractive index and nonplanar surfaces.

If we consider the 5 inch pressure seal window to induce a wavefront distortion no greater than $\lambda/5$ (no mean assumption considering its stress and environment), the remaining error budget must be shared by the gimballed mirror and large window. Sharing these tolerances equally, $e_2 = e_3 = e$, we see that

$$2e^2 = e_t^2 - e_1^2 = \lambda^2 (1/4 - 1/25), \quad (2)$$

resulting in $e \approx 0.325 \lambda$.

Mirror Flatness

This tolerance value of 0.325λ is, for the gimballed mirror, a fairly tight limit as we might expect for a high resolution system. For an example we can calculate the specified mirror flatness. Since a mirror induces a wavefront distortion of twice its surface figure, the portion of the mirror reflecting the 4 inch wide beam must be flat to $e/2$, or 0.1625λ . In addition, if the mirror is used at an incident angle of θ , this tolerance must be decreased by $\cos \theta$. Hence, for an average incident angle of 45° , the mirror should be flat to 0.1625λ over a $4\sqrt{2}$ inch diameter area. This surface tolerance does not include any allowance for mirror bending caused by its rotation and the effects of its own weight.

Wind Seal Window Sag

The large window in the aircraft skin has not only two possible surface irregularity tolerances but a homogeneity and a sag tolerance. These must add up to less than 0.325λ . We can consider first how much of this tolerance is used up by the sag of the window under its own weight. The sagitta of the circular window is given by the equation (see Fig. 2)

$$y = k w r^4 (Et)^{-1}, \quad (3)$$

which describes an unconstrained plate with uniform loading. In the last equation

- y is the center sag inches,
- k is an empirical constant,
- w = factor describing weight of window (psi),
- E = modulus (psi),
- t = window thickness (inches).

For the fused silica window being considered in our application,

$$r = 27/2 = 13.5 \text{ inches},$$

$$t = 1.75 \text{ inches},$$

$$E = 1.05 \times 10^7 \text{ psi},$$

$$k = 0.696,$$

$$w = .08 \times 1.75 = .14 \text{ psi},$$

REPRODUCIBILITY OF THE
ORIGINAL PAGES IS POOR

Hence:

$$y = (.696) (.14) (13.5)^4 (1.07 \times 10^7 \times 1.75)^3$$

$$y = 0.575 \times 10^{-4} \text{ inches.}$$

The radius of curvature R caused by this sag y is given by the sagitta formula

$$R = (y^2 + r^2) / (2y) \approx r^2 / 2y \quad (4)$$

We assume here (with less than 50% error) that both sides of the window have the same curvature. The focal length f of a thick lens with equal radii R is given by

$$f = nR^2 (n-1)^{-2} t^{-1} \quad (5)$$

This focal length f is also the radius of curvature of the wavefront after passing through the window. For a beam of diameter D, the peak-to-peak wave deviation from a plane is given by

$$e_{p-p} = \frac{\text{sagitta}}{2} = D^2 / 8f, \quad (6)$$

$$\begin{aligned} &= \frac{D^2 (n-1)^2 t}{8 nR^2}, \\ &= \frac{D^2 (n-1)^2 t y}{2 n r^4} = \frac{D^2 (n-1)^2 k w}{2 n E t^2} \end{aligned} \quad (7)$$

The last equation relates peak-to-peak wavefront distortion to window sag y, window thickness t, refractive index n, beam diameter D, and window semidiameter r. For our particular case, D = 4 inches and n = 1.46.

Hence:

$$e_{p-p} = \frac{16 (1.46)^2 (1.75) y}{2 (1.46) (13.5)^4} = 0.612 \times 10^{-4} y$$

For y = 0.575 × 10⁻⁴ inches, e_{p-p} = 0.35 × 10⁻⁸ inches ≈ λ / 6000, a negligible amount. Hence we may place all the optical tolerance on the window surface quality.

The 0.325λ tolerance must be shared by both window surfaces.

The tolerance may be specified in two different ways according as to how the window will be tested. If each surface is to be tested independently we may specify the maximum allowable deviations of each surface from a flat plane. This method however indicates a more stringent requirement than necessary (by about 40%). In this case we hope for random errors of the two surfaces so that we have the condition

$$(0.325 \lambda)^2 > 2 e_s^2 ; e_s < .23 \lambda$$

The allowable surface deformation is $e_s / (n-1)$, which for a refractive index n of 1.45 amounts to $\lambda/2$ over the beamwidth. As was mentioned before, if the window flatness test is made with Haidinger's fringes instead of Fizeau fringes, a more lenient tolerance can be observed.

This section investigated the first order effects of wind seal window sag on the AOCP system's resolution. Wavefront distortion caused by the window sag under its own weight was found to be negligible. A few surface optical tolerances were also calculated. However, these tolerances should be considered only suggestions, since the error budget must be shared by a number of components.

REPRODUCIBILITY OF THE
ORIGINAL PAGE IS POOR